Wanyi Nie
Krzysztof (Kris) Iniewski *Editors*

Metal-Halide Perovskite Semiconductors

From Physical Properties to Opto-electronic Devices and X-ray Sensors

Springer

Metal-Halide Perovskite Semiconductors

Wanyi Nie • Krzysztof (Kris) Iniewski
Editors

Metal-Halide Perovskite Semiconductors

From Physical Properties to Opto-electronic Devices and X-ray Sensors

Springer

Editors
Wanyi Nie
Los Alamos National Laboratory
Los Alamos, NM, USA

Krzysztof (Kris) Iniewski
Redlen Technologies
Saanichton, BC, Canada

ISBN 978-3-031-26891-5 ISBN 978-3-031-26892-2 (eBook)
https://doi.org/10.1007/978-3-031-26892-2

This Springer imprint is published by the registered company Springer Nature Switzerland AG
The registered company address is: Gewerbestrasse 11, 6330 Cham, Switzerland

Contents

About the Editors

Wanyi Nie graduated from Wake Forest University with a Ph.D. degree in physics in late 2012. Her Ph.D. thesis was on the optimization of organic photovoltaics. She later joined Los Alamos National Laboratory (LANL) in Material Physics and Application Division (MPA) as a postdoc associate and director's funded postdoc fellow from 2013 to 2016 working on interfacial charge transfer states of organic electronics. Since 2016, she has been working as a staff scientist at LANL leading a team to develop novel semiconductors and opto-electronic devices. The main research projects at her group include perovskite photovoltaics, light emitting diodes, X-ray/Gamma-ray detectors and imagers. She is also a scientist at Center of Integrated Nanotechnology at LANL, a DOE user facility. Wanyi is an active reviewer for peer-reviewed journals, such as *Nature*, *Nature Energy*, *Nature Electronics*, *Nature Communications*, *Science Advances*, *JACS*, *Advanced Materials* etc.; she also serves as a reviewer for several funding agents (LANL Laboratory Directed Research Direction Office, DOE office of science and other international grant offices).

Krzysztof (Kris) Iniewski is a director of Detector Architecture and Applications at Redlen Technologies Inc., a detector company based in British Columbia, Canada. During his 16 years at Redlen, he has managed development of highly integrated CZT detector products in medical imaging and security applications. Prior to Redlen, Kris hold various management and academic positions at PMC-Sierra, University of Alberta, SFU, UBC and University of Toronto. Dr. Iniewski has published over 150+ research papers in international journals and conferences. He holds 25+ international patents granted in USA, EU, Canada, France, Germany and Japan. He wrote and edited 75+ books for Wiley, Cambridge University Press, Mc-Graw Hill, CRC Press, and Springer. He is a frequent invited speaker and has consulted for multiple organizations internationally.

Perovskite Materials: Application Perspective

Krzysztof (Kris) Iniewski, Wanyi Nie, Yuki Haruta, and Makhsud Saidaminov

1 Introduction

Perovskite is a calcium titanium oxide mineral, with the chemical formula of $CaTiO_3$. The mineral was discovered in the Ural Mountains of Russia by Gustav Rose in 1839 and is named after the Russian mineralogist Lev Perovski (1792–1856). The terms "perovskite" and "perovskite structure" are often used interchangeably, but while true perovskite (the mineral) is formed of calcium, titanium, and oxygen in the form $CaTiO_3$, the perovskite structure is anything that has the generic form ABX_3 and the same crystallographic structure as perovskite mineral. The simplest way to describe ABX_3 perovskite structure is as a cubic unit cell with B in the center, X on the faces, and A in the vertices of the unit cell. In halide perovskites, X is a halogen (Cl^-, Br^-, I^-), B is a divalent cation typically Pb^{2+} and/or Sn^{2+}, and A is a large monovalent cation such as Cs^+, $CH_3NH_3^+$. From here on, we will focus on halide perovskites.

Perovskite's potential applications include catalyst electrodes, solar cells, lasers, memory devices, X-ray and gamma ray sensors, and spintronic applications. The book covers these applications in more depth in the following chapters, so the intent here is to provide some general guidance. Several chapters in various books and review papers can be referenced for earlier reports on perovskite materials [1–8].

Depending on the composition, perovskites can have an impressive array of interesting properties including wide bandgap tunability, nonlinear optics,

K. (Kris) Iniewski (✉)
Redlen Tehnologies, Saanichton, BC, Canada

W. Nie
Los Alamos National Lab, Los Alamos, NM, USA
e-mail: wanyi@lanl.gov

Y. Haruta · M. Saidaminov
University of Victoria, Victoria, BC, Canada
e-mail: msaidaminov@uvic.ca

W. Nie, K. (Kris) Iniewski (eds.), *Metal-Halide Perovskite Semiconductors*,
https://doi.org/10.1007/978-3-031-26892-2_1

ferroelectricity, charge ordering, spin-dependent transport, and others. Perovskites, therefore, hold exciting opportunities for physicists, chemists, and material scientists. Over the last two decades, halide perovskites (HPs) have been identified as one of the most promising materials in photovoltaic and light-emitting devices. This has led to major breakthroughs in materials science.

Recent advances in halide perovskite materials have resulted in impressive gains in solar cells, photon detectors, and light-emission diodes. This chapter briefly reviews recent advancements in perovskite materials for high-energy photon sensing and contrasts them against state-of-the-art semiconductors, as well as conventional scintillators. A new startup company Actinia is described as a case study.

Although the first halide perovskite ($CsPbX_3$) was already reported in 1893 [9], this class of materials received widespread attention only in the last 10 years. The technology development has been driven by the solar cell field since 2009 [10], and its X-ray detection capability has been recently recognized as a possibility to adopt. The development of the process to fabricate mm-scale perovskite single crystals paved the way for X-ray detection applications.

Halide perovskites do not perform well under very high-flux conditions, creating a barrier to entry into applications like computed tomography (CT); therefore, perovskite is not a significant threat to traditional semiconductor devices at the moment. But due to unique material properties, perovskites will likely find some entry points where low cost, ease of manufacture, and mechanical flexibility are attractive. They will likely displace some low-end scintillator solutions and perhaps with time applications like mammography/breast imaging where the flexible shape might be of premium.

It is challenging to forecast how this technology will move forward as every day new perovskite research papers are published. The citations of the first perovskite solar cell paper [10] have reached over 14,000 in 12 years, and the research on perovskite X-ray detectors is also accelerated (Fig. 1). Things can change quickly as perovskite materials have been very successful in raising research funds from both state and private sectors. Therefore, this chapter offers a sampling perspective in 2022. An example of recent government funding activity is Peroxis, an EU-funded research consortium (https://peroxis-project.eu/consortium/). Its objective is to develop a groundbreaking highly sensitive and high spatial resolution direct X-ray detection technology that will greatly improve the diagnosis of major diseases such as cancer, infectious, degenerative, or cardiovascular diseases. The consortium partners are CEA, Trixell, Siemens, University of Jaume (Spain), Philips and TNO, and Neel. Similar grant initiatives have been announced in the USA and other countries.

1.1 Perovskite as a Photovoltaics

Solar cells are currently the most prominent perovskite application, as perovskites are recognized as potential inexpensive base materials for high-efficiency commercial photovoltaics. Perovskite photovoltaics (PVs) are constantly undergoing

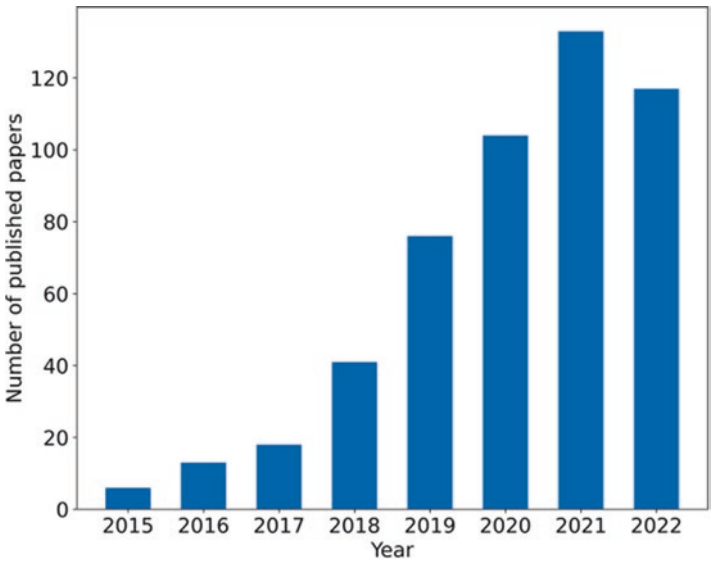

Fig. 1 Number of "perovskite X-ray detector" papers retrieved from *Web of Science* as of October 24, 2022

research and improvement, going from just 3.8% efficiency in 2009 to over 25% in 2022. Market research forecast that the market for perovskite PV will reach $214 million in 2025 [11].

The original perovskite photovoltaics started as a simple variant of dye-sensitized solar cells (DSSCs) in which a perovskite was just a dye [10] but the device structure has been evolving toward the planar architecture. Perovskites offer a significant advantage over silicon in PV applications since perovskites react to a broader range of visible light frequencies. In addition, perovskite PVs offer additional attributes like flexibility, semi-transparency, lightweight, and low processing costs [12].

Besides, the bandgap of perovskites can be tuned widely (~1.2 to ~3.0 eV). This creates an opportunity in pairing them up with low bandgap PV technology like silicon PVs, which will result in improved efficiency as tandem solar cells and will matter in a highly competitive market where system costs and performance levels depend on efficiencies.

The technology is, however, not fully commercially ready yet, and perovskite PVs will need to face several challenges before commercialization. Among these issues are the cells' long-term durability and toxicity (the risk is that these devices may release lead, a highly toxic element, into the environment). To avoid these issues, encapsulation technologies are being developed. A number of chapters in this book address photovoltaic applications.

1.2 Perovskite in X-ray Imaging

In addition to application in solar cells, the realization of perovskite-based X-ray imaging devices is expected as they show some promising properties such as a high X-ray sensitivity. Market research predicts that perovskite X-ray detectors will open new applications for X-rays, expanding what is already a multibillion-dollar industry [13]. More efficient imagers would draw less power, lending themselves to portable machines that run on batteries. Researchers have demonstrated a variety of tunable, color-emitting perovskite nanocrystals. That work could lead to multicolor X-ray displays, which are impossible with today's scintillator X-ray machines. Research continues in both indirect detection scintillator materials and direct conversion semiconductors. And because they use flexible substrates, perovskite imagers could conform to whatever is being scanned. Faster, more sensitive imagers might also reduce the radiation from dental and medical X-rays and airport security scanners.

One of the biggest issues in PV application, which is instability against the moisture, is not significant for X-ray imagers application because the environmental conditions they will face are more benign. In addition, one can wrap the detector in different materials while still seeing good X-ray penetration into it, which is not necessarily the case with a PV system that needs to absorb solar radiation efficiently. Solar panels need to perform even after 20 years, typically exposed to heat and light, both of which can degrade the perovskite compound. X-ray machines, by contrast, are typically used in climate-controlled settings. For these reasons, many researchers including us believe perovskite X-ray detectors will be commercialized much more quickly than other perovskite applications.

A big obstacle to the market is the lack of a scalable fabrication process for perovskite X-ray imagers. Although X-ray imagers require enough area comparable to the imaging area for the X-ray absorbing layers, the fabrication of such a large perovskite single crystal is still challenging. Polycrystalline perovskite thick films prepared by some scalable processes have been reported, but the X-ray detection performance is not enough compared to the single crystal-based devices and so needs to be improved [14].

1.3 Perovskite Quantum Dots and Lasers

Perovskite quantum dots (PQDs) are a class of quantum dots based on perovskite materials. While these are relatively new, they have already been shown to have properties matching or surpassing those of the metal chalcogenide QDs: they are more tolerant to defects and have excellent photoluminescence quantum yields and high color purity. Such attractive properties are extremely suited for electronic and optoelectronic applications, and so PQDs have significant potential for real-world applications, some of which are already emerging, including LED displays and quantum dot solar cells [15].

As direct bandgap semiconductors, perovskites exhibit the unique optical properties of bandgap tunability, charge-carrier mobility, defect tolerance, photoluminescence quantum efficiency, and power conversion efficiency. These properties make them promising light-emitting materials for high optical gain, low-threshold, and multicolor laser applications. The fact that they can be fabricated from low-cost precursors via simple processes makes them attractive as well.

Researchers have found that organometal halide-based perovskites (a combination of lead, organics, and halogens arranged into a perovskite crystal structure in the solid state) could be very suitable for making optoelectronic devices since they can be processed in solution and do not need to be heated to high temperatures. This means that large-area films of these materials can be deposited onto a wide range of flexible or rigid substrates. The perovskites also have an optical bandgap that can be tuned in the visible to infrared regions, which makes them very promising for a range of optoelectronic applications. These materials also emit light very strongly, which makes them very suitable for making LEDs. The wavelength of the light emitted by the perovskites can be easily tuned, which could make them ideal for color displays and lighting and in optical communication applications.

However, a major obstacle is that electrons and holes only weakly bind in perovskite thin films. This means that excitons (electron-hole pairs) spontaneously dissociate into free carriers in the bulk recombination layer, leading to low photoluminescence quantum efficiency (PLQE), high leakage current, and low luminous efficiency. This obviously impairs perovskites' ability to create high-performance LEDs, and for perovskite materials to make a comparable impact in light emission, it is necessary to overcome their slow radiative recombination kinetics. Researchers will have to find ways of effectively confining electrons and holes in the perovskite so that they can "recombine" to emit light. Major progress is already being made in this field, and it seems that perovskites might indeed open the door to a low-cost, color-tunable approach to LED development. One chapter in this book is devoted to this exciton problem.

2 Perovskites for X-Ray and Gamma-Ray Detection

2.1 Motivation

The interest in perovskites started with highly efficient photovoltaic cells. Researchers were also exploring perovskites' potential in transistors and LED lighting. There is yet another use for halide perovskites, likely the most promising of all: as X-ray and gamma-ray detectors. What makes perovskites so useful for X-ray detection is the same thing that makes them good for solar cells: they are excellent at converting photons into electrical charge. In a direct detector, X-ray photons are converted into electrons inside a semiconductor. In a scintillator imager, the X-ray photons are first converted into visible photons, which are then converted into electrons by a photodiode array. Interestingly, perovskites can be manufactured and

used as either direct conversion detectors (like silicon, CdTe, or CZT) or as traditional indirect scintillator materials (incumbent technology for X-ray detection) [6].

Many companies exploring this area and major X-ray imaging manufacturers are considering perovskite for their next-generation X-ray machines. Compared with today's X-ray imagers, detectors based on perovskite compounds can be more sensitive and use less power. And for certain applications, the materials can be tuned to emit color when irradiated.

Other researchers have demonstrated perovskites in direct X-ray detectors with superior performance to that of commercial imagers, but low-performing silicon or selenium is typically used in these comparisons. Research into perovskite materials for X-ray detection remains fertile. At the recent 2021 IEEE NSS MICS RSTD conference, there were more research papers on perovskites than on traditional CdTe and CZT semiconductor detectors [16–30]. Interestingly, there was a lack of any big original equipment manufacturers (OEMs) or startups presenting, which is an indication that the technology development is still in the research phase, with no clear indication of technology transfer or attempts to build commercially viable devices. We expect this trend to continue at the 2022 IEEE NSS MICS RSTD conference which at the time of this writing is about to start in Milano.

In addition to the ongoing material research activity that may benefit the development of new ionizing radiation detectors, it is attractive that the Pb-halide perovskites can be grown and processed in solution at relatively low temperatures and that the basic raw materials are earth-abundant. Furthermore, the $APbX_3$ perovskites have reasonably high density and high-Z elements (e.g., Pb, Cs, I), which are helpful in a radiation detector to stop and convert the incident X-ray or gamma photon to electron-hole pairs.

The lead-halide perovskites exhibit so-called defect tolerance, which is partly credited for transport properties beneficial in solar cells and high quantum yield from nanocrystals in LEDs. Defect tolerance is taken here to mean that defect trap levels lie within the bands rather than in the bandgap or are shallow if within the bandgap. Reviews and explanations have been offered in the literature and further in this book. The attractive properties of metal halides are accompanied by the fact that such salts generally are soft insulators prone to point and line defects. Many of the electron trap levels that would appear within the bandgaps of most other halide insulators become enveloped within the Pb-derived conduction band that is mainly responsible for narrowing the gap from typical metal halide insulators to $APbX_3$ semiconductors [31–33].

As suggested by the branching in the lower part of Fig. 2, it appears that lead-halide perovskites may be poised to furnish radiographic detectors by two different routes, one depending on defect tolerance-associated carrier lifetime in semiconductor mode for direct radiographic detection and the other depending on high quantum-yield light emission from excitons in semiconducting quantum dots (QDs). The following two sections examine these two paths separately. Section 2.2 focuses on the right branch seeking to exploit scintillating light emission for indirect radiography. Section 2.3 focuses on examining progress along the left branch using charge collection.

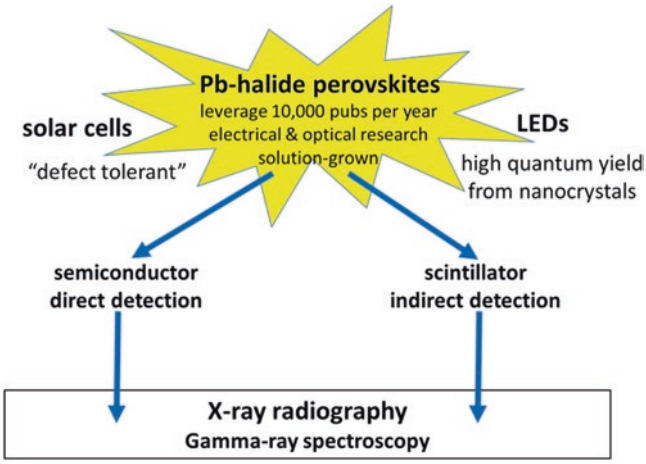

Fig. 2 Activity in photovoltaic and LED research on perovskites may be leveraged for two corresponding routes to radiation detection, particularly X-ray radiography and gamma ray spectroscopy [6]

2.2 Perovskites as Scintillators

Prospects for making room-temperature perovskite scintillators benefited from research and development on perovskite light-emitting diodes (LEDs), where it had been found that perovskite nanocrystals as light emitters avoid the room-temperature quenching of luminescence that occurs in extended 3D bulk crystals. The retention of light emission at room temperature in nanocrystals is generally attributed to the quantum confinement of electrons and holes together. Inorganic $CsPbBr_3$ or hybrid $(CH_3NH_3)PbBr_3$ (=$MAPbBr_3$) might attain a scintillation light yield as high as 156 photons/keV [6]. To realize them, an understanding of how the thermal quenching in microscopic and macroscopic crystals occurs and how quantum confinement defeats room-temperature quenching would be helpful. Although various strategies have been proposed to solve these fundamental perovskite scintillator problems, the applications in the industry are still challenging. On the other hand, the second path of using perovskites as direct detectors looks more promising as discussed below.

2.3 Perovskites as Direct Detectors

The research on perovskite direct X-ray detectors was triggered by the development of facile growth methods which provide high-quality mm-scale perovskite single crystals. In 2015, high-quality, hybrid perovskite single-crystal growth was first published using a low-cost, rapid growth technique, now known as inverse temperature crystallization (ITC) [34–37]. Soon thereafter, large, ongoing research efforts

have been placed in a variety of areas in solution-based hybrid perovskite single-crystal growth. There are a variety of other efficient solution-based growth techniques that have been successfully demonstrated to produce high-quality single crystals of hybrid and non-hybrid perovskite single crystals. These include anti-solvent vapor diffusion, temperature-lowering methods, and slow solvent evaporation [38].

Although the solution-based methods have been the most popular method for perovskite single-crystal growth, some groups have turned to melt growth methods for high-quality inorganic perovskite crystal growth (e.g., $CsPbBr_3$). This method provides accurate control to produce high-quality single crystals. However, in the realm of hybrid perovskites, this method cannot be used because the organic components in hybrid perovskites will be decomposed or volatilized.

Thanks to those developments in mm-scale single-crystal growth, many perovskites' direct X-ray detectors have been reported. As provided in the recent review paper [39–44], excellent X-ray detectors with high X-ray sensitivities over 10^4 μC Gy^{-1} cm^{-2} and low detection limits below 10 nGy s^{-1} have been reported. The sensitivity and detection limit of the perovskite X-ray detectors are several orders higher and lower than conventional detectors (amorphous Se, HgI_2, and CdTe), respectively. While those reports are supporting the promising future of perovskite-based direct X-ray detectors, further scale-up for imaging devices is still challenging. Therefore, polycrystalline thick films that can be easily scaled up for imaging devices are recently developed and described in one of the chapters in this book.

2.4 Perovskites as Flexible X-Ray Detectors

The world around us consists of a myriad of objects with curved geometries and complex surfaces, yet most sensors and detectors that we use to study them are rigid and planar. Confronting this incompatibility will allow for applications impossible to realize with current technologies. Ultra-flexible, low-cost, and highly sensitive high-energy radiation detectors are of great interest to the fields of medical diagnostics, dosimetry, industrial inspection, security, and defense. Low weight and high conformability of X-ray wearable dosimeters are appealing features for astronauts, nuclear power plants, and laboratory workers, as well as for imagers used in structural inspection and cultural heritage preservation. This research area is part of the major trends in electronics industry of producing flexible electronics/sensors products.

State-of-the-art solid-state X- and gamma ray detectors for large-area applications based on silicon (Si), amorphous selenium (a-Se), and cadmium (zinc) telluride (CdTe/CdZnTe) are mechanically stiff, difficult to scale up, and require high operating voltage. Organic semiconductors were the first group of materials that was able to overcome these issues, offering liquid phase, low-temperature, and low-cost deposition techniques that are scalable to large flexible substrates. Mechanical

flexibility, high X-ray sensitivity (up to 1.3×10^4 μC Gy^{-1} cm^{-2}), and low limit of detection (down to 0.29 μGy s^{-1}) have been demonstrated for both organic single-crystal and thin film direct X-ray detectors. Despite these encouraging results, organic semiconductors are intrinsically low-Z materials, therefore resulting in subpar high-energy photon absorption. Blends of organic semiconductors and heavy inorganic nanoparticles or lead-based quantum dots have been proposed to overcome such issues. On one hand, this approach offers a strategy to improve the material attenuation fraction, but on the other hand, it is intrinsically limited by the maximum nanoparticle concentration that can be dispersed in the blend before clustering and agglomeration occur, resulting in electronic transport degradation.

Recently, lead-halide perovskites emerged as an auspicious novel material family for X- and gamma ray detection. Their success can be attributed to strong absorption of ionizing radiation due to the presence of heavy atoms (e.g., Pb, I, and Br), high charge carrier mobilities, long exciton diffusion, long charge carrier lifetime, and excellent optical properties. Single-crystal and thick-film perovskite X-ray detectors have been the focal point of current research, often incorporated in a lateral photoconductor radiation detector architecture. This kind of device shows outstanding sensitivity as well as fast, stable, and reproducible responses. Increasing the thickness of crystals or films has been the primary way to raise the total radiation absorbance and thus improve the detector efficiency. Nevertheless, limited attention has been devoted to thin-film perovskite ionizing radiation detectors. Vertical configuration photodiode architecture based on thin films allows for lower dark current and faster response and stands out as the only viable candidate for flexible device implementation.

2.5 Case Study: $CsPbBr_3$

Actinia (https://actiniadetectors.com/) is developing one of the most studied perovskite materials, $CsPbBr_3$, that features a large bandgap of 2.3 eV which ensures low dark currents and robust performance well above room temperature. $CsPbBr_3$ has a pseudo-cubic perovskite structure (Fig. 3). Compared to organic-inorganic hybrid perovskites, the all-inorganic $CsPbBr_3$ perovskite features great advantages in chemical and device stability, due to the lack of organic molecules, while also exhibiting top-of-the-line performance that rivals the best room-temperature semiconductors. Unlike such materials, however, detector-quality $CsPbBr_3$ is inexpensive to synthesize, uses readily available starting materials, and tolerates crystal defects well.

Actinia has developed proprietary growth methods for high-quality crystal growth of $CsPbBr_3$. Growing crystals of $CsPbBr_3$ using Actinia's techniques has the advantage of producing size-controllable high-purity single crystals and provides a feasible path to mass production for commercial X-ray detection applications. Actinia's proprietary technology and methods produce large, high-performing $CsPbBr_3$ crystals. Actinia's $CsPbBr_3$ devices exhibit high-energy discrimination

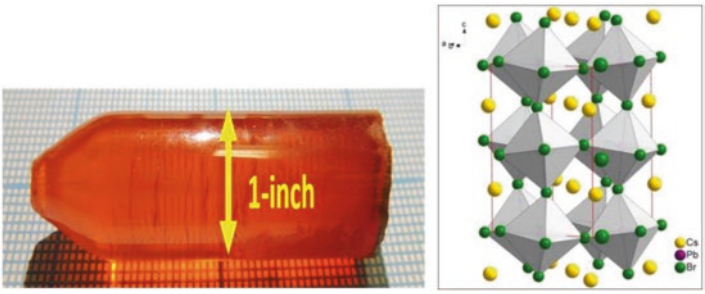

Fig. 3 $CsPbBr_3$ ingot produced by the other Actinia (middle) and three-dimensional (3D) perovskite structures of $CsPbBr_3$ (right)

ability and high X-ray sensitivity under a variety of X-ray sources with a continuum energy spectrum. The details of the performance can be found in these published papers [27–30]. The performance of the Actinia detectors can be summarized using *Nature Photonics* Abstract [27]: "Halide perovskite semiconductors are poised to revitalize the field of ionizing radiation detection as they have done to solar photovoltaics. We show that all-inorganic perovskite $CsPbBr_3$ devices resolve ^{137}Cs 662-keV γ-rays with 1.4% energy resolution, as well as other X- and γ-rays with energies ranging from tens of keV to over 1 MeV in ambipolar sensing and unipolar hole-only sensing modes with crystal volumes of 6.65 mm^3 and 297 mm^3, respectively. We demonstrate the scale-up of $CsPbBr_3$ ingots to up to 1.5 inches in diameter with an excellent hole mobility–lifetime product of 8×10^{-3} cm^2 V^{-1} and a long hole lifetime of up to 296 μs. $CsPbBr_3$ detectors demonstrate a wide temperature region from ~2 °C to ~70 °C for stable operation. Detectors protected with suitable encapsulants show a uniform response for over 18 months. Consequently, we identify perovskite $CsPbBr_3$ semiconductor as an excellent candidate for new-generation high-energy γ-ray detection."

3 Perovskite Material Properties

3.1 Perovskite Material Characterization

Once single crystals are grown and harvested from the solution, it is important to characterize them to ensure high quality, proper composition, and desired properties. In principle, this is not different than for CZT. There are abundant characterization techniques developed in the literature to understand the properties of hybrid perovskite single crystals, but the most important properties belong to structural, optical, and electronic categories for semiconductor device development.

When single crystals are first grown and harvested from solution, a well-utilized tool to initially characterize the quality of the growth is a visual inspection. When

the bromide- and chloride-based crystals are grown, they are transparent. When visually inspecting a single crystal, it is important to look for various signs. The most common visual inspection for these types of single crystals among the community relies on the transparency of the crystals without distortion of imagery or graphical lines placed underneath the crystal. However, if the crystal is not transparent or cloudy or even slightly distorts the image below, one can speculate on the quality of the crystal growth through a relative concentration of defects or microcracks in the bulk of the crystals. In the case of nontransparent single crystals, like the black, iodide-based single crystals, transparency cannot be utilized for quality checks. Instead, the quality inspection here comes from the smoothness and mirror-like finishes of the crystal faces. Other visual inspections include checking for smooth parallel sides without curvature for cubic crystals and sharp edges.

The visual inspection is a first, simple step to initially speculate on the quality of the bulk material; however, phase and defect concentration are very important properties in these materials for semiconductor applications and must be quantified properly. Powder X-ray diffraction (XRD) is commonly used to study the crystal structure of single crystals. In this method, the single crystal is finely ground into powder and an XRD pattern is collected. The data is then matched to the pure compound from a crystallographic database to ensure that the material is in the proper phase (i.e., $MAPbBr_3$ = cubic, $MAPbCl_3$ = cubic, $MAPbI_3$ = tetragonal for room-temperature structures). Other X-ray diffraction techniques can be used to understand imperfections in the crystallographic structure throughout the material such as Laue diffraction patterns to characterize the alignment of the crystal faces and high-resolution XRD (such as rocking curves) to see any deviations in the crystal structure. Temperature-dependent XRD can also be used to understand structure transitions such as in $MAPbI_3$ which undergoes a transition from cubic to tetragonal phase around 330 K and another transition to the orthorhombic phase around 160 K.

The next common characterization deals with quantifying defect concentration and characterizing the types of defects that directly play an important role in semiconductor optoelectronic applications. There are a wide variety of experimental techniques including secondary ion mass spectrometry, positron annihilation spectroscopy, X-ray measurements, electrical measurements, and optical measurements. Electrical measurements such as space charge limited current (SCLC) and Hall measurements can be also used to quantify defect concentrations. Meanwhile, other common techniques include the time of flight and temperature-modulated techniques to determine the levels of traps within the bandgaps, which helps to understand the roles of traps in charge transport processes. Again, similar techniques are used in the CZT world so there is little new here.

The following techniques to continue characterizing As-grown perovskite single crystals use optical spectroscopy. Absorption is used to directly measure the bandgap and states that below the gap, photoluminescence can be a close substitute for estimating the bandgap and trap density of the material. When they are excited by an absorbable wavelength, the excited states relax from the conduction band to the valence band, and the corresponding energy is released via light such as photoluminescence.

3.2 Perovskite Electronic Properties

The electronic band structure, charge transport, traps, and defects depend on the perovskite compositions and the crystal growth conditions. Here, we discuss the general electronic properties of perovskites relevant to radiation detection applications. Lead-halide perovskites have a strong radiation stopping power due to their high effective atomic number (consists of heavy elements like Pb, Cs, halides, etc.) and high density. The linear attenuation coefficients of hybrid perovskite materials ($MAPbI_3$, $CsPbBr_3$, 2D perovskite, and double perovskite) are comparable to conventional CZT and much higher than Si. Therefore, the quantum efficiency of a $MAPbI_3$ crystal with a 2 mm thickness (density 4.15 g/cm^3) for a radiation photon with an energy of 100 keV is about 99.9% (assuming the photon deposits all its energy in the crystal and all the electron-hole pairs generated are collected). Even at an energy of 300 keV, photoelectric absorption is the dominant interaction mechanism and Compton scattering is much smaller. The inorganic $CsPbBr_3$ perovskite has an even higher attenuation coefficient. Due to the tunable nature of the material compositions, other high atomic number elements can also be incorporated into the perovskite materials to further increase the stopping power. $Cs_2AgBiBr_6$ double perovskite is one example of high detection efficiency. Moreover, using the optical bandgap (E_g), one can estimate the ionization energy or the free electron-hole pair creation energy (W) using empirical relation $W = \sim 3E_g$. The bandgap for common perovskites falls within the range of 1.1–2.5 eV, which translates to ionization energies in the range of 3.3–7.5 eV comparable to 4.6 eV in CZT.

3.3 Perovskite Charge Transport Properties

Due to strong spin-orbit coupling, the electron and hole effective mass in $MAPbI_3$ is reduced to 0.1–0.3 of m_0. These effective mass values are comparable to Si. However, the carrier mobilities in halide perovskites are lower than that of Si. Depending on the measurement technique used and the quality of the single crystal, the chaptered electron and hole mobility values for $MAPbI_3$ are in the range of 24–800 cm^2/Vs. This range is large, indicating that many samples at the low end of reported mobilities were likely inferior, e.g., containing many trapping centers that lower the measured mobilities. In addition, the temperature dependence of mobility measurements indicates that these modest mobility values are mainly due to the scattering of electrons with longitudinal-optical phonons. Notably, the reported electron and hole mobilities are in the same range, which is consistent with effective mass. Therefore, ambipolar charge transport in lead-halide perovskites is ideal for the efficient extraction of both electrons and holes.

On the other hand, the perovskites have long carrier lifetimes and diffusion lengths [20]. The reported lifetimes of $MAPbI_3$ are around 10–17 μs while a record lifetime of $CsPbBr_3$ which is more than 25 μs has been reported [27]. The long

lifetimes also make up for the modest mobility values and result in mobility-lifetime ($\mu\tau$) products comparable to CZT materials. It might be worth noting here that some of these materials, $CsPbBr_3$ for example, are hole-dominant materials. The reported $\mu\tau$ product values for $MAPbI_3$, $MAPbBr_3$, and $CsPbBr_3$ are 0.8×10^{-3} cm^2/V, 1.2×10^{-2} cm^2/V, and $1.33–1.69 \times 10^{-3}$ cm^2/V, respectively [1–8]. In addition, a high $\mu\tau$ product of 1.8×10^{-2} cm^2/V for mixed-halide $MAPbBr_{2.94}Cl_{0.06}$ has been obtained by doping $MAPbBr_3$ with Cl.

Low trap state densities in the range 10^9–10^{10} cm^{-3} have been reported for solution-grown halide perovskite single crystals, again comparable to CZT. Using Bridgman melt growth method, centimeter-sized $CsPbBr_3$ crystals with impurity levels below 10 ppm for a total of 69 elements have also been obtained. The experimental results are consistent with theoretical studies which indicate that dominant intrinsic defects are shallow traps while deep defects located near the middle of the bandgap are unlikely to form due to high enthalpy of formation. This "defect tolerance" in perovskites has been attributed to the strong lone pair in Pb s-orbital, antibonding coupling in I p-orbital. Due to the low density of electrically active defects in halide perovskites, charge carriers excited by radiation can be extracted without being trapped. Moreover, the defect tolerance nature of perovskites also gives rise to radiation hardness.

4 Looking Ahead

What is ahead for perovskite materials? Research funds will likely continue to pour into this technology. Perovskite materials, after all, exhibit intriguing and unusual physical properties that will be extensively studied for both practical applications and theoretical modeling, and the materials science and applications of perovskites have already been a broad research area open to many revolutionary discoveries for new device concepts. At least 10,000 research papers have been published on this topic already.

It is generally recognized that it takes 20–30 years in materials science to reach production maturity although in the perovskite case one might argue it will be shortened, say down to 10–15 years, due to widespread application space and universality of the material solutions offered. That puts 2035 as a year of commercial deployment and 2030 as a year with some product samples being demonstrated. We forecast that low-end scintillator applications will be the first to use perovskite technology on par with some new unique applications that explore perovskites' unique properties like the flexibility of the substrate material. The perovskite mantra will be unique (flexibility in shape), low cost, and easy to manufacture (e.g., in amorphous/polycrystalline shape). But performance needs to follow if this is to become a real contender in the radiation detection space.

References

1. Pan, L., Kandlakunta, P., & Cao, L. R. (2021). Inorganic perovskite $CsPbBr_3$ gamma ray detector. In K. Iniewski (Ed.), *Advanced materials for radiation detection*. Springer.
2. Andričević, P. (2021). The impact of detection volume on hybrid halide perovskite-based radiation detectors. In K. Iniewski (Ed.), *Advanced materials for radiation detection*. Springer.
3. Manuel, Q.-L., Leunam, F.-I., Reyes-Banda, M. G., & Caraveo-Frescas, J. A. (2021). Inorganic halide perovskite thin films for neutron detection. In K. Iniewski (Ed.), *Advanced materials for radiation detection*. Springer.
4. Li, F., Yang, T., & Zheng, R. (2021). Radiation detection technologies enabled by halide perovskite single crystals. In K. Iniewski (Ed.), *Advanced materials for radiation detection*. Springer.
5. Gedda, M., Faber, H., Petridis, K., & Anthopoulos, T. D. (2021). Metal halide perovskites for high energy radiation detection. In K. Iniewski (Ed.), *Advanced materials for radiation detection*. Springer.
6. Wolszczak, W. W., Carroll, D. L., & Williams, R. T. (2022). Toward perovskite-related scintillators with necessary stokes shift and thickness for hard X-ray radiography and gamma spectroscopy. In K. Iniewski (Ed.), *Advanced X-ray detector technologies design and applications*. Springer.
7. Nie, W., Tsai, H., Liu, F., Shrestha, S., & Tisdale, J. (2022). Emerging lead-halide perovskite semiconductor for solid-state detectors. In K. Iniewski (Ed.), *Advanced X-ray detector technologies design and applications*. Springer.
8. Jena, A. K., Kulkarni, A., & Miyasaka, T. (2019). Halide perovskite photovoltaics: Background, status, and future prospects. *Chemical Reviews, 119*, 3036–3103.
9. Wells, H. L. (1893). Über die Cäsium- und Kalium-Bleihalogenide. *Zeitschrift für Anorganische Chemie, 3*, 195–210.
10. Kojima, A., Teshima, K., Shirai, Y., & Miyasaka, T. (2009). Organometal halide perovskites as visible-light sensitizers for photovoltaic cells. *Journal of the American Chemical Society, 131*, 6050–6051.
11. https://www.semiconductor-today.com/news_items/2015/jul/idtechx_160715.shtml
12. Min, H., Lee, D. Y., Kim, J., Kim, G., Lee, K. S., Kim, J., Paik, M. J., Kim, Y. K., Kim, K. S., Kim, M. G., Shin, T. J., & Seok, S. I. (2021). Perovskite solar cells with atomically coherent interlayers on SnO_2 electrodes. *Nature, 598*, 444–450.
13. https://site.ieee.org/sb-uol/x-ray-detection-may-be perovskites killer-app/.
14. Haruta, Y., Kawakami, M., Nakano, Y., Kundu, S., Wada, S., Ikenoue, T., Miyake, M., Hirato, T., & Saidaminov, M. I. (2022). Scalable fabrication of metal halide perovskites for direct X-ray flat panel detectors: A perspective. *Chemistry of Materials, 34*, 5323–5333.
15. Wang, H.-C., Bao, Z., Tsai, H.-Y., Tang, A.-C., & Liu, R.-S. (2018). Perovskite quantum dots and their application in light-emitting diodes. *Small, 14*, 1702433.
16. Hansen, K., Datta, A., & Motakef, S. *Perovskite semiconductor X-ray detectors for medical and synchrotron applications* (#1116). https://www.eventclass.org/contxt_ieee2021/
17. Datta, A., Hansen, K., Pinaroli, G., Carini, G., Deptuch, G., O'Connor, P., Herrmann, S., & Motakef, S. *Perovskite X-ray detectors for high spatial resolution synchrotron imaging* (#579). https://www.eventclass.org/contxt_ieee2021
18. Mayén Guillén, J. A., Baussens, O., Chapran, M., Verilhac, J.-M., Gros D'Aillon, E., Ibanez, A., & Zaccaro, J. *MAPb(Br1-xClx)3 perovskite materials for direct X-ray detection (#490).* https://www.eventclass.org/contxt_ieee2021/
19. Ciavatti, A., Ledee, F., Verdi, M., Basiricò, L., & Fraboni, B. *Ultra-stable and robust response to X-Rays in 2D layered perovskite micro-crystalline films directly deposited on flexible substrate (#358).* https://www.eventclass.org/contxt_ieee2021/
20. Bennett, S. H., Alghamdi, S. S., Braddock, I. H., O'Neill, J. G., Liu, X., Zhang, B., & Sellin, P. J. *Charge transport optimisation of FA lead halide perovskite radiation detectors (#556).* https://www.eventclass.org/contxt_ieee2021/

21. Alghamdi, S. S., Bennett, S. H., Braddock, I. H., Gibbard, H. J., O'Neill, J. G., Moss, R., & Sellin, P. J. *Large area polycrystalline perovskite X-ray detectors (#618).* https://www.eventclass.org/contxt_ieee2021/
22. Murgulov, V., Schweinle, C., Daub, M., Hillebrecht, H., & Fiederle, M. *Growth and characterisation of $Cs_2AgBiBr_6$ double perovskite single crystals for application in radiation sensing* (#489). https://www.eventclass.org/contxt_ieee2021/
23. Tan, R., Charest, J., Busch, C., Dryzhakov, B., Higgins, K., Ahmadi, M., Hu, B., & Lukosi, E. *Advanced techniques for gamma ray spectroscopy with metal halide perovskites (#658).* https://www.eventclass.org/contxt_ieee2021/
24. Boschetti, B., Toufanian, R., Datta, A., & Motakef, S. *Solution growth and detector performance of centimeter-scale lead halide perovskites (#1067).* https://www.eventclass.org/contxt_ieee2021/
25. Islam, M. M., Niraula, M., Nakashima, Y., Matsubara, T., Hirano, S., Takagi, Y., & Yasuda, K. *Growth and characterization of single-crystal lead halide perovskite for X-ray detector application (#182).* https://www.eventclass.org/contxt_ieee2021/
26. Brynza, M., Belas, E., Pipek, J., Betušiak, M., Praus, P., Ahmadi, M., Grill, R., & Musiienko, A. *Unravelling the electronic and charge transport properties in organic perovskites (#254).* https://www.eventclass.org/contxt_ieee2021/
27. Stoumpos, C. C., Malliakas, C. D., Peters, J. A., Liu, Z. F., Sebastian, M., Im, J., Chasapis, T. C., Wibowo, A. C., Chung, D. Y., Freeman, A. J., Wessels, B. W., & Kanatzidis, M. G. (2013). Crystal growth of the perovskite semiconductor $CsPbBr_3$: A new material for high-energy radiation detection. *Crystal Growth & Design, 13*(7), 2722–2727.
28. He, Y. H., Matei, L., Jung, H. J., McCall, K. M., Chen, M., Stoumpos, C. C., Liu, Z. F., Peters, J. A., Chung, D. Y., Wessels, B. W., Wasielewski, M. R., Dravid, V. P., Burger, A., & Kanatzidis, M. G. (2018). High spectral resolution of gamma-rays at room temperature by perovskite $CsPbBr_3$ single crystals. *Nature Communications, 9*, 8.1609.
29. He, Y. H., Liu, Z. F., McCall, K. M., Lin, W. W., Chung, D. Y., Wessels, B. W., & Kanatzidis, M. G. (2019). Perovskite $CsPbBr_3$ single crystal detector for alpha-particle spectroscopy. *Nuclear Instruments & Methods in Physics Research Section a-Accelerators Spectrometers Detectors and Associated Equipment, 922*, 217–221.
30. He, Y. H., Petryk, M., Liu, Z. F., Chica, D. G., Hadar, I., Leak, C., Ke, W. J., Spanopoulos, I., Lin, W. W., Chung, D. Y., Wessels, B. W., He, Z., & Kanatzidis, M. G. (2021). $CsPbBr_3$ perovskite detectors with 1.4% energy resolution for high-energy gamma-rays. *Nature Photonics, 15*, 36–42.
31. Zhou, Y., Chen, J., Bakr, O. M., & Mohammed, O. F. (2021). Metal halide perovskites for X-ray imaging scintillators and detectors. *ACS Energy Letters, 6*, 739–768.
32. Kang, J., & Wang, L.-W. (2017). High defect tolerance in lead halide perovskite $CsPbBr_3$. *The Journal of Physical Chemistry Letters, 8*, 489–493.
33. Meggiolaro, D., Motti, S. G., Mosconi, E., Barker, A. J., Ball, J., Perini, C. A. R., Deschler, F., Petrozza, A., & De Angelis, F. (2018). Iodine chemistry determines the defect tolerance of lead-halide perovskites. *Energy & Environmental Science, 11*, 702–713.
34. Saidaminov, M. I., Abdelhady, A. L., Maculan, G., & Bakr, O. M. (2015). Retrograde solubility of formamidinium and methylammonium lead halide perovskites enabling rapid single crystal growth. *Chemical Communications, 51*, 17658–17661.
35. Saidaminov, M. I., Abdelhady, A. L., Murali, B., Alarousu, E., Burlakov, V. M., Peng, W., Dursun, I., Wang, L., He, Y., Maculan, G., Goriely, A., Tom, W., Mohammed, O. F., & Bakr, O. M. (2015). High-quality bulk hybrid perovskite single crystals within minutes by inverse temperature crystallization. *Nature Communications, 6*, 7586.
36. Kadro, J. M., Nonomura, K., Gachet, D., Grätzel, M., & Hagfeldt, A. (2015). A facile route to freestanding $CH_3NH_3PbI_3$ crystals using inverse solubility. *Scientific Reports, 5*, 11654.
37. Liu, Y., Yang, Z., Cui, D., Ren, X., Sun, J., Liu, X., Zhang, J., Wei, Q., Fan, H., Fengyang, Y., Zhang, X., Zhao, C., & Liu, S. F. (2015). Two-inch-sized perovskite $CH_3NH_3PbX_3$ (X = Cl, Br, I) crystals: Growth and characterization. *Advanced Materials, 27*, 5176–5183.

38. Zhang, T., Yang, M., Benson, E. E., Li, Z., van de Lagemaat, J., Luther, J. M., Yan, Y., Zhu, K., & Zhao, Y. (2015). A facile solvothermal growth of single crystal mixed halide perovskite CH $_3NH_3Pb(Br_{1-x}Cl_x)_3$. *Chemical Communications, 51*, 7820–7823.
39. Li, J., Zeyao Han, Y. G., Dejian, Y., Liu, J., Dawei, H., Xiaobao, X., & Zeng, H. (2021). Perovskite single crystals: Synthesis, optoelectronic peroperties, and application. *Advance Functional Materials, 31*, 2008684.
40. Song, J., Cui, Q., Li, J., Jiayue, X., Wang, Y., Leimeng, X., Xue, J., Dong, Y., Tian, T., Sun, H., & Zeng, H. (2017). Ultralarge all-inorganic perovskite bulk single crystal for high-performance visible–infrared dual-modal photodetectors. *Advanced Optical Materials, 5*, 1700157.
41. Haodi, W., Ge, Y., Niu, G., & Tang, J. (2021). Metal halide perovskites for X-ray detection and imaging. *Matter, 4*, 144–163.
42. Turedi, B., Lintangpradipto, M. N., Sandberg, O. J., Yazmaciyan, A., Matt, G. J., Alsalloum, A. Y., Almasabi, K., Sakhatskyi, K., Yakunin, S., Zheng, X., Naphade, R., Nematulloev, S., Yeddu, V., Baran, D., Armin, A., Saidaminov, M. I., Kovalenko, M. V., Mohammed, O. F., & Bakr, O. M. (2022). Single-crystal perovskite solar cells exhibit close to half a millimeter electron-diffusion length. *Advanced Materials, 34*, 2202390.
43. Wei, H., DeSantis, D., Wei, W., Deng, Y., Guo, D., Savenije, T. J., Cao, L., & Huang, J. (2017). Dopant compensation in alloyed $CH_3NH_3PbBr_{3-x}Cl_x$ perovskite single crystals for gamma-ray spectroscopy. *Nature Materials, 16*, 826–823.
44. He, Y., Petryk, M., Liu, Z., Chica, D. G., Hadar, I., Leak, C., Ke, W., Spanopoulos, I., Lin, W., Chung, D. Y., Wessels, B. W., He, Z., & Kanatzidis, M. G. (2020). CsPbBr3 perovskite detectors with 1.4% energy resolution for high-energy γ-rays. *Nature Photonics, 15*, 36. https://doi.org/10.1038/s41566-020-00727-1

Perovskite Thin Film Growth Techniques

Cheng-Hung Hou and Wanyi Nie

1 Introduction

Perovskite semiconductors are low cost, solution processible materials that have enabled exciting optoelectronic devices. In addition to single crystals, perovskite polycrystalline thin films are widely utilized in optoelectronic devices that adapt a thin-film device architecture. Depositing a uniform perovskite thin film with desirable properties has been an essential task for the development various optoelectronic devices, including photovoltaics, light-emitting diodes, and photo-detectors. Spin coating is a widely used fabrication tool for lab-scale device fabrication. The uniformity and film thickness can be finely tuned by solution concentration, viscosity, and the spin-coating speed. In perovskite photovoltaic research, thin-film engineering approaches have been extensively investigated based on spin-coating methods. However, for building large devices, like solar panels at meter-scales, alternative coating methods need to be explored. And the optimal coating parameters can vary depending on the thin-film deposition mechanisms.

Here in this chapter, we will introduce the thin-film fabrication methods that are mainly used for perovskite photovoltaic development. We will first introduce lab-scale, spin-coating method for building perovskite thin films. One-step, two-step, and antisolvent processing methods are described which are popular way of making perovskite solar cells. Next, we will focus on large-scale solar cell fabrication techniques, such as spin coating, D-bar coating, chemical vapor deposition (CVD), blade coating, and slot-die coating. Among the solution-based approaches, we found that D-bar coating, blade coating, and slot-die coating are popular for building perovskite solar panels. CVD is a dry fabrication method where solvent residual

C.-H. Hou · W. Nie (✉)
Los Alamos National Laboratory, Los Alamos, NM, USA
e-mail: wanyi@lanl.gov

W. Nie, K. (Kris) Iniewski (eds.), *Metal-Halide Perovskite Semiconductors*,
https://doi.org/10.1007/978-3-031-26892-2_2

would not be not a concern. A precisely controlled deposition rate is possible with CVD which can produce ultra-uniform layer.

2 Lab-Scale Thin-Film Fabrication

Spin coating is the most thoroughly investigated and optimized deposition method for perovskite thin-film fabrication. Briefly, a motor can rotate the substrate from a few hundred to thousands of rams per minute (RPM). Once a small quantity of precursor is dropped on the substrate, the motor starts to spin and the solvent evaporates as the spin speed increases. Once all the solvent escapes from the liquid, a solid film deposition is completed. Normally, a post-annealing step is needed to drive away all the residual solvent which also completes the perovskite crystallization. It is a prevailing approach for making small-area devices. Significant amounts of efforts are invested in thin-film crystallinity and uniformity control via spin-coating methods to produce high-quality optoelectronic devices. Since the perovskite optoelectronics typically have a thin absorber of <500 nm, making a uniform, high-quality film has a direct impact on the efficiency of the devices. Because 3D and 2D perovskites have different transport properties, different film-making strategies are employed. The next sections will introduce the different ways of making high-quality films for each structure.

2.1 3D Perovskite Thin-Film Deposition

The main challenge of making 3D perovskite thin film is obtaining full coverage, high degree of crystallinity, large grain size, and low surface roughness. If defects are not a concern in the thin film, once the correct perovskite phase is fully converted delivering the expected optical band gap and the film is uniformly produced with a low surface roughness (< 10 nm), the solar cells made with these films should output a high-power conversion efficiency. In reality, the pin hole, defects, and grain boundaries often play deterministic roles in the final performances. A perovskite thin-film device is typically made in a "sandwich" device architecture (Fig. 1a) where two doped contacts (called selective contacts) are placed on each side of the intrinsic perovskite layer forming a p-i-n junction. Thin metal films are deposited on top of the selective contacts serving as the metal leads for current signal readout. If a single pin hole is present in the film as illustrated in Fig. 1b, the current will directly flow between the top and bottom electrodes causing a current leakage in the diode.

To eliminate the pin hole problem, extensive thin-film fabrication methods have been reported. The most straightforward method is to directly coat perovskite precursor on the substrate. The precursor contains lead iodide (PbI_2) and organo-halide salt (e.g., methylammonium iodide, MAI) in a common organic solvent, such as

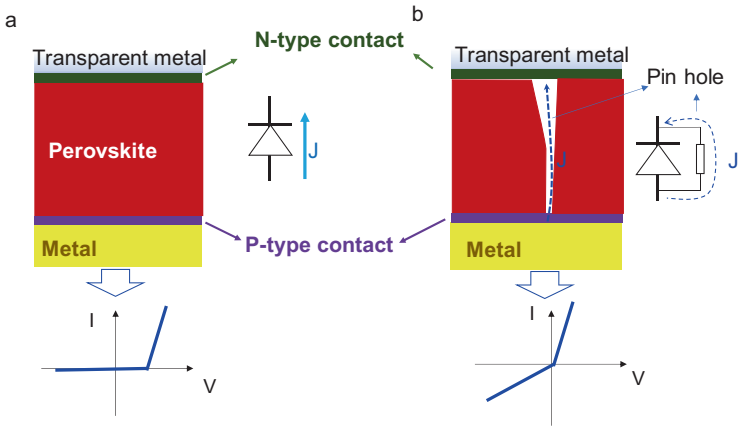

Fig. 1 Schematic illustration of an ideal thin-film device (a) and a device with pin hole (b). Their corresponding typical current-voltage characteristics are drawn below

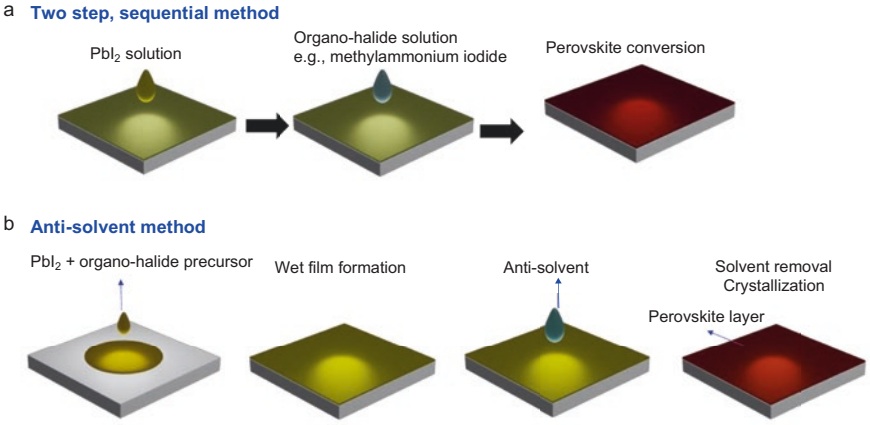

Fig. 2 Schematic illustration of the (**a**) two-step coating method and (**b**) antisolvent spin-coating method for producing uniform perovskite thin films

dimethylformamide (DMF), dimethyl sulfoxide (DMSO), or other polar solvents. Upon solvent removal, PbI_2 makes contact with MAI for perovskite phase conversion, and the perovskite crystalline grains start to grow. However, this method lacks control over the nucleation and reaction rate which often yields porous films. To circumvent this problem, more coating methods have been explored. The next method is called a "two-step" [1] fabrication approach as illustrated in Fig. 2a. In brief, PbI_2 solution is first coated on the substrate producing a pure PbI_2 thin film. After drying, an organo-halide precursor dissolved in a different organic solvent (usually an alcohol) is coated on the PbI_2 forming a double layer. A post-annealing step is performed after the two-step coating, promoting the perovskite phase

conversion in the wet film. And the annealing step also promotes a larger grain growth in the solid phase. This method will allow more control over the reaction and crystal growth rate in solid phase, yielding more uniform coating.

Another popular method that is currently widely employed is called "antisolvent" method. This approach is illustrated in Fig. 2. Briefly, a perovskite solution is first dropped on the substrate and spin coating starts. After the initial spinning stage, the precursor spreads over the substrate, and part of the solvent gets vaporized leaving a wet film. At a certain time stamp, an antisolvent that does not dissolve the perovskite precursor nor coordinate with the materials is quickly dropped onto the wet film. The antisolvent extracts the residual solvent that initiates the crystallization. After the spin-coating process, a post-annealing step is necessary to further promote the crystalline grain to grow. A variety of antisolvents have been investigated, most commonly used antisolvents include ether, toluene, chlorobenzene, etc. [2–5]. A proper choice of antisolvent is critical for making high-performance solar cells.

It is worth mentioning that to achieve the best film quality, a solvent additive such as DMSO is often added in the perovskite precursor in the "antisolvent" method. DMSO coordinates with the lead iodide in the precursor that retards the crystallization rate which is the key to fabricate uniform layers [6]. However, the DMSO-additive coupled with antisolvent method also possesses a narrow time window of producing high-quality film [7]. Specifically, the antisolvent must be dripped at a precise time stamp, i.e., 5–10 seconds after the high-speed coating starts. Once missing this time window, a porous structure can be produced which will harm the device performance [5, 8]. Although the antisolvent engineering and the two-step sequential solution deposition have been widely studied to realize the fabrication of high-performance small-area devices, these two approaches are not necessarily compatible with the high-throughput thin-film fabrications. For instance, the narrow time window of dripping the antisolvent can be a problem when producing larger panels. If the antisolvent does not arrive everywhere on the panel all at the desired time stamp, then high-quality film is not deposited through the full area of the panel. The resulting power conversion efficiency of the solar panel is capped by the poorest sub-cell.

To widen the time window, Zhao et al. [2] attempted to vary the DMSO ratio in the precursor which tuned the time window up to 25 seconds. They attributed it to the intermolecular hydrogen bonding forces in the precursor introduced by adding more DMSO that widened the time window. Similar fine tuning is reported by Chen et al. [9] and many others. Huang et al. reported an alternative solvent additive [5]; instead of using DMSO, the team used sulfolane as the retarding solvent. In this case, sulfolane coordinates with the organo-halide which further slowed down the reaction rate. As a result, the antisolvent dripping window was widened to over 90 seconds after spin coating. This allowed the team to fabricate a perovskite mini-module with a simpler dip-coating method with a high-power conversion efficiency over 16%. Other solvent additives like tert-butyl alcohol [10], 1,4,7,10,13,16-hexaoxacyclooctadecane [11], and others have been explored.

Apart from room temperature coating method, Nie et al. discovered a "hot-casting" method to fabricate crystalline layer with large grains. In particular, the team first preheated the perovskite precursor solution and substrate to coat perovskite thin films, which can produce high-quality, mm-scale large-grain perovskite thin films for reproducible perovskite solar cells [12–16]. This method also turned out to be useful for 2D perovskite thin-film deposition that will be elaborated in the next section.

2.2 2D Perovskite Thin-Film Fabrication

In 2016, Tsai et al. reported nearly single-crystal thin-film growth with controllable orientation for 2D lead halide perovskite materials [17–20]. Interestingly, the hot-cast 2D film showed near single crystalline crystal structures in the film, which is accompanied with a preferential orientation. Controlling the crystal alignment is essential to facilitate the charge transport, suppress the carrier recombination in the semiconductor, as well as improve the device operation stability under light and humidity conditions [17, 21, 22]. In this work, the crystal orientation and crystallinity of the 2D perovskite materials have been characterized by the powerful synchrotron grazing incidence wide-angle X-ray scattering (GIWAXS) [17, 18, 20, 23, 24].

Besides the temperature control, many other methods have been explored to fabricate 2D perovskite thin films with preferential orientations. Additives like molten salt and ammonium chloride have been added to the precursor which assisted the pure phase, vertically aligned 2D crystal growth in the thin film [25–28]. More recently, Chen et al. utilized strain engineering for epitaxial stabilization of halide perovskite thin films, which exhibit enhanced semiconductor device performance [29]. These studies have clearly shown that the quality of the grown perovskite crystals would greatly impact both the stability and performance of the optoelectronic devices.

3 Large-Scale Thin-Film Fabrication

To commercialize the perovskite photovoltaics, large-scale coating methods are needed to build panel scale (m^2) solar modules. While many mini-modules were produced by spin-coating methods, an issue that may result from the spin-coating process is the possible inhomogeneous crystalline structures as the device area increases. To address the inhomogeneity issue, the additive strategy, which can dramatically reduce the surface-property fluctuation, was developed. For example, an upscalable spin-coating manufacturing of perovskite module was found to be enabled by the NH_4Cl-additive strategy, and the high PCE values of 16.35% and 12.14% for modules with active areas of 22.4 cm^2 and 91.8 cm^2, respectively, were successfully demonstrated.

Besides the spin-coating process, D-bar, blade, and slot-die coating are solution-based deposition techniques that are compatible with continuous high-throughput thin-film fabrications. These methods are required for larger-scale (i.e., a few meter squares) panel manufacturing yielding an ultra-high uniformity. As a result, many research groups have tried to optimize this process and develop robust procedures for the fabrication of uniform and large-area perovskite thin films. For these techniques, solvent engineering is found to be crucial for realizing the deposition of a high-quality perovskite film. Besides, the air-knife technique, which enables the fast removal of the residual solvent during thin-film deposition, was also essential because it can significantly improve the film uniformity.

Among all the functional materials used in the module, forming a uniform thin film with desirable properties has been the most challenging for the light-harvesting perovskites. Although the antisolvent engineering and the two-step sequential solution deposition have been widely utilized to realize the fabrication of high-performance small cells, these two approaches are not necessarily compatible with the high-throughput thin-film fabrications.

Spin coating has been the most thoroughly investigated/optimized manufacturing process for perovskite thin-film fabrications. Therefore, it is still a preferable approach for making perovskite mini modules (e.g., modules with a photoactive area ≤ 25 cm^2). The main issue of the spin-coating process is that it results in a rougher and more inhomogeneous perovskite film comparing to those deposited via vapor depositions. In a study conducted by Tong, G. et al. [ref 3], the surface potential mappings obtained from $Cs_{0.05}FA_{0.54}MA_{0.41}Pb(I_{0.98}Br_{0.02})_3$ films fabricated via the two-step spin-coating process and thermal evaporation were compared. According to the Kelvin probe force microscopy (KPFM) images shown in Fig. 3a, the spin cast perovskite film has a more significant potential fluctuation (21.3 mV) than the thermal evaporated film (17.92 mV). To overcome the inherent surface inhomogeneity, Tong, G. et al. have developed an additive strategy to modify the surface morphology of the spin cast film. They demonstrated that if NH_4Cl additive was introduced into the perovskite precursor, the uniformity of the resultant perovskite film would be remarkable improved, yielding the smallest potential fluctuation (9.81 mV). An upscalable fabrication of perovskite module was therefore enabled by the additive strategy, as evidenced by the active area PCE of 16.35% and 12.14% for designated module area of 22.4 cm^2 and 91.8 cm^2, respectively.

D-bar coating is a solution-based deposition technique that is compatible with continuous high-throughput thin-film fabrications. Accordingly, many research groups have tried to replace the spin-coating process with the D-bar coating technique. In a recent study, Lim, K.-S. et al. successfully demonstrated a perovskite mini-module with an impressive PCE value of over 17% based on the D-bar coating technique. They verified that the key to successfully forming a high-quality $(FAPbI_3)_{0.875}(CsPbBr_3)_{0.125}$ film via D-bar deposition is introducing the Lewis base hexamethylphosphoramide (HMPA) additive into the precursor solution. Figure 3b shows the optical microscopy (OM) images obtained from the wet precursor films after different drying times. If dimethylformamide (DMF) was the only solvent used to prepare the perovskite ink, formation of the large precipitates would be

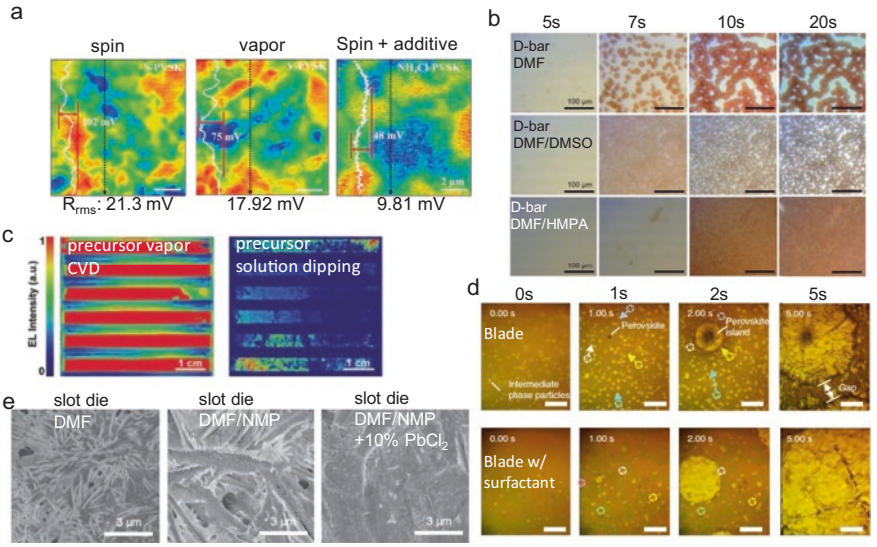

Fig. 3 Morphologies of perovskite thin films fabricated with scalable deposition tools. (**a**) KPFM mapping images showing surface potential fluctuations of the spin-cast and vapor-deposited perovskite films. The introduction of NH_4Cl additive was found to decrease the surface potential roughness from 21.3 mV to 9.81 mV, leading to the smallest surface potential fluctuation. [#3] (**b**) In situ OM images of wet precursor films deposited using the DMF, DMF/DMSO, and DMF/HMPA solutions. The island crystal growth was suppressed by the utilization of DMF/DMSO mixed solvent and eliminated by introducing the HMPA additive. [#8] (**c**) EL mapping images obtained from perovskite modules utilizing CVD and dip-cast perovskite films. The uniformly saturated EL signal in the sub-cell area confirmed the superior quality of the large-area CVD perovskite film. [#12] (**d**) In situ OM images acquired from the blade-cast perovskite films without and with surfactant. The introduction of the LP surfactant was found to remarkably increase the uniformity of the blade-cast film. [#30] (**e**) SEM images of the slot-die cast perovskite films using the DMF, DMF/NMP, and DMF/NMP with excess $PbCl_2$ inks. [#6] Fig. 3(**b–f**) was acquired from the original figures in the references and modified/reprinted with permissions

observed within 7 s. The large precipitates would subsequently lead to significant pinhole areas in the final perovskite film. It was also discovered that the pinhole density could be remarkably decreased by the utilization of DMF: dimethyl sulfoxide (DMSO) mixed solvent. Nevertheless, if a pinhole-free perovskite film is desired, introducing the HMPA additive into the solution would be required so the HMPA molecule could form a stable adduct intermediate phase with the precursor. The film uniformity was found to be dramatically improved due to the presence of the adduct intermediate phase. As a result, by using the HMPA-additive precursor, the D-bar coating technique had enabled the fabrication of a 17% perovskite mini-module with device area up to 25 cm^2.

Another promising perovskite thin-film deposition technique is chemical vapor deposition (CVD) that takes the advantage of forming perovskite films using vaporized precursors. Unlike the thermal evaporation process, which is another

vapor-based deposition technique that simultaneously introduces organic and inorganic precursors into the reacting chamber, the CVD process generally involves a pre-deposition of the inorganic precursor film (e.g., PbI_2) and a sequential conversion of the inorganic precursor into perovskite phase by exposing it to organic precursor vapors (e.g., FAI, MAI). The vapor-based sequential reaction route leads to a highly controllable crystallization process of the perovskite crystal, which is essential for achieving an ideal thin-film uniformity and a limited defect density over a large module area. As a result, many promising results of the large-area perovskite optoelectronics have been enabled by the CVD process.

4 Summary

This chapter summarizes the fabrication methods of perovskite photovoltaic devices. It is essential to obtain uniform, pin hole-free crystalline thin film to deliver high-performance solar cell. In lab-scale demonstration, spin coating is widely adapted for cell fabrication. One-step coating, two-step deposition, and antisolvent method are three typical ways of building high-quality layer for high-efficiency solar cell demonstrations. To achieve large-scale fabrication, alternative deposition tools such as blade coating, D-bar coating, slot-die coating, and chemical vapor deposition methods have been explored. The film morphology control has been a key challenge to obtain high efficiency. To further scale the perovskite photovoltaic technology to the commercial level, meter-scale fabrication method is needed. The film uniformity across the full area will be required to deliver a high efficiency.

References

1. Im, J.-H., et al. (2014). Morphology-photovoltaic property correlation in perovskite solar cells: One-step versus two-step deposition of CH3NH3PbI3. *APL Materials, 2*, 081510.
2. Zhao, P., et al. (2018). Antisolvent with an ultrawide processing window for the one-step fabrication of efficient and large-area perovskite solar cells. *Advanced Materials, 30*, 1802763.
3. Paek, S., et al. (2017). From nano- to micrometer scale: The role of antisolvent treatment on high performance perovskite solar cells. *Chemistry of Materials, 29*, 3490–3498.
4. Taylor, A. D., et al. (2021). A general approach to high-efficiency perovskite solar cells by any antisolvent. *Nature Communications, 12*, 1878.
5. Huang, H.-H., et al. (2021). A simple one-step method with wide processing window for high-quality perovskite mini-module fabrication. *Joule, 5*, 958–974.
6. Jeon, N. J., et al. (2014). Solvent engineering for high-performance inorganic–organic hybrid perovskite solar cells. *Nature Materials, 13*, 897–903.
7. Chen, C., et al. (2021). Understanding the effect of antisolvent on processing window and efficiency for large-area flexible perovskite solar cells. *Materials Today Physics, 21*, 100565.
8. Szostak, R., et al. (2019). Exploring the formation of formamidinium-based hybrid perovskites by antisolvent methods: In situ GIWAXS measurements during spin coating. *Sustainable Energy & Fuels, 3*, 2287–2297.

9. Chen, C., et al. (2022). Additive engineering in antisolvent for widening the processing window and promoting perovskite seed formation in perovskite solar cells. *ACS Applied Materials & Interfaces, 14*, 17348–17357.
10. Kim, Y. Y., et al. (2020). Roll-to-roll gravure-printed flexible perovskite solar cells using eco-friendly antisolvent bathing with wide processing window. *Nature Communications, 11*, 5146.
11. Kong, X., et al. (2021). Highly reproducible fabrication of perovskite films with an ultrawide antisolvent dripping window for large-scale flexible solar cells. *Solar RRL, 5*, 2000646.
12. Nie, W., et al. (2015). High-efficiency solution-processed perovskite solar cells with millimeter-scale grains. *Science, 347*, 522–525.
13. Tsai, H., et al. (2015). Optimizing composition and morphology for large-grain perovskite solar cells via chemical control. *Chemistry of Materials, 27*, 5570–5576.
14. Nie, W., et al. (2016). Light-activated photocurrent degradation and self-healing in perovskite solar cells. *Nature Communications, 7*, 11574.
15. Tsai, H., et al. (2017). Effect of precursor solution aging on the crystallinity and photovoltaic performance of perovskite solar cells. *Advanced Energy Materials, 7*, 1602159.
16. Nie, W., et al. (2018). Critical role of interface and crystallinity on the performance and photostability of perovskite solar cell on nickel oxide. *Advanced Materials, 30*, 1703879.
17. Tsai, H., et al. (2016). High-efficiency two-dimensional Ruddlesden–Popper perovskite solar cells. *Nature, 536*, 312–316.
18. Tsai, H., et al. (2018). Stable light-emitting diodes using phase-pure Ruddlesden–Popper layered perovskites. *Advanced Materials, 30*, 1704217.
19. Tsai, H., et al. (2020). Critical role of organic spacers for bright 2D layered perovskites light-emitting diodes. *Advanced Science, 7*, 1903202.
20. Tsai, H., et al. (2020). A sensitive and robust thin-film x-ray detector using 2D layered perovskite diodes. *Science Advances, 6*, eaay0815.
21. Tsai, H., et al. (2018). Design principles for electronic charge transport in solution-processed vertically stacked 2D perovskite quantum wells. *Nature Communications, 9*, 2130.
22. Tisdale, J. T., et al. (2020). Methylammonium Lead tribromide single crystal detectors towards robust gamma-ray photon sensing. *Advanced Optical Materials, 8*, 2000233.
23. Schlipf, J., et al. (2017). Structure of organometal halide perovskite films as determined with grazing-incidence X-ray scattering methods. *Advanced Energy Materials, 7*, 1700131.
24. Chen, A. Z., et al. (2018). Origin of vertical orientation in two-dimensional metal halide perovskites and its effect on photovoltaic performance. *Nature Communications, 9*, 1336.
25. Ren, H., et al. (2020). Efficient and stable Ruddlesden–Popper perovskite solar cell with tailored interlayer molecular interaction. *Nature Photonics, 14*, 154–163.
26. Liang, C., et al. (2021). Two-dimensional Ruddlesden–Popper layered perovskite solar cells based on phase-pure thin films. *Nature Energy, 6*, 38–45.
27. Zhang, X., et al. (2017). Vertically oriented 2D layered perovskite solar cells with enhanced efficiency and good stability. *Small, 13*, 1700611.
28. Zhang, X., et al. (2018). Orientation regulation of phenylethylammonium cation based 2D perovskite solar cell with efficiency higher than 11%. *Advanced Energy Materials, 8*, 1702498.
29. Chen, Y., et al. (2020). Strain engineering and epitaxial stabilization of halide perovskites. *Nature, 577*, 209–215.

Photophysics of Hybrid and Inorganic Lead Halide Perovskites

Masaru Kuno and Irina Gushchina

1 Introduction

This chapter focuses on the optoelectronic properties of hybrid and all-inorganic lead halide perovskites. Such materials adopt the chemical stoichiometry ABX_3 and are strong contenders for applications in solar photovoltaics. Among leading candidates are systems where the A cation is organic (e.g., methylammonium, $CH_3NH_3^+$, MA; formamidinium, $CH(NH_2)_2^+$, FA) or inorganic (e.g., Cs+), the B cation is Pb^{2+}, and the X anion is I^-, Br^-, or Cl^-. Important systems come from the methylammonium lead halide ($CH_3NH_3PbX_3$, or $MAPbX_3$), formamidinium lead halide [$CH(NH_2)_2PbX_3$, or $FAPbX_3$], and cesium lead halide ($CsPbX_3$) families. Alloys are also possible and $APbX_3$ materials can be produced as mixed cation, mixed anion, or even mixed cation/mixed anion alloys. Common mixed cation systems include A = FA/Cs or A = FA/MA alloys, e.g., $FA_{1-y}Cs_yPbI_3$ or $FA_{1-y}MA_yPbI_3$. Mixed anion materials are often mixtures of iodine and bromine such as $MAPb(I_{1-x}Br_x)_3$ and $FAPb(I_{1-x}Br_x)_3$ while mixed cation/anion systems include $FA_xMA_yCs_{1-x-y}Pb(I_{1-z}Br_z)_3$ (FAMACs).

Given prior discussion about the unique structural properties of ABX_3 materials, we simply recall here that $APbX_3$ perovskites adopt cubic/quasi-cubic structures at room temperature with corner sharing $[PbI_6]^{4-}$ octahedra and with A^+ cations (MA, FA, Cs) filling octahedral voids. Such structures satisfy the Goldschmidt tolerance factors required of ideal cubic structures ($0.9 \leq t \leq 1.0$) and for structures having tilted octahedra ($0.7 < t < 0.9$) [1]. The compositional diversity of mixed cation and mixed anion systems is limited by the existence of non-perovskite (δ_{ortho}- and δ_{hex}-phases) phases that appear when A^+ ionic radii are insufficient to stabilize interstitial voids in the structure [2, 3]. Although $APbX_3$ perovskites can adopt other (e.g.,

M. Kuno (✉) · I. Gushchina
University of Notre Dame, Notre Dame, IN, USA
e-mail: mkuno@nd.edu

W. Nie, K. (Kris) Iniewski (eds.), *Metal-Halide Perovskite Semiconductors*,
https://doi.org/10.1007/978-3-031-26892-2_3

orthorhombic) crystal structures at different temperatures [4], we focus on the photophysical properties of photovoltaically relevant cubic/pseudo-cubic structures in what follows.

The primary motivation for investigating and ultimately understanding the optical response of $APbX_3$ perovskites stems from their successful implementation in high-efficiency photovoltaics. Today, perovskite solar cell power conversion efficiencies (PCEs) routinely exceed 20%. A maximum PCE of 25.7% has been reported in NREL's benchmark efficiency chart [5] and will undoubtedly be supplanted shortly. These values collectively represent a remarkable rise of perovskite solar cell efficiencies given their modest starting value of 3.8% in 2009. In short, $APbX_3$ perovskite solar cells are, from a PCE perspective, on par with crystalline silicon.

Responsible for this success are extraordinary and fortuitous perovskite properties. This entails facile solution processability, crystallinity despite low temperature processing, chemical and stoichiometric diversity, and large absorption efficiencies, all simultaneously coupled to low exciton binding energies, large carrier mobilities, and favorable energetics to engender defect tolerance. However, despite extensive research into improving perovskite solar cell PCEs, performance bottlenecks still remain. This prevents them from reaching their full Shockley-Queisser efficiency of ~31% for single-junction devices. A need therefore exists to fully understand the fundamental optical and electrical properties of $APbX_3$ systems to realize their ultimate performance potentials.

2 Absorption

A key feature of lead halide perovskites is their favorable absorption properties. This includes sizable absorption coefficients (α), band edges close to the desired Shockley-Queisser value of 1.55 eV, and tunable absorption edges in mixed halide alloys. Figure 1a highlights these features by showing reported absorption spectra for common $APbX_3$ systems.

In the red, at approximately 1.6 eV lie $MAPbI_3$, $FAPbI_3$, and $CsPbI_3$. Near 2.2 eV are $MAPbBr_3$, $FAPbBr_3$, and $CsPbBr_3$. Further to the blue at ~3.1 eV is $MAPbCl_3$. The figure makes apparent that perovskite band gaps are sensitive to the choice of halide anion, whether I^-, Br^-, or Cl^-. This has previously suggested that the A-site cation plays a lesser role in determining the optical response of these materials. Instead, optical transitions are thought to be primarily established by perovskite's inorganic $[PbI_6]^{4-}$ framework [10]. This is supported by electronic structure calculations, which suggest A-site cation-related states being energetically removed from corresponding band edges. Cation-influenced octahedral tilting and lattice contraction [11] do, however, influence band edge energies, as evidenced by measurements on mixed cation perovskites such as $MA_{1-x}FA_xPbI_3$ or $FA_{1-x}Cs_xPbI_3$ where band gaps can be altered using cation stoichiometry [12–15].

Figure 1b further illustrates the sensitivity of perovskite band gaps to halide stoichiometry by showing how increasing the Br fraction (x) in a $MAPb(I_{1-x}Br_x)_3$ alloy

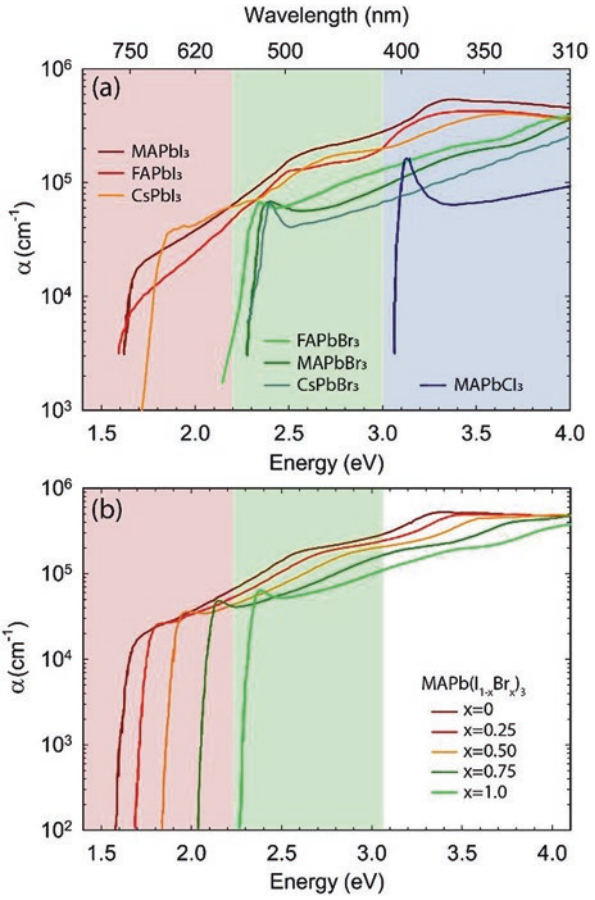

Fig. 1 Summary of the absorption spectra of various $APbX_3$ perovskites. Data extracted from References [6–9]. Spectral band edges highlighted using colored regions

causes its E_g to progressively shift towards the $MAPbBr_3$ limit. Analogous trends are observed with $MAPb(Cl_{1-x}Br_x)_3$ [16, 17] as well as with $FAPb(I_{1-x}Br_x)_3$ [18]. The formation of continuous $MAPb(I_{1-x}Cl_x)_3$ alloys is prevented by large differences in I^- and Cl^- ionic radii such that little if any Cl incorporation is achieved. Consequently, such systems are denoted $MAPbI_3(Cl)$ in what follows [19]. This ability to compositionally tune band gaps makes mixed halide alloys of potential use in tandem (perovskite/silicon) solar cells.

Figure 1 summarizes the absorption coefficients of these materials. Evident are sizable band edge values, which lie between 10^4 and 10^5 cm^{-1}. These α-values correspond favorably to those of other photovoltaically relevant semiconductors. To illustrate, GaAs has an absorption coefficient of $\alpha \sim 10^4$ cm^{-1} at its absorption edge. References [6, 20–22] highlight this favorable comparison by visually illustrating perovskite α-values relative to those of other semiconductors across a range of energies.

Table 1 summarizes compiled E_g and α-values for the various $APbX_3$ perovskites being discussed. Apart from the general trends noted above, there is a sizable variability in reported values. $MAPbI_3$ band gaps, for instance, range from 1.5 to

Table 1 Absorption parameters of various lead halide perovskites

System	E_g (eV)	E_b (meV)	$\alpha_{2.0\,eV}$ ($\times 10^5$ cm^{-1})	$\alpha_{2.3\,eV}$ ($\times 10^5$ cm^{-1})	$\alpha_{3.1\,eV}$ ($\times 10^5$ cm^{-1})
$MAPbI_3$	~1.5 [23] 1.55 [24, 25] 1.553 [26] 1.557 [27] 1.56 [28, 29] 1.574 [30] 1.59 [21, 31] 1.6 [32–35] 1.61 [36–38] 1.63 [39] 1.646 [40]	1.7–2.1 [31] 6 [41] 7.4 [42] 9 [43] 12.3 [40] 13.1 [44] 14–18 [45] 16–22 [46] 25 [47] 29 [48] 32 [49] 37 [50] 40 [51] 45 [52] 50 [53] 55 [54]	0.23 [24, 32] 0.24 [21] 0.26 [29] 0.38 [31, 55] 0.39 [36] 0.44 [56] 0.45 [26] 0.46 [23] 0.47 [33, 35] 0.50 [57] 0.58 [58] 0.60 [20] 0.66 [30, 38] 0.67 [20] 0.68 [25] 0.73 [39] 0.75 [59] 0.78 [46] 0.79 [37] 0.92 [28] 1.70 [34]	0.47 [32] 0.51 [29] 0.53 [24] 0.59 [21] 0.64 [31, 33] 0.86 [36] 0.91 [58] 0.93 [25] 0.94 [55] 0.95 [35] 1.01 [23] 1.04 [20, 26] 1.19 [56] 1.22 [38] 1.34 [59] 1.39 [46] 1.44 [39] 1.47 [30] 1.50 [37] 1.55 [28] 2.88 [34]	1.09 [29] 2.04 [25] 2.34 [21] 2.43 [58] 2.56 [24, 35] 2.76 [31] 2.80 [32] 2.86 [26] 2.89 [23] 2.94 [33] 2.99 [28] 3.02 [59] 3.15 [36] 3.24 [37] 3.31 [38] 3.33 [56] 3.38 [55] 3.51 [46] 3.68 [39] 4.19 [34] 4.51 [30]
$FAPbI_3$	1.45 [22] 1.55 [55] 1.566 [40]	8.4 [40] 10 [60] 31.6 [61]	0.25 [55] 0.43 [22]	0.71 [55] 1.62 [22]	3.59 [55] 4.52 [22]
$CsPbI_3$	1.738 [8]	20 [62]	–	0.71 [8]	2.34 [8]
$FAPbBr_3$	2.351 [40]	24 [60] 31.8 [40]	–	0.74 [63]	1.86 [63]
$MAPbBr_3$	2.24 [24] ~2.3 [56] 2.309 [64] 2.384–2.392 [40]	14 [65] 30.9–36.3 [40] 40.3 [44] 41 [66] 76 [53] 150 [67]	–	0.08 [55] 0.12 [24] 0.13 [56] 0.43 [64] 0.91 [63]	0.73 [64] 1.04 [24] 1.11 [55] 1.24 [56] 1.77 [63]
$CsPbBr_3$	2.3 [9] 2.37 [68] 2.39 [69] 2.4 [70]	40 [62]	–	0.02 [68] 0.13 [9] 0.23 [63] 0.31 [69] 0.57 [70]	0.78 [9] 0.89 [69] 1.02 [68] 1.36 [63] 1.45 [70]
$MAPbCl_3$	2.97 [24]	41 [71] 50 [72]	–	–	0.35 [24] 1.0 [55]

1.646 eV. This is also true of $MAPbBr_3$ where E_g-values range from 2.24 to 2.392 eV. In either case, E_g spreads are of order 150 meV.

Associated absorption coefficients are also highly variable, as evident from tabulated α-values compiled at three different energies (2.0 eV, 2.3 eV, and 3.1 eV). In particular, Table 1 shows that $MAPbI_3$ α-values at 2.0 eV range from 0.23 to

1.70×10^5 cm^{-1}. At 2.3 eV, α-values range from 0.47 to 2.88×10^5 cm^{-1}. Analogous variations exist with other perovskites. This variability and lack of accord are summarized visually in References [6, 36, 40, and 58].

Many reasons exist for apparent differences in reported optical parameters. Much has to do with variations in sample quality that stem from the numerous approaches used to prepare perovskite thin films. They include solution deposition (doctor blading, spray coating, slot-die coating, inkjet printing, etc.), solution deposition with solvent recrystallization (two-step spin-coating or antisolvent treatment), hot casting, chemical vapor deposition, and low-pressure vapor-assisted solution processing [73, 74]. Sample quality variability is especially highlighted when thin films are compared to $APbX_3$ single crystals, which possess larger grains, reduced morphological disorder, and correspondingly reduced surface roughness [75].

Consequently, what results are thin film/single crystal specimens that possess varying degrees of crystallinity, thicknesses, apparent grain sizes, surface roughness, etc. All lead to measurement variations. Fujiwara [6], for example, attributes reported E_g and α-value variations to surface roughness that introduces significant light scattering to spectroscopic ellipsometry measurements. This degrades subsequent model extraction of perovskite optical constants (i.e., frequency-dependent refractive indices and permittivities) and leads to an underestimation of perovskite band gaps. When such surface roughness variations are explicitly accounted for, a closer agreement between researcher-reported α and E_g values is realized.

Beyond band gaps and absorption coefficients, Fig. 1 reveals other intriguing features of $APbX_3$ materials. For $MAPbI_3$, $FAPbI_3$ and $CsPbI_3$, band edges resemble those of bulk, direct gap semiconductors. No apparent excitonic features are seen. The absence of an excitonic response is corroborated by numerous estimates of their exciton binding energies (E_b), as summarized in Table 1. These estimates arise from magnetoabsorption and temperature-dependent emission and absorption measurements as well as from modeling experimental $APbX_3$ band edge absorption spectra with Elliott's model [76].

Table 1 shows a spread of reported E_b values. As with E_g and α, large variations can be seen where for $MAPbI_3$ E_b ranges from 1.7 to 55 meV. Despite this, reported binding energies are of order kT and suggest that the optical response of $MAPbI_3$ and $FAPbI_3$ can be described in terms of free carriers. This conclusion is corroborated by time-resolved emission, transient differential absorption, and THz conductivity studies [76]. Note that this is not necessarily true of Br- and Cl-based $APbX_3$ materials such as $CsPbBr_3$ or $MAPbCl_3$ where prominent band edge excitonic features are seen in the linear absorption. The suggestion is supported by their generally larger E_b-values in Table 1.

The specific origin of the optical transitions in lead halide perovskites has been the subject of numerous studies. Most entail density functional theory calculations to varying degrees of approximation [24, 36, 77]. Without delving into specifics, consensus exists that valence to conduction band transitions occurs at the R symmetry point and involves valence bands that originate from the antibonding combination of halide p and Pb(6s) orbitals. Corresponding conduction bands largely arise from Pb(6p) orbitals [77]. These bands are also responsible for above gap

transitions and produce apparent structure at higher energies. For example, a feature in the absorption spectrum of $MAPbI_3$ close to 2.5 eV (Fig. 1) is attributed to a valence/conduction band transition at the M symmetry point [24, 76, 77]. The antibonding nature of the $APbX_3$ valence band is supported by apparent increases in perovskite band gap with increasing temperature. This contrasts itself to the response of traditional, tetrahedrally coordinated semiconductors where band gaps decrease (increase) with increasing (decreasing) temperature.

3 Carrier Dynamics

Having briefly summarized the general absorptive properties of $APbX_3$ perovskites, we now provide insight into their carrier recombination processes, following photoexcitation. This is important since the fate of photogenerated carriers is fundamental to device operation and ultimately to their efficiencies. A kinetic model is therefore developed that qualitatively and quantitatively rationalizes the intrinsic photophysics of $APbX_3$ systems [47, 78]. This includes experimental observations of photoluminescence, time-correlated emission decays, and transient differential absorption dynamics. In addition to numerical simulations, analytical approximations are provided to better visualize qualitative trends in both emission intensities and time-correlated decays. Although the model does not explicitly consider device operation, interested readers may refer to Reference [79] for an extension that includes charge extracting interfaces. Such a model has been used to establish the performance bottleneck(s) of a high-efficiency FAMACs solar cell.

In general, the primary recombination processes considered are (a) bimolecular (radiative) electron-hole recombination, (b) carrier trapping, and (c) nonradiative Auger recombination. The latter is nominally only important at high carrier densities, far beyond 1 sun conditions. These processes are summarized in Fig. 2 with the

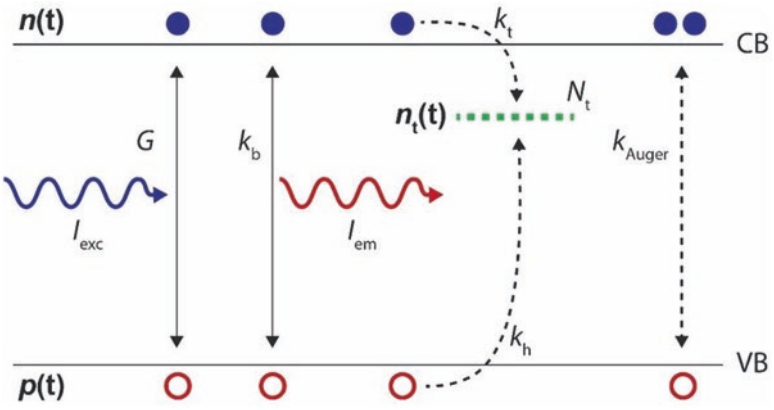

Fig. 2 Schematic illustration of photophysical processes occurring in lead halide perovskites, following photoexcitation

illustration showing photoexcitation creating transient electron and hole populations [$n(t)$ and $p(t)$] in the perovskite conduction and valence bands. Carriers subsequently recombine via the three processes outlined above. Although the identity of $APbX_3$ trap states remains debated, there appears to be some agreement that such states are electron traps. This is assumed in what follows. Note that other versions of this model exist, which account for exciton dissociation, unintentional doping, and carrier diffusion. The interested reader is therefore referred to References [80], [81], and [49] for details.

Kinetic expressions that summarize the model are

$$\begin{aligned}\frac{dn}{dt} &= G - k_t\left(N_t - n_t\right)n - k_b np - \frac{1}{2}k_{\text{Auger}}\left[n^2 p + np^2\right]\\ \frac{dp}{dt} &= G - k_h n_t p - k_b np - \frac{1}{2}k_{\text{Auger}}\left[n^2 p + np^2\right]\\ \frac{dn_t}{dt} &= k_t\left(N_t - n_t\right)n - k_h n_t p\end{aligned} \tag{1}$$

where G is the initial charge generation rate (cm^{-3} s^{-1}), linked to the excitation intensity (I_{exc}, W cm^{-2}), i.e., $G = \frac{I_{exc}\alpha}{h\nu}$ with α the absorption coefficient (cm^{-1}) and $h\nu$ the photon energy (J), n (p) is the electron (hole) concentration (cm^{-3}) in the perovskite conduction (valence) band, k_t is an electron trapping rate constant (cm^3 s^{-1}), N_t is a corresponding trap density (cm^{-3}), n_t is the trap population (cm^{-3}), k_b is a bimolecular radiative recombination rate constant (cm^3 s^{-1}, referred to as k_2 in the literature), and k_{Auger} is the Auger, three-carrier rate constant (cm^6 s^{-1}, referred to as k_3 in the literature).

Numerous studies now provided estimates for the various rate constants in Eq. (1) and Fig. 2. These literature estimates are summarized in Table 2 across various $APbX_3$ systems. An inspection shows that most work has focused on $MAPbI_3$ and $MAPbI_3$(Cl) thin films with relatively less work carried out on corresponding FA-based materials.

Table 2 also makes apparent that while variations in rate constants exist across systems and even within a given material, there is general consistency in their values. Bimolecular radiative rate constants are of order 10^{-10} cm^3 s^{-1}, while Auger rate constants are of order 10^{-28} cm^6 s^{-1} [85]. Measured pseudo-first-order rate constants for electron trapping are of order $k_1 \sim 10^7$ s^{-1} from where corresponding k_t values are of order $k_t \sim 10^{-10}$ cm^3 s^{-1}, provided estimated trap densities of order $N_t \sim 10^{-16}$ cm^{-3}.

The general photogenerated carrier dynamics, predicted by Eq. (1) at different excitation intensities, are now illustrated. Implicit to the discussion is continuous wave (CW) excitation. An identical analysis can be conducted assuming pulsed excitation. However, this is not pursued here since common applications of perovskite materials generally entail CW excitation conditions. Interested readers may refer to References [97] and [98] for details of a pulsed excitation analysis.

Table 2 Literature rate constants for various lead halide perovskites

	$MAPbI_3$	$MAPbI_3(Cl)$	$MAPbBr_3$	$FAPbI_3$	$FAPb(I_{1-x}Br_x)_3$	$FAPbBr_3$	FAMACs
$k_1 \approx k_t N_t$ ($\times 10^7$ s^{-1})	0.091 (TOPO) [82] 0.66 [82] 0.72–1.3 [83] 1.4–1.5 [84] 1.5 [85, 86] 1.8 [87]	0.49 [84] 1.2 [85] 1.2 [88]	–	0.7 [85]	–	2.1 [85]	0.4 [89]
N_t ($\times 10^{16}$ cm^{-3})	10^{-4}–10^{-3} (emissive) [90] 0.90–86 [78] 5.0–16 [59] 6.0 [80]	<0.05 [80] <0.1–4.0 [91] 1.0 [92] 2.5 [81]	–	–	–	–	0.54–60 [79]
k_b ($\times 10^{-10}$ cm^3 s^{-1})	0.1–1.0 [86] 0.35 [82] 0.4 (TOPO) [82] 0.60 [85] 1.5 [93] 1.7 [87] 3.5 [80] 6.0 [94] 6.2–37 [83] 9.2–9.4 [84] 13 [49] 23 [95]	0.23–0.78 [91] 0.87 [84] 1.1 [85, 88] 4.9 [80] 11 [96]	4.9 [93]	1.1 [85]	1.0–30 [18] (x = 0–1)	11 [85]	0.30 [89]
k_{Auger} ($\times 10^{-28}$ cm^6 s^{-1})	0.37–1.3 [84] ~1 [86] 1.6 [85] 3.4 [93] ~10 [94]	0.20 [85] 0.23 [88] 0.99 [84] 3.8 [96]	13.5 [93]	0.20 [85]	0.20–1.5 [18] (x = 0–1)	1.5 [85]	0.01 [89]

4 Low Excitation Intensities

At low excitation intensities, carrier trapping dominates radiative recombination. Low photogenerated carrier densities further mean that nonradiative Auger pathways can be ignored. Consequently, under the assumption that the material is intrinsic, Eq. (1) reduces to

$$\frac{dn}{dt} \approx G - k_t N_t n$$
$$\frac{dp}{dt} \approx G - k_h p^2$$

The equations make apparent that at steady state $n = \frac{G}{k_t N_t} \propto G$ and $p = \sqrt{\frac{G}{k_h}} \propto \sqrt{G}$. Since the emission rate and corresponding intensity, I_{em}, are proportional to the product of n and p, I_{em} grows with increasing I_{exc} (G) in a power law fashion. Its growth exponent is ~3/2, i.e., $I_{em} \propto G^{\frac{3}{2}}$.

Figure 3a illustrates this for the case where $N_t = 10^{16}$ cm^{-3}. Employed rate constants for the numerical simulation of Eq. (1) are $k_b = 10^{-10}$ cm^3 s^{-1}, $k_t = 10^{-9}$ cm^3 s^{-1}, $k_h = 10^{-11}$ cm^3 s^{-1}, and $k_{Auger} = 10^{-28}$ cm^6 s^{-1}. The model therefore reveals that I_{em} grows as $G^{1.6}$ at low G where recombination is primarily trap-mediated (shaded red region). Figure 3b shows identical behavior for simulations where N_t has been varied between $N_t = 10^{15}$ and 10^{18} cm^{-3}. In all cases, fit-extracted growth exponents range from $m = 1.5$ to 1.6. Of note is the increasing range of G-values where $m \sim 1.5$. This is rationalized by delayed trap saturation due to larger N_t-values.

Figure 3c shows experimental data for a $MAPbI_3$ single crystal and thin film [78] that corroborate these model predictions. Acquired over ~3 orders of magnitude in G, the data reveal $m \sim 1.5$ power law growth exponents for either material, as established by fits to low G I_{em}-values (dashed lines with fit-extracted m-values shown). Differences in the range of I_{em}-values over which $m \sim 1.5$ qualitatively agree with Fig. 3b and suggest underlying N_t-value variations between $MAPbI_3$ single crystals and thin films. Other data acquired on $MAPbI_3$ and $MAPbI_3$(Cl) over 8 orders of magnitude in G reveal identical $m \sim 1.5$ power law growth exponents at low G [47]. This further corroborates the analysis and conclusions drawn here. Note that under (low irradiance) *pulsed* excitation, analogous power law growth of the integrated emission intensity is predicted with an ideal model growth exponent of $m = 2.0$ [97, 98]. Such quadratic emission growth has previously been observed for $MAPbI_3$ and $MAPbI_3$(Cl) thin films [47].

Next, by assuming above-simplified kinetic expression for n and p, corresponding (normalized) photoluminescence decays take the form

$$\mathrm{PL}(t) = \frac{I_{em}(t)}{I_{em,max}} \approx \frac{e^{-k_t N_t t}}{1 + k_h G t}. \quad (2)$$

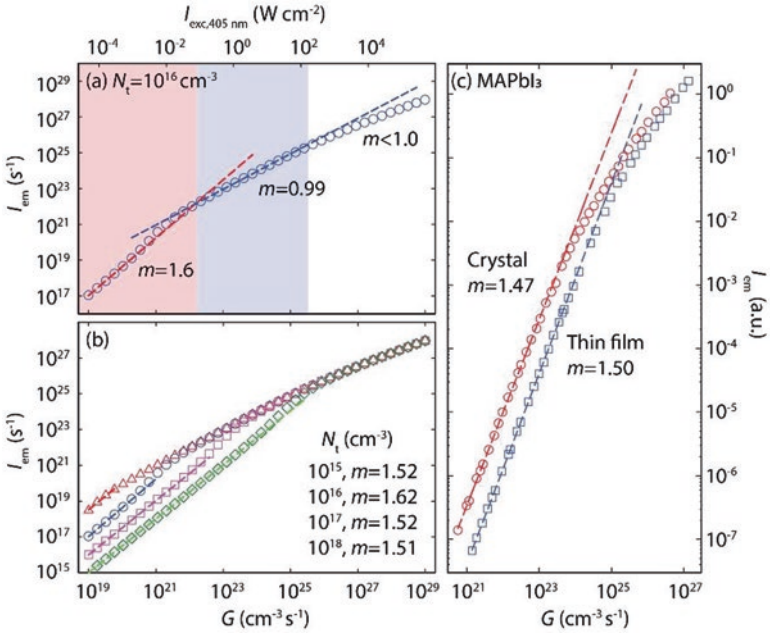

Fig. 3 (**a**) I_{em} versus G for $N_t = 10^{16}$ cm^{-3}. Dashed lines are linear fits to the data in a given growth regime (shaded regions). Fit-extracted growth exponents shown. G-values are linked to associated I_{exc}, assuming 405 nm excitation with $\alpha = 10^5$ cm^{-1}, for reference purposes. (**b**) I_{em} versus G for N_t varying between $N_t = 10^{15}$–10^{18} cm^{-3}. Dashed lines are linear fits in the trap-mediated recombination regime. Fit-extracted growth exponents shown. (**c**) I_{em} versus G data for a $MAPbI_3$ single crystal and thin film. Data from Reference [78]. Dashed lines are fits to the data at smaller G with fit-extracted growth exponents shown

At small G or short times, the numerator in Eq. (2) dominates. Decays are therefore near exponential with an associated pseudo-first-order decay constant of $k_t N_t \sim 10^7$ s^{-1} (Table 2). Figure 4a illustrates this for the model predicted decay when $G = 10^{15}$ cm^{-3}. An accompanying (superimposed) dotted line is Eq. (2). This qualitative prediction is supported by numerous studies, which report near exponential decays at low I_{exc} for various perovskite systems [80, 81, 84, 87, 99].

5 Intermediate Excitation Intensities

As I_{exc} increases, progressive trap filling ($n_t \rightarrow N_t$) reduces the electron trapping rate such that $n \rightarrow p$. This simplifies Eq. (1) and leads to the following effective rate expressions:

$$\frac{dn}{dt} \approx G - k_b n^2$$

$$\frac{dp}{dt} \approx G - k_h N_t p - k_b p^2.$$

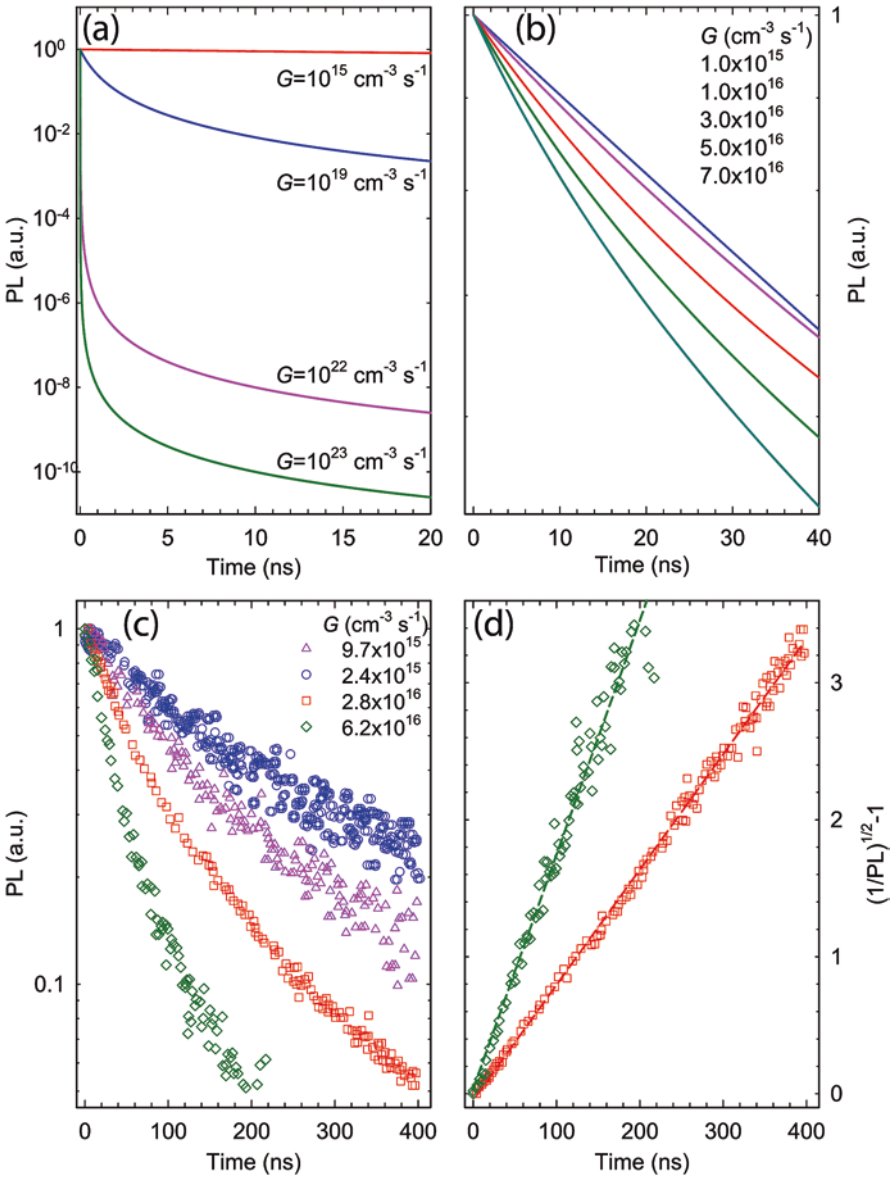

Fig. 4 (**a**) Predicted PL decays from Eq. (1) for variable G between $G = 10^{15}$ and 10^{23} cm^{-3}. Superimposed over the data are analytical predictions from Eqs. (2)–(4) (dotted lines). (**b**) Predicted decays for $G = 10^{15}$–7×10^{16} cm^{-3}. (**c**) $MAPbI_3$ PL decays from Reference [87]. (**d**) Large G $MAPbI_3$ PL decays from Reference [87] replotted. Dashed lines are linear fits to the data

Invoking steady state conditions then means that $n = \sqrt{\frac{G}{k_b}} \propto \sqrt{G}$ with $p = \frac{-k_t N_t + \sqrt{(k_t N_t)^2 + 4G}}{2} \propto \sqrt{G}$. The emission intensity therefore transitions to power law growth with a growth exponent of $m \sim 1$. Figure 3a illustrates this transition by showing a fit to the model data, highlighted in the shaded blue region. A fit-extracted power law growth exponent of $m = 0.99$ is found. Analogous behavior is observed in Fig. 3b when N_t is varied between 10^{15} and 10^{18} cm^{-3}. In whole, the model data makes evident that increasing N_t extends the region of trap-mediated recombination ($m \sim 1.5$) to larger G-values before bimolecular (radiative) recombination ($m \sim 1.0$) dominates carrier dynamics following photoexcitation.

Using the above simplified rate expressions, associated (normalized) photoluminescence decays adopt the following bimolecular form:

$$\mathrm{PL}(t) = \frac{I_{\mathrm{em}}(t)}{I_{\mathrm{em,max}}} = \frac{1}{(1 + k_b G t)\left[1 + (k_t N_t + k_b G t)\right]} \tag{3}$$

where Fig. 4a shows model-predicted decays for $G = 10^{19}$ and $G = 10^{22}$ cm^{-3} using the same parameters employed earlier at low I_{exc}. Analytical results from Eq. (3) are superimposed atop the model decays and are in excellent agreement. Model decays also highlight the transition in kinetic response in this I_{exc} regime. Figure 4b illustrates this for G-values between $G = 10^{16}$ and 10^{17} cm^{-3} where for smaller G-values, near exponential behavior is seen. With increasing G, an apparent near exponential to bimolecular transition occurs. Such PL(t) transitions have previously been reported in the literature [80, 81, 87, 99] and an example from a $MAPbI_3$ thin film is shown in Fig. 4c.

6 High Excitation Intensities

At sufficiently high excitation intensities, trap saturation causes bimolecular (radiative) recombination to dominate. In this limit, Eq. (1) effectively becomes

$$\frac{dn}{dt} \approx G - k_b n^2$$
$$\frac{dp}{dt} \approx G - k_b p^2$$

so that $n = p = \sqrt{\frac{G}{k_b}} \propto \sqrt{G}$. I_{em} thus continues to grow in a power law fashion with a growth exponent of $m \sim 1$. Figure 3 illustrates this for $N_t = 10^{16}$ cm^{-3} (Fig. 3a) and across N_t-values between $N_t = 10^{15}$ and 10^{18} cm^{-3} (Fig. 3b). It should be mentioned that a growth exponent of $m \sim 1$ is common to this intensity regime under pulsed excitation [47, 97, 98].

An associated (normalized) photoluminescence decay takes the bimolecular form

$$\mathrm{PL}(t) = \frac{I_{\mathrm{em}}(t)}{I_{\mathrm{em,max}}} \approx \frac{1}{\left(1 + k_b G t\right)^2}, \tag{4}$$

which is near identical to the expression derived earlier for intermediate excitation intensities (Eq. 3). Figure 4a plots a model-predicted decay for $G = 10^{23}$ cm^{-3} with Eq. (4) superimposed. Again, there is excellent agreement with the analytical approximation.

Beyond bimolecular fits, predicted bimolecular decays can be confirmed visually by plotting $\sqrt{\frac{I_{\mathrm{em,max}}}{I_{\mathrm{em}}(t)} - 1}$ versus time. In this case, linear behavior is expected [100]. Figure 4d illustrates this for the large G experimental data in Fig. 4c. Evident linear behavior is observed, as highlighted by dashed, linear fits.

Above this excitation regime, the onset of Auger-mediated nonradiative recombination causes emission efficiencies to decrease. This stems from competitive, nonradiative recombination of carriers. What results then is sublinear growth of I_{em} with an associated power law growth exponent $m < 1$. Figure 3a explicitly illustrates the onset of Auger recombination for $N_t = 10^{16}$ cm^{-3} at high G where the simulated data shows $m < 1$. It can also be shown that in this regime, plotting $\left[\frac{I_{\mathrm{em,max}}}{I_{\mathrm{em}}(t)} - 1\right]$ versus time yields linear behavior [100].

7 Emission Quantum Yields

Equation (1) simultaneously allows internal emission quantum yields (QYs) to be estimated through the ratio of the bimolecular radiative recombination rate to the initial carrier generation rate, i.e.

$$\mathrm{QY} = \frac{k_b np}{G}. \tag{5}$$

The importance of this metric is that high emission efficiencies are requisite for optimizing $APbX_3$ photovoltaic performance. More specifically, it is the associated external quantum efficiency (EQE, EQE = η_eQY where η_e is a photon extraction efficiency) that is fundamentally linked to the maximum open circuit voltage (and PCE) achievable in a solar cell [101]. The seemingly contradictory conclusion that arises then is that a good solar cell must also be a good light emitter [102].

Figure 5 shows model-predicted (internal) QYs plotted as functions of N_t when N_t is varied between 10^{15} cm^{-3} and 10^{18} cm^{-3}. As with Figs. 3 and 4, employed rate constants have been kept constant at their nominal literature values of $k_b \sim 10^{-10}$ cm^3 s^{-1}, $k_t \sim 10^{-9}$ cm^3 s^{-1}, and $k_h \sim 10^{-11}$ cm^3 s^{-1}. Fig. 5 also provides model-predicted EQEs via $\mathrm{EQE} = \frac{\eta_e (k_b np)}{G}$.

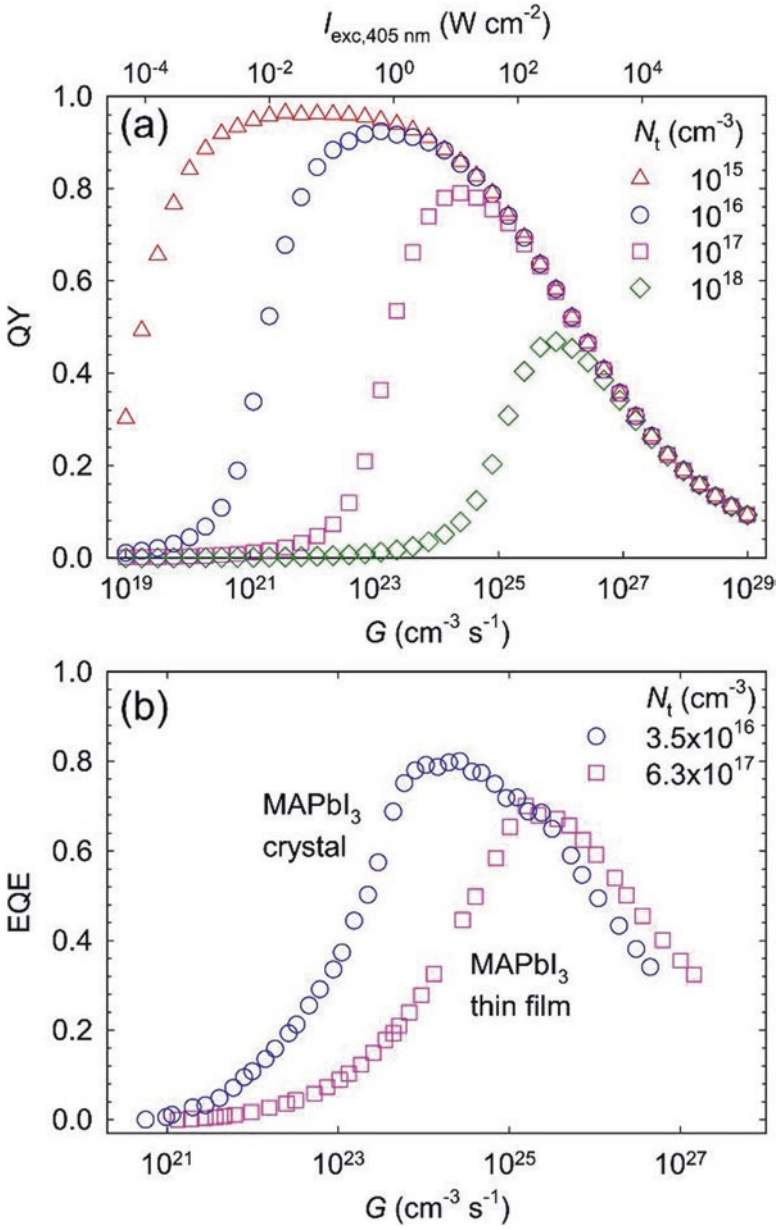

Fig. 5 (**a**) Predicted (internal) QYs for variable G between $G = 10^{19}$–10^{27} cm^{-3} and N_t between 10^{15} and 10^{18} cm^{-3}. For reference purposes, G-values are linked to associated I_{exc} assuming 405 nm excitation with $\alpha = 10^5$ cm^{-1}. (**b**) Experimental EQE estimates for a $MAPbI_3$ single crystal and thin film. Data from Reference [78]. Fit extracted N_t-values shown

Table 3 Literature $APbX_3$ emission EQEs under effective 1 sun conditions. Additives shown in parenthesis: K = potassium, Rb = rubidium, TOPO = trioctylphosphine oxide, pyr = pyridine, TPPO = triphenylphosphine oxide, SPPO = 9,9-spirobifluoren-2-yl-diphenyl-phosphine oxide)

Material	EQE film (%)	EQE film treated (%)	EQE device (%)
$MAPbI_3$	0.92 [103] 3 [82] 5 [104] 5.8 [78] 10 [105]	12–13 (TOPO) [106] 20.3 (TOPO) [103] 35 (TOPO) [82]	5 [106]
$MAPbI_3(Cl)$	20 [104] 50–60 [107]	24–25 (pyr) [108]	–
$MAPbBr_3$	2–3 [109] 15 [104]	1.2 [110] 32 (TPPO) [111] 85 (SPPO) [111]	–
FAMACs	2.4 [112] 66 (K) [113]	3.6 (Rb) [112]	0.43–2.83 [79] 14.5 (K) [113]
$FAMAPb(I_{1-x}Br_x)_3$	-	-	0.1–3.0 [114]

The resulting figure illustrates several things. First, as discussed earlier, at low I_{exc}, trapping dominates carrier recombination. This leads to low QYs. Attesting to this are experimental perovskite, 1 sun EQEs in Table 3. Values for thin films, (surface) treated thin films, and devices are shown. Inspection of the data reveals that reported 1 sun EQEs are generally on the order of several percent with some notable exceptions. This is consistent with the lower QYs seen at low G in Fig. 5. Of note is that this bulk perovskite data contrasts itself to analogous results, summarized in Reference [115] for perovskite nanocrystals (NCs). In these materials, EQEs regularly approach or attain unity values.

Next, Table 3 shows that treating lead halide perovskite thin films with Lewis bases such as trioctylphosphine oxide (TOPO) or pyridine improves their EQEs. However, they only increase values to numbers of order 10%. This indicates that while defect passivation is possible, significant trap densities still remain. This is again unlike the case of perovskite NCs where effective surface passivation does appear possible and which leads to unity EQEs [116]. Finally, Table 3 shows that device EQEs are all suppressed from corresponding thin film or treated thin film values due to the inevitable competition for carriers by electron and hole extraction interfaces present in working devices.

Figure 5 shows that maximal QYs are achieved upon trap saturation at high excitation intensities. In the case where $N_t = 10^{16}$ cm^{-3}, near unity internal QYs are realized close to 1 sun conditions. The figure further shows that increasing N_t simply leads to progressively larger I_{exc}-values required to achieve peak QYs, which themselves become progressively smaller. In all cases, maximum QYs persist until a critical G beyond which the onset of Auger-mediated carrier recombination causes them to fall as discussed earlier.

This QY behavior has previously been modeled by reducing the kinetics in Eq. (1) to [85].

$$\frac{dN}{dt} = G - \mathrm{AN} - \mathrm{BN}^2 - \mathrm{CN}^3. \tag{6}$$

In Eq. (6), N is an effective electron-hole density, A is a generic first-order rate constant that describes nonradiative, trap-mediated recombination of photogenerated carriers, B is a second-order (radiative) rate constant, and C is a third-order rate constant that accounts for nonradiative Auger recombination. The rate constants A, B, and C are effectively k_1, k_b, and k_{Auger} in Table 2. A corresponding internal QY is then

$$\mathrm{QY} = \frac{\mathrm{BN}^2}{\mathrm{AN} + \mathrm{BN}^2 + \mathrm{CN}^3}. \tag{7}$$

Equation (7) can be recast in terms of EQE via $\mathrm{EQE} = \dfrac{\eta_e \mathrm{BN}^2}{\mathrm{AN} + \eta_e \mathrm{BN}^2 + \mathrm{CN}^3}$. In either case, a peak QY can be found by taking the derivative of QY (EQE) with respect to N to find a critical point (i.e., $\dfrac{d\mathrm{QY}}{dN} = \dfrac{d\mathrm{EQE}}{dN} = 0$) [85]. A resulting optimal carrier density (N_{opt}) is then

$$N_{\mathrm{opt}} = \sqrt{\frac{A}{C}} \sim \sqrt{\frac{k_1}{k_{\mathrm{Auger}}}} \tag{8}$$

and is linked to a corresponding maximum internal QY of

$$\mathrm{QY}_{\mathrm{max}} = \frac{1}{1 + \dfrac{2\sqrt{AC}}{B}} \sim \frac{1}{1 + \dfrac{2\sqrt{k_1 k_{\mathrm{Auger}}}}{k_2}} \tag{9}$$

with a corresponding maximum EQE of $\mathrm{EQE}_{\mathrm{max}} = \dfrac{1}{1 + \dfrac{2\sqrt{AC}}{\eta_e B}} \sim \dfrac{1}{1 + \dfrac{2\sqrt{k_1 k_{\mathrm{Aug}}}}{\eta_e k_2}}$.

Equations (6) and (7) can be used to model experimental EQEs to extract relevant rate constants. They are, however, not predictive in that tabulated rate constants from Table 2 cannot be used to estimate QYs and EQE a priori. This is because Figs. 3–5 show that trap saturation occurs due to $n_t \rightarrow N_t$. Consequently, the pseudo-first-order trapping rate constant (here A) is I_{exc}-dependent. Immediate application of Eqs. (8) and (9) therefore leads to predicted N_{opt} and $\mathrm{QY}_{\mathrm{max}}$ smaller than those revealed by full numerical simulations of Eq. (1) (Fig. 5).

Finally, beyond trap-mediated recombination, an important reason for small overall EQE values and for why EQEs are smaller than internal QYs is photon trapping within the perovskite. This originates from refractive index differences with the surrounding medium and is most prominent in $APbX_3$ films and crystals where physical sizes approach the wavelength of light. This leads to estimated photon extraction efficiencies of $\eta_e \sim 10\%$ [104, 105]. Note that such trapping is not significant for NCs as they effectively behave as dipole emitters. This rationalizes why unity/near unity EQEs are readily seen with these materials [115].

8 Ion Migration

Finally, despite all of the notable properties of $APbX_3$ materials, preventing their widespread commercialization is their well-known environmental sensitivities. Addressing this have been a number of studies [117, 118]. Less recognized but equally important are intrinsic instabilities linked to ion migration. Namely, both cations and anions in $APbX_3$ materials are mobile with ion mobilities stemming from vacancy-mediated ion migration under bias or under illumination.

For cations, evidence for bias-induced A^+ migration comes from observed device hysteresis thought to stem from cation accumulation at electrodes [119–121]. The phenomenon is better illustrated using more direct measurements such as time-of-flight secondary ion mass spectrometry and super-resolution infrared absorption measurements [122, 123], which explicitly reveal cation migration and accumulation near electrodes.

For anions, a well-known phenomenon is light-induced photosegregation whereby shining light on mixed I^-/Br^- systems [e.g., $MAPb(I_{1-x}Br_x)_3$] induces halide segregation. This results in the formation of I-rich inclusions within parent, mixed halide perovskites. Such photoinduced halide segregation is experimentally observed as progressive photoluminescence redshifts due to photogenerated carriers being funneled to I-rich domains. Such domains act as emissive recombination centers because of favorable (valence) band offsets relative to those of parent mixed halide materials. Observed redshifts/photosegregation are reversible when specimens are no longer illuminated with remixing being entropically driven. References [4, 124, and 125] provide more details on the phenomenon.

At this point, an inevitable question that arises is the connection between the earlier photocarrier dynamics and the bias−/light-induced ion migration described here. Since ion migration, whether cation or anion, is thought to be vacancy-mediated and since point defects are likely responsible for carrier trapping, a connection between the two is suggested. Evidence for this can already be found in the literature where References [126, 127, and 128] already suggest that decreasing defect densities mitigates ion migration. Studies linking the two topics, however, are limited. Consequently, more work is required to establish a comprehensive picture of ion-inclusive carrier dynamics that follow photoexcitation of $APbX_3$ systems. As such, linking the two sets the direction for future investigations of these unique materials.

References

1. Goldschmidt, V. (1926). Die Gesetze der Krystallochemie. *Die Naturwissenschaften, 14*, 477–485.
2. Manser, J., Christians, J., & Kamat, P. (2016). Intriguing optoelectronic properties of metal halide perovskites. *Chemical Reviews, 116*, 12956–13008.
3. Stoumpos, C., & Kanatzidis, M. (2015). The renaissance of halide perovskites and their evolution as emerging semiconductors. *Accounts of Chemical Research, 48*, 2791–2802.
4. Brennan, M., Ruth, A., Kamat, P., & Kuno, M. (2020). Photoinduced anion segregation in mixed halide perovskites. *Trends in Chemistry, 2*, 282–301.
5. Best research-cell efficiency chart [Internet]. Nrel.gov. 2022 [cited 26 January 2022]. Available from https://www.nrel.gov/pv/cell-efficiency.html.
6. Fujiwara, H., Kato, M., Tamakoshi, M., Miyadera, T., & Chikamatsu, M. (2018). Optical characteristics and operational principles of hybrid perovskite solar cells. *Physica Status Solidi (a), 215*, 1700730.
7. Fujiwara, H., & Collins, R. W. (2018). Organic-inorganic hybrid perovskites. *Spectroscopic Ellipsometry for Photovoltaics, 2*, 471–493.
8. Yan, W., Guo, Y., Beri, D., Dottermusch, S., Chen, H., & Richards, B. S. (2020). Experimental determination of complex optical constants of air-stable inorganic $CsPbI_3$ perovskite thin films. *Physica Status Solidi (RRL)–Rapid Research Letters, 14*, 2000070.
9. Yan, W., Mao, L., Zhao, P., Mertens, A., Dottermusch, S., Hu, H., Jin, Z., & Richards, B. S. (2020). Determination of complex optical constants and photovoltaic device design of all-inorganic $CsPbBr_3$ perovskite thin films. *Optics Express, 28*, 15706–15717.
10. Chen, H., Lee, M., & Chen, C. (2016). Wavelength-dependent optical transition mechanisms for light-harvesting of perovskite $MAPbI_3$ solar cells using first-principles calculations. *Journal of Materials Chemistry C, 4*, 5248–5254.
11. Prasanna, R., Gold-Parker, A., Leijtens, T., Conings, B., Babayigit, A., Boyen, H. G., Toney, M. F., & McGehee, M. D. (2017). Band gap tuning via lattice contraction and octahedral tilting in perovskite materials for photovoltaics. *Journal of the American Chemical Society, 139*, 11117–11124.
12. Pellet, N., Gao, P., Gregori, G., Yang, T., Nazeeruddin, M., Maier, J., & Grätzel, M. (2014). Mixed-organic-cation perovskite photovoltaics for enhanced solar-light harvesting. *Angewandte Chemie International Edition, 53*, 3151–3157.
13. Ono, L., Juarez-Perez, E., & Qi, Y. (2017). Progress on perovskite materials and solar cells with mixed cations and halide anions. *ACS Applied Materials & Interfaces, 9*, 30197–30246.
14. Li, Z., Yang, M., Park, J., Wei, S., Berry, J., & Zhu, K. (2015). Stabilizing perovskite structures by tuning tolerance factor: Formation of formamidinium and cesium lead iodide solid-state alloys. *Chemistry of Materials, 28*, 284–292.
15. Weber, O., Charles, B., & Weller, M. T. (2016). Phase behaviour and composition in the formamidinium–methylammonium hybrid lead iodide perovskite solid solution. *Journal of Materials Chemistry A, 4*, 15375–15382.
16. Sadhanala, A., Ahmad, S., Zhao, B., Giesbrecht, N., Pearce, P., Deschler, F., Hoye, R. L. Z., Gödel, K. C., Bein, T., Docampo, P., Dutton, S. E., De Volder, M. F. L., & Friend, R. H. (2015). Blue-green color tunable solution processable organolead chloride–bromide mixed halide perovskites for optoelectronic applications. *Nano Letters, 15*, 6095–6101.
17. Tang, S., Xiao, X., Hu, J., Gao, B., Chen, H., Peng, Z., Wen, J., Era, M., & Zou, D. (2020). Solvent-free mechanochemical synthesis of a systematic series of pure-phase mixed-halide perovskites $MAPb(I_xBr_{1-x})_3$ and $MAPb(Br_xCl_{1-x})_3$ for continuous composition and band-gap tuning. *ChemPlusChem, 85*, 240–246.
18. Rehman, W., Milot, R. L., Eperon, G. E., Wehrenfennig, C., Boland, J. L., Snaith, H. J., Johnston, M. B., & Herz, L. M. (2015). Charge-carrier dynamics and mobilities in formamidinium lead mixed-halide perovskites. *Advanced Materials, 27*, 7938–7944.

19. Colella, S., Mosconi, E., Fedeli, P., Listorti, A., Gazza, F., Orlandi, F., Ferro, P., Besagni, T., Rizzo, A., Calestani, G., Gigli, G., De Angelis, F., Mosca, R., & Gigli, G. (2013). $MAPbI_{3-x}Cl_x$ mixed halide perovskite for hybrid solar cells: The role of chloride as dopant on the transport and structural properties. *Chemistry of Materials, 25*, 4613–4618.
20. De Wolf, S., Holovsky, J., Moon, S. J., Löper, P., Niesen, B., Ledinsky, M., Haug, F. J., Yum, J. H., & Ballif, C. (2014). Organometallic halide perovskites: Sharp optical absorption edge and its relation to photovoltaic performance. *Journal of Physical Chemistry Letters, 5*, 1035–1039.
21. Ziang, X., Shifeng, L., Laixiang, Q., Shuping, P., Wei, W., Yu, Y., Li, Y., Zhijian, C., Shufeng, W., Honglin, D., Minghui, Y., & Qin, G. G. (2015). Refractive index and extinction coefficient of $CH_3NH_3PbI_3$ studied by spectroscopic ellipsometry. *Optical Materials Express, 5*, 29–43.
22. Xie, Z., Sun, S., Yan, Y., Zhang, L., Hou, R., Tian, F., & Qin, G. G. (2017). Refractive index and extinction coefficient of $NH_2CH{=}NH_2PbI_3$ perovskite photovoltaic material. *Journal of Physics: Condensed Matter, 29*, 245702.
23. Ghimire, K., Cimaroli, A., Hong, F., Shi, T., Podraza, N., & Yan, Y.. (2015, June 14). Spectroscopic ellipsometry studies of $CH_3NH_3PbX_3$ thin films and their growth evolution. In *2015 IEEE 42nd Photovoltaic Specialist Conference (PVSC)* (pp. 1–5). IEEE.
24. Leguy, A. M., Azarhoosh, P., Alonso, M. I., Campoy-Quiles, M., Weber, O. J., Yao, J., Bryant, D., Weller, M. T., Nelson, J., Walsh, A., Van Schilfgaarde, M., & Barnes, P. R. F. (2016). Experimental and theoretical optical properties of methylammonium lead halide perovskites. *Nanoscale, 8*, 6317–6327.
25. Phillips, L. J., Rashed, A. M., Treharne, R. E., Kay, J., Yates, P., Mitrovic, I. Z., Weerakkody, A., Hall, S., & Durose, K. (2016). Maximizing the optical performance of planar $CH_3NH_3PbI_3$ hybrid perovskite heterojunction stacks. *Solar Energy Materials and Solar Cells, 147*, 327–233.
26. Loper, P., Stuckelberger, M., Niesen, B., Werner, J., Filipic, M., Moon, S. J., Yum, J. H., Topic, M., De Wolf, S., & Ballif, C. (2015). Complex refractive index spectra of $CH_3NH_3PbI_3$ perovskite thin films determined by spectroscopic ellipsometry and spectrophotometry. *Journal Physical Chemistry Letters, 6*, 66–71.
27. Manzoorm, S., Häusele, J., Bush, K. A., Palmstrom, A. F., Carpenter, J., Zhengshan, J. Y., Bent, S. F., Mcgehee, M. D., & Holman, Z. C. (2018). Optical modeling of wide-bandgap perovskite and perovskite/silicon tandem solar cells using complex refractive indices for arbitrary-bandgap perovskite absorbers. *Optics Express, 26*, 27441–27460.
28. Ball, J. M., Stranks, S. D., Hörantner, M. T., Hüttner, S., Zhang, W., Crossland, E. J., Ramirez, I., Riede, M., Johnston, M. B., Friend, R. H., & Snaith, H. J. (2015). Optical properties and limiting photocurrent of thin-film perovskite solar cells. *Energy & Environmental Science, 8*, 602–609.
29. Marronnier, A., Lee, H., Lee, H., Kim, M., Eypert, C., Gaston, J. P., Roma, G., Tondelier, D., Geffroy, B., & Bonnassieux, Y. (2018). Electrical and optical degradation study of methylammonium-based perovskite materials under ambient conditions. *Solar Energy Materials and Solar Cells, 178*, 179–185.
30. Bailey, C. G., Piana, G. M., & Lagoudakis, P. G. (2019). High-energy optical transitions and optical constants of $CH_3NH_3PbI_3$ measured by spectroscopic ellipsometry and spectrophotometry. *Journal of Physical Chemistry C, 123*, 28795–28801.
31. Lin, Q., Armin, A., Nagiri, R. C., Burn, P. L., & Meredith, P. (2015). Electro-optics of perovskite solar cells. *Nature Photonics, 9*, 106–112.
32. Leguy, A. M., Hu, Y., Campoy-Quiles, M., Alonso, M. I., Weber, O. J., Azarhoosh, P., Van Schilfgaarde, M., Weller, M. T., Bein, T., Nelson, J., Docampo, P., & Barnes, P. R. F. (2015). Reversible hydration of $CH_3NH_3PbI_3$ in films, single crystals, and solar cells. *Chemistry of Materials, 27*, 3397–3407.
33. Wang, Z., Yuan, S., Li, D., Jin, F., Zhang, R., Zhan, Y., Lu, M., Wang, S., Zheng, Y., Guo, J., Fan, Z., & Chen, L. (2016). Influence of hydration water on $CH_3NH_3PbI_3$ perovskite films prepared through one-step procedure. *Optics Express, 24*, A1431–A1443.

34. Wang, X., Gong, J., Shan, X., Zhang, M., Xu, Z., Dai, R., Wang, Z., Wang, S., Fang, X., & Zhang, Z. (2018). In situ monitoring of thermal degradation of $CH_3NH_3PbI_3$ films by spectroscopic ellipsometry. *Journal of Physical Chemistry C, 123*, 1362–1369.
35. Demchenko, D. O., Izyumskaya, N., Feneberg, M., Avrutin, V., Özgür, Ü., Goldhahn, R., & Morkoç, H. (2016). Optical properties of the organic-inorganic hybrid perovskite $CH_3NH_3PbI_3$: Theory and experiment. *Physical Review B, 94*, 075206.
36. Shirayama, M., Kadowaki, H., Miyadera, T., Sugita, T., Tamakoshi, M., Kato, M., Fujiseki, T., Murata, D., Hara, S., Murakami, T. N., Fujimoto, S., Chikamatsu, M., & Fujiwara, H. (2016). Optical transitions in hybrid perovskite solar cells: Ellipsometry, density functional theory, and quantum efficiency analyses for $CH_3NH_3PbI_3$. *Physical Review Applied, 5*, 014012.
37. Jiang, Y., Soufiani, A. M., Gentle, A., Huang, F., Ho-Baillie, A., & Green, M. A. (2016). Temperature dependent optical properties of $CH_3NH_3PbI_3$ perovskite by spectroscopic ellipsometry. *Applied Physics Letters, 108*, 061905.
38. Guerra, J. A., Tejada, A., Korte, L., Kegelmann, L., Töfflinger, J. A., Albrecht, S., Rech, B., & Weingärtner, R. (2017). Determination of the complex refractive index and optical bandgap of $CH_3NH_3PbI_3$ thin films. *Journal of Applied Physics, 121*, 173104.
39. Ghimire, K., Zhao, D., Cimaroli, A., Ke, W., Yan, Y., & Podraza, N. J. (2016). Optical monitoring of $CH_3NH_3PbI_3$ thin films upon atmospheric exposure. *Journal of Physics D: Applied Physics, 49*, 405102.
40. Green, M. A., Jiang, Y., Soufiani, A. M., & Ho-Baillie, A. (2015). Optical properties of photovoltaic organic–inorganic lead halide perovskites. *Journal Physical Chemistry Letters, 6*, 4774–4785.
41. Yamada, Y., Nakamura, T., Endo, M., Wakamiya, A., & Kanemitsu, Y. (2015). Photoelectronic responses in solution-processed perovskite $CH_3NH_3PbI_3$ solar cells studied by photoluminescence and photoabsorption spectroscopy. *IEEE Journal of Photovoltaics, 5*, 2156–3381.
42. Ziffer, M., Mohammed, J., & Ginger, D. S. (2016). Electroabsorption spectroscopy measurements of the exciton binding energy, electron–hole reduced effective mass, and band gap in the perovskite $CH_3NH_3PbI_3$. *ACS Photonics, 3*, 1060–1068.
43. Yang, Y., Ostrowski, D., France, R., Zhu, K., van de Lagemaat, J., Luther, J., & Beard, M. C. (2015). Observation of a hot-phonon bottleneck in lead-iodide perovskites. *Nature Photonics, 10*, 53–59.
44. Yang, Y., Yang, M., Li, Z., Crisp, R., Zhu, K., & Beard, M. C. (2015). Comparison of recombination dynamics in $CH_3NH_3PbBr_3$ and $CH_3NH_3PbI_3$ perovskite films: influence of exciton binding energy. *Journal of Physical Chemistry Letters, 6*, 4688–4692.
45. Miyata, A., Mitioglu, A., Plochocka, P., Portugall, O., Wang, J., Stranks, S., Snaith, H. J., & Nicholas, R. J. (2015). Direct measurement of the exciton binding energy and effective masses for charge carriers in organic–inorganic tri-halide perovskites. *Nature Physics, 11*, 582–587.
46. Sun, S., Salim, T., Mathews, N., Duchamp, M., Boothroyd, C., Xing, G., Sum, T. S., & Lam, Y. M. (2014). The origin of high efficiency in low-temperature solution-processable bilayer organometal halide hybrid solar cells. *Energy & Environmental Science, 7*, 399–407.
47. Saba, M., Cadelano, M., Marongiu, D., Chen, F., Sarritzu, V., Sestu, N., Figus, C., Aresti, M., Piras, R., Lehmann, A. G., Cannas, C., Musinu, A., Quochi, F., Mura, A., & Bongiovanni, G. (2014). Correlated electron–hole plasma in organometal perovskites. *Nature Communications, 5*, 5049.
48. Sestu, N., Cadelano, M., Sarritzu, V., Chen, F., Marongiu, D., Piras, R., Mainas, M., Quochi, F., Saba, M., Mura, A., & Bongiovanni, G. (2015). Absorption f-sum rule for the exciton binding energy in methylammonium lead halide perovskites. *Journal of Physical Chemistry Letters, 6*, 4566–4572.
49. Savenije, T. J., Ponseca, C. S., Jr., Kunneman, L., Abdellah, M., Zheng, K., Tian, Y., Zhu, Q., Canton, S. E., Scheblykin, I. G., Pullerits, T., Yartsev, A., & Sundström, V. (2014). Thermally activated exciton dissociation and recombination control the carrier dynamics in organometal halide perovskite. *Journal of Physical Chemistry Letters, 5*, 2189–2194.

50. Hirasawa, M., Ishihara, T., & Goto, T. (1994). Exciton features in 0-, 2-, and 3-dimensional networks of $[PbI_6]^{4-}$octahedra. *Journal of the Physical Society of Japan, 63*, 3870–3879.
51. Zhu, X., Su, H., Marcus, R., & Michel-Beyerle, M. E. (2014). Computed and experimental absorption spectra of the perovskite $CH_3NH_3PbI_3$. *Journal of Physical Chemistry Letters, 5*, 3061–3065.
52. Ishihara, T. (1994). Optical properties of PbI-based perovskite structures. *Journal of Luminescence, 60-61*, 269–274.
53. Tanaka, K., Takahashi, T., Ban, T., Kondo, T., Uchida, K., & Miura, N. (2003). Comparative study on the excitons in lead-halide-based perovskite-type crystals $CH_3NH_3PbBr_3$ $CH_3NH_3PbI_3$. *Solid State Communications, 127*(9–10), 619–623.
54. D'Innocenzo, V., Grancini, G., Alcocer, M., Kandada, A., Stranks, S. D., Lee, M. M., Lanzani, G., Snaith, H. J., & Petrozza, A. (2014). Excitons versus free charges in organo-lead tri-halide perovskites. *Nature Communications, 5*, 3586.
55. Kato, M., Fujiseki, T., Miyadera, T., Sugita, T., Fujimoto, S., Tamakoshi, M., Chikamatsu, M., & Fujiwara, H. (2017). Universal rules for visible-light absorption in hybrid perovskite materials. *Journal of Applied Physics, 121*, 115501.
56. Park, J. S., Choi, S., Yan, Y., Yang, Y., Luther, J. M., Wei, S. H., Parilla, P., & Zhu, K. (2015). Electronic structure and optical properties of α-$CH_3NH_3PbBr_3$ perovskite single crystal. *Journal of Physical Chemistry Letters, 6*, 4304–4308.
57. Xing, G., Mathews, N., Sun, S., Lim, S., Lam, Y., Grätzel, M., Mhaisalkar, S., & Sum, T. C. (2013). Long-range balanced electron- and hole-transport lengths in organic-inorganic $CH_3NH_3PbI_3$. *Science, 342*, 344–347.
58. Jiang, Y., Green, M. A., Sheng, R., & Ho-Baillie, A. (2015). Room temperature optical properties of organic–inorganic lead halide perovskites. *Solar Energy Materials and Solar Cells, 137*, 253–257.
59. Xing, G., Mathews, N., Lim, S. S., Yantara, N., Liu, X., Sabba, D., Grätzel, M., Mhaisalkar, S., & Sum, T. C. (2014). Low-temperature solution-processed wavelength-tunable perovskites for lasing. *Nature Materials, 13*, 476–480.
60. Galkowski, K., Mitioglu, A., Miyata, A., Plochocka, P., Portugall, O., Eperon, G., Wang, J., Stergiopoulos, J., Stranks, S., Snaith, H. J., & Nicholas, R. J. (2016). Determination of the exciton binding energy and effective masses for methylammonium and formamidinium lead tri-halide perovskite semiconductors. *Energy & Environmental Science, 9*, 962–970.
61. Liu, Y., Wang, J., Zhu, N., Liu, W., Wu, C., Liu, C., Xiao, L., Chen, Z., & Wang, S. (2019). Investigation on binding energy and reduced effective mass of exciton in organic–inorganic hybrid lead perovskite films by a pure optical method. *Optics Letters, 44*, 3474–3477.
62. Protesescu, L., Yakunin, S., Bodnarchuk, M., Krieg, F., Caputo, R., Hendon, C., Yang, R. X., Walsh, A., & Kovalenko, M. V. (2015). Nanocrystals of cesium lead halide perovskites ($CsPbX_3$, X = Cl, Br, and I): Novel optoelectronic materials showing bright emission with wide color gamut. *Nano Letters, 15*, 3692–3696.
63. Mannino, G., Deretzis, I., Smecca, E., La Magna, A., Alberti, A., Ceratti, D., & Cahen, D. (2020). Temperature-dependent optical band gap in $CsPbBr_3$, $MAPbBr_3$, and $FAPbBr_3$ single crystals. *Journal of Physical Chemistry Letters, 11*, 2490–2496.
64. Alias, M. S., Dursun, I., Saidaminov, M. I., Diallo, E. M., Mishra, P., Ng, T. K., Bakr, O. M., & Ooi, B. S. (2016). Optical constants of $CH_3NH_3PbBr_3$ perovskite thin films measured by spectroscopic ellipsometry. *Optics Express, 24*, 16586–16594.
65. Awasthi, K., Du, K., Wang, C., Tsai, C., Hamada, M., Narra, S., Diau, E., & Ohta, N. (2018). Electroabsorption studies of multicolored lead halide perovskite nanocrystalline solid films. *ACS Photonics, 5*, 2408–2417.
66. Ruf, F., Aygüler, M., Giesbrecht, N., Rendenbach, B., Magin, A., Docampo, P., Kalt, H., & Hetterich, M. (2019). Temperature-dependent studies of exciton binding energy and phase-transition suppression in $(Cs,FA,MA)Pb(I,Br)_3$ perovskites. *APL Materials, 7*, 031113.
67. Koutselas, I., Ducasse, L., & Papavassiliou, G. C. (1996). Electronic properties of three- and low-dimensional semiconducting materials with Pb halide and Sn halide units. *Journal of Physics: Condensed Matter, 8*, 1217–1227.

68. Chen, C., Wu, D., Yuan, M., Yu, C., Zhang, J., Li, C., & Duan, Y. (2021). Spectroscopic ellipsometry study of $CsPbBr_3$ perovskite thin films prepared by vacuum evaporation. *Journal of Physics D: Applied Physics, 54*, 224002.
69. Zhao, M., Shi, Y., Dai, J., & Lian, J. (2018). Ellipsometric study of the complex optical constants of a $CsPbBr_3$ perovskite thin film. *Journal of Materials Chemistry C, 6*, 10450–10455.
70. Chen, X., Wang, Y., Song, J., Li, X., Xu, J., Zeng, H., & Sun, H. (2019). Temperature dependent reflectance and ellipsometry studies on a $CsPbBr_3$ single crystal. *Journal of Physical Chemistry C, 123*, 10564–10570.
71. Yamada, T., Aharen, T., & Kanemitsu, Y. (2018). Near-band-edge optical responses of $CH_3NH_3PbCl_3$ single crystals: Photon recycling of excitonic luminescence. *Physical Review Letters, 120*, 057404.
72. Comin, R., Walters, G., Thibau, E., Voznyy, O., Lu, Z., & Sargent, E. H. (2015). Structural, optical, and electronic studies of wide-bandgap lead halide perovskites. *Journal of Materials Chemistry C, 3*, 8839–8843.
73. Abbas, M., Zeng, L., Guo, F., Rauf, M., Yuan, X., & Cai, B. (2020). A critical review on crystal growth techniques for scalable deposition of photovoltaic perovskite thin films. *Materials, 13*, 4851.
74. Saki, Z., Byranvand, M., Taghavinia, N., Kedia, M., & Saliba, M. (2021). Solution-processed perovskite thin-films: The journey from lab- to large-scale solar cells. *Energy & Environmental Science, 14*, 5690–5722.
75. Trivedi, S., Prochowicz, D., Parikh, N., Mahapatra, A., Pandey, M., Kalam, A., Tavakoli, M. M., & Yadav, P. (2021). Recent progress in growth of single-crystal perovskites for photovoltaic applications. *ACS Omega, 6*, 1030–1042.
76. Herz, L. M. (2016). Charge-carrier dynamics in organic-inorganic metal halide perovskites. *Annual Review of Physical Chemistry, 67*, 65–89.
77. Even, J., Pedesseau, L., Katan, C., Kepenekian, M., Lauret, J. S., Sapori, D., & Deleporte, E. (2015). Solid-state physics perspective on hybrid perovskite semiconductors. *Journal of Physical Chemistry C, 119*, 10161–10177.
78. Draguta, S., Thakur, S., Morozov, Y. V., Wang, Y., Manser, J. S., Kamat, P. V., & Kuno, M. (2016). Spatially non-uniform trap state densities in solution-processed hybrid perovskite thin films. *Journal of Physical Chemistry Letters, 7*, 715–721.
79. Draguta, S., Christians, J. A., Morozov, Y. V., Mucunzi, A., Manser, J. S., Kamat, P. V., Luther, J. M., & Kuno, M. (2018). A quantitative and spatially resolved analysis of the performance-bottleneck in high efficiency, planar hybrid perovskite solar cells. *Energy & Environmental Science, 11*, 960–969.
80. Hutter, E. M., Eperon, G. E., Stranks, S. D., & Savenije, T. J. (2015). Charge carriers in planar and meso-structured organic–inorganic perovskites: Mobilities, lifetimes, and concentrations of trap states. *Journal of Physical Chemistry Letters, 6*, 3082–3090.
81. Stranks, S. D., Burlakov, V. M., Leijtens, T., Ball, J. M., Goriely, A., & Snaith, H. J. (2014). Recombination kinetics in organic-inorganic perovskites: Excitons, free charge, and subgap states. *Physical Review Applied, 2*, 034007.
82. DeQuilettes, D. W., Koch, S., Burke, S., Paranji, R. K., Shropshire, A. J., Ziffer, M. E., & Ginger, D. S. (2016). Photoluminescence lifetimes exceeding 8 μs and quantum yields exceeding 30% in hybrid perovskite thin films by ligand passivation. *ACS Energy Letters, 1*, 438–444.
83. D'Innocenzo, V., Srimath Kandada, A. R., De Bastiani, M., Gandini, M., & Petrozza, A. (2014). Tuning the light emission properties by band gap engineering in hybrid lead halide perovskite. *Journal of the American Chemical Society, 136*, 17730–17733.
84. Wehrenfennig, C., Eperon, G. E., Johnston, M. B., Snaith, H. J., & Herz, L. M. (2014). High charge carrier mobilities and lifetimes in organolead trihalide perovskites. *Advanced Materials, 26*, 1584–1589.
85. Johnston, M. B., & Herz, L. M. (2016). Hybrid perovskites for photovoltaics: Charge-carrier recombination, diffusion, and radiative efficiencies. *Accounts of Chemical Research, 49*, 146–154.

86. Milot, R. L., Eperon, G. E., Snaith, H. J., Johnston, M. B., & Herz, L. M. (2015). Temperature-dependent charge-carrier dynamics in $CH_3NH_3PbI_3$ perovskite thin films. *Advanced Functional Materials, 25*, 6218–6227.
87. Yamada, Y., Nakamura, T., Endo, M., Wakamiya, A., & Kanemitsu, Y. (2014). Photocarrier recombination dynamics in perovskite $CH_3NH_3PbI_3$ for solar cell applications. *Journal of the American Chemical Society, 136*, 11610–11613.
88. Wehrenfennig, C., Liu, M., Snaith, H. J., Johnston, M. B., & Herz, L. M. (2014). Charge-carrier dynamics in vapour-deposited films of the organolead halide perovskite $CH_3NH_3PbI_{3-x}Cl_x$. *Energy & Environmental Science, 7*, 2269–2275.
89. Wolff, C. M., Bourelle, S. A., Phuong, L. Q., Kurpiers, J., Feldmann, S., Caprioglio, P., Marquez, J. A., Wolansky, J., Unold, T., Stolterfoht, M., Shoaee, S., Deschler, F., & Neher, D. (2021). Orders of recombination in complete perovskite solar cells-linking time-resolved and steady-state measurements. *Advanced Energy Materials, 45*, 2101823.
90. Dobrovolsky, A., Merdasa, A., Li, J., Hirselandt, K., Unger, E. L., & Scheblykin, I. G. (2020). Relating defect luminescence and nonradiative charge recombination in $MAPbI_3$ perovskite films. *Journal of Physical Chemistry Letters, 11*, 1714–1720.
91. de Quilettes, D. W., Vorpahl, S. M., Stranks, S. D., Nagaoka, H., Eperon, G. E., Ziffer, M. E., Snaith, H. J., & Ginger, D. S. (2015). Impact of microstructure on local carrier lifetime in perovskite solar cells. *Science, 348*, 683–686.
92. Samiee, M., Konduri, S., Ganapathy, B., Kottokkaran, R., Abbas, H. A., Kitahara, A., Joshi, P., Zhang, L., Noack, M., & Dalal, V. (2014). Defect density and dielectric constant in perovskite solar cells. *Applied Physics Letters, 105*, 153502.
93. Chen, X., Lu, H., Yang, Y., & Beard, M. C. (2018). Excitonic effects in methylammonium lead halide perovskites. *Journal of Physical Chemistry Letters, 9*, 2595–2603.
94. Guo, Z., Manser, J. S., Wan, Y., Kamat, P. V., & Huang, L. (2015). Spatial and temporal imaging of long-range charge transport in perovskite thin films by ultrafast microscopy. *Nature Communications, 6*, 7471.
95. Manser, J. S., & Kamat, P. V. (2014). Band filling with free charge carriers in organometal halide perovskites. *Nature Photonics, 8*, 737–743.
96. Trinh, M. T., Wu, X., Niesner, D., & Zhu, X. Y. (2015). Many-body interactions in photo-excited lead iodide perovskite. *Journal of Materials Chemistry A, 3*, 9285–9290.
97. Vietmeyer, F., Frantsuzov, P. A., Janko, B., & Kuno, M. (2011). Carrier recombination dynamics in individual CdSe nanowires. *Physical Review B, 83*, 115319.
98. Morozov, Y. V., Draguta, S., Zhang, S., Cadranel, A., Wang, Y., Janko, B., & Kuno, M. (2017). Defect-mediated CdS nanobelt photoluminescence up-conversion. *Journal of Physical Chemistry C, 121*, 16607–16616.
99. Stranks, S. D. (2017). Nonradiative losses in metal halide perovskites. *ACS Energy Letters, 2*, 1515–1525.
100. Puthussery, J., Lan, A., Kosel, T. H., & Kuno, M. (2008). Band-filling of solution-synthesized CdS nanowires. *ACS Nano, 2*, 357–367.
101. Ross, R. T. (1967). Some thermodynamics of photochemical systems. *The Journal of Chemical Physics, 46*, 4590–4593.
102. Miller, O. D., Yablonovitch, E., & Kurtz, S. R. (2012). Strong internal and external luminescence as solar cells approach the Shockley–Queisser limit. *IEEE Journal of Photovoltaics, 2*, 303–311.
103. Braly, I. L., de Quilettes, D. W., Pazos-Outón, L. M., Burke, S., Ziffer, M. E., Ginger, D. S., & Hillhouse, H. W. (2018). Hybrid perovskite films approaching the radiative limit with over 90% photoluminescence quantum efficiency. *Nature Photonics, 12*, 355–361.
104. Richter, J. M., Abdi-Jalebi, M., Sadhanala, A., Tabachnyk, M., Rivett, J. P., Pazos-Outón, L. M., Gödel, K. C., Price, M., Deschler, F., & Friend, R. H. (2016). Enhancing photoluminescence yields in lead halide perovskites by photon recycling and light out-coupling. *Nature Communications, 7*, 13941.

105. Pazos-Outón, L. M., Szumilo, M., Lamboll, R., Richter, J. M., Crespo-Quesada, M., Abdi-Jalebi, M., Beeson, H. J., Vrućinić, M., Alsari, M., Snaith, H. J., Ehrler, B., Friend, R. H., & Deschler, F. (2016). Photon recycling in lead iodide perovskite solar cells. *Science, 351*, 1430–1433.
106. Liu, Z., Krückemeier, L., Krogmeier, B., Klingebiel, B., Márquez, J. A., Levcenko, S., Öz, S., Mathur, S., Rau, U., Unold, T., & Kirchartz, T. (2018). Open-circuit voltages exceeding 1.26 V in planar methylammonium lead iodide perovskite solar cells. *ACS Energy Letters, 4*, 110–117.
107. Deschler, F., Price, M., Pathak, S., Klintberg, L. E., Jarausch, D. D., Higler, R., Hüttner, S., Leijtens, T., Stranks, S. D., Snaith, H. J., Atatüre, M., Phillips, R. T., & Friend, R. H. (2014). High photoluminescence efficiency and optically pumped lasing in solution-processed mixed halide perovskite semiconductors. *Journal of Physical Chemistry Letters, 5*, 1421–1426.
108. Noel, N. K., Abate, A., Stranks, S. D., Parrott, E. S., Burlakov, V. M., Goriely, A., & Snaith, H. J. (2014). Enhanced photoluminescence and solar cell performance via Lewis base passivation of organic–inorganic lead halide perovskites. *ACS Nano, 8*, 9815–9821.
109. Kojima, K., Ikemura, K., Matsumori, K., Yamada, Y., Kanemitsu, Y., & Chichibu, S. F. (2019). Internal quantum efficiency of radiation in a bulk $CH_3NH_3PbBr_3$ perovskite crystal quantified by using the omnidirectional photoluminescence spectroscopy. *APL Materials, 7*, 071116.
110. Droseros, N., Longo, G., Brauer, J., Sessolo, M., Bolink, H., & Banerji, N. (2018). Origin of the enhanced photoluminescence quantum yield in $MAPbBr_3$ perovskite with reduced crystal size. *ACS Energy Letters, 3*, 1458–1466.
111. Longo, G., La-Placa, M., Sessolo, M., & Bolink, H. J. (2017). High photoluminescence quantum yields in organic semiconductor-perovskite composite thin films. *ChemSusChem, 10*, 3788–3793.
112. Saliba, M., Matsui, T., Domanski, K., Seo, J. Y., Ummadisingu, A., Zakeeruddin, S. M., Correa-Baena, J. P., Tress, W. R., Abate, A., Hagfeldt, A., & Grätzel, M. (2016). Incorporation of rubidium cations into perovskite solar cells improves photovoltaic performance. *Science, 354*, 206–209.
113. Abdi-Jalebi, M., Andaji-Garmaroudi, Z., Cacovich, S., Stavrakas, C., Philippe, B., Richter, J. M., Alsari, M., Booker, E. P., Hutter, E. M., Pearson, A. J., Lilliu, S., Savenije, T. J., Rensmo, H., Divitini, G., Ducati, C., Friend, R. H., & Stranks, S. D. (2018). Maximizing and stabilizing luminescence from halide perovskites with potassium passivation. *Nature, 555*, 497–501.
114. Kramarenko, M., Ferreira, C. G., Martínez-Denegri, G., Sansierra, C., Toudert, J., & Martorell, J. (2020). Relation between fluorescence quantum yield and open-circuit voltage in complete perovskite solar cells. *Solar RRL, 4*, 1900554.
115. Zhang, S., Zhukovskyi, M., Jankó, B., & Kuno, M. (2019). Progress in laser cooling semiconductor nanocrystals and nanostructures. *NPG Asia Materials, 11*, 1–9.
116. Koscher, B. A., Swabeck, J. K., Bronstein, N. D., & Alivisatos, A. P. (2017). Essentially trap-free $CsPbBr_3$ colloidal nanocrystals by postsynthetic thiocyanate surface treatment. *Journal of the American Chemical Society, 139*, 6566–6569.
117. Mazumdar, S., Zhao, Y., & Zhang, X. (2021). Stability of perovskite solar cells: Degradation mechanisms and remedies. *Frontiers in Electronics, 2*, 712785.
118. Wang, R., Mujahid, M., Duan, Y., Wang, Z., Xue, J., & Yang, Y. (2019). A review of perovskites solar cell stability. *Advanced Functional Materials, 29*, 1808843.
119. Futscher, M., Lee, J., McGovern, L., Muscarella, L., Wang, T., Haider, M. C., Fakharuddin, A., Schmidt-Mende, L., & Ehrler, B. (2019). Quantification of ion migration in $CH_3NH_3PbI_3$ perovskite solar cells by transient capacitance measurements. *Materials Horizons, 6*, 1497–1503.
120. Calado, P., Telford, A., Bryant, D., Li, X., Nelson, J., O'Regan, B. C., & Barnes, P. R. (2016). Evidence for ion migration in hybrid perovskite solar cells with minimal hysteresis. *Nature Communications, 7*, 13831.

121. Singh, R., & Parashar, M. (2020). Origin of hysteresis in perovskite solar cells. In J. Ren & Z. Kan (Eds.), *Soft-Matter Thin Film Solar Cells* (pp. 1–42). AIP Publishing Books.
122. Pavlovetc, I. M., Brennan, M. C., Draguta, S., Ruth, A., Moot, T., Christians, J. A., Aleshire, K., Harvey, S. P., Toso, S., Nanayakkara, S. U., Messinger, J., Luther, J. M., & Kuno, M. (2020). Suppressing cation migration in triple-cation lead halide perovskites. *ACS Energy Letters, 5*, 2802–2810.
123. Lin, Y., Chen, B., Fang, Y., Zhao, J., Bao, C., Yu, Z., Deng, Y., Rudd, P. N., Yan, Y., Yuan, Y., & Huang, J. (2018). Excess charge-carrier induced instability of hybrid perovskites. *Nature Communications, 9*, 4981.
124. Brennan, M. C., Draguta, S., Kamat, P. V., & Kuno, M. (2017). Light-induced anion phase segregation in mixed halide perovskites. *ACS Energy Letters, 3*, 204–213.
125. Wang, Y., Quintana, X., Kim, J., Guan, X., Hu, L., Lin, C. H., Jones, B. T., Chen, W., Wen, X., Gao, H., & Wu, T. (2020). Phase segregation in inorganic mixed-halide perovskites: From phenomena to mechanisms. *Photonics Research, 8*, A56–A71.
126. Zhang, G., Long, R., Lu, Y., Zhang, S., Zhao, W., Yu, Y., Mi, Q., Qin, P., & Huang, F. (2021). Calcium-assisted in situ formation of perovskite nanocrystals for luminescent green and blue emitters. *ACS Applied Nano Materials, 4*, 14303–14311.
127. Zheng, X., Yuan, S., Liu, J., Yin, J., Yuan, F., Shen, W., Yao, K., Wei, M., Zhou, C., Song, K., Zhang, B., Lin, Y., Hedhili, M. N., Wehbe, N., Han, Y., Sun, H., Lu, Z., Anthopoulos, T. D., Mohammed, O. F., Sargent, E. H., Liao, L., & Bakr, O. M. (2020). Chlorine vacancy passivation in mixed halide perovskite quantum dots by organic pseudohalides enables efficient rec. 2020 blue light-emitting diodes. *ACS Energy Letters, 5*, 793–798.
128. Wang, F., Bai, S., Tress, W., Hagfeldt, A., & Gao, F. (2018). Defects engineering for high-performance perovskite solar cells. *Npj Flexible Electronics, 2*, 22.

Perovskite Light-Emitting Diodes

Dawei Di and Baodan Zhao

1 Introduction

Perovskite light-emitting diodes (PeLEDs) [1] are an emerging technology for next-generation display, lighting, and communications. They offer the combined advantages of excellent color purity, spectral tunability, high luminescence efficiencies, and low processing costs. Since the report of room-temperature electroluminescence (EL) from halide perovskite in 2014 [1], the field has been moving at an unprecedented pace; the external quantum efficiencies (EQEs) of PeLEDs exceeded the 20% milestone in 2018 [2–5], followed by more recent works improving the device EQEs to ~28% [6].

Advances in material development and device structures were the main driving forces for the rapid progresses in device performance. The device designs of early PeLEDs were heavily inspired by that of perovskite solar cells and polymer OLEDs [1, 7, 8]. While PeLEDs are typically processed very simply from solution, they show optoelectronic characteristics comparable to that of conventional III–V devices, which require demanding processing conditions [9, 10]. Similar to other types of LEDs, enhancing the radiative recombination processes while reducing the nonradiative recombination losses holds the key to raising the internal quantum efficiencies (IQEs) of PeLEDs toward 100% [3, 10]. To achieve this goal, the emissive layer materials were improved primarily by compositional engineering and dimensionality control [3, 11, 12].

Innovations in device architectures were critical to the realization of the current state-of-the-art devices [2–6, 13, 14]. For PeLEDs with different colors, device

D. Di (✉) · B. Zhao (✉)
State Key Laboratory of Extreme Photonics and Instrumentation, College of Optical Science and Engineering; International Research Center for Advanced Photonics, Zhejiang University, Hangzhou, China
e-mail: daweidi@zju.edu.cn; baodanzhao@zju.edu.cn

W. Nie, K. (Kris) Iniewski (eds.), *Metal-Halide Perovskite Semiconductors*,
https://doi.org/10.1007/978-3-031-26892-2_4

designs vary considerably due to the different scenarios of charge injection, blocking, and balance. It has been understood that reducing nonradiative recombination losses at the emissive layer/charge-transporter interfaces [3, 13, 15] of PeLEDs is equally crucial, if not more crucial than suppressing nonradiative recombination in the bulk region. While the IQEs of PeLEDs were found to approach unity [3], the EQEs are restricted by the relatively poor light extraction efficiency of the device architecture [3, 16, 17]. This indicates opportunities in improving device efficiency through light management.

While great progresses have been made in improving PeLEDs to become a commercially viable technology, many challenges remain. The poor device operational lifetimes are considered the main obstacle toward industrial applications. A recent breakthrough in this direction was the demonstration of ultrastable near-infrared (NIR) PeLEDs with device lifetimes meeting the demands of commercial applications [18]. However, the operational stability of visible PeLEDs remains poor. Among various stability-limiting mechanisms, ion migration and phase instability are some of the most crucial factors for the instability of PeLEDs. Besides, high-performance blue [19, 20] and white [21, 22] PeLEDs are still under active development, and they are important missing pieces for perovskite-based full-color display and solid-state lighting applications. Moreover, issues concerning the toxicity of lead [23, 24] and the progress in the development of mini- and micro-PeLEDs [25] require attention from researchers in the field.

2 Device Architectures

The commonly used device structures for PeLEDs were mostly inherited from that of planar perovskite solar cells and solution-processed OLEDs [1, 7, 8]. The perovskite emissive layer is normally placed in between charge-transport layers (CTLs) with different polarities (e.g., electron- and hole-transport layers) to form a sandwich-like device structure [1]. One of the CTLs is normally in contact with a conductive oxide-coated transparent substrate, while the other CTL is in contact with metal electrodes.

The CTLs are normally considered to serve two functions simultaneously: charge transport and charge injection into the perovskite emissive layers. Using terminologies borrowed from conventional semiconductor diodes, the current PeLED structures may be comparable to that of a PIN heterostructure LED. In direct reference to thin-film OLEDs, a “standard” device configuration refers to the structure in which the hole-transport layer (HTL) such as PEDOT:PSS is in contact with the transparent conductive substrate, while the electron-transport layer (ETL) such as TPBi is coated by thermally evaporated electrodes (e.g., LiF and Al) (Fig. 1a) [1, 13, 14]. An “inverted” device structure normally refers to the case where the ETL such as ZnO is deposited on top of the transparent conductive substrate and the HTL such as TFB polymer is coated by thermally evaporated electrodes (e.g., MoO_x and Au) (Fig. 1b) [12, 27].

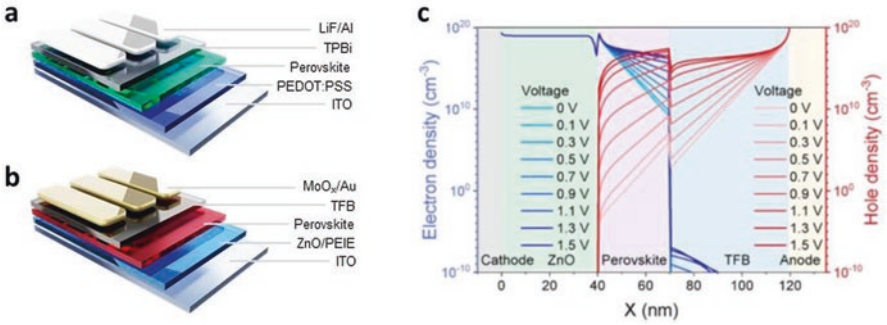

Fig. 1 Device structures and charge distribution of typical PeLEDs. Schematic illustrations of (**a**) the structure of a typical PeLED with a "standard" configuration and (**b**) the structure of a typical PeLED with an "inverted" configuration. (**c**) Simulated electron and hole density distributions in the perovskite LED under different voltages. The shaded regions in gray, light green, pink, light blue, and yellow correspond to cathode, ZnO, perovskite, TFB, and anode, respectively. Panels **a** and **b** were reproduced from [18]. Panel **c** was reproduced from [26]

3 General Device Operation

The basic operation principles of PeLEDs are similar to that of inorganic semiconductor heterojunction LEDs, with some deviations in charge injection and transport due to the commonly used device configurations in which organic CTLs are employed.

3.1 Charge Injection and Blocking

When an external bias is applied to a PeLED, charge injection from the electrodes to the CTLs occurs by drift and diffusion processes, followed by the subsequent injection of charges into the perovskite emissive layer. The simplest consideration for efficient charge injection is the correct alignment of energy levels between the neighboring materials in the PeLED structure. For example, the LUMO level of the ETL is normally close to the conduction band minimum (CB) of the perovskite emissive layer to ensure effective electron injection. At the same time, the ETL prevents excess hole current from passing through the device. This is normally ensured by the deep-lying HOMO level of the ETL. The distribution of charges across a typical PeLED is shown in Fig. 1c [26].

It should be noted that closely aligned energy levels are not strictly required for efficient charge injection in cases where the CTLs are highly conductive. For example, the valance band maximum (VBM) of ITO is around 4.5 eV, showing a considerable energy-level offset of ~0.6 eV with the commonly used PEDOT:PSS HTL (HOMO: 5.1 eV). ITO/PEDOT:PSS is known to be an excellent hole-transport interface for PeLEDs despite the large energetic offset. This could be understood by the high carrier concentrations and mobilities in both the ITO and PEDOT:PSS

materials, allowing the formation of ohmic contact at the interface without the need of closely aligned energy levels. The blocking of charges by CTLs of the opposite polarities prevents leakage currents, raising the chance of electron-hole encounter.

3.2 Charge Recombination

The recombination of carriers in halide perovskite materials shows many similarities to that of inorganic semiconductors such as III–V compounds [9, 10]. Excited-state carriers in typical three-dimensional (3D) halide perovskites are in the form of free carriers or loosely bound electron-hole pairs due to the large dielectric constants that screen Coulomb interactions, showing exciton binding energies on the order of 10 meV [28]. The optically or electrically injected carriers in the perovskite material relax radiatively through band-to-band recombination, giving rise to light emission.

In addition to the radiative recombination channel discussed above, there are non-radiative recombination losses that are responsible for the non-ideal light emission efficiencies of the perovskite materials and devices. Trap-assisted (Shockley-Read-Hall) recombination is the main mechanism for nonradiative losses at moderate to low carrier densities. For $MAPbI_3$ perovskite, trap-assisted recombination is expected to dominate at carrier density of $<10^{16}$ cm^{-3} [29], which is relevant to solar cell and LED operation. Trap passivation is therefore a critical consideration in raising PeLED performance. Under higher carrier densities, Auger recombination [29, 30] is expected to occur, leading to efficiency losses at higher current densities.

Assuming balanced electron and hole populations in the perovskite emitter, the recombination of injected carriers can be described by the following equation:

$$-\frac{dn}{dt} = k_1 n + k_2 n^2 + k_3 n^3 \tag{1}$$

where k_1 is the trap-assisted recombination rate, k_2 is the rate constant of band-to-band radiative recombination, k_3 is the Auger recombination constant, and n is the carrier concentration [28].

Assuming only band-to-band recombination contributes to the radiative process, the radiative efficiency η_{rad} is therefore given by Eq. (2) and is used to describe the power dependent PLQEs observed for typical perovskite emitters (Fig. 2a):

$$\eta \mathrm{rad} = k_2 n / \left(k_1 + k_2 n + k_3 n^2 \right) \tag{2}$$

It has been suggested that in low-dimensional perovskite emitters with lower dielectric constants, excited-state carriers may exist in the form of excitons which may recombine radiatively in a fashion more similar to that in organic semiconductors [31, 32]. This could make the first-order term ($k_1 n$) of Eq. (1) completely or partly radiative, raising the radiative efficiency at medium to low carrier densities.

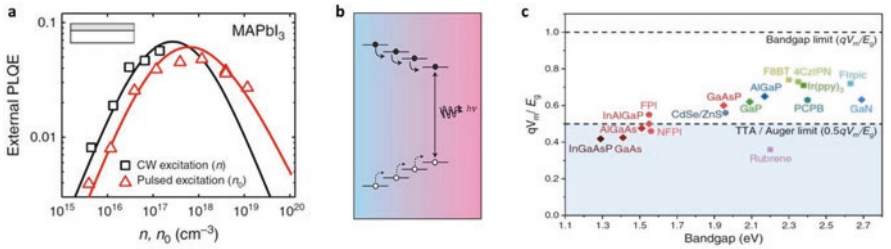

Fig. 2 Studies of radiative recombination for PeLEDs and related devices. (**a**) Measured external PLQEs for $MAPbI_3$ perovskite under steady state (black) and pulsed laser excitation (red) with the prediction from the recombination rate model (lines). Under pulsed excitation, the average PLQE is measured over the decay of the carrier density n. (**b**) Multi-phase perovskite material $PEA_2(CH_3NH_3)_{n-1}Pb_nI_{3n+1}$ channel energy across an inhomogeneous energy landscape, concentrating carriers to the smallest-bandgap emitters. The arrows represent the carrier transfer process. (**c**) Measured qV_m/E_g of different classes of LEDs. FPI, NFPI, and PCBP denote $FAPbI_3$, $NMA_2FA_{n-1}Pb_nI_{3n+1}$, and $PEA_2Cs_{n-1}Pb_nBr_{3n+1}$ perovskite, respectively. The shaded area denotes the region where the measured qV_m/E_g falls below the limits set by TTA or Auger processes. Panel **a** was reproduced from [29]. Panel **b** was reproduced from [11, 12]. Panel **c** was reproduced from [26]

3.3 *Energy Transfer/Funneling*

A distinct branch in PeLED research is the study of mixed-dimensional perovskite systems exhibiting efficient energy transfer/funneling from the higher-bandgap to the lower-bandgap perovskite phases. This mechanism confines charges at the lower-bandgap perovskite crystal domains, enabling interfacial passivation and an increased local carrier concentration that enhance radiative recombination processes (e.g., a larger k_2n^2 term in Eq. (1)).

Such mechanism was found to be effective in PeLEDs operating at moderate current densities. However, due to the high local carrier concentrations, Auger recombination in mixed-dimensional perovskite emitters were found to be more pronounced [33], contributing to efficiency roll-off at higher current densities.

3.4 *Operating Voltages*

Recently, it was reported that the minimum voltage required for observing EL from PeLEDs could be as low as $0.46E_g/q$, where E_g is the bandgap and q is the elementary charge [26]. Ultralow operating voltages were universally observed across many classes of semiconductors (Fig. 2b) [26], in contrast to earlier reports claiming up-conversion mechanisms exclusive to a few material systems. The ultralow-voltage EL phenomenon does not violate the energy conservation principle and can be explained by the recombination of band-edge carriers whose populations are determined by Fermi-Dirac functions perturbed by a small external bias. However, the apparent threshold voltages for a particular photon flux vary greatly for different classes of LEDs [26].

For example, a unique benefit of PeLEDs over OLEDs is that they generally operate at lower driving voltages for the same photon flux. This is primarily due to the reason that metal halide perovskites exhibit higher carrier concentrations and mobilities at room temperature compared to organic semiconductors. It was shown that PeLEDs can be driven at voltages below the bandgap of silicon, allowing potential integration with silicon electronics [26]. The low operating voltages of PeLEDs indicate opportunities in next-generation communications, computational and energy applications.

4 Achieving Near-Unity Internal Quantum Efficiencies

A critical step in establishing PeLED as a next-generation light source technology was the demonstration of high EL quantum efficiencies [2–6, 15]. The EQE and IQE of PeLEDs are correlated with each other according to the following equation:

$$EQE = IQE \times f_{\text{outcoupling}} = f_{\text{balance}} \times f_{\text{e-h}} \times \eta_{\text{rad}} \times f_{\text{outcoupling}} \tag{3}$$

where f_{balance} is the charge injection balance factor (with a maximum value of unity), $f_{\text{e-h}}$ is the probability of forming a correlated electron-hole pair from each pair of injected carriers, η_{rad} is the probability of radiative recombination for each electron-hole pair, and $f_{\text{outcoupling}}$ is the optical outcoupling coefficient [28].

It can be seen that IQE is determined by f_{balance}, $f_{\text{e-h}}$, and η_{rad}. Charge balance (f_{balance}) can be maximized by choosing functional layers with appropriate energy levels [3, 4, 34, 35] and charge-transport properties [13]. The main strategies for improving $f_{\text{e-h}}$ include the formation of charge-confinement structures that improve the chance of electron-hole encounters [11, 12, 35] and the enhancement of Coulomb interactions by reducing the dielectric constants of the materials [28, 33]. For perovskite emitters, the radiative efficiency of an electron-hole pair (η_{rad}) is determined by $\eta_{\text{radiative}} = k_{\text{rad}}/(k_{\text{rad}} + k_{\text{non-rad}})$, where k_{rad} is radiative recombination rate and $k_{\text{non-rad}}$ is the nonradiative recombination rate [28]. For emitters where only band-to-band recombination contributes to photon emission, η_{rad} can be obtained by Eq. (2) discussed earlier.

4.1 Suppressing Bulk Nonradiative Losses

The most intensively studied direction in the field of PeLEDs has been the suppression of nonradiative losses in the bulk region of the perovskite emissive layer. The suppression of nonradiative losses ties closely with the passivation of traps in the perovskite materials. This was typically achieved by compositional tuning of the perovskite precursors [14, 27], introduction of small molecule [36] and polymeric [3] trap passivators, dimensionality control [11, 12], and post-treatments [14, 20].

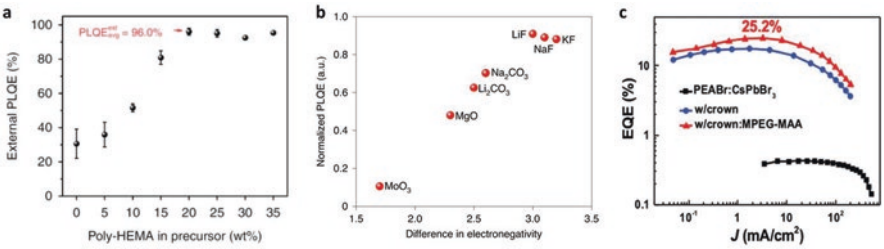

Fig. 3 Suppressing nonradiative losses for PeLED materials and devices. (**a**) External PLQE of perovskite-polymer bulk heterostructure films (on fused silica) as a function of poly-HEMA weight fraction in the solid precursors. The error bars show the highest and lowest external PLQEs measured for each weight fraction. The black dots represent the average external PLQEs. The optimized polymer weight fraction of 20% in precursor corresponds to a volume fraction of 28% in the emissive film. The excitation source used was a 532-nm c.w. laser with an intensity of 100 mW cm^{-2} (approximately 1 sun). (**b**) Normalized PLQEs of perovskite films formed on a range of thermally evaporated interfacial materials with different polarities, characterized by the relative electronegativity of the chemical bonds. (**c**) EQE−J characteristics of PeLEDs based on PEABr:CsPbBr perovskite with/without crown and with crown:MPEG-MAA. Panel **a** was reproduced from [3]. Panel **b** was reproduced from [13]. Panel **c** was reproduced from [6]

Photoluminescence quantum efficiencies (PLQEs) of perovskite emissive layers are an indication of the effectiveness of passivation. PLQEs of approaching 100% were reported for perovskite-polymer heterostructures (Fig. 3a) [3] and perovskite nanocrystals [5]. Deep-lying traps responsible for the loss of PLQEs were considered to primarily originate from uncoordinated lead (including Pb^{2+} and Pb^0) for the case of lead halide perovskite emitters. Other widely employed approaches for studying nonradiative losses are the characterization of trap density using space-charge limited current (SCLC) analysis [23] and the measurements of PL decay kinetics which are affected by the rates of both radiative and nonradiative recombination processes. The aforementioned methods are powerful tools in the development of perovskite emissive layers for PeLEDs.

4.2 Suppressing Interfacial Nonradiative Losses

Interfacial nonradiative recombination is a critical factor limiting the performance of PeLEDs. However, this issue did not receive as much attention as for the losses in the bulk. An example of interfacial nonradiative losses in PeLEDs is the reduction of PL lifetime and intensity (PLQE) when the emissive layer is in contact with the charge-transport layers [3]. Such processes prevent PeLEDs from achieving near-unity IQEs, despite the very high PLQEs of the perovskite emissive layers.

Interfacial nonradiative losses in PeLEDs can be suppressed in various ways. First, approaches that provide bulk passivation could normally lead to the passivation of interfacial traps at the same time. For example, perovskite-polymer bulk heterostructures were found to eliminate the effects of interfaces on PL decay

kinetics, leading to near-unity IQEs and EQEs of up to 20.1% [3]. It was reported that ultrathin polar interfaces including lithium fluoride (LiF) [13] (Fig. 3b) enable the formation of highly emissive and uniform perovskite films on hydrophobic polymeric charge transporters in an OLED-like device configuration. This led to the demonstration of efficient green quasi-2D PeLEDs with EQEs of up to 19.1% at >1500 cd m^{-2}. Similar interfacial modification and polymer passivation approaches were employed in green PeLEDs (Fig. 3c) showing exceptionally high EQEs of up to 28.1% [6]. Similarly, hydrophilic interfaces prepared using polymers such as polyethyleneimine [27], perfluorinated ionomer (PFI) [14], and small molecules including ethanolamine [37] and aluminum oxide [38] were found to allow the formation of high-quality perovskite films. Although these strategies have been proven useful for high-performance PeLEDs, further mechanistic investigations are required to reveal the origins of such improvements.

5 Light Outcoupling

While the IQEs in some of the best-performing PeLEDs approach 100%, around 80% of the internally generated photons are trapped in the device stack and eventually lose energy through a variety of loss channels owing to the non-ideal light outcoupling [2–5, 15].

Low light outcoupling yields in PeLEDs normally arise from (i) waveguide modes parallel to the substrate due to the larger refractive indices of perovskites (~2.5) compared to the commonly used charge-transport materials and transparent electrodes (~1.7–1.8) [3] and (ii) the total internal reflection of emitted photons over a wide range of emission angles owing to the difference between the refractive indices of the device substrate and the air. Consequently, only photons from a small emission cone can escape from the PeLED device (Fig. 3c), while the rest are trapped in waveguided and substrate modes.

Opportunities in improving EQEs further lie in the ability in extracting the trapped photons from PeLEDs. Light outcoupling strategies for PeLEDs can be briefly divided into two categories, modifications of the perovskite layer properties and the employment of external optical structures.

5.1 Modification of Perovskite Layer Properties

Some notable approaches for light outcoupling based on the modification of the perovskite layer properties are the reduction of refractive index (n) [3], control of transition dipole moment orientations [39–44], formation of light scattering structures within the emissive layer [2], and photon recycling [16]. According to the ray optics limit of $1/2n^2$, the reduction of n can increase η_{out} for planar PeLEDs. For typical 3D perovskites, n is ~2.5. Including 2D ligands with a significant fraction of

organic content in the perovskite composition lowers n to ~2.1 [3]. Introducing polymers into the perovskite emissive layers was reported to reduce n further to ~1.9 [3], resulting in an η_{out} of ~21% (Fig. 4a) and EQEs of up to 20.1% [3]. Orientation of transition dipole moments (TDMs) also plays an important role in the photon extraction processes. Emission from only horizontally oriented TDMs can be effectively extracted. The fraction of horizontal TDMs could be tuned by engineering the perovskite nanostructures [39–42, 44]. For PeLEDs based on nanoplatelets [39], a horizontal dipole fraction of ~84% and η_{out} of 31% were reported. Tuning of the fraction of horizontal TDMs can also be achieved for solution-processed polycrystalline perovskite films [43]. Light scattering in rough or structured emissive layers is expected to enhance η_{out}. PeLEDs based on submicrometer-scale structures were reported to have outcoupling efficiencies of ~30%, leading to peak EQEs of up to 20.7% (Fig. 4b) [2].

Photon recycling improves the light extraction from PeLEDs by randomizing the directions of trapped photons in a fashion similar to scattering, but through the reabsorption and re-emission of light (Fig. 4c) [16, 28, 29, 45]. It was reported that for PeLEDs based on perovskite emitters with high internal radiative efficiencies and small Stokes shifts (e.g., $PEA_2Cs_{n-1}Pb_nBr_{3n+1}$), about 30–70% of EL may originate from photon recycling [16]. The theoretical outcoupling efficiency of PeLEDs in the presence of photon recycling is given by

$$EQE_{PR} = f_{\text{balance}} \times f_{\text{out,direct}} \Big/ \left[f_{\text{out,direct}} + A_{\text{para}} + \frac{(1-\eta_{\text{rad}})}{\eta_{\text{rad}}} \right] \tag{4}$$

where f_{balance} is the charge balance factor, $f_{\text{out, direct}}$ is the direct light outcoupling efficiency, η_{rad} is the internal radiative efficiency of the perovskite layer, and A_{para} is the parasitic absorption loss external to the perovskite layer [16].

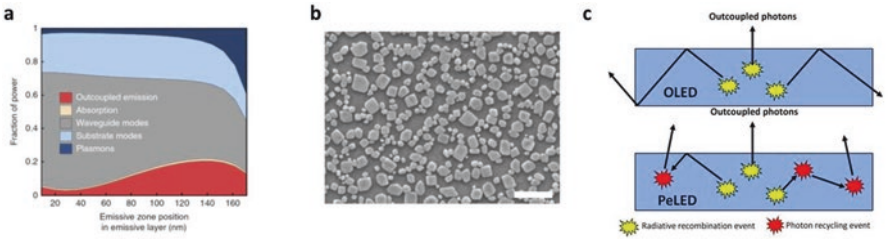

Fig. 4 Case studies of light outcoupling in PeLEDs. (**a**) Modeled fractional optical power distribution in the LED structure as a function of emissive zone position in the PPBH emissive layer with a thickness of 180 nm. The origin of the x-axis is the ETL/emissive layer interface. "Outcoupled emission" indicates the fraction of outcoupled light from the LED. Other modes lead to optical losses. (**b**) SEM image of the perovskite with submicrometer-scale structures. The scale bar represents 1 μm. (**c**) Simplified schematics for comparing light outcoupling processes in an OLED (upper panel) and PeLED (lower panel), with the arrows denoting photon trajectories. Panel **a** was reproduced from [3]. Panel **b** was reproduced from [2]. Panel **c** was reproduced from [28]

5.2 External Optical Structures

External optical structures such as lenses [39, 46, 47] and microcavities [48] are capable of converting optical power in substrate and waveguide modes into outcoupled modes, resulting in substantially increased η_{out}. It was reported that a light-outcoupling hemispherical lens improved the peak EQEs of perovskite nanocrystal LEDs from 23.4% to 45.5% [49]. Microcavities were used to improve η_{out} from ~20% to ~30% for top-emitting PeLEDs featuring transparent electrodes, leading to peak EQEs of up to 20.2% [50]. Similarly, other light outcoupling approaches employing plasmonic effects [51, 52] and refractive index matching [53–55] were found to improve η_{out} for PeLEDs.

6 Challenges

While the researchers in the field have witnessed a remarkable progress in improving PeLED performance, many challenges remain. Some of the most critical current shortcomings of PeLEDs include poor operational stability, the low efficiencies of blue PeLEDs, the toxicity of lead, and the difficulty in micropatterning for mini/micro-PeLED applications.

6.1 Operational Stability

The poor operational stability of PeLEDs is the grandest challenge in their journey toward commercialization. Halide perovskite materials were widely considered to be intrinsically unstable under electric fields due to the ionic nature of their crystal lattices. Device lifetimes (T_{50}) are typically on the order of 10–100 hours. This is clearly unsatisfactory as practical applications require much improved device longevity (longer than 10,000 h at useful photon fluxes) [56].

A recent breakthrough in this area was the demonstration of efficient (peak EQE =22.8%) $FAPbI_3$ PeLEDs with ultralong operational lifetimes meeting the demands of commercial applications. This was enabled by the introduction of a dipolar molecular stabilizer, SFB10 [18]. The PeLEDs showed no degradation over 3600 h (5 months) under continuous operation at a current density of 5 mA cm^{-2}. Accelerated aging tests at current densities of 10–200 mA cm^{-2} were performed to obtain the operational lifetimes of the PeLEDs, according to an empirical scaling law developed for modeling the degradation of LEDs:

$$R_0^{\,n} \times T_{50} = \text{constant} \tag{5}$$

where R_0 is the initial radiance of the LED and n is the acceleration factor. Based on the 62 data points acquired from the accelerated aging tests, T_{50} lifetimes were

estimated to be ~1.2 × 10^4 h (~1.3 years) and ~ 3.3 × 10^4 h (~3.7 years) at 3.7 W sr^{-1} m^{-2} (5 mA cm^{-2}) and 2.1 W sr^{-1} m^{-2} (3.2 mA cm^{-2}), respectively (Fig. 5a). Longer T_{50} lifetimes were estimated for lower radiances, for example, at 0.21 W sr^{-1} m^{-2} (0.7 mA cm^{-2}), the T_{50} lifetime was estimated to be 2.4 × 10^6 h (2.7 centuries). For reference, for high-efficiency OLEDs based on $Ir(ppy)_3$, a luminance of 1000 cd m^{-2} corresponds to a radiance of 2.1 W sr^{-1} m^{-2}, and a luminance of 100 cd m^{-2} corresponds to a radiance of 0.21 W sr^{-1} m^{-2}. The dipolar molecular stabilizer interacts with the cations (FA^+, Pb^{2+}) and anions (I^-) at the grain boundaries of the $FAPbI_3$ perovskite. This suppresses ion migration under electric fields, preventing the formation of lead iodide which mediates detrimental phase transformation. The ultralong device lifetimes could remove the critical concern that halide perovskite devices may be intrinsically unstable, paving the path toward industrial applications [18]. Despite these encouraging results, stable PeLEDs emitting in the visible spectral range are yet to be demonstrated.

Ion migration is a key mechanism limiting the operational stability of PeLEDs [59–61]. Owing to the soft and ionic crystal structure of the halide perovskites, ion migration may be triggered by external stimuli such as electric fields, heat, and light (Fig. 5b) [57, 59, 62]. Ionic movements would induce detrimental effects on the performance of PeLEDs through defect generation, lattice deformation, interfacial ion accumulation, ionic doping, and chemical interactions [59]. Apart from the aforementioned dipolar molecular stabilizer approach [18], a range of methods such as molecular passivation [2, 4, 63–68], dimensionality control [12, 69–71], and thermal management [72] were explored to suppress the effects of ion migration.

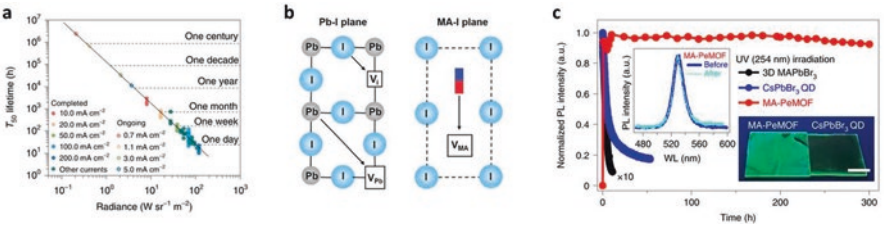

Fig. 5 Recent studies on PeLED operational stability and ion migration. (**a**) The T_{50} lifetimes as a function of initial radiance (R_0); the solid line is the fitting of the T_{50} data to equation $R_0^n \times T_{50} =$ constant, where n is the acceleration factor (n = 1.86). The data points marked by the solid dots are from completed T_{50} measurements (total data points, 62). The open circles are the extrapolated T_{50} lifetimes for the ongoing measurements at medium and low current densities, which are expected to finish after longer times. (**b**) Ionic transport mechanisms in a $CH_3NH_3PbI_3$ perovskite structure. Schematic illustration of the three ionic transport mechanisms involving conventional vacancy hopping between neighboring positions: I^- migration along an octahedron edge; Pb^{2+} migration along the diagonal direction <110>; $CH_3NH_3^+$ migration into a neighboring vacant A-site cage involving motion normal to the unit cell face composed of four iodide ions. (**c**) Normalized PL intensity as a function of time for 3D $MAPbBr_3$, $CsPbBr_3$ QD, and MA-PeMOF thin films in ambient air (relative humidity of 30%) under constant UV irradiation (254 nm). Insets show the PL spectrum of the MA-PeMOF thin film before and after irradiation for 200 hours (left) and their photographs under UV light (right). Scale bar, 1 cm. WL, wavelength. Panel **a** was reproduced from [18]. Panel **b** was reproduced from [57]. Panel **c** was reproduced from [58]

Metal-organic frameworks (MOF) were reported to enable enhanced operational stability of PeLEDs by preventing ion migration in the perovskite-MOF emissive films (Fig. 5c), achieving bright and stable (T_{50} > 50 h) green EL [58]. A cross-linking strategy using methylene-bis-acrylamide was reported to strengthen the binding of Br^- and increase the activation energy of ion migration in bromide perovskite-based LEDs, leading to a T_{50} lifetime of 208 h [63]. As halide ions are widely considered to be the primary contributor to ion migration [60, 61], further efforts in the control of halide ions are expected to show benefits in improving device stability. This could be achieved in a number of ways, including raising the barriers to ion migration using molecular stabilizers [18] and reducing halide vacancies [73].

Phase transformation and halide segregation are some of the main factors for the instability of blue and red PeLEDs based on mixed-halide [74] and mixed-dimensional perovskites [71] and perovskite structures with undesirable tolerance factors [67, 75]. Common triggers for these processes include unfavorable material composition [71], halide migration [74], lattice strain/stress, and externally induced structural evolution [67, 75]. It is possible to partially suppress halide segregation by modifying the nanocrystal surfaces with multidentate ligands, hindering the formation of iodine Frenkel defects [68]. Despite such improvements, the T_{50} lifetime at an initial luminance of 141 cd m^{-2} was only 30 min for these devices, indicating that considerable challenges remain for mixed-halide PeLEDs [68]. Interfacial chemical interactions [65, 75] and thermal degradation [65] are some of the additional contributors to the structural instability of halide perovskites.

6.2 Blue PeLEDs

Unlike near-infrared, red and green PeLEDs exhibiting high EQEs of over 20%, the efficiencies of blue PeLEDs are still low. For “standard” blue PeLEDs with peak wavelengths equal to or shorter than 470 nm, the EQEs are below 10%, limiting their potential application in wide-color-gamut displays. Moreover, the operational stability of blue PeLEDs is significantly worse compared to PeLEDs emitting at longer wavelengths.

The most widely used method for achieving blue PeLEDs is the mixing of bromide- and chloride-based perovskite precursors (i.e., halide mixing). However, the PLQEs of the blue perovskite emitters normally reduce as the chloride fraction increases, owing to the small formation energy of chloride vacancies [73]. Blue-emitting perovskites prepared from bromide-chloride mixing often show undesirable Goldschmidt tolerance factors, resulting in reduced stability [76]. Besides, the halide vacancies are active sites for ion migration, leading to spectral and structural instability [67, 75].

An alternative approach for attaining blue PeLEDs is through quantum confinement effects in reduced-dimensional bromide perovskites, shifting the emission

wavelengths from the green to blue regions. These typically include quasi-2D/3D perovskites [77] and perovskite nanocrystals/quantum dots [19]. Reduced-dimensional perovskites show advantages in PLQEs due to the generally larger exciton binding energies [28, 78] or fast-energy transfer/funneling processes [11, 12] that increase the probability of electron-hole encounters, and the improved passivation [3] of nanocrystalline perovskite grains. For quasi-2D/3D perovskite systems, a main challenge lies in the difficulty in attaining uniform phase distribution for blue EL with high spectral purity [77]. Similarly, for perovskite nanocrystals (including quantum dots), the broad distribution of nanocrystal sizes could result in a wider emission bandwidth due to the bandgap variations of the nanocrystals, affecting the spectral narrowness of EL.

While a few recent works reported efficient blue PeLEDs with EQEs>10% [20, 79, 80], the EL emission was still limited to the sky-blue spectral region (475–495 nm), deviating from the requirements of high-definition displays. Understanding the nucleation and crystallization processes and the origin of nonradiative losses in blue perovskite emitters may lead to further advances in this area. Achieving stable operation with blue PeLEDs presents even greater challenges and is expected to be a subject of future research.

6.3 Toxicity

Similar to perovskite solar cells, high-performance PeLEDs are typically based on lead halide perovskites. The potential toxicity of metallic lead (Pb) in the perovskite materials raises concerns over the possible impacts to human health and the natural environment, limiting the scope of practical applications. The search for eco-friendly alternatives to the lead-based perovskites is therefore an important direction in the area of PeLEDs.

Some of the most widely used methods for the reduction of toxicity include partial or complete replacement of Pb with other group-IV metals (e.g., Sn [81–83] and Ge [23]) and double perovskites [21]. As Pb-based perovskites generally show superior optoelectronic properties, replacing Pb with nontoxic elements while maintaining high device performance is a clear goal in this direction.

Replacing Pb with Sn was found to be effective in producing efficient perovskite solar cells with reduced toxicity. However, Sn-based (including Pb-Sn) perovskites generally show significantly reduced PLQEs compared to the Sn-free, Pb-based perovskites. This might be due to the reason that it is more likely to form a higher density of trap states related to the oxidation of Sn^{2+} and the rapid crystallization of Sn-based perovskites [81]. Decent EQEs of up to ~5% from Sn-based perovskite LEDs were reported [82, 83], but the overall device performance remained unsatisfactory.

Recently, it was shown that it is possible to prepare highly luminescent Ge-Pb perovskite films with PLQEs of up to ~71%. This led to the demonstration of

efficient green PeLEDs with EQEs of up to 13.1% [23]. While this indicates new opportunities in this direction, achieving high efficiencies for lead-free PeLEDs remains to be a challenging task.

Double perovskites, with a general formula of $A_2B^IB^{III}X_6$, is another important material class for lead-free devices [21]. While a wide variety of material compositions can be expected from this class of perovskites, currently they exhibit low PLQEs [84], largely due to the indirect bandgap nature and the high densities of traps for most of the double perovskites developed. Metal ion dopants were used to raise the PLQEs of double perovskites. For instance, by introducing Bi^{3+} and Na^+, $Cs_2Ag_{0.6}Na_{0.4}InCl_6$:0.04% Bi powders showed a PLQE of ~86%, three orders of magnitude higher than that of $Cs_2AgInCl_6$ [21]. However, preparing efficient PeLEDs based on double perovskites remains very challenging, partly owing to the limited quality of the perovskite films [21].

6.4 Mini- and Micro-PeLEDs

Mini- and micro-light-emitting diodes (mini/micro-LEDs) [85–88] have attracted much attention owing to their superior characteristics of low power consumption, high contrast ratio, high brightness, high response speed, and high efficiency. While the current mini/micro-LED technologies are known to be advantageous, the requirement for high-quality epitaxial III-V semiconductors becomes more stringent, as reducing the pixel sizes to the microscopic scale tends to generate nonradiative loss pathways near the sidewalls of the active regions [86, 89]. Besides, the mass-transfer process required for the production of mini/micro-LED displays reduces the manufacturing yields [90–92]. These factors inevitably increase the production costs of mini/micro-LEDs.

Despite the promise of PeLEDs as a low-cost alternative to the mainstream LED technologies, the options for creating efficient PeLEDs with microscopic pixel sizes remain limited, leading to moderate emission efficiencies from PeLEDs with micropatterned emissive arrays [93, 94]. The possibility of developing single-pixel mini/micro-PeLEDs is rarely explored.

Recently, efficient mini/micro-perovskite LEDs were reported. The compatibility of luminescent perovskite with self-aligned photolithography (Fig. 6) was enabled by the insertion of a lithium fluoride surface-tension-relief layer. Active-layer luminescence properties and morphological control are critical to mini/micro-PeLEDs. Following these design rules, proof-of-concept mini/micro-PeLEDs with active pixel areas of down to 100×200 um^2, and peak external quantum efficiencies of up to ~9.1%, were developed [25]. While this study indicated the potential of next-generation mini/micro-PeLED displays, such applications demand individually addressable pixel arrays with considerably smaller pixel sizes comparable to commercial micro-LEDs.

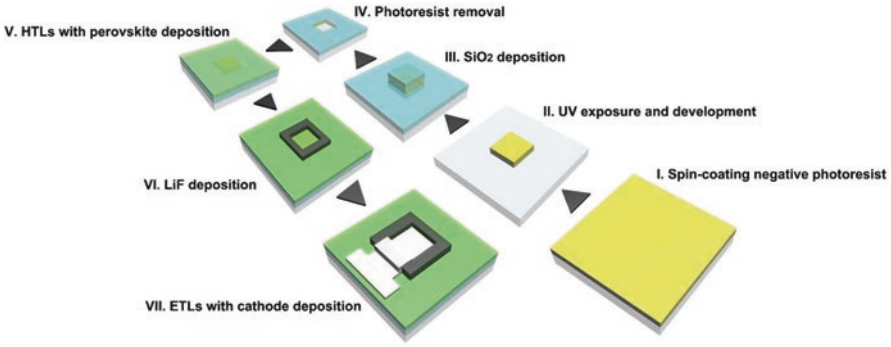

Fig. 6 Illustration of self-aligned micropatterning processes for mini/micro-PeLEDs. (I) Spin-coating negative photoresist. (II) UV exposure and development. (III) SiO_2 deposition. (IV) Photoresist removal. (V) HTLs with perovskite deposition. (VI) LiF deposition. (VII) ETLs with cathode deposition. Figure 6 was reproduced from [25]

7 Summary

PeLEDs have been recognized as an emerging technology for display, lighting, and communication applications. In this chapter, we have provided an overview of the basic designs, operating principles, and main challenges of PeLEDs. While the device architectures and fabrication processes of PeLEDs are similar to that of perovskite solar cells and solution-processed OLEDs, they exhibit some interesting light emission characteristics comparable to LEDs based on III-V semiconductors [9, 10]. The excellent spectral tunability and narrow emission linewidth of PeLEDs are potentially advantageous over that of OLEDs. The rapid progress in device efficiencies was primarily driven by material design and device engineering, leading to IQEs of approaching 100%. The suppression of both bulk and interfacial nonradiative recombination losses was key to reaching this goal. Opportunities in raising the EQEs of PeLEDs beyond the current state-of-the-art (20–28%) [2–6, 15] lie in the improvement of light outcoupling from the devices.

Looking forward, many challenges remain in developing PeLEDs from a laboratory curiosity to a commercially viable technology. A recent breakthrough was made in addressing the critical challenge of device instability [18], demonstrating NIR PeLEDs with ultralong operational lifetimes meeting the demands of practical applications. However, similar device stability is yet to be achieved for PeLEDs emitting in the visible region. Moreover, blue and low-toxicity PeLEDs face considerable challenges in raising the efficiency and stability beyond what can be currently achieved. While technical difficulties are present in the reliable micropatterning of perovskite devices, mini/micro-PeLEDs [25] are a promising research direction toward high-pixel-density display applications. Despite the challenges ahead, PeLEDs have set the sail for becoming a next-generation light source technology.

References

1. Tan, Z.-K., Moghaddam, R. S., Lai, M. L., Docampo, P., Higler, R., Deschler, F., Price, M., Sadhanala, A., Pazos, L. M., Credgington, D., Hanusch, F., Bein, T., Snaith, H. J., & Friend, R. H. (2014). *Nature Nanotechnology, 9*, 687.
2. Cao, Y., Wang, N., Tian, H., Guo, J., Wei, Y., Chen, H., Miao, Y., Zou, W., Pan, K., He, Y., Cao, H., Ke, Y., Xu, M., Wang, Y., Yang, M., Du, K., Fu, Z., Kong, D., Dai, D., Jin, Y., Li, G., Li, H., Peng, Q., Wang, J., & Huang, W. (2018). *Nature, 562*, 249.
3. Zhao, B., Bai, S., Kim, V., Lamboll, R., Shivanna, R., Auras, F., Richter, J. M., Yang, L., Dai, L., Alsari, M., She, X.-J., Liang, L., Zhang, J., Lilliu, S., Gao, P., Snaith, H. J., Wang, J., Greenham, N. C., Friend, R. H., & Di, D. (2018). *Nature Photonics, 12*, 783.
4. Lin, K., Xing, J., Quan, L. N., de Arquer, F. P. G., Gong, X., Lu, J., Xie, L., Zhao, W., Zhang, D., Yan, C., Li, W., Liu, X., Lu, Y., Kirman, J., Sargent, E. H., Xiong, Q., & Wei, Z. (2018). *Nature, 562*, 245.
5. Chiba, T., Hayashi, Y., Ebe, H., Hoshi, K., Sato, J., Sato, S., Pu, Y.-J., Ohisa, S., & Kido, J. (2018). *Nature Photonics, 12*, 681.
6. Liu, Z., Qiu, W., Peng, X., Sun, G., Liu, X., Liu, D., Li, Z., He, F., Shen, C., Gu, Q., Ma, F., Yip, H. L., Hou, L., Qi, Z., & Su, S. J. (2021). *Advanced Materials, 33*, 2103268.
7. Lee, M. M., Teuscher, J., Miyasaka, T., Murakami, T. N., & Snaith, H. J. (2012). *Science, 338*, 643.
8. Burroughes, J. H. H., Bradley, D. D. C., Brown, A. R., Marks, R. N., Mackay, K., Friend, R. H., Burns, P. L., Holmes, A. B., & Road, M. (1990). *Nature, 347*, 539.
9. Stranks, S. D., & Snaith, H. J. (2015). *Nature Nanotechnology, 10*, 391.
10. Liu, X. K., Xu, W., Bai, S., Jin, Y., Wang, J., Friend, R. H., & Gao, F. (2020). *Nature Materials, 20*(1), 10.
11. Yuan, M., Quan, L. N., Comin, R., Walters, G., Sabatini, R., Voznyy, O., Hoogland, S., Zhao, Y., Beauregard, E. M., Kanjanaboos, P., Lu, Z., Kim, D. H., & Sargent, E. H. (2016). *Nature Nanotechnology, 11*, 872.
12. Wang, N., Cheng, L., Ge, R., Zhang, S., Miao, Y., Zou, W., Yi, C., Sun, Y., Cao, Y., Yang, R., Wei, Y., Guo, Q., Ke, Y., Yu, M., Jin, Y., Liu, Y., Ding, Q., Di, D., Yang, L., Xing, G., Tian, H., Jin, C., Gao, F., Friend, R. H., Wang, J., & Huang, W. (2016). *Nature Photonics, 10*, 699.
13. Zhao, B., Lian, Y., Cui, L., Divitini, G., Kusch, G., Ruggeri, E., Auras, F., Li, W., Yang, D., Zhu, B., Oliver, R. A., MacManus-Driscoll, J. L., Stranks, S. D., Di, D., & Friend, R. H. (2020). *Nature Electronics, 3*, 704.
14. Cho, H., Jeong, S.-H., Park, M.-H., Kim, Y.-H., Wolf, C., Lee, C.-L., Heo, J. H., Sadhanala, A., Myoung, N., Yoo, S., Im, S. H., Friend, R. H., & Lee, T.-W. (2015). *Science, 350*, 1222.
15. Xu, W., Hu, Q., Bai, S., Bao, C., Miao, Y., Yuan, Z., Borzda, T., Barker, A. J., Tyukalova, E., Hu, Z., Kawecki, M., Wang, H., Yan, Z., Liu, X., Shi, X., Uvdal, K., Fahlman, M., Zhang, W., Duchamp, M., Liu, J.-M., Petrozza, A., Wang, J., Liu, L.-M., Huang, W., & Gao, F. (2019). *Nature Photonics, 13*, 418.
16. Cho, C., Zhao, B., Tainter, G. D., Lee, J. Y., Friend, R. H., Di, D., Deschler, F., & Greenham, N. C. (2020). *Nature Communications, 11*, 611.
17. Shi, X. B., Liu, Y., Yuan, Z., Liu, X. K., Miao, Y., Wang, J., Lenk, S., Reineke, S., & Gao, F. (2018). *Advanced Optical Materials, 6*, 1800667.
18. Guo, B., Lai, R., Jiang, S., Zhou, L., Ren, Z., Lian, Y., Li, P., Cao, X., Xing, S., Wang, Y., Li, W., Zou, C., Chen, M., Hong, Z., Li, C., Zhao, B., & Di, D. (2022). *Nature Photonics, 16*(9), 637.
19. Liu, Y., Cui, J., Du, K., Tian, H., He, Z., Zhou, Q., Yang, Z., Deng, Y., Chen, D., Zuo, X., Ren, Y., Wang, L., Zhu, H., Zhao, B., Di, D., Wang, J., Friend, R. H., & Jin, Y. (2019). *Nature Photonics, 13*, 760.
20. Karlsson, M., Yi, Z., Reichert, S., Luo, X., Lin, W., Zhang, Z., Bao, C., Zhang, R., Bai, S., Zheng, G., Teng, P., Duan, L., Lu, Y., Zheng, K., Pullerits, T., Deibel, C., Xu, W., Friend, R., & Gao, F. (2021). *Nature Communications, 12*, 1.

21. Luo, J., Wang, X., Li, S., Liu, J., Guo, Y., Niu, G., Yao, L., Fu, Y., Gao, L., Dong, Q., Zhao, C., Leng, M., Ma, F., Liang, W., Wang, L., Jin, S., Han, J., Zhang, L., Etheridge, J., Wang, J., Yan, Y., Sargent, E. H., & Tang, J. (2018). *Nature, 563*, 541.
22. Chen, J., Wang, J., Xu, X., Li, J., Song, J., Lan, S., Liu, S., Cai, B., Han, B., Precht, J. T., Ginger, D., & Zeng, H. (2020). *Nature Photonics, 15*, 238.
23. Yang, D., Zhang, G., Lai, R., Cheng, Y., Lian, Y., Rao, M., Huo, D., Lan, D., Zhao, B., & Di, D. (2021). *Nature Communications, 12*, 4295.
24. Lu, J., Guan, X., Li, Y., Lin, K., Feng, W., Zhao, Y., Yan, C., Li, M., Shen, Y., Qin, X., & Wei, Z. (2021). *Advanced Materials, 33*, 2104414.
25. Hsu, C., Tian, S., Lian, Y., Zhang, G., Zhou, Q., Cao, X., Zhao, B., & Di, D. (2021). *Cell Reports Physical Science, 2*, 100582.
26. Lian, Y., Lan, D., Xing, S., Guo, B., Ren, Z., Lai, R., Zou, C., Zhao, B., Friend, R. H., & Di, D. (2022). *Nature Communications, 13*, 3845.
27. Wang, J., Wang, N., Jin, Y., Si, J., Tan, Z.-K. K., Du, H., Cheng, L., Dai, X., Bai, S., He, H., Ye, Z., Lai, M. L., Friend, R. H., & Huang, W. (2015). *Advanced Materials, 27*. n/a.
28. Stranks, S. D., Hoye, R. L. Z., Di, D., Friend, R. H., Deschler, F., Stranks, S. D., Hoye, R. L. Z., Di, D., Friend, R. H., & Deschler, F. (2019). *Advanced Materials, 31*, 1803336.
29. Richter, J. M., Abdi-Jalebi, M., Sadhanala, A., Tabachnyk, M., Rivett, J. P. H., Pazos-Outón, L. M., Gödel, K. C., Price, M., Deschler, F., & Friend, R. H. (2016). *Nature Communications, 7*, 13941.
30. Landsberg, P. T. (1992). *Recombination in semiconductors*. Cambridge University Press. https://doi.org/10.1017/CBO9780511470769
31. Di, D., Yang, L., Richter, J. M., Meraldi, L., Altamimi, R. M., Alyamani, A. Y., Credgington, D., Musselman, K. P., MacManus-Driscoll, J. L., & Friend, R. H. (2017). *Advanced Materials, 29*, 1605987.
32. Di, D., Romanov, A. S., Yang, L., Richter, J. M., Rivett, J. P. H., Jones, S., Thomas, T. H., Abdi Jalebi, M., Friend, R. H., Linnolahti, M., Bochmann, M., & Credgington, D. (2017). *Science, 356*, 159.
33. Jiang, Y., Cui, M., Li, S., Sun, C., Huang, Y., Wei, J., Zhang, L., Lv, M., Qin, C., Liu, Y., & Yuan, M. (2021). *Nature Communications, 12*, 1.
34. Zhao, X., & Tan, Z. K. (2019). *Nature Photonics, 14*(4), 215.
35. Xiao, Z., Kerner, R. A., Zhao, L., Tran, N. L., Lee, K. M., Koh, T.-W., Scholes, G. D., & Rand, B. P. (2017). *Nature Photonics, 11*, 108.
36. Ban, M., Zou, Y., Rivett, J. P. H., Yang, Y., Thomas, T. H., Tan, Y., Song, T., Gao, X., Credgington, D., Deschler, F., Sirringhaus, H., & Sun, B. (2018). *Nature Communications, 9*, 3892.
37. Choul Yu, J., Kim, D. B., Baek, G., Lee, B. R., Jung, E. D., Lee, S., Chu, J. H., Lee, D.-K., Choi, K. J., Cho, S., Song, M. H., Yu, J. C., Kim, D. B., Lee, B. R., Jung, E. D., Lee, S., Choi, K. J., Song, M. H., Baek, G., Cho, S., Chu, J. H., & Lee, D. (2015). *Advanced Materials, 27*, 3492.
38. Li, G., Rivarola, F. W. R., Davis, N. J. L. K., Bai, S., Jellicoe, T. C., de la Peña, F., Hou, S., Ducati, C., Gao, F., Friend, R. H., Greenham, N. C., & Tan, Z.-K. (2016). *Advanced Materials, 28*, 3528.
39. Shen, Y., Cheng, L.-P., Li, Y.-Q., Li, W., Chen, J.-D., Lee, S.-T., Tang, J.-X., Shen, Y., Cheng, L.-P., Li, Y.-Q., Li, W., Chen, J.-D., Lee, S.-T., & Tang, J.-X. (2019). *Advanced Materials, 31*, 1901517.
40. Fieramosca, A., de Marco, L., Passoni, M., Polimeno, L., Rizzo, A., Rosa, B. L. T., Cruciani, G., Dominici, L., de Giorgi, M., Gigli, G., Andreani, L. C., Gerace, D., Ballarini, D., & Sanvitto, D. (2018). *ACS Photonics, 5*, 4179.
41. Walters, G., Haeberlé, L., Quintero-Bermudez, R., Brodeur, J., Kéna-Cohen, S., & Sargent, E. H. (2020). *Journal of Physical Chemistry Letters, 11*, 3458.
42. Jurow, M. J., Lampe, T., Penzo, E., Kang, J., Koc, M. A., Zechel, T., Nett, Z., Brady, M., Wang, L. W., Alivisatos, A. P., Cabrini, S., Brütting, W., & Liu, Y. (2017). *Nano Letters, 17*, 4534.
43. Zou, C., & Lin, L. Y. (2020). *Optics Letters, 45*(17), 4786–4789.

44. Jurow, M. J., Morgenstern, T., Eisler, C., Kang, J., Penzo, E., Do, M., Engelmayer, M., Osowiecki, W. T., Bekenstein, Y., Tassone, C., Wang, L. W., Alivisatos, A. P., Brütting, W., & Liu, Y. (2019). *Nano Letters, 19*, 2489.
45. Bowman, A. R., Anaya, M., Greenham, N. C., & Stranks, S. D. (2020). *Physical Review Letters, 125*, 067401.
46. Kim, H. P., Kim, J., Kim, B. S., Kim, H. M., Kim, J., Bin, A. R., Yusoff, M., Jang, J., & Nazeeruddin, M. K. (2017). *Advanced Optical Materials, 5*, 1600920.
47. Möller, S., & Forrest, S. R. (2002). *Journal of Applied Physics, 91*, 3324.
48. Schubert, E. F., Hunt, N. E. J., Micovic, M., Malik, R. J., Sivco, D. L., Cho, A. Y., & Zydzik, G. J. (1994). *Science (1979), 265*, 943.
49. Kim, Y. H., Kim, S., Kakekhani, A., Park, J., Park, J., Lee, Y. H., Xu, H., Nagane, S., Wexler, R. B., Kim, D. H., Jo, S. H., Martínez-Sarti, L., Tan, P., Sadhanala, A., Park, G. S., Kim, Y. W., Hu, B., Bolink, H. J., Yoo, S., Friend, R. H., Rappe, A. M., & Lee, T. W. (2021). *Nature Photonics, 15*(2), 148.
50. Miao, Y., Cheng, L., Zou, W., Gu, L., Zhang, J., Guo, Q., Peng, Q., Xu, M., He, Y., Zhang, S., Cao, Y., Li, R., Wang, N., Huang, W., & Wang, J. (2020). *Light: Science & Applications, 9*, 1.
51. Zhang, X., Xu, B., Wang, W., Liu, S., Zheng, Y., Chen, S., Wang, K., & Sun, X. W. (2017). *ACS Applied Materials & Interfaces, 9*, 4926.
52. Luo, Q., Zhang, C., Deng, X., Zhu, H., Li, Z., Wang, Z., Chen, X., & Huang, S. (2017). *ACS Applied Materials & Interfaces, 9*, 34821.
53. Berestennikov, A. S., Voroshilov, P. M., Makarov, S. V., & Kivshar, Y. S. (2019). *Applied Physics Reviews, 6*, 031307.
54. Lova, P., Cortecchia, D., Krishnamoorthy, H. N. S., Giusto, P., Bastianini, C., Bruno, A., Comoretto, D., & Soci, C. (2018). *ACS Photonics, 5*, 867.
55. Chen, S., & Nurmikko, A. (2017). *ACS Photonics, 4*, 2486.
56. Wellmann, P., Hofmann, M., Zeika, O., Werner, A., Birnstock, J., Meerheim, R., He, G., Walzer, K., Pfeiffer, M., & Leo, K. (2005). *Journal of the Society for Information Display, 13*, 393.
57. Eames, C., Frost, J. M., Barnes, P. R. F., O'Regan, B. C., Walsh, A., & Islam, M. S. (2015). *Nature Communications, 6*, 1.
58. Tsai, H., Shrestha, S., Vilá, R. A., Huang, W., Liu, C., Hou, C. H., Huang, H. H., Wen, X., Li, M., Wiederrecht, G., Cui, Y., Cotlet, M., Zhang, X., Ma, X., & Nie, W. (2021). *Nature Photonics, 15*, 843.
59. Dong, Q., Lei, L., Mendes, J., & So, F. (2020). *Journal of Physics: Materials, 3*, 012002.
60. Li, C., Wang, N., Guerrero, A., Zhong, Y., Long, H., Miao, Y., Bisquert, J., Wang, J., & Huettner, S. (2019). *Journal of Physical Chemistry Letters, 10*, 6857.
61. Li, C., Guerrero, A., Huettner, S., & Bisquert, J. (2018). *Nature Communications, 9*, 5113.
62. Boyd, C. C., Cheacharoen, R., Leijtens, T., & McGehee, M. D. (2019). *Chemical Reviews, 119*, 3418.
63. Han, B., Yuan, S., Cai, B., Song, J., Liu, W., Zhang, F., Fang, T., Wei, C., Zeng, H., Han, B., Yuan, S., Cai, B., Song, J., Liu, W., Zhang, F., Fang, T., Wei, C., & Zeng, H. (2021). *Advanced Functional Materials, 31*, 2011003.
64. Li, H., Lin, H., Ouyang, D., Yao, C., Li, C., Sun, J., Song, Y., Wang, Y., Yan, Y., Wang, Y., Dong, Q., & Choy, W. C. H. (2021). *Advanced Materials, 33*, 2008820.
65. Kuang, C., Hu, Z., Yuan, Z., Wen, K., Qing, J., Kobera, L., Abbrent, S., Brus, J., Yin, C., Wang, H., Xu, W., Wang, J., Bai, S., & Gao, F. (2021). *Joule, 5*, 618.
66. Wang, H., Zhang, X., Wu, Q., Cao, F., Yang, D., Shang, Y., Ning, Z., Zhang, W., Zheng, W., Yan, Y., Kershaw, S. V., Zhang, L., Rogach, A. L., & Yang, X. (2019). *Nature Communications, 10*, 1.
67. Jeong, B., Han, H., Ji Choi, Y., Hwan Cho, S., Hyuk Kim, E., Won Lee, S., Sung Kim, J., Park, C., Kim, D., Park, C., Jeong, B., Han, H., Cho, S. H., Kim, E. H., Lee, S. W., Kim, J. S., Park, C., Choi, Y. J., & Kim, D. (2018). *Advanced Functional Materials, 28*, 1706401.
68. Hassan, Y., Park, J. H., Crawford, M. L., Sadhanala, A., Lee, J., Sadighian, J. C., Mosconi, E., Shivanna, R., Radicchi, E., Jeong, M., Yang, C., Choi, H., Park, S. H., Song, M. H., de Angelis, F., Wong, C. Y., Friend, R. H., Lee, B. R., & Snaith, H. J. (2021). *Nature, 591*, 7848.

69. Ma, D., Lin, K., Dong, Y., Choubisa, H., Proppe, A. H., Wu, D., Wang, Y. K., Chen, B., Li, P., Fan, J. Z., Yuan, F., Johnston, A., Liu, Y., Kang, Y., Lu, Z. H., Wei, Z., & Sargent, E. H. (2021). *Nature, 599*, 7886.
70. Wang, Q., Wang, X., Yang, Z., Zhou, N., Deng, Y., Zhao, J., Xiao, X., Rudd, P., Moran, A., Yan, Y., & Huang, J. (2019). *Nature Communications, 10*, 1.
71. Xing, J., Zhao, Y., Askerka, M., Quan, L. N., Gong, X., Zhao, W., Zhao, J., Tan, H., Long, G., Gao, L., Yang, Z., Voznyy, O., Tang, J., Lu, Z. H., Xiong, Q., & Sargent, E. H. (2018). *Nature Communications, 9*, 1.
72. Zhao, L., Roh, K., Kacmoli, S., Al Kurdi, K., Jhulki, S., Barlow, S., Marder, S. R., Gmachl, C., & Rand, B. P. (2020). *Advanced Materials, 32*, 2000752.
73. Zheng, X., Yuan, S., Liu, J., Yin, J., Yuan, F., Shen, W. S., Yao, K., Wei, M., Zhou, C., Song, K., Zhang, B. B., Lin, Y., Hedhili, M. N., Wehbe, N., Han, Y., Sun, H. T., Lu, Z. H., Anthopoulos, T. D., Mohammed, O. F., Sargent, E. H., Liao, L. S., & Bakr, O. M. (2020). *ACS Energy Letters, 5*, 793.
74. Vashishtha, P., & Halpert, J. E. (2017). *Chemistry of Materials, 29*, 5965.
75. Yuan, Z., Miao, Y., Hu, Z., Xu, W., Kuang, C., Pan, K., Liu, P., Lai, J., Sun, B., Wang, J., Bai, S., & Gao, F. (2019). *Nature Communications, 10*, 1.
76. Yoon, S. J., Kuno, M., & Kamat, P. V. (2017). *ACS Energy Letters, 2*, 1507.
77. Yuan, S., Wang, Z.-K., Xiao, L.-X., Zhang, C.-F., Yang, S.-Y., Chen, B.-B., Ge, H.-T., Tian, Q.-S., Jin, Y., Liao, L.-S., Yuan, S., Wang, Z.-K., Yang, S.-Y., Ge, H.-T., Tian, Q.-S., Jin, Y., Liao, L.-S., Xiao, L.-X., Zhang, C.-F., & Chen, B.-B. (2019). *Advanced Materials, 31*, 1904319.
78. Congreve, D. N., Weidman, M. C., Seitz, M., Paritmongkol, W., Dahod, N. S., & Tisdale, W. A. (2017). *ACS Photonics, 4*, 476.
79. Yang, Y., Xu, S., Ni, Z., van Brackle, C. H., Zhao, L., Xiao, X., Dai, X., & Huang, J. (2021). *Advanced Materials, 33*, 2100783.
80. Liu, Y., Li, Z., Xu, J., Dong, Y., Chen, B., Park, S. M., Ma, D., Lee, S., Huang, J. E., Teale, S., Voznyy, O., & Sargent, E. H. (2022). *Journal of the American Chemical Society, 144*, 4009.
81. Jia, H., Shi, H., Yu, R., Ma, H., Wang, Z., Zou, C., Tan, Z. A., Jia, H., Shi, H., Yu, R., Ma, H., Tan, Z., Wang, Z., & Zou, C. (2022). *Small, 18*, 2200036.
82. Wang, Y., Zou, R., Chang, J., Fu, Z., Cao, Y., Zhang, L., Wei, Y., Kong, D., Zou, W., Wen, K., Fan, N., Wang, N., Huang, W., & Wang, J. (2019). *Journal of Physical Chemistry Letters, 10*, 453.
83. Lu, J., Guan, X., Li, Y., Lin, K., Feng, W., Zhao, Y., Yan, C., Li, M., Shen, Y., Qin, X., Wei, Z., Lu, J., Guan, X., Li, Y., Lin, K., Feng, W., Zhao, Y., Yan, C., Li, M., Shen, Y., Qin, X., & Wei, Z. (2021). *Advanced Materials, 33*, 2104414.
84. Wang, C. Y., Liang, P., Xie, R. J., Yao, Y., Liu, P., Yang, Y., Hu, J., Shao, L., Sun, X. W., Kang, F., & Wei, G. (2020). *Chemistry of Materials, 32*, 7814.
85. Jin, S. X., Li, J., Li, J. Z., Lin, J. Y., & Jiang, H. X. (2000). *Applied Physics Letters, 76*, 631.
86. Wong, M. S., Nakamura, S., & DenBaars, S. P. (2020). *ECS Journal of Solid State Science and Technology, 9*, 015012.
87. Lin, J. Y., & Jiang, H. X. (2020). *Applied Physics Letters, 116*, 100502.
88. Huang, Y., Hsiang, E. L., Deng, M. Y., & Wu, S. T. (2020). *Light: Science & Applications, 9*, 1.
89. Cao, X. A., Pearton, S. J., Zhang, A. P., Dang, G. T., Ren, F., Shul, R. J., Zhang, L., Hickman, R., & van Hove, J. M. (1999). *Applied Physics Letters, 75*, 2569.
90. Corbett, B., Loi, R., Zhou, W., Liu, D., & Ma, Z. (2017). *Progress in Quantum Electronics, 52*, 1.
91. Cok, R. S., Meitl, M., Rotzoll, R., Melnik, G., Fecioru, A., Trindade, A. J., Raymond, B., Bonafede, S., Gomez, D., Moore, T., Prevatte, C., Radauscher, E., Goodwin, S., Hines, P., & Bower, C. A. (2017). *Journal of the Society for Information Display, 25*, 589.
92. Zhang, L., Ou, F., Chong, W. C., Chen, Y., & Li, Q. (2018). *Journal of the Society for Information Display, 26*, 137.
93. Zou, C., Chang, C., Sun, D., Böhringer, K. F., & Lin, L. Y. (2020). *Nano Letters, 20*, 3710.
94. Zou, C., Liu, Y., Ginger, D. S., & Lin, L. Y. (2020). *ACS Nano, 14*, 6076.

Excitons in $CsPbBr_3$ Halide Perovskites

J. A. Peters, Z. Liu, O. Bulgin, Y. He, V. Klepov, M. De Siena, M. G. Kanatzidis, and B. W. Wessels

1 Introduction

Metal halide perovskites (MHPs) are currently being considered for many applications, including light-emitting diodes (LEDs) and room-temperature hard radiation detector devices. MHPs have been utilized in hard radiation detector devices due to their good physical properties and reasonably high atomic number elements. Moreover, they possess large bulk resistivity that leads to small dark currents and low noise for radiation detector devices. Recently, we have shown high-resolution radiation detectors with very narrow linewidths using $CsPbBr_3$ as the MHP [1–3]. Notwithstanding the considerable potential of halide perovskites for ionizing

J. A. Peters
Department of Materials Science and Engineering, Northwestern University, Evanston, IL, USA

Department of Chemistry, Physics, and Engineering Studies, Chicago State University, Chicago, IL, USA

Z. Liu · B. W. Wessels (✉)
Department of Materials Science and Engineering, Northwestern University, Evanston, IL, USA
e-mail: b-wessels@northwestern.edu

O. Bulgin
Department of Chemistry, Physics, and Engineering Studies, Chicago State University, Chicago, IL, USA

Y. He · V. Klepov · M. De Siena
Department of Chemistry, Northwestern University, Evanston, IL, USA

M. G. Kanatzidis
Department of Materials Science and Engineering, Northwestern University, Evanston, IL, USA

Department of Chemistry, Northwestern University, Evanston, IL, USA

W. Nie, K. (Kris) Iniewski (eds.), *Metal-Halide Perovskite Semiconductors*,
https://doi.org/10.1007/978-3-031-26892-2_5

radiation detection, there is no broad consensus on their charge transport characteristics. To further improve the detector performance, charge transport in the devices needs to be studied and optimized, while an understanding of the role of charge transport on detector efficiency is required [4]. There is a competition between recombination via extrinsic disorder and intrinsic disorder. Hence, native defects and impurities that scatter or trap carriers need to be removed or optimized, and intrinsic scattering and trapping mechanisms that limit mobility need to be resolved. Toward this end, several experimental and theoretical investigations on MHPs have been undertaken [5, 6]. One such investigation involved the interaction between a charge carrier and the lattice, attributing coupling to longitudinal optical (LO) phonons through the Coulomb interaction [7]. LO phonon scattering induces a mobility limit at room temperature for most polar materials [7]. Understanding the role of electron-phonon scattering interactions is needed to enhance detector performance. Two types of electron-phonon interactions have been previously described [8, 9]. They include acoustic deformation potential scattering and Frohlich-type polaron interactions. For Frohlich interactions, lattice polarization generates a large electric field via LO phonon modes. These Frohlich interactions strongly limit the room-temperature charge-carrier mobility in metal halide perovskite. Calculations indicate that the carrier mobility for $MAPbI_3$ is limited to 80 cm^2/Vs, which is close to the experimentally observed value [10]. Frohlich polar interactions also lead to polarons forming either highly localized (small polarons) or extended in space (large polarons) [11]. The movement of polarons is regulated by the nature of the polar lattice, with small polarons moving incoherently by way of a hopping mechanism and the large polarons moving coherently via scattering events [8, 12]. Small polarons have been optically revealed as a broad peak on the low energy side of the free exciton peak utilizing photoluminescence measurements. These low-energy near band edge states trap carriers and alter charge transport in the materials, including carrier mobility and mobility-lifetime products (μ-τ), which are important for developing halide perovskites for radiation detection applications. Ultimately, trap states could lead to peak broadening in radiation detectors.

Here, we investigate photogenerated charge carriers in bulk $CsPbBr_3$ single crystals using photoluminescence (PL) spectroscopy and time-resolved photoluminescence (TR-PL) spectroscopy to determine the nature of charge transport. Although there have been numerous reports of near band edge emission (NBE) in $CsPbBr_3$ via PL and TR-PL, most of these have been studied on nanocrystals, nanosheets/nanoplates, and quantum dot structures with very few studies on bulk single crystals with a view on applications to ionizing radiation detectors [13, 14]. The question arises as to the nature and identity of the background defects in the high-purity, Bridgman material. Knowledge of excitonic states and band tail states is necessary for understanding recombination and transport in these materials. Do band tail or Urbach-like states exist in single-crystalline materials? Previously we found in bulk $CsPbBr_3$ single crystals that a band edge luminescence at ~2.3 eV dominated the spectrum [15]. The PL peak was further resolved into two peaks at 2.29 eV and 2.33 eV. The emission peaks were attributed to free exciton recombination and bound exciton recombination. No evidence of deep-level emission was observed in the spectrum.

Using Toyazawa's analysis of FWHM of the NBE peak, a phonon energy of 16 meV was obtained [16]. We also reported on the temperature dependence and effect of excitation intensity on the time-resolved near band edge emission (NBE) PL. A simple rate equation, including single carrier recombination and electron-hole exciton recombination, was used to describe the NBE bands [17]. In that study, monomolecular and bimolecular recombination contributions were distinguished. A double exponential decay curve described the time-dependent PL. This finding was consistent with the thermal quenching measurements where the temperature dependence was well-described by a double exponential thermal quenching curve. The activation energies of thermal quenching were 17 meV and 0.7 meV. A question remains as to the identity of the exciton-related PL peaks. In the present study, we measure the thermal quenching of the spectrally resolved near band edge PL. In addition to excitonic states, we studied band-tail states near the conduction band edge. These band-tail states are involved in both charge transport and luminescence.

2 Experimental Methods

2.1 Synthesis

$CsPbBr_3$ (ID: YH2105) was synthesized via a solid-state reaction, and single crystals were grown using the Bridgman method and polished for optical measurements. These procedures are described in detail elsewhere [18]. Specifically, a Φ10 mm quartz tube was utilized for the melt growth, which was placed inside a two-zone Bridgman furnace. The overheating temperature and cooling rates were ~ 20–30 K and 1–5 K/h, respectively. The As-grown Φ10 mm ingot was then mechanically cut and polished for optical measurements.

2.2 Low-Temperature Photoluminescence Measurements

Temperature-dependent and excitation intensity-dependent photoluminescence (PL) were measured for the $CsPbBr_3$ compound. The sample mounting procedure and measurement setup were similar to those described by us previously [19]. A continuous wave diode laser (OBIS 405 nm LX, 100 mW) with a constant power of up to 100 mW and intensity of up to 6944 mW/ cm^2 was used as the excitation source of the PL measurements. A set of calibrated neutral optical density filters was used to tune the power from ~1.26 μ W to 50 mW, so as to limit the laser intensity between 1.4 and 3472 mW/cm^2 for temperature- and power-dependent measurements. Temperature-dependent PL measurements were made with 2 mW (intensity of ~140 mW/cm^2) laser power to ensure reproducibility. Power-dependent

PL measurement was conducted at 13 K. Repeating the measurements yields the same signal for the chosen laser powers, indicating that the samples are undamaged.

2.3 Time-Resolved Photoluminescence (TR-PL) Measurements

For the TR-PL measurements, the $CsPbBr_3$ perovskite crystal is illuminated with the 405-nm light pulses operated at 20–1000 Hz. The pulse width was kept at 1 μs or 100 μs and the spot size is ~1 mm^2. The measurement setup was like that previously reported [10]. The exposure of the sample to a laser pulse gives rise to a TR-PL response, which passes through a spectrophotometer (SPEX 500 M) and is picked up by the PMT. The signal after PMT is monitored by an oscilloscope with 50 or 75 Ω impedance. The low impedance is chosen to ensure that the trace of the TR-PL accurately reflects the time decay behavior. Since the lower limit of the oscilloscope is 1 mV, any TR-PL signal lower than 0.1 mV does not have a sufficient signal to noise ratio. For each given temperature, the peak or shoulder locations of PL is first scanned. Then the operating wavelength of the spectrophotometer is tuned to each wavelength of interest, and TR-PL measurement is subsequently conducted. Figure 1 shows a schematic of the measurement setups for PL and TR-PL measurements.

3 Results and Discussion

3.1 Low-Temperature Photoluminescence Spectroscopy

The spectrum of excitonic emission from the bulk Bridgman-grown $CsPbBr_3$ crystals, and its thermal quenching over the temperature range of 13–80 K, **is** shown in Fig. 2a. A long exponential tail is observed in the PL spectrum on the low-energy side of the main peak (~2.29 eV), and it is shown with greater clarity on a semi-log

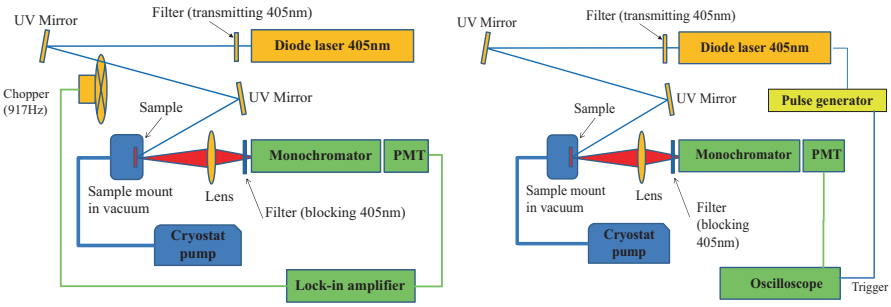

Fig. 1 Measurement setups for PL (LEFT) and TR-PL (RIGHT) spectroscopies

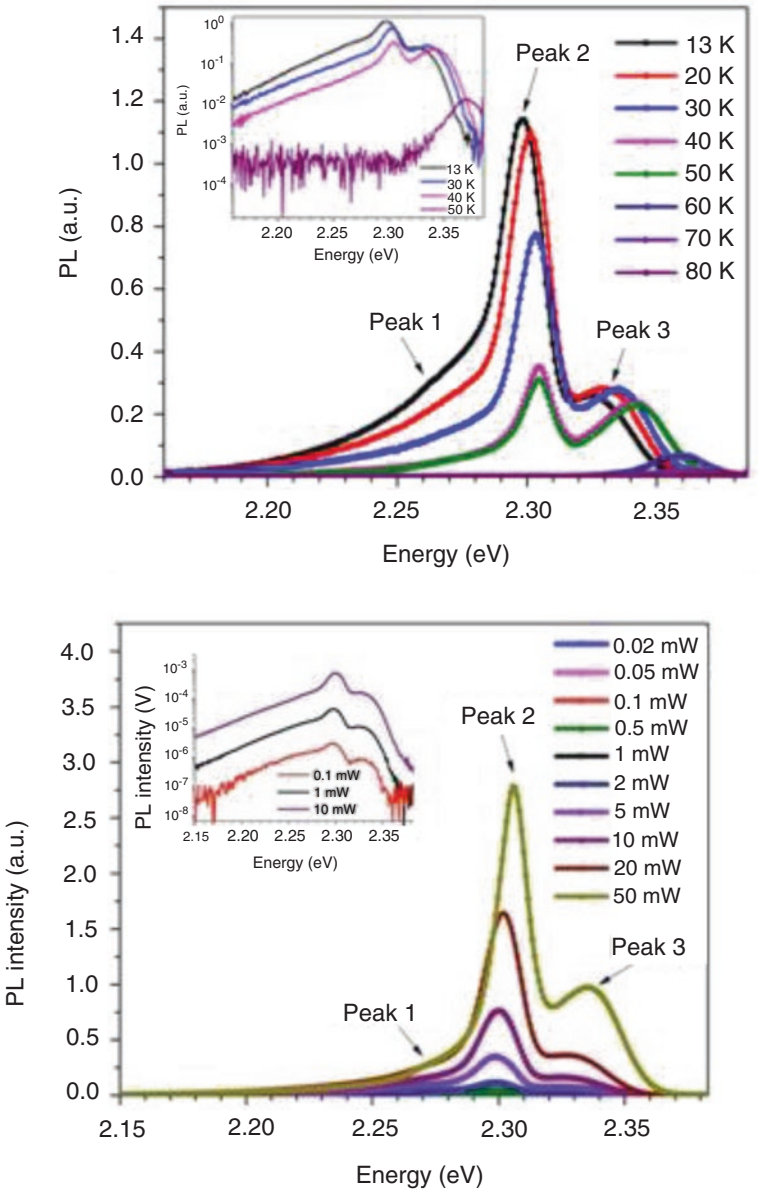

Fig. 2 (**a**) Spectrum of exciton emission for T = 13 K to 80 K. (**b**) PL spectra of different laser power at a temperature of 13 K. A band tail is observed at energies below 2.27 eV

plot in the inset of Fig. 1. Three bands are observed at 2.27, 2.29, and 2.33 eV. The band at 2.27 eV has a long shoulder on the low-energy side. Upon heating, the luminescence from the three bands decreases in intensity. At a temperature of 13 K, the full width at half-maximum (FWHM) for each of the observed peaks are 31.8, 19.4,

and 18.9 meV, respectively. By comparing the peaks detected here with previous work on $CsPbBr_3$, single-crystal peaks 2 and 3 can be attributed to free exciton recombination and bound exciton recombination [15]. The broader feature at 2.27 eV (peak 1) may be the result of the defect-related transitions linked to native and structural defects. Figure 2b shows the PL spectra at a temperature of 13 K for different excitation powers. A pronounced band tail is observed for different excitation levels.

The excitation power dependence of the PL intensity (Fig. 3) determines the type of recombination processes in these Bridgman grown crystals. It well known that the intensity I of the luminescence emission is proportional to L^{γ} where L is the power of the exciting laser radiation. An exponent (γ) value in the range $1 < \gamma < 2$ indicates exciton-like transitions, whereas $\gamma < 1$ suggests either free-to-bound or donor-acceptor pair transitions [20]. For the three peaks measured in the present study, the intensity I increases logarithmically with the excitation intensity L with the values of γ in the range $1 < \gamma < 2$. This result indicates exciton-like emission for all three peaks. For further confirmation of the excitonic nature of these peaks, the excitation power dependence of PL intensity was measured at temperatures $12 \leq T \leq 200$. It is found that the gamma value does depend on temperature. The results in Table 1 show that the values of γ were > 1 for all the peaks at all temperatures measured. This validates our initial assignment of the peaks to excitonic emission.

Trap ionization levels can be obtained from the peak intensity's temperature dependence. Figure 4a shows a plot of the measured peak intensities (solid symbols) of the three emission bands shown in Fig. 2a versus temperature. Also shown is the intensity versus reciprocal temperature in Fig. 4b. The intensity dependence of peak 2 reveals a monotonically decreasing behavior. Intensities of peaks 1 and 3 have a weaker temperature dependence. We observe from the temperature-dependent peak intensities in Fig. 2a that peak 1 becomes unobservable and quenches above

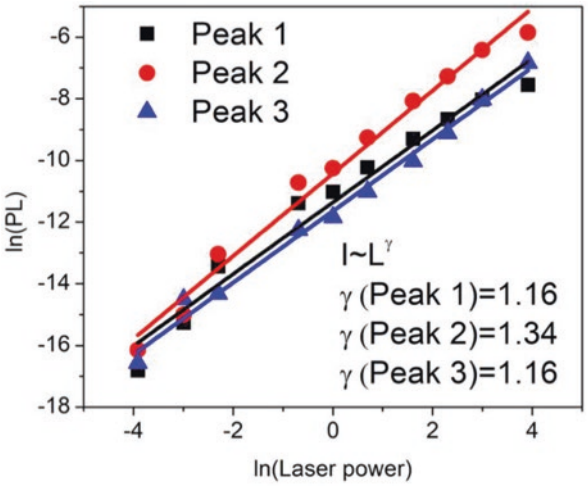

Fig. 3 PL intensity dependence on laser power for the three bands, with energies 2.27 eV, 2.29 eV, and 2.34 eV at 13 K

Table 1 Dependence of gamma parameter on temperature for three bands

Peak	$\gamma_{(12\ K)}$	$\gamma_{(35\ K)}$	$\gamma_{(65\ K)}$	$\gamma_{(95\ K)}$	$\gamma_{(200\ K)}$
2.27 eV	1.14	1.49	1.36	1.36	N/A
2.29 eV	1.38	1.38	1.53	1.53	1.46
2.33 eV	1.54	1.56	1.80	1.50	1.62

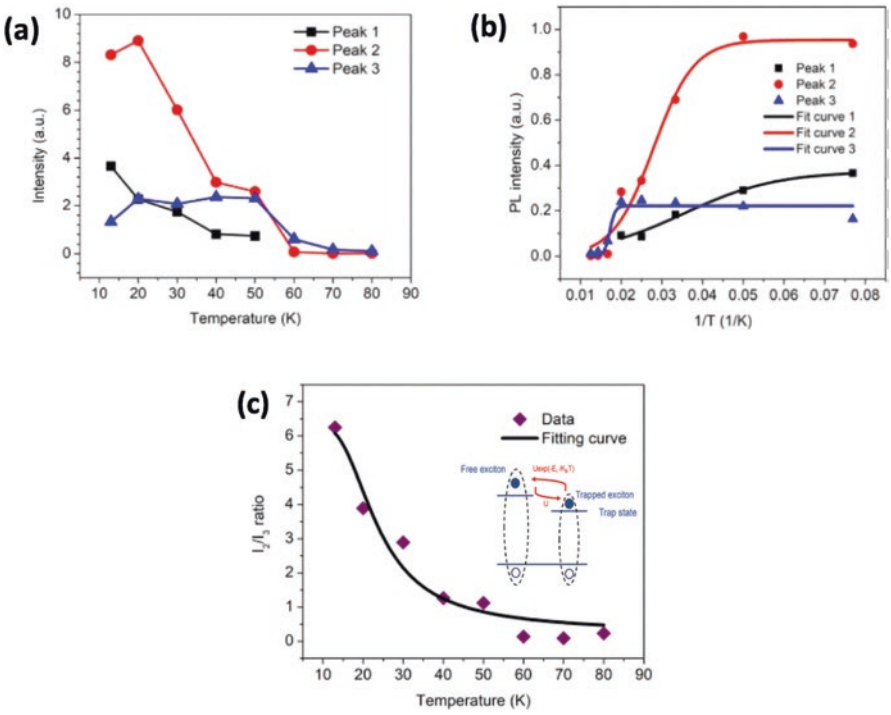

Fig. 4 (**a**) Dependence of peak intensity on T (K) for three peaks shown in Fig. 1a. (**b**) Intensity vs. 1/T for each of the peaks in Fig. 1a. (**c**) The ratio of intensities of exciton peaks versus temperature

50 K, while at ~55 K there is a temperature-induced intersection of the intensities of peaks 2 and 3. The ratio of the intensities of peaks 2 and 3 was analyzed using the following equation:

$$\frac{I_2}{I_3} = \frac{R_2}{R_3} \frac{U_0}{\left(R_{n_2} + R_2 T^{-2} + U_0 e^{-\frac{E_t}{k_B T}} \right)} \tag{1}$$

where I_2 and I_3 are the integrated intensities, R_2 and R_3 are the radiative recombination rates, and R_{n2} is the nonradiative recombination rate [21]. U_0 gives the trapping

rate while $U_0 exp \quad \frac{E_t}{k_B T}$ specifies the detrapping rate. E_t is the activation energy or the thermal detrapping barrier height of trapped/bound excitons [22]. As shown in Fig. 4c, the ratio of the two peaks I_2/I_3 systematically decreased with increasing temperature. The decrease could be described in terms of an activated process as shown by the inset in Fig. 4c where a trapped/bound exciton is thermalized forming a free exciton or large polaron [23]. It can therefore be reasonably assumed that thermal transfer between the trapped/bound excitons and free excitons accounts for the observed PL at 13 < T < 80 K. The activation energy E_t calculated using Eq. (1) above yielded a value of 7.6 meV which corresponds to the energy of thermalization of trapped/bound exciton to the free exciton. The dominance of the PL intensity of peak 2 over peak 3 at low temperatures (Fig. 4a) presumably indicates that the band at 2.29 eV (peak 2) is the free exciton emission. Free exciton trapping is known to be very efficient at low temperatures, with a trapping rate significantly greater than the detrapping rate of trapped/bound excitons [20]. An increase in temperature (15–30 K) causes a reduction in the population of filled trap states and gives rise to the high mobility of excitons or large polarons and a substantial decrease in PL intensity [21]. Polarons are formed when excess carriers interact and couple with ionic vibrations in polar materials such as $CsPbBr_3$. These quasiparticles are created via the separation of an exciton [8].

Alternatively, the binding energy of excitons can be determined from the thermal quenching of emission using the following equation: [24].

$$I(T) = \frac{I_0}{1 + C_1 e^{-\frac{E_B}{k_B T}}} \tag{2}$$

where I_0 and C_1 are constants and E_B is the binding energy. C_1 is associated with the intensity of the quenching process. By fitting the dependence of peak intensity on reciprocal temperature (Fig. 4b) with Eq. (2), the activation energy for the three peaks was determined to be 7.52, 17.3, and 130.6 meV, respectively. These activation energies can be ascribed to bound exciton formation involving different types of binding sites, such as intrinsic and extrinsic defects or lattice interactions. The quenching involves electron-phonon scattering, and the PL in $CsPbBr_3$ is a result of the recombination of excitons trapped by small polarons. The PL emission peaks are narrow for the case where electron-phonon interactions are weak but broad for the case where the Huang-Rhys parameter S is large [19]. S describes the strength of the electron-phonon coupling.

The detailed nature of the disorder responsible for the near band edge PL emission and its temperature dependence is under study. One possibility previously put forth to describe the emission in defect perovskites is the self-trapped exciton. In that case, the PL line shape is nearly Gaussian, and the peak energies are just a few meV below the free exciton peak [25]. In contrast, the recombination model discussed here presupposes that local fluctuations in the potential landscape have trapped excitons [21]. The origin of potential fluctuations that bind excitons is

related to the presence of point defects (e.g., vacancies and interstitials) as well as extended defects (e.g., twins and sub-grain boundaries). These fluctuations have been proposed by M. Baranowski [21] to be the source of the low carrier mobilities observed in these perovskite materials. From the Drude-Anderson model for mobility $\mu = e\tau/m^*$ where m^* is the carrier effective mass [8]. For the halide perovskites, there is a mobility edge between the free exciton level and the bound exciton level. An increase in m^* for carriers below the band edge is observed, resulting in lower mobilities for carriers. The presence of fluctuations gives rise to the mobility edge. Figure 5 shows a schematic representation of the model used to describe the near-band edge PL emission. The various pathways for the trapped/bound excitons, i.e., radiative recombination, hopping between different localized minima [26], or activation to a free exciton state, are indicated.

The thermal quenching of NBE PL in hybrid halide perovskites has been ascribed by M. Baranowski [21] to the thermalization of trapped/bound carriers into the conduction band. Here, the mobility and diffusion length of the excitons/polarons are larger and that enable their diffusion and capture by nonradiative, trapping centers near or at the surface. As the temperature increases, the bound excitons thermalize into the conduction band where higher mobilities are observed. That phonons are involved in the recombination can be observed in the prior studies of PL peak energy dependence on temperature $E(T)$ where a combination of the electron-phonon (EP) interaction and thermal expansion (TE) contributes to the luminescent peak shift according to the following equation: [27].

$$E(T) = E(0) + A_{TE}T - S\hbar\omega\left[\coth\left(\hbar\omega / 2k_BT\right) - 1\right] \tag{3}$$

where $E(0)$ is the peak energy at T = 0 K, A_{TE} is the thermal expansion parameter, S is the Huang-Rhys factor indicating electron-phonon coupling strength, and $\langle\hbar\omega\rangle$ is an average phonon energy. From the analysis of peak energy shown in Fig. 6, and using Eq. (3), an average phonon energy E of 6.5 meV and 27.4 meV was calculated for peaks 2 and 3, respectively. The Huang-Rhys parameter S was 3.81 and 1.51 for peaks 2 and 3, respectively, signifying a strong coupling. The effective phonon

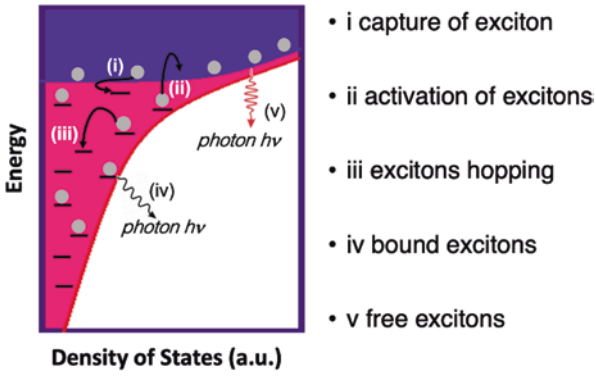

Fig. 5 Model for density of states versus energy. Excitons are trapped/bound below the conduction band edge in the band tail (after Ref. [21], Fig. 3a)

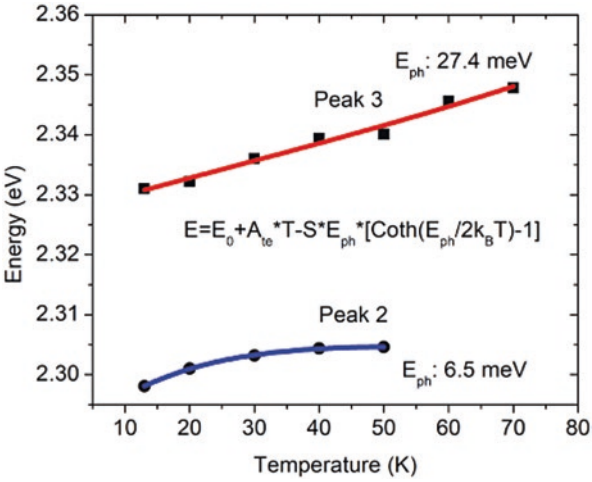

Fig. 6 Peak energy (E) vs. temperature (T) for phonon energy calculation using Eq. (3)

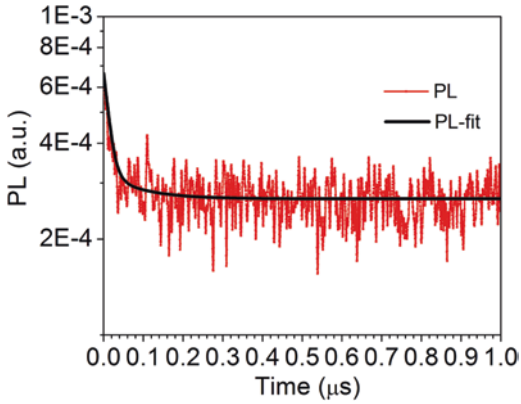

Fig. 7 Semi-log plot of the transient PL decay curve of peak 2 emission obtained at 20 K. Solid line is the fitting curve with the biexponential decay function as described in the text with $\tau_1 = 12$ ns, and $\tau_2 = 91.4$ ns

energy values of 6.5 and 27.4 meV are in fair agreement with prior values of 8.9 meV [28] and 20.5 meV [3] found using Raman spectroscopy.

3.2 Transient Photoluminescence Spectroscopy

The PL peak emission bands were further examined using time-resolved PL (TR-PL) spectroscopy. Figure 7 shows a typical decay curve for peak 2 (2.29 eV) at 20 K. The luminescence intensity $I(t)$ can be described by the following equation:

$$I(t) = C_1 e^{\frac{-t}{\tau_1}} + C_2 e^{\frac{-t}{\tau_2}} \tag{4}$$

where C_1 and C_2 are scaling parameters. By fitting the data to Eq. (4), a short time constant $\tau_1 = 12$ ns and a long time constant $\tau_2 = 91.4$ ns were determined for peak 2. For peak 3, $\tau_1 = 1.9$ ns and $\tau_2 = 18.3$ ns. A biexponential decay function with decay times indicates the presence of two separate processes [26] in the observed PL decay that leads to either radiative or nonradiative recombination. While multi-exponential fitting describes the shape of a decay curve, we cannot assign a distinguishable physical mechanism to each component; hence, a comprehensive kinetic analysis is needed. Further studies are in progress on our samples.

The average PL lifetimes of peaks 2 and 3 can be obtained using [29]

$$\tau_{ave} = \frac{\left(C_1 \times \tau_1^{\,2}\right) + \left(C_2 \times \tau_2^{\,2}\right)}{\left(C_1 \times \tau_1\right) + \left(C_2 \times \tau_2\right)} \tag{5}$$

From Eq. (5), average lifetimes of ~17 ns and ~ 38 ns were determined for peaks 2 and 3, respectively. The longer average lifetime of peak 3 may be attributable to the trapping of excitons (shown in the inset of Fig. 4c) by states that are formed by point defects (vacancies, interstitials, etc.) and extended defects (twins). Point defects trap charge carriers and control the carrier lifetime, thereby affecting radiation detector charge collection. In contrast, significant fluctuations initiated by extended defects can impair the performance of these detectors [30].

We carried out temperature-dependent TR-PL measurements to gain further information on decay dynamics. Our measurement of temperature-dependent CW PL allowed us to determine the locations of the points of interest. As shown in Fig. 8, a second peak with a relatively strong intensity on the lower energy side (2.30 eV) can be observed at ~50 K.

TR-PL measurements were carried out at temperatures ranging from 12 to 50 K (Fig. 9). Both a fast and a slow state are visible. Because the measurements had a low signal-to-noise ratio, no fit was reported for the other peaks other than the

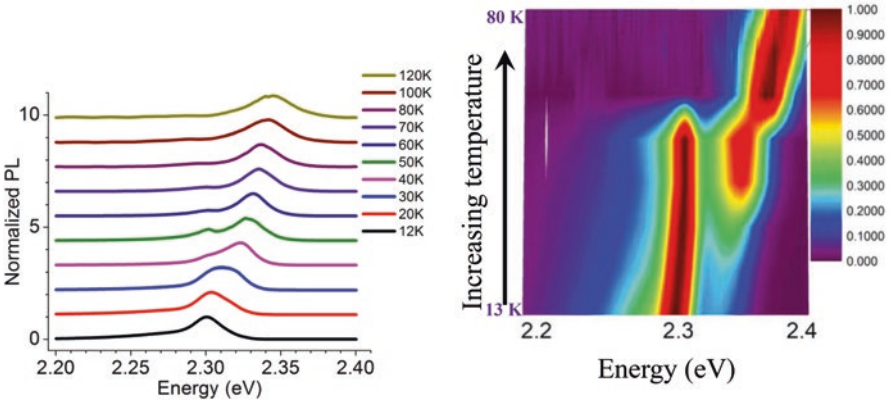

Fig. 8 (Left) Normalized PL intensity vs. temperature at excitation power of 2 mW. (Right) Three-dimensional map of the PL spectrum

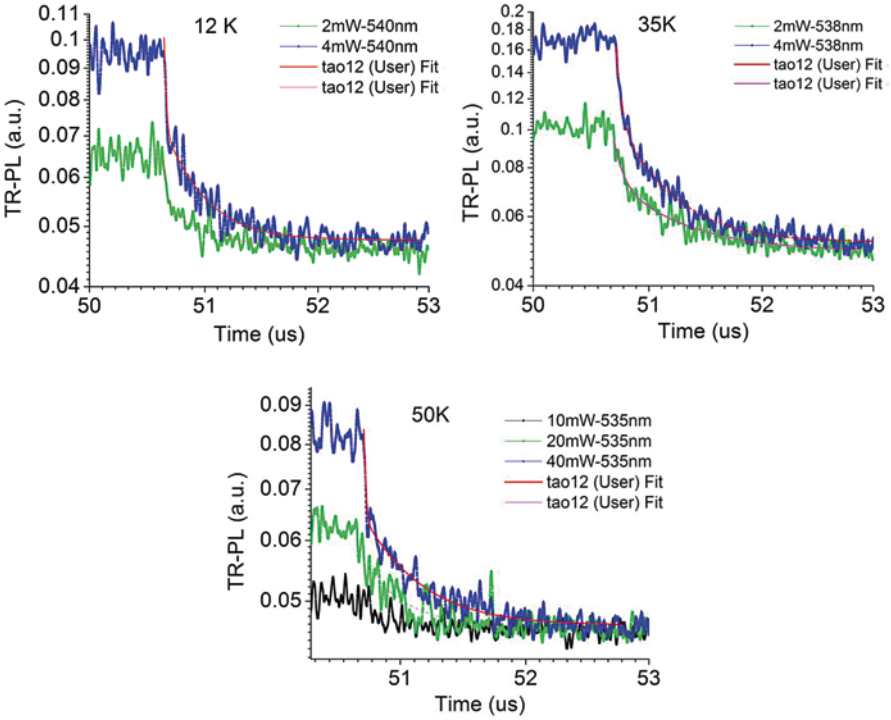

Fig. 9 TR-PL decays and fits at 12 K, 35 K, and 50 K

Table 2 Fitting parameters obtained from TR-PL datasets

Temperature	Excitation power	Excitation power	Excitation power	Excitation power	Excitation power
12 K	**2 mW**	**4 mW**			
C_1:C_2; ratio	9.87:8.07; 1.223	2.89:2.44; 1.185			
τ_1	29.27 ns	13.37 ns			
τ_2	401.13 ns	319.41 ns			
35 K	**2 mW**	**4 mW**			
C_1:C_2; ratio	2.17:2.45; 0.886	5.76:5.32; 1.083			
τ_1	74.82 ns	43.41 ns			
τ_2	566.26 ns	418.85 ns			
50 K			**10 mW**	**20 mW**	**40 mW**
C_1:C_2; ratio			3.61:1.97; 1.83	2.36:11.36; 0.208	1.94:1.78; 1.09
τ_1			6.33 ns	47.62 ns	11.20 ns
τ_2			521.03 ns	343.4 ns	416.14 ns

dominant peak (2.3 eV), which only produced significant lifetimes. Table 2 shows that shorter lifetimes are observed for higher excitation power (4 mW) for the dominant peak at 12 K and 35 K. This pattern can be explained using a bimolecular mode. It predicts that as excitation intensities increase, more bimolecular species will be formed, and recombination will occur more quickly. See Peters et al. (PRB 2019) for more detailed arguments [17].

As depicted in Fig. 8, the temperature-dependent PL spectrum exhibits an anomalous transition at about 50 K. In order to comprehend this better, we conducted a TR-PL measurement at 50 K. As the excitation power rises from 10 to 20 mW, the fast decay component of the main peak (2.325 eV), as shown in Table 2, slows down, while the slow decay component speeds up. Excitation power increases of 20–40 mW resulted in reverse trends. This unusual behavior at 50 K could be due to a power-dependent defect activation. We argue that the high 40 mW intensity on the sample may be sufficient to fill the defect states, which appear to be dynamically dormant.

3.3 Polaron Strength Estimation

We estimated the polaron strength parameter to ascertain the nature of polaron coupling and verify that the observed PL in CsPbBr3 is the result of the recombination of excitons trapped by small polarons. Several samples were used to test the correlation between the square of the refractive index and the square of the wavelength of the light source. This relation is used to fit the dielectric constant in Monte Carlo simulations. A silicon wafer larger than the instrument's aperture served as the standard in the infrared regime. Compound semiconductor samples are smaller in size and hence a correction is needed to calculate their reflectivity. A typical result for the substance $CsPbBr_3$ is shown in Fig. 9. The red curve in the figure represents the outcome of a Filmetrics measurement to align the results in the 0.2–0.9 μm wavelength range.

The anomalous sharp changes in n^2 observed in Fig. 10 are assumed to be caused by a change in detectors in the instrument as well as band edge absorption. The results were used in the simulation to calculate the compound's mobilities. The simulated results, which are 160 cm^2/Vs for $CsPbBr_3$, agree with the experimental results within a factor of 2 [31]. The dielectric constant limit, ε_∞, is estimated to be 4.3, which is consistent with what has been reported in the literature [32]. As a result, we evaluated our polaron strength parameter for zeroth-order approximation using the effective mass for hole carriers and omega therein, but with varying ε_0, the low limit dielectric constant, from 10 to 30. The polaron strength parameter is in the range of 1.8 and higher. We could argue that our case falls under the category of strong polaron coupling.

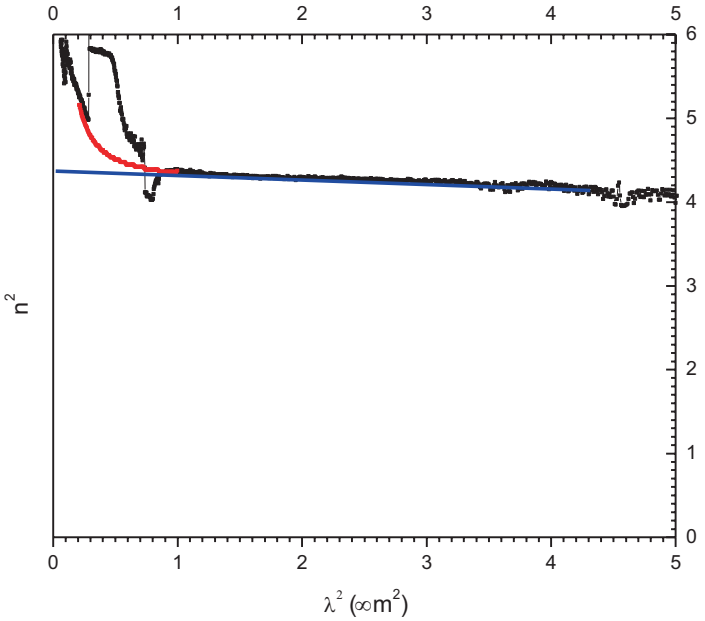

Fig. 10 The relationship between square of the refractive index vs. square of the wavelength of the light source (unit μm^2) for a $CsPbBr_3$ sample

4 Summary and Conclusions

In summary, excitons in Bridgman-grown halide perovskite $CsPbBr_3$ single crystals were examined using photoluminescence spectroscopy. The photoluminescence revealed the presence of three strong bands at the band edge temperatures below 80 K. From the spectral response of the PL intensity below the band edge, a band tail or Urbach-like tail is observed. The temperature dependence and excitation dependence of the three bands indicate that they originate from the radiative recombination of free excitons and trapped/bound excitons. The integrated intensity of the PL was strongly temperature-dependent and depended upon the specific exciton band. At low temperatures ($\leq$ 60 K) intrinsic disorder and its related shallow below bandgap tail states determine the emission properties. The disorder evolves with increasing temperature and accounts for the broad emission peak at 2.27 eV. The integrated PL intensity dependence on temperature also demonstrated strong electron-phonon coupling in $CsPbBr_3$ similar to other perovskites. The presence of electron-phonon interactions has implications for the utilization of $CsPbBr_3$ in ionizing radiation detectors. A significant number of electron-phonon interactions during charge transport result in carrier scattering and subsequently lower mobility. The time dependence of the luminescence intensity indicated a multi-phonon recombination process. Average lifetimes of ~17 ns and ~ 38 ns were measured for peaks 2 and 3, respectively. The origin of these edge states could be associated with point defects (metal/halide vacancies, interstitials, etc.), as well as twinning due to

the cubic-to-tetragonal phase transition in $CsPbBr_3$. Eliminating the trapping sites for excitons should lead to materials with improved mobilities, carrier lifetimes, and, ultimately, detector properties.

Acknowledgments The authors thank A. Benadia for technical assistance. This research is sponsored by the Defense Threat Reduction Agency (DTRA) as part of the Interaction of Ionizing Radiation with Matter University Research Alliance (IIRM-URA) under contract number HDTRA1-20-2-0002. This work made use of the Materials Processing and Microfabrication Facility supported by the MRSEC program of the National Science Foundation (DMR-1720139) at the Materials Research Center of Northwestern University.

References

1. He, Y., Petryk, M., Liu, Z., Chica, D. G., Hadar, I., Leak, C., Ke, W., Spanopoulos, I., Lin, W., Chung, D. Y., Wessels, B. W., & Kanatzidis, M. G. (2021). $CsPbBr_3$ perovskite detectors with 1.4% energy resolution for high-energy γ-rays. *Nature Photonics, 15*(1), 36–42.
2. He, Y., Matei, L., Jung, H. J., McCall, K. M., Chen, M., Stoumpos, C. C., Liu, Z., Peters, J. A., Chung, D. Y., Wessels, B. W., & Wasielewski, M. R. (2018). High spectral resolution of gamma-rays at room temperature by perovskite $CsPbBr_3$ single crystals. *Nature Communications, 9*(1), 1–8.
3. Stoumpos, C. C., Malliakas, C. D., Peters, J. A., Liu, Z., Sebastian, M., Im, J., Chasapis, T. C., Wibowo, A. C., Chung, D. Y., Freeman, A. J., & Wessels, B. W. (2013). Crystal growth of the perovskite semiconductor $CsPbBr_3$: A new material for high-energy radiation detection. *Crystal Growth & Design, 13*(7), 2722–2727.
4. Owens, A., & Peacock, A. (2004). Compound semiconductor radiation detectors. *Nuclear Instruments and Methods in Physics Research Section A: Accelerators, Spectrometers, Detectors and Associated Equipment, 531*(1–2), 18–37.
5. Wei, H., & Huang, J. (2019). Halide lead perovskites for ionizing radiation detection. *Nature Communications, 10*(1), 1–12.
6. Kakavelakis, G., Gedda, M., Panagiotopoulos, A., Kymakis, E., Anthopoulos, T. D., & Petridis, K. (2020). Metal halide perovskites for high-energy radiation detection. *Advanced Science, 7*(22), 2002098.
7. Iaru, C. M., Geuchies, J. J., Koenraad, P. M., Vanmaekelbergh, D., & Silov, A. Y. (2017). Strong carrier–phonon coupling in lead halide perovskite nanocrystals. *ACS Nano, 11*(11), 11024–11030. Sendner, M., Nayak, P.K., Egger, D.A., Beck, S., Müller, C., Epding, B., Kowalsky, W., Kronik, L., Snaith, H.J., Pucci, A. and Lovrinčić, R., 2016. Optical phonons in methylammonium lead halide perovskites and implications for charge transport. *Materials Horizons*, *3*(6), pp. 613–620.
8. Ghosh, D., Welch, E., Neukirch, A. J., Zakhidov, A., & Tretiak, S. (2020). Polarons in halide perovskites: A perspective. *The Journal of Physical Chemistry Letters, 11*(9), 3271–3286.
9. Lacroix, A., De Laissardiere, G. T., Quémerais, P., Julien, J. P., & Mayou, D. (2020). Modeling of electronic mobilities in halide perovskites: Adiabatic quantum localization scenario. *Physical Review Letters, 124*(19), 196601.
10. Budzinauskas, K., Ewertowski, S., Olthof, S., Meerholz, K., & Van Loosdrecht, P. H. (2019). Charge carrier migration and hole extraction from MAPbI3. *Journal of Physics: Conference Series, 1220*(1), 012053. IOP Publishing.
11. Firsov, Y. A. (2007). Small polarons: Transport phenomena. In A. S. Alexandrov (Ed.), *Polarons in advanced materials* (pp. 63–105). Springer.
12. Ortmann, F., Bechstedt, F., & Hannewald, K. (2009). Theory of charge transport in organic crystals: Beyond Holstein's small-polaron model. *Physical Review B, 79*(23), 235206.

13. Diroll, B. T., Zhou, H., & Schaller, R. D. (2018). Low-temperature absorption, photoluminescence, and lifetime of CsPbX3 (X= Cl, Br, I) nanocrystals. *Advanced Functional Materials, 28*(30), 1800945.
14. Wolf, C., & Lee, T. W. (2018). Exciton and lattice dynamics in low-temperature processable CsPbBr3 thin-films. *Materials Today Energy, 7*, 199–207.
15. Sebastian, M., Peters, J. A., Stoumpos, C. C., Im, J., Kostina, S. S., Liu, Z., Kanatzidis, M. G., Freeman, A. J., & Wessels, B. W. (2015). Excitonic emissions and above-band-gap luminescence in the single-crystal perovskite semiconductors $CsPbBr_3$ and $CsPbCl_3$. *Physical Review B, 92*(23), 235210.
16. Toyozawa, Y. (1981). Dynamics of excitons in deformable lattice. *Journal of Luminescence, 24*, 23–30.
17. Peters, J. A., Liu, Z., Yu, R., McCall, K. M., He, Y., Kanatzidis, M. G., & Wessels, B. W. (2019). Carrier recombination mechanism in $CsPbBr_3$ revealed by time-resolved photoluminescence spectroscopy. *Physical Review B, 100*(23), 235305.
18. He, Y., Liu, Z., McCall, K. M., Lin, W., Chung, D. Y., Wessels, B. W., & Kanatzidis, M. G. (2019). Perovskite $CsPbBr_3$ single crystal detector for alpha-particle spectroscopy. *Nuclear Instruments and Methods in Physics Research Section A: Accelerators, Spectrometers, Detectors and Associated Equipment, 922*, 217–221.
19. Kostina, S. S., Peters, J. A., Lin, W., Chen, P., Liu, Z., Wang, P. L., Kanatzidis, M. G., & Wessels, B. W. (2016). Photoluminescence fatigue and inhomogeneous line broadening in semi-insulating Tl_6SeI_4 single crystals. *Semiconductor Science and Technology, 31*(6), 065009.
20. Bimberg, D., Sondergeld, M., & Grobe, E. (1971). Thermal dissociation of excitons bounds to neutral acceptors in high-purity GaAs. *Physical Review B, 4*(10), 3451.
21. Lao, X., Yang, Z., Su, Z., Wang, Z., Ye, H., Wang, M., Yao, X., & Xu, S. (2018). Luminescence and thermal behaviors of free and trapped excitons in cesium lead halide perovskite nanosheets. *Nanoscale, 10*(21), 9949–9956.
22. Chua, S. J., Xu, S. J., Zhang, X. H., & Zhang, X. (1998). Carrier capture in InAs monolayer quantum wells grown on GaAs substrates. *Microelectronic Engineering, 43*, 287–293.
23. Baranowski, M., Urban, J. M., Zhang, N., Surrente, A., Maude, D. K., Andaji-Garmaroudi, Z., Stranks, S. D., & Plochocka, P. (2018). Static and dynamic disorder in triple-cation hybrid perovskites. *The Journal of Physical Chemistry C, 122*(30), 17473–17480.
24. Lohar, A. A., Shinde, A., Gahlaut, R., Sagdeo, A., & Mahamuni, S. (2018). Enhanced photoluminescence and stimulated emission in $CsPbCl_3$ nanocrystals at low temperature. *The Journal of Physical Chemistry C, 122*(43), 25014–25020.
25. Li, S., Luo, J., Liu, J., & Tang, J. (2019). Self-trapped excitons in all-inorganic halide perovskites: Fundamentals, status, and potential applications. *The Journal of Physical Chemistry Letters, 10*(8), 1999–2007.
26. Baranowski, M., & Plochocka, P. (2020). Excitons in metal-halide perovskites. *Advanced Energy Materials, 10*(26), 1903659.
27. Wei, K., Xu, Z., Chen, R., Zheng, X., Cheng, X., & Jiang, T. (2016). Temperature-dependent excitonic photoluminescence excited by two-photon absorption in perovskite $CsPbBr_3$ quantum dots. *Optics Letters, 41*(16), 3821–3824.
28. Cha, J. H., Han, J. H., Yin, W., Park, C., Park, Y., Ahn, T. K., Cho, J. H., & Jung, D. Y. (2017). Photoresponse of $CsPbBr_3$ and Cs_4PbBr_6 perovskite single crystals. *The Journal of Physical Chemistry Letters, 8*(3), 565–570.
29. Sillen, A., & Engelborghs, Y. (1998). The correct use of "average" fluorescence parameters. *Photochemistry and Photobiology, 67*(5), 475–486.
30. Bolotnikov, A. E., Babalola, S. O., Camarda, G. S., Chen, H., Awadalla, S., Cui, Y., Egarievwe, S. U., Fochuk, P. M., Hawrami, R., Hossain, A., & James, J. R. (2009). Extended defects in CdZnTe radiation detectors. *IEEE Transactions on Nuclear Science, 56*(4), 1775–1783.
31. Stoumpos, C. C., et al. (2013). Based on original dataset of TOF measurement of sample 3cs2a with pulsed nitrogen laser at 337 nm wavelength. Crystal growth of the perovskite semiconductor $CsPbBr_3$: A new material for high energy radiation detection. *Crystal Growth & Design, 13*, 2722–2727.
32. Miyata, K., et al. (2017). Large polarons in lead halide perovskites. *Science Advances, 3*, e1701217.

Charge Carrier Mobility of Metal Halide Perovskites: From Fundamentals to Ionizing Radiation Detection

Zheng Zhang and Bayram Saparov

1 Introduction

The detection of ionizing radiation (e.g., X-ray and γ-ray detection) plays a pivotal role for a wide range of practical applications, including medical imaging, national security, astrophysics and particle physics, national security, and high tech and consumer electronics [1–3]. Recently, three-dimensional (3D) metal halide perovskites (MHPs, Fig. 1a) with the general chemical formula ABX_3 (where A = methylammonium, formamidinium, or Cs^+; B = Pb^{2+}; X = I^-, Br^-, Cl^-) have shown great promise for radiation detection due to their suitable bandgap energies, high bulk crystal resistivity, superior charge carrier transport properties, and preparation using simple and low-cost solution-processing methods [5–7] (Fig. 2). However, the instability of semiconducting 3D halide perovskites under ambient air, irradiation, and heat exposure is a major concern; therefore, lower-dimensional perovskites (e.g., two-dimensional (2D), one-dimensional (1D), zero-dimensional (0D)), which incorporate larger organic spacers that serve as electrically insulating layers along the vertical direction (Fig. 1b), have been studied as alternatives to 3D perovskites. Among notable high-performance 3D perovskites is $CsPbBr_3$, which shows encouraging gamma photon detection performance with a superior detector energy resolution of 1.4% for 662 keV γ-ray radiation [12]. While materials and device performance-focused studies dominate the field, in-depth understanding of the charge carrier transport dynamics of halide perovskites is still limited [13]. This is at least in part due to the unusual fundamental chemical and physical properties of this new class of materials including the halide ion migration issues. Inherent limitations of the moderate charge carrier mobility of MHPs are not still fully explored and understood. In addition, the reported experimentally measured mobility values,

Z. Zhang (✉) · B. Saparov
Department of Chemistry & Biochemistry, The University of Oklahoma, Norman, OK, USA
e-mail: zzhang@ou.edu; saparov@ou.edu

W. Nie, K. (Kris) Iniewski (eds.), *Metal-Halide Perovskite Semiconductors*,
https://doi.org/10.1007/978-3-031-26892-2_6

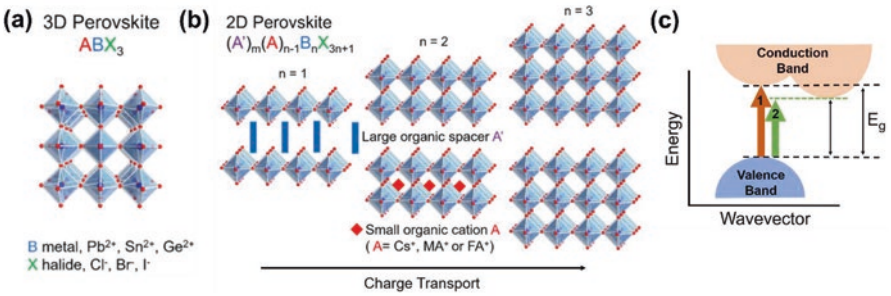

Fig. 1 (**a**) A polyhedral representation of the 3D crystal structure of the parent ABX_3 perovskite. (**b**) Sample 2D perovskite structures containing variable thickness inorganic layers; charge transport in 2D perovskites is expected to be anisotropic with the preferred charge transport direction along the inorganic layers (reproduced with permission from [4], American Chemical Society, Copyright 2019.). (**c**) Illustration of the direct and indirect band to band transitions (reproduced with permission from [5], AIP Publishing, Copyright 2021)

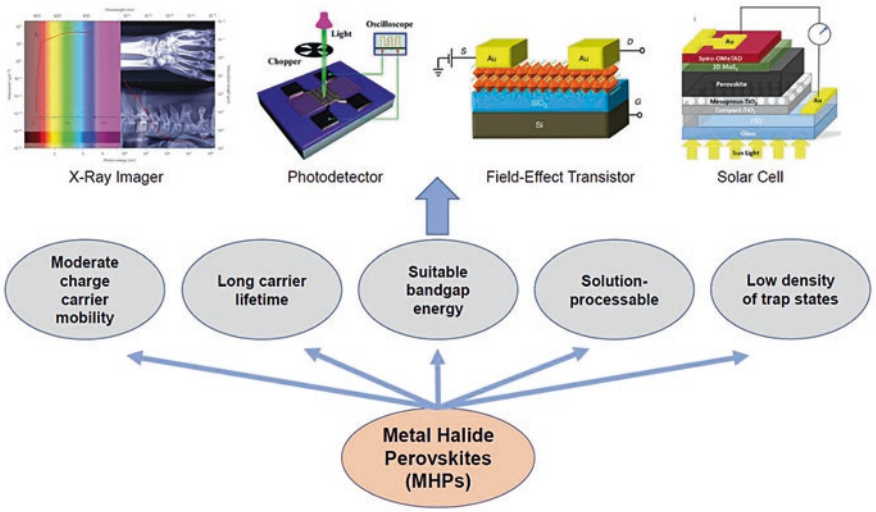

Fig. 2 Metal halide perovskites (MHPs) are an exciting new class of semiconductors with favorable chemical and physical properties that allow their consideration for several optical and electronic applications including ionizing radiation detection (reproduced with permission from [8], Springer Nature, Copyright 2020; [9], Springer Nature, Copyright 2018; [10], Royal Society of Chemistry, Copyright 2017; [11], Springer Nature, Copyright 2015)

even for the same material composition and stoichiometry, show a vast variation in literature. In this chapter, we aim to summarize the literature-reported carrier mobility values for MHPs and provide an explanation for the origin of the unusually high variation in the reported mobilities. Further, we outline several future research directions to ensure the accurate elucidation of the charge carrier dynamics and reveal the charge carrier mobility of MHPs. This chapter will cover the basics of

charge carrier transport of semiconductors including metal halide perovskites, measurement techniques and methods for determining the carrier mobility, and the current limitations in understanding the charge carrier dynamics of MHPs.

2 Basics of Carrier Transport

2.1 Optical Bandgap and Electron-Hole Pair Creation Energy

The charge carrier electron-hole pair creation energy (W) depends on the bandgap energy (E_g) of a semiconductor [14]:

$$W = 2E_g + 1.43 \tag{1}$$

In intrinsic semiconductors, carrier densities are low with most of the charge carrier electrons sitting in the valence band (VB). Through heat/photon excitation (including ionizing radiation such as X-rays, γ-rays, alpha particles), electrons gain sufficient energy and move to the conduction band (CB), and thus, they become free charge carriers. According to the bandgap nature of semiconductors, the VB to CB band-to-band transitions could be either direct or indirect type (Fig. 1c). For indirect bandgap semiconductors, the transition of electrons from VB to CB requires the participation of phonons to conserve the momentum. Therefore, direct bandgap semiconductors are preferred for applications that involve photo-absorption.

2.2 Carrier Mobility and Mobility-Lifetime Product

For ionizing radiation detection applications, charge transport is typically evaluated together with the carrier lifetime as a part of the mobility-lifetime (μ-τ) product, a metric typically cited when discussing the prospects of a given material system. The intrinsic charge carrier lifetime of semiconductors is the time from carrier production to carrier recombination and could be determined using the time-resolved photoluminescence (TRPL) technique. Charge carrier mobility is defined as the carrier velocity v (cm/s) divided by the drift time t (s) using the below formula:

$$\mu = \frac{v}{t} \tag{2}$$

Mobility-lifetime product is more representative of the carrier transport properties as compared to the carrier mobility. In literature, the μ-τ product for halide perovskite semiconductors has been determined using two ways: (i) the photocurrent approach enabled by measuring the induced current through X-ray or laser

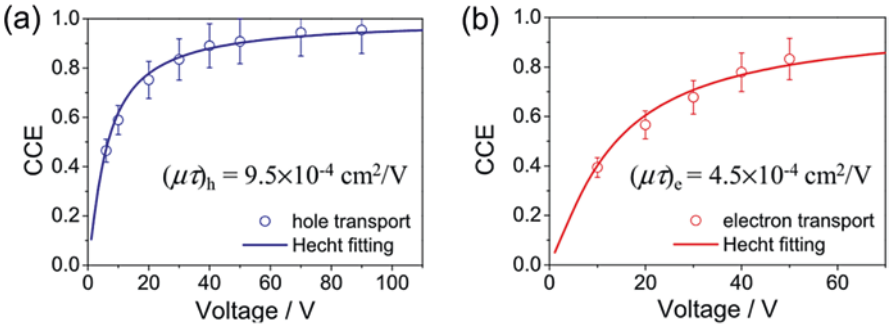

Fig. 3 The mobility-lifetime product extracted for electrons and holes using the $CsPbBr_3$ perovskite alpha particle detector (reproduced with permission from [16], Elsevier, Copyright 2019)

excitation, and then the μ-τ product can be determined using Many's equation [15], and (ii) plot of the charge collection efficiency (CCE) vs. peak centroid (e.g., γ-ray or alpha particle energy peak) to extract μ-τ product using the Hecht model [16] (see Fig. 3), which could be formulated as below [17]:

$$\mathrm{CCE} = \eta(x) = \frac{(\mu\tau)_e E}{d}\left(1 - \exp\left(-\frac{d-x}{(\mu\tau)_e E}\right)\right) + \frac{(\mu\tau)_h E}{d}\left(1 - \exp\left(-\frac{x}{(\mu\tau)_h E}\right)\right) \tag{3}$$

where d is the detector thickness and E is the electric field. It should be noted that Eq. (3) considers the contributions from both electron and hole carriers. For single-charge carrier transport, this equation could be simplified to [18]

$$\frac{Q}{Q_0} = \frac{\mu\tau E}{d}\left[1 - \exp\left(-\frac{d}{\mu\tau E}\right)\right] \tag{4}$$

where Q/Q_0 represents the charge collection efficiency.

2.3 *Defects, Doping, and Crystal Structures*

For the charge transport dynamics, it could be impacted by the temperature, structural phase transition, carrier concentration, doping levels, and material defects. For instance, measurements on $MAPbBr_3$ single crystals suggest that the measured Hall mobility is highly temperature-dependent across the cubic-to-tetragonal structural phase transition region, from $\mu \propto T^{-1.5}$ (for the cubic phase) to $\mu \propto T^{-0.5}$ (for the tetragonal phase) (Fig. 4) [19]. The results suggest that acoustic-phonon and space-charge carrier scattering mechanisms dominate at the cubic phase and tetragonal

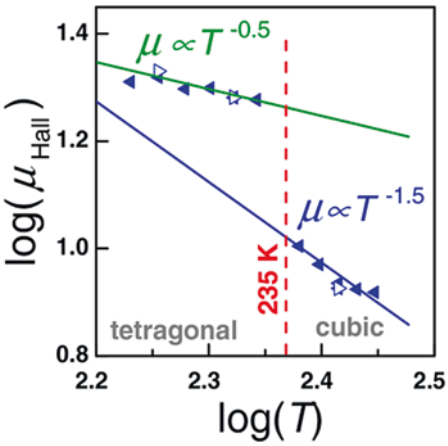

Fig. 4 A plot shows the temperature-dependent Hall mobility across the cubic phase to tetragonal phase regions for $MAPbBr_3$ perovskite (reproduced with permission from [19], John Wiley & Sons, Inc., Copyright 2016.)

phase regions, respectively. The impurity dopants could serve as either donors or acceptors to enhance the majority or minority carrier concentration and thus influence the charge transport dynamics. For Sn-doped $MA_3Sb_2I_9$, the mobility is two-fold raised to 43.05 cm^2/V-s in comparison to 16.68 cm^2/V-s for undoped $MA_3Sb_2I_9$ [20], although the inherent mechanisms seem to have not been fully explored. In addition, material defects play a pivotal role that impacts the charge carrier transport dynamics. Examples are that detrimental deep vacancy-type defects could trap electrons and dislocations enhance the scattering probability of charge carriers. As a result, the charge collection efficiency between the semiconductor detector metal contact electrodes is at some extent influenced by either the intrinsic or extrinsic defects. Although benign shallow defects are known to form in 3D halide perovskites such as $MAPbX_3$, given the rich chemistry and crystal structures of MHPs, some members may exhibit more harmful defects, e.g., deep level electron traps V_{Br} and Bi_{Ag} with formation energies above the thermal energy have been reported for the double perovskite $Cs_2AgBiBr_6$ [21].

2.4 Bulk Crystals Vs. Thin Films

For applications targeting radiation sensing, studies on both bulk single crystals and polycrystalline MHP thin films have been carried out [6, 22]. As the name suggests, single crystal is a continuous undisrupted crystal lattice, whereas polycrystalline films are comprised of many small crystallites (or crystal grains) that can have various orientations and sizes. Compared to single-crystal perovskites, carrier transport through thin film samples can be significantly impacted by the grain boundaries, which are the interfaces between neighboring grains. Hence, the mobility for thin films is usually orders of magnitude lower in contrast to single crystal counterparts. In addition, the compositional and structural uniformity of the thin film sample, film

thickness, surface roughness, grain sizes, and their distribution all could influence the measured mobility to some extent. In terms of the synthesis, single-crystal perovskites can be grown from solutions using inverse temperature crystallization (ITC), temperature-lowering, antisolvent slow diffusion, and slow evaporation techniques. Perovskite thin films are most often fabricated by using the spin coating method, which deposits thin layers (~ nm to micron thicknesses) onto glass substrates using the perovskite precursor solutions.

2.5 Radiative Vs. Nonradiative

The charge carrier recombination process could either be radiative or nonradiative. For radiative recombination, charge carrier electrons and holes recombine and emit the energy as photons. Perovskite light-emitting diodes (LEDs), in which minority and majority carriers recombine at the junction interface, are operated based on this principle. Contrary to radiative recombination, nonradiative process refers to the recombination process that emits phonons rather than photons. Auger recombination is an example of a nonradiative process, though this process is more favored for high carrier concentration semiconductors. In the Auger recombination, after electrons are excited from valence to conduction band, part of the energy could be transferred to nearby electrons and then the energy is lost through thermal vibrations (in the form of phonons) due to the unstable energetic state. Alternatively, excited electrons could decay back to valence band and recombine with the holes. Or along the decay route, when electrons encounter the intermediate energy levels formed by defects and get trapped then delocalize, the carrier recombination rate is therefore significantly reduced. Nonetheless, although the recombination rate is reduced, such trapping-detrapping process could be beneficial for enhancing the carrier lifetime. In other cases, electrons recombine with holes in the defect sites and emit photons; the rest energy is again lost as phonons.

3 Mobility Characterization Methods

3.1 Contact-Required Methods

The time-of-flight (ToF) method has been widely used to separately determine the mobility of electrons and holes for semiconductors, including leading room-temperature radiation detector material cadmium zinc telluride (CdZnTe) [23], thallium bromide (TlBr) [24], and lead halide perovskites such as cesium lead bromide $CsPbBr_3$ [25]. This technique essentially measures the carrier drift time from a

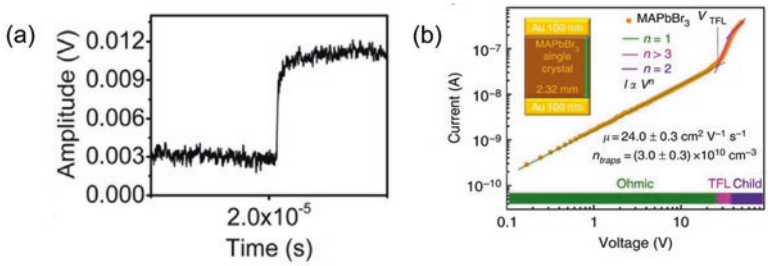

Fig. 5 (**a**) A measured ToF pulse trace using the $TlSn_2I_5$ halide anti-perovskite detector for estimating the mobility (reproduced with permission from [26], American Chemical Society, Copyright 2017). (**b**) SCLC curve for a solution-grown $MAPbBr_3$ perovskite single crystal with Ohmic, TFL, and Child transition regimes identified to extract the density of trap states and carrier mobility (reproduced with permission from [27], Nature Publishing Group, Copyright 2015)

typical ToF pulse trace (see Fig. 5a), and then the carrier mobility could be easily calculated using the below equation:

$$\mu = \frac{v}{t} = \frac{L/t}{t} = \frac{L}{t^2} \tag{5}$$

where L is the carrier drift distance, which could be simply taken as the sample thickness. The carrier drift time t is read from the ToF pulse trace as the time interval between 10% and 90% of the pulse amplitude or as double of the time it requires to reach half of the maximum pulse amplitude. Readers are further directed to read the ToF mobility studies of CdZnTe single crystals [23, 28].

Since the emergence of metal halide perovskites in the 2010s, space-charge-limited current (SCLC) technique has been the most often used method in literature for characterization of the charge carrier mobilities. This is due to the ease of measurement by using the SCLC technique, although the suitability of this method for mobility measurement of halide perovskites is questionable (see below). The SCLC method is essentially based on the balance between the injected charge carrier concentration from metal contact electrodes and the intrinsic charge carrier concentration of perovskite semiconductors. To use this method for mobility extraction, a perovskite single crystal is firstly sandwiched between two metal contact electrodes and then voltage bias is applied to the two electrodes. By varying the applied bias voltage, a SCLC curve (i.e., a current vs. voltage curve, Fig. 5b) that contains three transition regimes (namely, Ohmic, trap-filled-limited (TFL), and Child) could be identified. In the Ohmic regime, the current is linearly proportional to the applied voltage bias. Thus, the bulk crystal resistivity (which is a basic and yet important property to evaluate semiconductor's potential for ionizing radiation detector leakage current reduction) could be determined from this regime. Following the Ohmic regime, all intrinsic defect traps are filled by the injected charge carriers from metal contact electrodes; therefore, the second regime is named as TFL region. The onset

voltage (i.e., V_{TFL}) of the TFL regime could be used to estimate the density of trap states n_{trap} in halide perovskites using Eq. (6) [29]:

$$n_{trap} = \frac{2\varepsilon\varepsilon_0}{eL^2} V_{TFL} \tag{6}$$

where ε is the dielectric constant, ε_0 is the vacuum permittivity, e is the electronic charge, and L is the sample thickness or the distance between two electrodes. The carrier mobility could be determined from the third Child region, where the intrinsic charge carrier concentration is dominated over by the injected charge carriers from metal contacts, and thus, the carrier mobility is no longer a function of intrinsic carrier concentration. The mobility μ is evaluated from this regime using the Mott-Gurney law [30]

$$\mu = \frac{8J_D L^3}{9\varepsilon\varepsilon_0 V^2} \tag{7}$$

where J_D is the current density and V is the applied bias voltage.

Hall effect technique is the gold standard method for mobility measurement of semiconductors, e.g., detailed Hall effect measurements have been performed for beta-gallium oxide (β-Ga_2O_3) [31] and gallium arsenide (GaAs) [32]. The Hall effect evaluates the charge carrier behaviors under a combination of the electrical and magnetic fields. Under the electrical field, charge carriers are being pulled toward one side of the semiconductor solids depending on if the charge is positive/negative. The addition of magnetic field produces a Lorentz force on charge carriers, and thus the moving direction of charge carriers is deflected. Magnitude of the produced Lorentz force on one electron could be described using the below formula [33]:

$$\vec{F} = -e\left[\vec{E} + \vec{v} \times \vec{B}\right] \tag{8}$$

where e is the electronic charge, E is the electrical field, v is the velocity of electrons, and B is the magnetic field. A same equation can be written for holes with positive charge. The mobility can be determined from Hall effect using the below Eq. (9):

$$\mu = \frac{R_H}{\rho} \tag{9}$$

where R_H is the Hall coefficient (could be calculated using the electrical field, current density, and magnetic field) and ρ is the semiconductor resistivity (Ω·cm). The Hall effect method has been used for measuring the mobility of halide perovskites such as $MAPbI_3$, $MAPbBr_3$, and tin perovskite $CsSnI_3$ [19, 30, 34].

Fabrication of a field-effect transistor (FET) is another contact-required technique that may be used to determine the mobility; however, this method is more suitable for assessing the mobility of halide perovskites for transistor applications (i.e., the device-oriented mobility). Note that the charge carrier transport behaviors across the electrode-semiconductor interface (either being Ohmic or Schottky type) is another research topic that requires further studies for halide perovskites. The FET technique evaluates the carrier mobility from the saturation regime using the relationship between I_{DS} (drain current) and V_{GS} (gate voltage) through the equation below [9, 35]:

$$I_{DS} = \frac{W}{2L} C_i \mu \left(V_{GS} - V_{TH} \right)^2 \tag{10}$$

where W refers to the channel width, L is channel length, C_i is the capacitance of gate electrode, and V_{TH} is the threshold voltage. Carrier mobility extracted by the FET method is related to the surface morphology, temperature, grain size, and the electrode materials [9].

3.2 Contact-Free Techniques

The time-resolved terahertz spectroscopy (TRTS) and time-resolved microwave conductivity (TRMC) are both contactless measurement techniques [36–39] that can be used to determine carrier mobilities of materials. The TRTS technique

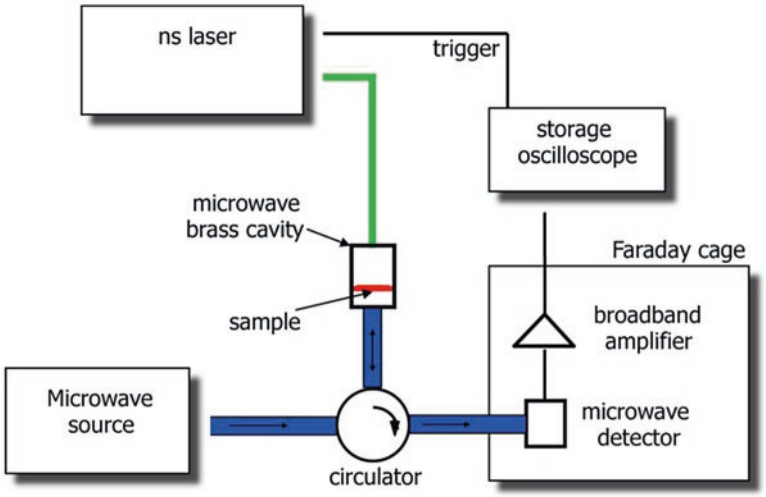

Fig. 6 Illustration of the TRMC setup, the measured sample is placed in the microwave cavity and microwaves are generated using the voltage-controlled oscillator (reproduced from permission from [40], American Chemical Society, Copyright 2013)

essentially uses visible excitations to excite the samples and then record the transient photoconductivity. TRTS method requires the sample to be transparent; for this reason, this method is usually used for studying the perovskite thin films. Nonetheless, using the TRTS technique, few successful measurements are made to determine the mobility of perovskite single crystals [36, 37]. As an alternative to TRTS, for the TRMC method (see Fig. 6 for a schematic plot of the measurement setup), a nanosecond laser pulse is used to photoexcite the sample and then the transient change in microwave reflectivity that is induced by the charge carriers is monitored [41]. Carrier mobility can be determined from the TRMC method using Eq. (11) (according to the relative change of microwave power) [42, 43]:

$$\frac{\Delta P(t)}{P} = Ae\sum_i \Delta n_i(t)\mu_i = Ae\left(\Delta n_e(t)\mu_e + \Delta n_h(t)\mu_h\right) \tag{11}$$

where μ_e and μ_h are electron and hole mobilities, respectively. Note that the mobility determined above from the TRMC measurement is a sum of electron and hole mobilities, although Eq. (11) has separated the contributions from the two types of charge carriers.

3.3 Cross-Comparison of the Measurement Techniques

Though the charge carrier mobility of semiconductors including MHPs could be determined using several contactless and contact-required methods discussed above, the measured mobility values tend to vary from method to method. Each technique comes with its own advantages and suitability. Contactless measurements are ideal when the deposition of high-quality metal electrodes is not accessible. However, TRTS and TRMC methods become complicated for thick single-crystal specimens. Consequently, they are generally used for determining the mobility of perovskite thin films. In addition, the TRTS and TRMC techniques could not distinguish the hole and electron contributions, as having been discussed from Eq. (11). This is not the case for device-oriented techniques, such as ToF. Since the ToF method could excite the sample from one electrode side and then collect the transported charges contributed by single-charge carrier on the other side, the mobility from either electrons or holes then could be extracted. Nevertheless, identical to the SCLC method, the ToF technique requires depositing electrode contacts to the measured sample. Thus, the mobility measured using the ToF or SCLC method could be influenced by the selected electrode contact materials. This is the reason why band alignment is very necessary for achieving high-efficiency charge transport. For the SCLC method, poor-quality electrode contacts could lead the trap-free SCLC conduction region to be difficult to reach for reliable mobility extraction.

There is also difference between the mobility evaluated from the ToF and Hall effect measurements. Hall mobility could be influenced by the electrical and

magnetic fields due to the different carrier scattering mechanisms, including lattice scattering and charged dislocation scattering. Charge carriers mainly undergo Coulomb and photon scattering at low electrical fields as they are almost in equilibrium with lattice vibrations [44]. However, the carrier mobility becomes a field-dependent parameter at high electrical fields. In addition, at low temperatures, the Coulomb scattering dominates over the phonon scattering. Due to the lattice thermal vibrations, Coulomb scattering and phonon scattering compete at high temperatures [45]. Such difference could be observed from the traditional semiconductor material silicon (Si). The measured drift mobility for single crystal silicon sample is 1360 cm^2/V-s (for electrons) and 510 cm^2/V-s (for holes), respectively. Hall mobility for the two types of charge carriers is determined to be 1560 cm^2/V-s (electrons) and 345 cm^2/V-s (holes) [46].

4 Discussion of the Reported Mobility: Theoretical and Experimental

Though many studies have been carried out for metal halide perovskites such as $MAPbI_3$, $FAPbI_3$, and $CsPbBr_3$, the literature reported charge carrier mobility for the same perovskite material composition and structure shows a large variance (see Table 1 for comparison of the reported mobility for single crystals). Therefore, this leads to an intuitive question: what causes this large variance in the reported carrier mobility even if the perovskite composition is the same? In part, some discrepancy is expected to originate from the measurement methods used for determining the mobility. As having been discussed above, drift mobility differs from the Hall mobility. In addition, this observation could be related to the unusual chemistry and physics of MHPs. Many of these studies used the facile SCLC method to estimate the carrier mobility of halide perovskites [27, 65, 76]. Although the SCLC method is relatively simple and straightforward, it is known that the halogen ionic migration is a critical issue for this class of materials [77, 78], e.g., the ionic migration negatively impacts the fabricated perovskite-based device performance including X-ray detectors and photodetectors. The device efficiency deteriorates under continuous operation due to the charge screening effect. Given the fact that MHPs may demonstrate changing chemistry under measurement conditions due to the movement of halide ions, the suitability of using SCLC method to measure the mobility becomes a question that should be addressed. In fact, this issue has long been observed in other halide-based radiation detector materials, such as thallium bromide (TlBr) [79]. Under external added bias, the halogen ions drift and form an electrical counterfield. Thus, the TFL and Child regimes could have been incorrectly identified if the migration of halogen ions is not considered. To understand the mechanism that drives the halogen migration, few studies have been carried out [77, 78, 80]. Pulsed SCLC is proposed as an alternative to traditional SCLC to reliably measure the carrier mobility [81].

Table 1 Summary of the mobility measured by different methods for metal halide perovskite single crystals. Note the mobility reported here is measured at room temperature, unless otherwise mentioned (h, hole; e, electron) (reproduced with permission from [5], AIP Publishing, Copyright 2021)

Perovskite	Mobility (cm^2/V-s)	Method	Reference
Three-dimensional (3D) perovskites			
$MAPbI_3$	105 ± 35 (h)	Hall	[30]
	164 ± 25 (h)	SCLC	
	24.0 ± 6.8 (e)	ToF	
	65 ± 6	SCLC	[47]
	60	TRTS	[48]
	620	TRTS	[36]
	35	TRTS	[49]
	130 ± 20 (n-type) 42 ± 5 (p-type)	TRMS	[50]
	< 4.7	FET	[9]
$MASnI_3$	2320 (e) 322 (h)	Hall	[51]
	200 (at 250 K)	Hall	[52]
$MAPbBr_3$	35 ± 2 (h)	SCLC	[53]
	24.0 15 (at 80 K)	SCLC FET	[27] [54]
$MAPbCl_3$	42 ± 9	SCLC	[55]
$FAPbI_3$	4.4	SCLC	[56]
	35 ± 7	SCLC	[57]
	40 ± 5	SCLC	[58]
	150 ± 15	SCLC	[47]
$FAPbBr_3$	62 ± 11 (h)	SCLC	[57]
	0.12	SCLC	[59]
$FAPbBr_{2.23}Cl_{0.77}$	12	SCLC	[59]
$FAPb_{0.97}Sn_{0.03}Br_3$	0.22	SCLC	[59]
$MA_{0.45}FA_{0.55}PbI_3$	271 ± 60	SCLC	[47]
$CsPbBr_3$	181 (e) 56.5 (h)	ToF	[25]
	63 (e) 49 (h)	ToF	[16]
	1.78 (h)	ToF	[60]
	9.71–38.5 < 2.3 0.32	Hall FET FET	[61] [62] [63]
$CsPbCl_3$	28 ± 1 (e) 20 ± 1 (h)	ToF	[64]
$FA_{0.9}Cs_{0.05}MA_{0.05}PbI_{2.7}Br_{0.3}$	197 (e) 219 ± 18 (h)	SCLC	[65]
$KTaO_3$	0.4	FET	[66]

(continued)

Table 1 (continued)

Perovskite	Mobility (cm^2/V-s)	Method	Reference
$Cs_2AgBiBr_6$	7.02	SCLC	[67]
	3.17	SCLC	[68]
	5	ToF	[2]
Two-dimensional (2D) perovskites			
$MA_3Sb_2I_9$	16.68	SCLC	[20]
Sn-doped $MA_3Sb_2I_9$	43.05	SCLC	[20]
$Rb_3Sb_2I_9$	0.32 (e)	ToF	[69]
$Cs_3Sb_2I_9$	0.14 (h)	ToF	[69]
$(NH_4)_3Bi_2I_9$	213	SCLC	[70]
$PEA_2MA_2Pb_3I_{10}$ $(BA)_2MAPb_2I_7$	4.4×10^{-2} 0.5 (at 80 K)	SCLC FET	[71] [72]
One-dimensional (1D) perovskites			
$(DME)PbBr_4$	> 4.51	SCLC	[34]
Zero-dimensional (0D) perovskites			
$Cs_3Bi_2I_9$	4.3 (e) 1.7 (h)	ToF	[69]
$FA_3Bi_2I_9$	4	Hall	[73]
$MA_3Bi_2I_9$	70	Hall	[74]
	1–6 (h) 2–8 (e)	ToF	
Metal-free perovskites			
$DABCO\text{-}NH_4Br_3$	2.00 (h) 0.67 (e)	SCLC	[75]
	2.08	Hall	

Another important factor that should be taken into consideration is the crystal quality. Depending on the chemical composition and crystal structure of the MHP, vacancy-type defects could act as deep-level defects to trap the charge carriers and thus reduce the mobility. The formed material defects are to some extent also depend on the crystal growth methods adopted. For high-quality single-crystal growth via solution methods, the choice of the appropriate solvent, growth temperature, crystal growth rate, purity of the selected reactants, etc. all play important roles. One of the major benefits of using MHPs for radiation detection is their solution processability. The estimated cost for growing perovskite single crystals from solutions is about \$0.5–1.0 per cm^3 [6]. In addition to solution methods, all-inorganic MHPs could also be produced using melt growth methods at relatively low temperatures. For instance, $CsPbBr_3$ crystals have been successfully grown using the Bridgman melt growth method; high-quality crystals of $CsPbBr_3$ can also be obtained from aqueous solutions. The reported mobility for this material shows a vast range, spanning from 1.78 to 56.5 cm^2/V-s for holes [16, 25, 60]. This difference is likely due to the single-crystal quality and the density of defect states.

It could be noticed that contact-free methods TRTS and TRMC yield very high mobility values up to 620 cm^2/V-s for $MAPbI_3$. Note that TRTS and TRMC

measurements are conducted on a localized small area from the sample in contrast to ToF and SCLC measurements. Thus, the contact-free measurements are less likely to be influenced by the material defects and grain boundaries (for thin film samples). As a result, the carrier mobility determined by contactless methods could serve as a guidance for the further material optimization. However, contactless methods will probably be less beneficial to reveal the carrier mobility for practical applications as most of these fabricated devices, including ionizing radiation detectors, require to have electrode contacts.

Density-functional theory (DFT) computational studies can in principle support the experimental characterization of charge transport in MHPs [82–84]. However, note that there are a number of prominent studies showing a significant discrepancy between the experimentally measured and theoretically predicted carrier mobility values. Thus, though $MAPbI_3$ has been identified as a promising radiation detector material that could resolve high-energy gamma rays [85], the theoretical mobility predicted by Motta et al. for this material is surprisingly low with a value of approximately 10 cm^2/V-s for electrons [82]; in contrast, the reported experimental mobility value for $MAPbI_3$ single crystals reach up to 620 cm^2/V-s. Similarly, for the tin-based perovskite $MASnCl_3$, Wang et al. predicted a very high mobility value of 1700 cm^2/V-s for electrons based on their computational studies [86]. In the meantime, the solar cell power conversion efficiency (PCE) is less than 1% for solar cells fabricated using $MASnCl_3$ single crystals [87], implying that there should be intrinsic limitations for this material. In fact, recent electronic structure calculations performed by Ouhbi et al. for tin perovskites including $CsSnI_3$, $CsSnCl_3$, $MASnBr_3$, and $FASnBr_3$ suggest that these materials demonstrate strong electron localizations possibly due to the charge-lattice coupling (i.e., formation of polarons) [88]. The polaron formation may be detrimental for employing tin perovskites for photovoltaic and radiation detection applications.

5 Conclusions and Future Development

This chapter summarizes the measured mobilities of metal halide perovskites from recent reports and discusses the inherent reasons for the large variance of the measured mobility in literature. Even though the pursuit of ideal semiconductor detector materials has been ongoing for over half a century (see Fig. 7 for a list of traditional semiconductor detector materials), there is yet no single material that possesses all desirable properties while offering excellent detector energy resolution and low costs. The recently developed halide perovskites have achieved some success over the past few years, yet understanding the carrier transport properties of this novel class of new materials is still at an early stage. The reported carrier mobility values, even for the same perovskite composition and structure, exhibit a notably large variance. In addition, for application of halide perovskites for semiconducting radiation detection, the carrier mobility is relatively low as compared to the traditional detector material CdZnTe, which has electron mobility above 1000 cm^2/V-s but suffers

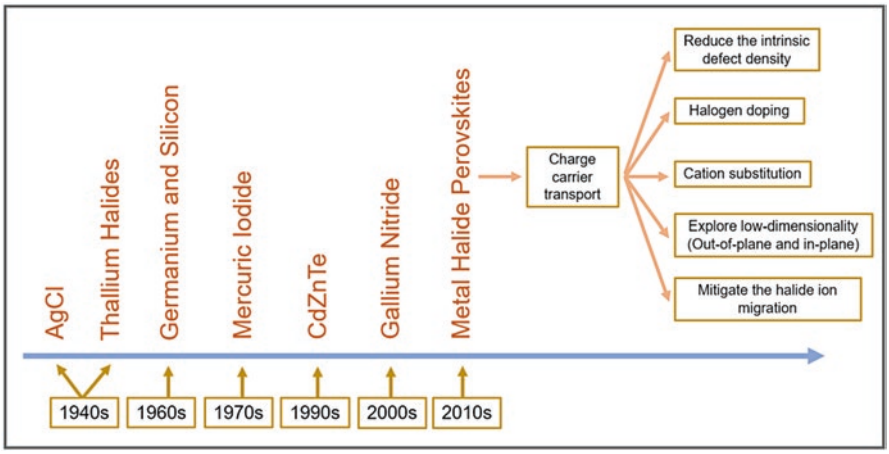

Fig. 7 List of the traditional semiconductor detector materials, including metal halide perovskites and the future development pathway to enhance the charge carrier dynamics of this class of materials

from poor hole transport. Thus, there is an urgent demand to understand the inherent factors that limit the charge transport to ensure the fabrication of high-performance detectors based on this class of materials. Polaron formation (dielectric electron-phonon coupling) has been investigated by computational tools and experimental studies [89, 90], yet the impact of polaron theory on carrier transport remains to be under debate. Polaron formation is relatively fast within femtoseconds in halide perovskites, and large polarons localize the charge carriers and thus reduce the carrier mobility. The polaron theory in part explains the moderate carrier mobility of halide perovskites, yet the measured mobility reported in literatures remains to be lower than the theoretical mobility predicted using the polaron theory [91]. This might indicate that more fundamental limitations (mainly should be from carrier scatterings) should be explored. To fully reveal the carrier scattering mechanisms and charge localization that limit the charge carrier mobility, temperature-dependent measurements may be carried out as the polaron formation and charge carrier behaviors vary with temperature.

To transform the perovskite technology from lab research to commercial applications, the detrimental influence of halide ion migration on mobility measurement should not be overlooked. In fact, as having been discussed by Corre et al. [81], the traditional manner of conducting SCLC measurement with no consideration of the halogen migration should be revisited. This should at least in part explain the vast disagreement of the reported carrier mobility among literatures. The intrinsic moderate mobility of halide perovskites may also be further enhanced. Halogen doping is one direction that requires further studies. On the other hand, more efforts could be placed to study the charge transport dynamics of lower-dimensionality perovskites. Among the $A_3B_2X_9$ perovskite family, $MA_3Sb_2I_9$ and $(NH_4)_3Bi_2I_9$ 2D perovskites showed a relatively high carrier mobility that is comparable to the 3D

family. For $(NH_4)_3Bi_2I_9$, a high mobility of 213 cm^2/V-s was revealed by SCLC measurement, although this value may be rechecked to consider the possible halogen migration. Thus, lower-dimensional perovskites including the 2D family which possess exceptional air stability with smaller activation energy for ionic conductivity that leads to suppressed halogen migration could be the next-step research focus for radiation detection.

References

1. Matt, G. J., Levchuk, I., Knüttel, J., Dallmann, J., Osvet, A., Sytnyk, M., Tang, X., Elia, J., Hock, R., Heiss, W., & Brabec, C. J. (2020). Sensitive direct converting X-ray detectors utilizing crystalline CsPbBr3 perovskite films fabricated via scalable melt processing. *Advanced Materials Interfaces, 7*(4), 1901575.
2. Zhang, Z., Cao, D., Huang, Z., Danilov, E. O., Chung, C. C., Sun, D., & Yang, G. (2021). Gamma-ray detection using bi-poor Cs2AgBiBr6 double perovskite single crystals. *Advanced Optical Materials, 9*(8), 2001575.
3. Weber, M. J. (2002). Inorganic scintillators: Today and tomorrow. *Journal of Luminescence, 100*(1–4), 35–45.
4. Mao, L., Stoumpos, C. C., & Kanatzidis, M. G. (2019). Two-dimensional hybrid halide perovskites: Principles and promises. *Journal of the American Chemical Society, 141*(3), 1171–1190.
5. Zhang, Z., & Saparov, B. (2021). Charge carrier mobility of halide perovskite single crystals for ionizing radiation detection. *Applied Physics Letters, 119*(3), 030502.
6. Yakunin, S., Dirin, D. N., Shynkarenko, Y., Morad, V., Cherniukh, I., Nazarenko, O., Kreil, D., Nauser, T., & Kovalenko, M. V. (2016). Detection of gamma photons using solution-grown single crystals of hybrid Lead halide perovskites. *Nature Photonics, 10*(9), 585–589.
7. López, C. A., Abia, C., Alvarez-Galván, M. C., Hong, B. K., Martínez-Huerta, M. V., Serrano-Sánchez, F., Carrascoso, F., Castellanos-Gómez, A., Fernández-DÍaz, M. T., & Alonso, J. A. (2020). Crystal structure features of CsPbBr3 perovskite prepared by mechanochemical synthesis. *ACS Omega, 5*(11), 5931–5938.
8. Liang, M., Ali, A., Belaidi, A., Hossain, M. I., Ronan, O., Downing, C., Tabet, N., Sanvito, S., EI-Mellouhi, F., & Nicolosi, V. (2020). Improving stability of organometallic-halide perovskite solar cells using exfoliation two-dimensional molybdenum chalcogenides. *npj 2D Materials and Applications, 4*(1), 1–8.
9. Yu, W., Li, F., Yu, L., Niazi, M. R., Zou, Y., Corzo, D., Basu, A., Ma, C., Dey, S., Tietze, M. L., Buttner, U., Wang, X., Wang, Z., Hedhili, M. N., Guo, C., Wu, T., & Amassian, A. (2018). Single crystal hybrid perovskite field-effect transistors. *Nature Communications, 9*(1), 1–10.
10. Li, Y., Shi, Z. F., Li, S., Lei, L. Z., Ji, H. F., Wu, D., Xu, T. T., Tian, Y. T., & Li, X. J. (2017). High-performance perovskite photodetectors based on solution-processed all-inorganic CsPbBr3 thin films. *Journal of Materials Chemistry C, 5*(33), 8355–8360.
11. Yakunin, S., Sytnyk, M., Kriegner, D., Shrestha, S., Richter, M., Matt, G. J., Azimi, H., Brabec, C. J., Stangl, J., Kovalenko, M. V., & Heiss, W. (2015). Detection of X-ray photons by solution-processed Lead halide perovskites. *Nature Photonics, 9*(7), 444–449.
12. He, Y., Petryk, M., Liu, Z., Chica, D. G., Hadar, I., Leak, C., Ke, W., Spanopoulos, I., Lin, W., Chung, D. Y., Wessels, B. W., He, Z., & Kanatzidis, M. G. (2021). CsPbBr3 perovskite detectors with 1.4% energy resolution for high-energy γ-rays. *Nature Photonics, 15*(1), 36–42.
13. Herz, L. M. (2016). Charge-carrier dynamics in organic-inorganic metal halide perovskites. *Annual Review of Physical Chemistry, 67*, 65–89.

14. Devanathan, R., Corrales, L. R., Gao, F., & Weber, W. J. (2006). Signal variance in gamma-ray detectors-a review. *Nuclear Instruments and Methods in Physics Research, Section A: Accelerators, Spectrometers, Detectors and Associated Equipment, 565*(2), 637–649.
15. Wei, H., Desantis, D., Wei, W., Deng, Y., Guo, D., Savenije, T. J., Cao, L., & Huang, J. (2017). Dopant compensation in alloyed $CH_3NH_3PbBr_{3-x}Cl_x$ perovskite single crystals for gamma-ray spectroscopy. *Nature Materials, 16*(8), 826–833.
16. He, Y., Liu, Z., McCall, K. M., Lin, W., Chung, D. Y., Wessels, B. W., & Kanatzidis, M. G. (2019). Perovskite CsPbBr 3 single crystal detector for alpha-particle spectroscopy. *Nuclear Instruments and Methods in Physics Research, Section A: Accelerators, Spectrometers, Detectors and Associated Equipment, 922*, 217–221.
17. Kim, K. O., Kwon, T. J., Kim, J. K., & Ha, J. H. (2011). A new approach for evaluating the mobility-lifetime products of electron-hole pairs in semiconductor detectors. *Journal of the Korean Physical Society, 59*(1), 20–26.
18. Street, R. A., Ready, S. E., Van Schuylenbergh, K., Ho, J., Boyce, J. B., Nylen, P., Shah, K., Melekhov, L., & Hermon, H. (2002). Comparison of PbI2 and HgI2 for direct detection active matrix X-ray image sensors. *Journal of Applied Physics, 91*(5), 3345–3355.
19. Yi, H. T., Wu, X., Zhu, X., & Podzorov, V. (2016). Intrinsic charge transport across phase transitions in hybrid Organo-inorganic perovskites. *Advanced Materials, 28*(30), 6509–6514.
20. Ju, D., Jiang, X., Xiao, H., Chen, X., Hu, X., & Tao, X. (2018). Narrow band gap and high mobility of Lead-free perovskite single crystal Sn-doped MA3Sb2I9. *Journal of Materials Chemistry A, 6*(42), 20753–20759.
21. Li, T., Zhao, X., Yang, D., Du, M. H., & Zhang, L. (2018). Intrinsic defect properties in halide double perovskites for optoelectronic applications. *Physical Review Applied, 10*(4), 041001.
22. Tsai, H., Liu, F., Shrestha, S., Fernando, K., Tretiak, S., Scott, B., Vo, D. T., Strzalka, J., & Nie, W. (2020). A sensitive and robust thin-film X-ray detector using 2D layered perovskite diodes. *Science Advances, 6*(15), 20200410.
23. Erickson, J. C., Yao, H. W., James, R. B., Hermon, H., & Greaves, M. (2000). Time of flight experimental studies of CdZnTe radiation detectors. *Journal of Electronic Materials, 29*(6), 699–703.
24. Suzuki, K., Shorohov, M., Sawada, T., & Seto, S. (2015). Time-of-flight measurements on TlBr detectors. *IEEE Transactions on Nuclear Science, 62*(2), 433–436.
25. Feng, Y., Pan, L., Wei, H., Liu, Y., Ni, Z., Zhao, J., Rudd, P. N., Cao, L. R., & Huang, J. (2020). Low defects density CsPbBr3single crystals grown by an additive assisted method for gamma-ray detection. *Journal of Materials Chemistry C, 8*(33), 11360–11368.
26. Lin, W., Stoumpos, C. C., Liu, Z., Das, S., Kontsevoi, O. Y., He, Y., Malliakas, C. D., Chen, H., Wessels, B. W., & Kanatzidis, M. G. (2017). TlSn2I5, a robust halide Antiperovskite semiconductor for γ-ray detection at room temperature. *ACS Photonics, 4*(7), 1805–1813.
27. Saidaminov, M. I., Abdelhady, A. L., Murali, B., Alarousu, E., Burlakov, V. M., Peng, W., Dursun, I., Wang, L., He, Y., MacUlan, G., Goriely, A., Wu, T., Mohammed, O. F., & Bakr, O. M. (2015). High-quality bulk hybrid perovskite single crystals within minutes by inverse temperature crystallization. *Nature Communications, 6*(1), 1–6.
28. Karasyuk, P., Shepelytskyi, Y., Semeniuk, O., Bubon, O., Juska, G., Blevis, I., & Reznik, A. (2018). Investigation of photoconductivity and electric field distribution in CZT detectors by time-of-flight (TOF) and charge extraction by linearly increasing voltage (CELIV). *Journal of Materials Science: Materials in Electronics, 29*(16), 13941–13951.
29. Bube, R. H. (1962). Trap density determination by space-charge-limited currents. *Journal of Applied Physics, 33*(5), 1733–1737.
30. Dong, Q., Fang, Y., Shao, Y., Mulligan, P., Qiu, J., Cao, L., & Huang, J. (2015). Electron-hole diffusion lengths > 175 μm in solution-grown CH3NH3PbI3 single crystals. *Science (80-), 347*(6225), 967–970.
31. Ahrling, R., Boy, J., Handwerg, M., Chiatti, O., Mitdank, R., Wagner, G., Galazka, Z., & Fischer, S. F. (2019). Transport properties and finite size effects in β-Ga2O3 thin films. *Scientific Reports, 9*(1), 13149.

32. Stillman, G. E., Wolfe, C. M., & Dimmock, J. O. (1970). Hall coefficient factor for polar mode scattering in N-type GaAs. *Journal of Physics and Chemistry of Solids, 31*(6), 1199–1204.
33. Dunlap, R. A. (2019). *Electrons in solids: Contemporary topics* (pp. 1–114). Morgan & Claypool Publishers. https://doi.org/10.1088/2053-2571/ab2f2c
34. Liu, T., Tang, W., Luong, S., & Fenwick, O. (2020). High charge carrier mobility in solution processed one-dimensional lead halide perovskite single crystals and their application as photodetectors. *Nanoscale, 12*(17), 9688–9695.
35. Matsushima, T., Leyden, M. R., Fujihara, T., Qin, C., Sandanayaka, A. S. D., & Adachi, C. (2019). Large metal halide perovskite crystals for field-effect transistor applications. *Applied Physics Letters, 115*(12), 120601.
36. Valverde-Chávez, D. A., Ponseca, C. S., Stoumpos, C. C., Yartsev, A., Kanatzidis, M. G., Sundström, V., & Cooke, D. G. (2015). Intrinsic femtosecond charge generation dynamics in single crystal CH3NH3PbI3. *Energy & Environmental Science, 8*(12), 3700–3707.
37. Xia, C. Q., Lin, Q., Patel, J. B., Wright, A. D., Crothers, T. W., Milot, R. L., Herz, L. M., & Johnston, M. B. (2019). *International conference on infrared, Millimeter, and terahertz waves, IRMMW-THz*. IEEE Computer Society.
38. Savenije, T. J., Guo, D., Caselli, V. M., & Hutter, E. M. (2020). Quantifying charge-carrier mobilities and recombination rates in metal halide perovskites from time-resolved microwave photoconductivity measurements. *Advanced Energy Materials, 10*(26), 1903788.
39. Guse, J. A., Soufiani, A. M., Jiang, L., Kim, J., Cheng, Y. B., Schmidt, T. W., Ho-Baillie, A., & McCamey, D. R. (2016). Spectral dependence of direct and trap-mediated recombination processes in lead halide perovskites using time resolved microwave conductivity. *Physical Chemistry Chemical Physics, 18*(17), 12043–12049.
40. Savenije, T. J., Ferguson, A. J., Kopidakis, N., & Rumbles, G. (2013). Revealing the dynamics of charge carriers in polymer: Fullerene blends using photoinduced time-resolved microwave conductivity. *Journal of Physical Chemistry C, 117*(46), 24085–24103.
41. Brenot, R., Vanderhaghen, R., Drevillon, B., French, I., Roca, I., & Cabarrocas, P. (1997). Time resolved microwave conductivity measurements for the characterization of transport properties in thin film micro-crystalline silicon. *Thin Solid Films, 296*(1–2), 94–97.
42. Peng, J., Chen, Y., Zheng, K., Pullerits, T., & Liang, Z. (2017). Insights into charge carrier dynamics in Organo-metal halide perovskites: From neat films to solar cells. *Chemical Society Reviews, 46*(19), 5714–5729.
43. Colbeau-Justin, C., & Valenzuela, M. A. (2013). Time-resolved microwave conductivity (TRMC) a useful characterization tool for charge carrier transfer in photocatalysis: A short review. *Revista Mexicana de Fisica, 59*(3), 191–200.
44. Schroder, D. K. (1987). *Advanced Mos devices (modular series on solid state devices)*. Addison-Wesley.
45. Hu, C., Khandelwal, S., Chauhan, Y. S., McKay, T., Watts, J., Duarte, J. P., Kushwaha, P., & Agarwal, H. (2019). *Industry standard FDSOI compact model BSIMIMG for IC design* (Vol. 1). Woodhead Publishing.
46. Cronemeyer, D. C. (1957). Hall and drift mobility in high-resistivity single-crystal silicon. *Physics Review, 105*(2), 522–523.
47. Li, W. G., Rao, H. S., Chen, B. X., Wang, X. D., & Kuang, D. B. (2017). A Formamidinium-methylammonium Lead iodide perovskite single crystal exhibiting exceptional optoelectronic properties and long-term stability. *Journal of Materials Chemistry A, 5*(36), 19431–19438.
48. Xia, C. Q., Lin, Q., Patel, J. B., Wright, A. D., Crothers, T. W., Milot, R. L., Herz, L. M., & Johnston, M. B. (2019). Time-resolved THz spectroscopy of metal-halide perovskite single crystals and polycrystalline thin films. *Int. Conf. Infrared, Millimeter, Terahertz Waves, IRMMW-THz, 2019-September*.
49. Valverde-Chávez, D. A., Ponseca, C. S., Stoumpos, C., Yartsev, A., Kanatzidis, M. G., Sundström, V., & Cooke, D. G. (2015). Optical pump - multi-THz probe spectroscopy of a single crystal organic hybrid lead halide perovskite. *CLEO: Science and Innovations*. CLEO-SI 2015*, 2015*, 2267.

50. Semonin, O. E., Elbaz, G. A., Straus, D. B., Hull, T. D., Paley, D. W., Van Der Zande, A. M., Hone, J. C., Kymissis, I., Kagan, C. R., Roy, X., & Owen, J. S. (2016). Limits of carrier diffusion in N-type and p-type CH3NH3PbI3 perovskite single crystals. *Journal of Physical Chemistry Letters, 7*(17), 3510–3518.
51. Stoumpos, C. C., Malliakas, C. D., & Kanatzidis, M. G. (2013). Semiconducting tin and Lead iodide perovskites with organic cations: Phase transitions, high mobilities, and near-infrared photoluminescent properties. *Inorganic Chemistry, 52*(15), 9019–9038.
52. Takahashi, Y., Hasegawa, H., Takahashi, Y., & Inabe, T. (2013). Hall mobility in tin iodide perovskite CH3NH3SnI 3: Evidence for a doped semiconductor. *Journal of Solid State Chemistry, 205*, 39–43.
53. Rong, S., Xiao, Y., Jiang, J., Zeng, Q., & Li, Y. (2020). Strongly enhanced photoluminescence and photoconductivity in erbium-doped MAPbBr3 single crystals. *Journal of Physical Chemistry C, 124*(16), 8992–8998.
54. Wang, J., Senanayak, S. P., Liu, J., Hu, Y., Shi, Y., Li, Z., Zhang, C., Yang, B., Jiang, L., Di, D., Ievlev, A. V., Ovchinnikova, O. S., Ding, T., Deng, H., Tang, L., Guo, Y., Wang, J., Xiao, K., Venkateshvaran, D., Jiang, L., Zhu, D., & Sirringhaus, H. (2019). Investigation of electrode electrochemical reactions in CH3NH3PbBr3 perovskite single-crystal field-effect transistors. *Advanced Materials, 31*(35), 1902618.
55. Maculan, G., Sheikh, A. D., Abdelhady, A. L., Saidaminov, M. I., Haque, M. A., Murali, B., Alarousu, E., Mohammed, O. F., Wu, T., & Bakr, O. M. (2015). CH3NH3PbCl3 single crystals: Inverse temperature crystallization and visible-blind UV-photodetector. *Journal of Physical Chemistry Letters, 6*(19), 3781–3786.
56. Han, Q., Bae, S. H., Sun, P., Hsieh, Y. T., Yang, Y., Rim, Y. S., Zhao, H., Chen, Q., Shi, W., Li, G., & Yeng, Y. (2016). Single crystal formamidinium lead iodide (FAPbI3): Insight into the structural, optical, and electrical properties. *Advanced Materials, 28*(11), 2253–2258.
57. Zhumekenov, A. A., Saidaminov, M. I., Haque, M. A., Alarousu, E., Sarmah, S. P., Murali, B., Dursun, I., Miao, X. H., Abdelhady, A. L., Wu, T., Mohammed, O. F., & Bakr, O. M. (2016). Formamidinium lead halide perovskite crystals with unprecedented Long carrier dynamics and diffusion length. *ACS Energy Letters, 1*(1), 32–37.
58. Liu, Y., Sun, J., Yang, Z., Yang, D., Ren, X., Xu, H., Yang, Z., & Liu, S. F. (2016). 20-mm-large single-crystalline Formamidinium-perovskite wafer for mass production of integrated photodetectors. *Advanced Optical Materials, 4*(11), 1829–1837.
59. Ng, M., & Halpert, J. E. (2020). Single crystals of mixed Br/Cl and Sn-doped formamidinium lead halide perovskites: Via inverse temperature crystallization. *RSC Advances, 10*(7), 3832–3836.
60. Pan, L., Feng, Y., Huang, J., & Cao, L. R. (2020). Comparison of Zr, Bi, Ti, and Ga as metal contacts in inorganic perovskite CsPbBr gamma-ray detector. *IEEE Transactions on Nuclear Science, 67*(10), 2255–2262.
61. Zhang, B. B., Wang, F., Zhang, H., Xiao, B., Sun, Q., Guo, J., Hafsia, A. B., Shao, A., Xu, Y., & Zhou, J. (2020). Defect proliferation in CsPbBr3 crystal induced by ion migration. *Applied Physics Letters, 116*(6), 063505.
62. Liu, J., Liu, F., Liu, H., Hou, R., Yue, J., Cai, J., Peng, Z., Impundu, J., Xie, L., Li, Y. J., & Sun, L. (2020). Direct growth of perovskite crystals on metallic electrodes for high-performance electronic and optoelectronic devices. *Small, 16*(3), 1906185.
63. Huo, C., Liu, X., Song, X., Wang, Z., & Zeng, H. (2017). Field-effect transistors based on van-Der-Waals-grown and dry-transferred all-inorganic perovskite ultrathin platelets. *Journal of Physical Chemistry Letters, 8*(19), 4785–4792.
64. He, Y., Stoumpos, C. C., Hadar, I., Luo, Z., McCall, K. M., Liu, Z., Chung, D. Y., Wessels, B. W., & Kanatzidis, M. G. (2021). Demonstration of energy-resolved γ-ray detection at room temperature by the CsPBCl3 perovskite semiconductor. *Journal of the American Chemical Society, 143*(4), 2068–2077.

65. Liu, Y., Zhang, Y., Zhu, X., Yang, Z., Ke, W., Feng, J., Ren, X., Zhao, K., Liu, M., Kanatzidis, M. G., & Liu, S. (2021). Inch-sized high-quality perovskite single crystals by suppressing phase segregation for light-powered integrated circuits. *Science Advances, 7*(7), 202102.
66. Ueno, K., Inoue, I. H., Yamada, T., Akoh, H., Tokura, Y., & Takagi, H. (2004). Field-effect transistor based on KTaO3 perovskite. *Applied Physics Letters, 84*(19), 3726–3728.
67. Zhang, Z., Chung, C. C., Huang, Z., Vetter, E., Seyitliyev, D., Sun, D., Gundogdu, K., Castellano, F. N., Danilov, E. O., & Yang, G. (2020). Towards radiation detection using Cs2AgBiBr6 double perovskite single crystals. *Materials Letters, 269*, 127667.
68. Pan, W., Wu, H., Luo, J., Deng, Z., Ge, C., Chen, C., Jiang, X., Yin, W. J., Niu, G., Zhu, L., Yin, L., Zhou, Y., Xie, Q., Ke, X., Sui, M., & Tang, J. (2017). Cs2AgBiBr6 single-crystal X-ray detectors with a low detection limit. *Nature Photonics, 11*(11), 726–732.
69. McCall, K. M., Liu, Z., Trimarchi, G., Stoumpos, C. C., Lin, W., He, Y., Hadar, I., Kanatzidis, M. G., & Wessels, B. W. (2018). α-Particle detection and charge transport characteristics in the A3M2I9 defect perovskites (A = Cs, Rb; M = Bi, Sb). *ACS Photonics, 5*(9), 3748–3762.
70. Zhuang, R., Wang, X., Ma, W., Wu, Y., Chen, X., Tang, L., Zhu, H., Liu, J., Wu, L., Zhou, W., Liu, X., & Yang, Y. M. (2019). Highly sensitive X-ray detector made of layered perovskite-like (NH4)3Bi2I9 single crystal with anisotropic response. *Nature Photonics, 13*(9), 602–608.
71. Zhang, Y., Sun, M., Zhou, N., Huang, B., & Zhou, H. (2020). Electronic tunability and mobility anisotropy of quasi-2D perovskite single crystals with varied spacer cations. *Journal of Physical Chemistry Letters, 11*(18), 7610–7616.
72. Liu, F., Wang, L., Wang, J., Wang, F., Chen, Y., Zhang, S., Sun, H., Liu, J., Wang, G., Hu, Y., & Jiang, C. (2021). 2D Ruddlesden–popper perovskite single crystal field-effect transistors. *Advanced Functional Materials, 31*(1), 2005662.
73. Li, W., Xin, D., Tie, S., Ren, J., Dong, S., Lei, L., Zheng, X., Zhao, Y., & Zhang, W. H. (2021). Zero-dimensional lead-free FA3Bi2I9 single crystals for high-performance X-ray detection. *Journal of Physical Chemistry Letters, 12*(7), 1778–1785.
74. Zheng, X., Zhao, W., Wang, P., Tan, H., Saidaminov, M. I., Tie, S., Chen, L., Peng, Y., Long, J., & Zhang, W. H. (2020). Ultrasensitive and stable X-ray detection using zero-dimensional lead-free perovskites. *Journal of Energy Chemistry, 49*, 299–306.
75. Song, X., Cui, Q., Liu, Y., Xu, Z., Cohen, H., Ma, C., Fan, Y., Zhang, Y., Ye, H., Peng, Z., Li, R., Chen, Y., Wang, J., Sun, H., Yang, Z., Liu, Z., Yang, Z., Huang, W., Hodes, G., Liu, S., & Zhao, K. (2020). Metal-free halide perovskite single crystals with very long charge lifetimes for efficient X-ray imaging. *Advanced Materials, 32*(42), 2003353.
76. Liu, Y., Zhang, Y., Zhu, X., Feng, J., Spanopoulos, I., Ke, W., He, Y., Ren, X., Yang, Z., Xiao, F., Zhao, K., Kanatzidis, M., & Liu, S. (2021). Triple-cation and mixed-halide perovskite single crystal for high-performance X-ray imaging. *Advanced Materials, 33*(8), 1.
77. Oranskaia, A., Yin, J., Bakr, O. M., Brédas, J. L., & Mohammed, O. F. (2018). Halogen migration in hybrid perovskites: The organic cation matters. *Journal of Physical Chemistry Letters, 9*(18), 5474–5480.
78. Liu, G., Wu, Y., Liu, Y., Cai, B., Dong, Y., Zhang, S., & Zeng, H. (2021). Halide ion migration in Lead-free all-inorganic Cesium tin perovskites. *Applied Physics Letters, 119*(3), 031902.
79. Datta, A., Fiala, J., Becla, P., & Motakef, S. (2017). Stable room-temperature thallium bromide semiconductor radiation detectors. *APL Materials, 5*(10), 106109.
80. Meggiolaro, D., Mosconi, E., & De Angelis, F. (2019). Formation of surface defects dominates ion migration in lead-halide perovskites. *ACS Energy Letters, 4*(3), 779–785.
81. Le Corre, V. M., Duijnstee, E. A., El Tambouli, O., Ball, J. M., Snaith, H. J., Lim, J., & Koster, L. J. A. (2021). Revealing charge carrier mobility and defect densities in metal halide perovskites via space-charge-limited current measurements. *ACS Energy Letters, 6*(3), 1087–1094.
82. Motta, C., El-Mellouhi, F., & Sanvito, S. (2015). Charge carrier mobility in hybrid halide perovskites. *Scientific Reports, 5*, 12746.

83. Meng, G., Feng, Y., Song, X., Shi, Y., Ji, M., Xue, Y., & Hao, C. (2018). Theoretical insight into the carrier mobility anisotropy of organic-inorganic perovskite CH3NH3PbI3. *Journal of Electroanalytical Chemistry, 810*, 11–17.
84. Zhao, Y. Q., Wu, L. J., Liu, B., Wang, L. Z., He, P. B., & Cai, M. Q. (2016). Tuning superior solar cell performance of carrier mobility and absorption in perovskite CH3NH3GeCl3: A density functional calculations. *Journal of Power Sources, 313*, 96–103.
85. He, Y., Ke, W., Alexander, G. C. B., McCall, K. M., Chica, D. G., Liu, Z., Hadar, I., Stoumpos, C. C., Wessels, B. W., & Kanatzidis, M. G. (2018). Resolving the energy of γ-ray photons with MAPbI3 single crystals. *ACS Photonics, 5*(10), 4132–4138.
86. Wang, L. Z., Zhao, Y. Q., Liu, B., Wu, L. J., & Cai, M. Q. (2016). First-principles study of photovoltaics and carrier mobility for non-toxic halide perovskite CH3NH3SnCl3: Theoretical prediction. *Physical Chemistry Chemical Physics, 18*(32), 22188–22195.
87. Rahul, Singh, P. K., Singh, R., Singh, V., Bhattacharya, B., & Khan, Z. H. (2018). New class of Lead free perovskite material for low-cost solar cell application. *Materials Research Bulletin, 97*, 572–577.
88. Ouhbi, H., Ambrosio, F., De Angelis, F., & Wiktor, J. (2021). Strong electron localization in tin halide perovskites. *Journal of Physical Chemistry Letters, 12*(22), 5339–5343.
89. Zheng, F., & Wang, L. W. (2019). Large polaron formation and its effect on electron transport in hybrid perovskites. *Energy & Environmental Science, 12*(4), 1219–1230.
90. Miyata, K., Meggiolaro, D., Tuan Trinh, M., Joshi, P. P., Mosconi, E., Jones, S. C., De Angelis, F., & Zhu, X. Y. (2017). Large polarons in lead halide perovskites. *Science Advances, 3*(8), 201708.
91. Bonn, M., Miyata, K., Hendry, E., & Zhu, X. Y. (2017). Role of dielectric drag in polaron mobility in lead halide perovskites. *ACS Energy Letters, 2*(11), 2555–2562.

Advances in Organometallic Perovskites Enabled Radiation Detection Technologies

Murali Gedda, Hendrik Faber, Konstantinos Petridis, and Thomas D. Anthopoulos

1 Introduction

Radiation is the transmission or emission of energy by means of direct ionization (ionization radiation: α-particles and β-particles) or indirect ionization (high-energy radiation: X-rays and γ-rays). This is a fast-growing area of research that has shown a strong impact on various fields, including materials science, structural chemistry, and molecular biology. X-rays and γ-rays are effective tools for nondestructive inspection such as medical imaging [1–3], industrial monitoring [4], and security inspection [5]. Crystallography [6, 7], astronomy [8], and particle physics [9] are some of the relevant fields of high-energy radiation. Hence, efficient radiation detectors are pivotal to fully extract information from high-energy photons and particles. Ionizing radiation is a type of radiation that possesses enough energy to ionize atoms or molecules. The electrons and protons are the particles in an atomic nucleus that are mainly included during direct ionizing radiation. On the contrary, indirectly ionizing radiation is typically photon radiation induced by electrically neutral particles. Photon radiation is also known as high-energy electromagnetic waves, including X-rays (0.1–100 keV) and γ-rays (0.1–100 MeV) [10, 11]. Figure 1 represents the formation of common radiation types, including high-energy particle beams and photo radiation, and their related energies. Thanks to their high penetration and ionization, high-energy radiation can widely be used in various emerging fields.

M. Gedda (✉) · H. Faber · T. D. Anthopoulos (✉)
Kaust Solar Center, King Abdullah University of Science and Technology (KAUST), Thuwal, Saudi Arabia
e-mail: murali.gedda@kaust.edu.sa; thomas.anthopoulos@kaust.edu.sa

K. Petridis
Department of Electronic Engineering, Hellenic Mediterranean University, Chania, Crete

W. Nie, K. (Kris) Iniewski (eds.), *Metal-Halide Perovskite Semiconductors*,
https://doi.org/10.1007/978-3-031-26892-2_7

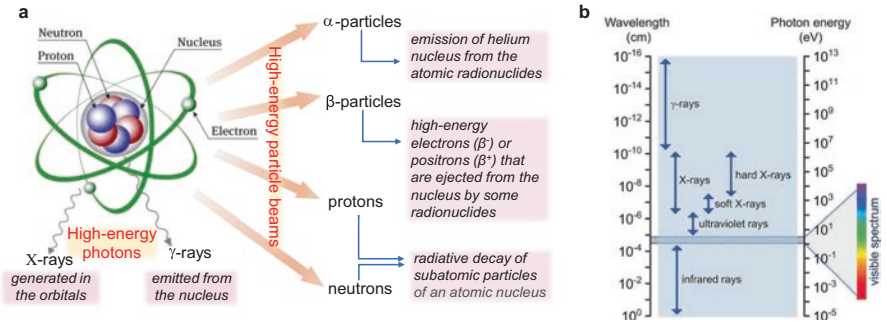

Fig. 1 (**a**) Schematic representation of particle and photon radiation and (**b**) the electromagnetic spectrum range from infrared to γ-rays

Semiconductors can detect radiation-induced free charge carriers with a suitable bandgap under suitably applied voltages. Analogous to normal photodetectors that work in UV-visible-infrared light ranges, semiconductor-based high-energy radiation detectors can also directly generate current from free-charge carriers excited through the photoelectric effect or by Coulomb force. Most of the existing radiation detection devices are based on silicon (Si), germanium (Ge), amorphous selenium (a-Se), cadmium telluride (CdTe), cadmium zinc telluride (CZT), or mercury iodide (HgI_2) [12]. Converting radiation into electrical or optical signals that can be further amplified using conventional electronics is the operational principle of most radiation detectors. Thus, along with the radiation-specific requirements, they must satisfy a few standard requirements. Primarily, the bandgap must be from 1.5 eV to 2.5 eV [13] to ensure a low dark current and to provide a sufficient energy barrier for electron-hole pair production; the semiconductor's large stopping power for effectively detecting high-energy radiation needs a high average atomic number Z and high mass density [14]. For example, the narrow bandgap (1.12 eV) and small atomic number of the widely used semiconductor Si yield a large dark current at room temperature, thus limiting the fabrication of high-performance radiation detectors based on Si. On the other hand, the relatively large bandgap (1.57 eV) and a high atomic number (49.3) of CZT materials show excellent performance in commercial radiation detectors [15, 16]. The carrier mobility-lifetime product $\mu_{h/e}\tau$ is another essential factor of semiconductors employed for radiation detection. A large $\mu_{h/e}\tau$ product enables a long carrier diffusion length, which indicates the reduced combination and possibility of a carrier being captured. In addition to direct detection, radiation can also be detected using scintillator and photodetector arrays, also known as indirect radiation detection. Conversion of high-energy photons and particles into visible light via scintillators followed by detection using sensitive photodetectors such as photodiode arrays and complementary metal-oxide semiconductors (CMOS), charged-coupled devices (CCD), etc. are the critical steps involved in indirect detection of radiation. Therefore, the scintillator is the crucial component

that determines conversion efficiency performance. Long-term stability, high energy resolution, and high light yield for generating enough detectable signals are the necessary traits of a high-quality scintillator. Inorganic crystals such as thallium-doped sodium and cesium iodides (NaI(Tl) and CsI(Tl)) are widely employed scintillator materials in the current market [17, 18]. However, complex growth methods and operating conditions are the limiting factors of these commercial semiconductors. Therefore, the demand for economical, facile processable semiconductors is rapidly raised.

Metal-halide perovskites (MHPs) emerged as a family of promising photoactive materials with excellent features over the past few years, including a long carrier lifetime, large absorption coefficient, high light yield, and cost-effective growth methods [19–21]. The general formula of MHPs is ABX_3, where A site represents inorganic cation such as Cs^+, a monovalent organic cation (e.g., methylammonium ($MA = CH_3NH_3$), formamidinium ($FA = CH(NH_2)_2$), or a mixture thereof and the B site is Pb or the recently focused non-Pb component, Sn, and X is a halide component Cl^-, Br^-, I^-, or a mixture thereof. The outstanding electronic and photophysical properties of halide perovskites also allow them as potential candidates for next-generation optoelectronic or electronic device applications beyond broadly investigated halide perovskite solar cells, such as light-emitting diodes [22–24], transistors [25, 26], lasers [27], and photodetectors [28, 29].

Since the first report that pointed out metal-halide perovskites can detect radiation [30], many radiation detectors based on MHPs have been fabricated, and their performance has further improved [31–33]. In this regard, the rapid research progress and great strides that metal-halide perovskites have made in ionizing radiation detection call for a swift and consistent survey into the state of the field. In addition, detecting the directly ionizing radiation particles using MHPs is another fascinating area of research. Therefore, this chapter aims to comprehensively summarize the recent successes, ongoing developments, and challenges of MHPs for radiation detection devices, emphasizing fundamental detection principles of various photons and charged particles. The beginning of the chapter presents the working mechanism of different radiation detectors. The subsequent section discusses the prominent physical characteristics of metal-halide perovskite materials for radiation detection. Recent accomplishments and ongoing efforts on MHP-based radiation detectors, particularly the detection of charged particles (alpha and beta particles), as well as high-energy photons (γ- and X-rays), are discussed in the following section. Since the area of MHP-based radiation detectors is rapidly evolving and numerous emerging technologies have been reported during the last 2 years, this chapter focuses mainly on summarizing the research findings during the past 2 years. The last part of the chapter consists of conclusions and presents a perspective for the future development of MHP materials for radiation detection applications. It also proposes some strategies to advance their enduring stability and device performance.

2 Working Principles of Radiation Detectors

2.1 Direct Radiation Detectors

Direct radiation detection can be attained by employing suitable semiconductors in the current or voltage modes. An ammeter is connected across the output of the detector in the current mode. Therefore, the measured current is the time average of all the individual pulses. The mean square voltage mode is effective when mixed radiation environments produce an uneven charge amount. The recorded detector's mean square of the time variance current is proportional to the square of the charge produced in each event and the rate of the event. However, the performance of the direct detector depends on the interaction of the incident particle or photon with the active semiconductors [34, 35].

2.1.1 Detection of Alpha (α) and Beta (β) Particles

The α-particles were named by Rutherford in 1899, and soon after, in 1907, these particles were confirmed to be helium nuclei. The energy of α-particles decayed from heavy atoms depends on the half-life of the emission process, i.e., a larger nucleus emits particles with higher energy. Due to their higher particle mass than other radiations, the energy of α-particles ranges between 3 and 7 MeV, with a speed of 15,000 km s^{-1}. Therefore, the penetration of α-particles is typically lower than that of β-particles or γ-rays, and a piece of paper or human skin could block it. However, it is the most harmful ionizing radiation; if the atoms that emit α-particles accidentally enter the human body, they could cause serious chromosomal damage to DNA which is 20 times worse than that caused by the same dose of γ-rays or β-particles [36]. In this regard, developing high-quality detectors for α-particle radiation is important. Such detectors are useful for environmental safety concerns and the nuclei information conducted by α-particles. An α-spectrum is commonly used to characterize α-particles ejected from the nuclei. Therefore, peak resolution is an important parameter for radiation detectors that helps in generating a spectrum with clear segregated radiation peaks. $\mu_{h/e}\tau$ product is another key parameter of α-particle detectors, related to the charge collection efficiency (CCE). The following Hecht equation is generally used to derive CCE for a single carrier [37]:

$$\eta = \frac{q}{q_0} = \frac{\mu\tau V}{d^2}\left(1 - e^{-\frac{d^2}{\mu\tau V}}\right) \tag{1}$$

where η is CCE, q and q_0 are the collected and the total injected charges, V is applied voltage, and d is the thickness of the detector.

The flux of high-energy particles like α-particles is weak and reaches the detector one after another. Therefore, the direct high-energy particle detector works in

voltage mode. The inelastic collisions of α-particles with the semiconductor lead to the generation of electron-hole pairs whose number depends proportionally on the energy of α-particle. The next step is separating and collecting generated charges in the form of current upon biasing voltage. As the originated current signal strength is low, integration of a charge-sensitive preamplifier with the semiconductors to boost the signal is the commonly employed process. The amplifier then combines the current signal and converts it into a voltage pulse, which is also proportional to α-particle energy. An α-particle spectrum as the final output is recorded by processing voltage pulses using a multiple-channel digitizer.

β-rays comprise electrons or positrons with reasonable penetration depths and are crucial in cancer cell treatment [38] and surface radiative contamination surveillance [39]. In addition to its higher speed and low energies than α-particles, β-particles possess different interactions when they meet atoms. When β-particles interact with the atom's nuclei, they get scattered elastically and change their trajectory. Interaction between β-particles and electrons in the atoms leads to inelastic scattering, which produces photons and other electron signals. For the element with a larger Z, the ratio of elastic and inelastic scattering (η) is higher. Therefore, inelastic scatterings in low-Z elements yield more photons. Similar to α-particle detection, β-particles can also be detected in the voltage mode using semiconductor-based detectors via separation and collection of generated electron-hole pairs.

2.1.2 X-Ray Detection

The current mode is commonly employed in direct X-ray detectors, where the photon flux is strong enough to generate current signals. The X-ray photons interact with the active semiconductors and converts into electron-hole pairs by photoelectric effect and Compton scattering. The generated charged carriers are further collected by electrodes under the applied voltage bias, producing the current signals. Key figures of merit (FOM) that determine the performance of a direct X-ray detector are discussed in the following.

Stopping Power

The rate of energy lost per unit of path length (x) by a charged particle with kinetic energy (T_E) in a medium of atomic number Z ($Z \propto \rho$, where ρ is the density of the material) is the stopping power. It is measured in MeV/cm or J/m. The following is the representative form of stopping power:

$$dT_E / \rho\, dx \tag{2}$$

Ionization Energy (W±)

The energy required to release an electron-hole pair in the photoconductor sensing material is ionization energy ($W_{\pm}$). The general representation of ionization energy in terms of energy bandgap (E_g) of the absorbing material and photon energy (E_{photon}) is as follows [40]:

$$W_{\pm} = 2.2E_g + E_{photon} \tag{3}$$

or

$$W_{\pm} = 3E_g \tag{4}$$

$\mu_{h/e}$ τ Product

High detection sensitivity is needed to generate good-quality images at any X-ray dose. The sensitivity of X-ray detectors can be enhanced through two different methods: (a) rising the mobility-lifetime ($\mu_{h/e}\tau$) product as it relates to the carrier drift length (L_D) given as $L_D = (k_BT\mu\tau/e)^{1/2}$ and (b) higher applied reverse bias. High $\mu_{h/e}\tau$ product and low trap density are essential for efficient direct X-ray detectors. The $\mu_{h/e}\tau$ product for a given sensing material can be estimated from the modified Hecht formula for photoconductivity (I) [41]:

$$I = \frac{I_o \mu\tau V}{L^2} \frac{1 - \exp\left(-\frac{L^2}{\mu\tau V}\right)}{1 + \frac{L}{V}\frac{s}{\mu}} \tag{5}$$

where I_o is the saturated photocurrent, L is the thickness of the material, V is the applied bias, and s is the surface recombination velocity.

Sensitivity

The ability to detect weak signals is known as sensitivity. The following formula can calculate the detector's sensitivity:

$$S = \frac{\int \left[I_{X-ray}(t) - I_{dark} \right] dt}{D \times V_d} \tag{6}$$

where $I_{X\text{-ray}}$ and I_{dark} are the generated currents with and without X-ray irradiation, D is the dose, and V_d is the detector volume.

The detector's linear dynamic range (LDR), which represents the range of X-ray dose rate under which the sensitivity remains constant, is a crucial parameter in describing a detector's properties. Large LDR will ensure that the detector delivers a precise measurement of the X-ray dose rate under a large deviation range.

Energy Resolution

The energy resolution is the detector's ability to determine the incident radiation energy [42]. It is derived from the ratio between the FWHM and the photo-peak centroid H_{max}. Thus, the energy resolution (R) is calculated from the following equation:

$$R\% = \frac{FWHM}{H_{\max}} \tag{7}$$

The thickness of the active layer should be three times larger than the attenuation length. The magnitude of the produced electrical current is proportional to the incident photon energy in direct radiation X-ray detectors operated in current mode. The key FOM parameters of high-energy radiation direct detectors and their significance are listed in Table 1.

2.2 *Indirect Radiation Detection*

The indirect radiation detectors consist of scintillator and photodiode arrays, which can also detect high-energy particles or photons [43]. As discussed in the previous section, high-energy particles can ionize the active semiconducting materials by Coulomb force. In contrast, photoelectrical effect, Compton scattering, and pair

Table 1 Some of the key direct radiation detectors' FOM parameters and their significance

FOM parameter	Significance
Mass attenuation coefficient	Determines the penetration depth
Density of the sensing material	Relies on the composition and structural properties of the active material
Signal-to-noise ratio	Describes dark current
Spatial resolution of the detector	Governs the image resolution
Response time	Photogenerated charges and transport
Uniformity of the sensing material	Processing versatility of the active material
Operational stability	Detector's performance during operation
Electron/hole mobility ($\mu_{h/e}$)—Lifetime (τ) product ($\mu_{h/e}\tau$)	Identifies the quality of a semiconductor

production generally occur in the materials when high-energy photons interact. The generated excitons through these processes will then be transferred to the defects states and recombined, yielding UV or visible light emission. Photo-sensitive photodetector arrays or cameras will further capture the emitted UV or visible light, and the output is generated as a current signal or image information. All processes are characterized by absorption coefficients determined by the scintillator material's atomic number (Z) and the photon energy. In the photoelectric effect dominant case, the linear absorption coefficient (μ_L) is given by

$$\mu_L \approx \rho Z^n / E^{3.5} \tag{8}$$

where E is the photon energy, ρ is the material density, and n is a constant that varies between 3 and 4.

Compton scattering, a part of the photon's energy transferred to the electron depending on the scattering angle, generally occurs at higher energies. The Compton scattering linear absorption coefficient (μ_C) is given by [44, 45]

$$\mu_C \approx \rho / (E)^{1/2} \tag{9}$$

The generation of low-energy excitons (pair production) usually occurs at very high-energy interactions that eventually produce visible light upon recombination. The emitted light can then be detected via photodetectors coupled with the scintillator element. The absorption coefficient (μ_P) associated with pair production is expressed as

$$\mu_P \approx \rho Z \ln(2E / (m_e c^2)) \tag{10}$$

where c is the speed of light and m_e is the mass of electrons. Conversion, energy transfer, and luminescence are the three main subprocesses involved in scintillation. The first stage of scintillation is photon absorption. Charge transport and energy transfer are the further steps. The final process comprises the transfer of energy of hot carriers to the luminescence centers that lead to visible light emission.

The number of electron-hole pairs generated during the ionization process per unit of energy is denoted by light yield (LY), measured as photons per MeV. The corresponding expression is as follows:

$$LY = 10^6 SQ / (\beta_c E_g) \tag{11}$$

where S is the efficiency of electron-hole transport to the optical (emissive) center, Q is the luminescence efficiency, and β_c is a constant with a characteristic value of 2.5. Some of the key FOMs of the scintillator are listed in Table 2.

Table 2 Important FOM parameters and their significance for high-energy scintillation detectors

FOM parameter	Significance
Radiation absorption efficiency	Relies on the density of scintillator material and Z
Light yield (LY)	Number of emitted photons per absorbed energy
Decay time	Kinetics of light response I(t) characterized by τ
Energy resolution	Ability to differentiate peak radiation energies
Spatial resolution	Governs the spatial frequency response of the photodetector
Radiation hardness	Characterizes the chemical and radiation stability
Proportionality	Linearity of the detected signal to the incoming radiation intensity
Afterglow	Residual light output occurring after the primary decay time of the main luminescent centers
Stopping power	Attenuation coefficient of the absorbed radiation

3 Desired Properties of Halide Perovskites for Radiation Detection

As discussed in the previous section, the superior electronic and photophysical properties of halide perovskites, including large absorption coefficients, long carrier lifetimes, high light yields, and cost-effective growth methods [46–49], put them in a position to be auspicious candidates for next-generation electronic [25, 26, 50] and optoelectronic devices, such as solar cells [51, 52], light-emitting diodes [27, 53, 54], LASERs [27], and photodetectors [55]. Furthermore, several prerequisites must be fulfilled to serve a semiconductor as a high-performance radiation detector. The attenuation coefficient is one of the important figures of merit (FOM) that decides the performance of the radiation detector. High-*Z* element semiconductors, such as CdTe and MHP, have higher attenuation than low-*Z* element semiconductors, such as Si and a-Se. Figure 2a shows the attenuation coefficient variation as a photon energy function. The inverse proportional relation of attenuation coefficient and energy implies that the detector's thickness and material choice must be tuned to achieve efficient absorption. Many research articles on radiation detectors based on inorganic and hybrid halide perovskites have also been fabricated for detecting high-energy charged particles and photons. The splendid features of halide perovskite materials for radiation detection applications have been detailed in the following subsection.

3.1 Large Stopping Power

Since high-energy particles/photons can be pulled down with more energy loss and thus more signal outputs, large stopping power is vital for high-performance radiation detectors. Perovskite with heavy metal ion lead (Pb) and halide components (typically Br or I) offer high average atomic numbers to achieve large stopping

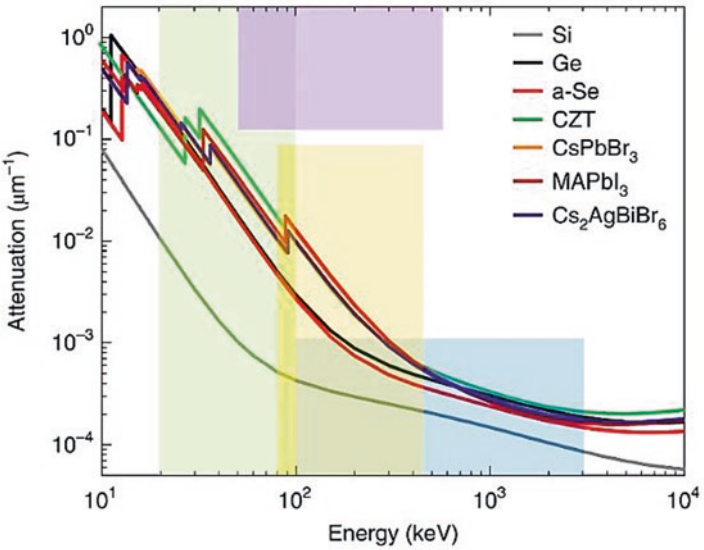

Fig. 2 The variation of the attenuation coefficient as a function of the photon energy of some popular perovskites and inorganic semiconductors. Reproduced with permission from Ref. [33]

power and consequently great detection efficiency. For instance, $CsPbBr_3$, an all-inorganic halide perovskite, has an average atomic number of about 65.9, which is even superior to that of 49.3 for the CZT material. The density of $MAPbI_3$ is 4 g cm^{-3}, and the corresponding linear attenuation coefficient is around 10 cm^{-1} at 100 keV, whereas inorganic perovskite $CsPbI_3$ even offers a larger linear attenuation coefficient of 14 cm^{-1}. Linear attenuation coefficients of some of the halide perovskites, $MAPbI_3$ and $CsPbBr_3$, and that of the commonly used Se, Ge, Si, and CdTe at different photon energies are shown in Fig. 2. It is clear from the figure that the halide perovskite materials exhibit the linear attenuation properties comparable and even higher than those commonly used materials.

3.2 Appropriate Bandgap and High Bulk Resistance

A large bulk resistance of a perovskite radiation detector is essential to ensure low dark currents and noise at room temperature, specifically when a high bias is employed. Currently, the estimated bulk resistances of lead-halide perovskites range from 10^7 to 10^9 Ω-cm, which can be further tuned by adjusting the halide component ratio in the perovskite [56, 57]. Also, metal-halide perovskites have tunable bandgaps ranging from 1.3 to 3.2 eV that can be adjusted through their halide components, making them ideal materials for radiation detectors.

3.3 High $\mu_{h/e}\tau$ Product

The recombination and trapping processes of charge carriers that are generated in the semiconductor by radiation depend on intrinsic and extrinsic defects of the material. Both processes effectively decrease the current flow, and thus the signal intensity is minimized. As a result of reduced recombination at defect sites, larger carrier-lifetime product $\mu_{h/e}\tau$ values can be achieved. Thus, the electrodes can collect more charge carriers, increasing the detector's efficiency. Most defect centers of halide perovskite films are generally situated at the surface or grain boundaries. This is the reason for exhibiting a low trap density of 10^7–10^9 cm^{-3} and thus high $\mu_{h/e}\tau$ products in grain boundary-free single crystals. The $MAPbI_3$ single crystal holds a high $\mu_{e/h}\tau$ product of 10^{-2} cm^2 V^{-1}, with an extended carrier diffusion length over 175 μm [58]. Besides, the internal quantum efficiency of a 3-mm-thick $MAPbI_3$ single crystal can also approach 100% under faint light illumination, which indicates a diffusion length almost exceeding 3 mm [59].

3.4 Inexpensive and Facile Growth Methods

Cost-effective crystal growth and device fabrication methods are halide perovskites' advantages. In comparison, the growth of widely used commercial semiconductors, like Si, Se, Ge, and CZT, typically requires very controlled and complex instruments. Contrarily, lead-halide perovskites can typically be produced at nominal temperatures (~150 °C) via solution methods. Moreover, the overall process is relatively inexpensive compared to the commonly used semiconductors mentioned above. For instance, a 1 cm^3 perovskite single-crystal growth costs around $0.3 when scaling up the production, which is four times lower than CZT crystal growth [32]. In addition, the facile fabrication of devices via a one-step spin or spray coating from dispersions of freshly grown perovskite crystals enables an enormous potential for further integration.

3.5 High Light Yield

Metal-halide perovskites are compatible with direct photoconductors and indirect scintillators for detecting high-energy radiation. When transforming from 3D to lower dimensional crystal forms, perovskites display robust radioluminescence under the excitation of high-energy radiations. For example, lead-halide perovskites showed optimal device performance with a higher light yield over 10^6 ph MeV^{-1} and a fast decay time of <1 ns, which are superior to conventional $LaBr_3$-Ce scintillators (light yield, 70,000 ph MeV^{-1}; decay time, 16 ns) [60]. Such high light yield and fast decay are required for first-class scintillators that allow measuring the

initial particle or radiation time with high accuracy and time resolution. Besides, halide perovskites also permit easy halide ion exchanges that promote a tunable luminescence spectrum over the visible region [61, 62].

4 Halide Perovskites for Particle Detection

4.1 α-Particle Detectors

4.1.1 Direct Detection of α-Particle

Due to the high charge carrier mobility, long diffusion length in the tens of micrometers range, and low trap density of 10^9 cm^{-3}, perovskite single crystals have been explored for direct and indirect ionized particle detection. Several reports on halide perovskites for α-particle detection include 3D, 2D, 0D, and other perovskite-related structures [63]. The primary attempt to detect α-particles using solid-state detectors based on $MAPbBr_3$ (density: 3.7 g/cm^3) halide perovskites was reported by Xu et al. [64]. The α-particle detectors were fabricated on bulk $MAPbBr_3$ single crystals ($5 \times 5 \times 2$ mm^3) in a metal-semiconductor-metal (MSM) structure. At the same time, BCP and C_{60} films coated all around served the purpose of both passivation and electron extraction. A series of energy spectrums were obtained under the exposure of a 0.8 mCi ^{241}Am source for 900 s at different biases. However, the energy spectra attained from the ^{241}Am α-source consists of broad spectral peaks and nonlinear peak position with the applied voltage (Fig. 3a). Unbalanced electron and hole transport induced high dark current (206 nA cm^{-2}) are the major attributes of this anomaly. Liu et al. adopted a modified antisolvent vapor-assisted crystallization (AVC) method (Fig. 3b) to improve the morphology and quality of $MAPbBr_3$ single crystal (Fig. 3c), thereby enhancing detector performance [65]. The devices fabricated in MSM structure with centimeter-sized $MAPbBr_3$ bulk crystals display bulk resistivity of about 5.6×10^8 Ω-cm and 400 nA leakage current under 100 V. The $\mu_{h/e}\tau$ products are 2.2×10^{-4} and 4.2×10^{-4} cm^2/V for electrons and holes. The electron and hole mobility is estimated to be 24.6 and 59.7 cm^2/(V-s), respectively, using a 0.8 μCi ^{241}Am α-source. $MAPbI_3$ single-crystal detectors reported by He et al. presented an enhanced performance in detecting ^{241}Am α-particles [68]. Balanced charge transport and low dark current of ~81 nA cm^{-2} have been reported. The ability to detect the 5.5 MeV ^{241}Am α-particles with an energy resolution of 14% is one of the key achievements of this work. Another work from the same group on an inorganic $CsPbBr_3$ single-crystal radiation detector [69] can simultaneously resolve the γ-ray (122 keV) and α-particle (5.5 MeV) peaks from a ^{57}Co source with energy resolutions of 4.8% and 15%, respectively (Fig. 3d,e). In general, due to their lower defect density, inorganic perovskites possess higher stability than organic-inorganic hybrid perovskites [66]. They have great potential to compete with the current technology for α-particle detection, especially considering the recent progress in high-resolution γ-ray detectors based on $CsPbBr_3$ [66, 70, 71].

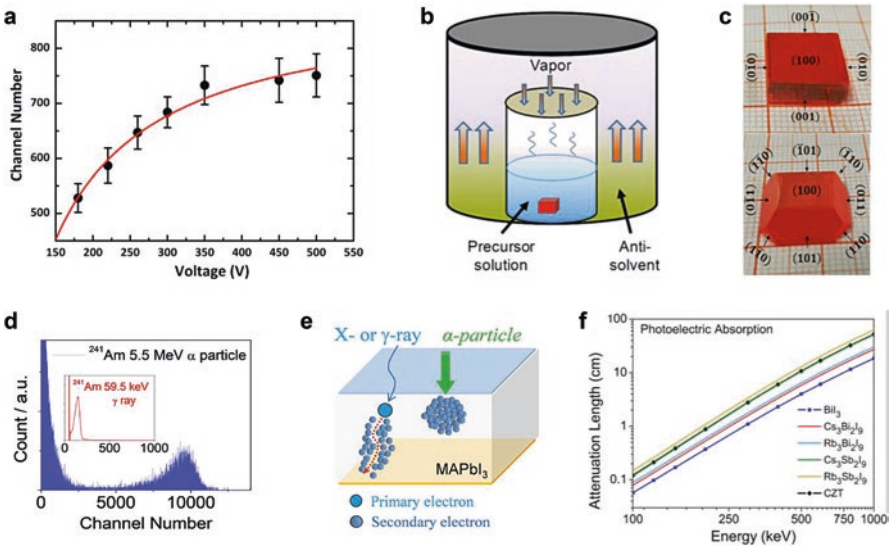

Fig. 3 (**a**) Spectral peak centroids obtained as a function of different applied voltages. (**b**) Representative diagram of $MAPbBr_3$ crystals grown from the solution by the AVC method. (**c**) As-grown cubic and polyhedral $MAPbBr_3$ crystal photograph. (**d**) Energy resolved spectrum Pb/$MAPbI_3$/Au detector under ^{241}Am radiation source. (**e**) Graphical representation of X- or γ-ray photon and charged particle (α-particle) interaction with $MAPbI_3$. (**f**) Attenuation length of $A_3M_2I_9$ compounds compared to CZT and BiI_3. **a** is reproduced with permission from [64], **b** and **c** are from [65], **d** and **e** are from [66], and **f** is from [67]

On the other hand, quantum well-structured 2D perovskites with lead-halide octahedra layers separated by bulk organic molecules yield great stability and extended exciton binding energies than 3D perovskites, favorable for optoelectronics [63]. For instance, direct detectors with 2D Dion-Jacobson perovskite (BDA) and $CsPb_2Br_7$ single crystals with a large bandgap of 2.76 eV and a high resistivity of 4.35×10^{10} Ω-cm exhibit a low dark current density of 34 nA cm^{-2} and 37% energy resolution for ^{241}Am α-particles [72]. Though the energy resolution still falls behind those of 3D perovskite, 2D perovskites hold great potential as α-particle detectors.

A few more perovskite-related structures have also been discovered as radiation detectors. The deformed perovskites with the formula $A_3M_2I_9$ ($Rb_3Bi_2I_9$, $Rb_3Sb_2I_9$, $Cs_3Bi_2I_9$, and $Cs_3Sb_2I_9$) were shown to detect α-particles as their attenuation length varies linearly with energy (Fig. 3f) [67]. Even though these materials could detect α-particles, their characteristic features, such as energy resolution, are far behind that of the conventional detectors [73]. The amount of collected charge concerning the generated charge, also known as charge collection efficiency (CCE), is another important performance factor, and it varies significantly with the number of charge traps. Perovskites with a high density of defects would cause lower CCE than conventional ones. Nevertheless, the prerequisite for good carrier transport abilities also restricts the choice of materials. Future studies must concentrate on enhancing

the crystal quality of halide perovskites and improving the device structure to increase both CCE and energy resolution.

4.1.2 Scintillators for α-Particle Detection

Perovskites with 2D and 0D structures are mostly explored to build scintillators for α-particle detection [63]. Li et al. synthesized $(BA)_2PbBr_4$ microcrystals for α-particle scintillation and achieved 24% energy resolution for α-particles from a ^{237}Np source [74]. The scintillator emitted 427 nm light with a reasonable yield of 7000 ph MeV^{-1}, analogous to a commercial plastic scintillator EJ228 (10,200 ph MeV^{-1}) (Fig. 4a, b). The 0D perovskite, Cs_4PbBr_6, in which the lead-halide octahedra are disjointed by Cs^+ cations, emits green light probably due to the presence of $CsPbBr_3$ impurities [76, 77]. The scintillators based on Cs_4PbBr_6 single crystals proposed by Li et al. displayed a high PLQY of 86.7% at 525 nm (Fig. 4c, d) [78]. Even though the scintillator showed high light yield, it suffered from poor

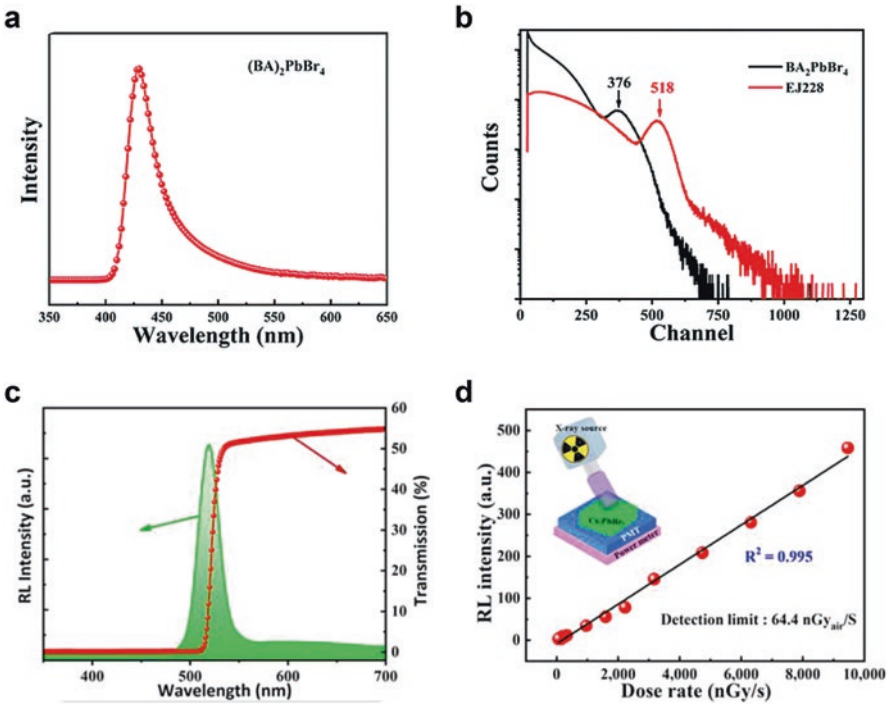

Fig. 4 (**a**) Radio luminescence (RL) spectrum of BA_2P microcrystals under 30 keV X-ray irradiation. (**b**) Pulse height spectrum of BA_2PbBr_4 microcrystals and the commercial plastic scintillator EJ228 under ^{137}Cs excitation. (**c**) Transmission and RL spectrum under 40 keV X-ray excitation. (**d**) Variation of RL as a function of dose rate. **a** and **b** are reproduced with permission from [74], **d** and **c** are from [75]

energy resolution (for 5.5 MeV α-particles was only 58.7%). Poor photon collection efficiency could be the possible reason for such low resolution. The same group further developed Cs_4PbI_6 single-crystal scintillators and attained an enhanced energy resolution of 43% for 5.5 MeV α-particles as well as a decent light yield of 50% [75].

While the recent progress on halide perovskite scintillators for α-particle detection emphasizes their great potential, unlike X-ray scintillators, very limited materials have been explored for α-particle scintillators [79]. There are still plenty of options to find better-performing compositions, particularly perovskite nanocrystals, which are highly promising X-ray scintillators [80].

4.2 β-Particle Detectors

High-energy electrons or positrons ejected by specific nuclides are known as β-particles. Detecting β-particles is vital for radioactive contamination surveillance [81]. β-particles have moderate penetration ability, higher than α-particles but lower than X-rays. Elastic or inelastic scattering are the two possible events that occur upon entering the β-particles into absorbing materials. Secondary emissions such as Auger electrons, secondary electrons, and X-rays are usually created in inelastic scattering. The electron-hole pairs that are yielded from secondary radiation contribute to the detector signal. Backscattering, which depends strongly on the Z value, usually originates from the elastic scattering between the β-particles and the nuclei [82]. Low-*Z* elements are ideal for β-particle detectors.

β-particle scintillators that are demonstrated so far are based on hybrid halide perovskites only. Due to their smaller average *Z* values than 3D perovskites and better irradiation hardness [83], Yu et al. choose 2D perovskite to fabricate β-scintillators [84]. To enhance PLQY and reduce reabsorption, Mn has been introduced as a dopant. The resultant Mn-doped STA_2PbBr_4 perovskite showed enhanced PLQY by 50% along with high scintillation light yield of 24,000 ph $MeV^{-}1$. Moreover, as displayed in Figs. 5a, b, the scintillator exhibited excellent linearity and superior

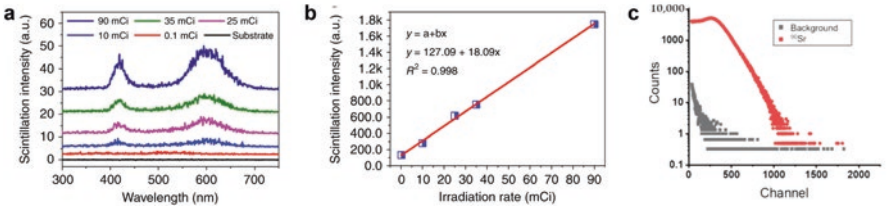

Fig. 5 (**a**) The scintillation spectra of the Mn-doped 2D HP scintillator under different β-ray irradiation intensities. (**b**) Linear response of the 2D HP scintillator down to the detection limit. (**c**) The spectrums of epoxy-PPO/perovskite plastic scintillators obtained by the ^{90}Sr planar source. **a** and **b** are reproduced with permission from [83] and **c** is from [85]

β-irradiation hardness. Hybrid perovskites that are implanted in the plastic scintillators are also found to be effective for β-scintillation. For example, a transparent scintillator with $CsPbBr_{3-x}Cl_x$ nanoclusters embedded in epoxy/PPO (PPO: 2,5-diphenyloxazole) featured a significant Stokes shift and substantially reduced reabsorption [85]. Moreover, the scintillator was able to produce an energy spectrum with higher counts that are superior to the commercial one, in the high energy range upon β-irradiation from a ^{90}Sr source (Fig. 5c). The demonstrated results disclosed the halide perovskites' potential applicability in plastic scintillators.

While the recent progress on halide perovskite β-particle scintillators is impressive in terms of light yield, the poor energy resolution is yet to be addressed. Detailed and comprehensive studies are required to answer the several open questions related to performance and material choice. Considering the similarities between X−/γ-ray detectors and β-particle detectors, impending studies could pursue similar material choices and device architectures for both direct detectors and scintillators, which would allow direct comparison between these two types of detectors. Perovskites with lighter elements such as Sn and Cu in place of Pb can be considered to solve the problem of electron backscattering triggered by atoms with high Z value.

5 Halide Perovskites for X-Ray Detection

5.1 Direct-Type X-Ray Detectors

X-ray detectors are not only attractive for scientific research but also have a wide range of applications in medical imaging and nondestructive inspection [63, 67, 72]. The conventional materials, CdZnTe, α-Se, HgI_2, and Si, are promising for X-ray photon detection, but their complex and energy-expensive fabrication process are the major hurdles to their wide spread [73, 74]. High-performing X-ray detectors with greater sensitivity, better-energy resolution, and low dose rate are vital for medical imaging applications. A large attenuation coefficient and high $\mu_{h/e}\tau$ product are some more important definitive parameters. In the recent past, due to their high and balanced carrier mobility, long carrier diffusion length, low trap density, and low processing cost, lead-based halide perovskite compounds with $APbX_3$ form were explored mostly for X-ray detectors [75, 78–80]. A summary of the achieved sensitivity values for single and multi-crystalline MHPs in recent years is given in Fig. 6a and combined with their respective mobility-lifetime products is shown in Fig. 6b. The increasing trend of sensitivity with $\mu_{h/e}\tau$ product unveils its potential for real-world applications.

$CsPbBr_3$ has an effective atomic number of 65.9 with a high attenuation coefficient, carrier mobility, and $\mu_{h/e}\tau$ products. Recent advancements in $CsPbBr_3$-based X-ray detectors dictate its great potential for high-sensitivity applications [109]. However, ion migration, especially under high applied electric fields, is one of the major issues of these 3D perovskites that limits the operational stability of the

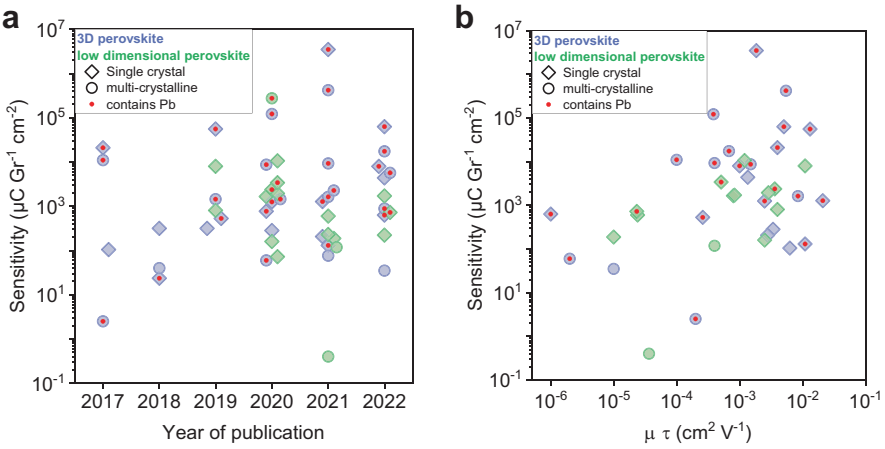

Fig. 6 (**a**) An overview of the attained sensitivity values for single and polycrystalline MHPs in the recent past and (**b**) combined with the corresponding mobility-lifetime products. The data has been extracted from the references [75, 86–108]

detector. The work by J. Wei et al. addressed the ion migration issue and proposed a "perovskite in a host" approach [110]. The authors proposed embedding $CsPbBr_3$ perovskite nanocrystal (PNC) in an organic semiconductor (P3HT:PCBM) percolating network (Fig. 7a). The presence of the surrounding organic phase blocks the ion migration and, at the same time, operates as the X-ray-generated charge transport pathways. The ability to tune the operational mode from indirect- to direct-type X-ray conversion by reducing the ligand density on the PNC surface is attractive figures of merits, among others. Suppressed ion migration, enhanced sensitivity to 5696 μC Gy_{air}^{-1} cm^{-2}, low detection limit down to 72 nGy_{air} s^{-1}, low dark-current even at higher voltage bias, and good operational stability are the important attributes of this method (Fig. 7b). The higher sensitivity, biasing stability, and solution processability further highlight the immense potential of this work for efficient X-ray imaging toward large-area flat panel imaging. Doping $CsPbBr_3$ with iodine atoms is another approach to enhance the impact of the $CsPbBr_3$ single crystal as an X-ray imaging detector proposed by P. Zhang et al. [109]. This work addresses the low resistivity and strong ion migration of $CsPbBr_3$ single crystals, which degrades their performance as direct X-ray detectors. Their findings were very encouraging since all the figures of merit of a direct X-ray detector measured were improved as a function of the doping level. More particular, the resistivity of $CsPbBr_{3-n}I_n$ single crystals increases from 10^9 Ω-cm ($CsPbBr_3$) to 10^{11} Ω-cm ($CsPbBr_2I$) that leads to enhanced $\mu_{h/e}\tau$ product and lowered detection limit (54 $nGys^{-1}$) for hard X-rays (120 keV) (Fig. 7c). The non-encapsulated single-crystal ($CsPbBr_{2.9}I_{0.1}$) imaging detector exhibits excellent ambient stability with stable dark current density (0.58 μA cm^{-2}). $CsPbBr_3$-based spectroscopic-grade detector for hard X-ray detection with an extremely low detection limit in energy-discrimination configuration is demonstrated by Y. He et al. [112]. This work dictates the potential of

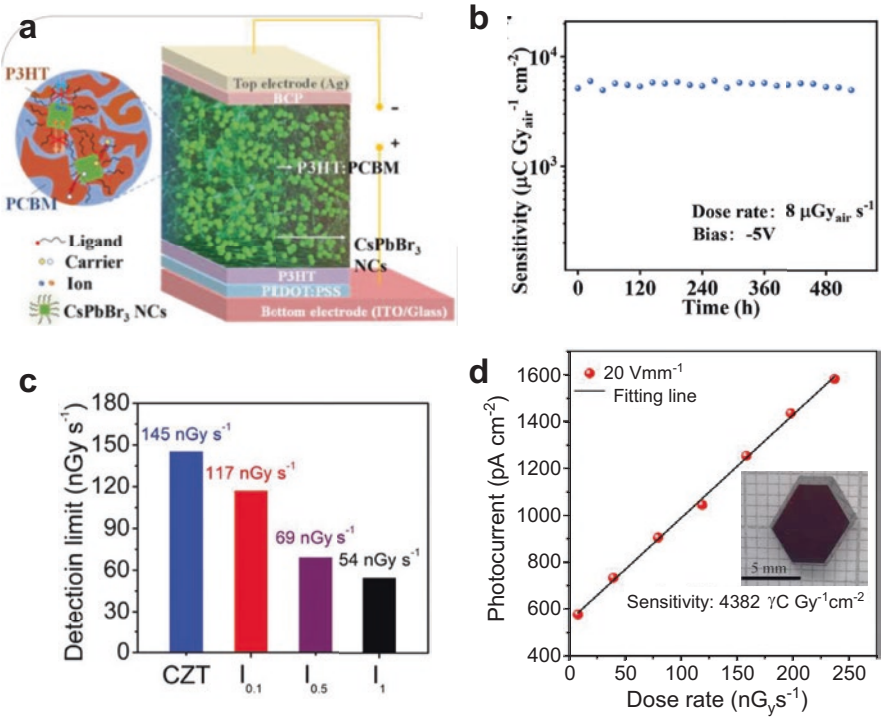

Fig. 7 (**a**) Schematic of direct-type PNC-based X-ray detectors. (**b**) Sensitivity variation of the device with storage time in an N_2 glove box for over 480 h. (**c**) Lowest detectable dose rate of the $CsPbBr_{3-n}I_n$ and CZT detectors. (**d**) The photocurrent density of the device was obtained at a different dose rate of X-ray irradiation. Inset: $Cs_3Bi_2I_9$ single-crystal grown by top-seed solution (TSS) method. **a** and **b** are reproduced with permission from [110], **c** is from [109], and **d** is from [111]

spectroscopic-grade $CsPbBr_3$ for X-ray photon counting. The proposed single-crystal X-ray detectors exhibit high X-ray sensitivity of about 5111 μC Gy_{air}^{-1} cm^{-2} at 50 kVp and an extremely low detectable dose rate of 0.02 nGy_{air} s^{-1}, which is far superior to traditional photoconductive X-ray detection systems. The photon counting method could revolutionize X-ray imaging in various medical and nondestructive probing applications [113, 114].

Organic-inorganic hybrid perovskite like $MAPbBr_3$ possesses a large X-ray attenuation coefficient, high resistivity, and large $\mu_{h/e}\tau$ product, which are promising for high-sensitivity radiation detectors (Fig. 2) [115]. However, the anisotropy during the perovskite single-crystal growth diminishes the figure of merits of the detector. Feng et al. introduced a facile fabrication technique of large-area single crystals directly onto substrates [116]. The proposed technique is based on controlling the distance between the solution surface and substrates. Posttreatment of the single crystals with UV/ozone further tailored their electrical properties by passivating the

surface traps. The X-ray response was tested under an X-ray source with energy up to 50 keV. The optimal devices display a sensitivity of 632 μC Gy_{air}^{-1} cm^{-2} under -5 V bias. This performance surpasses that of commercial α-Se X-ray detectors.

One of the biggest drawbacks of lead-based perovskite X-ray detectors is toxicity. One of the most promising candidates to replace Pb appears to be bismuth (Bi, Z = 83), with its atomic number among the largest nonradiative elements. Zhang et al. explored $Cs_3Bi_2I_9$ perovskite, which has the largest atomic number of 57.71 and enables 99% absorption of 40 keV X-rays [111]. The authors adopt the "top-seeded solution process" for fast, facile, and high-yield (86%) crystal growth. The constructed $Cs_3Bi_2I_9$-based direct X-ray detector yields the highest $\mu_{h/e}\tau$ product of 1.35×10^{-3} cm^2 V^{-1} and sensitivity of 4382 μCGy_{air}^{-1} cm^{-2} (Fig. 7d), which are superior to similar X-ray detectors fabricated using other growth techniques. The lower-dimensional perovskite crystals (2D, 1D, and 0D) consist of bulk organic cations, which function as a moisture-resistant layer, thus promoting higher ambient stability. Particularly, lead-free lower dimensional perovskites are more attractive due to their nontoxic nature. Zhang et al. report a large single 2D lead-free $Rb_4Ag_2BiBr_9$ crystals developed by the "slow cooling method" and employed in direct X-ray detectors [117]. The resistivity of the bulk crystal was reported as 2.59×10^9 Ω-cm, and the trap state density was estimated to be $\sim 10^{10}$ cm^{-3}. The resultant X-ray detector displays decent operational stability with the detector sensitivity of 222 μCGy^{-1} cm^{-2} at an electric field of 24 V/mm. Ease of preparation, high material stability, and inexpensive process of these materials are additional advantages. However, the X-ray detector's performance seems limited by intrinsic defects and needs further improvement.

Even though the halide perovskite semiconductors have been exposed as excellent materials for direct X-ray detectors, the ion migration effect when operating at a large electric field accelerates the degradation of perovskite-based electronic devices. On the other hand, limited indirect-type X-ray detectors (scintillators) are available due to the stringent requirements of ionizing radiation detection. Liu et al. attempted to address this pitfall by combining a direct-type X-ray detector based on $MAPbI_3$ with an indirect-type 0D $Cs_3Cu_2I_5$ scintillator [118]. The very successful energy transfer (type I energy level alignment) from $Cs_3Cu_2I_5$ to $MAPbI_3$ reduces the X-ray response time by 30 times (down to 36.6 ns from 1.07 μs of the single scintillator element of $Cs_3Cu_2I_5$) and is the main success factor of this next generation X-ray detection.

5.2 Indirect-Type X-Ray Detectors

Fast response time and good time resolution are key figures of merit of indirect X-ray detectors or scintillators. Applications such as time-of-flight positron emission tomography and time resolution measurements in synchrotron radiation facilities constantly demand scintillators. The introduction of all-inorganic halide

perovskite nanocrystals with high X-ray efficiency, good operational stability, and low-cost solution processability makes them excellent candidates for X-ray nanosecond detectors. However, numerous elements that have been reported are based on the defect-bound exciton emission, which provides large Stokes shifts, thus severely harming the stable luminescence. Li et al. proposed the 0D Cs_4PbI_6 nanocrystals for stable and fast X-ray detection [75]. The Cs_4PbI_6 single crystal-based scintillators showed a linear response to X-ray dose (from 145 nGy_{air}/s to 3.75 $\mu Gy_{air}/s$), highlighting its potential in X-ray imaging technology. The detection limit is 30-fold lower (187 $nGys^{-1}$) than the required X-ray diagnostics (5.5 $nGys^{-1}$), which is beneficial to avoid any adverse effects while diagnosing. Along with appreciable ambient stability, the Cs_4PbI_6 scintillators respond faster than existing plastic commercial devices.

6 Metal-Halide Perovskite Detectors for Space Applications

Despite the unique features of the perovskite semiconductors in detecting high-energy particles (alpha particles, electrons, protons) and photons (γ-rays and X-rays), the application that made them so popular was their application for energy harvesting and solar cells. Perovskite solar cells (PSCs) are now one of the main competitive technologies to silicon regarding solar energy harvesting. The currently reported power conversion efficiency has reached values higher than 25% [52]. Due to their high specific power (> 20 W/gr, and higher than any other space-based solar cell technology), low-temperature solution processability, power conversion performance, and radiation resistance, perovskite solar cell technology are very appealing for the next-generation space photovoltaic technology. This part reviews the approaches and consequences of PSCs for space applications and their resistance against high-energy particles and γ- and X-ray radiation.

Perovskites have aroused increasing interest in photovoltaics due to their flexible optoelectronic properties. Their outstanding optical and electrical properties, compatibility with flexible substrates, the highest specific power (12 times higher than that of c-Si or GaAs solar cells) for lightweight solar cell devices, and their excellent radiation resistance (superior to that of glass) make PSCs excellent candidates for space applications. Limited stability factors such as lead toxicity and instability issues due to oxygen and humidity are not valid factors in space. So, it is not surprising that there is an increased interest in investigating their performance (PCE and stability) in space environments (AM0, vacuum, and exposure to high-energy particles and radiation bombardment). Since the application of PSCs in space is a field in its infancy, there is a great interest in reviewing their performance under harsh space conditions and, for the sake of this chapter, their high-energy particle (electrons, protons, a-particles, and ions), and radiation (γ-rays, β-rays, x-rays) tolerance. High-energy radiation and high-energy particles interacting with matter will transfer their energy and momentum into the materials, resulting in damage and the generation of defects. The latter will reduce the device's performance for materials

that are part of PSCs. PSCs for space applications should therefore combine high performance with outstanding radiation resistance. The first work that reported the radiation tolerance of perovskites was one of Miyazawa et al. [119], who exposed an MA-based PSC against high-flux electron (1 MeV) and proton (150 keV) beams. No significant changes were measured in the PSCs' performance, skyrocketing the scientific community's interest in exploring the tolerance of other perovskite compositions under space conditions. Generally, radiation defects can be created that operate as majority carrier traps or minority carrier recombination centers under the impact of electron beams. However, high-energy particle beams, e.g., an electron beam with an energy of 1 MeV, cannot damage the PSC since it can penetrate all the cells' layers and accumulate at the substrate. However, these high particle beams generate UV-type radiation (Cerenkov radiation) that can be reflected from the metal electrode resulting in lower-energy electrons that can degrade the active layer [120]. For example, according to Huang et al. [121], a 10% degradation in device performance was reported when an electron beam of 1 MeV at the dose up to 10^{16} cm^{-2} bombarded an ITO/TiO_2/$FAPbI_3$/Spiro-OMeTAD/Ag PSC. Besides energy, the dose is also an important parameter affecting the PSC's stability against high-particle beams. The demonstrated perovskites show superior stability with dosage compared to popular materials like Si and GaAs that undergo degradation at lower doses (up to 10^{15} p cm^{-2}). Excellent electron beam hardness was also shown by other perovskite constructions like $MAPbI_3$ and $MA_{0.7}FA_{0.3}PbI_3$. No significant variation of the PCE was observed after the illumination of a $MAPbI_3$ solar cell due to a counterbalancing effect of lowering fill factor and the increase of J_{sc} after the electron beam illumination.

The work done by J.Ran et al. [122] summarizes that a high-energy electron beam can potentially induce (a) heating defects and (b) heating-induced phase transformations. The radiation tolerance of the PSCs was also investigated against proton irradiation (mainly existing in low Earth orbit of outer space), where particles of 2000 times more mass than an electron are expected to induce more extensive damage. Protons with energies close to 1 MeV have high stopping power and can cause severe damage to electronic devices. In general, it has been observed that high-energy proton beams (20–68 MeV) do not degrade the performance of PSC due to the degradation of the active layer. One of the possible reasons is the penetration of high-energy beams through the active layer without causing substantial collision events. In the case of $MAPbI_3$-based solar cells [123], a proton beam of 68 MeV at an accumulative dose rate of 10^{13} p cm^{-2} led to increased values in V_{oc} and FF (related to the active layer and the charge collection efficiency). Iodine atom displacement was observed by studying their recombination kinetics under high-energy proton atom illumination (10, 20, and 68 MeV) as a function of the proton's beam energy and dose [124]. As a result of iodine atom displacement, recombination centers (which appeared as sub-bandgap states) were built, leading to the degradation of the perovskite semiconductor. In the case of low-energy proton beams (50 keV), simulation work done by Miyazawa et al. [119] showed that for doses up to 10^{15} p cm^{-2}, the PSCs retained 50% of power conversion efficiency. It is an encouraging result compared to other solar cell technologies (Si, CIGS, and GaAs)

that did not survive under harsh conditions. This outstanding tolerance is attributed to the physical and electronic properties of the perovskite: long carrier diffusion length and excellent defect tolerance nature.

Moreover, stability of perovskite against exposure to other high-energy radiations like γ-ray (generated by fusion in the core of a star) has also been studied. This hardness level depends on the perovskite composition and accumulation radiation dose. More particular, whereas the hybrid perovskite PSCs ($Cs_{0.15}FA_{0.85}PbI_3$ and $Cs_{0.1}MA_{0.15}FA_{0.75}PbI_3$) show very poor stability against γ-rays (phase segregation), the inorganic PSCs showed excellent tolerance to an extreme γ-dose (1000 kRad) [125]. Moreover, the tolerance against γ-rays is superior to those of crystalline silicon or glass. The list of key figures of the merits of the radiation detectors that are explored for space applications is included in Table 3.

Table 3 Key figures of merits of radiation detectors demonstrated for space applications

Type of Radiation	Part of PSC exposed	Key Performance Indicator	Ref.
Electrons, 1 MeV Proton, 150 keV	Perovskite light absorber: $MAPbI_{3-x}Cl_x$	No change	[119]
Electrons, 1 MeV	Perovskite light absorber: $MA_{0.7}FA_{0.3}PbI_{3-x}Cl_x$	No change	[126]
Electrons, 1 MeV (dose: 10^{16} e/cm^2)	Perovskite light absorber: $MAPbI_3$	ΔPCE~0%	[120]
Proton beam: 68 MeV, dose at 10^{13} pcm^{-2}	Perovskite light absorber: $MAPbI_3$	ΔPCE~0%	[123]
Proton beam: 10, 20 and 68 MeV	Perovskite light absorber: Triple cation	ΔPCE~0%	[124]
γ-Ray (1000 kRad)	Perovskite light absorber: All inorganic HTL: PEDOT:PSS	No variation of any of the Photovoltaic parameters	[125]
Proton beam: 150 keV, dose 10^{14} protons cm^{-2}	HTL: Spiro-OMeTAD	Degradation of the chemical structure of HTL.	[121]
Electron beam: 100 keV, 10^{15} electrons cm^{-2}	HTL: Spiro-OMeTAD	Reduction in conductivity	[127]
Protons, 68 MeV, 10^{12}–10^{13} protons cm^{-2}	Transparent conductive electrode: Glass	Reduction in J_{sc} and PCE (10% and 40% reduction)	[128]
γ-Ray (2.3 Mrad)	Transparent conductive electrode: Glass	96.8% retained their initial PCE after 1535 hrs of irradiation—The reduction was attributed to glass darkening	[129]
Electrons, 1 MeV Proton, 150 keV	Transparent conductive electrode: Glass	Reduction of J_{sc}	[130]

6.1 Charge Transport Layers

The charge transport layers (hole transport layer (HTL), electron transport layer (ETL)) in PSCs play an important role in their stability against various parameters, including radiation experienced under space conditions. Understanding the impact of the transport layers' physical and electrical properties on the long-term stability of PSCs against high-energy radiation is essential. One of the most used HTLs in PSC is the Spiro-OMeTAD. The device did show degradation when subjected to proton radiation of 150 keV and at a dose of 1014 protons/cm2 [121]. More investigations on the stability of Spiro-OMeTAD against electron beams were carried out by Murakami et al. [127]. The observed lowering of conductivity was assigned to the bleaching of Li dopant upon electron beam exposure. An alternative HTL, P3HT, seems stable with no noticeable material degradation under ionizing radiation exposure [131], More work is required to study the effect of radiation particles on other common HTLs (e.g., CuO and CuSCN). γ-Ray radiation of 150, 300, and 500 Gy doses were applied to the $Cs_{0.15}MA_{0.10}FA_{0.75}Pb(Br_{0.17}I_{0.83})_3$ perovskite absorber that was combined with HTL PEDOT:PSS. The effect of the γ-rays on doses up to 500 Gy was negligible to PEDOT:PSS HTL [128]. A thorough assessment of the impact of high-energy radiation in ETL employed in PSCs' technology is highly required.

6.2 Substrate and Electrode

One of the primary appeals of using PSCs for space application is rooted in a reduced payload, i.e., the reduced mass of a solar cell that has to be lifted into space due to the PSCs' higher specific power compared to their conventional counterparts. Thus, the fabrication and evaluation of PSCs on lighter, flexible, conductive, and transparent substrates (e.g., PEN, PET) is an objective. However, most reports testing particle (e-beams) and radiation (γ-rays) stability of PSCs use rigid substrates, and a darkening of the rigid conductive glass is often observed [128]. The negative impact of this is lower J_{sc} and thus reduced PCE. The observed darkening is attributed to the formation of extra absorption bands due to the production of structural defects within the glass. Incorporating commercially available quartz or cesium-doped glass [121] is a solution for excellent radiation stability and low absorption [132].

6.3 Encapsulation Materials

Encapsulation of PSCs for space applications has been proven one of the most efficient ways to address instability issues due to the high-energy radiation of their various building blocks [133]. Soft matter materials with radioprotective properties seem to be a very promising way of encapsulation.

7 Challenges and Outlook

Metal-halide perovskites with superb optoelectronic and charge transport properties have attracted extensive research attention for various emerging energy and optoelectronic applications. While tremendous progress is achieved in the perovskite solar cell technology, the outstanding photophysical properties of these materials also enable them to serve as direct as well as indirect (scintillators) radiation detectors for both high-energy photons and charged particle radiation. Compared to traditional detectors, the advantages of halide perovskites are the widely tunable compositions that allow interactions with different types of radiation, the versatile and low-cost synthesis for large-scale production, and superior electronic and optical properties for fast and efficient detection. Ease of integration with other device components and better detector characteristics of halide perovskite detectors than commercial ones point toward MPL's bright future for next-generation radiation detection applications.

However, high ambient stability, large-area fabrication (commercial digital radiography detectors require an area larger than 1000 cm^2), low spectral resolution (15% is achieved but required is 0.25% for α-particles), and toxicity are the major challenges that need to be resolved in order to introduce perovskite radiation detectors into the commercial market. Some of the current hurdles that are still limiting the full potential of perovskite-charged particle radiation detectors are severe ion migration, relatively low resistance (10^7–10^9 Ω-cm) compared to inorganic semiconductors like 4H-SiC (10^{11} Ω-cm), environmental safety, low device retention, and poor ambient stability. Photon radiation detectors share the same challenges as those of charged particle detectors. Low dark current, lowest detectable limit, and robust material characteristics under high-energy radiation exposure are the extra factors that should be considered for photon radiation detectors. In addition, the detection efficiencies are also so far still much lower than those of established materials. Therefore, more efforts are needed to develop practical particle radiation detectors using halide perovskites.

Even though their energy resolution is lower than the conventional detectors, perovskites have been explored for direct detection of α-particles. Further advancements in material synthesis and device architecture are essential to improve energy resolution and detection efficiency. Perovskite crystals with reduced thickness with coplanar electrodes might enhance the detector performance for α-particle, whose penetration depth is shorter than other radiations. On the contrary, very few perovskite systems have been explored for β-particle detection via indirect mode. As the detection mechanism of both β-particles and photon radiation is similar, where the incident radiation tends to generate secondary electrons, the efficient photon detector material should work efficiently even for β-particle; thus, the effect of electron backscattering needs to be addressed. Advancing perovskite-based high-energy radiation detectors to detect ionized particles would create tremendous opportunities.

The skyrocketing advancement of PSC technology regarding their photovoltaic performance (above 25%), specific power (29.4 W/gr), and operational stability (reported operations for more than 10,000 hours, maintain more than 90% of initial PCE) drive their potential applicability for space applications. As single devices or part of tandem configurations, PSCs appear as an appealing alternative to power supply spacecraft and space-based equipment due to their unique and desirable properties. Their low cost, high radiation tolerance (more than 1500 h continuous operation under γ-rays and light illumination), and compatibility with flexible materials further boost their use as power suppliers for spacecraft and space equipment. However, the PSC technology in space faces some key challenges. The robustness and stability against AM0 conditions (extreme temperature cycles, high vacuum, solar (mainly due to excess UV radiation), and cosmic radiation) must be improved. Special attention needs to be given to the functional materials consisting of the active layer (perovskite absorption layer), mainly the transporting layers and the electrodes of the PSC. The selection of materials with equal or closer to equal temperature coefficients probably is a possible solution. Introducing interlayers that shield the active layer from UV radiation can also boost PSC performance in applications beyond Earth. The darkening of the glass substrates as a result of its interaction with high-energy particle radiation can be easily solved with the selection of quartz substrates. Finally, since one of the figures of merit for space applications is the specific power, developing thermally stable flexible substrates is critical to making PSCs competitive for space applications.

References

1. Darambara, D. G. (2006). *Nuclear Instruments and Methods in Physics Research – Section A, 569*, 153.
2. Seco, J., Clasie, B., & Partridge, M. (2014). *Physics in Medicine and Biology, 59*, R303.
3. Gill, H. S., Elshahat, B., Kokil, A., Li, L., Mosurkal, R., Zygmanski, P., Sajo, E., & Kumar, J. (2018). *Physics in Medicine, 5*, 20.
4. Ruddy, F. H., Dulloo, A. R., Seidel, J. G., Hantz, F. W., & Grobmyer, L. R. (2017). *Nuclear Technology, 140*, 198. https://doi.org/10.13182/NT02-A3333
5. Udod, V., & Nazarenko, S. (2023). X-ray Inspection Systems with Sandwich Radiation Detectors: A Survey. In E. Lysenko, A. Rogachev, & O. Starý (Eds.), *Recent Developments in the Field of Non-Destructive Testing, Safety and Materials Science*. ICMTNT 2021. Studies in Systems, Decision and Control, vol 433. Springer, Cham. https://doi.org/10.1007/978-3-030-99060-2_2
6. Abola, E., Kuhn, P., Earnest, T., & Stevens, R. C. (2000). *Nature Structural Biology, 7*, 973.
7. Yelon, W. B., & Ross, F. K. (1982). *Nuclear Instruments and Methods in Physics Research, 193*, 285.
8. Burla, M., Roeloffzen, C. G. H., Zhuang, L., Marpaung, D., Khan, M. R., Maat, P., Dijkstra, K., Leinse, A., Hoekman, M., & Heideman, R. (2012). *Applied Optics, 51*(7), 789–802.
9. Hassard, J. (1995). *Nuclear Instruments and Methods in Physics Research - Section A, 368*, 217.
10. Cleveland, C., & Morris, C. (2013). *Handbook of energy* (Vol. 405). Elsevier Science.
11. Kaplon, M. F., Peters, B., Reynolds, H. L., & Ritson, D. M. (1952). *Physical Review, 85*, 295.

12. McGregor, D., & Shultis, J. K. (2020). Radiation Detection: Concepts, Methods, and Devices (1st ed.). CRC Press. https://doi.org/10.1201/9781439819401
13. Alig, R. C., & Bloom, S. (1975). *Physical Review Letters, 35*, 1522.
14. Ohira, S., Washio, H., Yagi, M., Karino, T., Nakamura, K., Ueda, Y., Miyazaki, M., Koizumi, M., & Teshima, T. (2018). *Physica Medica, 56*, 34.
15. Erickson, J. C., Yao, H. W., James, R. B., Hermon, H., & Greaves, M. (2000). *Journal of Electronic Materials, 29*, 699.
16. Abbaszadeh, S., Gu, Y., & Reynolds, P. D. (2014). *Journal of Instrumentation, 9*, C11001.
17. Koba, Y., Iwamoto, H., Kiyohara, K., Nagasaki, T., Wakabayashi, G., Uozumi, Y., Matsufuji, N., & Inage-ku, A. (2011). *Scintillation Efficiency of Inorganic Scintillators for Intermediate-Energy Charged Particles. Progress in Nuclear Science and Technology, 1*(0), 218-221. https://www.semanticscholar.org/paper/Scintillation-Efficiency-of-Inorganic-Scintillators-Koba-Iwamoto/7bfc8cc5731f62727651c688444c453481b43636
18. Tsuda, S., & Saito, K. (2017). *Journal of Environmental Radioactivity, 166*, 419.
19. Rong, Y., Hu, Y., Mei, A., Tan, H., Saidaminov, M. I., Seok, S. I., McGehee, M. D., Sargent, E. H., & Han, H. (2018). *Science (1979), 361*.
20. Leijtens, T., Eperon, G. E., Noel, N. K., Habisreutinger, S. N., Petrozza, A., & Snaith, H. J. (2015). *Advanced Energy Materials, 5*, 1500963.
21. Xiao, Z., Yan, Y., Xiao, Z., & Yan, Y. (2017). *Advanced Energy Materials, 7*, 1701136.
22. Worku, M., Ben-Akacha, A., Shonde, T. B., Liu, H., & Ma, B. (2021). *Small Science, 1*, 2000072.
23. Liu, X. K., Xu, W., Bai, S., Jin, Y., Wang, J., Friend, R. H., & Gao, F. (2020). *Nature Materials, 20*, 10.
24. Gedda, M., Gkeka, D., Nugraha, M. I., Scaccabarozzi, A. D., Yengel, E., Khan, J. I., Hamilton, I., Lin, Y., Deconinck, M., Vaynzof, Y., Laquai, F., Bradley, D. D. C., Anthopoulos, T. D., Gedda, M., Gkeka, D., Nugraha, M. I., Scaccabarozzi, A. D., Yengel, E., Khan, J. I., Lin, Y., Laquai, F., Anthopoulos, T. D., Hamilton, I., Bradley, D. D. C., Deconinck, M., & Vaynzof, Y. (2022). *Advanced Energy Materials, 1*, 2201396.
25. Lin, Y. H., Pattanasattayavong, P., & Anthopoulos, T. D. (2017). *Advanced Materials, 29*, 1702838.
26. Gedda, M., Yengel, E., Faber, H., Paulus, F., Kreß, J. A., Tang, M.-C., Zhang, S., Hacker, C. A., Kumar, P., Naphade, D. R., et al. (2021). *Advanced Materials, 33*, 2003137.
27. Lei, L., Dong, Q., Gundogdu, K., So, F., Lei, L., Dong, Q., So, F., & Gundogdu, K. (2021). *Advanced Functional Materials, 31*, 2010144.
28. Dong, Y., Zou, Y., Song, J., Song, X., & Zeng, H. (2017). *Journal of Materials Chemistry C, 5*, 11369.
29. Khan, J. I., Gedda, M., Wang, M., Yengel, E., Kreß, J. A., Vaynzof, Y., Anthopoulos, T. D., & Laquai, F. (2022). *ACS Energy Letters, 7*, 2450.
30. Stoumpos, C. C., Malliakas, C. D., Peters, J. A., Liu, Z., Sebastian, M., Im, J., Chasapis, T. C., Wibowo, A. C., Chung, D. Y., Freeman, A. J., Wessels, B. W., & Kanatzidis, M. G. (2013). *Crystal Growth & Design, 13*, 2722.
31. Gedda, M., Faber, H., Petridis, K., & Anthopoulos, T. D. (2022). *Advanced Materials for Radiation Detection, 119*.
32. Wei, H., & Huang, J. (2019). *Nature Communications, 10*, 1066.
33. He, Y., Hadar, I., & Kanatzidis, M. G. (2021). *Nature Photonics, 16*(1), 14.
34. Eskin, J. D., Barrett, H. H., & Barber, H. B. (1998). *Journal of Applied Physics, 85*, 647.
35. del Sordo, S., Abbene, L., Caroli, E., Mancini, A. M., Zappettini, A., & Ubertini, P. (2009). *Sensors, 9*, 3491–3526.
36. Grellier, J., Atkinson, W., Bérard, P., Bingham, D., Birchall, A., Blanchardon, E., Bull, R., Guseva Canu, I., Challeton-De Vathaire, C., Cockerill, R., Do, M. T., Engels, H., Figuerola, J., Foster, A., Holmstock, L., Hurtgen, C., Laurier, D., Puncher, M., Riddell, A. E., Samson, E., Thierry-Chef, I., Tirmarche, M., Vrijheid, M., & Cardis, E. (2017). *Epidemiology, 28*, 675.

37. Shah, K. S., Lund, J. C., Olschner, F., Moy, L., & Squillante, M. R. (1989). *IEEE Transactions on Nuclear Science, 36*, 199.
38. Lommatzsch, P. (1976). *American Journal of Ophthalmology, 81*, 198.
39. Furuta, E., Yoshizawa, Y., Natake, T., & Takiue, M. (1997). *Radioisotopes, 46*, 912.
40. Que, W., & Rowlands, J. A. (1995). *Medical Physics, 22*, 365.
41. Zanichelli, M., Santi, A., Pavesi, M., & Zappettini, A. (2013). *Journal of Physics D: Applied Physics, 46*, 365103.
42. Gerrish, V. M. (1995). *Semiconductors and semimetals* (pp. 493–530). Elsevier.
43. Moseley, O. D. I., Doherty, T. A. S., Parmee, R., Anaya, M., & Stranks, S. D. (2021). *Journal of Materials Chemistry C, 9*, 11588.
44. Guerra, M., Manso, M., Longelin, S., Pessanha, S., & Carvalho, M. L. (2012). *Journal of Instrumentation, 7*, C10004.
45. Martz, H. E., Logan, C. M., Schneberk, D. J., & Shull, P. J. (2017). *X-Ray imaging: Fundamentals, industrial techniques, and applications*. CRC Press.
46. Protesescu, L., Yakunin, S., Bodnarchuk, M. I., Krieg, F., Caputo, R., Hendon, C. H., Yang, R. X., Walsh, A., & Kovalenko, M. V. (2015). *Nano Letters, 15*, 3692.
47. Dou, L., Yang, Y. M., You, J., Hong, Z., Chang, W. H., Li, G., & Yang, Y. (2014). *Nature Communications, 5*, 1.
48. Kovalenko, M. V., Protesescu, L., & Bodnarchuk, M. I. (2017). *Science (1979), 358*, 745.
49. Saidaminov, M. I., Haque, M. A., Almutlaq, J., Sarmah, S., Miao, X. H., Begum, R., Zhumekenov, A. A., Dursun, I., Cho, N., Murali, B., Mohammed, O. F., Wu, T., & Bakr, O. M. (2017). *Advanced Optical Materials, 5*, 1600704.
50. Chen, C., Zhang, X., Wu, G., Li, H., & Chen, H. (2017). *Advanced Optical Materials, 5*, 1600539.
51. Chen, W., Wu, Y., Yue, Y., Liu, J., Zhang, W., Yang, X., Chen, H., Bi, E., Ashraful, I., Grätzel, M., & Han, L. (2015). *Science (1979), 350*, 944.
52. Green, M. A., Ho-Baillie, A., & Snaith, H. J. (2014). *Nature Photonics, 8*, 506.
53. van Le, Q., Jang, H. W., & Kim, S. Y. (2018). *Small Methods, 2*, 1700419.
54. Fakharuddin, A., Gangishetty, M. K., Abdi-Jalebi, M., Chin, S. H., Yusoff, A. R. B. M., Congreve, D. N., Tress, W., Deschler, F., Vasilopoulou, M., & Bolink, H. J. (2022). *Nature Electronics, 5*(4), 203.
55. Wang, H., & Kim, D. H. (2017). *Chemical Society Reviews, 46*, 5204.
56. Eperon, G. E., Stranks, S. D., Menelaou, C., Johnston, M. B., Herz, L. M., & Snaith, H. J. (2014). *Energy & Environmental Science, 7*, 982.
57. Albero, J., Asiri, A. M., & García, H. (2016). *Journal of Materials Chemistry A, 4*, 4353.
58. Dong, Q., Fang, Y., Shao, Y., Mulligan, P., Qiu, J., Cao, L., & Huang, J. (n.d.).
59. Gao, F., Gao, R., Liu, H., Yang, Z., Hua, X., Wu, X., Shengzhong, L. (2019). More than 3-mm-long carrier diffusion and strong absorption over the full solar spectrum in copper oxide andselenium composite film. arXive. https://doi.org/10.48550/arXiv.1905.03432
60. Mykhaylyk, V. B., Kraus, H., & Saliba, M. (2019). *Materials Horizons, 6*, 1740.
61. Schmidt, L. C., Pertegás, A., González-Carrero, S., Malinkiewicz, O., Agouram, S., Mínguez Espallargas, G., Bolink, H. J., Galian, R. E., & Pérez-Prieto, J. (2014). *Journal of the American Chemical Society, 136*, 850.
62. Akkerman, Q. A., D'Innocenzo, V., Accornero, S., Scarpellini, A., Petrozza, A., Prato, M., & Manna, L. (2015). *Journal of the American Chemical Society, 137*, 10276.
63. Liu, F., Wu, R., Zeng, Y., Wei, J., Li, H., Manna, L., & Mohite, A. D. (2022). *Nanoscale, 14*, 6743.
64. Xu, Q., Wei, H., Wei, W., Chuirazzi, W., DeSantis, D., Huang, J., & Cao, L. (2017). *Nuclear Instruments and Methods in Physics Research - Section A, 848*, 106.
65. Liu, X., Zhang, H., Zhang, B., Dong, J., Jie, W., & Xu, Y. (2018). *Journal of Physical Chemistry C, 122*, 14355.
66. Liu, F., Wu, R., Wei, J., Nie, W., Mohite, A. D., Brovelli, S., Manna, L., & Li, H. (2022). *ACS Energy Letters, 7*, 1066.

67. McCall, K. M., Liu, Z., Trimarchi, G., Stoumpos, C. C., Lin, W., He, Y., Hadar, I., Kanatzidis, M. G., & Wessels, B. W. (2018). *ACS Photonics, 5*, 3748.
68. He, Y., Ke, W., Alexander, G. C. B., McCall, K. M., Chica, D. G., Liu, Z., Hadar, I., Stoumpos, C. C., Wessels, B. W., & Kanatzidis, M. G. (2018). *ACS Photonics, 5*, 4132.
69. He, Y., & Kanatzidis, M. (2019). *HDIAC Journal, 6*, 16.
70. Wang, F., Bai, R., Sun, Q., Liu, X., Cheng, Y., Xi, S., Zhang, B., Zhu, M., Jiang, S., Jie, W., & Xu, Y. (2022). *Chemistry of Materials, 2022*, 4000.
71. Gao, L., Sun, J.-L., Li, Q., & Yan, Q. (2022). *ACS Applied Materials & Interfaces, 14*, 37904.
72. Xiao, B., Sun, Q., Wang, S., Ji, L., Li, Y., Xi, S., Zhang, B. B., Wang, J., Jie, W., & Xu, Y. (2022). *Journal of Physical Chemistry Letters, 13*, 1187.
73. Shimaoka, T., Kaneko, J. H., Tsubota, M., Shimmyo, H., Watanabe, H., Chayahara, A., Umezawa, H., & Shikata, S. I. (2016). *Europhysics Letters, 113*, 62001.
74. Li, Y., Chen, L., Liu, B., Jin, P., Gao, R., Zhou, L., Wan, P., Xu, Q., & Ouyang, X. (2021). *Journal of Materials Chemistry C, 9*, 17124.
75. Li, Y., Chen, L., Gao, R., Liu, B., Zheng, W., Zhu, Y., Ruan, J., Ouyang, X., & Xu, Q. (2022). *ACS Applied Materials & Interfaces, 14*, 1489.
76. Ray, A., Maggioni, D., Baranov, D., Dang, Z., Prato, M., Akkerman, Q. A., Goldoni, L., Caneva, E., Manna, L., & Abdelhady, A. L. (2019). *Chemistry of Materials, 31*, 7761.
77. Saidaminov, M. I., Almutlaq, J., Sarmah, S., Dursun, I., Zhumekenov, A. A., Begum, R., Pan, J., Cho, N., Mohammed, O. F., & Bakr, O. M. (2016). *ACS Energy Letters, 1*, 840.
78. Li, Y., Shao, W., Chen, L., Wang, J., Nie, J., Zhang, H., Zhang, S., Gao, R., Ouyang, X., Ouyang, X., & Xu, Q. (2021). *NPG Asia Materials, 13*, 1.
79. Chen, Q., Wu, J., Ou, X., Huang, B., Almutlaq, J., Zhumekenov, A. A., Guan, X., Han, S., Liang, L., Yi, Z., Li, J., Xie, X., Wang, Y., Li, Y., Fan, D., Teh, D. B. L., All, A. H., Mohammed, O. F., Bakr, O. M., Wu, T., Bettinelli, M., Yang, H., Huang, W., & Liu, X. (2018). *Nature, 561*, 88.
80. Zhou, Y., Chen, J., Bakr, O. M., & Mohammed, O. F. (2021). *ACS Energy Letters, 6*, 739.
81. Ogundare, F. O., & Adekoya, O. I. (2015). *Journal of Radiation Research and Applied Science, 8*, 411.
82. Tabata, T., Ito, R., & Okabe, S. (1971). *Nuclear Instruments and Methods, 94*, 509.
83. Quan, L. N., Yuan, M., Comin, R., Voznyy, O., Beauregard, E. M., Hoogland, S., Buin, A., Kirmani, A. R., Zhao, K., Amassian, A., Kim, D. H., & Sargent, E. H. (2016). *Journal of the American Chemical Society, 138*, 2649.
84. Yu, D., Wang, P., Cao, F., Gu, Y., Liu, J., Han, Z., Huang, B., Zou, Y., Xu, X., & Zeng, H. (2020). *Nature Communications, 11*, 1.
85. Kang, H., Min, S., Seo, B., Roh, C., Hong, S., & Cheong, J. H. (2021). *Chemosensors, 9*, 53.
86. Steele, J. A., Pan, W., Martin, C., Keshavarz, M., Debroye, E., Yuan, H., Banerjee, S., Fron, E., Jonckheere, D., Kim, C. W., Baekelant, W., Niu, G., Tang, J., Vanacken, J., van der Auweraer, M., Hofkens, J., & Roeffaers, M. B. J. (2018). *Advanced Materials, 30*, 1804450.
87. Yakunin, S., Sytnyk, M., Kriegner, D., Shrestha, S., Richter, M., Matt, G. J., Azimi, H., Brabec, C. J., Stangl, J., Kovalenko, M. V., & Heiss, W. (2015). *Nature Photonics, 9*, 444.
88. Kasap, S., Frey, J. B., Belev, G., Tousignant, O., Mani, H., Greenspan, J., Laperriere, L., Bubon, O., Reznik, A., DeCrescenzo, G., Karim, K. S., & Rowlands, J. A. (2011). *Sensors, 11*, 5112.
89. Kim, Y. C., Kim, K. H., Son, D.-Y., Jeong, D.-N., Seo, J.-Y., Choi, Y. S., Han, I. T., Lee, S. Y., & Park, N.-G. (2017). *Nature, 550*, 87.
90. Xing, G., Mathews, N., Sun, S., Lim, S. S., Lam, Y. M., Graïzel, M., Mhaisalkar, S., & Sum, T. C. (2013). *Science (1979), 342*, 344.
91. Wang, X., Zhang, T., Lou, Y., & Zhao, Y. (2019). *Materials Chemistry Frontiers, 3*, 365.
92. Chotas, H. G., Dobbins, J. T., Floyd, C. E., & Ravin, C. E. (1991). *Investigative Radiology, 26*, 438.
93. Street, R. A., Ready, S. E., van Schuylenbergh, K., Ho, J., Boyce, J. B., Nylen, P., Shah, K., Melekhov, L., & Hermon, H. (2002). *Journal of Applied Physics, 91*, 3345.

94. Basiricò, L., Ciavatti, A., Fratelli, I., Dreossi, D., Tromba, G., Lai, S., Cosseddu, P., Bonfiglio, A., Mariotti, F., Dalla Val, C., Bellucci, V., Anthony, J. E., & Fraboni, B. (2020). *Frontiers of Physics, 8*, 13.
95. Martens, K., Chui, C. O., Brammertz, G., de Jaeger, B., Kuzum, D., Meuris, M., Heyns, M. M., Krishnamohan, T., Saraswat, K., Maes, H. E., & Groeseneken, G. (2008). *IEEE Transactions on Electron Devices, 55*, 547.
96. Yao, L., Niu, G., Yin, L., Du, X., Lin, Y., Den, X., Zhang, J., & Tang, J. (2020). *Journal of Materials Chemistry C, 8*, 1239.
97. Öz, S., Hebig, J. C., Jung, E., Singh, T., Lepcha, A., Olthof, S., Jan, F., Gao, Y., German, R., van Loosdrecht, P. H. M., Meerholz, K., Kirchartz, T., & Mathur, S. (2016). *Solar Energy Materials and Solar Cells, 158*, 195.
98. Mescher, H., Schackmar, F., Eggers, H., Abzieher, T., Zuber, M., Hamann, E., Baumbach, T., Richards, B. S., Hernandez-Sosa, G., Paetzold, U. W., & Lemmer, U. (2020). *ACS Applied Materials & Interfaces, 12*, 15774.
99. Zhao, J., Zhao, L., Deng, Y., Xiao, X., Ni, Z., Xu, S., & Huang, J. (2020). *Nature Photonics, 14*, 612.
100. Xu, T., Li, Y., Nikl, M., Kucerkova, R., Zhou, Z., Chen, J., Sun, Y. Y., Niu, G., Tang, J., Wang, Q., Ren, G., & Wu, Y. (2022). *ACS Applied Materials & Interfaces, 14*, 14157.
101. Zhang, H., Yang, Z., Zhou, M., Zhao, L., Jiang, T., Yang, H., Yu, X., Qiu, J., Yang, Y., Xu, X., Zhang, H., Yang, Z., Yu, X., Qiu, J., Xu, X., Zhou, M., Zhao, L., Jiang, T., Yang, Y., & Yang, H. (2021). *Advanced Materials, 33*, 2102529.
102. Datta, A., Fiala, J., & Motakef, S. (2021). *Scientific Reports, 11*, 1.
103. Deumel, S., van Breemen, A., Gelinck, G., Peeters, B., Maas, J., Verbeek, R., Shanmugam, S., Akkerman, H., Meulenkamp, E., Huerdler, J. E., Acharya, M., García-Batlle, M., Almora, O., Guerrero, A., Garcia-Belmonte, G., Heiss, W., Schmidt, O., & Tedde, S. F. (2021). *Nature Electronics, 4*, 681.
104. Liu, Y., Zhang, Y., Zhu, X., Feng, J., Spanopoulos, I., Ke, W., He, Y., Ren, X., Yang, Z., Xiao, F., Zhao, K., Kanatzidis, M., & Liu, S. (2021). *Advanced Materials, 33*, 2006010.
105. Xiao, Y., Jia, S., Bu, N., Li, N., Liu, Y., Liu, M., Yang, Z., & Liu, S. (2021). *Journal of Materials Chemistry A, 9*, 25603.
106. Xia, M., Song, Z., Wu, H., Du, X., He, X., Pang, J., Luo, H., Jin, L., Li, G., Niu, G., Tang, J., Xia, M., Song, Z., Wu, H., Du, X., He, X., Pang, J., Niu, G., Tang, J., Luo, H., Jin, L., & Li, G. (2022). *Advanced Functional Materials, 32*, 2110729.
107. Hu, M., Jia, S., Liu, Y., Cui, J., Zhang, Y., Su, H., Cao, S., Mo, L., Chu, D., Zhao, G., Zhao, K., Yang, Z., & Liu, S. F. (2020). *ACS Applied Materials & Interfaces, 12*, 16592.
108. Li, X., Zhang, P., Hua, Y., Cui, F., Sun, X., Liu, L., Bi, Y., Yue, Z., Zhang, G., & Tao, X. (2022). *ACS Applied Materials & Interfaces, 14*, 9340.
109. Zhang, P., Hua, Y., Xu, Y., Sun, Q., Li, X., Cui, F., Liu, L., Bi, Y., Zhang, G., Tao, X., Zhang, P., Hua, Y., Li, X., Cui, F., Liu, L., Bi, Y., Zhang, G., Tao, X., Xu, Y., & Sun, Q. (2022). *Advanced Materials, 34*, 2106562.
110. Wei, J., Tao, L., Li, L., Yan, M., Wang, C., Sun, W., Yang, D., Fang, Y., Wei, J., Tao, L., Li, L., Yan, M., Wang, C., Sun, W., Yang, D., & Fang, Y. (2022). *Advanced Optical Materials, 10*, 2102320.
111. Zhang, J., Li, A., Li, B., Yang, M., Hao, X., Wu, L., Zhao, D., Xia, G., Ren, Z., Tian, W., Yang, D., & Zhang, J. (2022). *ACS Photonics, 9*, 641.
112. He, Y., Hadar, I., De Siena, M. C., Klepov, V. V., Pan, L., Chung, D. Y., & Kanatzidis, M. G. (2022). *Advanced Functional Materials, 32*, 2112925.
113. Cahn, R. N., Cederström, B., Danielsson, M., Hall, A., Lundqvist, M., & Nygren, D. (1999). *Medical Physics, 26*, 2680.
114. Förster, A., Brandstetter, S., & Schulze-Briese, C. (2019). *Philosophical Transactions of the Royal Society A, 377*, 20180241.
115. Li, L., Liu, X., Zhang, H., Zhang, B., Jie, W., Sellin, P. J., Hu, C., Zeng, G., & Xu, Y. (2019). *ACS Applied Materials & Interfaces, 11*, 7522.

116. Feng, A., Xie, S., Fu, X., Chen, Z., & Zhu, W. (2022). *Frontiers in Chemistry, 9*, 1179.
117. Zhang, Z., Ma, Y. Z., Thomas, L., Gofryk, K., & Saparov, B. (2022). *Crystal Growth & Design, 22*, 1066.
118. Liu, L., Li, W., Feng, X., Guo, C., Zhang, H., Wei, H., Yang, B., Liu, L., Li, W., Feng, X., Wei, H., Yang, B., Guo, C., & Zhang, H. (2022). *Advanced Science, 9*, 2103735.
119. Miyazawa, Y., Ikegami, M., Chen, H. W., Ohshima, T., Imaizumi, M., Hirose, K., & Miyasaka, T. (2018). *IScience, 2*, 148.
120. Pérez-del-Rey, D., Dreessen, C., Igual-Muñoz, A. M., van den Hengel, L., Gélvez-Rueda, M. C., Savenije, T. J., Grozema, F. C., Zimmermann, C., & Bolink, H. J. (2020). *Solar RRL, 4*, 2000447.
121. Barbé, J., Hughes, D., Wei, Z., Pockett, A., Lee, H. K. H., Heasman, K. C., Carnie, M. J., Watson, T. M., & Tsoi, W. C. (2019). *Solar RRL, 3*, 1900219.
122. Ran, J., Dyck, O., Wang, X., Yang, B., Geohegan, D. B., & Xiao, K. (2020). *Advanced Energy Materials, 10*, 1903191.
123. Brus, V. V., Lang, F., Bundesmann, J., Seidel, S., Denker, A., Rech, B., Landi, G., Neitzert, H. C., Rappich, J., & Nickel, N. H. (2017). *Advanced Electronic Materials, 3*, 1600438.
124. Lang, F., Jošt, M., Bundesmann, J., Denker, A., Albrecht, S., Landi, G., Neitzert, H. C., Rappich, J., & Nickel, N. H. (2019). *Energy & Environmental Science, 12*, 1634.
125. Boldyreva, A. G., Frolova, L. A., Zhidkov, I. S., Gutsev, L. G., Kurmaev, E. Z., Ramachandran, B. R., Petrov, V. G., Stevenson, K. J., Aldoshin, S. M., & Troshin, P. A. (2020). *Journal of Physical Chemistry Letters, 11*, 2630.
126. Standard: Qualification and Quality Requirements for Space Solar Cells (AIAA S-111A-2014), 1 2014. https://arc.aiaa.org/doi/abs/10.2514/4.102806
127. Murakami, Y., Ishiwari, F., Okamoto, K., Kozawa, T., & Saeki, A. (2021). *ACS Applied Materials & Interfaces, 13*.
128. Lang, F., Nickel, N. H., Bundesmann, J., Seidel, S., Denker, A., Albrecht, S., Brus, V. V., Rappich, J., Rech, B., Landi, G., Lang, H. C. N. F., Nickel, N. H., Albrecht, S., Brus, V. V., Rappich, J., Rech, B., Bundesmann, J., Seidel, S., Denker, A., Landi, G., & Neitzert, H. C. (2016). *Advanced Materials, 28*, 8726.
129. Wang, Z., Lin, Q., Wenger, B., Christoforo, M. G., Lin, Y. H., Klug, M. T., Johnston, M. B., Herz, L. M., & Snaith, H. J. (2018). *Nature Energy, 3*(10), 855.
130. Miyazawa, Y., Ikegami, M., Miyasaka, T., Ohshima, T., Imaizumi, M., & Hirose, K. *2015 IEEE 42nd photovoltaic specialist conference* (Vol. 2015). PVSC.
131. Jung, E. H., Jeon, N. J., Park, E. Y., Moon, C. S., Shin, T. J., Yang, T. Y., Noh, J. H., & Seo, J. (2019). *Nature, 567*, 511.
132. Price, M., Kitchen, C., Eaves, H., Crabb, R., & Buia, P. (1998). *European Space Agency, (Special Publication) ESASP, 569*.
133. Wang, Y., Ahmad, I., Leung, T., Lin, J., Chen, W., Liu, F., Ng, A. M. C., Zhang, Y., & Djurišić, A. B. (2021). *ACS Materials Au*.

Solution Processable Metal-Halide Perovskites for Printable and Flexible Ionizing Radiation Detectors

Jessie A. Posar, Chwenhaw Liao, Levi Tegg, Anita Ho-Baillie, Marco Petasecca, and Matthew J. Griffith

1 Introduction

Detection of ionizing radiation is one of the foundations of modern society, with critical technological applications in medical diagnostics and treatment, space exploration, the nuclear energy industry, and border security. However, the rapidly increasing use of radiation in recent decades has correlated to higher radiation exposure in the population, with corresponding harmful effects to the health of workers and patients. Active monitoring of radiation doses has now become compulsory in many countries to instantaneously detect, evaluate, and correct for any deviations

J. A. Posar · M. J. Griffith (✉)
School of Aerospace, Mechanical and Mechatronic Engineering, University of Sydney, Camperdown, NSW, Australia

Australian Centre for Microscopy and Microanalysis, The University of Sydney, Camperdown, NSW, Australia

Sydney Nano Institute, University of Sydney, Camperdown, NSW, Australia
e-mail: matthew.griffith@sydney.edu.au

C. Liao · A. Ho-Baillie
Sydney Nano Institute, University of Sydney, Camperdown, NSW, Australia

School of Physics, University of Sydney, Camperdown, NSW, Australia

L. Tegg
School of Aerospace, Mechanical and Mechatronic Engineering, University of Sydney, Camperdown, NSW, Australia

Australian Centre for Microscopy and Microanalysis, The University of Sydney, Camperdown, NSW, Australia

M. Petasecca
Centre for Medical Radiation Physics, University of Wollongong, Wollongong, NSW, Australia

W. Nie, K. (Kris) Iniewski (eds.), *Metal-Halide Perovskite Semiconductors*,
https://doi.org/10.1007/978-3-031-26892-2_8

from planned exposure events. Current technologies for detecting ionizing radiation are composed of thick and mechanically rigid solid-state semiconductors, including silicon, selenium, and cadmium telluride; however, these materials are expensive to manufacture and cannot be easily fabricated into flexible or large-area sensing arrays. While such technologies exhibit excellent performance, they cannot satisfy all the demands for real-time monitoring of radiation in complex environments, where materials and devices should ideally be portable, lightweight, flexible, and with low operating power requirements. New hybrid materials must therefore be developed for radiation detection, combining the performance of inorganic semiconductors with these other desirable properties (Fig. 1).

Solution-processable alternative materials such as organic semiconductors have attracted substantial recent interest for radiation detection due to the appealing prospect of low-cost processing via industrial-scale printing techniques [1, 2]. However, the low atomic number of organic materials results in weak radiation attenuation, and the unique photophysics of organic materials typically results in poor photon-to-electronic conversion performance in comparison to inorganic semiconductors. Accordingly, there has been substantial recent interest devoted to hybrid organic/inorganic metal-halide perovskites. These materials couple the performance benefits of inorganic semiconductors (high atomic number elements for strong radiation attenuation and high mobility-lifetime products for good electrical performance) with the solution state processability of organic semiconductors, thus offering an exciting avenue to achieve low-cost flexible X-ray detectors with high performance [3].

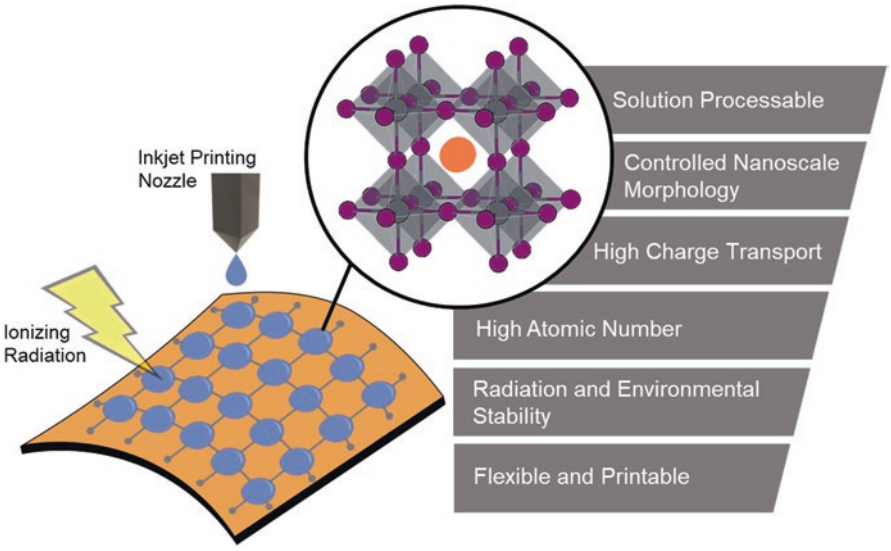

Fig. 1 Schematic summary of material and device properties for scalable direct ionizing radiation detectors

Despite the impressive radiation detection performances that have been achieved with perovskite single-crystal detectors, the research in this arena currently does not exploit one of their most significant advantages: the ability to be printed into flexible detectors with low-cost processing techniques. Significant gaps in performance still exist between perovskite materials and devices fabricated from complex deposition techniques on rigid substrates compared to the same materials deposited onto flexible substrates with innovative printing techniques [4]. To fully unlock the potential of perovskite materials for flexible radiation detection, a number of innovations are still required, including materials and device fabrication protocols suitable for high-quality crystal formation at low temperature, translation of the precise nanostructures successfully achieved in controlled laboratory environments to devices fabricated with printing techniques across large areas, and demonstration of practical stability for thin-film flexible devices in demanding environments.

In this work we will review the key material properties of metal-halide perovskites for printable ionizing radiation detection, techniques to form them into devices from solution, and the breakthroughs enabled by, and challenges remaining for, printable perovskites for radiation detection.

2 Material Considerations for Radiation Detection

2.1 Tailoring Perovskite Materials for Multifunctional Applications

Ionizing radiation sensors require a material that absorbs the incident radiation, converts it to free charge carriers, and then outputs an electrical signal. The material composition defines the probability of different interaction mechanisms for specific radiation sources and energies. During each direct interaction, a certain amount of energy is deposited into the material, termed absorbed dose. Charged particles interact through the Coulomb force, depositing energy along their path as defined by the stopping power $S = -\frac{dE}{dx} \sim NZ$ where NZ is the electron density of the material [5]. Photons can interact by transferring all their energy (photoelectric effect), or only part of their energy (Compton effect or coherent scattering), to the bound electrons of the detecting material [6]. The probability of each interaction is illustrated in the inset of Fig. 2, demonstrating the dependence of the interaction probability on the energy of the incident photons, E, and the atomic number of the absorbing material, Z. Specifically, the photoelectric effect is dominant for the majority of practical ionizing radiation energies for high Z materials such as perovskites.

As the interaction probability with ionizing radiation increases exponentially with atomic number, the traditional approach to developing direct radiation detectors is to employ high-Z electronic materials. However, this approach becomes more complex when considering the wide range of demands from modern applications. Wearable and flexible monitoring for dosimetry aims to determine the energy

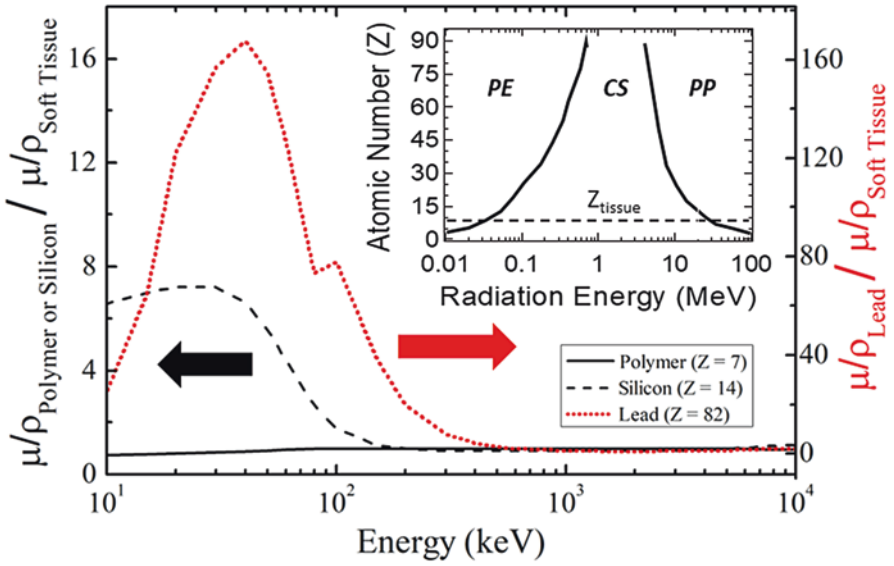

Fig. 2 Attenuation coefficient of materials for radiation detection, including polymers (solid black line), silicon (dotted black line), and lead (dotted black line) normalized to soft tissue as a function of energy. The inset displays the interaction type between the incident photons and absorbing material. Data from the National Institute of Standards and Technology (NIST) database [7]

deposited in a target material to measure radiation exposure in real time and thus permit advanced healthcare decisions. However, since the human body is formed mostly of water and carbon, it can be extremely complex to calibrate the energy deposited in a singular high-Z material into the equivalent response for human tissue. The interaction probabilities of detecting materials with ionizing radiation vary with distance from the source, radiation energy, dose rate, temperature, and incident angle, meaning multiple calibration factors are required to convert the signals measured by high-Z materials into the equivalent response from the low-Z human body [8, 9]. Figure 2 compares the energy dependence of silicon ($Z = 14$, $\rho = 2.33$ g/cm^3), which exhibits a seven-fold overresponse, and lead ($Z = 82$, $\rho = 11.29$ g/cm^3), exhibiting a 170-fold overresponse, for the relatively low energies typical of medical imaging ($E < 100$ keV) in comparison to the human body when normalized to the higher energies typical of space or radiation therapy ($E > 1$ MeV). This is advantageous for sensors developed for specifically targeted and narrow energy ranges, for example, X-ray imaging where high-Z materials increase likelihood of the photoelectric effect, improving contrast resolution [10]. However, such environments are not typical in high-radiation environments where monitoring or dosimetry is usually required, such as in outer space, medical clinics, or industrial applications of nuclear radiation. Here it is beneficial to use a sensing materials with a similar Z and ρ to human tissue, targeting a response independent of energy or other beam properties [11].

To accommodate the variation in demands for radiation sensors, a material would exhibit a high interaction probability with incident radiation but aim to present a flat energy response for widespread use in mixed radiation fields, superior electronic performance (defined by the materials ability to convert, transport, and extract free charge carriers), while balancing the ability to be developed using simple fabrication protocols at low manufacturing costs. Ideally, such protocols would have avenues towards depositing pixelated arrays of small detecting volumes onto a range of flexible substrates to meet the demand for low-cost and lightweight X-ray sensors by acting as a portable and/or wearable electronic for a wide range of applications not limited to personal radiation monitoring (for industries including nuclear energy and space exploration), border security scanning, curved digital X-ray imagers, and in vivo dosimetry.

Many of these requirements for next-gen radiation detectors can be uniquely solved with solution processable materials. Solution processability allows materials to be combined with a high degree of control to tune the detection properties, forming new electroactive inks that can be cast onto flexible substrates with a variety of simple deposition techniques at low temperatures [12]. Such inks have been extensively explored in solar cell research for low-cost manufacturing toward industrial-scale roll-to-roll printing techniques. Solution processable perovskites are a unique class of semiconducting materials that have the potential to maintain crystalline, polycrystalline, or nanocrystal structures during solution processable fabrication and deposition. The crystalline structure of perovskites facilitates their superior mobility, long carrier lifetimes, high carrier diffusion lengths, and low trap density, and they are recognized as the top-performing solution processable material in a range of applications. Their high-Z composition results in a high interaction probability with ionizing radiation from extremely thin layers (on the order of hundreds of nanometers), and they exhibit high bandgaps attributed to intrinsically superior radiation tolerance [13]. Accordingly, the material composition, structure, and bandgap of perovskites are key tools that should be considered when tuning detector materials for radiation absorption cross sections that are desirable for specific beam properties, including source type and energy.

2.2 Perovskite Materials and Structures

Metal-halide perovskites are a class of materials of the form ABX_3, where A is a monovalent cation (such as Cs^+ or a small organic molecule), B is a divalent metal cation (usually Pb^{2+}), and X is the halide anion (usually Cl^-, Br^-, or I^-) [14]. The crystal structure of three-dimensional (3D) perovskites can be understood as a network of corner-sharing metal-halide octahedra, as illustrated in Fig. 1 for the aristotype $Pm\bar{3}m$ cubic structure [15]. For cubic crystal structures, the unit cell dimensions (also known as the lattice parameters, a, b, and c) are equal and the angles between them (α, β, and γ) are 90°. Varying A, B, or X will change the unit cell dimensions [16], and may also change the crystal symmetry (e.g., $a = b \neq c$ in

a tetragonal structure) [17], or result in completely different structure types [18]. As discussed later, the type and arrangement of the atoms in the unit cell dominates the valence electronic structure and optical properties [19], so crystallographic characterizations are important for determining structure-property relationships.

Due to their high crystallinity [20], diffraction techniques are ideal for characterizing the crystal structures of perovskite materials. X-ray diffraction (XRD) is well-suited for the study of lead-halide perovskites as X-ray scattering intensity generally increases with Z^2 [21], so data with high signal-to-noise ratio can be obtained even with short acquisition times. Changes in the unit cell dimensions or symmetry lead to changes in peak positions or the appearance of new peaks. Qualitatively, an expansion of a unit cell (i.e., an increase in lattice parameter) will shift peaks to lower angles, with high-angle peaks shifting more than low-angle peaks. A reduction in crystal symmetry will generally result in additional peaks, though for subtle distortions (e.g., when $a = b \approx c$) the additional peaks may not be easily resolved [21, 22]. As an example, Noh et al. studied the methylammonium ($CH_3NH_3^+$, MA) lead-halide series $MAPb(I_{1-x}Br_x)_3$ by varying the anion between Br and I and observing the change in crystal structure and optical properties [16]. Between $x = 0.2$ ($MAPbI_{2.4}Br_{0.6}$) and $x = 1$ ($MAPbBr_3$), the structure is cubic, and the lattice parameter decreases linearly with x, following a standard Vegard relationship [23, 24] due to the differing ionic radii of the anions. Below $x \leq 0.13$ there is a reduction in slope of $a(x)$ and a slight broadening of the (020) reflection. However, at $x = 0$ (i.e., $MAPbI_3$) it becomes clear that this broadening was actually the splitting of the (200) peak into two new peaks due to a transition to a tetragonal crystal structure.

For materials containing both low-Z and high-Z elements, such as $MAPbI_3$, the X-ray diffraction pattern is not sensitive to the positions of the low-Z elements. Neutron diffraction can be used when the crystallographic role of the low-Z elements is important. Unlike the Z^2 scaling for X-ray scattering, the scattering cross section for neutrons is essentially random across isotopes [25], meaning low-Z elements are more easily observed against high-Z ones. Weller et al. illustrate this in their method for solving the structure of powdered formamidinium ($HC(NH_2)_2^+$, FA) lead iodide, $FAPbI_3$ [26]. The neutron powder diffraction pattern was collected, and the peak positions were manually indexed (i.e., assigned a Miller index corresponding to a lattice plane [22]) to a cubic unit cell. Accurate measurement of the lattice parameters was performed using XRD due to the strong scattering from the Pb sites on the cube corners.

X-ray and neutron powder diffraction are well-suited for the in situ or *in operando* characterizations of perovskite materials or devices. This permits the study of phase changes while a material or device is undergoing synthesis [27, 28], corrosion, irradiation [29], or any change in environment. Figure 3 shows diffraction patterns from Weller et al. as a sample of powdered $MAPbI_3$ is heated [30]. As the temperature is increased from 100 K to 165 K, the peaks shift to lower angles due to thermal expansion. At 165 K there is a transition from the orthorhombic to tetragonal structure resulting in a completely different diffraction pattern. As the temperature continues to increase, the peaks begin to merge as the PbI_6 octahedra rotate and straighten, before the cubic to tetragonal phase transition occurs at 327 K.

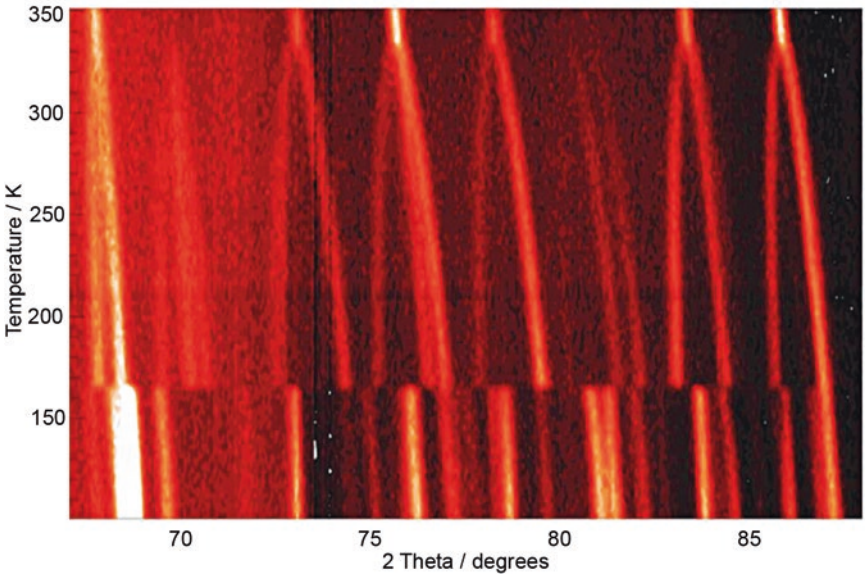

Fig. 3 In situ neutron powder diffraction data showing the slow heating of $MAPbI_3$. The shade corresponds to the intensity at each angle and temperature step, with lighter shades representing more counts and dark shades representing fewer counts. Reproduced from [30] under a CC-BY 3.0 from the Royal Society of Chemistry

The near-valence electronic structure of perovskites determines the radiation detection response and is dominated by the geometry and chemistry of the BX_6 octahedra. For lead-halide perovskites such as $MAPbBr_3$, the valence band mainly consists of Br 4*p* states (with some hybridization with Pb 6*s*) and the conduction band of Pb 6*p* states [31], with the electronic structures of other lead-halide perovskites being similar [14]. Exchanging or mixing different ions at the A or X sites results in different electrical properties, particularly the energy levels of the conduction band minimum (CBM) and valence band maximum (VBM). The difference between the CBM and the VBM is the bandgap. The CBM, VBM, and bandgap of some common lead-halide perovskites are shown in Fig. 4.

Decreasing the mass of the X anions (from I to Br to Cl) increases the energy of the CBM. Tao et al. indicate this might be affected by the confinement effect: when the Pb–X distance decreases, the orbitals of the Pb atom become more confined, which increases their self-energy [32]. Modulating the energy of the VBM is more complicated and influenced by three competing effects. First, lighter X anions have lower *p* orbital energy levels due to greater electronegativity, decreasing the overall energy of the valence band. Second, the same confinement effect reported by Tao et al. causes the Pb 6*s* atomic level to rise in energy, increasing the VBM. Lastly, the increasing hybridization strength between the Pb 6*s* states and X-site *p* states simultaneously increases the CBM and decreases the VBM. This also increases the bandgap.

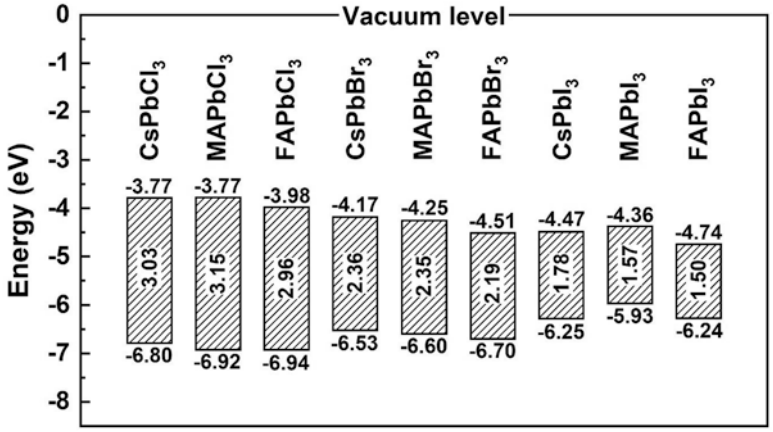

Fig. 4 The band diagram of $CsPbX_3$, $MAPbX_3$, and $FAPbX_3$ (X = Cl, Br, and I). For each bar, the lower number represents the VBM, the middle number the bandgap energy, and the upper number the CBM. The energy levels were extracted from [32]

Notably, the A cation does not contribute states near the Fermi level, though it still influences the electronic structure by modifying the unit cell dimensions or symmetry through steric effects. The change to the unit cell in turn affects B-X bonding, which modifies the electronic properties [14, 33]. Increasing the A-site cation size (from Cs to MA to FA) generally increases the unit cell volume. The greater Pb–X distance lowers the Pb 6*p* orbital energy, lowering the CB energy due to the confinement effect. Additionally, the degree of tilting and distortion of the PbX_6 octahedra reduces the hybridization between Pb and the halide states, reducing both the VBM and CBM.

Despite spontaneous formation of a 3D morphology, ABX_3 perovskite materials can also form into 2D (such as nanosheet, microplate) and 1D (nanowire, microwire, microrod) structures. This dimensionality can be achieved by either self-assembly or geometry design of the components during the crystallization process. Zhang et al. report a self-assembled $CsPbBr_3$ nanosheet prepared from low-speed centrifugation without using any polar solvents [34]. The material was formed into an X-ray scintillator by drop-casting the self-assembled $CsPbBr_3$ nanosheet onto a glass substrate and subsequently drying the film at room temperature in ambient conditions. The 2D perovskite demonstrated a high light yield (~21,000 photons/MeV), notably higher than the benchmark commercial Ce:LuAG single-crystal scintillator. Wang et al. demonstrated a wafer-scale perovskite microplate array device using a PbI_2 seed crystal array coupled with a solution flow chemistry process. Chemical vapor deposition was applied to the PbI_2 seed crystal arrays to fabricate the 2D $MAPbI_3$ microplate array (Fig. 5a) [35]. The microplate array demonstrated direct growth of patterned arrays from solution, thus presenting a solution to the challenges of incompatibility of perovskite crystals with typical lithographic processing. The entire crystal growth and device fabrication procedure

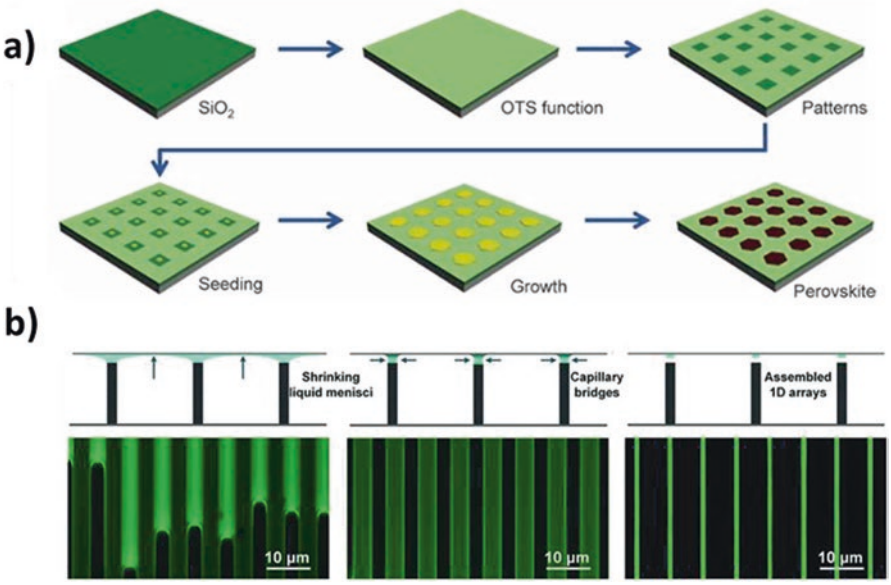

Fig. 5 Schematic illustration of (**a**) the procedure of fabricating the MAPbI3 microplate array on a patterned substrate. Reproduced from [35] under a CC-BY-NC Copyright © 2015, the authors. (**b**) The controlled dewetting assembly method to prepare a 1D perovskite array. Reproduced from [36] with permission from Copyright © 2018 WILEY-VCH Verlag GmbH & Co. KGaA, Weinheim

occur below 120 °C and are thus well suited to fabrication of perovskite arrays on typical low-cost substrates used for large-area flexible electronic applications, including plastics. A related approach to utilizing low-dimensionality perovskites to enhance solution processing was reported by Gao et al., who demonstrated a $MAPbX_3$ single-crystal microwire array through modification-free silicon pillars (Fig. 5b) [36]. In addition to patterning the detector into pixels using the microwires, the $MAPbX_3$ microwire array demonstrated high-quality crystallinity and a continuously tunable bandgap. The 1D arrays exhibited a high photodetector responsivity (3.2×10^3 AW^{-1}), with superior performance to perovskite thin films due to significant reduction of carrier recombination in the 1D crystalline arrays.

3 Printing Perovskite Devices

3.1 Perovskite Film Fabrication Methods

Metal-halide perovskite films can be fabricated into large-scale arrays on flexible substrates using low-cost printing and coating solution processing. Numerous deposition techniques have been developed over the years, each targeting unique advantages in the control of various parameters such as uniform thin-film deposition,

uniform thick layers, or tunable layer thickness by controlling the deposition parameters. At the heart of each technique is the challenge of translating the exquisite control of film nanostructure that can be obtained at the laboratory scale with spin coating in inert environments through to open atmosphere solution printing and coating techniques [12, 37]. In addition to this challenge, the need to develop new methods that can upscale materials and fabrication and assessment tools must be simultaneously solved, which has proven to be a longstanding challenge in the fabrication of photodiodes from printable semiconductors [38–41].

3.2 Printing Techniques

3.2.1 Spray Coating

The spray coating technique has been widely applied in organic photovoltaic and metal oxide thin-film deposition and provides a promising pathway for low-cost scalable perovskite film fabrication. The spray coating system operates via a two-step procedure, which includes atomizing and deposition systems as shown in Fig. 6a. First, an ultrasonic atomizer disperses the perovskite precursor solution into tiny droplets. Then, a low-pressure carrier gas, such as N_2, ejects these droplets onto the substrate through a nozzle. After the solvent is evaporated rapidly, homogenous films with tunable thickness can be formed by varying the deposition parameters (pressure, precursor concentration) and the duration time. Spray-coated perovskite X-ray detectors have exhibited thicknesses from 10 to 100 μm and recently unique in situ deposition reached large areas above 10 × 10 cm^2 [42–44]. A significant advantage of this technique is that the bottom-up crystal growth process results in

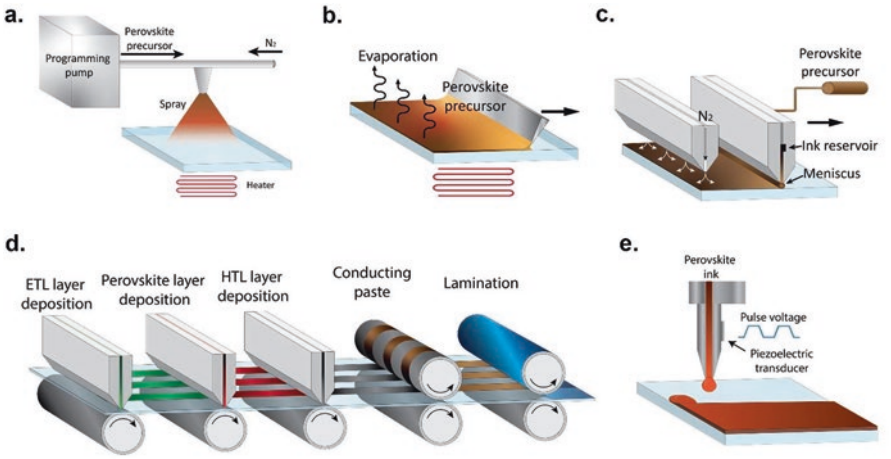

Fig. 6 The illustrations of different printing techniques, (**a**) spray coating, (**b**) blade coating, (**c**) slot-die printing, (**d**) roll-to-roll printing, and (**e**) inkjet printing, for perovskite film fabrication

compact columnar grains with limited grain boundaries in the direction of charge collection, enabling improved charge transport and collection in radiation detection devices [45, 46]. Spray coating is emerging as a powerful process for next-generation industrial-scale translation of perovskite technologies due to its ability to produce uniform, thick, and large-area films from a wide range of materials, including 3D ($CsPbI_2Br$ and $MAPbI_3$), 2D [$(PEA)_2PbI_4$], quasi-2D [$(PEA)_2MA_3Pb_4I_{13}$], and 0D ($Cs_3Sb_2I_9$) perovskites [43, 47].

3.2.2 Doctor-Blade Coating

Doctor-blading is a simple, cheap, and versatile continuous fabrication technique that has been applied extensively to the fabrication of perovskite films for photodiode detectors. This technique operates by spreading the precursor solution across the substrate with a blade, which can be moved at various speeds to control the thickness of the subsequent films. Typically doctor-blading is suited to highly viscous films and thus has been most frequently applied to fabricating thick active layer films (500 μm–1 mm) that are used for high attenuation direct radiation detectors [48]. Following film deposition, a heating process is applied to evaporate the solvent and construct a uniform film with the desired nanostructure, as shown in Fig. 6b. While doctor-blading has been shown to synthesize devices with areas over 10 cm^2 [49], the blade-coated layer can often incorporate significant porosity due to solvent evaporation from a thick film, which in turn limits both the attenuation of X-rays and the strength of adhesion of subsequent layers [50]. Attempts to address these limitations include a soft-pressing post-treatment of doctor-bladed perovskite films used to make a TFT array to remove porosity and improve the dark current and device signal-to-noise ratio [51]. The technique has also been used recently to fabricate a series of low-dimensional perovskite materials, including 2D $(PEA)_2MA_8Pb_9I_{28}$ and the 0D material $MA_3Bi_2I_9$, with results indicating a significant reduction in the device dark current due to a suppression of ion migration [52, 53].

3.2.3 Slot-Die Coating

The ability of slot-die coating to create large area devices has been widely demonstrated in the scalable fabrication of perovskite photovoltaic devices [54, 55]. This method involves containing the perovskite precursor ink inside a pressurized vessel, with a pump used to force ink out of this reservoir through a thin customized slit onto a moving substrate. The film thickness and lateral dimensions are controlled by the pump pressure and reservoir exit slits, respectively. The deposition of the precursor is often followed by a gas-quenching treatment to promote nucleation. This technique is a highly promising translation toward roll-to-roll printing given the ability to couple the coating procedure with a moving substrate, with previous research on printable photodiodes providing a rich suite of information on the

ability to obtain constant uniform ink flow by adjusting the angle of the ink reservoir, solution pumping velocity, flow rate, and substrate pre-wetting [56, 57]. A machined insert known as a meniscus guide can be placed inside the ink reservoir to control the coating width at the exit slits, and the distance between the meniscus guide and the substrate also determines perovskite layer thickness and pattern integrity. However, unlike the doctor-blade coating, the wet film thickness is determined by the flow rate instead of the gap height. Thus, it is crucial to have a continuous meniscus for high-quality perovskite films.

3.2.4 Inkjet Printing

Inkjet printing is a high-resolution digital printing technique based on drop-on-demand transfer of picoliters of material onto a substrate in an extremely material-efficient and contactless deposition procedure [58, 59]. A typical inkjet printing process is shown in Fig. 6e. This method can be divided into drop-on-demand (DOD), continuous inkjet (CIJ), and field- or flow-induced tip streaming (FITS) techniques [60]. The DOD printer is the most advanced technology widely used for large-area perovskite thin film fabrication. During the inkjet printing process, a droplet is generated by mechanical compression through a piezoelectric nozzle. Then, an electrically charged droplet is accelerated toward the substrate by an electric field. The small volume of delivered droplets has seen this technique find strong benefits in low temperature (<100 °C) perovskite thin film deposition process on a flexible substrate for high-performance X-ray detectors [61–63]. Furthermore, the ability of inkjet printing to achieve mask-free patterned perovskite deposition has strong potential to create complex device architectures such as folded perovskite X-ray detectors, as recently proposed [64].

3.2.5 Roll-to-Roll Printing

A particularly attractive route for processing perovskite films with large areas at low cost is to couple the printing and coating techniques described above with high-throughput roll-to-roll (R2R) fabrication [65]. Recently, gravure [66], doctor-blading [67], and slot-die coating [68] methods have been applied in roll-to-roll printing to fabricate perovskite photodetector devices. In principle, the addition of R2R capabilities to solution processing is simple, consisting of a motorized substrate control with an unwinder reel that feeds the flexible substrate through the printing or coating station and a rewinder reel that collects the substrate on another reel. In the middle of these two reels, several printing or coating units can be mounted, as shown in Fig. 6d. This integrated fabrication process has significantly reduced the handling damage and improved the throughput of device fabrication. However, in practice there are a substantial number of challenges that must be solved in order to enable full R2R fabrication of perovskite films. These include the

alteration of thickness of the layers that is introduced by parameters in the R2R system, such as the velocity of the substrate feed and its relationship with the printing or coating solution flow rate [69]. Additionally, the tension of the flexible substrate created by the winding and unwinding reels can influence the interactions between the substrate and the solution as it is deposited, which has a corresponding effect on the uniformity and thickness of the deposited layer [70]. Perhaps one of the larger practical challenges of R2R techniques is the trade-off between speed of substrate movement and the effective drying time required to cure the perovskite film. If the substrate moves too slowly, then a layer deposition becomes uncontrollably thick; however, if it moves too rapidly, then the films transit the drying stations too quickly to dry before reaching the rewinder reel [71].

3.3 Challenges for Printable and Flexible Metal-Halide Perovskite Films

Despite steady research progress on materials and device performance at the laboratory scale, long-term durability concerns, toxicity issues of both materials and manufacturing process, and a lack of robust high-throughput production technology for fabricating efficient large-area modules remain major obstacles toward commercialization of these materials using industrial-scale solution processing techniques [72].

It is important to note that the significant stability issues currently facing conventional lab-scale fabrication of perovskite materials including thermal, oxygen, and moisture exposure will remain problematic and likely become more difficult to overcome when upscaling due to the limited control levers available during printing deposition [73]. Therefore, stability studies on large-area devices will need to be extensively explored and understood. Moreover, the printing industry are currently focused on transitioning away from the toxic chemical solvents in which many perovskite inks are currently formulated, in particular halogenated organic solvents, for greener manufacturing processes [74, 75]. A substantial material challenge for solution processable perovskites will be their suspension in greener solvents while maintaining desirable morphologies once deposited with high device efficiencies.

On the manufacturing side of the equation, although an enormous number of high performance perovskite systems continue to be developed in the laboratory, the major restrictions on transitioning these materials to low-cost and large-area devices remains an inability to control the precise film nanoscale using these printing and coating techniques [50]. This can lead to inhomogeneous crystallization across the large-area perovskite film resulting in poor charge transport properties [76]. Large-area perovskite films also suffer from an increase in series resistance [77], requiring new device designs to be explored including isolated pixels, subcells, or metal grids [72].

4 Printable Metal-Halide Perovskites for Radiation Detection

The application of printable materials such as perovskites for radiation detection has gained significant momentum in recent years [1, 50]. The impact of ionizing radiation on perovskite devices, both in terms of performance (sensitivity) and stability (radiation hardness), is a key parameter that has been the focus of recent characterization efforts. This behavior is particularly dependent on photon energy, though the vast majority of studies to date have focused on the performance of perovskite radiation detectors at low energy. However, due to the emerging applications in both space and advanced medical treatment protocols, the high energy regime is beginning to attract significant attention on the development of novel materials for X-ray detection [78, 79].

4.1 Advances in Radiation Detection Performance

Radiation detection capabilities of perovskites focused on harnessing the excellent mobility characteristics and high-Z of thick single crystals perovskites to maximize their absorption and detection performance. The highest radiation sensitivity of 1.22×10^5 μCGy^{-1} cm^{-2} was demonstrated with an 800-μm-thick $MAPbI_3$ wafer at an operational voltage of 10 V [80]. Ultra-low detectable dose rate limits have also been demonstrated with perovskites, as low as 7.6 $nGys^{-1}$ with a 2-mm-thick Cl-doped $MAPbBr_3$ single crystal at −5 V; however, it is important to note that there has been some contention regarding the correct determination of the detection limit [81, 82]. Perovskite single crystals are mechanically rigid and require complex and expensive synthesis procedures that include high-vacuum deposition techniques that are not translational to low-cost large-area production onto flexible substrates. This section will focus on solution processable perovskites as an innovative solution to combine high-performance radiation sensing with large-area and flexible electronics. To evaluate the potential of these materials, we will expand the figures of merits from radiation sensitivity and detection limit to include flexibility, printability, and operational voltage. We will also include a discussion of the radiation stability of perovskites to evaluate their shelf-life and address concerns regarding their radiation damage susceptibility.

The first solution-processed perovskite for X-ray detection was achieved by spin coating four layers onto ITO-coated glass using common solar cell interlayers as a p-i-n diode structure PEDOT:PSS/$MAPbI_3$/PCBM/ZnO/Ag structure [42]. Three different spin-coated perovskite layers were chosen for this study: 260 nm, 360 nm, and 600 nm. The 600-nm-thick device demonstrated a competitive sensitivity of 25×10^3 μCGy^{-1} cm^{-3} (or 1.5 μCGy^{-1} cm^{-2}) at short circuit from a 75 kVp (<E > ~37 keV) source. Recent work has explored how the material composition of the perovskite layer can be optimized to improve the detection performance.

Basiricò et al. demonstrated that Cs mixed triple cation perovskites $Cs_{0.05}FA_{0.79}MA_{0.1}Pb(I_{0.8}\ Br_{0.2})_3$ increased the sensitivity to 3.7 $\mu CGy^{-1}\ cm^{-2}$ at short circuit and 97 $\mu CGy^{-1}\ cm^{-2}$ with a small operational voltage of −0.4 V [83]. The enhanced sensitivity was suggested to be due to differences in the charge transport and collection properties of the perovskite layer including an increase in grain size from 60 nm for $MAPbI_3$ to 200 nm as shown in Fig. 7a, a longer carrier lifetime, and a decrease in the nonradiative surface defects with no differences observed for the radiation absorption properties of the two films. The perovskite film thickness in this study was tuned to 450 nm, suggesting that while thicker films can absorb a higher percentage of incident ionizing radiation, it significantly reduced the charge collection and transport within the bulk of the film. This is likely due to poor crystallinity of the thicker films during spin coating deposition compared to single-crystal synthesis [87]. Bruzzi et al. presented the first investigation of drop-cast $CsPbBr_3$ films for medical applications, shown in Fig. 7b, demonstrating clinically acceptable reconstruction (within 5%) of the dose profile across the treatment field [84]. The authors showed that theoretically, perovskites are capable of superior radiation sensitivities compared to materials found in commercial radiation sensors like silicon and

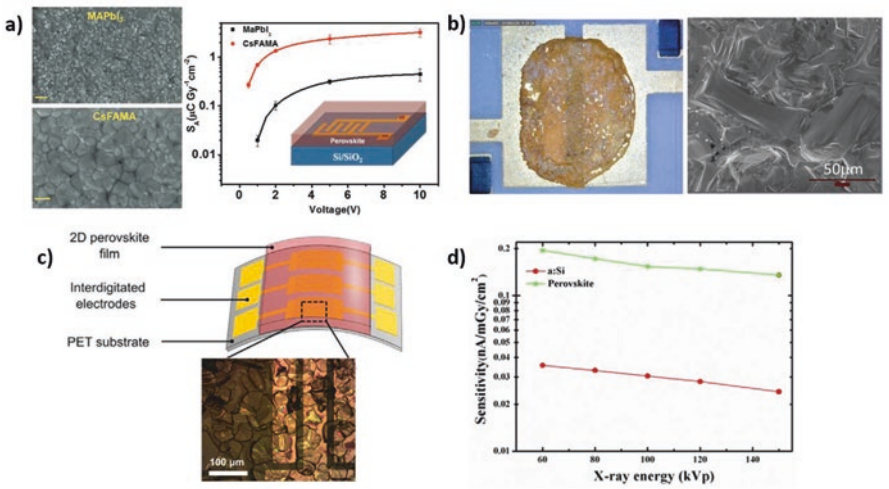

Fig. 7 Small-scale deposition of solution processable perovskites for radiation sensing. (**a**) Comparison of spin-coated deposition of triple cation CsFAMA perovskite and $MAPbI_3$ showing differences in the gain sizes (SEM on LHS) and radiation sensitivity (RHS) to a 35 kV Mo source. Reproduced from [83] with permission from Copyright © 2019 WILEY-VCH Verlag GmbH & Co. KGaA, Weinheim. (**b**) Picture (LHS) and SEM image (RHS) of a drop-cast $CsPbBr_3$ film developed for clinical radiation treatment applications. Reproduced from [84] under a CC-BY 4.0 Copyright © 2022 AIP Publishing LLC. (**c**) Schematic (top) and microscope image (bottom) of a novel 2D PEA_2PbBr_4 perovskite demonstrating microcrystalline film morphology after spin-coating deposition. Reproduced from [85] under a CC-BY Copyright © 2021, the authors. Advanced Optical Materials published by Wiley-VCH GmbH. (**d**) Energy response of a 270-nm-thick spin-coated $MAPbI_2Cl$ photovoltaic device from a tungsten-rhenium target compared to amorphous silicon. Reproduced from [86] under a CC BY 4.0

diamond due to their high density and low ionization energy (ease to create electron-hole pairs). However, experimentally the drop-cast perovskite film was significantly lower, reporting a sensitivity per unit area of 1.4 μCGy^{-1} cm^{-2} for 6 MV photons. The sensitivity was 15-fold higher for single-crystal perovskite films under the same conditions, suggesting drop-cast films form highly disordered structures [88]. It is obvious from both spin-coated and drop-cast perovskite films studied for radiation sensing that lab-scale solution processed deposition techniques result in poor film morphology and reduced charge transport properties compared to single crystals. Novel strategies to increase film morphology and crystallization of spin-coated or drop-cast films have recently been explored, including dissolution-recrystallization [89] and intermittent or two-step spin-coating methods [87, 90], which may be an advantage for radiation sensing, especially when thicker films are desired to absorb a higher percentage of incident ionizing radiation. Low-dimensional perovskites have been explored for radiation sensing, which may also mitigate the crystallinity issues of spin-coated or drop-cast layers [91]. A recent study demonstrated 2D PEA_2PbBr_3 (PEA = $C_6H_5C_2H_4NH_3^+$) formed microcrystalline films after standard spin-coating deposition onto flexible PET substrates, as shown in Fig. 7c [85]. The crystalline form led to a high radiation sensitivity of 806 μCGy^{-1} cm^{-2} and an ultra-low detection limit of 42 $nGys^{-1}$ at 150 kVp using a 1.9-μm-thick layer. The device was deposited onto flexible PET, showing a promising capacity to conform to complex contours; however, the detector was biased with a high operational voltage of 80 V, requiring a large power source which is not safe for wearable electronics.

Throughout the literature, only the theoretical X-ray mass attenuation coefficients across a wide energy range have been referenced to demonstrate superior absorption qualities of high-Z materials in perovskite films. It would be valuable to experimentally determine the energy dependence of a range of perovskite materials to use as a guide to develop a device that exhibits a flat response across a desired energy range as achieved with other novel sensing materials [92]. One study presented an order of magnitude increase in the sensitivity between 40 kVp and 150 kVp X-ray sources for a 10-μm-thick $MAPbI_3$ film as shown in Fig. 7c, suggesting a strong energy dependence for low keV [93]. Another study compared the response of a 270-nm-thick $MAPbI_2Cl$ between 60 kVp and 150 kVp [86]. When shown as a log scale in Fig. 7d, the response follows a similar shape to amorphous silicon, suggesting that if similar overresponse issues occur when compared to high X-ray energies, further consideration of the material composition of perovskite films will need to occur to flatten out the energy response across a desired range.

Scalable deposition techniques have become gradually more studied for perovskite radiation sensors for large-area imaging. The first method in 2015 spray coated $MAPbI_3$ onto glass substrates with interdigitated electrodes in a photoconductor device configuration [42]. Spray coating allows thicker films (10–100 μm) to be deposited as uniform films compared to spin coating. A 60 μm-thick single-element (non-pixelated) perovskite photoconductor demonstrated well-resolved images when scanned across the *x*–*y* plane of the field at a 40 V operational voltage with the resolution limited to the size of the single cell. For thicker films, large grain sizes in the polycrystalline structures must be fabricated to ensure printed perovskite

films function efficiently. Kim et al. demonstrated that printed $MAPbI_3$ films as thick as 830 μm with an average grain size of 30 μm via doctor blading exhibited optoelectronic characteristics approaching that of single crystals with a μτ product in the order of 1×10^{-4} cm^2 V^{-1} [48]. The article optimized the perovskite detector by adding additional layers between the contacts (polyimide perovskite composites) to lower the dark current to increase the signal-to-noise ratio for high-quality X-ray imaging when coupled with a rigid TFT backplane. A single-cell detector was capable of sensitivities as high as 11×10^3 μCGy^{-1} cm^{-2} from an 830-μm-thick film; however, it required a large operational bias of 200 V. The sensitivity of the pixelated device was lower than the single cell reaching 3.8×10^3 μCGy^{-1} cm^{-2}, suggested by the authors to result from incomplete charge collection in the gaps between the pixels, imperfect device contacts, and insufficient applied bias. In recent years, Qian and colleagues produced a 6 × 6 64 mm^2 pixelated in situ spray-coated $CsPbI_2Br$ 40-μm-thick X-ray detector. The sensitivity from a 50 kV X-ray source was ~1.48×10^5 μCGy_{air}^{-1} cm^{-2} with a dose rate limit of 280 $nGys^{-1}$ at a low operational voltage of 5 V [43].

Solution processable perovskites can also be deposited onto flexible substrates, opening avenues toward wearable technology. Ciavatti et al. deposited $MAPbI_3$ nanocrystals onto PEN by bar coating multiple layers on top of the previous film to maximize the thickness for high X-ray attenuation while maintaining high uniformity for efficient charge transport [93]. To further improve the optoelectronic performance, PCBM was added on top of the perovskite layer to fill the porous film and passivate any surface traps. The flexible single cell exhibited a good performance up to an active layer thickness of 10 μm with sensitivities of 494 μCGy^{-1} cm^{-2} from a 150 kVp X-ray source at an operational voltage of 4 V as shown in Fig. 8b. Thicker films exhibited high resistivity and electrical instability, unable to extract charges at the electrodes across the large bulk film with extremely large dark currents (above 2 V). The sensitivity was 3.5 times smaller than the same devices on glass substrates, and there was a significant variation in the X-ray performance across all ten flexible devices, suggesting that instability and reproducibility issues need to be addressed during fabrication. Bending cycles at a radius of 0.63 mm resulted in a larger dark current after the first bend, however remained stable with subsequent bending; furthermore, the sensitivity remained constant, implying steady X-ray monitoring for wearable electronics. Perovskite X-ray detectors have also been doctor-bladed onto a flexible pressure-sensitive air-dielectric IGZO TFT backplane for innovative two sensing modalities [94]. Guanidinium-doped $MAPbI_3$ was chosen as the X-ray sensing layer for its higher environmental stability, and the authors suggested its increased charge carrier lifetime will also benefit X-ray detection [95]. The sensitivity to 50 kV X-rays was 6.74×10^3 μCGy^{-1} cm^{-2} at 30 V. A 300-μm-thick perovskite film was used; however, it demonstrated excellent stability to bending after 2000 cycles, suggesting thicker films can be used for flexible sensors.

Inkjet printing has been explored for larger area flexible perovskite X-ray detectors due to its high spatial deposition control and combability with roll-to-roll printing. Mescher et al. demonstrated that an inkjet-printed single-cell triple cation perovskite $Cs_{0.1}(FA_{0.83}MA_{0.17})_{0.9}Pb(Br_{0.17}I_{0.83})_3$ could achieve sensitivities as high as

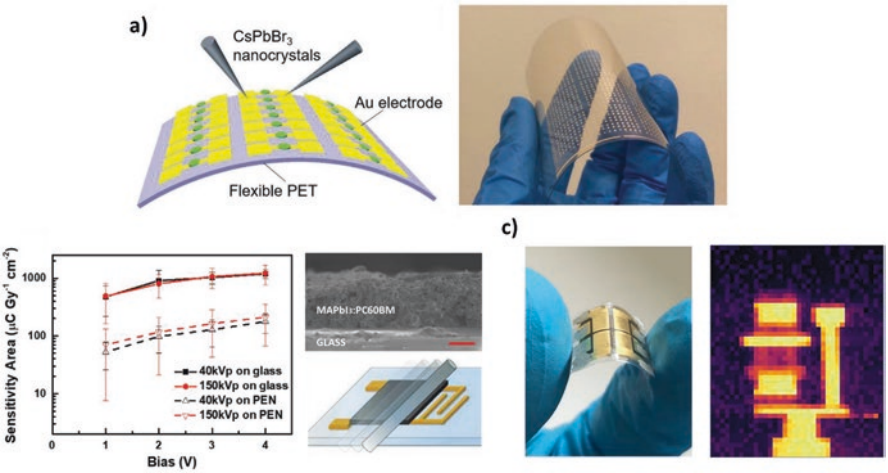

Fig. 8 Scalable deposition technique solution processable perovskites for radiation sensing. (**a**) Schematic (LHS) and picture (RHS) of an inkjet-printed array of $CsPbBr_3$ quantum dots deposited onto a flexible substrate. Reproduced from [61] with permission from Copyright © 2019 WILEY-VCH Verlag GmbH & Co. KGaA, Weinheim. (**b**) Highly uniform $MAPbI_3$ film (SEM image top RHS) via blade coating deposition (schematic bottom RHS). The image on the LHS presents the sensitivity at two radiation energies (40 kVp and 150 kVp) for substrates deposited onto glass and flexible PEN. Reproduced from [93] with permission from Copyright © 2021 WILEY-VCH Verlag GmbH & Co. KGaA, Weinheim. (**c**) Flexible inkjet-printed triple cation $CsFAMAPb(BrI)_3$ perovskite (LHS) used to image a pneumatic connector with a single pixel under 70 kVp X-ray radiation. Reproduced from [62] with permission from Copyright © 2020 American Chemical Society

59.9 $\mu CGy^{-1}\ cm^{-2}$ with a detection limit of 12 μGy/s to a 70 kVp X-ray source at a low operational voltage of 0.1 V, suggesting safe use for wearable electronics [62]. The flexible device was scanned under a metal pneumatic connector showing a clear X-ray image presented in Fig. 8c. A triple cation perovskite was chosen for a reliable translation to large area printing due to their improved stability, reproducibility, and high X-ray performances when spin coated [83, 96]. The device exhibited high reproducibility after multiple bending cycles stable down to a radius of 6 mm with a slight change after a high radius of 3 mm. However, there were still significant variations in the X-ray performance across 46 different devices compared to devices deposited onto glass. Pixelated and flexible perovskite X-ray detectors have also been realized with inkjet printing. Lui et al. developed a pixelated perovskite device shown in Fig. 8a from an extremely thin ~20 nm film of $CsPbBr_3$ quantum dots reaching extremely high sensitivity per unit area of 17.7 $\mu CGy^{-1}\ cm^{-2}$ when inkjet printed onto PET under synchrotron X-rays between 0.1 keV and 2.5 keV with a low operational bias of 0.1 V [61]. The flexible device was bent up to an angle of 120° showing a 25% reduction in the current. The sensitivity of the flexible device was lower than achieved for a rigid substrate under the same conditions at 83 $\mu CGy^{-1}\ cm^{-2}$. The ability to pixelate perovskite X-ray sensors while maintaining

extremely high X-ray sensitivities from ultra-thin and flexible active layers is extremely exciting and unique to the high-*Z* absorbing materials found in perovskites.

4.2 Radiation Stability

A majority of the radiation hardness studies for perovskites have focused on changes to the optoelectronic characteristics, including power conversion efficiency (PCE), external quantum efficiency (EQE), photoluminescence, and transmittance, due to their established use as solar cells for novel applications in space environments. While this is not directly relatable to their radiation detection performance, these metrics do give an insight into the effects of radiation damage on the transport properties within the perovskite which, we accept in some way, impacts the device performance for radiation sensing. Therefore, the optical properties are still an important figure of merit to discuss. Furthermore, many of the studies have explored radiation damage for single-crystal perovskites, which needs to be considered when comparing to perovskites deposited via solution processable techniques. This discussion focuses on the radiation hardness to gamma or X-ray irradiation; however, it is important to note that the effects investigated for other ionizing radiation sources including neutrons, electrons, and protons that are common in space environments or innovative radiation treatments have been discussed elsewhere [79, 97–99].

Yang et al. demonstrated that $Cs_{0.05}FA_{0.81}MA_{0.14}PbI_{2.55}Br_{0.45}$ perovskites in a glass/ITO/PTAA/perovskite/fullerene(C_{60})/BCP/Cu device structure exhibit extremely high radiation hardness [100]. Initial exposure to a ^{137}Cs gamma-ray radiation source up to a total irradiation dose (TID) of 75 Gy decreased the PCE by 18% and was attributed to a reduction in the diode fill factor. Long-term measurements showed extreme stability after the initial decrease, up to a TID of 15 kGy as shown in Fig. 9a (left plot). Noise in Fig. 9a (right plot) between a TID of 15 kGy and 22.5 kGy was the result of radiation damage directly to the copper electrode causing physical cracks in the coating. However, the reduced PCE was determined by the authors to be due to optical darkening in the glass substrate after irradiation that attenuated the 1 sun light source. Applying a correction factor to account for the attenuated light, the perovskite was reported to retain 96.8% of the PCE after a TID of 22.5 kGy. Xu et al. found that $MAPbBr_3$ exhibits significant defects after exposure up to 16.56 kGy from a Co60 gamma source causing surface morphologies of the single crystals to break into smaller pieces as shown in Fig. 9b. Following irradiation, the diffraction peak ratios flattened resulting in a reduction of the transmittance and a red shift of the optical bandgap [101]. The authors suggested that the observations were a result of changes in the crystal structure from radiation damage distorting the lattice. While Boldyreva et al. suggested that for a spin-coated triple cation $Cs_{0.05}FA_{0.81}MA_{0.14}Pb(Br_{0.17}I_{0.83})_3$ perovskite, the increase and redshift of the PL after a TID of 500 Gy were due to phase segregation of I- and B-rich domains [103]. The authors also commented on the spin-coated interlayers, stating that the

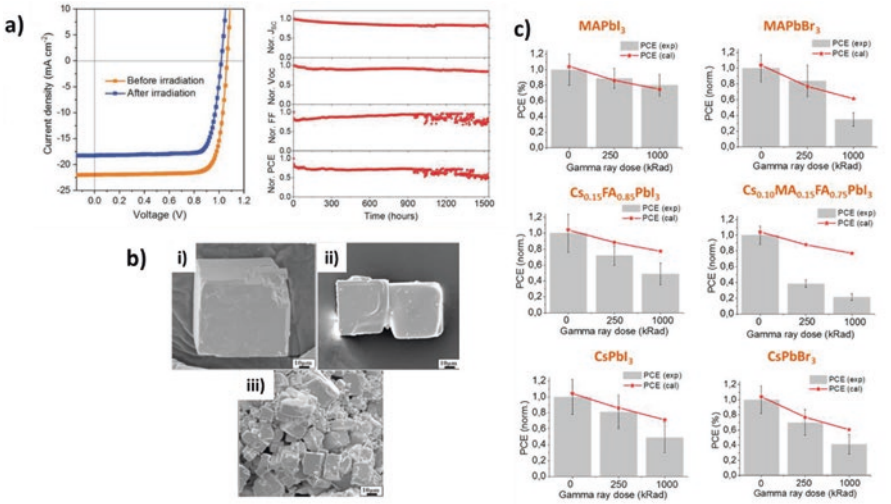

Fig. 9 Radiation damage studies of perovskites. (**a**) J–V curves under a solar sun simulator for a CFAMAPbIBr device before and after 15 kGy from a ^{137}Cs irradiation source. Reproduced from [100] with permission from Copyright © 2018 WILEY-VCH Verlag GmbH & Co. KGaA, Weinheim. (**b**) SEM images of $CH_3NH_3PbBr_3$ single crystal (i) before and following, (ii) 11.04 kGy, (iii) 16.56 kGy irradiation from a high-dose rate ^{60}Co source. Reproduced from [101] with permission from Copyright © 2022 Elsevier B.V. c) Power conversion efficiency under a solar sun simulator for $MAPbI_3$, $MAPbBr_3$, $Cs_{0.15}FA_{0.85}PbI_3$, $Cs_{0.10}MA_{0.15}FA_{0.75}PbI_3$, $CsPbI_3$, and $CsPbBr_3$ devices following 2.5 kGy and 10 kGy from a ^{137}Cs irradiation source normalized to pristine conditions. Reproduced from [102] with permission from Copyright © 2020 American Chemical Society

addition of PCBM did not stabilize the perovskite layer to radiation damage, showing a 40% reduction in the PCE attributed mainly to a 39% loss in photocurrent (compared to a photocurrent loss of 28% without PCBM), as confirmed by other works [104].

The observable changes in the electronic characteristics are valuable to gain an overall estimation of the working lifetime of devices; however, a fundamental explanation of the radiation-induced modifications is ideal to understand and ultimately model radiation damage in novel materials. A model would facilitate researchers to optimize their active layer composition to achieve high radiation hardness under a specific radiation source and energy, while balancing performance, as has been achieved previously for optical photodetectors [105]. There are some limited studies that have explored the microscopic reasoning for the radiation effects in perovskites. One group reported the appearance of a second Pb peak on the Pb $4f_{7/2}$ spectra under a 10 kV source during XPS measurements after a TID of 5.8 kGy. The amplitude of the second peak continued to rise after each scan up to a TID of 29 kGy, where the peak was identified to be the formation of metallic Pb from 10% of the Pb in a $MAPbBr_3$ single crystal [106]. However, Boldyreva et al. found that spin-coated triple cation perovskite films did not produce any additional peaks at a

TID of 5 kGy [103]. The authors only commented on a slight broadening of the Pb $4f_{7/2}$ peak that may be attributed to radiation-induced gradients in the material composition, not the formation of metallic Pb, and concluded that triple cation perovskites are more resistant to radiation. Other works at lower TIDs have also not found evidence of metallic Pb [107].

Boldyreva et al. in another work found that the composition of spin-coated perovskite determines the radiation hardness and the ability to "self-heal" [102]. The work explored the effects of radiation damage to $MAPbI_3$, $MAPbBr_3$, $Cs_{0.15}FA_{0.85}PbI_3$, $Cs_{0.10}MA_{0.15}FA_{0.75}PbI_3$, $CsPbI_3$, and $CsPbBr_3$ as solar cells after exposure to a ^{137}Cs gamma-ray source as shown in Fig. 9c. $MAPbI_3$ exhibited the greatest radiation hardness after a TID of 10 kGy, with no changes in the diode fill factor or open-circuit voltage and a slight decrease in the photocurrent and PCE due to the darkening of the glass following irradiation. On the other hand, $Cs_{0.15}FA_{0.85}PbI_3$ and $Cs_{0.10}MA_{0.15}FA_{0.75}PbI_3$ were the least stable, with a PCE loss of approximately 50% and 75%, respectively. The authors suggested that the superior radiation stability of $MAPbI_3$ was due to a gas-phase chemistry that promotes self-healing. Self-healing, or performance recovery of perovskites following exposure to ionizing radiation, has been suggested in multiple works [100, 101, 107, 108]. Yang et al. outlined that self-healing was due to displaced ions from the incident radiation simply migrating back to their lattice position after irradiation has ceased because of the thermodynamically lower energy level of the sites [100]. Armaroli et al. associated the recovery of $MAPbBr_3$ to environmental oxygen and water filling Br vacancies [107]. The authors suggest that the filling reverses the effects of these radiation-induced vacancies that, when left unoccupied, create large polarons through the coupling of photogenerated carriers and phonons.

A few studies have investigated the radiation detection performance of perovskites following irradiation, demonstrating high reproducibility after the multiple radiation cycles required for accurate dosimetry [83, 84, 101]. Small TID up to 4 Gy found no change in sensitivity from $Cs_{0.1}(FA_{0.83}MA_{0.17})_{0.9}Pb(Br_{0.17}I_{0.83})_3$ perovskites, suggesting reliable use for low-dose imaging. Exposure to larger TID that X-ray sensors will experience in harsher environments for applications including radiotherapy treatments observed an increase in the radiation sensitivity by an order of magnitude after 5.52 kGy. The changes were attributed to material decomposition and seal-healing of the perovskite [101]. However, a twofold increase in the dark current was also observed, which will affect the detection limit of the devices, thereby restricting the application in low-dose imaging.

These studies have outlined that perovskite samples exhibit reasonable radiation tolerance to low energies for low-dose X-ray imaging. However, the findings of gamma-ray-induced changes to perovskites from high doses do not provide a particularly clear outcome. The development of a radiation damage mechanism for high-dose exposures is required to allow researchers to manipulate the material formulation and morphology to enhance the radiation tolerance of perovskite X-ray detectors.

5 Conclusion and Outlook

The extensive research efforts in perovskite photodetector materials have seen a recent transition to the application radiation detectors. Increasing exposure to high levels of radiation from emerging applications in space, personal dosimetry, and medicine has led to a drive for more efficient and low-cost materials capable of monitoring and measuring these increased radiation doses. In this chapter we have described the key material physics of perovskites under ionizing radiation beams, discussing first the material innovations to improve detector performance and then outlining the key printing and coating techniques that can translate these materials to industrially relevant devices before finishing with an overview of the current status of solution processed radiation detection devices. Innovative synthesis strategies for perovskite structures continue to be developed at a rapid pace to combine the high performance of crystalline structures with mechanically flexible substrates that may increase their compatibility with printing techniques.

Although these materials exhibit excellent performance and compatibility with R2R printing and coating techniques, a considerable gap remains with respect to optimizing material performance and nanostructure using large-scale fabrication techniques in order to enhance their responsiveness and stability to all types of radiation sources. Controlling the nanoscale morphology of perovskite films has been shown to be essential in the creation of high-performance radiation detectors, with substantial further work required in order to translate the high precision laboratory fabrication procedures into the large-scale printed fabrication arena where the length scales rapidly increase and temperature, atmospheric composition, and other similar variables become far less controlled. Unlocking new printing fabrication procedures for these solution processable perovskite materials provides an avenue toward upscaled low-cost manufacture of radiation detectors using roll-to-roll machinery, which is an exciting prospect for future industrial translation of these technologies.

References

1. Griffith, M. J., et al. (2020). Printable organic semiconductors for radiation detection: From fundamentals to fabrication and functionality. *Frontiers in Physics*, 8.
2. Posar, J. A., et al. (2021). Polymer photodetectors for printable, flexible, and fully tissue equivalent X-ray detection with zero-bias operation and ultrafast temporal responses. *Advanced Materials Technologies*, *6*(9), 2001298–n/a.
3. Wei, H., & Huang, J. (2019). Halide lead perovskites for ionizing radiation detection. *Nature Communications, 10*(1), 1066–1066.
4. Basiricò, L., Ciavatti, A., & Fraboni, B. (2021). Solution-grown organic and perovskite X-ray detectors: A new paradigm for the direct detection of ionizing radiation. *Advanced Materials Technologies*, *6*(1), 2000475–n/a.
5. Attix, F. H. (1986). *Introduction to radiological physics and radiation dosimetry*. Wiley.
6. Knoll, G. F. (2010). *Radiation detection and measurement* (4th ed.). Wiley.

7. Hubbell, J. H., & Seltzer, S. M. (2004). *X-ray mass attenuation coefficients NIST standard reference database 126*. Radiation Physics Division, PML, NIST.
8. De Martin, E., et al. (2021). On the evaluation of edgeless diode detectors for patient-specific QA in high-dose stereotactic radiosurgery. *Physica Medica, 89*, 20–28.
9. Fidanzio, A., et al. (2000). PTW-diamond detector: Dose rate and particle type dependence. *Medical Physics (Lancaster), 27*(11), 2589–2593.
10. Martin, C. (2007). The importance of radiation quality for optimisation in radiology. *Biomedical Imaging and Intervention Journal, 3*(2), e38–e38.
11. Posar, J. A., et al. (2020). Characterization of a plastic dosimeter based on organic semiconductor photodiodes and scintillator. *Physics and Imaging in Radiation Oncology, 14*, 48–52.
12. Griffith, M. J., et al. (2019). Manipulating nanoscale structure to control functionality in printed organic photovoltaic, transistor and bioelectronic devices. *Nanotechnology, 31*(9), 92002–092002.
13. Klein, C. A. (1968). Bandgap dependence and related features of radiation ionization energies in semiconductors. *Journal of Applied Physics, 39*(4), 2029–2038.
14. Zhao, Y., & Zhu, K. (2016). Organic-inorganic hybrid lead halide perovskites for optoelectronic and electronic applications. *Chemical Society Reviews, 45*(3), 655–689.
15. Kim, T. W., & Park, N.-G. (2020). Methodologies for structural investigations of organic lead halide perovskites. *Materials Today (Kidlington, England), 38*, 67–83.
16. Noh, J. H., et al. (2013). Chemical management for colorful, efficient, and stable inorganic–organic hybrid nanostructured solar cells. *Nano Letters, 13*(4), 1764–1769.
17. Li, Z., et al. (2016). Stabilizing perovskite structures by tuning tolerance factor: Formation of formamidinium and cesium lead iodide solid-state alloys. *Chemistry of Materials, 28*(1), 284–292.
18. García-Fernández, A., et al. (2019). Hybrid lead halide [(CH3)2NH2]PbX3 (X = Cl− and Br−) hexagonal perovskites with multiple functional properties. *Journal of Materials Chemistry. C, Materials for Optical and Electronic Devices, 7*(32), 10008–10018.
19. Akkerman, Q. A., et al. (2018). Genesis, challenges and opportunities for colloidal lead halide perovskite nanocrystals. *Nature Materials, 17*(5), 394–405.
20. Huang, H., et al. (2017). Lead halide perovskite nanocrystals in the research spotlight: stability and defect tolerance. *ACS Energy Letters, 2*(9), 2071–2083.
21. Waseda, Y., Matsubara, E., & Shinoda, K. (Eds.). (2011). *X-ray diffraction crystallography introduction, examples and solved problems* (1st ed.). Springer.
22. Kisi, E. H., & Howard, C. J. (2008) Applications of neutron powder diffraction. In: *Oxford series on neutron scattering in condensed matter*, 15. : Oxford University Press.
23. Vegard, L. (1921). Die Konstitution der Mischkristalle und die Raumfüllung der Atome. *Zeitschrift für Physik, 5*, 17–26.
24. Denton, A. R., & Ashcroft, N. W. (1991). Vegard's law. *Physical Review. A, Atomic, Molecular, and Optical Physics, 43*(6), 3161–3164.
25. Sears, V. F. (1992). Neutron scattering lengths and cross sections. *Neurtron News, 3*, 26–37.
26. Weller, M. T., et al. (2015). Cubic perovskite structure of black formamidinium lead iodide, α-[HC(NH2)2]PbI3, at 298 K. *The Journal of Physical Chemistry Letters, 6*(16), 3209–3212.
27. Pistor, P., et al. (2014). Monitoring the phase formation of coevaporated lead halide perovskite thin films by in situ X-ray diffraction. *The Journal of Physical Chemistry Letters, 5*(19), 3308–3312.
28. Barrit, D., et al. (2022). Processing of lead halide perovskite thin films studied with in-situ real-time X-ray scattering. *ACS Applied Materials & Interfaces, 14*(23), 26315–26326.
29. Fransishyn, K. M., Kundu, S., & Kelly, T. L. (2018). Elucidating the failure mechanisms of perovskite solar cells in humid environments using in situ grazing-incidence wide-angle X-ray scattering. *ACS Energy Letters, 3*(9), 2127–2133.
30. Weller, M. T., et al. (2015). Complete structure and cation orientation in the perovskite photovoltaic methylammonium lead iodide between 100 and 352 K. *Chemical Communications (Cambridge, England), 51*(20), 4180–4183.

31. Park, J.-S., et al. (2015). Electronic structure and optical properties of α-CH3NH3PbBr3 perovskite single crystal. *The Journal of Physical Chemistry Letters, 6*(21), 4304–4308.
32. Tao, S., et al. (2019). Absolute energy level positions in tin- and lead-based halide perovskites. *Nature Communications, 10*(1), 2560–2560.
33. Saparov, B., & Mitzi, D. B. (2016). Organic–inorganic perovskites: Structural versatility for functional materials design. *Chemical Reviews, 116*(7), 4558–4596.
34. Zhang, Y., et al. (2019). Metal halide perovskite nanosheet for X-ray high-resolution scintillation imaging screens. *ACS Nano, 13*(2), 2520–2525.
35. Wang, G., et al. (2015). Wafer-scale growth of large arrays of perovskite microplate crystals for functional electronics and optoelectronics. *Science Advances, 1*(9), e1500613–e1500613.
36. Gao, H., et al. (2018). Bandgap engineering of single-crystalline perovskite arrays for high-performance photodetectors. *Advanced Functional Materials*, *28*(46), 1804349–n/a.
37. Carlé, J. E., et al. (2014). Upscaling from single cells to modules – fabrication of vacuum- and ITO-free polymer solar cells on flexible substrates with long lifetime. *Journal of Materials Chemistry. C, Materials for Optical and Electronic Devices, 2*(7), 1290–1297.
38. Cooling, N. A., et al. (2016). A low-cost mixed fullerene acceptor blend for printed electronics. *Journal of Materials Chemistry. A, Materials for Energy and Sustainability, 4*(26), 10274–10281.
39. Griffith, M. J., et al. (2015). Roll-to-roll sputter coating of aluminum cathodes for large-scale fabrication of organic photovoltaic devices. *Energy Technology (Weinheim, Germany), 3*(4), 428–436.
40. Al-Ahmad, A. Y., et al. (2020). A nuanced approach for assessing OPV materials for large scale applications. *Sustainable Energy & Fuels, 4*(2), 94–949.
41. Carlé, J. E., et al. (2017). Overcoming the scaling lag for polymer solar cells. *Joule, 1*(2), 274–289.
42. Yakunin, S., et al. (2015). Detection of X-ray photons by solution-processed lead halide perovskites. *Nature Photonics, 9*(7), 444–449.
43. Qian, W., et al. (2021). An aerosol-liquid-solid process for the general synthesis of halide perovskite thick films for direct-conversion X-ray detectors. *Matter, 4*(3), 942–954.
44. Haruta, Y., et al. (2020). Fabrication of CsPbBr3 thick films by using a mist deposition method for highly sensitive X-ray detection. *MRS Advances, 5*(8–9), 395–401.
45. Haruta, Y., et al. (2019). Fabrication of (101)-oriented CsPbBr3 thick films with high carrier mobility using a mist deposition method. *Applied Physics Express, 12*(8).
46. Haruta, Y., et al. (2021). Columnar grain growth of lead-free double perovskite using mist deposition method for sensitive X-ray detectors. *Crystal Growth & Design, 21*(7), 4030–4037.
47. Xu, X., et al. (2021). Sequential growth of 2D/3D double-layer perovskite films with superior X-ray detection performance. *Advanced Science*, *8*(21), 2102730–n/a.
48. Kim, Y. C., et al. (2017). Printable organometallic perovskite enables large-area, low-dose X-ray imaging. *Nature, 550*(7674), 87–91.
49. Deng, Y., et al. (2015). Scalable fabrication of efficient organolead trihalide perovskite solar cells with doctor-bladed active layers. *Energy & Environmental Science, 8*(5), 1544–1550.
50. Haruta, Y., et al. (2022). Scalable fabrication of metal halide perovskites for direct X-ray flat-panel detectors: A perspective. *Chemistry of Materials, 34*(12), 5323–5333.
51. Xia, M., et al. (2022). Compact and large-area perovskite films achieved via soft-pressing and multi-functional polymerizable binder for flat-panel X-ray imager. *Advanced Functional Materials*, *32*(16), 2110729–n/a.
52. Dong, S., et al. (2022). Green solvent blade-coated MA 3 Bi 2 I 9 for direct-conversion X-ray detectors. *Journal of Materials Chemistry. C, Materials for Optical and Electronic Devices, 10*(16), 6236–6242.
53. He, X., et al. (2022). Quasi-2D perovskite thick film for X-ray detection with low detection limit. *Advanced Functional Materials*, *32*(7), 2109458–n/a.

54. Huang, S. H., et al. (2020). Toward all slot-die fabricated high efficiency large area perovskite solar cell using rapid near infrared heating in ambient air. *Advanced Energy Materials*, *10*(37), 2001567–n/a.
55. Li, J., et al. (2021). 20.8% Slot-die coated MAPbI3 perovskite solar cells by optimal DMSO-content and age of 2-ME based precursor inks. *Advanced Energy Materials*, *11*(10), n/a.
56. Andersen, T. R., et al. (2016). Fully roll-to-roll prepared organic solar cells in normal geometry with a sputter-coated aluminium top-electrode. *Solar Energy Materials and Solar Cells, 149*, 103–109.
57. Andersen, T. R., et al. (2016). Comparison of inorganic electron transport layers in fully roll-to-roll coated/printed organic photovoltaics in normal geometry. *Journal of Materials Chemistry. A, Materials for Energy and Sustainability, 4*(41), 15986–15996.
58. Griffith, M. J., et al. (2021). Controlling nanostructure in inkjet printed organic transistors for pressure sensing applications. *Nanomaterials (Basel, Switzerland), 11*(5), 1185.
59. Griffith, M. J., et al. (2014). Printable sensors for explosive detonation. *Applied Physics Letters, 105*(14), 143301.
60. Basaran, O. A., Gao, H., & Bhat, P. P. (2013). Nonstandard Inkjets. *Annual Review of Fluid Mechanics, 45*(1), 85–113.
61. Liu, J., et al. (2019). Flexible, printable soft-X-ray detectors based on all-inorganic perovskite quantum dots. *Advanced Materials, 31*(1901644).
62. Mescher, H., et al. (2020). Flexible inkjet-printed triple cation perovskite X-ray detectors. *ACS Applied Materials & Interfaces, 12*(13), 15774–15784.
63. Glushkova, A., et al. (2021). Ultrasensitive 3D aerosol-jet-printed perovskite X-ray photodetector. *ACS Nano, 15*(3), 4077–4084.
64. Mescher, H., Hamann, E., & Lemmer, U. (2019). Simulation and design of folded perovskite X-ray detectors. *Scientific Reports, 9*(1), 5231–5231.
65. Griffith, M. J., et al. (2016). Combining printing, coating, and vacuum deposition on the roll-to-roll scale: A hybrid organic photovoltaics fabrication. *IEEE Journal of Selected Topics in Quantum Electronics, 22*(1), 112–125.
66. Kim, Y. Y., et al. (2019). Gravure-printed flexible perovskite solar cells: Toward roll-to-roll manufacturing. *Advanced Science*, *6*(7), 1802094–n/a.
67. Dou, B., et al. (2018). Roll-to-roll printing of perovskite solar cells. *ACS Energy Letters, 3*(10), 2558–2565.
68. Galagan, Y., et al. (2018). Roll-to-roll slot die coated perovskite for efficient flexible solar cells. *Advanced Energy Materials*, *8*(32), 1801935–n/a.
69. Li, H., et al. (2022). Fully roll-to-roll processed efficient perovskite solar cells via precise control on the morphology of PbI2:CsI layer. *Nano-micro Letters, 14*(1), 79–79.
70. Lee, C., et al. (2010). A novel method to guarantee the specified thickness and surface roughness of the roll-to-roll printed patterns using the tension of a moving substrate. *Journal of Microelectromechanical Systems, 19*(5), 1243–1253.
71. Benitez-Rodriguez, J. F., et al. (2021). Roll-to-roll processes for the fabrication of perovskite solar cells under ambient conditions. *Solar RRL*, *5*(9), 2100341–n/a.
72. Kim, J., et al. (2017). Overcoming the challenges of large-area high-efficiency perovskite solar cells. *ACS Energy Letters, 2*(9), 1978–1984.
73. Shi, L., et al. (2020). Gas chromatography-mass spectrometry analyses of encapsulated stable perovskite solar cells. *Science, 368*(6497).
74. Anderson, D., et al. (2019). Printable ionizing radiation sensors fabricated from nanoparticulate blends of organic scintillators and polymer semiconductors. *MRS Communications, 9*(4), 1206–1213.
75. Sunahara, K., et al. (2013). A nonconjugated bridge in dimer-sensitized solar cells retards charge recombination without decreasing charge injection efficiency. *ACS Applied Materials & Interfaces, 5*(21), 10824–10829.
76. Rong, Y., et al. (2018). Challenges for commercializing perovskite solar cells. *Science, 361*(6408), 1214.

77. Chen, Y., et al. (2018). Large-area perovskite solar cells – A review of recent progress and issues. *RSC Advances, 8*(19), 1489–1158.
78. Posar, J. A., et al. (2021). Towards high spatial resolution tissue-equivalent dosimetry for microbeam radiation therapy using organic semiconductors. *Journal of Synchrotron Radiation, 28*(5), 1444–1454.
79. Ho-Baillie, A. W. Y., et al. (2021). Deployment opportunities for space photovoltaics and the prospects for perovskite solar cells. *Advanced Materials Technologies*, 2101059.
80. Hu, M., et al. (2020). Large and dense organic–inorganic hybrid perovskite CH3NH3PbI3 wafer fabricated by one-step reactive direct wafer production with high X-ray sensitivity. *ACS Applied Materials & Interfaces, 12*(14), 16592–16600.
81. Pan, L., et al. (2021). Determination of X-ray detection limit and applications in perovskite X-ray detectors. *Nature Communications, 12*(1), 5258–5258.
82. Wei, H., et al. (2017). Dopant compensation in alloyed CH3NH3PbBr3−xClx perovskite single crystals for gamma-ray spectroscopy. *Nature Materials, 16*(8), 826–833.
83. Basiricò, L., et al. (2019). Detection of X-rays by solution-processed cesium-containing mixed triple cation perovskite thin films. *Advanced Functional Materials, 29*(34), 1902346.
84. Bruzzi, M., et al. (2019). First proof-of-principle of inorganic perovskites clinical radiotherapy dosimeters. *APL Materials*, *7*(5), 51101–051101-6.
85. Lédée, F., et al. (2022). Ultra-stable and robust response to X-rays in 2D layered perovskite micro-crystalline films directly deposited on flexible substrate. *Advanced Optical Materials, 10*(1), 2101145.
86. Gill, H. S., et al. (2018). Flexible perovskite based X-ray detectors for dose monitoring in medical imaging applications. *Physics in Medicine, 5*(C), 20–23.
87. Hamukwaya, S. L., et al. (2022). A review of recent developments in preparation methods for large-area perovskite solar cells. *Coatings, 12*(2), 252.
88. Bruzzi, M., & Talamonti, C. (2021). Characterization of crystalline CsPbBr3 perovksite dosimeters for clinical radiotherapy. *Frontiers in Physics*, 9.
89. Li, X., et al. (2016). Healing all-inorganic perovskite films via recyclable dissolution-recyrstallization for compact and smooth carrier channels of optoelectronic devices with high stability. *Advanced Functional Materials, 26*(32), 5903–5912.
90. Yan, Y., et al. (2021). Implementing an intermittent spin-coating strategy to enable bottom-up crystallization in layered halide perovskites. *Nature Communications, 12*(1), 6603–6603.
91. Xiao, B., et al. (2021). Towards superior X-ray detection performance of two-dimensional halide perovskite crystals by adjusting the anisotropic transport behavior. *Journal of Materials Chemistry. A, Materials for Energy and Sustainability, 9*(22), 1329–13219.
92. Posar, J. A., et al. (2020). Characterization of an organic semiconductor diode for dosimetry in radiotherapy. *Medical Physics (Lancaster), 47*(8), 3658–3668.
93. Ciavatti, A., et al. (2021). High-sensitivity flexible X-ray detectors based on printed perovskite inks. *Advanced Functional Materials, 31*(11), 2009072.
94. Jang, J., et al. (2021). Multimodal digital X-ray scanners with synchronous mapping of tactile pressure distributions using perovskites. *Advanced materials (Weinheim)*, *33*(30), 2008539–n/a.
95. Kubicki, D. J., et al. (2018). Formation of stable mixed guanidinium–methylammonium phases with exceptionally long carrier lifetimes for high-efficiency lead iodide-based perovskite photovoltaics. *Journal of the American Chemical Society, 140*(9), 3345–3351.
96. Saliba, M., et al. (2016). Cesium-containing triple cation perovskite solar cells: improved stability, reproducibility and high efficiency. *Energy & Environmental Science, 9*(6), 1989–1997.
97. Posar, J. A., Petasecca, M., & Griffith, M. J. (2021). A review of printable, flexible and tissue equivalent materials for ionizing radiation detection. *Flexible and Printed Electronics*.
98. Lang, F., et al. (2018). Influence of radiation on the properties and the stability of hybrid perovskites. *Advanced Materials, 30*(3), 1702905.
99. Paternò, G. M., et al. (2019). Perovskite solar cell resilience to fast neutrons. *Sustainable Energy & Fuels, 3*(1), 2561–2566.

100. Yang, S., et al. (2019). Organohalide lead perovskites: More stable than glass under gamma-ray radiation. *Advanced Materials, 31*, 1805547.
101. Xu, Q., et al. (2021). Effect of methylammonium lead tribromide perovskite based-photoconductor under gamma photons radiation. *Radiation Physics and Chemistry, 181*, 109337.
102. Boldyreva, A. G., et al. (2020). Unravelling the material composition effects on the gamma ray stability of lead halide perovskite solar cells: MAPbI3 breaks the records. *The Journal of Physical Chemistry Letters, 11*(7), 2630–2636.
103. Boldyreva, A. G., et al. (2019). γ-ray-induced degradation in the triple-cation perovskite solar cells. *The Journal of Physical Chemistry Letters, 10*(4), 813–818.
104. Large, M. J., et al. (2021). Flexible polymer X-ray detectors with non-fullerene acceptors for enhanced stability: Toward printable tissue equivalent devices for medical applications. *ACS Applied Materials & Interfaces*.
105. van der Salm, H., et al. (2015). Probing Donor–acceptor interactions in meso-substituted Zn(II) porphyrins using resonance Raman spectroscopy and computational chemistry. *Journal of physical chemistry. C, 119*(39), 22379–22391.
106. Wang, C., et al. (2018). Environmental surface stability of the MAPbBr3 single crystal. *Journal of Physical Chemistry C, 122*(6), 3513–3522.
107. Armaroli, G., et al. (2021). X-ray-induced modification of the photophysical properties of MAPbBr3 single crystals. *ACS Applied Materials & Interfaces, 13*(49), 58301–58308.
108. Lang, F., et al. (2016). Radiation hardness and self-healing of perovskite solar cells. *Advanced Materials, 28*, 8726–8731.

Two-Dimensional Halide Perovskites for Radiation Detection

Bao Xiao and Yadong Xu

1 Introduction

The demand for large-volume radiation detectors based on scintillation and semiconductor materials has triggered tremendous opportunities in the field of astronomy, high energy physics, nuclear medicine, nondestructive inspection, national security, etc. [1–3]. Depending on the detection modes, the radiation detectors can be classified into direct detection by solid-state semiconductors and indirect detection by scintillators. The former detectors directly convert photons to electrons by the semiconductor materials that are sensitive to high-energy radiation, while the scintillation detectors firstly convert high-energy radiation to ultraviolet or visible light, which can further be detected by the arrayed photodetectors.

Generally, radiation detector materials need to fulfill simultaneously several desirable properties. The direct detection semiconductor materials should possess a suitable bandgap (E_g), high resistivity (ρ), high average atomic number (Z), high mobility-lifetime product ($\mu\tau$), etc., whereas scintillation detectors should have the traits of high light yield, long-term stability, and high energy resolution. On this premise, current semiconductor detectors are mainly based on CdTe, TlBr, α-HgI_2, and $Cd_{0.9}Zn_{0.1}Te$ (CZT) [4–8], and the most commercially used scintillators are bulk crystals of NaI:Tl and CsI:Tl [9, 10]. However, each suffers from unsolved issues associated with the crystal growth, device operation conditions, or the manufacturing cost, which limits there widespread development [11]. Therefore, the quest for new detection materials is required in the field of high-energy radiation detection.

B. Xiao · Y. Xu (✉)
State Key Laboratory of Solidification Processing & Key Laboratory of Radiation Detection Materials and Devices, Ministry of Industry and Information Technology, Northwestern Polytechnical University, Xi'an, China
e-mail: fsnhxiaobao@mail.nwpu.edu.cn; xyd220@nwpu.edu.cn

W. Nie, K. (Kris) Iniewski (eds.), *Metal-Halide Perovskite Semiconductors*,
https://doi.org/10.1007/978-3-031-26892-2_9

Recently, the rapidly expanding class of halide perovskites have emerged as promising candidates for radiation detection materials, owing to their high attenuation coefficient, long carrier diffusion length and lifetime, and large mobility-lifetime product [12–14]. Compared to the degradation of the three-dimensional (3D) halide perovskite devices for long-term operations resulting from the poor air stability and ionic migration, two-dimensional (2D) halide perovskites present remarkable environmental and device stability and large Stokes shifts coupled with very broad emission, making it suitable as radiation detection materials [15, 16]. Therefore, this book chapter aims to summarize the recent research progress of 2D halide perovskite single crystals as X-ray detectors and then briefly talk about 2D halide perovskite scintillators applied in α-, β-particles, X-, and γ-ray detection.

2 Crystal Structure of 2D Halide Perovskites

Halide perovskites with the empirical formula of ABX_3 ($A = Cs^+$, MA^+, FA^+; $B = Sn^{2+}$, Pb^{2+}, Ge^{2+}; $X = Cl^-$, Br^-, I^-) are classified as 3D perovskite, in which BX_6 octahedra are corner-shared along three octahedral axes. However, the perovskites can be cut into slices from the 3D structure to a lower-dimensional layered configuration, all the way down to eventually isolated, zero-dimensional (0D) BX_6 octahedral clusters [17]. As the dimensional reduction of perovskites structure, the size restrictions, as outlined by the tolerance factor for the 3D structures, are gradually lifted. The layered 2D perovskites organized from BX_6 octahedra connected along two octahedral axes can be derived by slicing the 3D perovskites along the <100>, <110>, or <111> crystallographic planes and then inserting larger spacer cations to produce <100>-oriented, <110>-oriented, and <111>-oriented 2D perovskites, as shown in Fig. 1. The number of perovskite (inorganic) layers in 2D perovskites can be controlled by adjusting the stoichiometric ratio between A-site cations and larger spacer cations A′.

Among the three classifications, the <100>-oriented perovskites are the most widely investigated 2D layered perovskites, which can be further divided into Ruddlesden-Popper (RP) phase, Dion-Jacobson (DJ) phase, and alternating cations in the interlayer (ACI) phase depending on the larger spacer cations, with the general formulas of $A'_2A_{n-1}B_nX_{3n+1}$, $A''A_{n-1}B_nX_{3n+1}$, and $A'A_nB_nX_{3n+1}$, respectively. The spacer layer in RP perovskites is composed of two layers of monoammonium cations, which are bound to the inorganic layers from one side by hydrogen bonds (N–H•••X) between the ammonium groups and halide anions [18]. The adjacent inorganic octahedral layer misaligned by half an octahedral unit, showing a (1/2, 1/2) in-plane displacement [19]. However, for the DJ perovskites, the monoammonium cations in the organic layer are replaced by the diammonium cations that contain two amino groups at both ends connecting to the inorganic layers by hydrogen bonds (N–H•••X) [20], which leads to an eclipsed stacking of the adjacent inorganic layers exactly on top of each other with non-displacement (0, 0) [19]. The adjacent inorganic layers in ACI perovskites are eclipsed looking from *a* (or *b*)

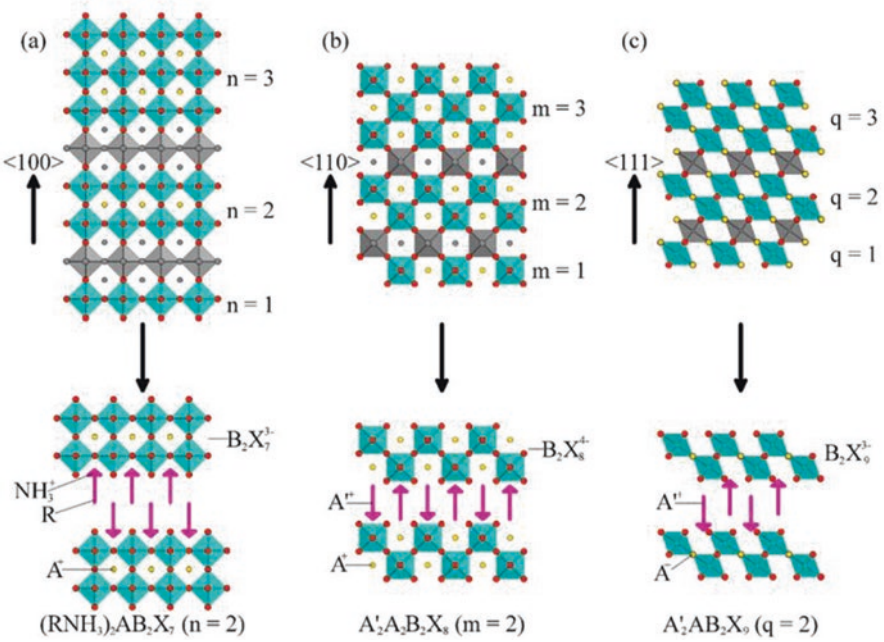

Fig. 1 Schematic representation of different families of layered perovskites: (**a**) <100>-oriented 2D perovskites with a general formula of $A'_2A_{n-1}B_nX_{3n+1}$, (**b**) <110>-oriented 2D perovskites with a general formula of $A'_2A_mB_mX_{3m+2}$, (**c**) <111>-oriented 2D perovskites with a general formula of $A'_2A_{q-1}B_qX_{3q+3}$ [24]. Reprinted with permission from Ref. [24]. Copyright 2016 American Chemical Society

direction, but staggered from *b* (or *a*) direction, leading to a (0, 1/2) or (1/2, 0) displacement [19]. Moreover, the A-site cation exists not only inside the octahedral cage but also between the layers alternating with larger organic cation (A′). To date, only the guanidinium cation can template this type of structure [21].

Compared to 3D halide perovskites, the interchangeability of the large organic cations (A′) and the control of layer dimensionality (*n*) offer 2D layered perovskites with greater structure tenability and further exhibit flexibility physical and optoelectronic properties, enabling them applied in various optoelectronic devices such as solar cells, light-emitting diodes (LED), radiation detectors, etc. [22, 23].

3 Advances in the Development of 2D Halide Perovskites X-Ray Direct Detectors

As mentioned above, the flexibility physical and optoelectronic properties of 2D halide perovskites enable them as promising candidates for radiation detectors, especially as X-ray detectors. In this section, the key parameters for X-ray direct

detection and the advances in the development of 2D halide perovskites X-ray direct detectors are systematically summarized.

3.1 The Key Parameters for X-Ray Direct Detectors

The performance of X-ray detector is largely limited by the properties of the X-ray absorber materials, which play vital roles in the processes of X-ray absorption, electron-hole pair generation, and transport. This section is aimed to introduce some key parameters for choosing X-ray detector materials and evaluating the X-ray detection performance.

(1) *The Selection of Perovskites for X-Ray Detectors.*

Stopping Power The stopping power is defined as the capability of a given material to completely absorb X-ray, which is usually quantified by the X-ray attenuation ratio (ε):

$$\varepsilon = 1 - \frac{I(x)}{I(0)} = 1 - e^{-\mu x} \tag{1}$$

where x is the material thickness and μ is the attenuation coefficient of the material, which is proportional to Z^4/E^3 (where Z is the atomic number and E is the X-ray photon energy). Thus, halide perovskite materials with high-Z elements enable them as ideal X-ray detector materials.

Ionization Energy The ionization energy ($W_{\pm}$) is defined as the energy required of the given material absorbing the X-ray to produce one free electron-hole pair, which is proportional to the energy bandgap (E_g) of the given material, and can be written as [25]:

$$W_{\pm} = 2E_g + 1.43 \tag{2}$$

Obviously, the narrower bandgap would result in a lower ionization energy ($W_{\pm}$), which is beneficial for the production of electron-hole pair in a given halide perovskite material. However, the perovskites with small bandgap also bring a large dark current and high noise. Therefore, suitable bandgap is necessary for halide perovskites operated as X-ray detectors [26].

Mobility-Lifetime Product The mobility-lifetime product ($\mu\tau$) is used to estimate the ability of charge carriers to drift before recombination in a given material and can be derived by the modified Hecht equation [27]:

$$I = \frac{I_0 \mu\tau V}{L^2} \cdot \frac{1 - \exp\left(-\frac{L^2}{\mu\tau V}\right)}{1 + \frac{L}{V} \cdot \frac{s}{\mu}} \tag{3}$$

where I and I_0 are the measured photocurrent and saturated photocurrent, respectively. L is the material thickness, V is the applied bias, and s is the surface recombination velocity. Thus, high $\mu\tau$ product directly determines the charge collection efficiency of given halide perovskites, which is essential to enhance the X-ray sensitivity.

(2) *The Key Performance Parameters for X-Ray Detectors.*

Sensitivity Sensitivity (S) is a key parameter for X-ray detectors, which reflects the ability of a detector to convert incident X-ray photons into current signals, and can be estimated by [28]:

$$S = \frac{I_p - I_d}{A \times D} \tag{4}$$

where I_p and I_d are the measured photocurrent and dark current, respectively. A is the effective area of X-ray detector and D is the dose rate. Therefore, X-ray detectors with high sensitivity can generate large current signals at a low dose rate, which is beneficial for reducing the risk of ionizing radiation [29].

Detection Limit The detection limit is another critical parameter for X-ray detectors, which determines the lowest detectable X-ray dose rate. The International Union of Pure and Applied Chemistry (IU-PAC) defines the detection limit as the equivalent dose rate to produce a signal greater than three times the noise level, so the signal-to-noise ratio (SNR) of 3 is used to define the detection limit in X-ray detectors [30]. Generally, the SNR can be calculated by:

$$SNR = \frac{I_{signal}}{I_{noise}} = \frac{I_p - I_d}{\sqrt{\frac{1}{N}\sum_{i}^{N}\left(I_i - I_p\right)^2}} \tag{5}$$

where I_{signal} and I_{noise} are the signal current and noise current, whereas I_p and I_d are the average photocurrent and dark current, respectively. A low detection limit not only allows for a reduced dose rate for X-ray examination, which significantly suppresses the risk of cancer, but also favors of high-resolution images acquisition.

Response Speed Response speed is defined as the time taken for the detector to respond to an external stimulus of detector, which is highly dependent on the carrier transport and collection processes in the detector. Therefore, the rise time (τ_r, the

time required for the current rising from 10% to 90% of the saturated photocurrent) and fall time (τ_f, the time required for the current falling from 90% to 10% of the saturated photocurrent) are often adopted to estimate the response capability of the detector. It is significant the X-ray detector should possess short response time, which can shorten the X-ray exposure time and enable higher frame rate during imaging [31].

3.2 2D Halide Perovskites X-Ray Direct Detectors

Currently, 3D halide perovskites, possessing high attenuation coefficient, long carrier diffusion length and lifetime, and large mobility-lifetime product, have shown great potential for direct X-ray detectors. However, their inherent stability (moisture, light, heat, etc.) and operational stability hinder the further applications of 3D halide perovskites in X-ray detection. 2D halide perovskites generally possess suppressed ion migration along with intrinsic chemical and moisture stability, showing more promising X-ray detection performance.

In 2019, 2D layered $(NH_4)_3Bi_2I_9$ perovskite single crystal has been proposed as X-ray direct detectors, which exhibits a unique anisotropic detection performance mainly ascribed to its anisotropic structure. For example, the $\mu\tau$ product for the direction parallel to the cleavage (001) surface is 1.1×10^{-2} $cm^2 \bullet V^{-1}$, which is almost three times than that of the direction perpendicular to (001) plane of 4.0×10^{-3} $cm^2 \bullet V^{-1}$. Consequently, the resulting parallel direction $(NH_4)_3Bi_2I_9$ detector exhibits a much higher X-ray sensitivity of 8.2×10^3 $\mu C \bullet Gy^{-1} \bullet cm^{-2}$ than the perpendicular direction detector of 803 $\mu C \bullet Gy^{-1} \bullet cm^{-2}$ due to charge transport and collection anisotropy, as shown in Fig. 2a–c. However, the perpendicular direction $(NH_4)_3Bi_2I_9$ detector exhibits a much lower X-ray detection limit of 55 $nGy \bullet s^{-1}$ than the parallel direction detector of 210 $nGy \bullet s^{-1}$, ascribed to the suppressed ion migration. Moreover, both parallel and perpendicular $(NH_4)_3Bi_2I_9$ X-ray detectors show an excellent operational stability under continuous working biases on a 10-h scale. It is highlighted that the anisotropic X-ray detection property enables $(NH_4)_3Bi_2I_9$ X-ray detector to be utilized in different practical conditions [32]. Then, centimeter-size all-inorganic 2D perovskite $Cs_3Bi_2I_6Br_3$ have been reported for X-ray detection, which shows a high sensitivity of 3194.59 $\mu C \bullet Gy^{-1} \bullet cm^{-2}$, much higher than its 0D counterpart $Cs_3Bi_2I_9$ of 707.81 $\mu C \bullet Gy^{-1} \bullet cm^{-2}$, ascribed to the enhancement of carrier transport (Fig. 2d–e). Moreover, the fabricated $Cs_3Bi_2I_6Br_3$ detector exhibits an outstanding operational stability under continuous working at a relatively high electric field [33]. By the way, both the perovskites $(NH_4)_3Bi_2I_9$ and $Cs_3Bi_2I_6Br_3$ can be considered as the derivatives ($A' = A$ and $q = 2$, i.e., $A_3B_2X_9$) by slinging the 3D perovskites along the <111> crystallographic planes, resulting in the <111>-oriented 2D perovskites.

In addition, <100>-oriented 2D Ruddlesden-Popper (RP) and Dion-Jacobson (DJ) perovskites have recently shown very promising performance in X-ray detection. For example, the insulating butylamine (BA) organic cation has been

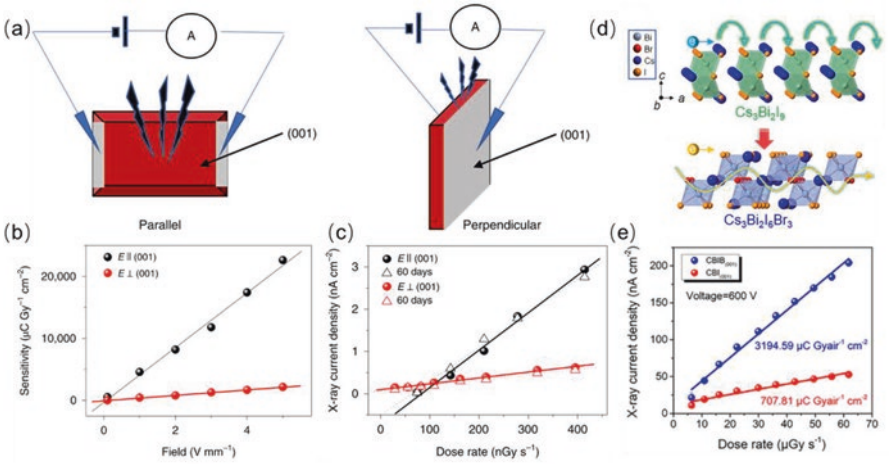

Fig. 2 (**a**) Illustration of parallel and perpendicular device structure of $(NH_4)_3Bi_2I_9$. (**b**) X-ray sensitivities of the $(NH_4)_3Bi_2I_9$ devices in direction parallel and perpendicular to the (001) surface. (**c**) Anisotropic X-ray photocurrent densities at different dose rates under pristine conditions (solid lines) and after 60 days of ambient air aging (dotted lines) [32]. Reprinted with permission from Ref. [32]. Copyright 2019 Springer Nature. (**d**) Schematic assumption of the carrier transport path in $Cs_3Bi_2I_9$ and $Cs_3Bi_2I_6Br_3$. (**e**) Electric field-dependent extracted X-ray sensitivities of $Cs_3Bi_2I_9$ and $Cs_3Bi_2I_6Br_3$ at 600 V [33]. Reprinted with permission from Ref. [33]. Copyright 2022 Elsevier

introduced into $Cs_2AgBiBr_6$ to generate a 2D layered RP perovskite $(BA)_2CsAgBiBr_7$, which could serve as the potential X-ray direct detector. The 2D $(BA)_2CsAgBiBr_7$ single crystal possesses a high resistivity of 1.5×10^{11} Ω•cm and large $\mu\tau$ product up to 1.21×10^{-3} $cm^2 \bullet V^{-1}$, which enables the fabricated detector to yield a superior X-sensitivity of 4.2 $\mu C \bullet Gy^{-1} \bullet cm^{-2}$ [34] (Fig. 3a–c). Then, Wei et al. found that introducing electron-deficient F atoms with neighbor benzene rings could enhance the supramolecular electrostatic interaction as supramolecular anchor, leading to a 2D RP perovskite 4-fluorophenethylammonium lead iodide $(F\text{-}PEA)_2PbI_4$. The fabricated $(F\text{-}PEA)_2PbI_4$ single-crystal detector yields an X-ray sensitivity of 3402 $\mu C \bullet Gy^{-1} \bullet cm^{-2}$ to 120 keVp hard X-ray with lowest detectable X-ray dose rate of 23 $nGy \bullet s^{-1}$. Moreover, the detector also exhibits excellent operation stability under ambient condition at 200 V high bias, showing stable response to hard X-ray pulses with no signal-to-noise ratio loss after over 1-month storage [35] (Fig. 3d–e).

The natural multiple quantum well (MQW) structure enables 2D RP perovskites with anisotropic X-ray detection performance. For example, the detector based on 2D $(BA)_2CsPb_2Br_7$ single crystal along *ab* plane exhibited superior X-ray sensitivity up to 13.26 $mC \bullet Gy^{-1} \bullet cm^{-2}$ at a relatively low electric field of 2.53 V mm^{-1}, while lower than 20 $\mu C \bullet Gy^{-1} \bullet cm^{-2}$ along *c* direction even at a pretty high electric field of 70 V mm^{-1} under the same irradiation of 40 kVp. However, the anisotropic detection performance could be adjusted by shortening the spacer cation from butylamine (BA) to isobutylamine (i-BA) to reduce the interlayer distance and barrier

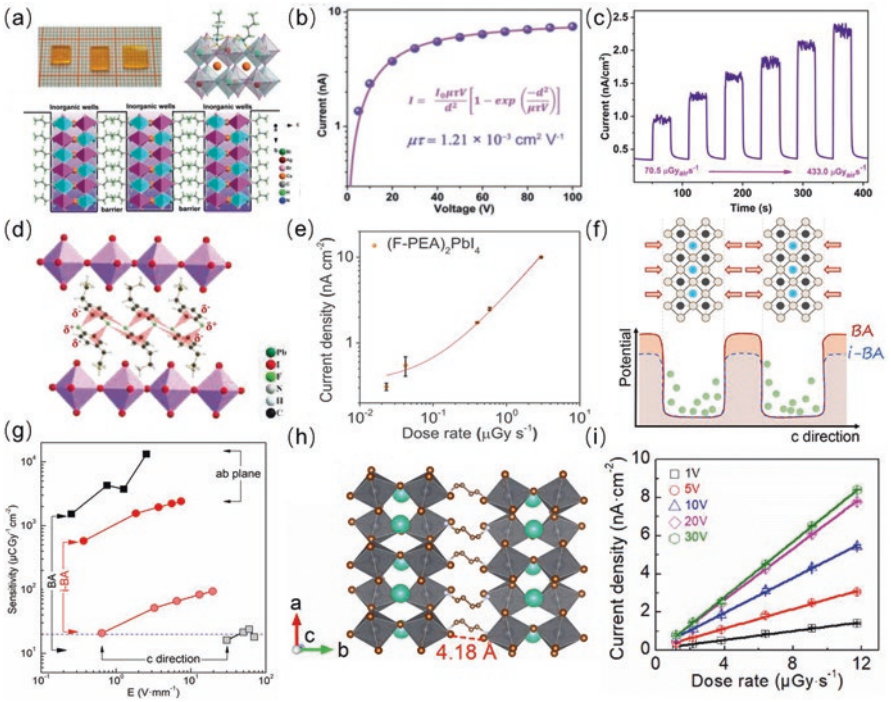

Fig. 3 (**a**) Photograph and crystal structure of $(BA)_2CsAgBiBr_7$. (**b**) Photoconductivity of single-crystalline $(BA)_2CsAgBiBr_7$. (**c**) X-ray response of $(BA)_2CsAgBiBr_7$ detector with varied dose rate [34]. Reprinted with permission from Ref. [34]. Copyright 2019 Wiley-VCH. (**d**) The crystal structure of $(F\text{-}PEA)_2PbI_4$, where electron-deficient F atoms form supramolecular electrostatic interaction with neighbor benzene rings. (**e**) The current density of $(F\text{-}PEA)_2PbI_4$ single-crystal device at different X-ray dose rates [35]. Reprinted with permission from Ref. [35]. Copyright 2020 Wiley-VCH. (**f**) Schematic diagram of charge transport restriction along the *c* direction in 2D perovskites $(BA)_2CsPb_2Br_7$ and $(i\text{-}BA)_2CsPb_2Br_7$. (**g**) Electric field-dependent X-ray sensitivities of $(BA)_2CsPb_2Br_7$ and $(i\text{-}BA)_2CsPb_2Br_7$ crystal detectors along the *ab* plane and *c* direction, respectively [36]. Reprinted with permission from Ref. [36]. Copyright 2021 Royal Society of Chemistry. (**h**) The crystal structure of $(BDA)CsPb_2Br_7$. (**i**) Dose rate-dependent current densities of $(BDA)CsPb_2Br_7$ detector under various biases [38]. Reprinted with permission from Ref. [38]. Copyright 2022 American Chemical Society

height, which resulted in lower X-ray sensitivity along *ab* plane and higher *c* direction X-ray sensitivity in 2D RP perovskite $(i\text{-}BA)_2CsPb_2Br_7$ [36] (Fig. 3f–g).

Furthermore, compared with the 2D RP perovskites, 2D Dion-Jacobson (DJ) perovskites have exhibited improved stability and electrical properties. The diammonium cations ($NH_3C_4H_8NH_3^{2+}$, BDA^{2+}) have been employed to form a 2D DJ perovskite $BDAPbI_4$, which also exhibits an excellent sensitivity of 242 $\mu C \bullet Gy^{-1} \bullet cm^{-2}$ under the 10 V bias with a detection limit as low as 430 $nGy \bullet s^{-1}$ [37]. Moreover, the diammonium cations (BDA^{2+}) have also been introduced to $CsPbBr_3$ to obtain a novel 2D DJ perovskite $(BDA)CsPb_2Br_7$, which enables the resulting detector along the out-of-plane direction to achieve a high X-ray sensitivity of 725.5 $\mu C \bullet Gy^{-1} \bullet cm^{-2}$ with excellent working stability [38] (Fig. 3h–i).

4 2D Halide Perovskite Semiconductor for Alpha Particle Detection

For the high-energy alpha particles (~3–7 MeV), the direct radiation detectors usually work in voltage mode, since the particle flux is relatively weak and alpha particles will come into the detector one by one with a shallow penetration depth. However, alpha particle is still destructive ionizing radiation, and it is very important for developing high-performance detectors for alpha particle detection. Recently, Xu et al. have developed a novel alpha detector based on a 2D DJ perovskite (BDA) $CsPb_2Br_7$ single crystal (inset in Fig. 4b). Then, a 5.48 MeV ^{241}Am α-particle source was adopted to analyze the radiation detection performance of resulting Au/(BDA) $CsPb_2Br_7$/Au device, as shown in Fig. 4a. A voltage-dependent energy spectra of (BDA)$CsPb_2Br_7$ detector with the bias changing from −100 V to −300 V can be seen in Fig. 4c. Specially, a superior energy resolution of 37% (FWHM) was achieved at −260 V bias (inset in Fig. 4c). The hole mobility-lifetime product $(\mu\tau)_h$ could be evaluated using the single charge carrier approximation Hecht equation [39]:

$$CCE = \frac{\mu\tau V}{d^2} \cdot \left(1 - \exp\left(-\frac{d^2}{\mu\tau V}\right)\right) \tag{6}$$

Therefore, the hole mobility-lifetime product $(\mu\tau)_h$ of (BDA)$CsPb_2Br_7$ crystal was calculated to be $(2.33 \pm 0.08) \times 10^{-5}$ $cm^2 \cdot V^{-1}$ by fitting the peak centroid channel vs. the bias voltage using Eq. (3), as shown in Fig. 4d [38]. The results suggest that the 2D DJ perovskite (BDA)$CsPb_2Br_7$ could serve as the potential alpha particle-detecting material.

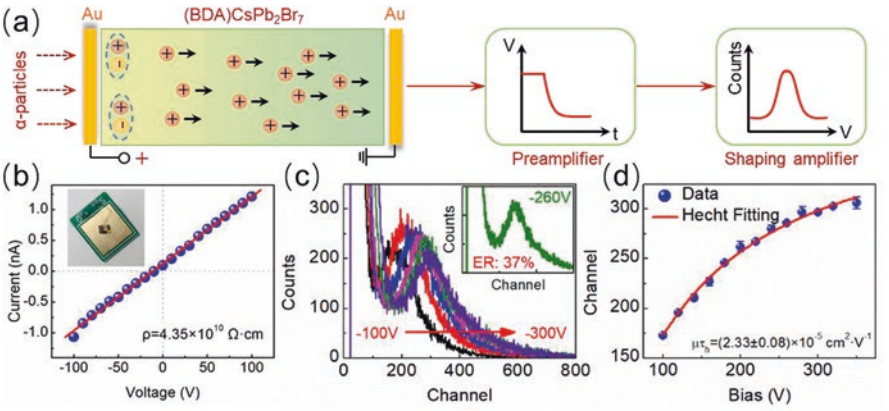

Fig. 4 (**a**) Hole transport process in Au/(BDA)$CsPb_2Br_7$/Au device illuminated by ^{241}Am α-particles. (**b**) The typical I-V curve of (BDA)$CsPb_2Br_7$; the inset is the fabricated Au/(BDA) $CsPb_2Br_7$/Au detector. (**c**) The energy spectra of (BDA)$CsPb_2Br_7$ detector under various voltages, respectively. The inset is the typical energy spectra under −260 V with a resolution of 37%. (**d**) The hole mobility-lifetime product evaluation of (BDA)$CsPb_2Br_7$ according to the Hecht equation [38]. Reprinted with permission from Ref. [38]. Copyright 2022 American Chemical Society

5 Advances in the Development of 2D Halide Perovskite Scintillators for Radiation Detection

The scintillation detectors are also capable of detecting high-energy particles or photons by indirect detection mode. Generally, the scintillation detectors firstly convert high-energy radiation to ultraviolet or visible light, which can further be detected by the arrayed photodetectors. Light yield (LY) and decay time are the most important figures of merit for scintillation detectors. LY indicates the number of photons that can be converted by the scintillator per photon or particle energy (in unit) and can be calculated by:

$$LY = 10^6 \frac{SQ}{\beta E_g} \tag{7}$$

where S is the efficiency of the transport of electron-hole pairs to the emission center, Q is the luminescence efficiency, and β is usually a constant with a value of 2.5. A high LY value indicates the high number of photons emitted from the scintillator which leads to a high signal output. It is generally believed that 2D perovskites are able to show high scintillation light yield and faster decay due to their higher exciton binding energy (hundreds of meV) [40]. In this section, the advances in the development of 2D halide perovskite scintillators are systematically summarized.

5.1 Alpha Particle Detectors

Developing high-performance detectors for alpha particle is important for environmental safety. Recently, lithium-doped 2D RP perovskite $(PEA)_2PbBr_4$ has been synthesized for multiple radiation detectors and scintillators for the first time (Fig. 5a). With a lithium dopant, the 1:1 Li-doped $(PEA)_2PbBr_4$ scintillator demonstrated a fast decay time of 11 ns and a high scintillation yield light of 11,000 photons per MeV (Fig. 5b). Figure 5c shows the pulse-height spectra results of the Li-doped $(PEA)_2PbBr_4$ scintillator using ^{241}Am and ^{224}Cm as the alpha particle sources [41].

5.2 Beta Particle Detectors

Beta particle with a moderate penetrating power is an important signal for surface radiative contamination surveillance. In general, the incident β-particles go through elastic scattering with nuclei and inelastic scattering with electrons in solids. Currently β-particle detectors are mainly based on the organic scintillators, including single crystal, liquid, and plastic types, which was limited by the issues of high

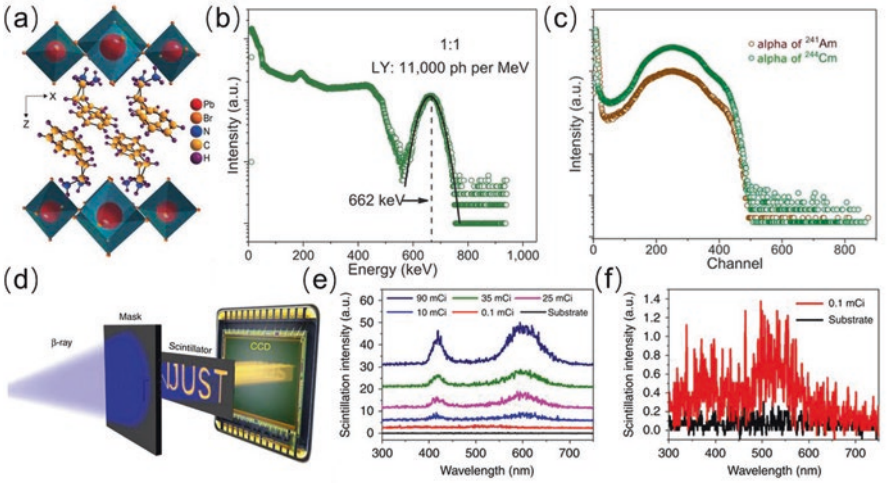

Fig. 5 (**a**) Crystal structure of $(PEA)_2PbBr_4$. (**b**) Pulse-height spectra of Li-doped $(PEA)_2PbBr_4$ with Gaussian fitting to extract light yield. (**c**) Alpha particle pulse-height spectra of Li-doped $(PEA)_2PbBr_4$ scintillator [41]. Reprinted with permission from Ref. [41]. Copyright 2020 Spring Nature. (**d**) Illustration of the setup of the system for β-particle detection by the 2D perovskite scintillator. (**e**) The scintillation spectra of the 2D perovskite scintillator under different β-particle irradiation intensity. (**f**) The scintillation spectrum under the irradiation activity of 0.1 mCi [42]. Reprinted with permission from Ref. [42]. Copyright 2020 Spring Nature

cost, poor irradiation hardness, carcinogenicity, complex fabrication, or thermal deterioration.

Recently, a type of β-particle scintillator with good thermotolerance and irradiation hardness based on 2D RP perovskites has been proposed by Zeng et al. A series of bulky organic cations in 2D RP perovskite $(A)_2PbBr_4$ (A = butylamine, BA; octylamine, OA; stearamine, STA; and dodecylamine, DA) have been explored to enhance the capturing of β-particle. Additionally, extrinsic manganese (Mn) dopants were adopted to improve the scintillation performance via serving as emitting centers with no self-absorption. Figure 5d shows the setup of the system for the β-particle detection by the 2D perovskite scintillator. The resultant 2D perovskite scintillator exhibited an effective β-particle detection performance with no functionality decay or hysteresis under an accumulated radiation dose of 10 kGy (dose rate 0.67 kGy•h^{-1}) and exhibited a low detection limit of 0.1 mCi (Fig. 5e–f) [42].

5.3 Gamma-Ray Detectors

Gamma-rays, as a form of electromagnetic waves, have the shortest wavelength and the highest energy and are usually emitted from atomic nuclei. 2D perovskite scintillator also exhibits good potential as γ-ray detection material. For example, Dang

et al. have investigated the scintillation properties from 11 different 2D organic-inorganic hybrid perovskites and found that the 3 2D perovskite $(PEA)_2PbBr_4$, $(EDBE)_2PbBr_4$, and $(BA)_2PbBr_4$ crystals have the higher light yield. Specially, $(BA)_2PbBr_4$ scintillator exhibits the highest light yield and 3.7 times greater than that of $(PEA)_2PbBr_4$ (~40,000 photons per MeV at RT), as well as being more stable from 10 K to 350 K compared to other 2D scintillators. In conjunction with the 5.3 ns fast decay time, $(BA)_2PbBr_4$ scintillator shows the energy resolution as low as 13% to resolve the 662 keV ^{137}Cs γ-ray, suggesting it can be a potential superior scintillator detector. Furthermore, Li-doped $(PEA)_2PbBr_4$ scintillator exhibits the light yield 2.009 times higher than that of undoped $(PEA)_2PbBr_4$ scintillator and achieves the best energy resolution of 7.7% at 662 keV from the ^{137}Cs γ-ray source for Li-doped $(PEA)_2PbBr_4$ scintillator [43, 44].

5.4 Neutron Detectors

A fast neutron has strong penetration ability through dense and bulky objects, which makes it an ideal nondestructive technology for detecting voids, cracks, or other defects inside large equipment. Recently, a hydrogen-rich 2D perovskite Mn-$(C_{18}H_{37}NH_3)_2PbBr_4$ (Mn-STA_2PbBr_4) has been demonstrated as fast neutron scintillator detector, where the hydrogen-rich long-chain organic amine ions lead to a high capturing efficiency of fast neutrons, and the Mn^{2+} dopants as the emitting centers improve the optical performance with no self-absorption (Fig. 6d). The fabricated large-area self-standing fast neutron scintillator plates based on 2D perovskite Mn-STA_2PbBr_4 deliver high light yields and good spatial resolution (0.5 lp/mm (lp, line pairs)), as shown in Fig. 6e–i [45]. The results open up a new route for the design of fast neutron scintillator materials and promote the development of fast neutron radiography-based nondestructive testing technologies.

6 Conclusion

In summary, the rise of halide perovskites as promising candidates for radiation detection materials has been witnessed from recent reports. Compared to the well-studied three-dimensional (3D) halide perovskite, two-dimensional (2D) halide perovskites could be obtained by slicing the 3D perovskites along different crystallographic planes with larger insulating organic cations to generate <100>-oriented, <110>-oriented, and <111>-oriented 2D perovskites, respectively. 2D layered perovskites with remarkable environmental and device stability have been reported to exhibit good potential in high-energy radiation detection in two types, namely, direct semiconductor detector and indirect scintillator detector.

The 2D perovskites have recently shown very promising performance in X-ray detection as a direct semiconductor detector. For example, the detector based on

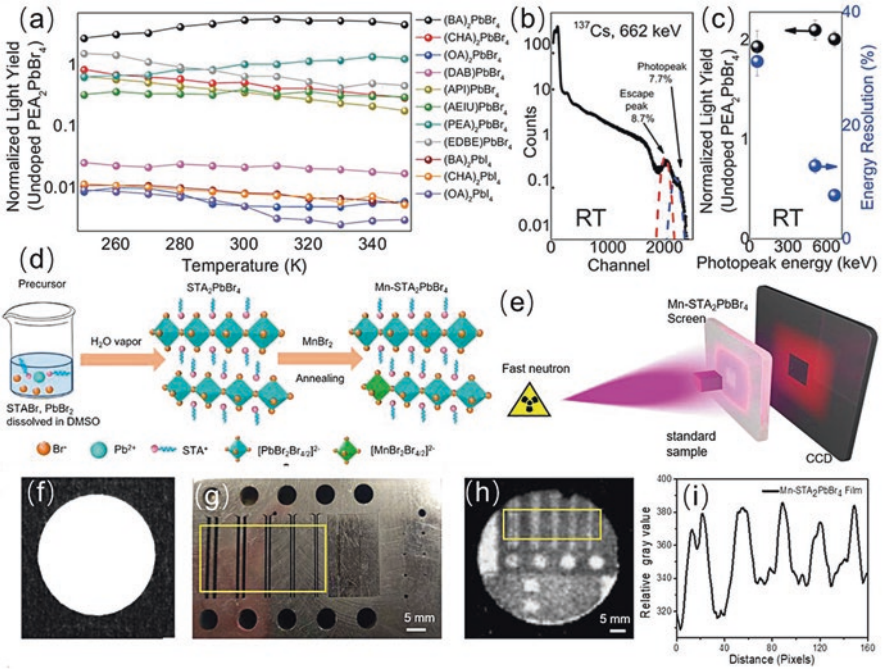

Fig. 6 (**a**) Temperature-dependent light yield of 2D perovskite for temperature between 250 and 350 K. (**b**) Pulse-height spectra of Li-doped $(PEA)_2PbBr_4$ under 662 keV gamma-ray from the ^{137}Cs source. (**c**) Light yield and energy resolution as a function of photopeak energies for different gamma-ray sources of ^{241}Am, ^{22}Na, and ^{137}Cs. The y-axis is normalized with the light yields of undoped $(PEA)_2PbBr_4$ under 662 keV gamma-ray at RT [43]. Reprinted with permission from ref. 43. Copyright 2020 American Chemical Society. (**d**) Synthesis scheme of Mn-STA_2PbBr_4. (**e**) Schematic of the experimental setup used for fast neutron radiography of a resolution test standard sample. The sample is placed between the fast neutron source and the Mn-STA_2PbBr_4 screen. (**f**) Fast neutron radiograph is generated by a 1 mm thick Mn-STA_2PbBr_4 plate. (**g**) Resolution test standard sample (steel plate with slits, holes of different depths). (**h**) Fast neutron imaging of resolution test standard sample. Each frame of the image is exposed for 100 s under a 14 MeV fast neutron accelerator for a total of 20 times. (**i**) Curve of the relative gray value distribution of (**h**), which can distinguish the fissure evidently [45]. Reprinted with permission from Ref. [45]. Copyright 2021 American Chemical Society

$(BA)_2CsPb_2Br_7$ single crystal along *ab* plane exhibited superior X-ray sensitivity up to 13.26 $mC•Gy^{-1}•cm^{-2}$ at a relatively low electric field of 2.53 V mm^{-1}. The natural multiple quantum well structure enables 2D perovskite detectors with anisotropic detection performance, which can be adjusted by shortening the spacer cation to reduce the interlayer distance and barrier height. The anisotropic X-ray detection property enables 2D perovskite to be utilized in different practical conditions. Except for the semiconductor detector, 2D perovskite scintillator detectors have also exhibited excellent performance in α-, β-particles, neutron, and γ-ray detection. For example, a type of 2D perovskite scintillator was developed to detect β-ray with good thermotolerance and irradiation hardness. Li-doped $(PEA)_2PbBr_4$ scintillator

was demonstrated to resolve 662 keV γ-rays with an energy resolution of 7.7% and has been proven to be useful in neutron detection through ^{6}Li enrichment. Although 2D perovskites have been proven to have good potential applied in high-energy radiation detection, the properties are still to be improved for producing better 2D perovskite semiconductor detector or scintillator detector.

Acknowledgments This work was supported by the National Natural Science Foundations of China (No. 51872228, 51802262, and U2032170), the Natural Science Foundation of Shaanxi Province (2020JC-12), and the Natural Science Basic Research Plan in Shaanxi Province of China (2019ZDLGY04-07).

References

1. Owens, A., & Peacock, A. (2004). Compound semiconductor radiation detectors. *Nuclear Instruments and Methods in Physics Research Section A: Accelerators, Spectrometers, Detectors and Associated Equipment, 531*(1–2), 18–37.
2. Szeles, C. (2004). CdZnTe and CdTe materials for X-ray and gamma ray radiation detector applications. *Physica Status Solidi B: Basic Solid State Physics, 241*(3), 783–790.
3. Kim, Y. C., Kim, K. H., Son, D. Y., Jeong, D. N., Seo, J. Y., Choi, Y. S., Han, I. T., Lee, S. Y., & Park, N. G. (2017). Printable organometallic perovskite enables large-area, low-dose X-ray imaging. *Nature, 550*(7674), 87–91.
4. Schlesinger, T. E., Toney, J. E., Yoon, H., Lee, E. Y., Brunett, B. A., Franks, L., & James, R. B. (2001). Cadmium zinc telluride and its use as a nuclear radiation detector material. *Materials Science and Engineering R, 32*(4), 103–189.
5. Locker, M., Fischer, P., Krimmel, S., Kruger, H., Lindner, M., Nakazawa, K., Takahashi, T., & Wermes, N. (2004). Single photon counting X-ray imaging with Si and CdTe single chip pixel detectors and multichip pixel modules. *IEEE Transactions on Nuclear Science, 51*(4), 1717–1723.
6. Melnikov, A. (1999). CdZnTe radiation detectors. *Journal of Crystal Growth, 197*(3), 663–665.
7. Gits, S., & Authier, A. (1982). Plastic defects in α-HgI_2 single crystals. *Journal of Crystal Growth, 58*(3), 473–485.
8. Hitomi, K., Onodera, T., & Shoji, T. (2007). Influence of zone purification process on TlBr crystals for radiation detector fabrication. *Nuclear Instruments and Methods in Physics Research Section A: Accelerators, Spectrometers, Detectors and Associated Equipment, 579*(1), 153–156.
9. Moszyński, M., Zalipska, J., Balcerzyk, M., Kapusta, M., Mengesha, W., & Valentine, J. D. (2002). Intrinsic energy resolution of NaI(Tl). *Nuclear Instruments and Methods in Physics Research Section A: Accelerators, Spectrometers, Detectors and Associated Equipment, 484*(1), 259–269.
10. Nagarkar, V. V., Gupta, T. K., Miller, S. R., Klugerman, Y., Squillante, M. R., & Entine, G. (1998). Structured CsI(Tl) scintillators for X-ray imaging applications. *IEEE Transactions on Nuclear Science, 45*(3), 492–496.
11. Owens, A. (2006). Semiconductor materials and radiation detection. *Journal of Synchrotron Radiation, 13*(2), 143–150.
12. Dong, Q., Fang, Y., Shao, Y., Mulligan, P., Qiu, J., Cao, L., & Huang, J. (2015). Electron-hole diffusion lengths>175 μm in solution-grown $CH_3NH_3PbI_3$ single crystals. *Science, 347*(6225), 967–970.
13. McMeekin, D. P., Sadoughi, G., Rehman, W., Eperon, G. E., Saliba, M., Hörantner, M. T., Haghighirad, A., Sakai, N., Korte, L., Rech, B., Johnston, M. B., Herz, L. M., & Snaith,

H. J. (2016). A mixed-cation lead mixed-halide perovskite absorber for tandem solar cells. *Science, 351*(6269), 151–155.
14. Shi, D., Adinolfi, V., Comin, R., Yuan, M., Alarousu, E., Buin, A., Chen, Y., Hoogland, S., Rothenberger, A., Katsiev, K., Losovyj, Y., Zhang, X., Dowben, P. A., Mohammed, O. F., Sargent, E. H., & Bakr, O. M. (2015). Low trap-state density and long carrier diffusion in organolead trihalide perovskite single crystals. *Science, 347*(6221), 519–522.
15. Smith, I. C., Hoke, E. T., Solisibarra, D., Mcgehee, M. D., & Karunadasa, H. I. (2014). A layered hybrid perovskite solar-cell absorber with enhanced moisture stability. *Angewandte Chemie, International Edition, 53*(42), 11232–11235.
16. Lin, Y., Bai, Y., Fang, Y., Wang, Q., Deng, Y., & Huang, J. (2017). Suppressed ion migration in low-dimensional perovskites. *ACS Energy Letters, 2*(7), 1571–1572.
17. Saidaminov, M. I., Mohammed, O. F., & Bakr, O. M. (2017). Low-dimensional-networked metal halide perovskites: The next big thing. *ACS Energy Letters, 2*(4), 889–896.
18. Stoumpos, C. C., Cao, D. H., Clark, D. J., Young, J., Rondinelli, J. M., Jang, J. I., Hupp, J. T., & Kanatzidis, M. G. (2016). Ruddlesden-Popper hybrid lead iodide perovskite 2D homologous semiconductors. *Chemistry of Materials, 28*(8), 2852–2867.
19. Blancon, J. C., Even, J., Stoumpos, C. C., Kanatzidis, M. G., & Mohite, A. D. (2020). Semiconductor physics of organic-inorganic 2D halide perovskites. *Nature Nanotechnology, 15*(12), 969–985.
20. Li, X., Hoffman, J., Ke, W., Chen, M., Tsai, H., Nie, W., Mohite, A. D., Kepenekian, M., Katan, C., Even, J., Wasielewski, M. R., Stoumpos, C. C., & Kanatzidis, M. G. (2018). Two-dimensional halide perovskites incorporating straight chain symmetric diammonium ions, $(NH_3C_mH_{2m}NH_3)(CH_3NH_3)_{n-1}Pb_nI_{3n+1}$ (m= 4-9; n= 1-4). *Journal of the American Chemical Society, 140*(38), 12226–12238.
21. Soe, C. M. M., Stoumpos, C. C., Kepenekian, M., Traoré, B., Tsai, H., Nie, W., Wang, B., Katan, C., Seshadri, R., & Mohite, A. D. (2017). New type of 2D perovskites with alternating cations in the interlayer space, $(C(NH_2)_3)(CH_3NH_3)_nPb_nI_{3n+1}$: Structure, properties, and photovoltaic performance. *Journal of the American Chemical Society, 139*(45), 16297–16309.
22. Chen, P., Bai, Y., Lyu, M., Yun, J.-H., Hao, M., & Wang, L. (2018). Progress and perspective in low-dimensional metal halide perovskites for optoelectronic applications. *Solar RRL, 2*(3), 1700186.
23. Wong, J., & Yang, K. (2021). 2D hybrid halide perovskites: Synthesis, properties, and applications. *Solar RRL, 5*(1), 2000395.
24. Saparov, B., & Mitzi, D. B. (2016). Organic-inorganic perovskites: Structural versatility for functional materials design. *Chemical Reviews, 116*(7), 4558–4596.
25. Devanathan, R., Corrales, L. R., Gao, F., & Weber, W. J. (2006). Signal variance in gamma-ray detectors – A review. *Nuclear Instruments and Methods in Physics Research Section A: Accelerators, Spectrometers, Detectors and Associated Equipment, 565*(2), 637–649.
26. Li, Z., Zhou, F., Yao, H., Ci, Z., Yang, Z., & Jin, Z. (2021). Halide perovskites for high-performance X-ray detector. *Materials Today, 48*, 155–175.
27. Stoumpos, C. C., Malliakas, C. D., Peters, J. A., Liu, Z., Sebastian, M., Im, J., Chasapis, T. C., Wibowo, A. C., Chung, D. Y., Freeman, A. J., Wessels, B. W., & Kanatzidis, M. G. (2013). Crystal growth of the perovskite semiconductor $CsPbBr_3$: A new material for high-energy radiation detection. *Crystal Growth & Design, 13*(7), 2722–2727.
28. Kasap, S. (2000). X-ray sensitivity of photoconductors: Application to stabilized a-Se. *Journal of Physics D: Applied Physics, 33*(21), 2853–2865.
29. Wei, H., Fang, Y., Mulligan, P., Chuirazzi, W., Fang, H.-H., Wang, C., Ecker, B. R., Gao, Y., Loi, M. A., Cao, L., & Huang, J. (2016). Sensitive X-ray detectors made of methylammonium lead tribromide perovskite single crystals. *Nature Photonics, 10*(5), 333–339.
30. Thompson, M., Ellison, S. L., & Wood, R. (2002). Harmonized guidelines for single-laboratory validation of methods of analysis (IUPAC Technical Report). *Pure and Applied Chemistry, 74*(5), 835–855.

31. Kakavelakis, G., Gedda, M., Panagiotopoulos, A., Kymakis, E., Anthopoulos, T. D., & Petridis, K. (2020). Metal halide perovskites for high-energy radiation detection. *Advancement of Science, 7*(22), 2002098.
32. Zhuang, R., Wang, X., Ma, W., Wu, Y., Chen, X., Tang, L., Zhu, H., Liu, J., Wu, L., Zhou, W., Liu, X., & Yang, Y. (2019). Highly sensitive X-ray detector made of layered perovskite-like $(NH_4)_3Bi_2I_9$ single crystal with anisotropic response. *Nature Photonics, 13*(9), 602–608.
33. Sun, Q., Xiao, B., Ji, L., Zhao, D., Liu, J., Zhang, W., Zhu, M., Jie, W., Zhang, B.-B., & Xu, Y. (2022). Effect of dimensional expansion on carrier transport behaviors of the hexagonal Bi-based perovskite crystals. *Journal of Energy Chemistry, 66*, 459–465.
34. Xu, Z., Liu, X., Li, Y., Liu, X., Yang, T., Ji, C., Han, S., Xu, Y., Luo, J., & Sun, Z. (2019). Exploring lead-free hybrid double perovskite crystals of $(BA)_2CsAgBiBr_7$ with large mobility-lifetime product toward X-ray detection. *Angewandte Chemie, International Edition, 58*(44), 15757–15761.
35. Li, H., Song, J., Pan, W., Xu, D., Zhu, W.-A., Wei, H., & Yang, B. (2020). Sensitive and stable 2D perovskite single-crystal X-ray detectors enabled by a supramolecular anchor. *Advanced Materials, 32*(40), 2003790.
36. Xiao, B., Sun, Q., Wang, F., Wang, S., Zhang, B., Wang, J., Jie, W., Sellin, P., & Xu, Y. (2021). Towards superior X-ray detection performance of two-dimensional halide perovskite crystals by adjusting anisotropic transport behavior. *Journal of Materials Chemistry A, 9*(22), 13209–13219.
37. Shen, Y., Liu, Y., Ye, H., Zheng, Y., Wei, Q., Xia, Y., Chen, Y., Zhao, K., Huang, W., & Liu, S. (2020). Centimeter-sized single crystal of two-dimensional halide perovskites incorporating straight chain symmetric diammonium ion for efficient X-ray detection. *Angewandte Chemie, International Edition, 59*(35), 14896–14902.
38. Xiao, B., Sun, Q., Wang, S., Ji, L., Li, Y., Xi, S., Zhang, B.-B., Wang, J., Jie, W., & Xu, Y. (2022). Two-dimensional Dion-Jacobson perovskite $(NH_3C_4H_8NH_3)CsPb_2Br_7$ with high X-ray sensitivity and peak discrimination of α-particles. *Journal of Physical Chemistry Letters, 13*(5), 1187–1193.
39. Sellin, P. J., Davies, A. W., Gkoumas, S., Lohstroh, A., Özsan, M. E., Parkin, J., Perumal, V., Prekas, G., & Veale, M. (2008). Ion beam induced charge imaging of charge transport in CdTe and CdZnTe. *Nuclear Instruments and Methods in Physics Research Section B: Beam Interactions with Materials and Atoms, 266*(8), 1300–1306.
40. Blancon, J. C., Stier, A. V., Tsai, H., Nie, W., Stoumpos, C. C., Traoré, B., Pedesseau, L., Kepenekian, M., Katsutani, F., Noe, G. T., Kono, J., Tretiak, S., Crooker, S. A., Katan, C., Kanatzidis, M. G., Crochet, J. J., Even, J., & Mohite, A. D. (2018). Scaling law for excitons in 2D perovskite quantum wells. *Nature Communications, 9, (1)*, 2254.
41. Xie, A., Hettiarachchi, C., Maddalena, F., Witkowski, M. E., Makowski, M., Drozdowski, W., Arramel, A., Wee, A. T. S., Springham, S. V., Vuong, P. Q., Kim, H. J., Dujardin, C., Coquet, P., Birowosuto, M. D., & Dang, C. (2020). Lithium-doped two-dimensional perovskite scintillator for wide-range radiation detection. *Communications Materials, 1*(1), 37.
42. Yu, D., Wang, P., Cao, F., Gu, Y., Liu, J., Han, Z., Huang, B., Zou, Y., Xu, X., & Zeng, H. (2020). Two-dimensional halide perovskite as β-ray scintillator for nuclear radiation monitoring. *Nature Communications, 11*(1), 3395.
43. Xie, A., Maddalena, F., Witkowski, M. E., Makowski, M., Mahler, B., Drozdowski, W., Springham, S. V., Coquet, P., Dujardin, C., Birowosuto, M. D., & Dang, C. (2020). Library of two-dimensional hybrid lead halide perovskite scintillator crystals. *Chemistry of Materials, 32*(19), 8530–8539.
44. Maddalena, F., Xie, A., Arramel, Witkowski, M. E., Makowski, M., Mahler, B., Drozdowski, W., Mariyappan, T., Springham, S. V., Coquet, P., Dujardin, C., Birowosuto, M. D., & Dang, C. (2021). Effect of commensurate lithium doping on the scintillation of two-dimensional perovskite crystals. *Journal of Materials Chemistry C, 9*(7), 2504–2512.
45. Zheng, J., Zeng, Y., Wang, J., Sun, C., Tang, B., Wu, Y., Zhang, Y., Yi, Y., Wang, N., Zhao, Y., & Zhou, S. (2021). Hydrogen-rich 2D halide perovskite scintillators for fast neutron radiography. *Journal of the American Chemical Society, 143*(50), 21302–21311.

Nonlinear Optical Properties in Perovskite Structure and Their Applications

José Luis Clabel Huamán, Leandro H. Zucolotto Cocca, André G. Pelosi, Rafael de Queiroz Garcia, Leonardo De Boni, and Cleber Renato Mendonça

1 Introduction

Nonlinear optics (NLO) research is considered one of the most revolutionary fields in the innovation of optics and photonics, an emerging field in the frontier of science, because of its potential applications [1]. Nonlinear optics arise from the interaction between the propagation of intense light waves and induced polarization in a medium [2]. As a consequence, it experiments effects such as multiple-frequency generation, two-photon absorption (2PA), Stark effect, electromagnetically induced transparency (EIT), stimulated Raman scattering (SRS), stimulated Brillouin scattering (SBS), and stimulated light scattering (SLS) [3–5]. Although the NLO response of a material is shown to require intense optical fields, a new material with controllable physicochemical properties enables occurrence at certain lower optical powers.

Perovskite structures have received great scientific interest in the last decades due to their excellent functional performance and unique optical and electronic properties, which has motivated an increase of use in applications including optical switches, lasers, modulators, and optical sensors, among others [6–9]. The particular properties include electro-optical, bandgap tunability, narrow bandgap, fast charge mobility, high absorption coefficients, and low defect concentration. The perovskite structure has a stoichiometric ABX_3, where A-site ions are generally rare earth elements and B-site ions are usually transitioned metal elements, frequently occupied by a larger-size and smaller-size cation, respectively, and X is often a chalcogen or halogen. The stability and distortion of perovskite structure are governed by the tolerance factor initially proposed by Goldschmidt [10] and recently

J. L. Clabel Huamán · L. H. Zucolotto Cocca · A. G. Pelosi · R. de Queiroz Garcia
L. De Boni · C. R. Mendonça (✉)
São Carlos Institute of Physics, University of São Paulo, São Carlos, SP, Brazil
e-mail: jclabel@ifsc.usp.br; crmendon@ifsc.usp.br

W. Nie, K. (Kris) Iniewski (eds.), *Metal-Halide Perovskite Semiconductors*,
https://doi.org/10.1007/978-3-031-26892-2_10

modified by Bartel et al. [11]. The equation expresses the tolerance factor: $\tau = (r_X/r_B) - n_A[n_A - (r_A/r_B)/ ln\ (r_A/r_B)]$, where r_A, r_B, and r_X are ionic radii of each ion (A, B, and X), n_A is the oxidation state of A, $r_A > r_B$, and $\tau < 4.18$ indicates perovskite. It determines a better accuracy of τ, mainly oxides of 83–92%.

In this regard, materials displaying interesting optical responses, such as oxide perovskites, show remarkable performance in nonlinear optics (NLO), owing to their noncentrosymmetry structure, high absorption, high exciton binding energy, large nonlinear coefficients, and high absorption band edges [12], which can be used for nonlinear optoelectronic devices. Besides, the optimization of the synthesis methods, affordable and nontoxic, and the ease of fabrication of perovskite oxides allow obtaining materials with different structures. During the synthesis process, the stoichiometric composition, presence of dopant, and processing parameters (pH, temperature, reaction times, among others) play an essential role in the pure phase of perovskite oxide. The manipulation and effective control of these correlated parameters influence the surface area, porosity, density of defect, and degree of octahedral distortion. They are an efficient strategy to achieve an increase in nonlinear optical response. Their unique properties and facile fabrication open up many opportunities for nonlinear optics and optoelectronic devices.

Thus, the present chapter introduces the main synthesis methods for perovskite formation. In the sequence, we will briefly introduce some principles of nonlinear optics. Moreover, we will review some of the characterization techniques frequently used to study various properties of materials. Following this principle, we will discuss the advantages and limitations of different nonlinear optical characterization techniques, and complementary experimental configurations of optical techniques will be provided. Thereby, considering the benefits of facile processing and high nonlinear optical response, we will scrutinize their advanced technological applications linked to developing nonlinear optical materials of the perovskite types.

2 Synthesis and Processing of Perovskite Structures

2.1 Coprecipitation Method

The coprecipitation method is used for synthesizing perovskite powder (ABO_3), with nanometer particle sizes and high homogeneity. This method requires the solubility of the metal cations. The process starts with the simultaneous precipitation of the suspension of soluble metal cations through a precipitation agent; see Fig. 1a. The latter decreases the solubility range and leads to a supersaturation condition [13]. Optimizing the perovskite particles through particle size control and the absence of agglomeration improves the material's functionality. In this sense, pH solution, solution uniformity, reaction times, temperature, and concentration are essential to obtain pure perovskite.

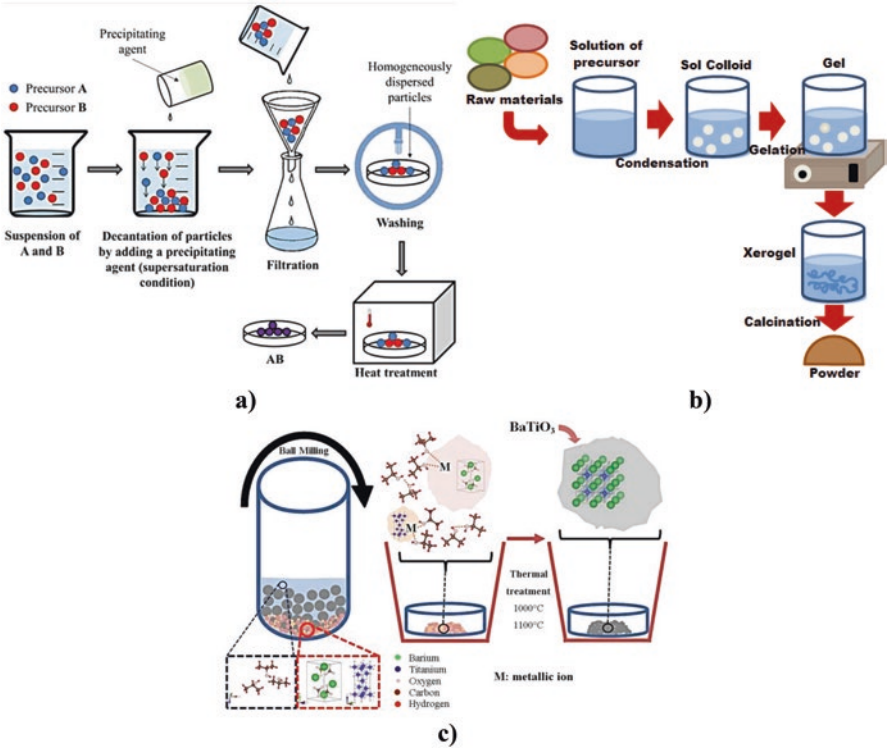

Fig. 1 Schematic representation of the (**a**) co-precipitation. Reprinted from Athayde et al. [13], with permission from Elsevier. Copyright (2016). (**b**) Sol-gel and (**c**) reaction state-solid method. Reprinted from Clabel et al. [14], with permission from Elsevier. Copyright (2020)

Zhang et al. prepared highly stable tetragonal $BaTiO_3$ nanopowder through the coprecipitation method, using barium chloride ($BaCl_2$) and titanium tetrachloride ($TiCl_4$) as raw materials and tartaric acid ($C_4H_6O_6$) as a precipitant agent [15]. Firstly, $BaTiO_3$ nanopowder was obtained through two solutions: the $BaCl_2$ was dissolved in deionized water (solution 1), while $TiCl_4$ and $C_4H_6O_6$ were dissolved in a mixture of isopropanol and deionized water (solution 2). The resultant precipitation was filtered and washed several times with distilled water to remove byproducts. Finally, $BaTiO_3$ nanopowder was obtained with good dispersibility and a homogeneous particle size of about 75 nm. Other authors investigated the influence of oxalate ligand in the coprecipitation method on the morphology and structural phase of undoped and Rh-doped $BaTiO_3$ nanoparticles [16]. Haron et al. [17] fabricated $LaMO_3$ (M = Al, Co, Fe) by using the coprecipitation method. Synthesis of $LaAlO_3$ was obtained using $LaAlO_3$, $Al(NO_3)_3{\cdot}6H_2O$, and $Al(NO_3)_3{\cdot}6H_2O$ as raw materials and dissolved in distilled water. For $LaCoO_3$ and $LaFeO_3$, the second raw material $Al(NO_3)_3{\cdot}6H_2O$ was replaced by $Co(NO_3)_2{\bullet}6H_2O$ and $Fe(NO_3)_3{\cdot}9H_2O$). Then NaOH solution as a precipitant agent was introduced, and after precipitation, it was filtered and washed with distilled water several times until the water became neutral

(pH = 7). Another study found that the nanosized structure of perovskite synthesized by coprecipitation includes $NdFeO_3$ and $CaTiO_3$ [18, 19]. Other advantages of the coprecipitation method are simple and rapid preparation, cost-effectiveness, good chemical homogeneity in the final product, high-phase purity, and fine particle or grain size. From the reported results, the physical and chemical parameters of the solvents used for the synthesis strongly affect the formation stages of the perovskite particle. So, different shapes, sizes, and orientations can be observed when appropriate solvents are used for the synthesis process.

2.2 Sol-Gel Method

The sol-gel method is a process of forming oxide linkages through an inorganic polymerization reaction. The synthesis starts with the mixture of precursor materials (metal alkoxide, metal-organic, or metal-inorganic salt) and solvent to form organic metal complexes. Among the variants of sol-gel methods, the Pechini method became the most used due to its versatility in preparing perovskite powders. During the sol colloid step, the pH, stirring, and temperature adjustment play an essential role in the condensation of the gel. After gel formation, a pre-calcination process is considered to eliminate organic material. Finally, the calcination process at low temperatures leads to great stoichiometry control, enhanced reactivity, distinct structures, high surface area, and greater particle homogeneity, thus producing the desired perovskite; see Fig. 1b. Also, gel formation is used to manufacture thin films [20, 21]. The calcination temperature for the formation of the perovskite structure, in this case, is much lower than that of the solid-state reaction method.

2.3 Solid-State Reaction Method

The fabrication of perovskite materials results from a high-temperature solid-state reaction. The desired stoichiometry of the perovskite can be obtained from the mixture of solid reactants (raw precursors), frequently nitrates, hydroxides, oxalates, alkoxides, carbonates, acetate, and oxides, with a pre-established ratio. The process involves the raw precursors, milling intensively (which allows high homogeneity), and calcination at high temperatures to enable interdiffusion of the cations, as shown in Fig. 1c. During the first stage, the reaction starts at the point of contact between the particles' surfaces. At this point, the thermodynamical processes of diffusion and interdiffusion by the particle boundary occur with a determinate reaction kinetic rate [14, 22, 23]. The last one depends on the reaction conditions, the structure of the raw precursor, surface area, reactivity, and thermodynamic free energy [24]. Sometimes, organic solvents (propanol-2 and acetone, among others) are used as a mixing medium to get a homogeneous mixture. Recently, it was shown that the use of organic solvent changes the particle size and functional group absorption, this

last owing to the active site generated on the particle surface [14, 25]. On the other hand, mechanical impacts during ball milling, powder charge, spinning rate, critical time, and calcination are highly sensitive for obtaining single phases [26].

2.4 Hydrothermal and Solvothermal Methods

The hydrothermal method is a chemical process applied to synthesize nanoparticles, which leads to crystalline forms with good properties, such as high yield, simple control, low pollution, and minimal energy consumption. This aqueous chemical process is developed in autoclaves under high temperatures and pressure (15 MPa). This implies the ions dissociated precipitate from the solvent, leading to the direct formation of oxide nanopowders. Hydrothermal and solvothermal methods are analogous; the first has water as a solvent, while the second can be realized using any other solvent. Among the advantages of these methods are the use of inexpensive raw materials (oxides, hydroxides, chlorides, and nitrates), control of the particle size, stoichiometry, particle shapes, and avoidance of the secondary phase. The controlled growth of nanoparticles with size and shape selection is essential for exploring their unique physical and chemical properties. The key to the control is during the dissolution-nucleation-growth process, which is an environment favoring the predominance of size and shape growth over particle-particle aggregation and finite diffusion on the nanoparticle. In the case of the hydrothermal method, the amount of water and the use of organic stabilizers contribute to controlling the size and shape of the nanoparticle. In addition, controlled synthesis conditions such as time, pH, temperature, and pressure are of major relevance.

Long and coworkers [27] have studied the formation of alkali metal lead halide nitrate, $Cs_2Pb(NO_3)_2Br_2$, obtained by the hydrothermal method. Raw materials such as CsBr and $Pb(NO_3)_2$ and deionized water solvent were placed in a 23 mL autoclave with a Teflon liner, which was heated at 200 °C for 5 days. Introducing Pb^{2+} cations with active lone-pair electrons in the nitrate system induces an enhanced luminescence property and increases the birefringence. Another study has been reported for the synthesis based on nanoporous titanates such as $SrTiO_3$, $BaTiO_3$, and $PbTiO_3$ for chemical catalysis applications, electrochemical catalysis, and photocatalysis [28]. Recent efforts have been made to understand the solvothermal method for growing $CH_3NH_3PbX_3$ (X = I, Br, Cl) crystals using various acids (HI, HBr, and HCl) as halogen sources and to study the growth behavior as a function of reaction conditions and halide composition [29].

2.5 Freeze-Drying Method

Freeze-drying (lyophilization) method appears to be one of the most attractive due to its remarkable ability to stabilize and facilitate the handling of colloidal suspensions. In this method, adding additives are necessary to obtain successful results.

This process allows converting solutions or colloidal suspensions into highly stable solids. Three consecutive synthesis steps are required, from the spraying of fine droplets of solution into liquid nitrogen until the sublimation of the solvent in the absence of the liquid phase: the freezing step, a primary drying step, and secondary drying [30]. Freezing (from liquid suspension) is an essential parameter since it defines the crystalline structure of ice. In contrast, the primary and secondary drying stages involve the sublimation of ice from the frozen product (due to the reduced pressure) and the removal of absorbed water from the product (water of non-sublimated ice), respectively. Thus, the crystalline ice structure depends on the cooling rate, degree of supercooling, and annealing [31]. The advantage of freeze-drying is that it enables monodisperse particle sizes and homogeneous distributions, which have been obtained due to the fast freezing of solvent and drying process of solvent sublimation.

Double perovskite structures, such as Sr_2CoTeO_6 and $Sr_2(Mg_{0.99}Co_{0.01})TeO_6$, were synthesized by freeze-drying [32]. Desired stoichiometric ratios of raw material of $SrCO_3$, $Co(C_2H_3O_2)_2$, $Mg(C_2H_3O_2)_2$, and TeO_2 were dissolved in dilute aqueous nitric acid, and the solutions were cooled under liquid nitrogen. The frozen solutions were subsequently freeze-dried, and the powders obtained were ground and heat treated. The synthesis of $CsPbBr_3$ perovskite nanocrystals was obtained from a mixture of docusate sodium, PbX_2, and CsX (X = Cl, Br) [33]. The precursor solution was immersed in liquid nitrogen and then freeze-dried to form $CsPbBr_3$ powder. Other examples of perovskite production include $NaNbO_3$ [34], $MTiO_3$ (M = Ca, Sr, Ba) [35], and $SrMo_{0.9}Co_{0.1}O_{3-\delta}$ [36], among others.

2.6 Magnetron Sputtering Deposition

Magnetron sputtering is a powerful technique widely used in thin-film deposition. Magnetron sputtering is a process in which the atoms are ejected from the surface of a bulk target material under ion bombardment of sufficient energy and subsequently deposited on the substrate [37]. The sputtering system consists of a pair of electrodes (cathode and anode) within an isolated chamber. The cathode assembly consists of an electrode and a bulk target material. The target is fabricated out of materials that are to be deposited. Substrates are placed on the anode. The process involves the creation of a plasma using inert gases such as argon at a high electric field. The positively charged ions from the plasma are accelerated toward the cathode and strike the negative electrode with sufficient force to eject atoms out of the target. The dislodged particles from the face of the target will condense on surfaces that are placed in proximity to the cathode. Conductive materials can be deposited using a DC power supply, and insulators are deposited using an RF power supply. The main advantages of this process can be highlighted: its comparably high deposition rates, ease of sputtering any compound, extremely high adhesion of films, ability to coat heat-sensitive substrates, and high purity of the deposited films [38]. A broader discussion on magnetron sputtering can be found in the literature [39].

Several materials can be evaporated, among them oxide and halide perovskites, offering the possibility to grow consecutive layers of different materials with a nanometric-micrometric control of the thickness, high homogeneity, high level of crystallization, and reduced surface roughness. In addition, the growth can be performed at room temperature, avoiding the material stress, which can be understood as a consequence of the significant mismatch between the thermal expansion coefficient of the perovskites and the substrate and could be responsible for the layers cracking and degradation [38]. Recently, Yasunori et al. [40] developed a rotational maze-shaped RF magnetron sputtering plasma by combining three kinds of rod magnets for improving target utilization and thin-film preparation. The target utilization rate can reach approximately 64.8%, which is two to three times that of conventional stable sputtering.

Recently, Peddigari et al. [41] reported that Dy_2O_3-doped $(K_{0.5}Na_{0.5})NbO_3$ thin films were deposited onto quartz and Pt/Ti/SiO2/Si substrates by RF magnetron sputtering. The effect of oxygen mixing percentage (OMP) on physical properties was reported. The change in the deposition rate with OMP significantly modifies the third-order nonlinear optical properties. The third-order nonlinear susceptibility ($|\chi^{(3)}|$) values of $(K_{0.5}Na_{0.5})NbO_3 + 0.5$ wt%Dy_2O_3 films increased from 0.69×10^{-3} esu to 1.40×10^{-3} esu with an increase in OMP. Besides, the nonlinear absorption coefficient $\beta = 1.70$ cm/W was obtained for the 100% OMP film. Likewise, the effect on the target-substrate distances (D = 30–70 mm) in the deposition process by RF magnetron sputtering of perovskite thin films was investigated [42]. The sputter deposition rate in the indicated interval of target-substrate distances decreased by more than twice. The study by nonlinear optical microscopy in perovskite films revealed the inhomogeneous distribution of second-harmonic generation, which is related to a nonuniform distribution of mechanical stresses in the medium. Other compounds with perovskite structures were excellently deposited $Pb(Zr,Ti)O_3$ [43], $CH_3NH_3PbI_3$ (MAPI) [44], and $CsPbBr_3$ and $CsPbCl_3$ [45].

2.7 Pulsed Laser Deposition (PLD)

Pulsed laser deposition (PLD) is a flexible technique where, through the process of ablation (i.e., the photonic energy is coupled to the bulk target material via electronic processes and chemical reactivity) of various materials, the perovskite film growth takes place. The operating principle of PLD involves the direct irradiation of a high-energy pulsed laser beam on the surface of a target material (source) over a period [46, 47]. This process can be conducted in ultrahigh vacuum conditions or in the presence of inert or chemically reactive gases (helium, nitrogen, or argon) [48]. During interaction with the incident laser beam, the temperature of the laser-irradiated surface of the bulk material increases rapidly, resulting in matter vaporizing and ionization processes. The ejected vapor (containing many energetic species—atoms, clusters, ions, and/or molecules) in the form of a plasma plume

expands perpendicularly away from the irradiated area. If a substrate is positioned in front of the plume's expansion trajectory, a fraction of the vaporized species condenses on this target surface into agglomerates and particles, promoting the uniform growth of thin films [49]. Thus, basicament, the PLD process, consists of the following steps: (i) interaction of the laser beam with the solid; (ii) plasma formation, heating, and initial isothermal expansion; (iii) adiabatic expansion; (iv) the interaction of the plume with the environment; and (v) nucleation and growth of the thin films on a substrate.

In this process, thermodynamic factors such as lattice misfits and chemical defects can be excluded, and the growth can be described entirely kinetically. The PLD method requires detailed knowledge of the plasma plume characteristics as a function of the different deposition parameters, which allows determining whether these parameters can control the plume's composition. Besides, the epitaxial growth of the perovskite thin films is strongly correlated to the laser fluence (which generates the plasma plume), composition, background gas pressure, and environmental conditions [46–49]. In general, PLD has attractive advantages compared to other film deposition methods 146, such as the stoichiometric condition of the target material transferred to the substrate is preserved; versatility in the homogenous growth of multilayer structures, heterostructures, and superlattices by manipulating different target materials; the film thickness can be controlled by fixing the operating parameters; high structural quality of the films; and fast and scalable [50, 51]. However, some drawbacks limit the improved performance of this technique, including the deposition process being restricted to substrates of small geometric dimensions (usually not more than 1 cm^2) and the appearance of surface roughness in the films because of large clusters and droplets arising from the chosen target material.

Substitution of three oxygen ions (O^{2-}) with two nitrogen ions (N^{3-}) in a layered perovskite $SrTiO_3$ yields a three-dimensional perovskite-type $SrTiO_3$:N film [52]. The incorporation of nitrogen results in a reduction in the optical bandgap energy, which allows visible light absorption [52]. Also, structures of $BaTiO_3$ (BTO) and $Ba_{0.5}Sr_{0.5}TiO_3$ (BST) thin films were fabricated at a substrate temperature of 700 °C and oxygen pressure of 0.1 mbar on quartz substrate via PLD [53]. The nonlinear absorption coefficients (β) of the thin films via the modified Z-scan technique were found to be 87 cm/W and 130 cm/W for BTO and BST thin films, respectively, at a wavelength of 488 nm. Similar work was reported on the effects of substrate temperature and oxygen pressure on nonlinear optical properties of PLD-deposited $BaTiO_3$ thin films [54]. The value of β is found to increase with the substrate temperature (9.28 to 57.54 cm/W), while it increases with an increase in oxygen pressure to 0.1 mbar (52.93 to 57.54 cm/W) and falls for higher oxygen pressure (57.54 to 46.52 cm/W) [54]. Thickness-dependent nonlinear optical properties of $Bi_{0.5}Na_{0.5}TiO_3$ thin-film growth by PLD were shown [55]. The impact of thickness is reflected in the β, which decreased with the increase of the thickness from 208 to 1300 nm at 0.796 to 0.157 cm/W.

3 Nonlinear Optical Characterization Techniques and Recent Advances

Nonlinear optics is the field concerned with explaining the modification of optical properties of a material by the presence of intense light [56]. Nonlinear optical phenomena usually become important when the intensity of the optical fields is high, which most frequently can only be achieved by using lasers. A useful way of formalizing the notion of nonlinear optical interaction is by writing a generalized nonlinear polarization (P^{NL}) expression for a medium as a function of the driving electric field E:

$$P^{NL} = \varepsilon_0 \left[\chi^{(1)} E + \chi^{(2)} E^2 + \chi^{(3)} E^3 + \ldots + \chi^{(N)} E^N \right]. \quad (1)$$

This polarization will define how the medium is influenced by light and also how, in a feedback mechanism, the medium will influence the propagation of light inside it. In Eq. (1), $\chi^{(i)}$ represents the electrical susceptibility of "ith" order. In a more general version of this equation, the $\chi^{(i)}$ have a tensorial nature, and the generation of a particular effect will depend on the orientation of the perovskite crystal planes relative to the electric fields.

The first term in the summation represents the usual linear response of the medium. The second term, with $\chi^{(2)}$, is responsible for phenomena like second-harmonic generation (SHG), sum-frequency generation (SFG), difference-frequency generation (DFG), and optical rectification. This term will only contribute to non-centrosymmetric crystals and at surfaces, where inversion symmetry breaks. SHG, when driven by an ultrashort pulse of central photon frequency ω, generates light at a central frequency of 2ω. This takes place only using virtual states of matter and with no absorption processes (see Fig. 2b). The coherence of the produced light will depend on the type of sample being used. If an ordered material is present, the generated light may have a good temporal and spatial coherence. However, for nanocrystals in a solution, for example, the random orientations and positions will

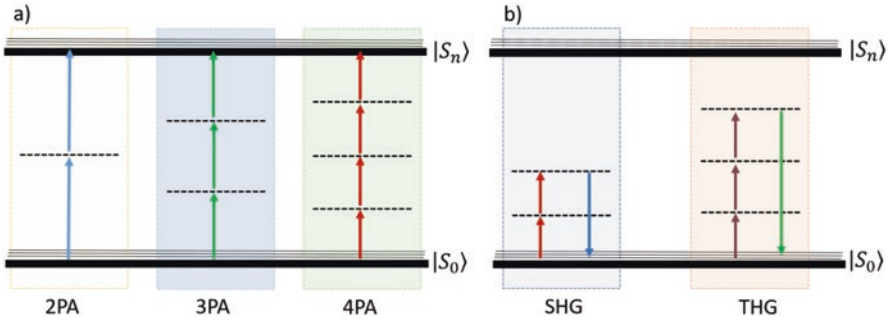

Fig. 2 Diagram of energy describing the multiphoton absorption (**a**) and SHG and THG processes (**b**)

produce incoherent scattered light. When this situation is present, the phenomenon is called hyper-Rayleigh scattering [57]. Usually, the second-harmonic generation ability of a material is reported by the first optical hyperpolarizability (β), which is associated with the microscopic second-harmonic generation and is evaluated as $\beta = \varepsilon_0\chi^{(2)}/N$, in which ε_0 is the vacuum dielectric constant and N is the number of molecules per cm^3. Previous works that studied SHG in perovskites will be discussed in Sect. 3.2. Another $\chi^{(2)}$ effect is the so-called optical rectification and is associated with the generation of a quasi-DC polarization component at the medium. When ultrashort pulsed light is used, the fast oscillation of this nonlinear component can generate radiation at the THz frequency range [58]. Some oxide perovskites and distorted oxide perovskites are used for producing such an effect [59] because of their high $\chi^{(2)}$ values.

The third term in Eq. (1), relative to $\chi^{(3)}$, includes processes like third-harmonic generation (THG, Fig. 2b), two-photon absorption (2PA, Fig. 2a), and the generation of a nonlinear refractive index (Kerr effect) proportional to the light intensity. The THG is analog to SHG and is a process responsible for generating light at three times (3 ω) the driving frequency of the incident light (ω). Furthermore, it does not have a symmetry selection rule as SHG. The two-photon absorption is a process that allows the electronic transition of a lower energy state to a higher one that would not be possible with the energy of a single photon. With two photons, this transition becomes possible by an intermediate virtual state created by the nonlinear interaction of light with the energy states of matter. The sum of the energies of the photons must be enough to surpass the energy difference of the states.

Furthermore, concerning higher-order nonlinearities and their applications, it is interesting to mention that all the odd terms ($\chi^{(i)}$, $i \geq 3$) lead to multiphoton absorption, like $i = 3$ in 2PA and $i = 5$ in 3PA (Fig. 2a). The parameter used to quantify the magnitude of these effects is the multiphoton absorption cross section ($\sigma^{(N)}$) which is a purely molecular parameter. Such coefficient can be defined as $\sigma^{(N)} = R^{(N)}/I^N$, where N is referred to the number of absorbed photons, I is the intensity, and R is the rate of transition given by [1]:

$$R_{ng}^{(2)} = \left| \sum_m \frac{\mu_{nm}\mu_{mg}E^2}{\hbar^2\left(\omega_{mg} - \omega\right)} \right|^2 2\pi\rho_f\left(\omega_{ng} - 2\omega\right) \tag{2}$$

$$R_{og}^{(3)} = \left| \sum_{mn} \frac{\mu_{on}\mu_{nm}\mu_{mg}E^3}{\hbar^3\left(\omega_{ng} - 2\omega\right)\left(\omega_{mg} - \omega\right)} \right|^2 2\pi\rho_f\left(\omega_{og} - 3\omega\right) \tag{3}$$

$$R_{pg}^{(4)} = \left| \sum_{omn} \frac{\mu_{on}\mu_{nm}\mu_{mg}E^4}{\hbar^4\left(\omega_{og} - 3\omega\right)\left(\omega_{ng} - 2\omega\right)\left(\omega_{mg} - \omega\right)} \right|^2 2\pi\rho_f\left(\omega_{pg} - 4\omega\right) \tag{4}$$

Since multiphoton absorption can be described as the imaginary part of the odd terms of the electronic susceptibility, the nonlinear refraction can be written as a

function of the real part. The most significant nonlinear refraction contribution is the third-order one ($\chi^{(3)}$), given rise to the nonlinear refractive index n_2. The total refractive index is written as $n = n_0 + n_2 I$, with n_0 representing the linear refractive index and n_2 given by [60]:

$$n_2 = \frac{2\pi\omega_p e^2}{n_0^2 m^2 c^3 \omega^4} \tag{5}$$

in which ω_p is the plasma frequency; e and m are the electron charge and mass, respectively; c is the light speed; and ω is the laser frequency. Perovskites have been reported as promising in the framework of new materials for nonlinear optical applications since they allow modulating, by the synthesis processes, the quantum confinement effect in lower-dimensional structures. With this, consequently, high values of nonlinear optical coefficients are reached. This way, the following subsections will show a series of results of multiphoton absorption, nonlinear refraction, second-harmonic generation, and third-harmonic generation obtained in oxide perovskites.

The nonlinear optical phenomena discussed until now by considering Eq. (1) are all restricted to the time interval in which E is applied, i.e., the time width of the light pulse. However, in a more general description of nonlinear optics, the interaction of a light pulse with matter can induce transient or permanent changes in matter, which persist beyond the time of the pulse. As a first example, this includes the generation of an excited state by the absorption of light. Such a phenomenon can change the local optical absorption and refraction characteristics of a material. One can imagine an experiment in which a pulse with intensity $I_p \propto |E_p|^2$ creates a transient change in absorption proportional to its intensity. This is a frequent case in a transient absorption (TA) experiment [61]. By sending a weaker pulse to investigate the sample (with an electric field E_{p2}) at a time τ after the first one, the nonlinear polarization experienced in the material could be written as $P^{NL} = \varepsilon_0[\chi^{(1)}E_{p2} + Im(\chi^{(3)'})|E_p|^2E_{p2}]$. Here, $\chi^{(3)'}(\tau)$ is the time-dependent proportionality constant that describes the change in absorption. The "(3)" is used because the second term in the expression can be interpreted as a third-order process on the electric field ($|E_p|^2 E_{p2}$). Because of this, experiments that investigate photoinduced dynamics of matter can be understood within the scope of nonlinear optics. This particular TA experiment illustrates one type of optical response measured in time-resolved ultrafast optical spectroscopy (TRUS) setups. So, apart from absorption changes, there are many other types of probing methods. They include measuring changes in reflectivity, birefringence, Faraday rotation, etc. [62–64]. The excitation (pumping) of materials is also done with nonresonant light and can be driven by multiple pulses at different wavelengths. The applications of TRUS to oxide perovskites will be treated in Sect. 3.3. There, it will be possible to address how the optical transients provide an essential characterization tool for investigating the states and dynamics of materials after light excitation has taken place.

3.1 Multiphoton Absorption and Nonlinear Refractive Index

Concerning techniques for determining the magnitude of multiphoton absorption (usually, absorption cross section) and the nonlinear refractive index, the Z-scan technique [65, 66], see Fig. 3a), is the most used one due to its ease of implementation and data acquisition. Fundamentally, Z-scan is based on translating the sample of optical length (L) around a focal region (z_0) and acquiring the experimental normalized transmittance (NT) as a function of the sample position (z). The NT is given by the transmittance measured closer to focus (where nonlinear effects are more pronounced) divided by transmittance far from focus. The experimental NT can be fitted by $T_N(z) = \frac{1}{\sqrt{\pi} q_0(z,0)} \int_{-\infty}^{\infty} \ln\left[1 + q_0(z,0) e^{-t^2}\right] dt$, in which $q_0 = \beta I_0 L \left(1 + \left(z^2 / z_0^2\right)\right)^{-1}$, such that, for example, the two-photon absorption cross section is obtained by $\sigma_{A2F} = \hbar\nu\, \beta / N$, being β the nonlinear absorption coeficient. For nonlinear refractive index determination, the NT is measured through an iris place in the far field; this setup is called close-aperture Z-scan. On the other hand, for MPA cross-section determination, the total signal is acquired by the photodetector and is called open-aperture Z-scan. Examples of typical nonlinear refractive index and multiphoton absorption are shown in Fig. 3b and c, respectively.

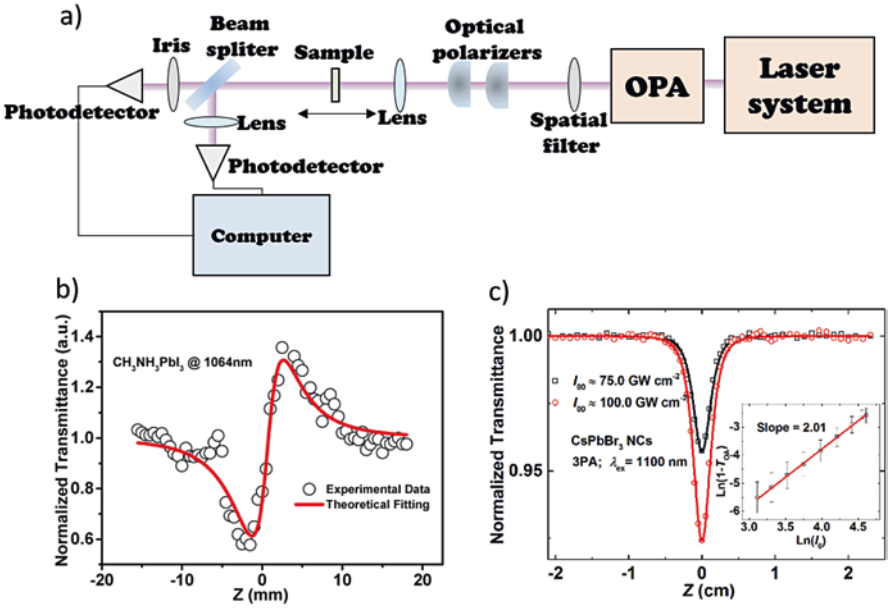

Fig. 3 (**a**) Representation of the Z-scan technique experimental setup and its typical signal for (**b**) nonlinear refraction obtained from close-aperture configuration. Reprinted from Zhang et al. [2], with permission from American Chemical Society. Copyright (2016). (**c**) Nonlinear absorption obtained from open-aperture configuration. Reprinted from Chen et al. [67], with permission from Springer Nature. Copyright (2017)

To avoid spurious effects in the MPA and nonlinear refraction, it is usually more suitable to employ femtosecond laser systems (30–200 fs) with KHz repetition rate [68]. Feng Zhou et al. [68] extensively analyzed the MPA process in several types of perovskites, and most of the studies employed systems with such configuration for the determination of the MPA magnitude.

Another route to determine the MPA cross section for fluorescent samples is the multiphoton fluorescence excitation (MPFE); see Fig. 4a. Such a technique is based on monitoring the fluorescence signal for different multiphoton excitation wavelengths. It is important to highlight that some experimental parameters, such as the temporal width of the laser pulse (τ_p), beam waist (w_0), and collection efficiency of

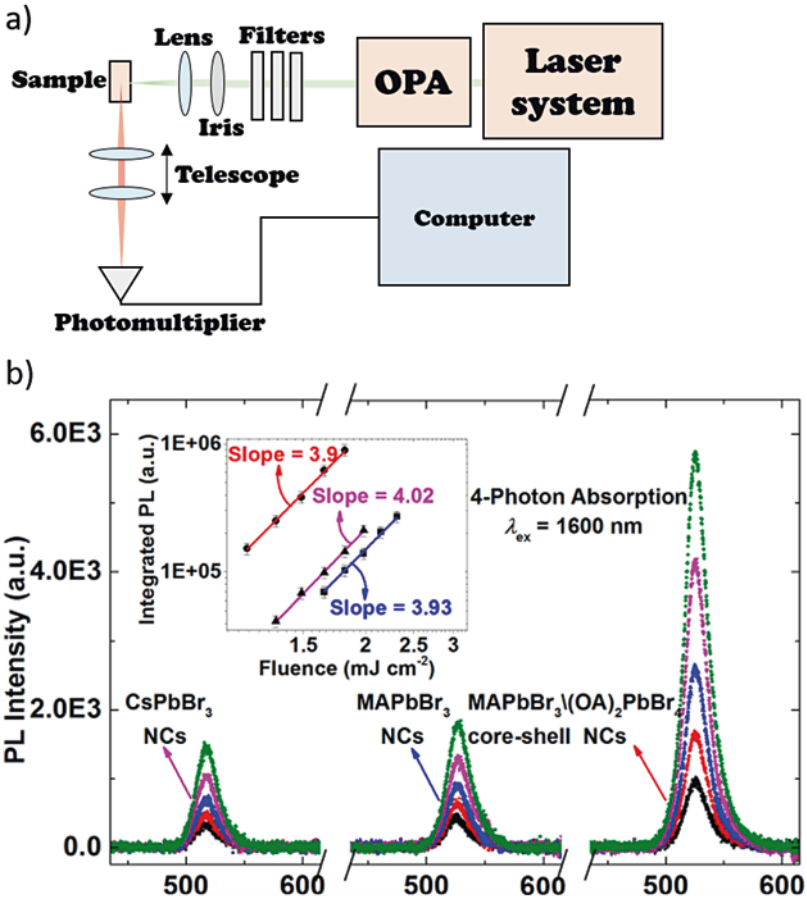

Fig. 4 (**a**) MPFE experimental setup representation and (**b**) fluorescence signal obtained through four-photon excitation. Reprinted from Chen et al. [67], with permission from Springer Nature. Copyright (2017). The inset of Fig. 4b shows the angular coefficient of the integrated fluorescence signal as a function of the laser power, indicating that the collected fluorescence is due to a four-photon absorption process

the system (η), need to be previously determined. In addition, the studied sample's fluorescence quantum yield (ϕ) and molar concentration (N) also need to be known. Details about the technique are described by W. Chen et al. [67]. In this paper, distinct multiphoton absorptions in perovskites are reported; see Fig. 4b. It should be mentioned that the MPFE technique does not need a high sample molar concentration to determine the fluorescence signal. Furthermore, low laser power can be used to excite the sample, once the experimental acquisition is carried out by a photomultiplier or a high sensibility spectrometer. Such features bring some advantages to the MPFE over the Z-scan.

Considering some of the works about nonlinear optical processes in oxide perovskites, Bing Gu et al. is worth mentioning [69]. This paper determined the refractive index and MPA of thin polycrystalline films of bismuth ferrite ($BiFeO_3$). This compound has received significant attention owing to its applications in several technological areas, such as, for instance, sensors and actuators [70]. Moreover, $BiFeO_3$ can present notable physical features [71–75]. Regarding ferroelectric nonlinear optical properties of thin films, researchers have shown that these kinds of compounds have good capabilities for employment as optical devices due to their optical transparency and great nonlinearities [76, 77]. Regarding linear optical properties, the transparency of $BiFeO_3$ thin film was determined, ranging from 58% up to 91% from visible to the infrared spectral window. Concerning the third-order optical nonlinearities, the femtosecond Z-scan technique was used. NLO results revealed a two-photon absorption coefficient, β, of 16.0 ± 0.6 cm/GW and a nonlinear refractive index, n_2, of (1.46 ± 0.06) × 10^{-4} cm^2/GW at 780 nm. Bing Gu et al. compared their results with other reported works [78–81] and have shown that $BiFeO_3$ thin films are a promising material for nonlinear optical devices.

Materials with ferroelectric properties are excellent materials for a large number of applications: memories devices, oscillators, filters, and tunable phase shifters [82–84]. In this context, Saravanan et al. [82] reported a large three-photon absorption in $Ba_{0.5}Sr_{0.5}TiO_3$ (BST) films at 800 nm. Nonlinearities were studied through the Z-scan technique for different growth temperatures (500–800 °C with 100 °C steps) and pulse durations (25 ps, 2 ps, and 6 ns). Three-photon absorption coefficients (α_3) of 45 × 10^{-22} cm^3/W^2 and 60 × 10^{-22} cm^3/W^2, for samples growth at 700 and 800°, respectively, were obtained. Regarding measurements with 2 ps, it was observed a decrease of α_3 for BTS at 700 nm (α_3= 15 × 10^{-22} cm^3/W^2) in comparison to 800 nm (α_3= 85 × 10^{-22} cm^3/W^2). A two-photon absorption coefficient (β) was obtained for BTS at 500, 600, 700, and 800 nm for 6-ns pulses. The results showed values of 30, 40, 55, and 110 cm/GW, respectively. Finally, results of n_2 were also performed for different temperatures and pulse temporal width. Considering measurements with 25 ps and 2 ps, n_2 displays an increase with growth temperature (from 500 °C up to 800 °C with 100 °C steps), ranging from 0.11 × 10^{-14} cm^2/W up to 3.25 × 10^{-14} cm^2/W and 0.18 × 10^{-14} cm^2/W up to 1.0 × 10^{-14} cm^2/W, respectively.

In the same vein of ferroelectric materials, S. Li et al. [85] reported a study of $Bi_{3.15}Nd_{0.85}TiO_{12}$ ($BNT_{0.85}$) thin films. Nonlinear optical measurements were performed through the Z-scan technique at 800 nm, 300 ps, and a 10 Hz repetition rate. The two-photon absorption coefficient and nonlinear refraction index were

Table 1 Nonlinear absorption and refraction coefficient for different perovskite oxides

Sample	$\lambda(nm)$, τ_p	β(cm/GW)	γ(cm²/GW)
$Bi_2Nd_2Ti_3O_{12}$	532, 35 ps	3.10×10^5	0.70
$Bi_{3.75}Nd_{0.25}Ti_3O_{12}$	532, 35 ps	5.24×10^4	0.94
$Bi_{3.25}La_{0.75}Ti_3O_{12}$	532, 35 ps	3.00×10^4	0.31
$Bi_{3.25}La_{0.75}Ti_3O_{12}$	800, 140 fs	-6.67×10^3	1.92×10^{-3}
$Bi_{3.25}Nd_{0.85}Ti_3O_{12}$	800, 300 fs	1.15×10^2	-8.15×10^{-3}
$BiFeO_3$	780, 350 fs	16	1.5×10^{-4}

Adapted from [85]

determined. It was observed a two-photon absorption coefficient and nonlinear refraction of 1.15×10^2 cm/GW and -8.15×10^{-3} cm²/GW, respectively. Nonlinear absorption processes are linked to oxygens vacancies, which are mainly responsible for indirect transition processes via defect levels. Also, values of β and γ were compared with similar materials, and values are displayed in Table 1.

3.2 Second-Harmonic Generation Techniques

Second-harmonic generation (SHG) is defined by the incidence of two photons ω and the generation of one photon of frequency 2 ω. SHG can be measured by using different approaches [86]. In general, techniques to measure SHG are classified into four groups [86]: far-field SHG polarimetry, wide-field SHG interference imaging, scanning SHG microscopy, and near-field SHG microscopy.

The most used technique is the far-field SHG polarimetry [86], which was proposed by Franken in 1961 [87]. This method is based on the incidence, in a specific angle, of polarized light at frequency ω in the sample surface and the measurement of light at frequency 2 ω, in the transmission or reflection configuration, by a sensitive photomultiplier. Denev et al. [86] illustrate the experimental setup, considering the transmission configuration, in the case of transparent compounds or in the reflection configuration for nontransparent compounds. At this point, it is relevant to highlight that the far-field SHG polarimetry is similar to scanning SHG microscopy [86]. The main difference is that in scanning SHG microscopy, an objective focuses the excitation beam (with frequency ω) on the sample being scanned across its surface.

The wide-field SHG interference contrast imaging technique is based on the fact that each part of the compound can generate second-harmonic signals with different amplitudes and phases. Therefore, it is possible to produce images from different parts of the sample using the phase change through this technique. An external reference beam (in the same frequency of the generated second harmonic (2 ω)) [88] is used to interfere with the second harmonic of the sample generating a phase contrast which is converted into an intensity one [89]. In order to amplify the SHG phase contrast, it is possible to adjust the relative phase of the reference and the

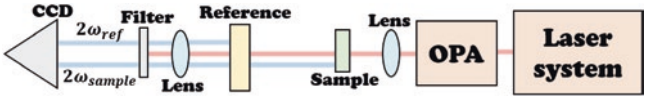

Fig. 5 Illustration of the experimental setup of the wide-field SHG interference contrast imaging technique

second harmonic of the sample [88]. A simple way to do that is by turning the reference crystal in its azimuthal axis. Figure 5 illustrates a basic concept of this technique.

Finally, the near-field SHG microscopy technique is based on the principles of near-field scanning optical microscopy (NSOM). In other words, NSOM is a technique that acquires the evanescent optical waves in the near field through a probe (usually a fiber probe) applied nearby the sample surface [90]. In the near-field SHG microscopy technique, a pulsed laser is used to pump the sample, and a probe (similar to the NSOM) is employed to acquire the SHG signal in the near field nearby the surface sample. It should be mentioned that there are other possible experimental setups regarding this technique [91, 92]. A possible experimental setup for a near-field SHG microscopy is shown in ref. [86].

A convenient method of quantifying the capacity of SHG microscopically is by determining the first hyperpolarizability (β). Such parameter is commonly determined by the hyper-Rayleigh scattering (HRS) technique which is usually performed with a reference sample with β value well known. To perform such a technique, the laser beam is focalized in the sample with an intensity I(ω), and a nonlinear scattering with an intensity $I(2\ \omega)$ is collected by a photomultiplier tube. Experimental details such as a dark box and bandpass filters need to be used to avoid spurious signals. Figure 6 also shows the experimental setup of the hyper-Rayleigh scattering (HRS) technique (Fig. 6a) and typical signals of second-harmonic generation (Fig. 6b), which was obtained through HRS technique.

It is important to mention that the frequency of excitation is usually far from resonance to avoid enhancement effects. Usually, HRS measurements are performed with a wavelength of excitation at 1064 nm, resulting in a β at 532 nm. Another point that should be highlighted, for fluorescent samples, is that the analysis should be carefully performed to guarantee that the collected signal originates from the nonlinear scattering and not from fluorescence generated by multiphoton excitation. Considering all these factors, a relationship between the intensities $I(\omega)$ and $I(2\ \omega)$ can be written as follows:

$$I\left(2\omega\right) = G\sum_{i=1}^{M} N_i \beta_i^2 I^2\left(\omega\right) \tag{6}$$

in which G is an instrumental factor, N_i is the concentration of scattering elements, and the index i represents the number of scattering elements in the sample. The instrument factor can be determined by performing HRS measurements in a

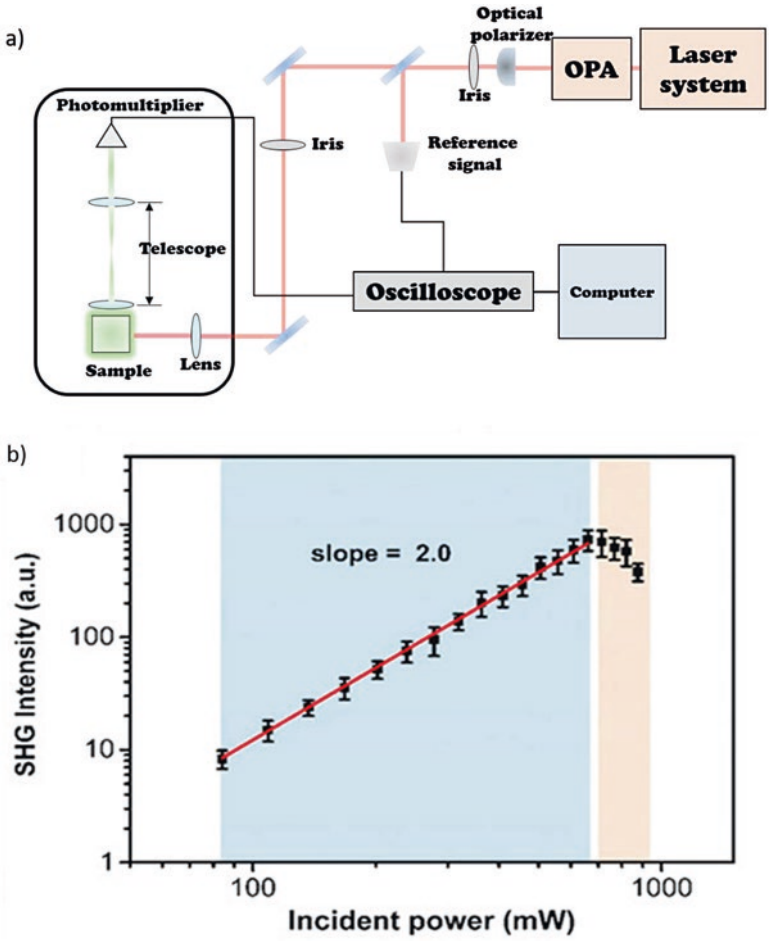

Fig. 6 (**a**) Representation of experimental setup of the hyper-Rayleigh scattering technique, and (**b**) shows the linear behavior in log-log scale (blue region) of SHG signal in function of the incident intensity of 1D quiral lead perovskite. Reprinted from Abdelwahab et al. [93], with permission from American Chemical Society. Copyright (2018). The figure also shows (red region) the damage caused owing the high incident power. Figure 6b adapted from [93]

sample with a value of β already known. In this way, the first hyperpolarizability can be determined by applying the following equation:

$$\beta^{\text{sample}} = \sqrt{\frac{\beta_{\text{ref}}^2 \alpha_{\text{sample}}}{\alpha_{\text{ref}}}} \tag{7}$$

in which α_{sample} and α_{ref} are the angular coefficients of the linear behavior between the nonlinear scattering intensity (I(2 ω)) and the concentration of the scattering element (N) for the sample and the reference, respectively.

Table 2 First hyperpolarizability for several perovskite oxides

	$BaTiO_3$	$KNbO_3$	KTP	$LiNbO_3$	ZnO 90–200	ZnO 20
β (10^{-24} esu/nm^3)	5.16	21.8	33.5	16.3	7.12	0.33

Adapted from [97]

Nowadays, many authors have considered using perovskite alkaline niobates (PAN) as compounds for second-harmonic bioimaging microscopy [94–96]. In this way, it is essential to study such compounds to verify their employment capacity. For this purpose, the most used method for determining the nonlinear optical properties is usually hyper-Rayleigh Scattering (HRS) measurements [94]. For instance, Silva et al. performed a nonlinear study, through the external reference HRS method [94], in $NaNbO_3$ nanocrystals with an orthorhombic crystalline structure. Their results showed that the first hyperpolarizability per volume is 0.93×10^{-29} esu/nm^3. In the same context, Joulaud et al. [97] investigated the SHG employing the HRS in several nanocrystals colloidal suspensions ($BaTiO_3$, $KNbO_3$, $KiTiOPO_4$ (KTP), $LiNbO_3$, and ZnO) (Table 2).

3.3 Time-Resolved Ultrafast Optical Spectroscopy in Oxide Perovskites

Time-resolved ultrafast optical spectroscopy (TRUS) is used to study the dynamics of oxide perovskite materials when excited by resonant and nonresonant ultrashort pulses of light [61]. This is done by monitoring the nonlinear optical response of the medium beyond the temporal width of excitation pulses by using delayed probe pulses. The TRUS experiments may use more than one excitation (pump) and probe pulses to cover all the characterization needs of a material. The resolution of the experiment may range from tens of attoseconds to a few picoseconds. Furthermore, the spectral content of the pulses can span from X-ray wavelengths to optical, IR, and THz frequencies. A depiction of a simple TRUS technique is shown in Fig. 7. It will be used as a comprehensive example for guiding the discussion of this section. In it, the delay between pump and probe is produced by using a mechanical delay line, and then both pulses are spatially overlapped at the sample. This generally allows one to measure the nonlinear optical response induced by the intense pump pulse at the material. Particularly, this setup allows one to measure the sample's transient absorption (TA) and reflectance (TR) by measuring the transmission and reflection of the probe pulse. This can be done with single-pixel detectors (P for TA and P2 for TR), as in Fig. 7, or with spectrometers, depending on the relevance of resolving the spectral content of the probe. An element like an optical chopper can be used for alternately exciting the sample with the pump pulse. This allows the transient effects to be measured for each time delay between pumps and probes. With this in mind, the applications of TRUS experiments to oxide perovskites can be discussed. Because of the variety of physical properties in the oxide perovskites, the works on the topic vary greatly in the choice of the TRUS methods. So now, an

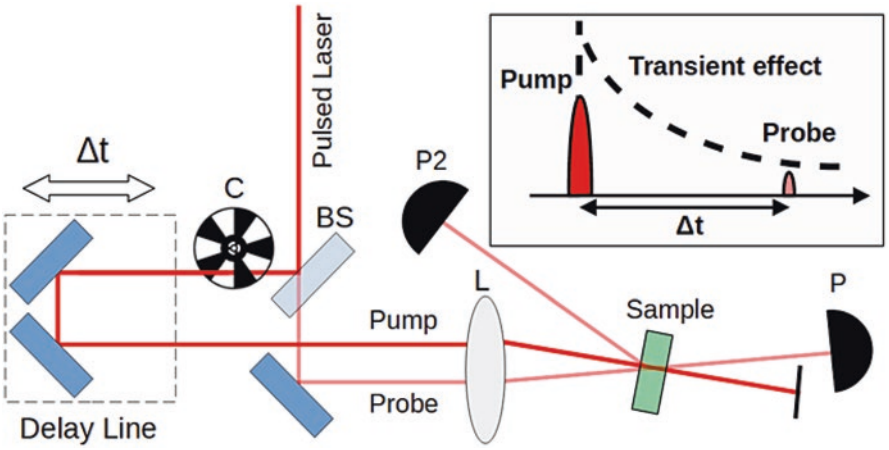

Fig. 7 A simple TRUS experiment using a pump-probe approach for simultaneously measuring TA and TR. The photodetectors are named P for TA and P2 for TR. The convergent lens is L. The adjustable time between pump and probe is Δt

overview will be presented considering some classes of studies in perovskites, relating them to the type of TRUS experiments that take part in the investigations.

First, it is important to remark that the nature of the transient effects in TRUS can be dubious if experiments are not performed to sort them out. An important work by Smolin et al. [62] corrects the interpretation of the TR spectra of epitaxial $LaFeO_3$ thin films [98]. By performing TA and TR measurements on $LaFeO_3$, $LaMnO_3$, and $LaMnO_3/LaFeO_3$ type I heterojunction thin films, it was possible to separate the thermal contributions of $LaFeO_3$ from the electronic contributions. This was possible because $LaMnO_3$ is a semiconductor with a lower bandgap (0.6 e V) compared to $LaFeO_3$ (2.4 eV), so the optical excitation of $LaMnO_3$ carriers at photon energies below the bandgap of $LaFeO_3$ does not allow any carriers to flow to it. Thus, in this case, only heat flows to the $LaFeO_3$ layers. Hence, the only transient response from $LaFeO_3$ seen in the transient spectra of the bilayers is related to thermal effects. This result made it possible to reassign a whole region of the transients previously associated with carriers to a thermal effect. The same thermal spectral dependence was confirmed by ellipsometry measurements with varying temperatures. Determining the correct electronic and thermal effects in TA and TR was important in this article to obtain the correct carrier lifetime and the correct interpretation of the carrier dynamics. This information is very important for appropriately designing light-harvesting materials, like in photovoltaic and photocatalytic applications. For more studies and considerations about thermal effects affecting perovskites and related systems, there are other relevant published works [99–101]. Another recent work proposes a method using Kramers-Kronig relations for discerning between the changes in the TA and TR spectra caused by the real or imaginary parts of the dielectric constant [102]. This is not normally considered in interpreting these spectra and can be relevant principally on thin films. One of the applications of the work

was on a halide perovskite, but the method can be directly applied to oxide perovskites and may provide new insights for these materials.

Another recent work with perovskite heterostructures, by Hoglund et al. [103], has explored time-domain Brillouin scattering (TDBS) to measure the phonon scattering times of $SrTiO_3$–$CaTiO_3$ superlattices. The authors wanted to study the properties of this class of materials as a function of the $SrTiO_3$/$CaTiO_3$ layer's thicknesses in the regime of very few unit cells per layer (from 2 to 27). Two structural transitions between the samples could be identified by the change in the phonon scattering times, which also exhibited a strong correlation with the changes in thermal conductivity in the material. To understand how this result was obtained, it is important to explain the technique. The TDBS experiment is closely related to the TR experiment depicted in Fig. 8. The principal addition to the experimental setup is the use of an acoustic transducer which is in touch with the sample and is excited by the pump pulse (400 nm in this experiment). This excitation provides ultrafast heating of the transducer, producing coherent acoustic waves that will propagate throughout the sample of interest. This means that the pump pulse does not need to be resonant with the sample, only with the transducer absorption spectrum. The propagating waves produce modulations of the refractive index, and this Brillouin response can then be sensed by a NIR probe (800 nm). The modulations act in analogy to a Fabry-Perot interferometer, producing partial constructive and destructive interferences. By measuring the lifetime of these oscillations at the TDBS signal, one measures the phonon scattering times. This, and related techniques, are already extensively applied in the literature on oxide perovskites [104–107]. The discussed work serves

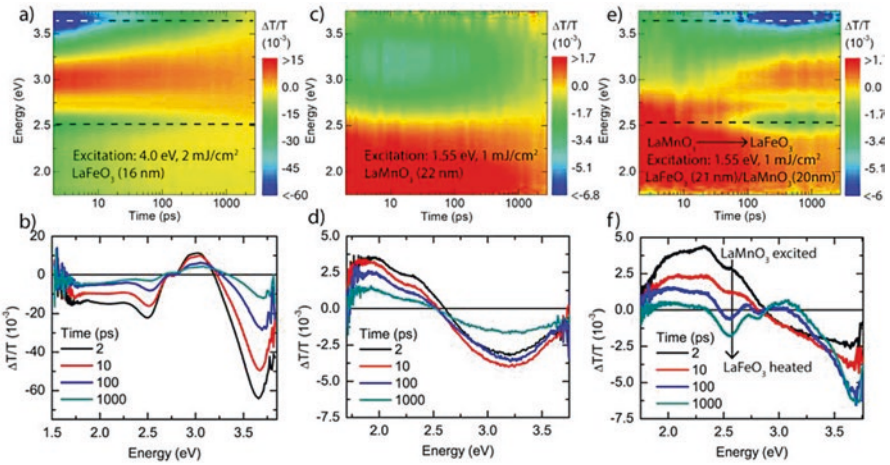

Fig. 8 The TA measurements performed on $LaFeO_3$ (**a**), $LaMnO_3$ (**c**), and $LaFeO_3$/$LaMnO_3$ bilayers (**e**). In (**b**, **d**, and **f**), it is possible to see slices for specific times of the transients in (**a**, **c**, and **e**), respectively. In (**e** or **f**), one observes the thermal transient response of $LaFeO_3$ at the heterojunction and its similarity with the response in (**a** or **b**) in the 2.5 to 3.6 eV region (dashed lines). Reprinted from Smolin et al. [62], with permission from American Chemical Society. Copyright (2022)

as an additional example of the usefulness of this acousto-optical TRUS method to the characterization and applications of perovskites and, more specifically, for pursuing sophisticated thermal and infrared responses in these materials [103].

An important emphasis of TRUS studies in oxide perovskites is in the field of correlated and quantum materials. Particularly, transition metal oxides (TMOs) and other quantum materials already have extensive literature on ultrafast spectroscopy, and extensive reviews on the field, including some perovskites, were already written [108–112]. This chapter's subset of TMOs includes doped and undoped perovskite, double perovskite, perovskite-like, and distorted perovskite structures. What is interesting in correlated materials is the coupling between their different degrees of freedom (DOF). Charge, lattice, spin, and orbital DOF combine to give TMOs unique properties, sensitive to variations in temperature, pressure, chemical doping, and electric and magnetic fields [108]. The states of these materials can range from Mott-Hubbard insulators to correlated or superconducting metals. What is important in using TRUS in TMOs is not only the characterization scope (a) but also the possibility of using TMOs as nonlinear and optical control materials (b). Concerning (a), TRUS can excite specific DOF of the materials and then probe the coupling of the other ones in space and time. This is particularly important to match experiment and theory on TMOs but is itself the straightforward path to applications (b). It is important to emphasize that photoinduced phase transitions (PIPTs) frequently occur when correlated materials are excited, and this is considered a form of optical (coherent) control. A plethora of studies explores metal-to-insulator transitions (MITs), photoinduced transient superconductive phases, modulation of ferroelectric or magnetic order, and many other examples. Some recent works spanning different applications and discoveries will be highlighted.

Recent work on the distorted perovskite $LiNbO_3$ has promoted the idea of nonlocal nonlinear phononics [113]. In this work, a vibrational mode was excited on the surface of ferroelectric $LiNbO_3$ with a mid-IR pump pulse (20 THz central frequency, 150 fs pulse duration). A nonlinear coupling mechanism with the excited phonons produced polaritons, which could be seen to propagate to a length of the material beyond the excitation region. Moreover, these polaritons produced a significant change in the ferroelectric polarization, even being able to reverse it. This was observed using femtosecond stimulated Raman spectroscopy (FSRS) as a probing method for the polariton and vibrational Raman modes. More specifically, the change of the Raman coefficient was evidence of a change in ferroelectric polarization, illustrating the usefulness of FSRS for probing ferroelectric states. So, the nonlocal use of phononics produced desired macroscopic transient changes on the material and effectively avoided the unwanted effects of phononic excitation, which include, e.g., heating. Another recent work involving magnetic order was published for the $DyFeO_3$ perovskite [63]. This material exhibited a PIPT from an antiferromagnetic (AFM) phase to a weak ferromagnetic (WFM) one. This phase was coherently produced by using mid-IR pulses and probed by measuring the Faraday rotation of a 1.55 eV (~800 nm) transmitted probe. The PIPT can be explained as a photomagnetic effect in which the mid-IR pump induces lattice distortions and coherently changes the exchange interaction between Fe and Dy. This change

creates the new nonequilibrium metastable phase (WFM), with a lifetime superior to 250 ps. This phenomenon is essentially different from a direct phonon-magnon coupling, in analogy with the phonon-polariton coupling from ref. [113]. Hence, it shows how the mid-IR response of correlated materials can be rich. Furthermore, a change in magnetic order is also possible to be obtained in $DyFeO_3$ with excitation at optical [114, 115] and THz frequencies [116]. In the former, the authors used the optomagnetic inverse Faraday effect. This effect is responsible for coherently controlling the sample's spins, altering the magnetic moment in an ultrafast time. This is done with an intense circularly polarized pump at 1.55 eV, and the effect is probed as in [63] (Faraday rotation probe). For the THz experiments in $DyFeO_3$, the production of magnons presented good tunability by exciting the spins directly at their quasi-ferromagnetic and quasi-antiferromagnetic modes. Furthermore, when electronic transitions are also present in the THz spectrum, their resonant excitation causes an enormous change in the magnetic anisotropy of the material. This then promotes a nonlinear excitation of the spins with a higher strength than the pure Zeeman interaction with the ferromagnetic and quasi-antiferromagnetic modes. Changing the THz pulse's spectral content makes it possible to control the nonlinearity of the spin excitations. This experiment used the same type of faraday NIR probe as in [18, 20]. These examples illustrate part of the landscape of ferroelectric and ferromagnetic TRUS studies of oxide perovskites.

Various double perovskite systems are also known for their magnetic phase transitions and MITs, which were already studied by TRUS [117]. Furthermore, many of such materials exhibit oxygen transport [118]. Recent work had successfully used a TR setup to study the $EuBaCo_2O_{5.39}$ perovskite [119]. By pumping the material at ~3.1 eV, it was possible to probe the oxygen displacement dynamics with pulses ranging from 650 nm (1.9 eV) until 7800 nm (0.16 eV). Both pump and probe had pulse widths on the order of 120 fs. The dynamics observed upon excitation yielded a fast component of 1–3 ps, associated with a strong electron-phonon interaction due to charge transfer from the O orbital to the Co orbital upon the UV excitation (Fig. 9). The lifetime of coherent phonons associated with oxygen movement matches this time scale, thus supporting this interpretation.

Additionally, another slow component was detected, with lifetimes on the 100–1000 ps time scales. This was associated with the motion of the oxide ions in the CoO layer of the material. More interestingly, the transport of the material occurs on an ultrafast time scale. It happens right after the charge transfer lifts the degeneracy of the e_g Co orbital due to the Jahn-Teller effect. This change in the orbital configuration perturbs the surroundings of the Co ions, favoring the transport of O ions due to the decrease in the potential barrier of crossing to a different position in the EuO layer. Additionally, the same UV pump was used to perform time-resolved electron diffraction, with electron probes accelerated at 75 keV and with picosecond time resolution. Diffraction probes with electrons or X-rays are very important in studying correlated materials, providing direct evidence of transient lattice changes. So, the crossover between optical and other ultrafast methods always contributes to the characterization objectives. This was verified in this work, because the transients of the optical spectroscopy and electron diffraction had the same dynamics within the time resolution of the experiment.

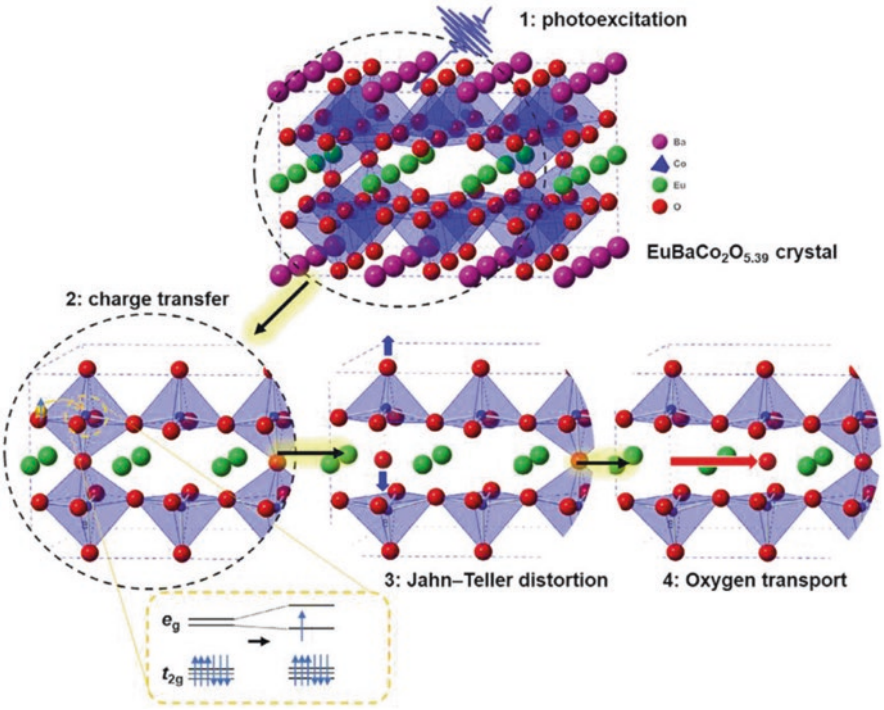

Fig. 9 The process of oxygen transport in the $EuBaCo_2O_{5.39}$ double perovskite is summarized in this figure. Reprinted from Hada et al. [119], with permission from Elsevier. Copyright (2021)

4 Applications of Perovskite Oxide in Photonic Devices

With the development of frequency doubling in ruby laser by Franken in 1961 [87] and the subsequent observation of other nonlinear optical effects, applications based on nonlinear properties have prompted a significant development in material science, laser technology, and information technology. Next, some photonic applications on perovskites are presented.

4.1 Nonlinear Waveguides

Waveguides require developing materials with significant electro-optical coefficients, high optical transparency, high second-order nonlinear coefficients, low scattering losses, and high modulation speeds [120]. The optimization of electro-optical coefficients in $BaTiO_3$ from 148 pm V^{-1} to 1000 pm V^{-1} makes them attractive for nonlinear waveguides (see Fig. 10a) [121]. Eltes and co-workers [121] show that the low-loss slot-waveguide structures ($\alpha_p = 6$ dB cm^{-1}) and high-Q ring resonator cavities ($Q > 20{,}000$) enhanced the optical confinement in the $BaTiO_3$ layer and reduced

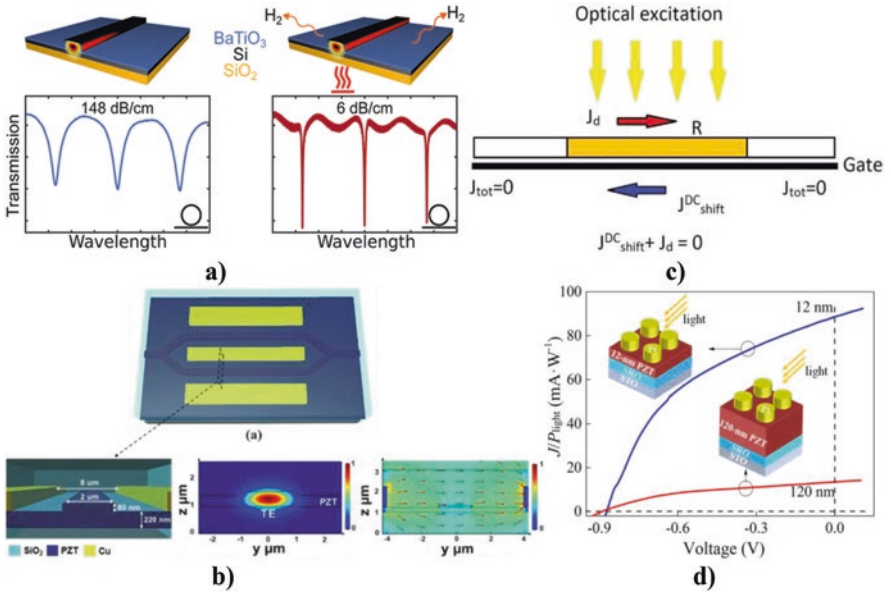

Fig. 10 (**a**) Schematics of waveguide and propagation losses at different stages during the processing. Comparison of ring resonator spectra before and after annealing. The spectra are taken from ring resonators with a 75 μm radius and gap sizes close to critical coupling. Reprinted from Eltes et al. [121], with permission from American Chemical Society. Copyright (2016). (**b**) Schematic of the designed PZT EO modulator. 3D view: two arms of the MZI waveguide act as phase modulators and are driven via a push-pull dual-drive electrode structure (upper). Cross section: 300 nm PZT film is deposited on SiO_2/Si substrate (lower left). A ridge waveguide is formed by etching 80 nm thick PZT (lower middle). DC field distribution in the modulator (lower right). Reprinted from Ban et al. [124], with permission from IEEE Xplore. Copyright (2022). (**c**) In the optically excited region, R, shift current, J_{DC} shift is countered by the diffusion current, J_d, so that the total current is divergence less in the steady state. A gate in proximity can be used to measure the charge density profile capacitively and hence the shift current in a steady state. Reprinted from Barik et al. [125], with permission from American Physical Society. Copyright (2020). (**d**) Comparison of *J*–*V* of the Pt/PZT structure at different light intensities and thickness-dependent. Reprinted from Tan et al. [126], with permission from Springer Nature. Copyright (2019)

bending losses. Fabrication of low-loss $BaTiO_3$-based slot-waveguide structures was obtained by annealing the waveguides in oxygen at 350 °C for 60 min. Theoretical modeling indicates that $BaTiO_3$ exhibits a strong nonlinear conversion between electrical and optical properties [122]. These studies have shown that the nonlinear electro-optical coefficients, low scattering losses, and optimization of optical confinement play an essential role in the incorporation of functional and high nonlinear $BaTiO_3$ in a nonlinear waveguide. Likewise, the $LiNb_6Ba_5Ti_4O_{30}$ thin film exhibits high transparency, anisotropic performance, and strong nonlinearity. The strong nonlinear response, measured by SHG (excitation at 800 nm) as a function of the incident beam polarization, with the output polarization fixed at 0 (P-out) and 90° (S-out), is attributed to the LNBTO phase and the interface between $LiNb_6Ba_5Ti_4O_{30}$ and $LiTiO_2$ [123].

4.2 Eletro-optic Modulators

High-performance solid-state electro-optic oxides possess both significant and fast electro-optic effects. Lithium niobate ($LiNbO_3$) is one of the best candidates widely used as an electro-optical modulator in telecommunications [127]. However, $LiNbO_3$ is less efficient as it has a low electro-optic effect and high-temperature dependence. Contrarily, $BaTiO_3$ is a highly promising material for developing high-performance electro-optical modulators due to its large Pockels coefficients [128]. This last is several orders of magnitude higher than $LiNbO_3$. Eltes et al. [129] fabricated electro-optic high-speed modulators based on the Pockels effect in barium titanate $BaTiO_3$ thin films into the back end of line of a photonic integrated circuit (PIC) platform (see Fig. 10b). The devices show excellent induced phase shift as a function of the applied voltage ($V_\pi L$) of 0.2 V cm, and considering the propagation losses α, the value is $V_\pi L\alpha$ of 1.3 VdB, which works at high speed (25 Gbit s^{-1}), and can be tuned at low-static power consumption (100 nW). Similar results in $BaTiO_3$ deposited by MBE show a large Pockels coefficient of 923 pm/V and electro-optic modulators response measured in photonic waveguides translate to a $V_\pi L$ of 0.45 V cm and achieve a high modulation bandwidth until 50 Gbit s^{-1} [130]. However, ferroelectric lanthanum-modified lead zirconate titanate (PLZT) thin film epitaxially grown showed significant enhancement when compared to $BaTiO_3$, due to control of PLZT material phase [131]. This process has the advantage of enhancing the electro-optic coefficient (>120 pm/V) and lowering the propagation loss (1.1 dB/cm) of PLZT compared with $BaTiO_3$. The optical modulator exhibited a half-wave voltage (V_π) of 6.0 V ($V_\pi L$ = 4.5 V cm) and optical modulation of up to 56 Gbit s^{-1}. Electro-optical modulators developed with another material type, lead zirconate titanate (PZT) thin film on the SiO_2/Si substrate, shows $V_\pi L$ of 1.4 V cm, propagation loss of 1.8 dB/cm, and 3-dB bandwidth of 12 GHz [124]. Recently shown was the influence of deposition method parameters as gun position, substrate height, and sputtering pressure on the quality of film and, consequently, on their electro-optical operation [132]. In this sense, thick epitaxial $BaTiO_3$ films grown by RF magnetron sputtering on $SrTiO_3$-templated silicon-on-insulator substrates, using the optimized conditions, yield an equivalent Pockels coefficient as high as 157 pm/V and $V_\pi L$ of 0.421 V cm.

4.3 Photovoltaic Solar Cells

The bulk photovoltaic effect (BPVE), in general, creates a steady photocurrent (or photovoltage) from sunlight, which occurs in noncentrosymmetric materials (or lacking inversion symmetry), such as ferroelectrics, possessing an above-bandgap [133]. BPVE-based solar cells include, among others, ferroelectric materials that have the capacity to minimize the energy loss due to the shift current mechanism. The general formalism developed by Sipe and Shkrebtii [134] shows that the shift

current is related to nonlinear optical effects, due to the second-order susceptibility tensor interaction with monochromatic light. In this sense, the second-order optical response to an optical excitation in noncentrosymmetric materials is a kinetic effect and includes a DC current and shift currents. This last one is generated by the sequential tunneling of electrons in one direction (see Fig. 10c). It is noted that intraband and interband contributions are considered in the formalism, and that applies to a semiconductor under optical excitation with photon energy $\hbar\omega < E_g$ (E_g bandgap). Thus, when electrons are excited from the valence band to the conduction bands in a noncentrosymmetric material, the charge center of the electrons is also shifted, giving rise to a nonlinear current.

Tan et al. [126] designed a ferroelectric $Pb(Zr_{0.2}Ti_{0.8})O_3$ ultrathin-film material, which can fulfill these criteria for better photovoltaic response. By reducing the film thickness, they achieved high power conversion efficiencies in ferroelectric photovoltaics. As the light intensity increases from 8.9 to 22.3 mW/cm^2, the current density (J_{SC}) increases correspondingly from 0.68 to 1.94 mA/cm^2, while the open-circuit voltage (V_{OC}) remains at ~ −0.84 V. Compared with the 120-nm film, the 12-nm ultrathin film exhibits a nearly 6.5-fold enhancement in J_{SC} per unit light intensity, which is attributed to the reduced recombination and lower areal series resistance, as shown Fig. 10d. Although BPVE and depolarization field (E_{dp}) effect are bulk effects, nonlinear optical effects of perovskite and Schottky barrier effect contribute to the optimization. Considering that formalism is applied to single phase, Pal et al. [135] modified the phenomenological model to a two-phase system and calculated experimentally in $Ba_{1-x}(Bi_{0.5}Li_{0.5})_xTiO_3$ system [136, 137]. Other reports in perovskite-type $BaTiO_3$ thin films and Bi_2FeCrO_6 multilayer thin films exhibit a solar cell conversion efficiency of 0.6% and 8.1%, respectively, overcoming the suggested limitations on power conversion efficiencies in the photovoltaic effect [138]. The ferroelectricity in Bi_2FeCrO_6 films originates from the $6s^2$ lone pair on Bi^{3+} ions, as is the case in $BiFeO_3$, $BiMnO_3$, and Bi_2FeMnO_3.

4.4 Nonlinear Phononics

The emerging area of nonlinear phononics studies what happens after large-amplitude coherent phonon oscillations are produced in materials [139]. If linear phononic excitation by IR light would lead to an average zero displacement of an oscillating mode, a nonlinear excitation can, e.g., provide nonzero net transient displacements of atoms in a lattice. This, of course, in a general sense, changes the properties of a material in a nonequilibrium, controllable, and totally unique manner. This signifies another way of manipulating materials that are beyond changing pressure, temperature, chemical doping, etc. [140]. So, it is seen as highly valuable in the field of highly correlated materials, in which many oxide perovskites are included. Only recently, with intense mid-IR laser sources, it has become possible to excite large-amplitude oscillations in IR-active phonons and observe this class of phenomena, including nonlinear couplings between different vibrational modes

[141], and degrees of freedom of the material. Particularly, near structural phase transitions, the nonlinear phononical response is amplified, making oxide perovskites very good candidates for this kind of application [142]. In Sect. 3.3, some works were already cited showing the possibilities of controlling electric and magnetic order [63, 143] in perovskites and, particularly, how the nonlinear coupling of phonons and polaritons is an example of nonlocal phononics [113]. Another very explored research topic is the tuning of superconductivity in cuprates, which remains a challenge [139, 144, 145].

5 Conclusion and Perspectives

A comprehensive and critical review of the nonlinear optical properties of oxide perovskites and their applications has been addressed. Moreover, the preparation methods are accompanied by particulars of synthesis of thin films, characterization techniques, and results emanating from them. Subsequently, devices based on the nonlinear properties of oxide perovskite materials and some projections into their future use have been provided. This review is motivated by the recent resurgence of complex oxides owing to their Pockels effect, multiple-frequency generation, two-photon absorption (2PA), Stark effect, electromagnetically induced transparency (EIT), stimulated Raman scattering (SRS), stimulated Brillouin scattering (SBS), and stimulated light scattering (SLS) that, in principle, would pave the way for unique multifunctional devices for heat and optical sensors, nonlinear waveguides, electro-optic modulators, and photovoltaic solar cell, to cite a few.

Acknowledgments The authors acknowledge financial support from the Brazilian institutions: São Paulo Research Foundation (FAPESP) under the grants 2020/04835-3, 2018/11283-7, and 2021/11484-5.

References

1. Boyd, R. W. (2008). *Nonlinear optics* (3rd ed.).
2. Zhang, R., Fan, J., Zhang, X., Yu, H., Zhang, H., Mai, Y., Xu, T., Wang, J., & Snaith, H. J. (2016). Nonlinear optical response of organic-inorganic halide perovskites. *ACS Photonics, 3*, 371–377.
3. Sadighian, J. C., Wilson, K. S., Crawford, M. L., & Wong, C. Y. (2020). Evolving stark effect during growth of perovskite nanocrystals measured using transient absorption. *Frontiers in Chemistry, 8*, 1–8.
4. Shi, L., Gayen, T., Budansky, Y., Yoo, K., Secor, J., Harvey, T., Harvey, G., Shumyatsky, P., Nolan, D., & Alfano, R. (2020). Enhanced stimulated raman scattering of solvent due to anharmonic energy transfer from resonance Raman solute molecules. *Optics Express, 28*, 21792.
5. Lembrikov, B. I. (2019). Introductory chapter: Nonlinear optical phenomena. In: *Nonlinear Optical – Novels Results in Theory and Applications*, pp. 1–13.

6. Perovskite fever. *Nature Materials*, *13* (2014) 2014.
7. Rottwitt, K., & Tidemand-Lichtenberg, P. (2014). *Nonlinear optics: Principles and applications*.
8. Clabel H, J. L., Zabotto, F. L., Nogueira, I. C., Schio, P., Garcia, D., De Lima, O. F., Leite, E. R., Moreira, F. M. A., & Cardoso, C. A. (2014). Magnetoelectric properties of laminated $La_{0.7}Ba_{0.3}MnO_3$–$BaTiO_3$ ceramic composites. *Journal of Magnetism and Magnetic Materials, 364*, 18–23.
9. Clabel H, J. L., Ferri, F. A., Zabotto, F. L., Rivera, V. A. G., Nogueira, I. C., Garcia, D., De Lima, O. F., Leite, E. R., Pereira-da-silva, M. A., & Cardoso, C. A. (2016). Grain size and interfacial interdiffusion influence on the magnetic and dielectric properties of magnetoelectric $La_{0.7}Ba_{0.3}MnO_3$–$BaTiO_3$ composites. *Journal of Magnetism and Magnetic Materials, 407*, 160–166.
10. Golsdschmidt, V. V. M. (1962). Die gesetze der krystallochemie. *Naturwissenschaften Naturwissenschaften, 14*, 477–485.
11. Bartel, C. J., Sutton, C., Goldsmith, B. R., Ouyang, R., Musgrave, C. B., Ghiringhelli, L. M., & Scheffler, M. (2019). New tolerance factor to predict the stability of perovskite oxides and halides. *Science Advances, 5*, 1–10.
12. Hwang, J., Ha, N. Y., Chang, H. J., Park, B., & Wu, J. W. (2004). Enhanced optical nonlinearity near the photonic bandgap edges of a cholesteric liquid crystal. *Optics Letters, 29*, 2644.
13. Athayde, D. D., Souza, D. F., Silva, A. M. A., Vasconcelos, D., Nunes, E. H. M., Da Costa, J. C. D., & Vasconcelos, W. L. (2016). Review of perovskite ceramic synthesis and membrane preparation methods. *Ceramics International, 42*, 6555–6571.
14. Clabel H, J. L., Awan, I. T., Pinto, A. H., Nogueira, I. C., Bezzon, V. D. N., Leite, E. R., Balogh, D. T., Mastelaro, V. R., Ferreira, S. O., & Marega, E. (2020). Insights on the mechanism of solid state reaction between TiO_2 and $BaCO_3$ to produce $BaTiO_3$ powders: The role of calcination, milling, and mixing solvent. *Ceramics International, 46*, 2987–3001.
15. Zhang, X., Yue, J., Zhao, Y., Yan, Z., Zhu, G., Liu, L., Xu, H., & Yu, A. (2021). Synthesis of tetragonal $BaTiO_3$ nano-particle via a novel tartaric acid co-precipitation process. *Ceramics International, 47*, 7263–7267.
16. Fomekong, R. L., You, S., Enrichi, F., Vomiero, A., & Saruhan, B. (2019). Impact of oxalate ligand in co-precipitation route on morphological properties and phase constitution of undoped and Rh-Doped $BaTiO_3$ nanoparticles. *Nanomaterials, 9*, 1–13.
17. Haron, W., Wisitsoraat, A., & Wongnawa, S. (2017). Nanostructured perovskite oxides – $LaMO_3$ (M=Al, Co, Fe) prepared by co-precipitation method and their ethanol-sensing characteristics. *Ceramics International, 43*, 5032–5040.
18. Hu, H., Huang, C. E., Nan, J., Wang, H., & Shen, C. (2019). Effects of co-precipitation method on microwave dielectric properties of $0.7CaTiO_3$–$0.3SmAlO_3$ ceramics. *Materials Research Express, 7*, 0–9.
19. Nguyen, T. A., Pham, V., Pham, T. L., Nguyen, L. T. T., Mittova, I. Y., Mittova, V. O., Vo, L. N., Nguyen, B. T. T., Bui, V. X., & Viryutina, E. L. (2020). Simple synthesis of $NdFeO_3$ nanoparticles by the co-precipitation method based on a study of thermal behaviors of Fe (III) and Nd (III) hydroxides. *Crystals, 10*, 219.
20. Clabel H, J. L., Ferreira, S. O., & Marega, E. (2018). Fluorescence by confocal scanning microscopy in $Ba(Ti_{0.97}Er_{0.03})O_3$ thin films. In: *Latin America Optics and Photonics Conference. OSA Technical Digest (Optica Publishing Group, 2018)*. p. Tu5A.4.
21. Clabel H, J. L., Awan, I. T., Lozano, G., Pereira-Da-Silva, M. A., Romano, R. A., Rivera, V. A. G., Ferreira, S. O., & Marega, E. (2020). Understanding the electronic properties of $BaTiO_3$ and Er^{3+} doped $BaTiO_3$ films through confocal scanning microscopy and XPS: The role of oxygen vacancies. *Physical Chemistry Chemical Physics, 22*, 15022–15034.
22. Buscaglia, M. T., Bassoli, M., Buscaglia, V., & Vormberg, R. (2008). Solid-state synthesis of nanocrystalline $BaTiO_3$: Reaction kinetics and powder properties. *Journal of the American Ceramic Society, 91*, 2862–2869.

23. Carter, R. E. (1961). Kinetic model for solid-state reactions. *The Journal of Chemical Physics, 34*, 2010–2015.
24. Anthony, R. (2014). *West, Solid state chemistry and its applications*.
25. Clabel H, J. L., Nicolodelli, G., Lozano, G. C., Rivera, V. A. G., Ferreira, S. O., Pinto, A. H., Li, M. S., & Marega, E. (2021). The extrinsic nature of double broadband photoluminescence from the $BaTiO_3$ perovskite: generation of white light emitters. *Physical Chemistry Chemical Physics, 23*, 18694–18706.
26. Gotor, F. J., Achimovicova, M., Real, C., & Balaz, P. (2013). Influence of the milling parameters on the mechanical work intensity in planetary mills. *Powder Technology, 233*, 1–7.
27. Long, Y., Dong, X., Zeng, H., Lin, Z., & Zou, G. (2022). Layered Perovskite-like Nitrate $Cs_2Pb(NO_3)2Br_2$ as a multifunctional optical material. *Inorganic Chemistry, 61*, 4184–4192.
28. Huang, X., Zhao, G., Wang, G., & Irvine, J. T. S. (2018). Synthesis and applications of nanoporous perovskite metal oxides. *Chemical Science, 9*, 3623–3637.
29. Guo, F., Zhang, B., Wang, J., Bai, H., Guo, R., Huang, Y., & Ren, P. (2018). Facile solvothermal method to synthesize hybrid perovskite CH_3NH_3PbX_3 (X = I, Br, Cl) crystals: publisher's note. *Optical Materials Express, 8*, 210.
30. Chen, G., & Wang, W. (2007). Role of freeze drying in nanotechnology. *Drying Technology, 25*, 29–35.
31. Eggenhuisen, T. M., Munnik, P., Talsma, H., De Jongh, P. E., & De Jong, K. P. (2013). Freeze-drying for controlled nanoparticle distribution in Co/SiO_2 Fischer-Tropsch catalysts. *Journal of Catalysis, 297*, 306–313.
32. Ortega-San Martin, L., Chapman, J. P., Lezama, L., Sánchez-Marcos, J., Rodríguez-Fernández, J., Arriortua, M. I., & Rojo, T. (2005). Factors determining the effect of Co(II) in the ordered double perovskite structure: Sr_2CoTeO_6. *Journal of Materials Chemistry, 15*, 183–193.
33. Zhang, X., Gao, L., Zhao, M., Miao, Y., Wang, Z., Wang, C., Liu, P., Xu, B., & Guo, J. (2020). Low-temperature direct synthesis of perovskite nanocrystals in water and their application in light-emitting diodes. *Nanoscale, 12*, 6522–6528.
34. Qin, L., Liu, Y., Zhu, S., Wu, D., Wang, G., Zhang, J., Wang, Y., Hou, L., & Yuan, C. (2021). Formation and operating mechanisms of single-crystalline perovskite $NaNbO_3$ nanocubes/few-layered Nb2CTxMXene hybrids towards Li-ion capacitors. *Journal of Materials Chemistry A, 9*, 20405–20416.
35. Groves, A. R., Ashton, T. E., & Darr, J. A. (2020). High throughput synthesis and screening of oxygen reduction catalysts in the $MTiO_3$(M = Ca, Sr, Ba) perovskite phase diagram. *ACS Combinatorial Science, 22*, 750–756.
36. Acuña, L. M., Cabezas, M. D., Fuentes, R. O., & Muñoz, F. F. (2021). Strong Co-Mo interaction behind unexpected physicochemical properties in $SrMo_{0.9}Co_{0.1}O_3$-δ Perovskite. *Journal of Physical Chemistry C, 125*, 17342–17354.
37. Deng, Y., Chen, W., Li, B., Wang, C., Kuang, T., & Li, Y. (2020). Physical vapor deposition technology for coated cutting tools: A review. *Ceramics International, 46*, 18373–18390.
38. Depla, D. (2021). Sputter deposition with powder targets: An overview. *Vacuum, 184*, 109892.
39. Rofifah, D. (2020). *High power impulse magnetron sputtering*. Elsevier.
40. Ohtsu, Y., Tanaka, R., & Nakashima, T. (2021). Development of rotational maze-shaped RF magnetron plasma for successful target utilization and thin-film preparation. *Japanese Journal of Applied Physics, 60*.
41. Peddigari, M., Patel, V., Bharti, G. P., Khare, A., & Pamu, D. (2017). Microwave dielectric and nonlinear optical studies on radio-frequency sputtered Dy_2O_3-doped KNN thin films. *Journal of the American Ceramic Society, 100*, 3013–3023.
42. Elshin, A. S., Pronin, I. P., Senkevich, S. V., & Mishina, E. D. (2020). Nonlinear optical diagnostics of thin polycrystalline lead zirconate titanate films. *Technical Physics Letters, 46*, 385–388.

43. Akhtari Zavareh, M., Abd Razak, B., Bin Wahab, M. H., Goh, B. T., Mahmoodian, R., & Wasa, K. (2020). Fabrication of $Pb(Zr,Ti)O_3$ thin films utilizing unconventional powder magnetron sputtering (PMS). *Ceramics International, 46*, 1281–1296.
44. Bonomi, S., Marongiu, D., Sestu, N., Saba, M., Patrini, M., Bongiovanni, G., & Malavasi, L. (2018). Novel physical vapor deposition approach to hybrid perovskites: Growth of MAPbI3 thin films by RF-magnetron sputtering. *Scientific Reports, 8*, 1–8.
45. Falsini, N., Ristori, A., Biccari, F., Calisi, N., Roini, G., Scardi, P., Caporali, S., & Vinattieri, A. (2021). A new route for caesium lead halide perovskite deposition. *Journal of the European Optical Society-Rapid Publications, 17*, 0–6.
46. Ogugua, S. N., Ntwaeaborwa, O. M., & Swart, H. C. (2020). Latest development on pulsed laser deposited thin films for advanced luminescence applications. *Coatings, 10*, 1–22.
47. Eason, R. (2007). *Pulsed laser deposition of thin films: Applications-led growth of functional materials*. Wiley.
48. Kek, R., Yap, S. L., Koh, S. F., Nee, C. H., Tou, T. Y., & Yap, S. S. (2020). Effects of background gases and pressure in pulsed laser deposition of Al-doped ZnO. *Thin Solid Films, 701*, 137953.
49. Dawood, M. S., Hamdan, A., & Margot, J. (2015). Influence of surrounding gas, composition and pressure on plasma plume dynamics of nanosecond pulsed laser-induced aluminum plasmas. *AIP Advances, 5*.
50. Bakin, A., & Waag, A. (2011). ZnO epitaxial growth. In *Comprehensive semiconductor science and technology* (pp. 368–395). Elsevier.
51. Ma, C., & Chen, C. (2016). *Advanced nano deposition methods* (pp. 1–31). Wiley.
52. Marozau, I., Döbeli, M., Lippert, T., Logvinovich, D., Mallepell, M., Shkabko, A., Weidenkaff, A., & Wokaun, A. (2007). One-step preparation of N-doped strontium titanate films by pulsed laser deposition. *Applied Physics A: Materials Science & Processing, 89*, 933–940.
53. Behera, S., & Khare, A. (2019). Linear and nonlinear optical properties of $BaTiO_3$ and $Ba_{0.5}Sr_{0.5}TiO_3$ thin films fabricated by pulsed laser deposition technique. *AIP Conference Proceedings*, 2082, 0–4.
54. Behera, S., & Khare, A. (2022). Influence of substrate temperature and oxygen pressure on the structural and optical properties of polycrystalline $BaTiO_3$ thin films grown by PLD. *Materials Science in Semiconductor Processing, 140*, 106379.
55. Pattipaka, S., Joseph, A., Bharti, G. P., Raju, K. C. J., Khare, A., & Pamu, D. (2019). Thickness-dependent microwave dielectric and nonlinear optical properties of $Bi_{0.5}Na_{0.5}TiO_3$ thin films. *Applied Surface Science, 488*, 391–403.
56. Boyd, R. W. (1992). *Nonlinear optics*. Academic Press.
57. Gupta, V. P. (2018). *Molecular and laser spectroscopy: Advances and applications*. Elsevier.
58. Hebling, J., Yeh, K.-L., Hoffmann, M. C., Bartal, B., & Nelson, K. A. (2008). Generation of high-power terahertz pulses by tilted-pulse-front excitation and their application possibilities. *Journal of the Optical Society of America B: Optical Physics, 25*, B6.
59. Dutta, M., Peralta, X. G., Bhalla, A., & Guo, R. (2015). Current status of oxide dielectric materials for terahertz applications-an overview. *Integrated Ferroelectrics, 166*, 108–139.
60. Gaeta, A. L., & Boyd, R. W. (2005). Nonlinear optics, basics | Ultrafast and intense-field nonlinear optics. In: *Encycl. Mod. Opt.* Elsevier, pp. 258–262.
61. Maiuri, M., Garavelli, M., & Cerullo, G. (2020). Ultrafast spectroscopy: State of the art and open challenges. *Journal of the American Chemical Society, 142*, 3–15.
62. Smolin, S. Y., Choquette, A. K., Wang, J., May, S. J., & Baxter, J. B. (2018). Distinguishing thermal and electronic effects in ultrafast optical spectroscopy using oxide heterostructures. *Journal of Physical Chemistry C, 122*, 115–123.
63. Afanasiev, D., Hortensius, J. R., Ivanov, B. A., Sasani, A., Bousquet, E., Blanter, Y. M., Mikhaylovskiy, R. V., Kimel, A. V., & Caviglia, A. D. (2021). Ultrafast control of magnetic interactions via light-driven phonons. *Nature Materials, 20*, 607–611.
64. Ho, P. P., & Alfano, R. R. (1979). Optical Kerr effect in liquids. *Physical Review A, 20*, 2170–2187.

65. Sheik-bahae, M., Said, A. A., & Van Stryland, E. W. (1989). High-sensitivity, single-beam n2 measurements. *Optics Letters, 14*, 955–957.
66. Sheik-Bahae, M., Said, A. A., Wei, T., Hagan, D. J., & Van Stryland, E. W. (1990). Sensitive measurement of optical nonlinearities using a single beam. *IEEE Journal of Quantum Electronics, 26*, 760–769.
67. Chen, W., Bhaumik, S., Veldhuis, S. A., Xing, G., Xu, Q., Grätzel, M., Mhaisalkar, S., Mathews, N., & Sum, T. C. (2017). Giant five-photon absorption from multidimensional core-shell halide perovskite colloidal nanocrystals. *Nature Communications, 8*, 15198.
68. Zhou, F., Ran, X., Fan, D., Lu, S., & Ji, W. (2021). Perovskites: Multiphoton absorption and applications. *Advanced Optical Materials, 9*, 2100292.
69. Gu, B., Wang, Y., Wang, J., & Ji, W. (2009). Femtosecond third-order optical nonlinearity of $BiFeO_3$. *Optics Express, 17*, 10970.
70. Wang, J., Neaton, J. B., Zheng, H., Nagarajan, V., Ogale, S. B., Liu, B., Viehland, D., Vaithyanathan, V., Schlom, D. G., Waghmare, U. V., Spaldin, N. A., Rabe, K. M., Wuttig, M., & Ramesh, R. (2003). Epitaxial $BiFeO_3$ multiferroic thin film heterostructures. *Science (80), 299*, 1719–1722.
71. Yun, K. Y., Noda, M., & Okuyama, M. (2003). Prominent ferroelectricity of $BiFeO_3$ thin films prepared by pulsed-laser deposition. *Applied Physics Letters, 83*, 3981–3983.
72. Basu, S. R., Martin, L. W., Chu, Y. H., Gajek, M., Ramesh, R., Rai, R. C., Xu, X., & Musfeldt, J. L. (2008). Photoconductivity in $BiFeO_3$ thin films. *Applied Physics Letters, 92*, 091905.
73. Pradhan, A. K., Zhang, K., Hunter, D., Dadson, J. B., Loiutts, G. B., Bhattacharya, P., Katiyar, R., Zhang, J., Sellmyer, D. J., Roy, U. N., Cui, Y., & Burger, A. (2005). Magnetic and electrical properties of single-phase multiferroic $BiFeO_3$. *Journal of Applied Physics, 97*, 093903.
74. Wang, Y., Zheng, R. Y., Sim, C. H., & Wang, J. (2009). Charged defects and their effects on electrical behavior in Bi1−xLaxFeO$_3$ thin films. *Journal of Applied Physics, 105*, 016106.
75. Kumar, A., Rai, R. C., Podraza, N. J., Denev, S., Ramirez, M., Chu, Y.-H., Martin, L. W., Ihlefeld, J., Heeg, T., Schubert, J., Schlom, D. G., Orenstein, J., Ramesh, R., Collins, R. W., Musfeldt, J. L., & Gopalan, V. (2008). Linear and nonlinear optical properties of $BiFeO_3$. *Applied Physics Letters, 92*, 121915.
76. Shin, H., Chang, H. J., Boyd, R. W., Choi, M. R., & Jo, W. (2007). Large nonlinear optical response of polycrystalline Bi_325La_075Ti_3O_12 ferroelectric thin films on quartz substrates. *Optics Letters, 32*, 2453.
77. Gu, B., Wang, Y.-H., Peng, X.-C., Ding, J.-P., He, J.-L., & Wang, H.-T. (2004). Giant optical nonlinearity of a $Bi_2Nd_2Ti_3O_{12}$ ferroelectric thin film. *Applied Physics Letters, 85*, 3687–3689.
78. Liu, S. W., Xu, J., Guzun, D., Salamo, G. J., Chen, C. L., Lin, Y., & Xiao, M. (2006). Nonlinear optical absorption and refraction of epitaxial $Ba_{0.6}Sr_{0.4}TiO_3$ thin films on (001) MgO substrates. *Applied Physics B: Lasers and Optics, 82*, 443–447.
79. Elim, H. I., Ji, W., Ma, G. H., Lim, K. Y., Sow, C. H., & Huan, C. H. A. (2004). Ultrafast absorptive and refractive nonlinearities in multiwalled carbon nanotube films. *Applied Physics Letters, 85*, 1799–1801.
80. Rativa, D., de Araujo, R. E., de Araújo, C. B., Gomes, A. S. L., & Kassab, L. R. P. (2007). Femtosecond nonlinear optical properties of lead-germanium oxide amorphous films. *Applied Physics Letters, 90*, 231906.
81. Lopez, R., Haglund, R. F., Feldman, L. C., Boatner, L. A., & Haynes, T. E. (2004). Optical nonlinearities in VO_2 nanoparticles and thin films. *Applied Physics Letters, 85*, 5191–5193.
82. Saravanan, K. V., Raju, K. C. J., Krishna, M. G., Tewari, S. P., & Rao, S. V. (2010). Large three-photon absorption in $Ba_{0.5}Sr_{0.5}TiO_3$ films studied using Z-scan technique. *Applied Physics Letters, 96*, 232905.
83. Saravanan, K. V., Krishna, M. G., & Raju, K. C. J. (2009). Effect of misfit strain and surface roughness on the tunable dielectric behavior of $Ba_{0.5}Sr_{0.5}TiO_3$ thin films. *Journal of Applied Physics, 106*, 114102.
84. Wang, F., & Ma, W. (2019). Phase stability and dielectric properties of (011) epitaxial $(Ba_{0.6}Sr_{0.4})TiO_3$ films. *Journal of Applied Physics, 125*, 082528.

85. Li, S., Zhong, X. L., Cheng, G. H., Liu, X., Wang, J. B., Huang, J., Song, H. J., Tan, C. B., Li, B., & Zhou, Y. C. (2014). Large femtosecond third-order optical nonlinearity of $Bi_{3.15}Nd_{0.85}Ti_3O_{12}$ ferroelectric thin films. *Applied Physics Letters, 105*, 192901.
86. Denev, S. A., Lummen, T. T. A., Barnes, E., Kumar, A., & Gopalan, V. (2011). Probing ferroelectrics using optical second harmonic generation. *Journal of the American Ceramic Society, 94*, 2699–2727.
87. Franken, P. A., Hill, A. E., Peters, C. W., & Weinreich, G. (1961). Generation of optical harmonics. *Physical Review Letters, 7*, 118–119.
88. Fiebig, M., Fröhlich, D., Leute, S., & Pisarev, R. V. (1998). Topography of antiferromagnetic domains using second harmonic generation with an external reference. *Applied Physics B: Lasers and Optics, 66*, 265–270.
89. Kurimura, S., & Uesu, Y. (1997). Application of the second harmonic generation microscope to nondestructive observation of periodically poled ferroelectric domains in quasi-phase-matched wavelength converters. *Journal of Applied Physics, 81*, 369–375.
90. Hecht, B., Sick, B., Wild, U. P., Deckert, V., Zenobi, R., Martin, O. J. F., & Pohl, D. W. (2000). Scanning near-field optical microscopy with aperture probes: Fundamentals and applications. *The Journal of Chemical Physics, 112*, 7761–7774.
91. Bozhevolnyi, S. I., Pedersen, K., Skettrup, T., Zhang, X., & Belmonte, M. (1998). Far- and near-field second-harmonic imaging of ferroelectric domain walls. *Optics Communication, 152*, 221–224.
92. Zayats, A. V., Smolyaninov, I. I., & Davis, C. C. (1999). Near-field microscopy of second-harmonic generation. In: Chikishev, A. Y., Zadkov, V. N., Zheltikov, A. M. (Eds.), *ICONO '98 Laser Spectrosc. Opt. Diagnostics Nov. Trends Appl. Laser Chem. Biophys. Biomed.*, SPIE, pp. 81–92.
93. Abdelwahab, I., Grinblat, G., Leng, K., Li, Y., Chi, X., Rusydi, A., Maier, S. A., & Loh, K. P. (2018). Highly enhanced third-harmonic generation in 2D perovskites at excitonic resonances. *ACS Nano, 12*, 644–650.
94. Barbosa-Silva, R., Silva, J. F., Rocha, U., Jacinto, C., & de Araújo, C. B. (2019). Second-order nonlinearity of $NaNbO_3$ nanocrystals with orthorhombic crystalline structure. *Journal of Luminescence, 211*, 121–126.
95. Thyagarajan, K., Rivier, S., Lovera, A., & Martin, O. J. F. (2012). Enhanced second-harmonic generation from double resonant plasmonic antennae. *Optics Express, 20*, 12860.
96. Nakayama, Y., Pauzauskie, P. J., Radenovic, A., Onorato, R. M., Saykally, R. J., Liphardt, J., & Yang, P. (2007). Tunable nanowire nonlinear optical probe. *Nature, 447*, 1098–1101.
97. Joulaud, C., Mugnier, Y., Djanta, G., Dubled, M., Marty, J.-C., Galez, C., Wolf, J.-P., Bonacina, L., & Le Dantec, R. (2013). Characterization of the nonlinear optical properties of nanocrystals by Hyper Rayleigh Scattering. *Journal of Nanobiotechnology, 11*, S8.
98. Smolin, S. Y., Scafetta, M. D., Guglietta, G. W., Baxter, J. B., & May, S. J. (2014). Ultrafast transient reflectance of epitaxial semiconducting perovskite thin films. *Applied Physics Letters, 105*.
99. Knowles, K. E., Koch, M. D., & Shelton, J. L. (2018). Three applications of ultrafast transient absorption spectroscopy of semiconductor thin films: Spectroelectrochemistry, microscopy, and identification of thermal contributions. *Journal of Materials Chemistry C, 6*, 11853–11867.
100. Forster, M., Cheung, D. W. F., Gardner, A. M., & Cowan, A. J. (2020). Potential and pitfalls: On the use of transient absorption spectroscopy for in situ and operando studies of photoelectrodes. *The Journal of Chemical Physics, 153*.
101. Sheu, Y. M., Trugman, S. A., Park, Y. S., Lee, S., Yi, H. T., Cheong, S. W., Jia, Q. X., Taylor, A. J., & Prasankumar, R. P. (2012). Ultrafast carrier dynamics and radiative recombination in multiferroic $BiFeO_3$. *Applied Physics Letters, 100*.
102. Ashoka, A., Tamming, R. R., Girija, A. V., Bretscher, H., Verma, S. D., Yang, S.-D., Lu, C.-H., Hodgkiss, J. M., Ritchie, D., Chen, C., Smith, C. G., Schnedermann, C., Price, M. B., Chen, K., & Rao, A. (2022). Extracting quantitative dielectric properties from pump-probe spectroscopy. *Nature Communications, 13*, 1437.

103. Hoglund, E. R., Bao, D. L., O'Hara, A., Makarem, S., Piontkowski, Z. T., Matson, J. R., Yadav, A. K., Haislmaier, R. C., Engel-Herbert, R., Ihlefeld, J. F., Ravichandran, J., Ramesh, R., Caldwell, J. D., Beechem, T. E., Tomko, J. A., Hachtel, J. A., Pantelides, S. T., Hopkins, P. E., & Howe, J. M. (2022). Emergent interface vibrational structure of oxide superlattices. *Nature, 601*, 556–561.
104. Lejman, M., Vaudel, G., Infante, I. C., Gemeiner, P., Gusev, V. E., Dkhil, B., & Ruello, P. (2014). Giant ultrafast photo-induced shear strain in ferroelectric $BiFeO_3$. *Nature Communications, 5*, 1–7.
105. Aryana, K., Tomko, J. A., Gao, R., Hoglund, E. R., Mimura, T., Makarem, S., Salanova, A., Bin Hoque, M. S., Pfeifer, T. W., Olson, D. H., Braun, J. L., Nag, J., Read, J. C., Howe, J. M., Opila, E. J., Martin, L. W., Ihlefeld, J. F., & P.E. (2022). Hopkins, observation of solid-state bidirectional thermal conductivity switching in antiferroelectric lead zirconate ($PbZrO_3$). *Nature Communications, 13*, 1–9.
106. Sharma, Y., Musico, B. L., Gao, X., Hua, C., May, A. F., Herklotz, A., Rastogi, A., Mandrus, D., Yan, J., Lee, H. N., Chisholm, M. F., Keppens, V., & Ward, T. Z. (2018). Single-crystal high entropy perovskite oxide epitaxial films. *Physical Review Materials, 2*, 1–6.
107. Yang, C. Y., Wu, P. C., Chu, Y. H., & Lin, K. H. (2021). Generation and coherent control of terahertz acoustic phonons in superlattices of perovskite oxides. *New Journal of Physics, 23*.
108. Zhang, J., & Averitt, R. D. (2014). Dynamics and control in complex transition metal oxides. *Annual Review of Materials Research, 44*, 19–43.
109. Giannetti, C., Capone, M., Fausti, D., Fabrizio, M., Parmigiani, F., & Mihailovic, D. (2016). Ultrafast optical spectroscopy of strongly correlated materials and high-temperature superconductors: a non-equilibrium approach. *Advances in Physics, 65*, 58–238.
110. Metcalf, M., Lazerson, S. A., Ford, O. P., Pickem, M., Giustino, F., Lee, J. H., Trier, F., Bibes, M., Winter, S. M., Valentí, R., Son, Y., Taillefer, L., Heil, C., Figueroa, A. I., Plaçais, B., Wu, Q., Yazyev, O. V., & Bakkers, E. P. A. M. (2020). The 2021 quantum materials roadmap. *Journal of Physics: Materials* OPEN ACCESS The 2021 quantum materials roadmap.
111. Katifori, E. (2021). Comptes rendus physique. *Comptes Rendus Physique, 22*, 3–14.
112. De La Torre, A., Kennes, D. M., Claassen, M., Gerber, S., McIver, J. W., & Sentef, M. A. (2021). Colloquium: Nonthermal pathways to ultrafast control in quantum materials. *Reviews of Modern Physics, 93*.
113. Henstridge, M., Först, M., Rowe, E., Fechner, M., & Cavalleri, A. (2022). Nonlocal nonlinear phononics. *Nature Physics, 18*, 457–461.
114. Kirilyuk, A., Kimel, A. V., & Rasing, T. (2010). Ultrafast optical manipulation of magnetic order. *Reviews of Modern Physics, 82*, 2731–2784.
115. Kimel, A. V., Kirilyuk, A., Usachev, P. A., Pisarev, R. V., Balbashov, A. M., & Rasing, T. (2005). Ultrafast non-thermal control of magnetization by instantaneous photomagnetic pulses. *Nature, 435*, 655–657.
116. Baierl, S., Hohenleutner, M., Kampfrath, T., Zvezdin, A. K., Kimel, A. V., Huber, R., & Mikhaylovskiy, R. V. (2016). Nonlinear spin control by terahertz-driven anisotropy fields. *Nature Photonics, 10*, 715–718.
117. Zhang, Y., Katayama, T., Chikamatsu, A., Schüßler-Langeheine, C., Pontius, N., Hirata, Y., Takubo, K., Yamagami, K., Ikeda, K., Yamamoto, K., Hasegawa, T., & Wadati, H. (2022). Photo-induced antiferromagnetic-ferromagnetic and spin-state transition in a double-perovskite cobalt oxide thin film. *Communications on Physics, 5*, 1–9.
118. Bao, S., Ma, C., Chen, G., Xu, X., Enriquez, E., Chen, C., Zhang, Y., Bettis, J. L., Whangbo, M. H., Dong, C., & Zhang, Q. (2014). Ultrafast atomic layer-by-layer oxygen vacancy-exchange diffusion in double-perovskite $LnBaCo_2O_{5.5}+\delta$ thin films. *Scientific Reports, 4*, 1–5.
119. Hada, M., Ohmura, S., Ishikawa, T., Saigo, M., Keio, N., Yajima, W., Suzuki, T., Urushihara, D., Takubo, K., Masaki, Y., Kuwahara, M., Tsuruta, K., Hayashi, Y., Matsuo, J., Yokoya, T., Onda, K., Shimojo, F., Hase, M., Ishihara, S., Asaka, T., Abe, N., Arima, T., Koshihara, S., & Okimoto, Y. (2021). Photoinduced oxygen transport in cobalt double-perovskite crystal $EuBaCo_2O_{5.39}$. *Applied Materials Today, 24*, 101167.

120. Zgonik, M., Bernasconi, P., Duelli, M., Schlesser, R., Günter, P., Garrett, M. H., Rytz, D., Zhu, Y., & Wu, X. (1994). Dielectric, elastic, piezoelectric, electro-optic, and elasto-optic tensors of $BaTiO_3$ crystals. *Physical Review B, 50*, 5941–5949.
121. Eltes, F., Caimi, D., Fallegger, F., Sousa, M., O'Connor, E., Rossell, M. D., Offrein, B., Fompeyrine, J., & Abel, S. (2016). Low-loss $BaTiO_3$-Si waveguides for nonlinear integrated photonics. *ACS Photonics, 3*, 1698–1703.
122. Jiang, Z., Paillard, C., Xiang, H., & Bellaiche, L. (2020). Linear versus nonlinear electro-optic effects in materials. *Physical Review Letters, 125*, 17401.
123. Huang, J., Wang, H., Li, D., Qi, Z., Zhang, D., Lu, P., Chen, H. T., Yarotski, D. A., Lin, P. T., Zhang, X., & Wang, H. (2020). Room-temperature ferroelectric $LiNb_6Ba_5Ti_4O_{30}$ spinel phase in a nanocomposite thin film form for nonlinear photonics. *ACS Applied Materials & Interfaces, 12*, 23076–23083.
124. Ban, D., Liu, G., Yu, H., Wu, Y., & Qiu, F. (2022). Low driving voltage and low optical loss electro-optic modulators based on lead zirconate titanate thin film on silicon substrate. *Journal of Lightwave Technology, 40*, 2939–2943.
125. Barik, T., & Sau, J. D. (2020). Nonequilibrium nature of nonlinear optical response: Application to the bulk photovoltaic effect. *Physical Review B, 101*, 45201.
126. Tan, Z., Hong, L., Fan, Z., Tian, J., Zhang, L., Jiang, Y., Hou, Z., Chen, D., Qin, M., Zeng, M., Gao, J., Lu, X., Zhou, G., Gao, X., & Liu, J. M. (2019). Thinning ferroelectric films for high-efficiency photovoltaics based on the Schottky barrier effect. *NPG Asia Materials, 11*.
127. Rabiei, P., Ma, J., Khan, S., Chiles, J., & Fathpour, S. (2013). Heterogeneous lithium niobate photonics on silicon substrates. *Optics Express, 21*, 25573.
128. Rosa, A., Tulli, D., Castera, P., Gutierrez, A. M., Griol, A., Baquero, M., Vilquin, B., Eltes, F., Abel, S., Fompeyrine, J., & Sanchis, P. (2017). Barium titanate (BaTiO_3) RF characterization for application in electro-optic modulators. *Optical Materials Express, 7*, 4328.
129. Eltes, F., Mai, C., Caimi, D., Kroh, M., Popoff, Y., Winzer, G., Petousi, D., Lischke, S., Ortmann, J. E., Czornomaz, L., Zimmermann, L., Fompeyrine, J., & Abel, S. (2019). A $BaTiO_3$-based electro-optic pockels modulator monolithically integrated on an advanced silicon photonics platform. *Journal of Lightwave Technology, 37*, 1456–1462.
130. Abel, S., Eltes, F., Ortmann, J. E., Messner, A., Castera, P., Wagner, T., Urbonas, D., Rosa, A., Gutierrez, A. M., Tulli, D., Ma, P., Baeuerle, B., Josten, A., Heni, W., Caimi, D., Czornomaz, L., Demkov, A. A., Leuthold, J., Sanchis, P., & Fompeyrine, J. (2019). Large Pockels effect in micro- and nanostructured barium titanate integrated on silicon. *Nature Materials, 18*, 42–47.
131. Abe, S., Joichi, T., Uekusa, K., Hara, H., & Masuda, S. (2019). Photonic integration based on a ferroelectric thin-film platform. *Scientific Reports, 9*, 16548.
132. Posadas, A. B., Park, H., Reynaud, M., Cao, W., Reynolds, J. D., Guo, W., Jeyaselvan, V., Beskin, I., Mashanovich, G. Z., Warner, J. H., & Demkov, A. A. (2021). Thick $BaTiO_3$ epitaxial films integrated on Si by RF sputtering for electro-optic modulators in Si photonics. *ACS Applied Materials & Interfaces, 13*, 51230–51244.
133. Tan, L. Z., Zheng, F., Young, S. M., Wang, F., Liu, S., & Rappe, A. M. (2016). Shift current bulk photovoltaic effect in polar materials-hybrid and oxide perovskites and beyond. *NPJ Computational Materials, 2*.
134. Cabellos, J. L. (2009). *Optical response in semiconductors*. Cent. Investig. En Óptica, PhD Thesis. 61.
135. Pal, S., Swain, A. B., Biswas, P. P., & Murugavel, P. (2020). Linear bulk photovoltaic effect and phenomenological study in multi-phase co-existing ferroelectric system. *Journal of Physics. Condensed Matter, 32*.
136. Pal, S., Swain, A. B., Biswas, P. P., Murali, D., Pal, A., Nanda, B. R. K., & Murugavel, P. (2018). Giant photovoltaic response in band engineered ferroelectric perovskite. *Scientific Reports, 8*, 1–7.
137. Yuan, Y., Reece, T. J., Sharma, P., Poddar, S., Ducharme, S., Gruverman, A., Yang, Y., & Huang, J. (2011). Efficiency enhancement in organic solar cells with ferroelectric polymers. *Nature Materials, 10*, 296–302.

138. Nechache, R., Harnagea, C., Li, S., Cardenas, L., Huang, W., Chakrabartty, J., & Rosei, F. (2014). Bandgap tuning of multiferroic oxide solar cells. *Nature Photonics, 9*, 61–67.
139. Subedi, A. (2021). Light-control of materials via nonlinear phononics. *Comptes Rendus Physique, 22*, 161.
140. Disa, A. S., Nova, T. F., & Cavalleri, A. (2021). Engineering crystal structures with light. *Nature Physics, 17*, 1087–1092.
141. Juraschek, D. M., Fechner, M., & Spaldin, N. A. (2017). Ultrafast structure switching through nonlinear phononics. *Physical Review Letters, 118*, 1–5.
142. Kaaret, J. Z., Khalsa, G., & Benedek, N. A. (2022). A strategy to identify materials exhibiting a large nonlinear phononics response: Tuning the ultrafast structural response of $LaAlO_3$ with pressure. *Journal of Physics. Condensed Matter, 34*.
143. Feng, N., Han, J., Lan, C., Xu, B., Bi, K., Lin, Y., & Nan, C. (2022). Selective tuning of order parameters of multiferroic $BiFeO_3$ in picoseconds using midinfrared terahertz laser pulses. *Physical Review B, 105*, 1–10.
144. Cavalleri, A. (2018). Photo-induced superconductivity. *Contemporary Physics, 59*, 31–46.
145. Mankowsky, R., Subedi, A., Först, M., Mariager, S. O., Chollet, M., Lemke, H. T., Robinson, J. S., Glownia, J. M., Minitti, M. P., Frano, A., Fechner, M., Spaldin, N. A., Loew, T., Keimer, B., Georges, A., & Cavalleri, A. (2014). Nonlinear lattice dynamics as a basis for enhanced superconductivity in $YBa_2Cu_3O_{6.5}$. *Nature, 516*, 71–73.
146. J.L. Clabel H., et al. (2023). Methods for the synthesis of ceramic materials with perovskite structure (pp. 31-75). Elsevier.

Perovskites as Catalyst Precursor for Hydrogen Production from Ammonia Decomposition

M. Pinzón, A. Sánchez-Sánchez, P. Sánchez, A. R. de la Osa, and A. Romero

1 Introduction

Green hydrogen has focused relevance as an ideal (high productivity for energy conversion) and clean energy carrier (CO_x-free fuel). Nevertheless, the main drawbacks associated with hydrogen (H_2) are its low volumetric energy density (8.96 $GJ{\cdot}m^{-3}$) and the difficulties related with gas handling, which increases the cost of the H_2-based technologies [1]. These involve a low acceptance for viable application, being necessary to use liquid chemical compounds to store H_2.

In this sense, ammonia (NH_3) is a promising "hydrogen carrier," which has generated high interest because of suitable qualities such as it is a carbon-free hydrogen vector and presents high gravimetric/volumetric hydrogen density. Moreover, it can be easily liquefied to store and transport and directly used electrochemically (fuel cells), thermochemically (combustion), and/or by cracking (ammonia decomposition) [2]. Thus, hydrogen production from ammonia (cracking) requires a highly efficient catalytic system which allows to decrease the energy requirements (reaction temperature) and the hydrogen purity (high ammonia conversion) to couple this reaction to PEM fuel cells.

While ruthenium catalysts have been proposed as the most active catalyst from a range of different metals (Rh, I, Ni, Co, Fe, etc.) [3–5], the use of non-noble metals (Ni or Co) has gained great attention as active phase, owing to their suitable catalytic performance under slight conditions and economic cost [6, 7]. Besides,

M. Pinzón · A. Sánchez-Sánchez · P. Sánchez · A. R. de la Osa
Department of Chemical Engineering, Faculty of Chemical Sciences and Technologies, University of Castilla-La Mancha, Ciudad Real, Spain

A. Romero (✉)
Department of Chemical Engineering, Higher Technical School of Agronomical Engineers, University of Castilla-La Mancha, Ciudad Real, Spain
e-mail: Amaya.Romero@uclm.es

W. Nie, K. (Kris) Iniewski (eds.), *Metal-Halide Perovskite Semiconductors*,
https://doi.org/10.1007/978-3-031-26892-2_11

bimetallic catalysts (Ni–Co) supported on different metal oxide have enhanced the reaction as consequence of the formation of Ni–Co alloy [8, 9]. Note that the catalytic activity is also influenced by supports, which must deliver high conductivity and basicity, and metallic crystallite size; preferably crystals in small size enhance ammonia decomposition [3, 10, 11].

On the other hand, the synthesis method affects the catalyst properties [3]. Thus, the impregnation method generates crystallites of too large size, and the coprecipitation method does not allow to precipitate nickel completely leading to low amount in the final catalyst [10]. In this sense, materials with the single-phase $LaNiO_3$ (perovskite structure) have allowed to develop catalysts with new metallic (Ni^0) and support (La_2O_3) phases, after reduction, with excellent results in ammonia decomposition reaction [7, 10, 12].

In light with this, the self-combustion method, which involves an exothermic reaction between an organic compound as fuel and metal nitrates, has been described to deliver homogeneous perovskite-type oxides ($LaBO_3$, B = non-noble metals) with slow reaction time and without intermediate of decomposition [13]. However, it is necessary an additional step of calcination to achieve the completely well-defined crystalline structure. Indeed, the modification of the fuel-to-metal nitrates molar ratio and calcination temperature generate perovskites with different properties [10, 13, 14].

In order to perform highly efficient and economical catalysts for H_2 production from NH_3 decomposition, this work involves a facile, low-cost, and environment-friendly approach toward synthesis of non-noble mono- and bimetallic catalyst for this reaction. Additionally, the effect of the synthesis parameters such as the molar ratio (fuel to metal nitrates) and the calcination temperature have been discussed.

2 Experimental

2.1 Catalyst Synthesis

Catalyst precursors (i.e., $LaCo_{1-x}Ni_xO_3$ perovskites where x = 0, 0.2, 0.4, 0.6, 0.8, and 1, molar basis) were synthesized by the self-combustion method using an organic fuel (citric acid) following the procedure described previously [7]. The relation of citric acid to metal nitrates varied from 0.5 to 1.25, and the powder obtained was calcined in an air at 600, 650, 700, 750, and 900 °C for 4 h (2 °C min^{-1} heating rate) resulting in MR $LaNiO_3$ or $LaCoO_3$, where *MR* refers to the molar ratio (citric acid to metal nitrates). The final catalysts (perovskite-derived catalyst) were prepared after reduction in 50% v/v H_2 flow (100 mL min^{-1} diluted with Ar) at 550 °C (10 °C min^{-1}) for 1 h, prior to the reaction.

2.2 Physicochemical Characterization

XRD patterns of the calcined and reduced perovskites were recorded on a Philips X'Pert MPD diffractometer using nickel-filtered Cu-Kα radiation in the range 20°–80° (2θ) using 0.02° step^{-1} (4 s step^{-1}). Textural properties were determined using a QUADRASORB 3SI through adsorption-desorption isotherms at liquid N_2. Structural morphology and elemental mapping (EDX) of calcined bimetallic perovskites were obtained using ZEISS GeminiSEM 500 FE-SEM with a PIN-diode BSE detector. Temperature-programmed reduction (H_2-TPR) essays were conducted in an AutoChem 2950 HP unit with a TCD detector. Samples (0.08 g) were heated from room temperature to 900 °C (10 °C min^{-1}), under 5% v/v H_2/Ar mixed gas, 60 mL min^{-1}. In the same equip, the total basic sites were determined from CO_2-TPD profiles. Samples (0.08 g) were reduced at 550 °C, cooling to 50 °C in argon flow and exposed to a CO_2 flow (40 mL min^{-1}) at 50 °C for 30 min. Finally, the samples were heated from room temperature to 900 °C (10 °C min^{-1}) under Ar flow. Images HRTEM of the final catalysts were performed in a TalosTM F200X (FEI-200 kV), and elemental mapping associated with images was carried out with an energy-dispersive X-ray spectrometer (X-Max Oxford). The crystallite size distribution was estimated by HRTEM, where more than 600 crystallites were measured for each material showing a Gaussian distribution.

2.3 Catalyst Activity

NH_3 decomposition tests (0.08 g of perovskite) were performed under 1 bar in a fixed-bed reactor. The sample were in situ reduced at 550 °C (10 °C min^{-1}) for 1 h (50% v/v H_2/Ar flow 100 mL min^{-1}) to obtain the final catalyst. Catalytic activity was evaluated in the temperature range of 250–450 °C under 5% v/v NH_3 (100 mL min^{-1} diluted with Ar), corresponding to a gas hourly space velocity (GHSV) of 75,000 mL g_{cat}^{-1} h^{-1}. Effluent gas composition after reaction was analyzed on-line through a gas chromatograph (Agilent 7820A) and allowed to determine H_2 formation (mmol H_2 g_{cat}^{-1} min^{-1}) rate and NH_3 conversion (x_{NH_3}) [7]. Arrhenius plot (Ln mmol H_2 g_{cat}^{-1} min^{-1} vs. 1/T) was employed to estimate the apparent activation energy (E_a), considering that NH_3 decomposition reaction happened into differential requirements. Finally, stability test for selected catalysts was carried out at 450 °C over 40 h.

3 Results

3.1 *Effect of Fuel-to-Metal Nitrates Molar Ratio and Calcination Temperature*

Aiming for optimizing the catalytic activity of the monometallic perovskites ($LaNiO_3$), the influence of the molar ratio and calcination temperature were investigated. First, the fuel-to-metal nitrates molar ratio was varied from 1.25 to 0.5, and the samples were calcined in air at 650 °C for 4 h. Then, the optimized sample was calcined at different temperature (600, 650, 700, 750, and 900 °C). All samples were reduced in situ at 550 °C for 1 h.

The catalytic activity of reduced MR $LaNiO_3$ samples at 350 °C was shown in Table 1. Note that the ammonia conversion was clearly influenced by the fuel-to-metal nitrates molar ratio, showing the catalytic activity an increase with the molar ratio. However, 1.25 $LaNiO_3$ perovskite-derived catalyst led to the lowest ammonia conversion at 350 °C (33.6%), while 1 $LaNiO_3$ resulted in the highest conversion at 350 °C (55.9%). In order to correlate the catalytic performance with the structural properties of the samples, different techniques have been used to the characterization of the precursors and the final catalysts.

All samples presented similar low surface area around 10 $m^2\ g^{-1}$ (Table 1), typical of these types of materials due to the high heat of combustion during synthesis and the calcination step [15, 16].

Despite the similarity in S_{BET}, the fuel-to-metal nitrates molar ratio affected the crystalline structure formed during synthesis, identified by XRD patterns (Fig. 1a). It was observed that perovskites synthesized with molar ratio equal to 0.75 and 1 only exhibited peaks related to rhombohedral $LaNiO_3$ (PDF, 11-0711) [7], which could justify the high catalytic activity of these perovskite-derived catalysts. However, 1.25 $LaNiO_3$ and 0.5 $LaNiO_3$ perovskites displayed peaks associated with $LaNiO_3$, tetragonal La_2NiO_4, and NiO impurities. These phases (La_2NiO_4 and NiO), considered impurities, appeared due to the low or high quantity of citric acid [13], and they were responsible of the low ammonia conversion reached. However, the perovskites were in situ reduced, and therefore, the crystalline structure changed as can be observed by XRD (Fig. 1b). In this sense, all perovskite-derived catalysts

Table 1 Ammonia conversion at 350 °C and physicochemical properties of *MR* $LaNiO_3$ perovskites calcined at 650 °C

Samples	Ammonia conversion (%)	S_{BET} ($m^2\ g^{-1}$)	Crystallite size (nm)[ab] Ni^0 ($2\theta = 44.5°$)	Total basic sites (μmol $CO_2\ g^{-1}$)[a]
1.25 $LaNiO_3$	33.6	10	8.1	5.2
1 $LaNiO_3$	55.9	12	5.5	18
0.75 $LaNiO_3$	48.3	9	4.8	17.8
0.5 $LaNiO_3$	36.7	9	13.2	4.3

[a]From the reduced perovskites
[b]Calculated by the Scherrer equation

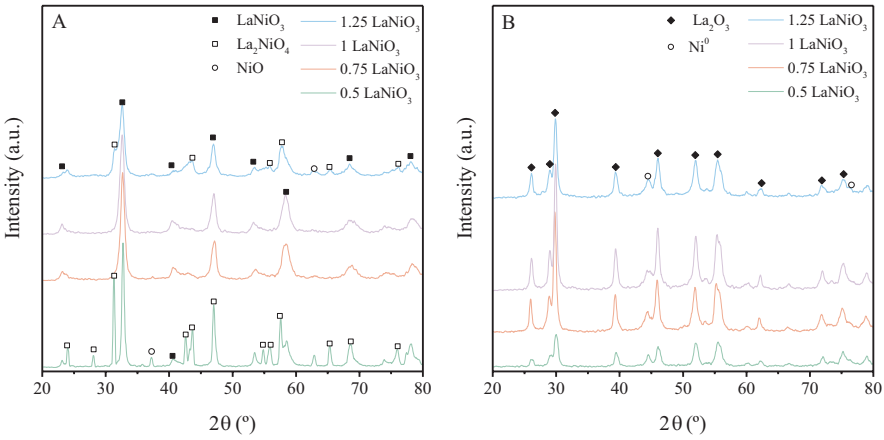

Fig. 1 (**a**) XRD pattern of MR $LaNiO_3$ perovskites calcined at 650 °C and (**b**) XRD pattern of final catalysts

(reduced perovskites) presented peaks linked to lanthanum oxide (La_2O_3) and metallic nickel (Ni^0) being the main phases of the final catalysts. Although the catalysts had the same crystalline structure, the ammonia conversion was distinctive, which indicated some differences in Ni^0 crystallite size. Then, nickel size was estimated from Scherrer equation at peak $2\theta = 44.5°$ and it is shown in Table 1. Note that 1.25 and 0.5 $LaNiO_3$ final catalysts showed larger crystallite size (8.1 and 13.1 nm, respectively) than 1 and 0.75 $LaNiO_3$ final catalysts (5.5 and 4.8 nm, respectively). The difference in crystallite size was consequence of the presence of La_2NiO_4 and NiO before reduction [13]. Moreover, it is well-known that small nickel sizes enhance the ammonia decomposition reaction because of its dependence on the structure and size of metal [17, 18]. Therefore, it is likely that the lower the nickel size of 1 and 0.75 $LaNiO_3$ final catalysts, the higher the catalytic activity.

On the other hand, high basicity is a key factor of catalysts in ammonia decomposition reaction. Hence the effect the citric acid-to-metal nitrates ratio has on the basicity of the final catalysts was discussed using CO_2-TPD profiles. The total basic sites of the final catalysts were estimated from the integration of the peaks, and it is indicated in Table 1. Note that the total basic sites increased as the molar ratio increased until a value of 1 (18 μmol CO_2 g^{-1}), and then it decreased again (5.2 μmol CO_2 g^{-1} for 1.25 $LaNiO_3$). This fact confirmed that the molar ratio affected the basic properties, despite of the phases observed after reduction. Moreover, the difference in crystallite size could rise the basic sites, achieving high basicity with small metal size [19]. In fact, the perovskite-derived catalyst with molar ratio equal to 1 and 0.75 exhibited the higher total basic sites (minor crystallite size) and, hence, the superior basicity, which justified the greater catalytic activity of 1 $LaNiO_3$ and 0.75 $LaNiO_3$ perovskite-derived catalyst.

In view of the results, the fuel-to-metal nitrates molar ratio influenced on the catalytic properties of the final catalysts and, so, the catalytic activity. Indeed,

crystalline phases after calcination compromised the nickel size and the total basic sites of the final catalysts. Thus, the 1 and 0.75 perovskites exhibited the main phase of $LaNiO_3$ (rhombohedral) without impurities (La_2NiO_4 and NiO) before reduction which resulted in the smallest nickel crystallite and the highest basicity. For that reason, this molar ratio was selected as the optimal to carry out the following studies.

Apart from that, the calcination temperature of the 1 $LaNiO_3$ perovskites was optimized and tested on hydrogen production from ammonia. In addition, the ammonia conversion at 400 °C as function of the calcination temperature is presented in Fig. 2. The results showed that the optimum calcination temperature was 650 °C, displaying the materials calcined at 700, 750, and 900 °C the lower catalytic activity. In fact, the material calcined at 900 °C achieved an ammonia conversion of 78.2% at 400 °C in comparison with 97.5% of conversion of the material calcined at 650 °C.

Toward to relate the catalytic activity with the materials characterization, different techniques have been used. As above mentioned, the crystalline phase seems to be crucial in the development of an adequate nickel catalyst; thus the XRD of the calcined perovskites is presented in Fig. 3a. Note that the calcination temperature did not influence on the phase formed after calcination. Actually, all perovskites presented the peaks associated with the rhombohedral $LaNiO_3$ (PDF, 11-0711), and

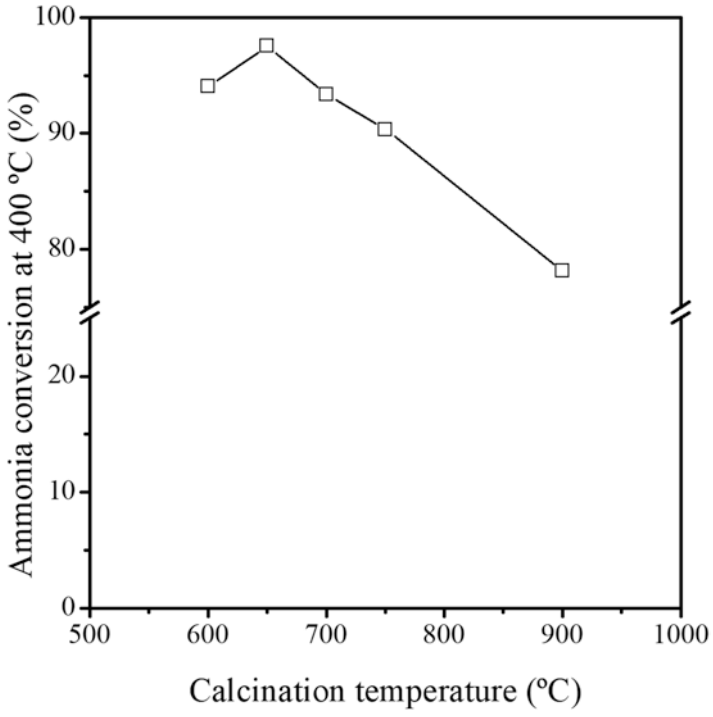

Fig. 2 Ammonia conversion at 400 °C as function of the calcination temperature for 1 $LaNiO_3$ perovskite-derived catalysts

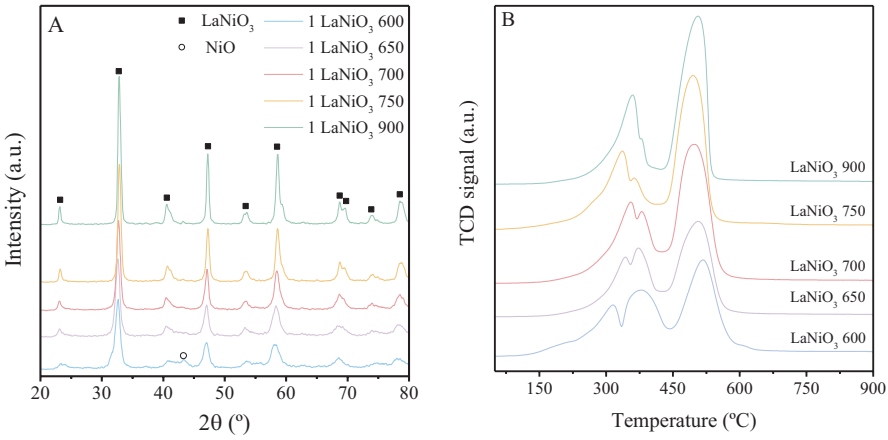

Fig. 3 (**a**) XRD pattern and (**b**) H_2-TPR for the 1 $LaNiO_3$ perovskites calcined at different temperature

Table 2 Physicochemical properties and hydrogen consumption of 1 $LaNiO_3$ perovskites calcined at different temperatures

Calcination temperature (°C)	S_{BET} ($m^2\ g^{-1}$)	Crystallite size (nm)[a]	Hydrogen consumption (mmol H_2 g^{-1})
		Ni^0 ($2\theta = 44.5°$)	
600	14	5.0	4.6
650	12	5.5	4.8
700	10	8.5	4.6
750	8	9.0	4.6
900	3	11.9	4.7

[a]Calculated by the Scherrer equation from the reduced perovskites

these peaks also increased with the temperature, indicating higher crystallite size [15]. However, the perovskite calcined at 600 °C showed another peak at 43.4° related to nickel oxide, which suggested an insufficient temperature to develop the structure of perovskite. In this sense, the presence of other different phase, such as NiO, caused a decrease in the catalytic activity. An influence of the calcination temperature was observed with the surface area (Table 2), i.e., the S_{BET} decreases as the calcination temperature raised as consequence of the increase of reaction rate [20]. This might have an effect in the catalytic activity although almost negligible due to the low surface area values.

Moreover, the reduction of the perovskite was studied by H_2-TPR, and the profile is exposed in Fig. 3b. Three hydrogen desorption peaks were observed for all perovskites at temperatures around 350 °C, 370 °C, and >500 °C. The low temperature peak was associated with first reduction of $LaNiO_3$ to give $La_2Ni_2O_5$, the middle temperature peak ascribed to NiO reduction, and the high temperature peak related with the final reduction of the perovskite to obtain Ni^0 and La_2O_3 [15]. Note that the

perovskite calcined at 600 °C exhibited the higher peak at middle temperature, indicating higher amount of NiO species, as can be seen by XRD.

In the same way, the crystalline structure of the perovskites reduced at 550 °C was analyzed by XRD (not shown here). All perovskite-derived catalysts presented metallic nickel and lanthanum oxide as two phases after reduction, suggesting that calcination temperature did not affect the crystalline structure of the final catalysts. However, considering the crystallite size of Ni^0 (Table 2), the calcination temperature influenced in this parameter. The higher nickel size the higher calcination temperature. In this sense, the perovskite calcined at a temperature higher than 650 °C generated nickel sizes higher than 6 nm which declined the ammonia conversion. In particular, an average nickel size between 3 and 5 nm has been established to enhance the ammonia decomposition [18].

Note that the perovskite calcined at 600 °C showed the lowest nickel size, but the presence of NiO before reduction led to lower catalytic activity than perovskite calcined at 650 °C, which could be related to the hydrogen consumption (calculated from H_2-TPR curves, Table 2) during reduction. It was observed that hydrogen consumption of perovskite calcined at 600 °C was 4.6 mmol H_2 g^{-1} and the perovskite calcined at 650 °C was 4.8 mmol H_2 g^{-1} showing higher reduction degree and hence superior catalytic activity.

In view of the results, this work has allowed to achieve the synthesis of nickel-based perovskites as catalyst precursors for the ammonia decomposition reaction. Besides, the fuel-to-metal nitrates molar ratio and calcination temperature were optimized to synthesize the suitable nickel catalyst. The 1 $LaNiO_3$ calcined at 650 °C and reduced at 550 °C exhibited suitable physicochemical properties (lower impurities before reduction, higher hydrogen consumption, small and well-dispersed Ni^0 crystallite size) which led to an excellent nickel catalyst with great catalytic activity. For that reason, a fuel-to-metal nitrates molar ratio equal to 1 and a calcination temperature of 650 °C were selected as optimal to carry out the synthesis of bimetallic perovskites.

3.2 Synthesis of Bimetallic Ni–Co Perovskites

In order to generate Ni–Co bimetallic catalysts, different $LaCo_{1-x}Ni_xO_3$ (x = 0, 0.2, 0.4, 0.6, 0.8, and 1 molar basis) perovskites were synthesized, tested, and optimized as catalyst precursors for the hydrogen production from ammonia.

The SEM images of calcined bimetallic perovskites are shown in Fig. 4, showing a characteristic nonporous structure with crystallite of different size and shapes. In addition, the higher the cobalt content, the lower the porosity and the higher the crystallite size [21].

From the EXD analysis, it could be observed the elements of perovskites (La, Ni, Co, and O) evenly distributed over the surface. This analysis was also used to corroborate that the synthesis was correctly carried out, and then, the Ni/Co weight ratio was measured (Table 3). This ratio absolutely set the theoretical ratio indicating the synthesis was perfectly performed (error of ±0.5%).

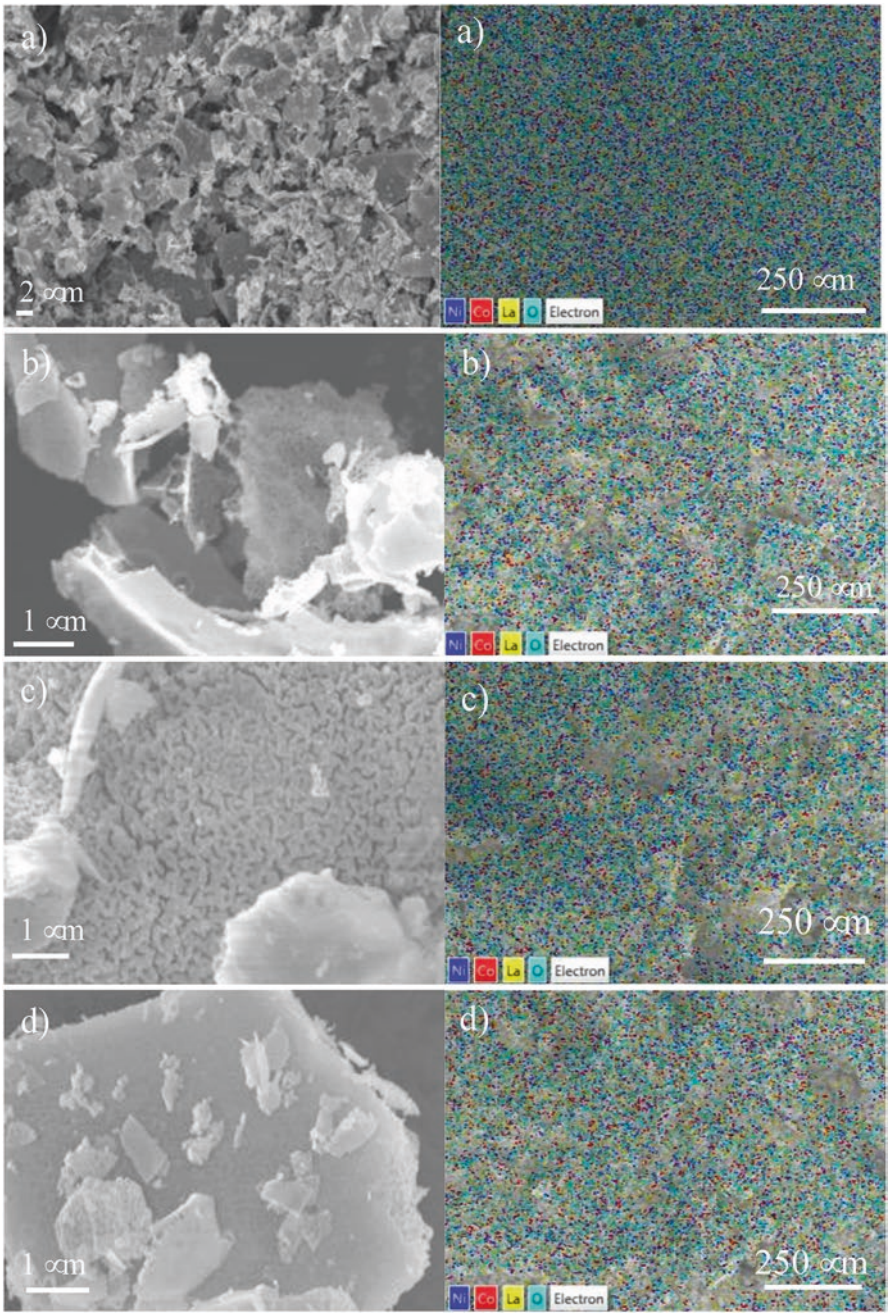

Fig. 4 HRSEM images and EDX elemental mapping of the calcined bimetallic perovskites: (**a**) $LaCo_{0.2}Ni_{0.8}O_3$, (**b**) $LaCo_{0.4}Ni_{0.6}O_3$, (**c**) $LaCo_{0.6}Ni_{0.4}O_3$, (**d**) $LaCo_{0.8}Ni_{0.2}O_3$

XRD patterns before reduction of the bimetallic perovskites are shown in Fig. 5a. Note that all bimetallic perovskites exhibited well-defined crystalline structure linked to rhombohedral $LaNiO_3$ or $LaCoO_3$ structure (PDF, 33-0711 or PDF, 48-0123) [21]. Additionally, no peaks related to nickel and cobalt oxide were detected. An increase in the cobalt content caused a splitting of the peaks to reach cobalt perovskite structure. However, in the XRD pattern of the reduced perovskites (Fig. 5b), there were differences as function of the Ni/Co ratio. In this sense, all perovskite-derived catalysts presented signals for metallic Ni or Co and La_2O_3, while final catalysts of perovskites with Ni/Co weigh ratio equal to 3.7 and 1.5 also exhibited peaks of tetragonal La_2NiO_4 or La_2CoO_4 phases. Santana et al. [22] suggested that during reduction treatment of the bimetallic perovskites, oxygen deficiency was generated leading to tetragonal phases formation and they required higher reduction temperatures.

In line with XRD analysis, H_2-TPR of the samples were carried out to estimate the reduction degree (Table 3). This parameter was calculated from the ratio of the real H_2 consumption (H_2-TPR curves, not shown here) to the theoretical amount of H_2 required for the reduction of perovskites. It should be mentioned that reduction process was affected by Co amount [23], and the perovskites with Ni/Co ratio 3.7 and 1.5 possessed the lower reduction degree. In fact, they showed an intermediate phase of reduction when they were reduced at 550 °C, as can be observed by XRD (Fig. 5b). These events (low reduction degree and tetragonal phase over surface after reduction) may cause metallic crystallites of bigger size, influencing the ammonia conversion.

Accordingly, TEM and elemental mapping of the perovskite-derived catalysts were carried out. The final catalysts were represented by highly dispersed spherical crystallite of metallic Ni/Co supported over homogeneous matrix [22], as can be seen in EDX images (Fig. 6). Furthermore, all elements of the final catalysts (Ni, Co, La, and O) were highly distributed, indicating that both metals (Ni and Co) coexist on the catalyst surface. From the TEM images (not shown here) and the crystallite size distribution, the average size of metallic Ni and/or Co was estimated, and it is shown in Table 3 for all perovskite-derived catalysts. Note that the higher crystallite size the higher cobalt amount, which could be due to the presence of the intermediate phase after reduction, the lower reduction degree, and the presence of

Table 3 Ni/Co weight ratio, reduction degree, and crystallite size of reduced bimetallic perovskites

	Ni/Co (wt/wt)[a]	Reduction degree (%)[b]	Crystallite size (nm)[c]
$LaNiO_3$	–	81	4.2 ± 0.1
$LaCo_{0.2}Ni_{0.8}O_3$	3.7	65	7.8 ± 0.1
$LaCo_{0.4}Ni_{0.6}O_3$	1.5	66	7.9 ± 0.1
$LaCo_{0.6}Ni_{0.4}O_3$	0.7	90	7.0 ± 0.1
$LaCo_{0.8}Ni_{0.2}O_3$	0.3	91	5.7 ± 0.1
$LaCoO_3$	–	70	7.7 ± 0.1

[a]Measured by EDX of calcined perovskites
[b]Calculate from H_2-TPR curves
[c]Calculate from TEM images (crystallite size distribution)

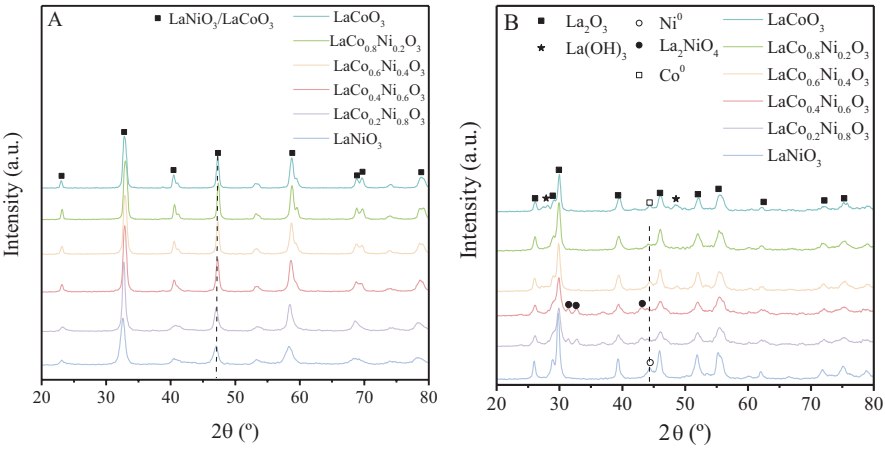

Fig. 5 (**a**) XRD pattern before and (**b**) XRD pattern after reduction of the perovskites

the two metals [22]. Samples with Ni/Co ratio equal to 0.7 and 0.3 showed a crystallite size of 7.0 nm and 5.7 nm, respectively, i.e., the bimetallic perovskite without intermediate phase and higher reduction degree presented lower crystallite size. Indeed, higher Ni and/or Co crystallite size was generated with the tetragonal La_2NiO_4 phase as catalyst precursors [22]. Apart from this, the lowest metal size was developed with the pure nickel perovskite ($LaNiO_3$) displaying a nickel size of 4.2 nm, which could influence on the catalytic activity.

Finally, the perovskite-derived catalysts were tested on the ammonia decomposition reaction. The catalytic activity was evaluated as hydrogen formation rate (mmol H_2 g_{cat}^{-1} min^{-1}) at 350 °C for all catalysts, and it is shown in Table 4.

Perovskite-derived catalysts synthesized with Ni/Co ratio of 3.7 and 1.5 exhibited the lower hydrogen production rate with a value of 1.3 mmol H_2 g_{cat}^{-1} min^{-1}, followed by the catalysts with Ni/Co ratio of 0.7 and 0.3 with a 1.6 mmol H_2 g_{cat}^{-1} min^{-1}; after these, the pure cobalt perovskite-derived catalyst showed 1.9 mmol H_2 g_{cat}^{-1} min^{-1}; and the highest catalytic activity was achieved by pure nickel perovskite-derived catalyst (2.5 mmol H_2 g_{cat}^{-1} min^{-1}). It was found that the catalytic performance was altered by Co amount and the main reason to the low activity of bimetallic and pure Co perovskite-derived catalysts in comparison with pure Ni final catalyst was the smaller crystallite size of the last catalyst (4.2 nm), although other parameters such as the reduction degree and the presence of tetragonal phase after reduction influenced the catalytic activity, decreasing it. In this sense, it is well-known that ammonia decomposition reaction is influenced by the metal size [17]. Thus, the bimetallic perovskites are not preferably as catalyst precursors because of the higher metal size generated after reduction.

On the other hand, Huang et al. [8] attributed the higher activity of bimetallic catalysts to the presence of Ni–Co alloys, so it might be likely that bimetallic catalysts of this work did not present Ni–Co alloys because these showed worse catalytic activity than monometallic ones. Thus, the drop in the overall activity of the

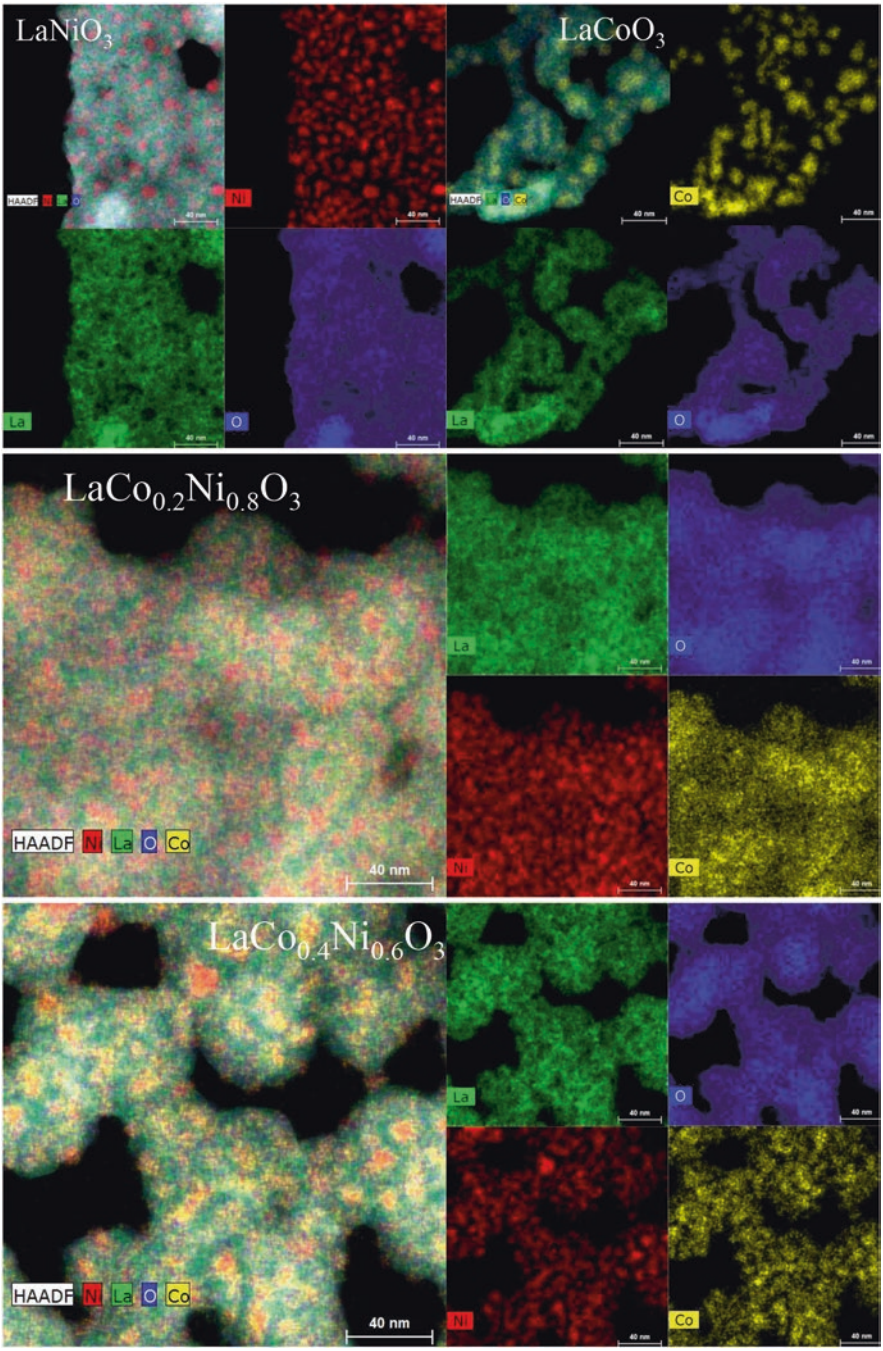

Fig. 6 EDX elemental mapping of the monometallic and bimetallic perovskites reduced at 550 °C

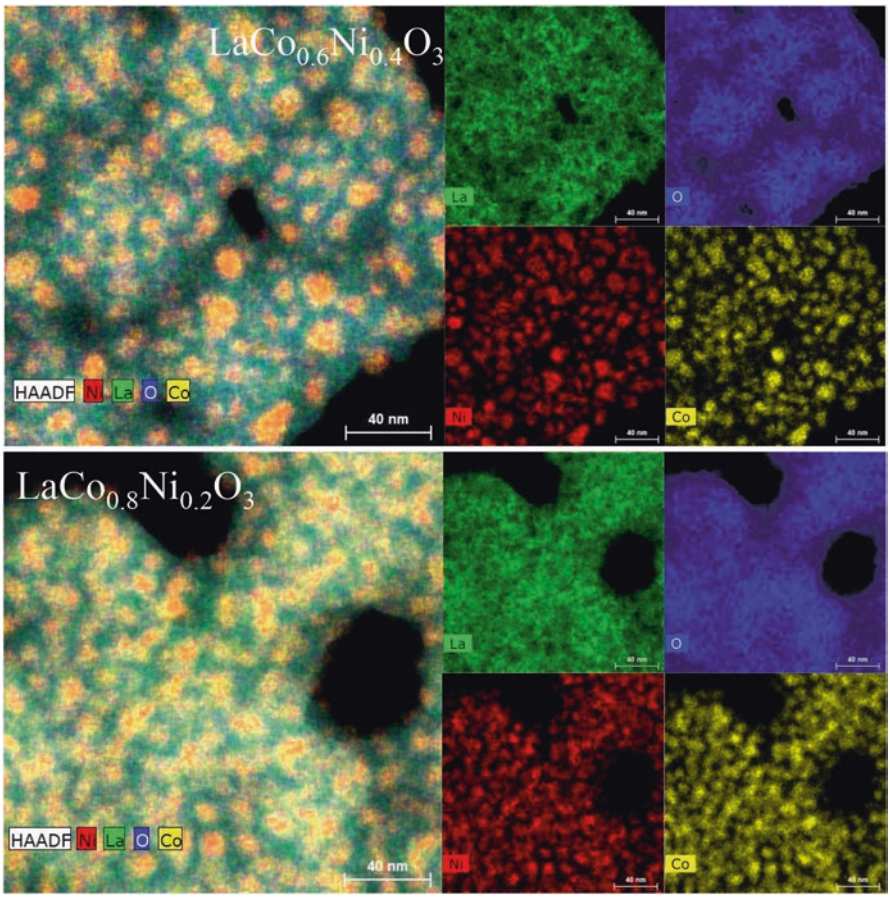

Fig. 6 (continued)

bimetallic catalysts could be due to the presence of individual Ni and Co active sites coexisting on catalytic surface, as shown by EDX (Fig. 6). In line with this, the rate-determining step of ammonia decomposition (recombinative desorption of adsorbed N atoms) is influenced by bond strengths (M–N where M = Ni, Co, and Fe), because N atoms are absorbed on metal surface generating strong bonds [27]. In addition, Wang et al. [27] have been proven by temperature-program desorption (TPD) experiments that Ni–N bond strength is weaker than Co–N bond, which enhanced the rate-determining step and hence the ammonia decomposition rate [28].

Subsequently, the difference in catalytic activity of perovskite-derived catalysts of $LaNiO_3$ and $LaCoO_3$ could be related to the basic properties, which have been estimated with CO_2-TPD (Fig. 7). Regarding the literature, the temperature of the desorption peaks was associated with the CO_2 interaction with basic sites of varying strength [29]. Thus, reduced $LaNiO_3$ perovskite displayed three desorption peaks at (i) 100–250 °C (weak basic sites), (ii) 250–500 °C (moderate basic sites), and (iii)

Table 4 Catalytic activity of perovskite-derived catalysts and comparative with other nickel catalysts of literature

Materials	GHSV (mL g_{cat}^{-1} h^{-1})	T (°C)	H_2 formation rate (mmol H_2 g_{cat}^{-1} min^{-1})	Ratio H_2 experimental/ H_2 maximum theoretical (%)	Ref.
$LaNiO_3$	75,000 (5% v/v NH_3-Ar)	350	2.5	56	This work
$LaCo_{0.2}Ni_{0.8}O_3$			1.3	30	
$LaCo_{0.4}Ni_{0.6}O_3$			1.3	31	
$LaCo_{0.6}Ni_{0.4}O_3$			1.6	37	
$LaCo_{0.8}Ni_{0.2}O_3$			1.6	38	
$LaCoO_3$			1.9	43	
Ni/CeO_2	13,800 (57% v/v NH_3-Ar)	350	1.5	4	[24]
Ni/GNP	15,000 (10% v/v NH_3-He)	375	0.8	17	[25]
$Ni/NaNH_2$-GNP			1.5	33	
Ni/KNH_2-GNP			2.0	44	
$Ni_{0.6}(Mg_{0.29}Al_{0.57}O_n)$	30,000 (pure ammonia)	350	3.4	10	[26]
1Ni–9Co/ $Ce_{0.6}Zr_{0.3}Y_{0.1}O_2$	6000 (pure ammonia)	350	1.0	15	[8]
Ni_5-Co_5/SiO_2	30,000 (pure ammonia)	350	5.0	15	[9]

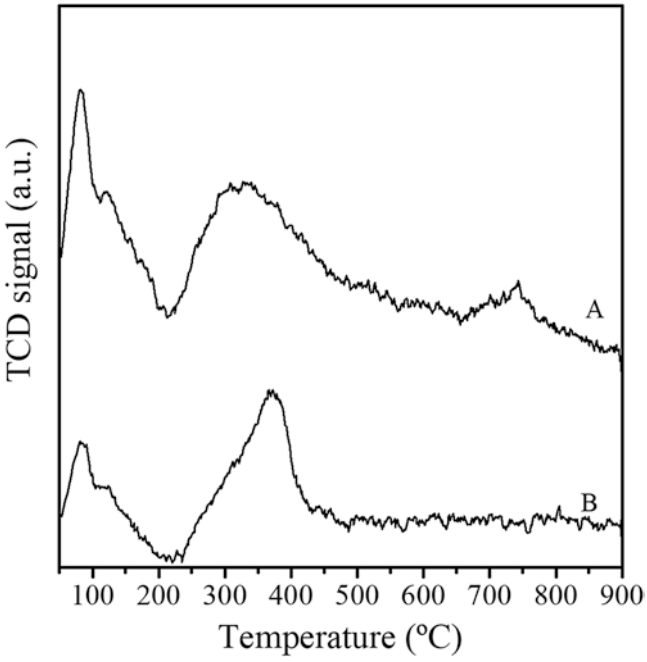

Fig. 7 CO_2-TPD profiles of a: $LaNiO_3$ and b: $LaCoO_3$ calcined at 650 °C (reduced at 550 °C)

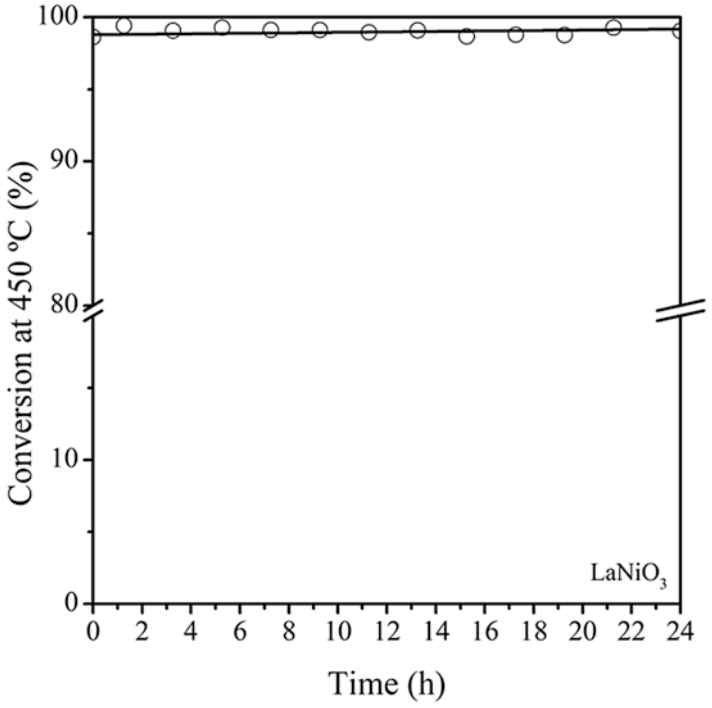

Fig. 8 Stability test for reduced $LaNiO_3$ (0.08 g catalyst, 75,000 $mL \cdot h^{-1} \cdot g_{cat}^{-1}$, atmospheric pressure)

>500 °C (strong basic sites), which corresponded to desorption amount (or total basic sites) of 18 μmol CO_2 g^{-1}. For reduced $LaCoO_3$ perovskite, only two desorption peaks were observed correlated to weak and moderate basic sites, and it presented a total basic site of a half the one of nickel (9.5 μmol CO_2 g^{-1}). In this respect, it is possible to adjust the basic properties by changing the B-site cation in the $LaBO_3$ structure.

Table 4 also shows the comparative of the hydrogen production rate of the final mono- and bimetallic catalysts developed in this work with nickel and Ni–Co catalysts accessible in the literature. Point out that catalysts of this work exhibited admirable hydrogen production rate at the highest gas hourly space velocity (GHSV) of the comparative, although the feeding gas composition was the lowest. Nevertheless, these conditions might be related to real application, and the materials could take advantage of diluted ammonia feed to generate hydrogen and get energy. In short, the pure nickel perovskite allowed to achieve a nickel-based catalyst with adequate nickel metal size, without intermediate of reduction, superior basic sites, and with higher active sites to improve the rate-determining step of ammonia decomposition reaction.

Finally, for real application the stability of the optimal catalyst (reduced $LaNiO_3$) is very important, and durability test was performed at 450 °C for 24 h (Fig. 8). The

catalyst demonstrated to be stable at high temperature with an ammonia conversion of 99% constant for long reaction times.

It has been demonstrated that self-combustion method with an additional step of calcination allowed to synthesize well-defined perovskites, which have been proven to be excellent catalyst precursors for ammonia decomposition reaction.

4 Conclusions

Perovskites, ($LaBO_3$, B = non-noble metals) prepared by self-combustion method, were demonstrated to be exceptional catalyst precursors of Ni-based catalysts. The synthesis parameters (fuel-to-metal nitrates molar ratio, calcination temperature, and Ni/Co weight ratio) affected the catalytic activity. The characterization of the samples (impurities, physicochemical properties, basicity, metal size, and reduction degree) together with the catalytic essays revealed that the 1 $LaNiO_3$ calcined at 650 °C displayed the most favorable properties for the ammonia decomposition. This material presented well-defined $LaNiO_3$ phase before reduction, small, well-dispersed Ni^0, high basicity after reduction, and the most active sites, exhibiting an ammonia conversion of 99% at 450 °C for 24 h (great stability). This work offers new perception in aiming cost-effective Ni-based catalysts to improve the NH_3 assessment as hydrogen carrier.

Acknowledgments This work was supported by the Regional Government of Castilla-La Mancha and the European Union [FEDER funds SBPLY/21/180501/000165]. M. Pinzón thanks the University of Castilla-La Mancha for the predoctoral contract within the framework of the Plan Propio I + D + i (grant number 2022-PRED-20658).

References

1. Cechetto, V., Di Felice, L., Medrano, J. A., et al. (2021). H_2 production via ammonia decomposition in a catalytic membrane reactor. *Fuel Processing Technology, 216*, 106772. https://doi.org/10.1016/j.fuproc.2021.106772
2. Valera-Medina, A., Amer-Hatem, F., Azad, A. K., et al. (2021). Review on ammonia as a potential fuel: From synthesis to economics. *Energy and Fuels, 35*, 6964–7029.
3. Lucentini, I., Garcia, X., Vendrell, X., & Llorca, J. (2021b). Review of the decomposition of ammonia to generate hydrogen. *Industrial and Engineering Chemistry Research, 60*, 18560–18611. https://doi.org/10.1021/acs.iecr.1c00843
4. Pinzón, M., Avilés-García, O., de la Osa, A. R., et al. (2022a). New catalysts based on reduced graphene oxide for hydrogen production from ammonia decomposition. *Sustainable Chemistry and Pharmacy, 25*, 100615. https://doi.org/10.1016/j.scp.2022.100615
5. Pinzón, M., Romero, A., de Lucas, C. A., et al. (2021a). Hydrogen production by ammonia decomposition over ruthenium supported on SiC catalyst. *Journal of Industrial and Engineering Chemistry, 94*, 326–335. https://doi.org/10.1016/j.jiec.2020.11.003

6. Pinzón, M., Romero, A., de Lucas-Consuegra, A., et al. (2022b). COx-free hydrogen production from ammonia at low temperature using Co/SiC catalyst: Effect of promoter. *Catalysis Today, 390–391*, 34–47. https://doi.org/10.1016/j.cattod.2021.12.005
7. Pinzón, M., Sánchez-Sánchez, A., Sánchez, P., et al. (2021b). Ammonia as a carrier for hydrogen production by using lanthanum based perovskites. *Energy Conversion and Management, 246*, 114681. https://doi.org/10.1016/j.enconman.2021.114681
8. Huang, C., Li, H., Yang, J., et al. (2019). $Ce_{0.6}Zr_{0.3}Y_{0.1}O_2$ solid solutions-supported Ni Co bimetal nanocatalysts for NH_3 decomposition. *Applied Surface Science, 478*, 708–716. https://doi.org/10.1016/j.apsusc.2019.01.269
9. Wu, Z. W., Li, X., Qin, Y. H., et al. (2020). Ammonia decomposition over SiO_2-supported Ni–Co bimetallic catalyst for COx-free hydrogen generation. *International Journal of Hydrogen Energy, 45*, 15263–15269. https://doi.org/10.1016/j.ijhydene.2020.04.007
10. Muroyama, H., Saburi, C., Matsui, T., & Eguchi, K. (2012). Ammonia decomposition over Ni/La_2O_3 catalyst for on-site generation of hydrogen. *Applied Catalysis A: General, 443–444*, 119–124. https://doi.org/10.1016/j.apcata.2012.07.031
11. Tran, D. T., Nguyen, T. H., Jeong, H., et al. (2022). Recent engineering advances in nanocatalysts for NH_3-to-H_2 conversion technologies. *Nano Energy, 94*, 106929.
12. Pinzón, M., Sánchez-Sánchez, A., Romero, A., et al. (2022c). Self-combustion Ni and Co-based perovskites as catalyst precursors for ammonia decomposition. Effect of Ce and Mg doping. *Fuel, 323*, 124384. https://doi.org/10.1016/J.FUEL.2022.124384
13. Da Silva, A. A. A., Da Costa, L. O. O., Mattos, L. V., & Noronha, F. B. (2013). The study of the performance of Ni-based catalysts obtained from $LaNiO_3$ perovskite-type oxides synthesized by the combustion method for the production of hydrogen by reforming of ethanol. *Catalysis Today, 213*, 25–32. https://doi.org/10.1016/j.cattod.2013.04.033
14. Sadabadi, H., Allahkaram, S. R., Kordijazi, A., et al. (2021). Structural characterization of $LaCoO_3$ perovskite nanoparticles synthesized by sol–gel autocombustion method. *Engineering Reports, 3*, 91–96. https://doi.org/10.1002/eng2.12335
15. Liu, L., Zhang, Z., Das, S., et al. (2020). $LaNiO_3$ as a precursor of Ni/La_2O_3 for reverse water-gas shift in DBD plasma: Effect of calcination temperature. *Energy Conversion and Management, 206*, 112475. https://doi.org/10.1016/j.enconman.2020.112475
16. Sihaib, Z., Puleo, F., Pantaleo, G., et al. (2019). The effect of citric acid concentration on the properties of $LaMnO_3$ as a catalyst for hydrocarbon oxidation. *Catalysts, 9*, 226. https://doi.org/10.3390/catal9030226
17. Li, Y., Wen, J., Ali, A. M., et al. (2018). Size structure–catalytic performance correlation of supported Ni/MCF-17 catalysts for COx-free hydrogen production. *Chemical Communications, 54*, 6364–6367. https://doi.org/10.1039/C8CC01884G
18. Okura, K., Okanishi, T., Muroyama, H., et al. (2016). Ammonia decomposition over nickel catalysts supported on rare-earth oxides for the on-site generation of hydrogen. *ChemCatChem, 8*, 2988–2995. https://doi.org/10.1002/cctc.201600610
19. Li, X., Li, D., Tian, H., et al. (2017). Dry reforming of methane over Ni/La_2O_3 nanorod catalysts with stabilized Ni nanoparticles. *Applied Catalysis B: Environmental, 202*, 683–694. https://doi.org/10.1016/j.apcatb.2016.09.071
20. Civera, A., Pavese, M., Saracco, G., & Specchia, V. (2003). Combustion synthesis of perovskite-type catalysts for natural gas combustion. *Catalysis Today, 83*, 199–211. https://doi.org/10.1016/S0920-5861(03)00220-7
21. Omari, E., Makhloufi, S., & Omari, M. (2017). Preparation by sol–gel method and characterization of Co-doped $LaNiO_3$ perovskite. *Journal of Inorganic and Organometallic Polymers and Materials, 27*, 1466–1472. https://doi.org/10.1007/s10904-017-0604-y
22. Santos, M. d. S., RCR, N., Noronha, F. B., et al. (2018). Perovskite as catalyst precursors in the partial oxidation of methane: The effect of cobalt, nickel and pretreatment. *Catalysis Today, 299*, 229–241. https://doi.org/10.1016/j.cattod.2017.06.027

23. Zhang, T., & Liu, Q. (2020). Mesostructured cellular foam silica supported bimetallic $LaNi_{1-x}CoxO_3$ catalyst for CO_2 methanation. *International Journal of Hydrogen Energy, 45*, 4417–4426. https://doi.org/10.1016/j.ijhydene.2019.12.006
24. Lucentini, I., García Colli, G., Luzi, C. D., et al. (2021a). Catalytic ammonia decomposition over Ni-Ru supported on CeO_2 for hydrogen production: Effect of metal loading and kinetic analysis. *Applied Catalysis B: Environmental, 286*. https://doi.org/10.1016/j.apcatb.2021.119896
25. Chang, F., Wu, H., Van Der, P. R., et al. (2019). Effect of pore confinement of $NaNH_2$ and KNH_2 on hydrogen generation from ammonia. *Journal of Physical Chemistry C, 123*, 21487–21496. https://doi.org/10.1021/acs.jpcc.9b03878
26. Su, Q., Gu, L., Yao, Y., et al. (2017). Layered double hydroxides derived Nix(MgyAlzOn) catalysts: Enhanced ammonia decomposition by hydrogen spillover effect. *Applied Catalysis B: Environmental, 201*, 451–460. https://doi.org/10.1016/j.apcatb.2016.08.051
27. Wang, L., Yi, Y., Zhao, Y., et al. (2015). NH_3 Decomposition for H_2 generation: Effects of cheap metals and supports on plasma-catalyst synergy. *ACS Catalysis, 5*, 4167–4174. https://doi.org/10.1021/acscatal.5b00728
28. Ganley, J. C., Thomas, F. S., Seebauer, E. G., & Masel, R. I. (2004). A priori catalytic activity correlations: The difficult case of hydrogen production from ammonia. *Catal Letters, 96*, 117–122. https://doi.org/10.1023/B:CATL.0000030108.50691.d4
29. Yu, Y., Gan, Y., Huang, C., et al. (2020). Ni/La_2O_3 and $Ni/MgO–La_2O_3$ catalysts for the decomposition of NH_3 into hydrogen. *International Journal of Hydrogen Energy, 45*, 16528–16539. https://doi.org/10.1016/j.ijhydene.2020.04.127

Defect Origin of the Light-Soaking Effects in Hybrid Perovskite Solar Cells

Jing Wang and Wan-Jian Yin

1 Introduction

The past decade has witnessed the rapid development of organic-inorganic hybrid perovskites (OIHPs), particularly their power conversion efficiency (PCE), which has dramatically increased from 3.8% in 2009 to a record 25.7%; this is comparable to the performance of commercial thin-film solar cells, such as Si, CdTe, and $Cu(In,Ga)Se_2$ [1]. Some studies have demonstrated that the excellent properties of OIHPs are mainly attributed to their large absorption coefficient [2, 3], high carrier diffusion length [4, 5], high charge carrier mobility [6], and unique defect tolerance [7, 8]. However, in practice, OIHPs inevitably suffer from the critical stability problems because their facile decomposition is exacerbated by external stimuli, such as air (oxygen), moisture, and solar illumination, which is a major obstacle for commercial applications. To mitigate these negative effects, device encapsulation has been employed to effectively minimize exposure to oxygen and humidity [9, 10]. However, the photostability issues of perovskite cells, such as light-soaking effects (LSEs), remain highly challenging because solar cells must work under light illumination.

J. Wang
School of Physical Science and Technology, Ningbo University, Ningbo, People's Republic of China

College of Energy, Soochow Institute for Energy and Materials InnovationS (SIEMIS), Soochow University, Suzhou, People's Republic of China

W.-J. Yin (✉)
College of Energy, Soochow Institute for Energy and Materials InnovationS (SIEMIS), Soochow University, Suzhou, People's Republic of China

Jiangsu Provincial Key Laboratory for Advanced Carbon Materials and Wearable Energy Technologies, Soochow University, Suzhou, People's Republic of China
e-mail: wjyin@suda.edu.cn

W. Nie, K. (Kris) Iniewski (eds.), *Metal-Halide Perovskite Semiconductors*,
https://doi.org/10.1007/978-3-031-26892-2_12

Based on existing reports, the PCE of perovskites exhibits two typical modes of LSEs under working conditions: (i) The device shows a decrease in PCE after storage in the dark and a gradual recovery of PCE to its initial state under light illumination (called the self-healing process) [11]. (ii) The PCE of the device gradually decreases under continuous illumination and shows a partial or complete self-healing process when placed in the dark [12, 13]. This anomalous behavior of LSEs has not been observed in conventional inorganic photovoltaic (PV) semiconductors.

In this chapter, by combining the methods of first-principles defect calculations, time-dependent density-functional theory (TD-DFT), and non-adiabatic molecular dynamics (NAMD), we discuss the defect properties of hybrid perovskite $CH_3NH_3PbI_3$ ($MAPbI_3$) cell materials and analyze why they exhibit giant, reversible, and bidirectional LSEs, unlike traditional semiconductor cells. This study focuses on three typical defects (I_{Pb}, I_i, and V_I) as examples to further reveal the behaviors of LSEs, and the results show that these abnormal LSEs are closely related to the stable configurations and properties of defects, ion diffusion barriers, carrier lifetimes, etc. Based on these, we develop a unified defect theory for LSEs. More importantly, we propose potential strategies for minimizing the LSEs to achieve high-performance and long-term stable PSCs.

2 Calculations Details

The structural, electronic, and defect properties of the $MAPbI_3$ were calculated using the Vienna *ab* initio simulation package (VASP) [14]. Here, the frozen projector-augmented wave (PAW) method [15] was used to address the interaction between electrons and ions, and the generalized gradient approximation (GGA) [16] describes the exchange correlation. The cutoff energy of the plane-wave basis was set to 300 eV throughout the calculation process. For crystal relaxation (unit cell), the convergence criteria for the total energy and force were set to less than 1×10^{-5} eV and 0.01 eV/Å, respectively. For the Monkhorst-Pack (MP) mesh [17] (k-point) within the first Brillouin zone (BZ), the k-points multiplied by the corresponding lattice constant, which was approximately equal to 30, were used as the benchmark. Since this chapter focuses on the properties of intrinsic defects and how the device performance is affected with/without external factors, considering that a relatively large supercell system is required for these studies, we used a $1 \times 1 \times 1$ single k-point to perform the simulation because $MAPbI_3$ belongs to a direct-bandgap system (at the Γ-point). In general, although the GGA functional can obtain reliable structures, it is often underestimated in bandgap predictions for semiconductor materials. To improve the accuracy of the bandgap, more advanced functionals, such as HSE and GW [18, 19], are commonly used. Unfortunately, these functionals are mainly suitable for relatively small systems and impractical for studying large systems with point defects because of their extremely high computational cost. Interestingly, for $MAPbI_3$, the GGA method can yield a bandgap value

close to the experimental measurements, which is because the errors generated by GGA and non-spin-orbit coupling (SOC) cancel each other when they are used simultaneously. Thus, the studies on the nature of the intrinsic defects in $MAPbI_3$ were performed based on the non-SOC-GGA method. Additionally, the climbing image-nudged elastic band (CI-NEB) [20] was used to calculate the diffusion energy barriers of ion migration.

To investigate the electron-hole recombination dynamic process, we combined the Quantum Espresso (QE) [21] and PYthon eXtension for Ab Initio Dynamics (PYXAID) [22, 23] packages to perform non-adiabatic molecular dynamics (NAMD) simulations. This process is roughly divided into three calculation steps: (i) After the optimized structures were obtained at 0 K, all systems were heated to 300 K in a canonical ensemble using the Nos e thermostat [24]. Thereafter, a 3 ps adiabatic MD trajectory was obtained with an integration time step of 1 fs and an Andersen thermostat collision frequency of 0.05 fs^{-1}. (ii) Along the 3 ps MD trajectory, the electronic structure of each frame was used by the QE code, and PYXAID analyzed the transition matrix elements and NA electron-phonon coupling (EPC) strength between the pairwise states. These time-dependent results were used for subsequent NAMD simulations and data analysis. Considering that $MAPbI_3$ is a system with a direct bandgap, the calculations for the two parts above were performed under a single k-point ($1 \times 1 \times 1$). (iii) NAMD was performed using the semiclassical decoherence-induced surface-hopping (DISH) method [25]. The carrier lifetimes (τ) were obtained by exponentially fitting the data with the relationship $p(t) = \exp(-t/\tau)$, where $p(t)$ is the population evolution between the pairwise states. To obtain better statistical calculations, we repeated NA coupling once to double the data as input for NAMD, where the first half of the data was regarded as the initial condition.

3 Results and Discussions

The LSEs of perovskite solar cell materials are affected by many factors, such as defect properties, ion-diffusion energy barriers, carrier lifetime, and light illumination. Therefore, it is necessary to systematically understand the correlation between these factors and the LSEs to guide the improvement of the PV performance of perovskites.

3.1 Defect Properties in Perovskite $MAPbI_3$

In practice, the preparation of perovskites using the solution method near room temperature inevitably produces various defects. Although these defects appear to be insignificant in size and quantity, they may have effects on some physical properties of PV materials; they may even directly determine the application direction.

Therefore, the theoretical study of the inherent defects of perovskite cells is important, and it is necessary to deepen our understanding of these defects.

3.1.1 Defective Behavior of the Rigid Models

Figure 1a shows the thermodynamic growth environment of cubic-phase (α-phase) $MAPbI_3$, based on the first-principles calculations. We can see from the results that if the synthesis conditions (or chemical potential) are limited to the red narrow range, it will be beneficial to promote the synthesis of $MAPbI_3$. Otherwise, binary impurity materials, such as CH_3NH_3I and PbI_2, are generated, which affects the perovskite quality. This emphasizes that the delicate control of the synthesis conditions is central to realizing the ideal crystal of $MAPbI_3$. Meanwhile, similar behavior is observed in other phases of $MAPbI_3$ [26], including all-inorganic perovskite systems, such as $CsPbI_3$ [27]. This may be related to the ionic character of the crystal lattices. In contrast, the growth conditions for conventional semiconductor materials with covalent bonds are not particularly significant [28, 29].

For the α-phase $MAPbI_3$ perovskite, we investigated all possible intrinsic defects, including two cation substitutions (MA_{Pb}, Pb_{MA}), three vacancies (V_{MA}, $V_{Pb,}$ V_I), three interstitials (MA_i, Pb_i, I_i), and four anion-cation substitutions (MA_I, Pb_I, I_{MA}, I_{Pb}). Since the formation of these defects varies in difficulty during the preparation process and depends on the chemical potential, studying the formation energies of the defects helps to understand which defects are prone to forming and how the defect properties can be regulated by chemical potential. The results are shown in Fig. 1b–d, which describe the formation energies under the Pb-poor/I-rich (A), moderate (B), and Pb-rich/I-poor (C) states shown in Fig. 1a, respectively. The smaller the formation energy, the easier it is for defects to form. For clarity, defects with low formation energies are depicted by thick-colored lines, whereas the gray dashed lines represent defects with high formation energies. Additionally, Fermi

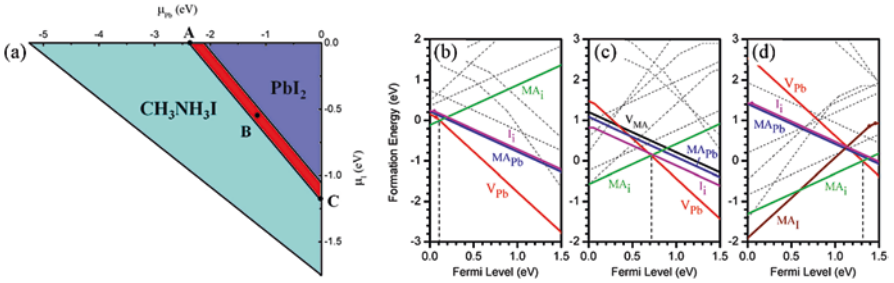

Fig. 1 (**a**) Thermodynamically stable ranges of α-phase $MAPbI_3$, CH_3NH_3I, and PbI_2; points A, B, and C represent three different chemical growth environments: A ($\mu_{MA} = -2.87$ eV, $\mu_{Pb} = -2.39$ eV, $\mu_I = 0$ eV), B ($\mu_{MA} = -2.41$ eV, $\mu_{Pb} = -1.06$ eV, $\mu_I = -0.60$ eV), and C ($\mu_{MA} = -1.68$ eV, $\mu_{Pb} = 0$ eV, $\mu_I = -1.19$ eV). (**b–d**) show the relationship between formation energy and Fermi levels at the chemical potentials A, B, and C, respectively. Adapted with permission from Ref. [7]. Copyright 2014 AIP Publishing LLC

pinning evolved from low energy to high energy as the chemical potentials increased (A to B to C), implying that the electrical conductivity of $MAPbI_3$ can be transformed from a very good *p*-type to a very good *n*-type system. However, such tunable behavior is not observed for other semiconductor solar cell materials. For example, the *p*-type doping of $Cu(In,Ga)Se_2$ and $Cu_2ZnSn(S,Se)_4$ is relatively easy; however, the *n*-type doping becomes difficult under equilibrium growth conditions [30, 31].

The effect of defects on the performance of PV materials depends on the defect formation energy and the electrical properties of the defects. Thus, we calculated the transition energy levels for all defects in $MAPbI_3$ (see Fig. 2), describing the corresponding Fermi levels when the formation energies of two charged states (*q* and *q′*) are equal and reflecting the difficulty of carrier transition from defect levels to band edges in the process of gaining or losing electrons. Combined with the results in Fig. 1, it was found that most defects with low formation energies were benign because of the shallow transition levels, such as MA_i and V_I. For defects with relatively deep transition levels, such as I_{MA}, I_{Pb}, Pb_i, and Pb_I, the formation energies of these harmful defects were considerably high, implying that they were not easily formed during the growth of $MAPbI_3$. With this unique defect property, OIHPs can achieve a PCE higher than 20% by solution synthesis at room temperature.

3.1.2 Anomalous Defects in $MAPbI_3$

In traditional semiconductor cells, once a defect is formed, the defect properties typically do not change accordingly because of the strong covalent nature of the crystal, resulting in a slight distortion near the defect. However, such defect characteristics are unsuitable for perovskites because of the soft lattice formed by ionic bonds.

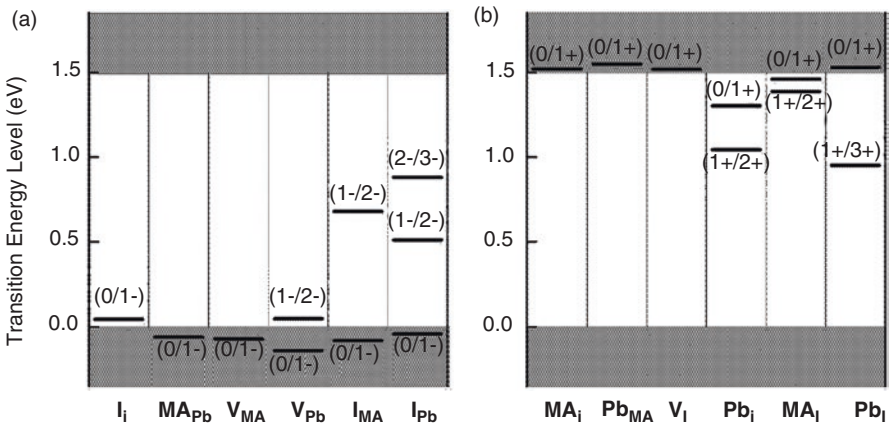

Fig. 2 Transition energy levels of 12 intrinsic defects in $MAPbI_3$, including (**a**) intrinsic acceptors and (**b**) donors; adapted with permission from Ref. [7]. Copyright 2014 AIP Publishing LLC

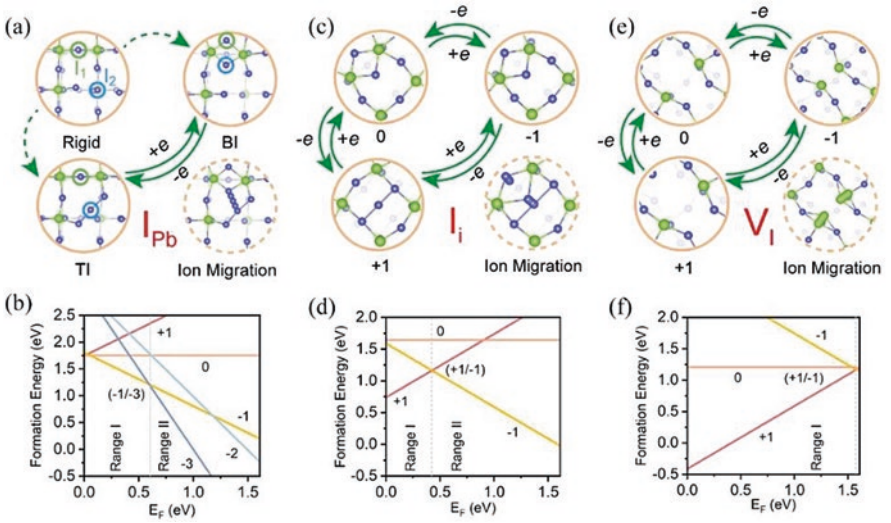

Fig. 3 (**a**, **c**, **e**) represent the local configurations of I_{Pb}, I_i, and V_I defects and their transitions via electron gains and losses and ionic migration, respectively. (**b**, **d**, **f**) represent the calculated formation energies of I_{Pb}, I_i, and V_I defects, respectively, at the selected chemical potential (point B in the study conducted in Ref. [7]). E_F is the Fermi energy referenced to the valence band maximum (VBM) level. Adapted with permission from Refs. [32]. Copyright 2021, American Chemical Society

Here, we take the above I_{Pb} defect as an example to reveal the anomalous behavior, the rigid mode of which is shown in Fig. 3a. The electronic properties demonstrate that regardless of the charge state of the defect, the defect states within the bandgap always originate from the dislocation bonds between the iodide ions on the lattice and the iodide ions on the replacement lead [26], which is in agreement with previous theoretical reports [33]. Notably, the above conclusions are based on the structures at 0 K; however, it has not been determined if they still hold at room temperature.

To address this issue, we performed NVT MD simulations at 300 K and found that the rigid model of I_{Pb} spontaneously transformed into stable configurations depending on the charge states, as shown in Fig. 3a for the bridge-iodine (BI) and trimer-iodine (TI) structures. The new structures can be viewed as the complex defects of both I_i and V_{Pb}, as supported by the theoretical work of Buin et al. [33], who showed that the rigid model is unstable based on the defect binding energies. Comparing their total energies, it was found that TI was more stable than the other structures (i.e., the rigid and BI models) for +1, 0, and −1 charged I_{Pb}, while for −2 and −3 charged states, BI became stable. Based on these results, we propose two possible points: (i) It was revealed that the rigid model I_{Pb} is unfavorable to form under the actual synthesis process of $MAPbI_3$, which mainly exists in BI or TI structures. (ii) Once the defect gains/loses electrons, iodine ions driven by the energy provided by the external thermal annealing or light soaking are beneficial for overcoming the kinetic barriers and realizing the transition between BI and TI

structures, as shown in Fig. 3a. Additionally, electronic structure studies showed that the BI structures in I_{Pb}^{-2} and I_{Pb}^{-3} were defect-free within the bandgap, implying that the effect of new structures on the device performance may be different from that of traditional rigid models.

Figure 3b shows the formation energies of stable I_{Pb} at moderate chemical potentials, which are significantly lower than those of the rigid model [7]. In particular, the high stability of I_{Pb}^{-3} afforded only one transition level within the bandgap, (−1/−3), which evolved from both (−1/−2) and (−2/−3) in the rigid model. When the Fermi level of the system was lower than 0.59 eV, the dominant charge state for I_{Pb} was −1, and it aggravated the recombination rate of carriers because of the strongly localized trapping state caused by iodine dislocation bonds, which is very unfavorable for PV performance. If the Fermi level is higher than 0.59 eV, the −3 charged state becomes the main defect. Owing to the absence of a defect state, the device performance is typically not affected.

Additionally, such abnormal behavior was found in other intrinsic defects, such as the I_i and V_I in $MAPbI_3$; their localized structures are shown in Fig. 3c and e, respectively. The results demonstrated that I_i in the low-charge state (−1) was the BI structure, while the high-charge state (+1) was the TI model. Owing to their structural similarities, the electronic natures of defects I_i^{+1} (I_i^0) and I_i^{-1} were similar to those of I_{Pb}^{-1} and I_{Pb}^{-3}, respectively. For stability, Fig. 3d indicates that I_i^0 is energetically unfavorable compared to either I_i^{+1} or I_i^{-1} over the entire range of Fermi levels within the bandgap, and it is a characteristic of typical negative-U defects. Among them, the relatively deep transition level (+1/−1) located at 0.41 eV above the VBM may accelerate carrier recombination, thereby resulting in a detrimental defect in $MAPbI_3$. This is consistent with previously published results [34, 35]. For V_I, unlike I_{Pb} and I_i, the local structures are Pb dimer (V_I^{-1}) and non-dimer (V_I^{+1} and V_I^0), respectively, and we observed that V_I^{+1} dominated the Fermi level over the entire range of the bandgap (see Fig. 3f). However, Agiorgousis et al. [36] demonstrated that V_I^{-1} with a Pb-dimer configuration is stable if the Fermi level is 0.19 below the conduction band maximum (CBM), which is obtained based on the PBE functional. Kang et al. considered SOC in the optimization of V_{Br} in $CsPbBr_3$ and found that two Pb ions near V_{Br} were converted from a dimer structure without the SOC method to a non-dimer structure, and the defect state disappeared [37].

Pb_i, Pb_{MA}, and I_{MA} have similar characteristics; their common feature is the formation of strong covalent bonds via Pb dimers and I trimers in their stable structures [36]. These cases reveal that when studying the PV properties of perovskites, the stable structure of intrinsic defects should be verified from the following aspects:

(i) MD simulations. The structure obtained based on the 0 K optimization may be a metastable configuration, while the MD simulation using 300 K reproduces the actual environment, which is beneficial for defects to tend to a more stable state.
(ii) Optimization algorithm. Since perovskite contains the heavy element Pb, the influence of the SOC effect on structural stability is worth considering.

3.2 Calculation of the Ion-Migration Barriers

Experiments have demonstrated that ion migration in perovskites can produce numerous observable phenomena, such as photocurrent hysteresis, LSEs, and light-induced phase separation. Therefore, understanding the microscopic mechanism behind ion migration is very important because it can provide clues for the development of perovskites with high stability and improved PV performance.

Although most studies have calculated the ion-migration barrier of $MAPbI_3$, there are significant discrepancies in the values [38–40]. Such discrepancies depend on many factors, such as the selection of the perovskite phase and parameter setting, which significantly hinder the understanding of the ion-migration process, as well as the evaluation of the dominant migratory ion. To exclude the interference of external factors, Yang et al. calculated the diffusion barriers of four low-energy defects in $MAPbI_3$ using a unified standard [41]. The results shown in Table 1 indicate that ions are more likely to migrate along the *ab* plane than the *c* axis. Meanwhile, V_I^{+1}, I_i^{-1}, and MA_i^{+1} have low diffusion barriers (0.19–0.38 eV), revealing that these defects can diffuse through iodine and MA ions at room temperature, and the corresponding diffusion paths are shown in Fig. 4, which describes the geometric structures at the initial, transition, and final states, respectively. Additionally, V_I^{+1} exhibited a significantly low defect formation energy according to the analysis in Sect. 3.1. Therefore, the combination of these factors suggests that V_I^{+1} was the dominant diffusion defect in $MAPbI_3$.

Notably, in early studies, ion migration was mainly analyzed and discussed from the point of view that the system was in equilibrium, and its initial and final states were typically the same structure. However, the physical mechanism by which external factors, such as illumination, regulate the ion-migration process is still lacking because perovskite cells must operate under solar illumination.

Figure 2 shows that the defect configurations and their properties in the ground state depend on the Fermi level of the system. If the Fermi level was higher than 0.59 eV, the defect states (DS) in stable I_{Pb}^{-3} with the BI configuration resonated with the VB. Under light illumination, the electrons in the VB were excited to the CB, as shown in Fig. 5a. This caused the dominant I_{Pb}^{-3} to lose electrons and transform into the relatively high-charge states (I_{Pb}^{-2}, I_{Pb}^{-1}, I_{Pb}^{0}, and I_{Pb}^{+1}) at BI, which was because the geometrical response lagged far behind that of electrons. Since BI structures at this time were metastable for I_{Pb}^{-1}, I_{Pb}^{0}, and I_{Pb}^{+1}, these defects evolved into stable TI

Table 1 Diffusion barriers (in eV) for V_I^{+1}, V_{MA}^{-1}, I_i^{-1}, and MA_i^{+1} along the *ab* plane and *c* axis in β-$MAPbI_3$

	V_I^{+1}	V_{MA}^{-1}	I_i^{-1}	MA_i^{+1}
ab plane	0.26	0.62	0.19	0.38
c axis	0.34	0.89	0.33	0.48

Adapted with permission from Ref. [41]. Copyright 2016 American Chemical Society

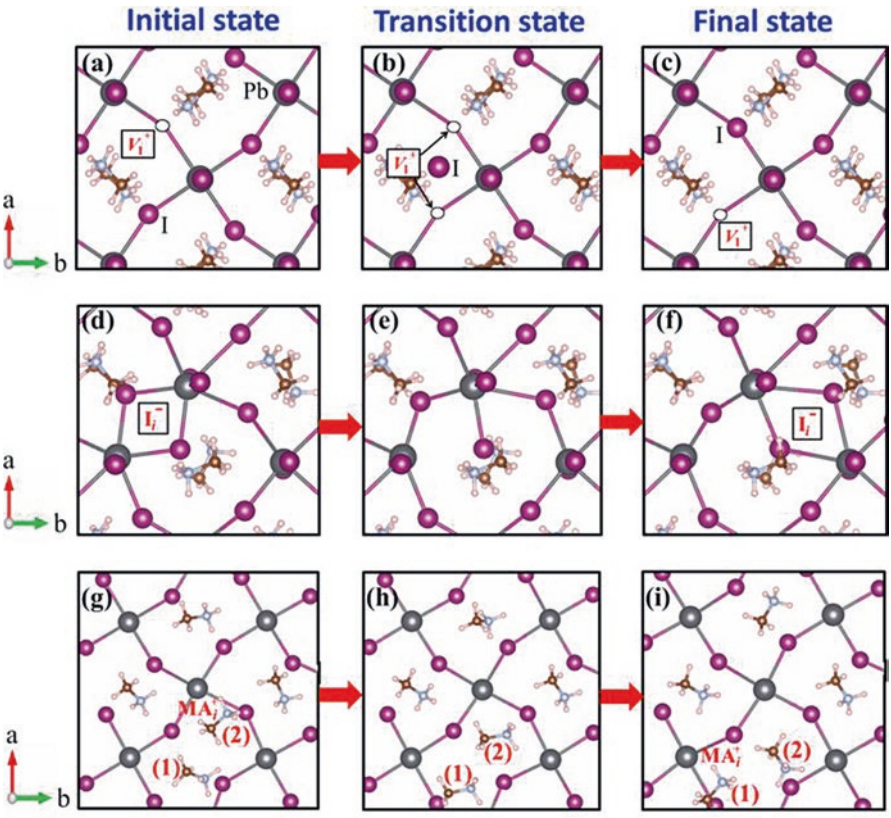

Fig. 4 Diffusion paths of V_I^{+1}, I_i^{-1}, and MA_i^{+1} along ab plane: the initial (**a**, **d**, **g**), the transition (**b**, **e**, **h**), and the final (**c**, **f**, **i**) state; in parts (**g**–**i**), the two MA ions involved in the kick-out process of the MA_i^{+1} diffusion are labeled (1) and (2). Adapted with permission from Ref. [41]. Copyright 2016 American Chemical Society

structures through ion migration (see the diffusion path shown in Fig. 3). The transition barrier between different configurations of I_{Pb}, as shown in Fig. 5b, indicated that the metastable BI structure only needed to cross a small activation energy barrier to transform into a stable TI structure, while the inverse process became difficult. In this case, illumination promoted the population transition from the BI to TI structure. When the Fermi level was less than 0.59 eV, for the stable I_{Pb}^{-1}, the antibonding $pp\sigma^*$ state formed by the dislocated bonds obtained electrons from the VB under illumination, as shown in Fig. 5c, and transitioned into low-charge states (I_{Pb}^{-2} and I_{Pb}^{-3}) and vice versa for ion diffusion. Both I_i and V_I had similar defect behaviors, except that the metastable structures for I_i^{-1} in the TI configuration and V_I^{+1} in the Pb-dimer configuration did not exist, and the transition barriers are shown in Fig. 5d and f, respectively.

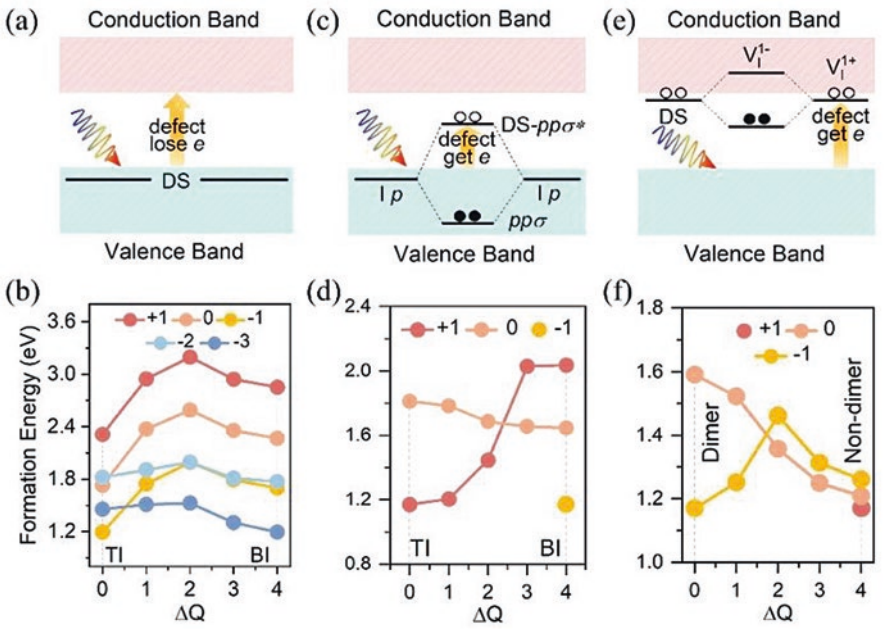

Fig. 5 (**a**, **c**, **e**) represent the formation mechanisms of the defect levels for I_{Pb}^{-3} (I_i^{-1}), I_{Pb}^{-3} (I_i^{-1}), and V_I^{+1} (V_I^{-1}), respectively, and the corresponding electron gains and losses in the DS under illumination. (**b**, **d**, **f**) Represent the transition barriers between different configurations for each charge state of I_{Pb}, I_i, and V_I defects, respectively. Adapted with permission from Refs. [32]. Copyright 2021, American Chemical Society

Interestingly, the surface of $MAPbI_3$ was favored for the formation of V_I because V_I has a relatively low formation energy, which is even lower than that of the bulk phase (see Fig. 6a), exhibiting a negative-U behavior. The transition level (+1/−1) was located at 1.18 eV above the VBM. Based on the transition energy barriers and their stable local structures, as shown in Fig. 6b and c, it was observed that V_I defects under illumination can realize the transformation of both defect configurations and positions between the first layer and second layer through the iodine migration [26].

3.3 Effect of Doping on Ion Migration in Perovskite

Cao et al. incorporated extrinsic alkali cations (including Cs^+, Rb^+, K^+, Na^+, and Li^+) into perovskite $FAPbI_3$ based on DFT calculations and proposed a new mechanism for the inhibition of ion migration [42]. Figure 7a shows possible structures for alkali cation substitution at an A site and occupancy at an interstitial site, and their local configurations are shown in the red-dashed box (b) and blue-dashed boxes (d),

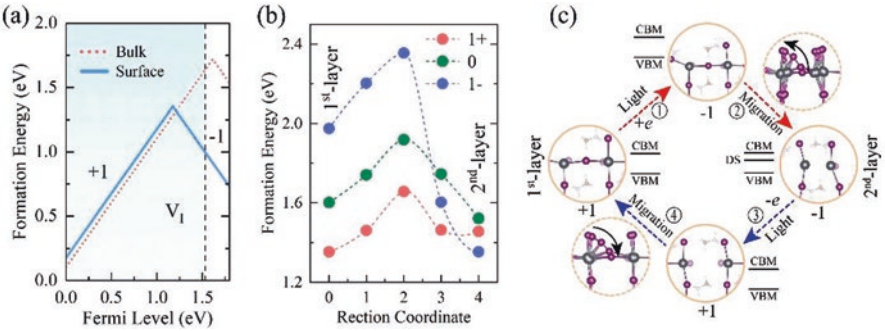

Fig. 6 (**a**) Formation energies of V_I defect as a function of the Fermi level at a specific chemical potential (point B) [26]; the red-dashed line and blue-solid line represent the formation energies of V_I in the bulk and near the surface, respectively. (**b**) The transition barriers between the outermost layer (first layer) and subsurface layer (second layer) for each charge state of V_I defect; (**c**) the structural evolution of the dominant surface V_I^{+1} in the first layer and V_I^{-1} in the second layer, marked with the red and blue arrows, respectively; the black arrows represent the migration direction of the iodine ions. Adapted with permission from Ref. [26]. Copyright 2022 American Chemical Society

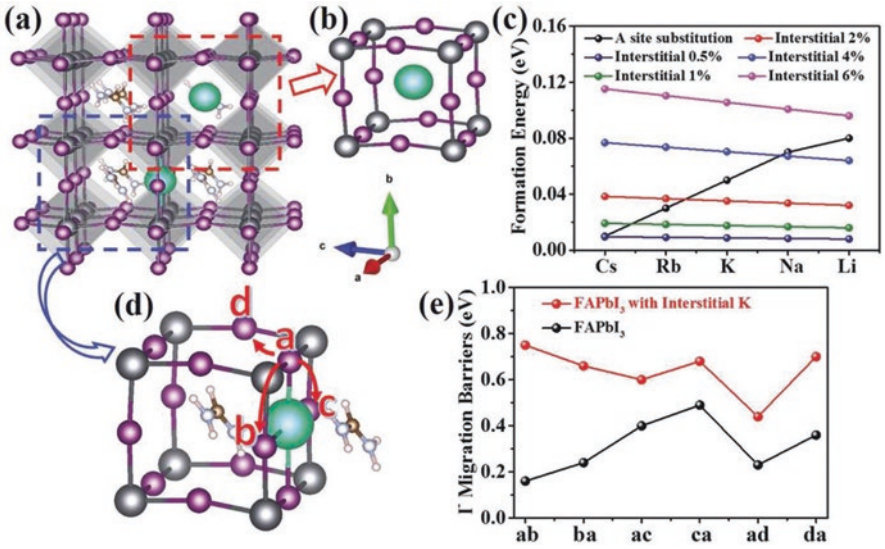

Fig. 7 Thermodynamic and kinetic properties of alkali cation incorporation (Cs^+, Rb^+, K^+, Na^+, and Li^+); (**a**) the possible locations of alkali cations in $FAPbI_3$, (**b**) at the A site and (**d**) at the interstitial site; (**c**) ΔH of alkali cation incorporation at an A site and an interstitial site; (**d**) the illustration of the I^- diffusion pathways, using $FAPbI_3$ with K^+ at an interstitial site as an example; (**e**) the comparison of the I^- diffusion barriers in $FAPbI_3$ with and without interstitial K^+; adapted with permission from Ref. [42]. Copyright 2018 WILEY-VCH Verlag GmbH & Co. KGaA, Weinheim

respectively. The formation energies (ΔH) of alkali cation incorporation at several concentrations in $FAPbI_3$ were analyzed; see Fig. 7c. From these results, the following conclusions can be drawn. (i) Both types of occupancy are thermodynamically possible when the percentage of alkali cations is small (≤6%). (ii) Interstitial occupation becomes more favorable as the concentration of alkali cations decreases. (iii) For the largest alkali (Cs^+) ions at considerably low concentrations (0.5%), the interstitial occupancy is even more stable than the A-site occupancy. Additionally, the authors studied the substitution of Pb ions at the B site with alkali cations and found that the formation energy was significantly higher than that of both types of occupancy.

Figure 7d shows the diffusion paths of I along several different directions with and without the interstitial occupancy of K^+. The calculated results of I^- migration barriers for each diffusion path are shown in Fig. 7e, from which it can be seen that the introduction of K^+ effectively raises the diffusion barriers in all diffusion paths, including ab, ac, ad, and reverse migrations. This was mainly attributed to three factors: (*i*) K^+ ions suppressed the iodine diffusion by blocking part of the diffusion path, such as the diffusion processes of ab (or ba) and ac (or ca). (*ii*) When K ions were incorporated into the system, the formation of V_I (i.e., the generation of free iodine ions) required more energy than that required in the pure perovskite host, as reflected by the defect formation energy [42, 43]. (*iii*) The introduction of K ions perturbed the original periodic potential field, resulting in the reorientation of FA^+, thereby enhancing the interaction between cations (FA^+) and anions (I^-). Therefore, the combined effect of these factors suppressed iodine ion diffusion, reduced the hysteresis of the I–V curve, and improved the photostability of $FAPbI_3$ solar cells.

Additionally, the incorporation (doping) of extrinsic ions effectively suppressed the formation of detrimental defects. Here, for example, Fig. 8a and b shows the stable crystal structures of V_I^{-1} without and with Br doping, respectively, and it can be seen that Br doping causes V_I^{-1} defects to transition from dimer to non-dimer structures. The breakdown of the original Pb-dimer bonds can be ascribed to the following two reasons [44]. First, the bond length of Pb-Br was shorter than that of Pb-I, as reflected by the small radius of Br^- (1.96 Å) than I^- (2.20 Å) and smaller lattice constant of $MAPbBr_3$ (5.94 Å) than $MAPbI_3$ (6.31 Å). Second, the bond energy of Pb-Br was stronger than that of Pb-I because of the strong electronegativity of Br, which can be reflected by the bulk moduli of $MAPbBr_3$ (26.42 GPa) and $MAPbI_3$ (20.24 GPa). Resultantly, Br had a relatively strong driving force to break the Pb-Pb dimer and drag the Pb atoms to their original lattice sites. For the barriers for the transition between the dimer and non-dimer structures, as shown in Fig. 8c, compared with the case without Br doping, it was observed that the Pb-Pb dimer became a metastable structure after Br doping. Further, the diffusion barrier decreased to 0.06 eV, implying that the Pb-dimer structure easily transformed into the non-dimer structure. Meanwhile, the transition from a non-dimer structure to a detrimental dimer structure became very difficult because this process needed to overcome a large energy barrier of 0.24 eV.

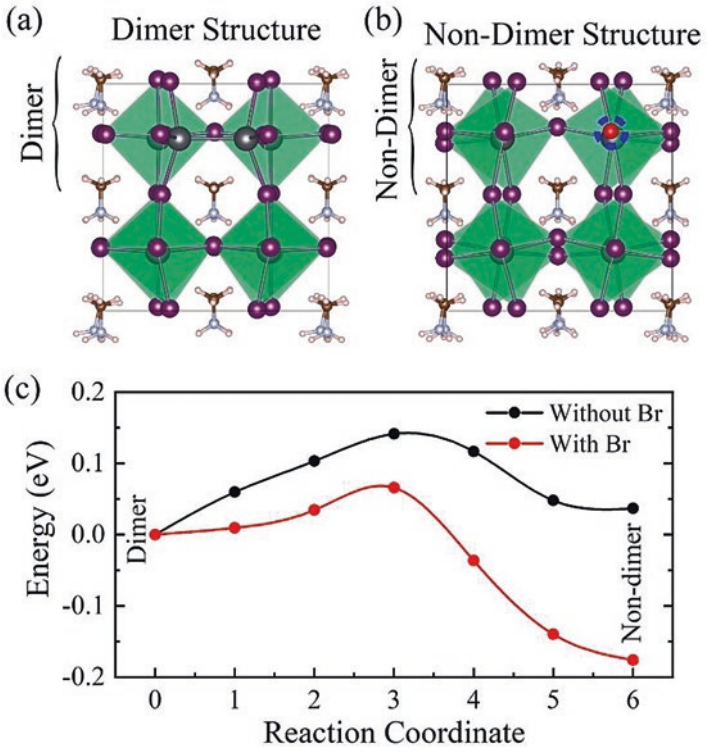

Fig. 8 (**a**) and (**b**) show the stable crystal structures of V_I^{-1} before and after Br doping, respectively. (**c**) The transition barriers between the dimer and non-dimer structures for $MAPbI_3$ and $MAPb(I_{0.96}Br_{0.04})_3$; adapted with permission from Refs. [44]. Copyright 2019 WILEY-VCH Verlag GmbH & Co. KGaA, Weinheim

3.4 Carrier Dynamic Behavior in Defective Systems

Previous studies on the influence of intrinsic defects on solar cell performance (carrier lifetime) were mainly based on qualitative analysis of both the defect transition level and the Shockley-Read-Hall (SRH) theory. Since the electron-phonon coupling (EPC) effects were not considered, quantifying the carrier lifetime of defects from first-principles simulations became difficult and relied mainly on experimental measurements. However, experimentally obtained carrier lifetimes were often the result of the combined effects of multiple defects, making it difficult to assess the degree to which each type of defect affected the device performance and what role they play (i.e., benign or detrimental defects). In recent years, the EPC in semiconductor materials has been efficiently calculated based on a variety of new algorithms to realize the quantitative analysis of carrier-capture rate and the carrier lifetime of defects, determine if it is an effective non-radiative recombination center,

and limit the PV efficiency. These methods have been applied to a wide range of photoexcitation dynamics studies, including defects, grain boundaries, dopings, and interfaces [26, 44–48], and provide an important means for understanding the dynamic process of carriers.

3.4.1 Analysis of Defect Carriers Based on Static Coupling Formalism

For example, although the calculations by Buin et al. [33, 49] demonstrated that the anti-site Pb_I defect in $MAPbI_3$ perovskite has a deep energy level within the band-gap and shows a high concentration under I-poor growth conditions, the problem of the carrier-capture rate is still unclear. Li et al. calculated the non-radiative recombination rate of the Pb_I defects using the static coupling formalism [50], where the non-radiative recombination probability is given by the following formula [51]:

$$W_{fi} = \frac{2\pi}{\hbar}\sum_m\sum_n p(i,m)\left|\sum_k \psi_f\left|\frac{\partial H}{\partial Q_k}\right|\psi_i\chi_n\left|Q_k\right|\chi_m\right|^2 \delta\left(\Delta E + E_m - E_n\right),$$

where indicators $i(m)$ and $f(\mathrm{n})$ represent the initial and final electronic (phonon) states, respectively, and k pervades the entire phonon mode. ΔE represents the energy difference between the initial E_{i0} and final E_{f0} states. E_m and E_n are the phonon energies of the initial and final states, respectively. $p(i, m)$ is the probability that the entire system is in its initial phonon state. The EPC strength is described by $\psi_f\left|\frac{\partial H}{\partial Q_k}\right|\psi_i$, and $\langle\chi_n|Q_k|\chi_m\rangle$ is defined as the lattice transition matrix element, which can be obtained using path integral techniques and Gaussian integration [52–54].

The carrier-capture rate (B) of defects can be calculated using the formula $B = W_{fi}V$, where V represents the volume of the entire supercell. The capture cross section σ is described by $B/\langle v\rangle$, where $\langle v\rangle$ is the thermal velocity, $\sqrt{\frac{3k_BT}{m^*}}$, which depends on the temperature T and effective mass m^* of the electron or hole carriers. According to previous theoretical studies, the effective masses of the electron and hole carriers for $MAPbI_3$ are $m_e^* = 0.19\ m_0$ and $m_h^* = 0.25\ m_0$, respectively [55].

Figure 9a shows the formation energies of Pb_I at all charge states in β-$MAPbI_3$. Since the probability of trapping more holes (electrons) simultaneously is typically very small, the main concern here is to capture carriers via the (+/2+) transition level, i.e., Pb_I^+ captures a hole from the VBM and transitions into Pb_I^{+2}, and Pb_I^{+2} captures an electron from the CBM and transitions into Pb_I^+. Figure 9b describes the process of carrier trapping by the deep-level defect states, that is, capturing holes from the VBM and electrons from the CBM, and generating phonons. The calculated results of the carrier-capture rate showed that it was positively correlated with the temperature (Fig. 9c and d). For Pb_I^+, its hole-capture rate and cross section at 300 K were $B_h = 4.1 \times 10^{-7}\ \mathrm{cm^3/s}$ and $\sigma_h = 1.8 \times 10^{-14}\ \mathrm{cm^2}$, respectively. For Pb_I^{+2},

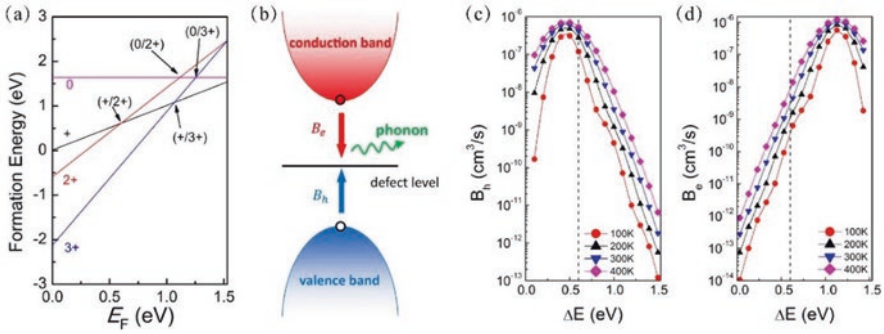

Fig. 9 (**a**) The formation energy of anti-site Pb_I defect at different charge states; (**b**) the schematic of the non-radiative carrier capture of the electron or hole through the defect level within the band-gap; (**c**) and (**d**) represent the relationship between the hole and electron-capture rates of Pb_I and transition levels at different temperatures, respectively. Adapted with permission from Ref. [51]. Copyright 2017 American Physical Society

they were $B_e = 2.8 \times 10^{-9}$ cm^3/s and $\sigma_e = 1.0 \times 10^{-16}$ cm^2, respectively. These values are larger than those of conventional semiconductors. To give a few examples, when Au is doped in silicon, the σ_e and σ_h are 3.5×10^{-15} cm^2 and 3.5×10^{-15} cm^2 [56], respectively; $\sigma_e\left(Sn_{Zn}^{+}\right)$ in Cu_2ZnSnS_4 is 4.7×10^{-18} cm^2 [57]. The large cross section of $MAPbI_3$ was mainly due to the heavy Pb-I atoms and soft phonon modes. To achieve carrier lifetimes higher than 1 μs, the concentrations of Pb_I^{+} and Pb_I^{+2} should be lower than 2.4×10^{12} cm^2 and 3.6×10^{14} cm^2, respectively. Based on this, they proposed an empirical criterion for the quick identification of effective non-radiative recombination centers [57]: when the defect captures carriers, the nearby configuration undergoes considerable structural relaxation, implying that there may be a large carrier-capture cross section.

3.4.2 Analysis of Carrier Dynamic Behavior via the NAMD Method

To understand the dynamic behavior of carriers after photoexcitation, it is necessary to understand the dynamic process of carriers trapped by defect states according to their electronic structures. Figure 10a–d shows the process of trapping the carriers of three defects (I_{Pb}, I_i, and V_I) in different charge states using the defect states in β-phase $MAPbI_3$, where the red and blue arrows indicate the relaxation/trapping process of electrons and holes, respectively. It was observed that the defect states in the bandgap made the recombination channel of the carriers more complicated.

Figure 10e–g plots the evolution of the population of the first excited state in the three defect systems, using the recombination rate to solve the coupled kinetic equation [48]. The results showed that the carrier lifetime of the defect with the deep level in the bandgap was one order of magnitude lower than that of the defect-free systems. For example, the TI configuration of I_{Pb} was only 3–6 ns, while BI had the order of tens of nanoseconds. This behavior was similarly possessed in iodine

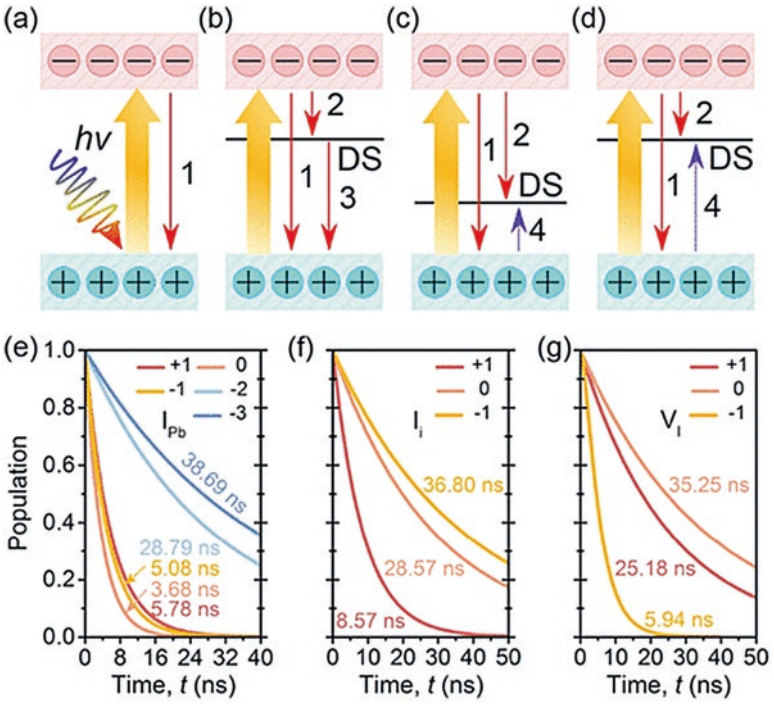

Fig. 10 Electron-hole recombination channels of (**a**) I_{Pb}^{-2}, I_{Pb}^{-3}, I_i^{-1}, and V_I^{+1}; (**b**) I_{Pb}^{+1}, I_{Pb}^{0}, I_{Pb}^{+1}, and I_i^{+1}; (**c**) I_i^0; and (**d**) V_I^0 and V_I^{-1}. Number 1 indicates the direct non-radiative recombination between the electrons in the CBM and the holes in the VBM. Number 2 is the electron trapping from the CBM to DS. Number 3 is the recombination of the trapped electron in DS with holes in VBM. Number 4 is the hole trapping from VBM to DS. (**e**–**g**) are the non-radiative e–h recombination dynamics for I_{Pb}, I_i, and V_I at different charge states. Adapted with permission from Ref. [32]. Copyright 2021 American Chemical Society

interstitials and vacancies. Among them, I_i^{+1} (8.57 ns) and V_I^{-1} (5.94 ns) were significantly lower than the other charge state systems. These data revealed that the deep DSs accelerated the recombination rate of photogenerated carriers, which was attributed to the strong EPC strength between DSs and band edges, thereby affecting the PCE of the $MAPbI_3$ cell.

Conversely, ion migration under nonequilibrium had a strong effect on the carrier lifetime. Tong et al. combined TD-DFT and NAMD methods to study the correlation between V_I migration and the carrier recombination rate in the α-$MAPbI_3$, as shown in Fig. 11. Further, they demonstrated that ion migration accelerates carrier recombination because the carrier lifetime scale (~10^{-2} ns) is significantly shorter than that of pristine perovskite (~ns) [58]. This result indicates that the beginning of the V_I defect no longer begins a defect during the migration process, which is consistent with the conclusions reported by many experiments [59–61].

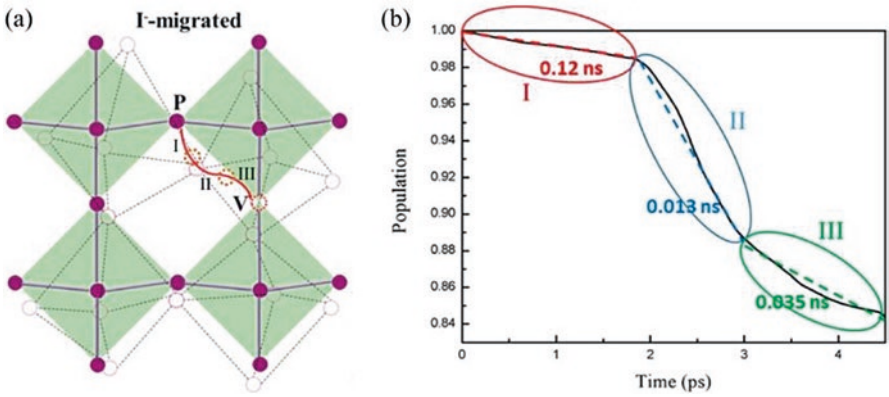

Fig. 11 (**a**) Schematic of I^- diffusion in the α-$MAPbI_3$. (**b**) The decay of the excited-state population in the iodine-migrated perovskite; the entire process is divided into three steps, including I, II, and III. Adapted with permission from Ref. [58]. Copyright 2020 American Chemical Society

Therefore, ion migration should be avoided to reduce the charge carrier losses and improve the PCE of halide perovskites.

To suppress the influence of negative factors on PV performance, we investigated the doping of a small amount of Br in α-$MAPbI_3$ and analyzed its effects on the carrier lifetime of V_I before and after doping. In the previous section, based on first-principles calculations, we qualitatively understood how Br doping passivates the DX center. The corresponding results for the carrier transition and recombination dynamic processes are shown in Fig. 12. Br doping increased the lifetime of excited electrons in the conduction band, from 3.2 ns to 19 ns, depending on the following aspects: (*i*) Decreased defect states. As shown in Figure (c), it is reflected that the carrier recombination channels are reduced. (*ii*) Reduced EPC. This is because the Pb-Pb-dimer bond was broken, saturating the iodine dangling bond (Fig. 8). Further, this can be reflected by calculating the standard deviation of the inorganic atoms at 300 K, as shown in Table 2, where small deviations indicate small atomic fluctuations. The calculation of the carrier lifetime provided direct theoretical evidence that Br doping can effectively passivate the detrimental V_I^- in $MAPbI_3$, as supported by the experimental conclusions [62–64]. For example, Kiermasch et al. found that the introduction of Br increased the carrier lifetime by ~2.75 times compared with the pristine system through transient photovoltage (TPV) and charge carrier extraction (CE) measurements [64].

3.5 LSEs in Perovskite

LSEs refer to the change in solar cell performance over time when exposed to light illumination. This behavior is common in PV materials, including traditional semiconductor cells, such as Si, CdTe, and $Cu(In,Ga)Se_2$, as well as novel perovskites,

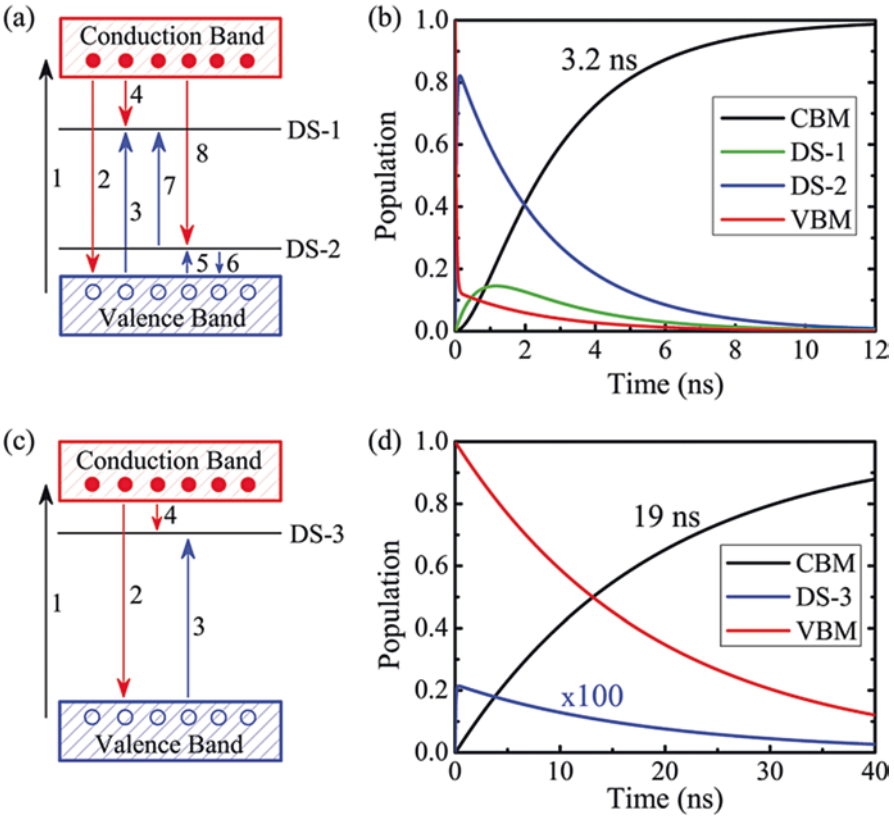

Fig. 12 Investigation of the carrier recombination process of V_I^- in $MAPbI_3$ (**a**) and $MAPb(I_{0.96}Br_{0.04})_3$ (**c**); among them, 1, formation of photoexcited holes and electrons; 2, direct non-radiative recombination between the VBM and CBM; 3, 5, the capture of holes by defect states (DS-1, DS-2, or DS-3); 4, 8, the trap-assisted recombinations of electrons from the CBM; 6, the detrapping of holes from shallow defect level (DS-2) to VBM; 7, the decay of trapped holes from DS-2 to DS-1; (**b**) and (**d**) are the evolution of the population of the key states in (**a**) and (**c**), respectively; adapted with permission from Ref. [44]. Copyright 2019 WILEY-VCH Verlag GmbH & Co. KGaA, Weinheim

Table 2 Standard deviation (Å) of atomic positions in $MAPbI_3$ and $MAPb(I_{0.96}Br_{0.04})_3$

	Pb-I/Br[a]	I[b]
$MAPbI_3$	0.495	0.635
$MAPb(I_{0.96}Br_{0.04})_3$	0.469	0.427

[a]Average over Pb and I/Br atoms

[b]I atom with the dangling bond; adapted with permission from Ref. [44]. Copyright 2019 WILEY-VCH Verlag GmbH & Co. KGaA, Weinheim

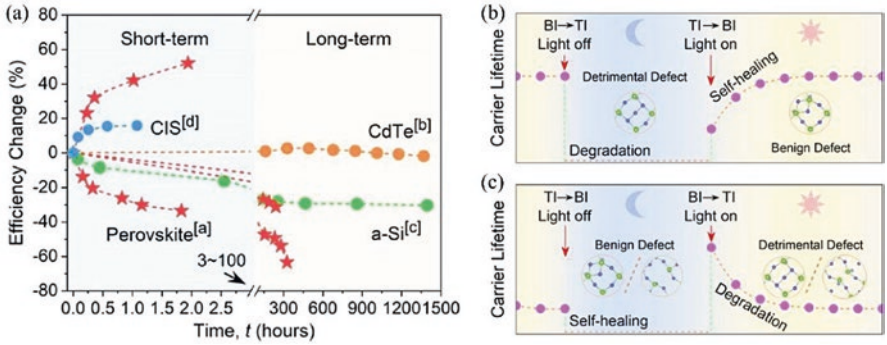

Fig. 13 (**a**) The efficiency of various PV materials changes over time. [**a**] Perovskite [11, 12]; [**b**] CdTe [65]; [**c**] Si [65]; [**d**] CIS [65, 66]. Two self-healing modes: (**b**) degradation in the dark and recovery under light illumination; (**c**) degradation under light illumination and recovery in the dark; adapted with permission from Ref. [32]. Copyright 2021 American Chemical Society

such as typical $MAPbI_3$, as shown in Fig. 13a. Notably, the PCE of perovskites shows a change (~50%) in just a few hours and even shows a different trend of change under illumination.

Taking I_{Pb} defect as an example, combined with the analysis of defect formation energy, ion diffusion barrier, and carrier lifetime calculation in the previous sections, if the Fermi energy level is below the VBM of +0.59 eV in the dark, the TI structures of I_{Pb}^{-1} are dominant and act as effective carrier centers because of the short carrier lifetime. Once illuminated, the detrimental I_{Pb}^{-1} defects trap electrons and transform into the BI structures of I_{Pb}^{-2} and I_{Pb}^{-3}, thereby exhibiting long carrier lifetimes. This process corresponds to the "self-healing under illuminant" observed in the experiment, as shown in Fig. 13b. If the light is turned off, the high-energy BI structures transform into the stable TI structures of I_{Pb}^{-1} under the ground state, corresponding to the "degradation in the dark" process.

Conversely, if the Fermi level is higher than VBM of +0.59 eV, the BI structures of I_{Pb}^{-3} with a long carrier lifetime are dominant. Upon illumination, the benign I_{Pb}^{-3} defects lose the electrons and transition into the TI structures (I_{Pb}^{-1}, I_{Pb}^{0}, and I_{Pb}^{+1}) with a short carrier lifetime, which corresponds to the process of "degradation under light," as shown in Fig. 13c. When the light was turned off, the TI structures in the excited state were unstable and transformed into stable BI structures under an equilibrium state, making the BI structures of I_{Pb}^{-3} dominant again, corresponding to the process of "self-healing in the dark."

Further, the other defect-induced LSEs can be explained by the analytical methods described above, such as I_i and V_I. They have the following common features. (i) The defect configurations depend on the charge states: the defects in different charge states have different stable configurations. (ii) There are differences in the carrier lifetimes of the different configurations. (iii) The transition barriers between the different defect configurations are low. As a result, perovskites exhibit the grant, reversible, and bidirectional LSEs observed experimentally. Additionally,

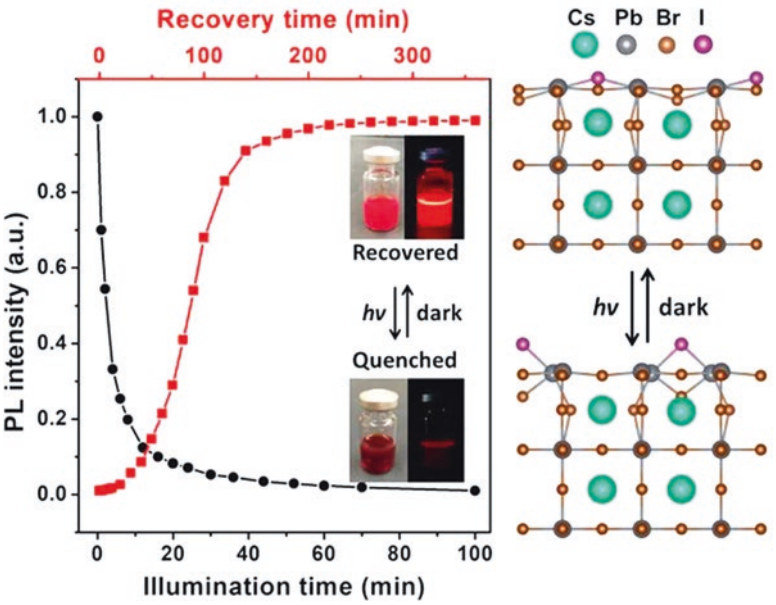

Fig. 14 Left panel: the degradation process of photoluminescence (PL) intensity under light illumination and PL recovery in the dark. Right panel: the evolution of two configurations at the atomic level corresponding to the left panel; adapted with permission from Ref. [67]. Copyright 2020 American Chemical Society

all-inorganic $CsPbBr_3$ perovskite quantum dots (PQD) exhibit the behavior of LSEs [67], as shown in Fig. 14, which is ascribed to the migration of iodide ions on the PQD surface. Under illumination, the iodine ion migration forms V_I, lattice distortion, and fluorescence quenching. In the dark, the migrated iodine ions spontaneously migrate back and fill V_I defects, resulting in fluorescence recovery.

To mitigate the impact of LSEs on the performance and stability of perovskite solar cells, we propose three possible methods based on the defect commonality that causes LSEs:

(i) Decreasing the defect concentration. This requires the synthesis of high-quality perovskite crystals to avoid the formation of numerous defect configurations.
(ii) Minimizing the number of different defect configurations. For example, we can effectively suppress the formation of detrimental Pb-dimer defects after electron capture by introducing an appropriate amount of Br.
(iii) Raise the diffusion energy barrier of ions, particularly halogen ions. For example, A-site and B-site doping have been shown to increase the ion diffusion barrier and phase stability of perovskites [42, 68–70], thereby reducing LSEs.

4 Conclusions

In conclusion, this chapter systematically discusses why perovskite solar cells, unlike traditional PV materials, exhibit giant, reversible, and bidirectional LSEs from an atomic-level perspective. First, we concluded that $MAPbI_3$ perovskite has excellent photoelectric performance, which is attributed to its unique defect characteristics. Second, it was found that some abnormal configurations of intrinsic defects are stable at specific charge states, thereby affecting the defect properties, such as I_{Pb}, I_i, and V_I. Third, by combining the factors of illumination and ion diffusion, we established a transition mechanism between the different defect configurations. Additionally, NAMD demonstrated that both deep-level defects and ion diffusion accelerate the carrier recombination rate and revealed the effectiveness of external ion doping on the enhancement of the carrier lifetime and diffusion barrier. The combined effects of these factors enabled us to gain a relatively deep understanding of the physical picture behind LSEs. More importantly, based on these results, we propose potential strategies for minimizing LSEs to achieve high-performance and long-term stable PSCs.

Acknowledgments This work was supported by the National Natural Science Foundation of China (Grant Nos. 12204256, 12147121, 11974257, and 11904246), China Postdoctoral Science Foundation (Grant 2020 M671570), Jiangsu Distinguished Young Talent Funding (Grant BK20200003), and National Key Research and Development Program of China (Grant 2020YFB1506400). The DFT calculations were performed at the National Supercomputer Center in Tianjin [TianHe-1(A)].

References

1. NPEL. *Best research-cell efficiency chart.* https://www.nrel.gov/pv/cell-efficiency.html.
2. Yin, W. J., Shi, T., & Yan, Y. (2014). Unique properties of halide perovskites as possible origins of the superior solar cell performance. *Advanced Materials, 26*(27), 4653.
3. De Wolf, S., Holovsky, J., Moon, S. J., Loper, P., Niesen, B., Ledinsky, M., et al. (2014). Organometallic halide perovskites: Sharp optical absorption edge and its relation to photovoltaic performance. *Journal of Physical Chemistry Letters, 5*(6), 1035.
4. Stranks, S. D., Eperon, G. E., Grancini, G., Menelaou, C., Alcocer, M. J., Leijtens, T., et al. (2013). Electron-hole diffusion lengths exceeding 1 micrometer in an organometal trihalide perovskite absorber. *Science, 342*(6156), 341.
5. Wehrenfennig, C., Eperon, G. E., Johnston, M. B., Snaith, H. J., & Herz, L. M. (2014). High charge carrier mobilities and lifetimes in organolead trihalide perovskites. *Advanced Materials, 26*(10), 1584.
6. Ponseca, C. S., Jr., Savenije, T. J., Abdellah, M., Zheng, K., Yartsev, A., Pascher, T., et al. (2014). Organometal halide perovskite solar cell materials rationalized: Ultrafast charge generation, high and microsecond-long balanced mobilities, and slow recombination. *Journal of the American Chemical Society, 136*(14), 5189.
7. Yin, W.-J., Shi, T., & Yan, Y. (2014). Unusual defect physics in $CH_3NH_3PbI_3$ perovskite solar cell absorber. *Applied Physics Letters, 104*(6), 063903.

8. Yin, W.-J., Chen, H., Shi, T., Wei, S.-H., & Yan, Y. (2015). Origin of high electronic quality in structurally disordered $CH_3NH_3PbI_3$ and the passivation effect of Cl and O at grain boundaries. *Advanced Electronic Materials, 1*(6), 1500044.
9. Jiang, Y., Qiu, L., Juarez-Perez, E. J., Ono, L. K., Hu, Z., Liu, Z., et al. (2019). Reduction of lead leakage from damaged lead halide perovskite solar modules using self-healing polymer-based encapsulation. *Nature Energy, 4*(7), 585.
10. Ma, S., Bai, Y., Wang, H., Zai, H., Wu, J., Li, L., et al. (2020). 1000 h Operational lifetime perovskite solar cells by ambient melting encapsulation. *Advanced Energy Materials, 10*(9), 1902472.
11. Huang, F., Jiang, L., Pascoe, A. R., Yan, Y., Bach, U., Spiccia, L., et al. (2016). Fatigue behavior of planar $CH_3NH_3PbI_3$ perovskite solar cells revealed by light on/off diurnal cycling. *Nano Energy, 27*, 509.
12. Nie, W., Blancon, J.-C., Neukirch, A. J., Appavoo, K., Tsai, H., Chhowalla, M., et al. (2016). Light-activated photocurrent degradation and self-healing in perovskite solar cells. *Nature Communications, 7*(1), 11574.
13. Cheng, Y., Liu, X., Guan, Z., Li, M., Zeng, Z., Li, H. W., et al. (2021). Revealing the degradation and self-healing mechanisms in perovskite solar cells by sub-bandgap external quantum efficiency spectroscopy. *Advanced Materials, 33*(3), e2006170.
14. Kresse, K. G. G., & Furthmüller, J. (1996). Efficient iterative schemes for ab initio total-energy calculations using a plane-wave basis set. *Physical Review B, 54*, 11169.
15. Kresse, G., & Joubert, D. (1999). From ultrasoft pseudopotentials to the projector augmented-wave method. *Physical Review B, 59*(3), 1758.
16. Perdew, J. P., Burke, K., & Ernzerhof, M. (1996). Generalized gradient approximation made simple. *Physical Review Letters, 77*(18), 3865.
17. Monkhorst, H. J., & Pack, J. D. (1976). Special points for Brillouin-zone integrations. *Physical Review B, 13*(12), 5188.
18. Heyd, J., Scuseria, G. E., & Ernzerhof, M. (2003). Hybrid functionals based on a screened Coulomb potential. *Journal of Chemical Physics, 118*(18), 8207.
19. Shishkin, M., & Kresse, G. (2007). Self-consistent G W calculations for semiconductors and insulators. *Physical Review B, 75*(23), 235102.
20. Henkelman, G., Uberuaga, B. P., & Jónsson, H. (2000). A climbing image nudged elastic band method for finding saddle points and minimum energy paths. *Journal of Chemical Physics, 113*(22), 9901.
21. Giannozzi, P., Baroni, S., Bonini, N., Calandra, M., Car, R., Cavazzoni, C., et al. (2009). Quantum Espresso: A modular and open-source software project for quantum simulations of materials. *Journal of Physics Condensed Matter, 21*(39), 395502.
22. Akimov, A. V., & Prezhdo, O. V. (2013). The PYXAID program for non-adiabatic molecular dynamics in condensed matter systems. *Journal of Chemical Theory and Computation, 9*(11), 4959.
23. Akimov, A. V., & Prezhdo, O. V. (2014). Advanced capabilities of the PYXAID program: Integration schemes, decoherence effects, multiexcitonic states, and field-matter interaction. *Journal of Chemical Theory and Computation, 10*(2), 789.
24. Nosé, S. (1984). A unified formulation of the constant temperature molecular dynamics methods. *Journal of Chemical Physics, 81*(1), 511.
25. Jaeger, H. M., Fischer, S., & Prezhdo, O. V. (2012). Decoherence-induced surface hopping. *Journal of Chemical Physics, 137*(22), 22A545.
26. Wang, J., & Yin, W. J. (2022). Revisiting the iodine vacancy surface defects to rationalize passivation strategies in perovskite solar cells. *Journal of Physical Chemistry Letters, 13*(29), 6694.
27. Huang, Y., Yin, W.-J., & He, Y. (2018). Intrinsic point defects in inorganic cesium lead iodide perovskite $CsPbI_3$. *The Journal of Physical Chemistry C, 122*(2), 1345.

28. Malitckaya, M., Komsa, H.-P., Havu, V., & Puska, M. J. (2017). First-principles modeling of point defects and complexes in thin-film solar-cell absorber $CuInSe_2$. *Advanced Electronic Materials, 3*(6), 1600353.
29. Bailey, C. L., Liborio, L., Mallia, G., Tomić, S., & Harrison, N. M. (2010). Defect physics of $CuGaS_2$. *Physical Review B, 81*(20), 205214.
30. Chen, S., Gong, X. G., Walsh, A., et al. (2010). Defect physics of the kesterite thin-film solar cell absorber Cu_2ZnSnS_4. *Applied Physics Letters, 96*(2), 021902.
31. Zhang, S., Wei, S.-H., Zunger, A., & Katayama-Yoshida, H. (1998). Defect physics of the $CuInSe_2$ chalcopyrite semiconductor. *Physical Review B, 57*(16), 9642.
32. Wang, J., Duan, X., & Yin, W. J. (2021). Photoinduced dynamic defects responsible for the giant, reversible, and bidirectional light-soaking effect in perovskite solar cells. *Journal of Physical Chemistry Letters, 12*(38), 9328.
33. Buin, A., Comin, R., Xu, J., Ip, A. H., & Sargent, E. H. (2015). Halide-dependent electronic structure of organolead perovskite materials. *Chemistry of Materials, 27*(12), 4405.
34. Zhang, X., Turiansky, M. E., Shen, J.-X., & Van de Walle, C. G. (2020). Iodine interstitials as a cause of nonradiative recombination in hybrid perovskites. *Physical Review B, 101*(14), 140101.
35. Meggiolaro, D., Motti, S. G., Mosconi, E., Barker, A. J., Ball, J., Andrea Riccardo Perini, C., et al. (2018). Iodine chemistry determines the defect tolerance of lead-halide perovskites. *Energy & Environmental Science, 11*(3), 702.
36. Agiorgousis, M. L., Sun, Y. Y., Zeng, H., & Zhang, S. (2014). Strong covalency-induced recombination centers in perovskite solar cell material $CH_3NH_3PbI_3$. *Journal of the American Chemical Society, 136*(41), 14570.
37. Kang, J. (2020). Effects of band edge positions on defect structure in lead halide perovskites: A case study on the Br vacancy in $CsPbBr_3$. *Physical Review Materials, 4*(8), 085405.
38. Eames, C., Frost, J. M., Barnes, P. R., O'Regan, B. C., Walsh, A., & Islam, M. S. (2015). Ionic transport in hybrid lead iodide perovskite solar cells. *Nature Communications, 6*(1), 7497.
39. Azpiroz, J. M., Mosconi, E., Bisquert, J., & De Angelis, F. (2015). Defect migration in methylammonium lead iodide and its role in perovskite solar cell operation. *Energy & Environmental Science, 8*(7), 2118.
40. Haruyama, J., Sodeyama, K., Han, L., & Tateyama, Y. (2015). First-principles study of ion diffusion in perovskite solar cell sensitizers. *Journal of the American Chemical Society, 137*(32), 10048.
41. Yang, D., Ming, W., Shi, H., Zhang, L., & Du, M.-H. (2016). Fast diffusion of native defects and impurities in perovskite solar cell material $CH_3NH_3PbI_3$. *Chemistry of Materials, 28*(12), 4349.
42. Cao, J., Tao, S. X., Bobbert, P. A., Wong, C. P., & Zhao, N. (2018). Interstitial occupancy by extrinsic Alkali cations in perovskites and its impact on ion migration. *Advanced Materials, 30*(26), e1707350.
43. Shi, T., Yin, W.-J., & Yan, Y. (2014). Predictions for p-type $CH_3NH_3PbI_3$ perovskites. *Journal of Physical Chemistry C, 118*(44), 25350.
44. Wang, J., Li, W., & Yin, W. J. (2020). Passivating detrimental DX centers in $CH_3NH_3PbI_3$ for reducing nonradiative recombination and elongating carrier lifetime. *Advanced Materials, 32*(6), e1906115.
45. Long, R., Liu, J., & Prezhdo, O. V. (2016). Unravelling the effects of grain boundary and chemical doping on electron-hole recombination in $CH_3NH_3PbI_3$ perovskite by time-domain atomistic simulation. *Journal of the American Chemical Society, 138*(11), 3884.
46. Long, R., English, N. J., & Prezhdo, O. V. (2012). Photo-induced charge separation across the graphene-TiO_2 interface is faster than energy losses: a time-domain ab initio analysis. *Journal of the American Chemical Society, 134*(34), 14238.
47. Liu, J., & Prezhdo, O. V. (2015). Chlorine doping reduces electron-hole recombination in lead iodide perovskites: Time-domain ab initio analysis. *Journal of Physical Chemistry Letters, 6*(22), 4463.

48. Li, W., Sun, Y. Y., Li, L., Zhou, Z., Tang, J., & Prezhdo, O. V. (2018). Control of charge recombination in perovskites by oxidation state of halide vacancy. *Journal of the American Chemical Society, 140*(46), 15753.
49. Buin, A., Pietsch, P., Xu, J., Voznyy, O., Ip, A. H., Comin, R., et al. (2014). Materials processing routes to trap-free halide perovskites. *Nano Letters, 14*(11), 6281.
50. Shi, L., Xu, K., & Wang, L.-W. (2015). Comparative study of ab initio nonradiative recombination rate calculations under different formalisms. *Physical Review B, 91*(20), 205315.
51. Li, J., Zhu, H.-F., Zhang, Y.-Y., Yuan, Z.-K., Chen, S., & Gong, X.-G. (2017). Large carrier-capture rate of Pb_I antisite in $CH_3NH_3PbI_3$ induced by heavy atoms and soft phonon modes. *Physical Review B, 96*(10), 104103.
52. Ferrer, F. J. A., Cerezo, J., Soto, J., Improta, R., Santoro, F. J. C., & Chemistry, T. (2014). First-principle computation of absorption and fluorescence spectra in solution accounting for vibronic structure, temperature effects and solvent inhomogenous broadening. *Computational and Theoretical Chemistry, 1040*, 328.
53. Borrelli, R., Capobianco, A., & Peluso, A. (2012). Generating function approach to the calculation of spectral band shapes of free-base chlorin including Duschinsky and Herzberg–Teller effects. *Journal of Physical Chemistry A, 116*(40), 9934.
54. Baiardi, A., Bloino, J., & Barone, V. (2013). General time dependent approach to vibronic spectroscopy including Franck–Condon, Herzberg–Teller, and Duschinsky effects. *Journal of Chemical Theory and Computation, 9*(9), 4097.
55. Yin, W.-J., Yang, J.-H., Kang, J., Yan, Y., & Wei, S.-H. (2015). Halide perovskite materials for solar cells: A theoretical review. *Journal of Materials Chemistry A, 3*(17), 8926.
56. Bemski, G. (1958). Recombination properties of gold in silicon. *Physical Review, 111*(6), 1515.
57. Li, J., Yuan, Z.-K., Chen, S., Gong, X.-G., & Wei, S.-H. (2019). Effective and noneffective recombination center defects in Cu_2ZnSnS_4: Significant difference in carrier capture cross sections. *Chemistry of Materials, 31*(3), 826.
58. Tong, C. J., Li, L., Liu, L. M., & Prezhdo, O. V. (2020). Synergy between ion migration and charge carrier recombination in metal-halide perovskites. *Journal of the American Chemical Society, 142*(6), 3060.
59. Tress, W., Yavari, M., Domanski, K., Yadav, P., Niesen, B., Correa Baena, J. P., et al. (2018). Interpretation and evolution of open-circuit voltage, recombination, ideality factor and subgap defect states during reversible light-soaking and irreversible degradation of perovskite solar cells. *Energy & Environmental Science, 11*(1), 151.
60. Gerhard, M., Louis, B., Camacho, R., Merdasa, A., Li, J., Kiligaridis, A., et al. (2019). Microscopic insight into non-radiative decay in perovskite semiconductors from temperature-dependent luminescence blinking. *Nature Communications, 10*(1), 1698.
61. deQuilettes, D. W., Zhang, W., Burlakov, V. M., Graham, D. J., Leijtens, T., Osherov, A., et al. (2016). Photo-induced halide redistribution in organic-inorganic perovskite films. *Nature Communications, 7*(1), 11683.
62. Cao, K., Cui, J., Zhang, H., Li, H., Song, J., Shen, Y., et al. (2015). Efficient mesoscopic perovskite solar cells based on the $CH_3NH_3PbI_2Br$ light absorber. *Journal of Materials Chemistry A, 3*(17), 9116.
63. Zhang, F., Yang, B., Mao, X., Yang, R., Jiang, L., Li, Y., et al. (2017). Perovskite $CH_3NH_3PbI_{3-x}Br_x$ single crystals with charge-carrier lifetimes exceeding 260 μs. *ACS Applied Materials & Interfaces, 9*(17), 14827.
64. Kiermasch, D., Rieder, P., Tvingstedt, K., Baumann, A., & Dyakonov, V. (2016). Improved charge carrier lifetime in planar perovskite solar cells by bromine doping. *Scientific Reports, 6*(1), 39333.
65. Gostein, M., & Dunn, L. (2011). Light soaking effects on photovoltaic modules: Overview and literature review. *2011 37th IEEE photovoltaic specialists conference: IEEE*. p. 003126.
66. Willett, D., & Kuriyagawa, S. (1993). The effects of sweep rate, voltage bias and light soaking on the measurement of CIS-based solar cell characteristics. *Conference record of the twenty third IEEE photovoltaic specialists conference-1993* (Cat No 93CH3283–9): IEEE. p. 495.

67. Wang, H., Zhang, X., Sui, N., Hu, Y., Colvin, V. L., Bai, X., et al. (2020). Emission quenching and recovery of illuminated perovskite quantum dots due to iodide ion migration. *Journal of Physical Chemistry Letters, 11*(15), 6168.
68. Jena, A. K., Kulkarni, A., Sanehira, Y., Ikegami, M., & Miyasaka, T. (2018). Stabilization of α-$CsPbI_3$ in ambient room temperature conditions by incorporating Eu into $CsPbI_3$. *Chemistry of Materials, 30*(19), 6668.
69. Yao, J. S., Ge, J., Wang, K. H., Zhang, G., Zhu, B. S., Chen, C., et al. (2019). Few-nanometer-sized alpha-$CsPbI_3$ quantum dots enabled by strontium substitution and iodide passivation for efficient red-light emitting diodes. *Journal of the American Chemical Society, 141*(5), 2069.
70. Zheng, F., Chen, W., Bu, T., Ghiggino, K. P., Huang, F., Cheng, Y., et al. (2019). Triggering the passivation effect of potassium doping in mixed-cation mixed-halide perovskite by light illumination. *Advanced Energy Materials, 9*(24), 1901016.

Single-Crystal Halide Perovskites for Transistor Applications

Feng Li

Halide perovskites have emerged as a promising family of candidates with a unique combination of extraordinary optoelectronic properties and facile solution-processed synthetic and fabrication routes, gaining tremendous achievements in broadly ranged energy-related and optoelectronic applications, such as solar cells, light-emitting diodes, photodetectors, and photocatalysis. Recent advances have also demonstrated the extraordinary electronic properties, mainly including high carrier mobilities and ambipolar characteristics, making this class of semiconductors ideal for high-performance transistor devices with multifunctions. In comparison to the polycrystalline counterparts, halide perovskite single crystals featuring low defects and trap densities exhibit more remarkable carrier dynamics and enhanced stabilities, holding significant potentials for transistor applications. In this chapter, we overview the field of emerging transistors that are made by solution-processed single-crystal perovskites as well as discuss the remained challenges and future opportunities. We begin with the brief introductions on the basics of transistors; then, we discuss the unique features of these perovskite crystals in detail, such as tunable bandgap, reasonable carrier mobility, ambipolar charge transport, and defect and trap characteristics, facilitating the transistor devices. Thereafter, we highlight the survey on the recent achievements regarding transistors based on single-crystal perovskites in various forms. Finally, we provide our perspectives on the main challenges and future developments of this research field.

F. Li (✉)
The School of Physics, the University of Sydney, Sydney, NSW, Australia

College of Physics, Sichuan University, Chengdu, Sichuan, China
e-mail: feng.li2@sydney.edu.au

W. Nie, K. (Kris) Iniewski (eds.), *Metal-Halide Perovskite Semiconductors*,
https://doi.org/10.1007/978-3-031-26892-2_13

1 Introduction

Perovskite halide materials, described by ABX_3 (where A stands for monovalent metal/organic cation, B represents divalent metal cation, and X is halogen anion), as a promising family of light-sensitive materials have aroused remarkable interest in a series of optoelectronic, energy-related, sensing, and radiation detection applications, owing to their eminent optoelectronic and physical features, including strong light absorption, ultralong carrier lifetime, and high photoemission, along with their facile synthesis and fabrication processing [1–4]. In general, the applications based on halide perovskites in optoelectronics are cantered mainly on their polycrystalline thin-film ones. In spite of the great achievements received in various device applications, perovskite polycrystalline films typically suffer from grain boundaries, relatively higher trap densities and defects, and low stability; these would hinder the enhancements of device performance and impede further industrialization [5–10]. Closely following the rapid development of perovskite polycrystalline samples and the related devices, there existed various forms and dimensions of halide perovskites, such as single crystals, low-dimensional perovskites in both the "structure level" and "molecular level", or nanostructured ones, which have also evoked attractive interests in both the fundamental research and practical device applications.

Impressively, halide perovskite single crystals demonstrate the outstanding characteristics such as free of grain boundaries, ultralow trap density and defects, excellent optical features, and highly improved carrier lifetimes, being attractive in photovoltaics and various optoelectronics [6, 11–16]. More importantly, intensive theoretical calculations and experimental investigations on perovskite crystals also showed promising charge carrier dynamics, in particular ambipolar transport behaviors, high carrier mobilities, and ultralong carrier diffusion lengths [16–18]. Benefiting from these advantages combined with the cost-effectiveness, excellent stabilities, and solution-phase procedures, single-crystal perovskites also demonstrate great potentials as the leading successor via alternating with the traditional semiconducting materials for electronics. In this sense, single-crystal perovskites in both the bulk and thin forms have recently been applied in the prototypical electronic devices, field-effect transistors (FETs); at the same time, there have been extensive research efforts devoted to developing effective strategies for the improvements of perovskite crystal qualities and FET device performance, as well as for the probing of carrier transport mechanism within perovskite crystals, including carrier scattering and trapping, ion migration effect, hysteresis, and electronic structure through such a device platform.

Despite the ongoing processes and growing research efforts on the FETs based on perovskite single crystals, demonstrating considerable advantages and potentials, there still exist some limitations and challenges, like working mechanism, device yield, ion migration, as well as environmental stability and circuit integrations; addressing them would allow for enabling the real-world electronic applications. In this chapter, we comprehensively review the recent advances and facing challenges of solution-grown perovskite crystals for FETs. We begin by briefly introducing the fundamentals of transistors. Following by presenting the unique

features of perovskite crystals that are critical to the advanced FETs as well as the solution-based syntheses for different forms and dimensions of perovskite crystals, recent achievements on perovskite crystal FETs along with their working mechanism are detailly summarized and discussed. At last, we identify the main challenges faced by the community and explore the possible opportunities to develop optimized perovskite crystal FETs for practical applications.

2 Fundamentals of Field-Effect Transistors

2.1 Device Structure

FET devices are the essential building blocks in various electronic devices, which mainly possess the function of switching and/or amplifying electronic signals via applying an additional gate field. Normally, a FET is constructed using three main components, including (i) active semiconductor channel, (ii) dielectric layer, and (iii) source/drain and gate electrodes. In detail, FETs, as the typical three-terminal devices, consist of the source, drain, and gate contacts [19–23], where the dielectric layer separate the active semiconductor layer and the gate electrode (Fig. 1a). Both the source and drain electrodes contact the active channel directly; the distance between the source and drain electrodes is defined as the channel length (L), and the width of them is the channel width (W).

Generally, FETs mainly have four types of device configurations, including bottom-gate/top-contact (BGTC), bottom-gate/bottom-contact (BGBC), top-gate/bottom-contact (TGBC), and top-gate/top-contact (TGTC) (Fig. 1a–d) [21]. The performance of FET devices employing the same semiconductor materials and active channels but different device structures may differ somehow, which can originate from the different interface properties, mainly including the ones between active channels and electrodes and/or dielectrics. As to perovskite FETs, although all the abovementioned four device structures have been reported [19, 20, 23–25], most of them were still produced on the basis of the bottom-gate constructions considering their facile fabrication processing [19, 24, 26–29]. It is noted that the top-gate structured FETs could offer the benefits of controlling or tuning the interfaces between perovskite active layer and/or dielectric layer and/or gate electrode, thus optimizing device performance.

2.2 Device Characterization

The standard characterizations of FET devices embody the tests of transfer (Fig. 1e and f) and output characteristics (Fig. 1g) [20, 22]. As for the transfer mode, the drain currents (I_{ds}) are tested with the sweeping gate voltage (V_{gs}) while keeping the constant drain-source voltage (V_{ds}). The output curves are obtained by measuring I_{ds}

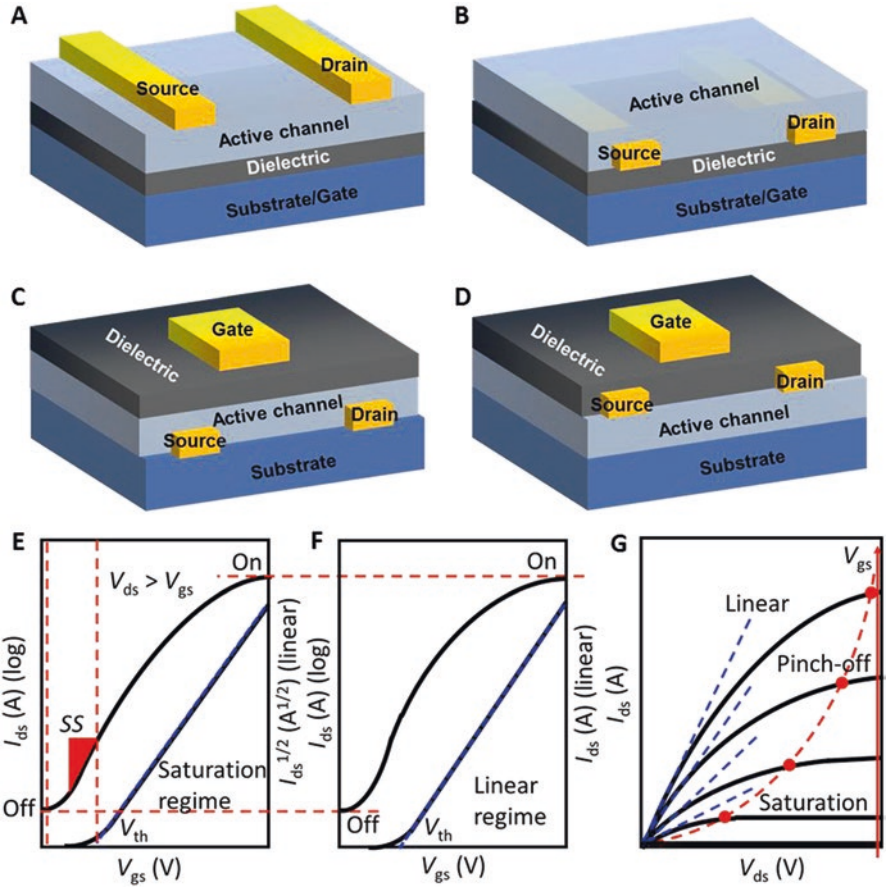

Fig. 1 Transistor structures and characterizations. (**a**) Typical three-terminal top-contact/bottom-gate (TCBG) transistor, consisting of source/drain electrodes, semiconductor active channel, dielectric, and gate electrode. (**b**) Bottom-contact/bottom-gate (BCBG), (**c**) bottom-contact/top-gate (BCTG), and (**d**) top-contact/top-gate (TCTG) transistors. (**e**) Transfer characteristic in saturation regime. (**f**) Transfer characteristic in linear regime. (**g**) Output characteristic showing drain current as a function of drain bias with setting a series of different constant gate voltages

as a function of V_{ds} while setting V_{gs} at the different step values. Normally, the FET device performance can be assessed through the following parameters, including charge carrier mobility (μ), on/off ratio (I_{on}/I_{off}), threshold voltage (V_{th}), and sub-threshold swing (*SS*).

Charge carrier mobility – μ – is a key parameter for characterizing FET device performance and semiconductor properties, in particular the carrier transport capacity. In detail, in the saturation regime, I_{ds} values can be obtained by (Fig. 1e) [22, 23]:

$$I_{ds} = \frac{W}{2L}\mu C_i \left(V_{gs} - V_{th}\right)^2 \tag{1}$$

in which C_i is the capacitance per unit area of the dielectric. From this equation, the square root of I_{ds} is directly proportional to V_{gs}; thus, the saturation carrier mobility (μ_{sat}) is extracted via [22, 23]:

$$\mu = \frac{2L}{WC_i\left(V_{gs} - V_{th}\right)} \cdot \frac{\partial I_{ds}}{\partial V_{gs}} = \frac{2L}{WC_i}\left(\frac{\partial\sqrt{I_{ds}}}{\partial V_{gs}}\right)^2 \tag{2}$$

In the linear regime ($V_{ds} > V_{gs}$) (Fig. 1f), the *I*–*V* curves can be expressed analytically as [22, 23]:

$$I_{ds} = \frac{W}{L}\mu C_i\left(V_{gs} - V_{th}\right)V_{ds} \tag{3}$$

The linear carrier mobility (μ_{lin}) can thus be extracted from the transfer curves of FETs in the linear regime and via using the following formula [22, 23]:

$$\mu = \frac{L}{WC_iV_{ds}} \cdot \frac{\partial I_{ds}}{\partial V_{gs}} \tag{4}$$

On/off ratio—I_{on}/I_{off}—is another important factor, that is, the ratio between the I_{ds} value at the on-state and that at the off-state, which can be obtained from the transfer curves directly (Fig. 1e and f) [22, 30]. Such a parameter describes the ability of controlling the I_{ds} values with the varied V_{gs} values; as for the high-quality FET devices, it should be as large as possible.

The threshold voltage—V_{th}—value is mainly depending on the charge carrier traps at the related interfaces in FET devices, which describes the offset of charges that contribute to (or hinder) the total charge transport properties within the active semiconductor channel even without using V_{gs}.

Subthreshold swing—*SS*—indicates the ability of a FET device to switch between the on-site and the off-state, and its value can also be obtained from the transfer curve (Fig. 1e) via employing the equation as shown below [22, 23]:

$$SS = \frac{\partial V_{gs}}{\partial\left(\log_{10} I_{ds}\right)} \tag{5}$$

The *SS* value can highly rely on the capacitance of dielectric layer and the trap states at the interfaces in FET devices.

Notably, these equations are mainly on the basis of the ideal operating conditions for FETs. For the practical FETs made by different semiconductor materials, there would somehow exist unexpected pitfalls for the extractions key parameters from the device tests, thus resulting in over- or underestimation of the device performance. Till now, FET technologies have highly matured and been widely applied in

almost all electronic products in people's daily life; however, seeking for suitable active semiconductor materials combining cost-effectiveness and promising physical features and designing novel device contractures and integration technologies are still significantly rewarding.

3 Main Features and Solution Processability of Perovskite Crystals

3.1 Materials Structures

Perovskite materials stand for a family of compounds (with a general chemical formula of ABX_3), processing the same type of crystal structure of inorganic $CaTiO_3$ (first discovered by German mineralogist G. Rose and then named after Russian mineralogist L. A. Perovski) [31]. As for halide perovskite semiconductors (Fig. 2a), A-site monovalent cation can be organic groups (such as methylammonium, MA^+, or formamidinium—FA^+) or inorganic cations (like Cs^+), referring to the organic-inorganic hybrid or all-inorganic perovskites, respectively [1, 2, 35–37], while B normally stands for the divalent metal cation (like Pb^{2+} or Sn^{2+}) [1, 2, 38, 39], and X represents the halide anion (I-, Br-, Cl-, or their mixtures) [1, 2].

Regarding the geometric structures, the three-dimensional (3D) network can be constructed via linking the framework of perovskite unit cells through the $[BX_6]^{4-}$ octahedra [40]. To quantitatively survey the perovskite structure stability, a Goldschmidt tolerance factor (*t.f.*) was introduced, which can be described by $t.f. = \left(r_A + r_X\right) / \sqrt{2}\left(r_B - r_X\right)$ (where r_A, r_B, and r_X are the radii of A, B, and X atoms, respectively) [41]. It was empirically shown that the values of $0.89 < t.f. < 1.0$ can frame the stable cubic structure 3D perovskites [42]. The small A-site cation radius can cause the tilt of $[BX_6]^{4-}$ octahedron, thus leading to the lower-symmetrical perovskite crystal structures with the smaller *t.f.* values (< 0.89), like tetragonal or orthorhombic. If A-site is occupied by large organic groups, thus, the "molecular-level" low-dimensional perovskites with the *t.f.* values larger than 1, such as two-dimensional (2D) layered or one-dimensional (1D) linear ones (which mainly focus on the material compositions and molecular structures), can be obtained (Fig. 2b) [32, 43, 44]. Notably, the low dimensionality of halide perovskites can also refer to the "structure level", namely, the nanostructured materials with different forms or morphologies, like 2D micro−/nanoplatelets, 1D nanowires (NWs), and zero-dimensional (0D) nanocrystals (NCs). The "structure-level" low-dimensional perovskites contain the same composition as 3D perovskites, so the intrinsic physical features are derived from 3D perovskite counterparts with additional quantum confinement effects along at least one direction.

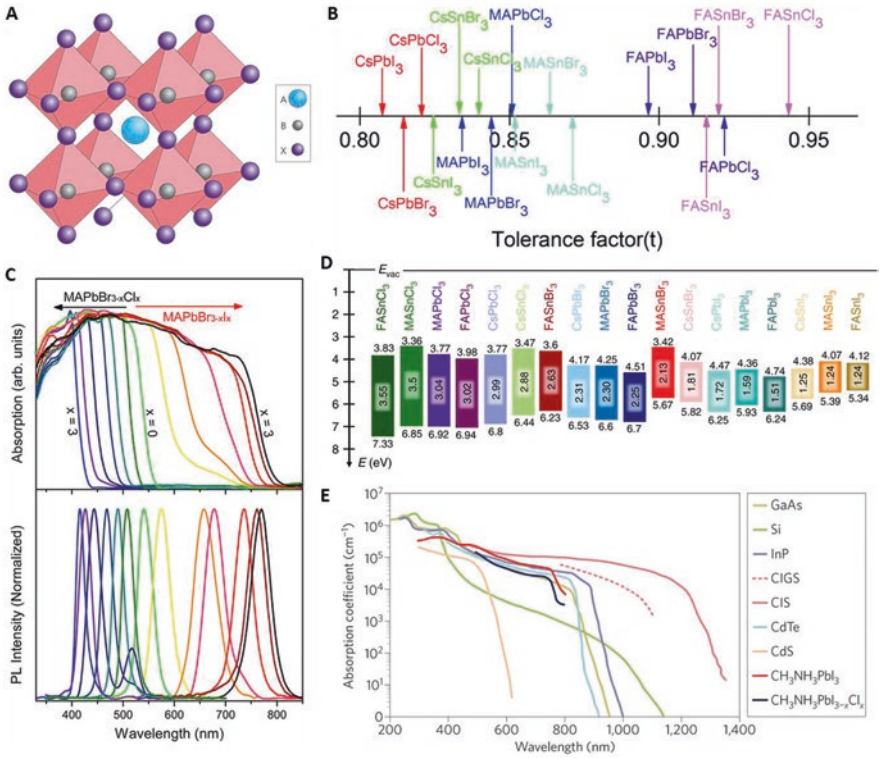

Fig. 2 Structures and optical properties of halide perovskites. (**a**) Crystal structure of perovskite material. Reproduced with permission from Ref. 2, Springer Nature. (**b**) Tolerance factor (*t.f.*) values of various halide perovskites. Reproduced with permission from Ref. 32, RSC. (**c**) Ultraviolet-visible absorption spectrum and photoluminescence spectrum of $MAPbBr_{3-x}Cl_x$ and $MAPbBr_{3-x}I_x$ thin films. Reproduced with permission from Ref. 33, ACS. (**d**) Energy-level diagram of various halide perovskites. Reproduced with permission from Ref. 34, Springer Nature. (**e**) Absorption coefficients for widely used $MAPbI_3$ and $MAPbI_{3-x}Cl_x$ compared with other light-sensitive inorganic materials. Reproduced with permission from Ref. 2, Springer Nature

3.2 Structure Diversity and Bandgap Tunability

According to the *t.f.* factor for checking the structural stability, a series of halide perovskites with different forms and dimensions have been developed for exploring new properties and multiple device functionalities. Theoretically calculated results on the representative halide perovskite—$MAPbI_3$—showed that the valence band maximum (VBM) can mainly be depending on both *s*-orbitals of divalent metal cations (Pb^{2+}) and *p*-orbitals of halide anions (I^-) [45]. Therefore, substituting the chemical composition(s) at each site and effectively modifying the coupling of the related orbitals could be the effective strategies for tuning the band structures of perovskites. In detail, beyond the normally applied MA^+, FA^+, or Cs^+, A-site cations

can also be alternated or occupied by the variety-sized monovalent metal cations or organic groups, leading to diverse perovskite dimensions/structures, including 2D layered or 1D linear structures, such as the Ruddlesden-Popper (RP) phase, the Dion-Jacobson (DJ) phase, and the alternating-cation (ACI) phase, as well as the tunable bandgaps [44, 46].

B-site divalent cations have the higher formation energy as compared to A-site cations, and their sizes may not change much, and, thus, the *t.f.* values would not be changed too much for perovskite crystals [44]. Notably, the bond angles between B-site cations and X-site halide anions can have the great impact on the bandgaps of perovskite crystals [1]; for example, the light absorption range of Pb-Sn mixed perovskites by controlling the ratio between Pb and Sn can be extended into near-infrared region, which are considered as highly suitable candidate for high-performance optoelectronic devices [2, 31, 46].

Plus, X-site halide anions' sizes could effectively affect the crystal structure of perovskites [44, 46, 47]. In this sense, the X-site anion doping could be a promising strategy to tune the band structures and optical properties of perovskites, referring to bathochromic-shift effect [23, 44]. Through tuning different X-site halogen anion(s), perovskites can exhibit tunable direct bandgaps ranging from 1.2 eV to 3.6 eV, covering the visible spectrum (Fig. 2c) [33]. Additionally, appropriately tuning X-site anions along with both A- and B-site cations could result in the different bandgaps laying over the entire ultraviolet-visible-near-infrared spectrum (Fig. 2d) [34, 48]. It has also been widely reported that the bandgaps of perovskite polycrystalline films could be further experimentally regulated up to a certain target range by advisably tuning all the involved element ratios, thus rationally promoted for controlling the target perovskite crystals [45, 49]. Thus, the high chemical composition tunability and structure versatility pave the effective routine for modifying the electronic band structures of perovskite crystals, leading to a wide range of electronic applications with multiple functionalities.

3.3 Optical Features

The optical properties of semiconductors, like their light absorption properties, can be directly determined by their band structures, affecting their optoelectronic devices. Halide perovskites can experimentally and theoretically demonstrate ultra-high absorption coefficients up to 10^5 cm^{-1} in the entire visible range (because of the strong inter-band transition) [50–52], comparable with and even much higher than those of the conventional semiconductors (Fig. 2e) [2, 53]. As compared to the polycrystalline films, perovskite crystals can show the extended absorption range (due to the sharp band edge cutoffs with no excitonic signature and the enhanced below-bandgap absorption), indicating the excellent feature of less in-gap defect states [6, 16, 54]. The extended absorption range of perovskite crystals could make more photons absorbed, thus increasing the short-circuit current density in the related devices, helpful for the light-harvesting devices, particularly solar cells and

photodetectors [55]. Perovskites, depending on their compositions and molecular dimensions, also demonstrated the tunable binding energies of excitons (bound electron-hole pairs) [44]. Correspondingly, the exciton binding energies of perovskite crystals can also be effectively tuned via substituting chemical compositions. In detail, excitons with the lower binding energy can overcome the Coulombic interaction easily; thus, under light excitation, they can be separated into free holes and electrons, enabling high-efficiency photovoltaics and photodetection devices [44, 56].

On the contrary, substituting the halide ions or reducing the perovskite crystal dimensions can increase the exciton binding energy, facilitating high-performance light-emitting devices, which can originate from the enhanced radiative recombination effect of charge carriers [30, 44, 57]. These promising features would help with the design of novel FETs with multiple functionalities, like light-emitting transistors or phototransistors [19, 58].

3.4 Solution-Based Processability

Regarding the growth of perovskite crystals, even though different techniques have been adopted to synthesize perovskite crystals with diverse dimensions and shapes [4, 59], the facile solution-based crystallizations at the relatively low temperatures are the most widely used approaches (due to the high temperature-dependent solubility of halide perovskites in the solvents) [16, 23]. While for the traditional inorganic semiconductors, they often require the demanding deposition equipment in ultrahigh vacuum atmosphere and/or at high temperatures. Being different from the solution-processable organic semiconductors with the relatively high defect densities, perovskite crystals grown via the solution processes can also possess high crystal quality [6, 16, 23]. Moreover, the solution-based processability of perovskite crystals can make them ideal candidates with cost-effectiveness for large-scaled flexible electronics and stretchable devices, thereby advancing the development of perovskite crystal electronics toward practical industrialization.

3.4.1 3D Single-Crystal Perovskites

Bulk Single Crystals Solution temperature lowering (STL) method was developed by Tao's group to synthesize bulk $MAPbI_3$ crystals (Fig. 3a), considering these perovskite materials can show the decreased solubility in the related HX (X = Cl, Br, and I) solution with lowering temperatures [60]. Other types of mixed-halogen perovskite crystals like $MAPbBr_{3-x}Cl_x$ and $MAPbI_{3-x}Br_x$ were also prepared successfully via such a method. To obtain larger-sized perovskite bulk crystals, the selected high-quality crystal seeds from this method could be dropped into the fresh solution again for further growth(s) with the careful controls. Notably, this growth method would need ultralong time to obtain perovskite crystals with high quality (in several

days). Notably, the time-consumption factor would be the main drawback of this method; thus, synthesis approaches with much faster process for perovskite crystals would be required.

In this regard, inverse temperature crystallization (ITC) approach was also widely applied in synthesizing perovskite crystals (because of decreased solubility in certain solvents with increasing temperature); it has been demonstrated that the obtained samples could be with the advantages of rapid crystallization, improved quality, and controlled shapes and sizes. Bakr et al. introduced this method to synthesize the high-quality $MAPbI_3$ and $MAPbBr_3$ bulk crystals, and the whole process just needed 3 h (Fig. 3b) [61]. Thereafter, this ITC method was further modified to get the large-sized perovskite crystals. Liu et al. further combined this ITC approach and the seed crystallization process with the precise controls to synthesize the large-scaled single-crystal perovskites [65].

The anti-solvent vapor-assisted crystallization (AVC) is also a normally applied approach for the growth of single-crystal perovskites. This method was first employed by Bakr et al. to grow high-quality $MAPbBr_3$ and $MAPbI_3$ crystals [6]. In particular, two or more solvents are required for this method, where at least one of them serves as a good solvent with less volatile property and the other(s) should be the bad solvent(s) that is/are more volatile (Fig. 3c) [6, 66]. Generally, it would be better to behave the insolubility property of perovskite materials in the bad solvent; with slowly diffusing the bad solvent into the perovskite precursor solution, the related crystallization could be highly improved. As compared to the ITC method, this AVC method could require relatively more crystallization time; however, it is still much faster than the STL process, together with the temperature-independent behavior and room temperature operation, making it attractive for the widespread usage.

Thin Single Crystals Within the perovskite bulk crystals with large thicknesses, the light-generated and/or free charge carriers would undergo scattering and/or recombination before reaching the electrodes, thus leading to the mediocre device performance and obstructing the real-world commercialization. In this regard, to overcome such a barrier, it would be promising to explore effective strategies for synthesizing the perovskite crystals with controllable sizes, beneficial for advancing the practical device applications with high performance. An effective strategy termed cavitation-triggered asymmetrical crystallization was used by Bakr et al. to grow perovskite thin crystals with the μm-sized thicknesses (Fig. 3d), for which the short ultrasonic pulse (≈1 s) was performed onto the low-supersaturation solution during the entire process [62]. Benefiting from the capillary pressure in the whole space between two clean flat substrates, space-confined strategies have been widely adopted, combined with the normal growth routines for bulk crystals, to synthesize perovskite crystals with controllable thickness [67]. For instance, Chen et al. reported that perovskite thin crystals with the tunable thicknesses from nanometers to micrometers could be obtained via space-confined solution-processed method (Fig. 3e) [63]. To produce large-scaled high-quality perovskite thin crystals, more promising strategies, such as one-step printing geometrically confined lateral crys-

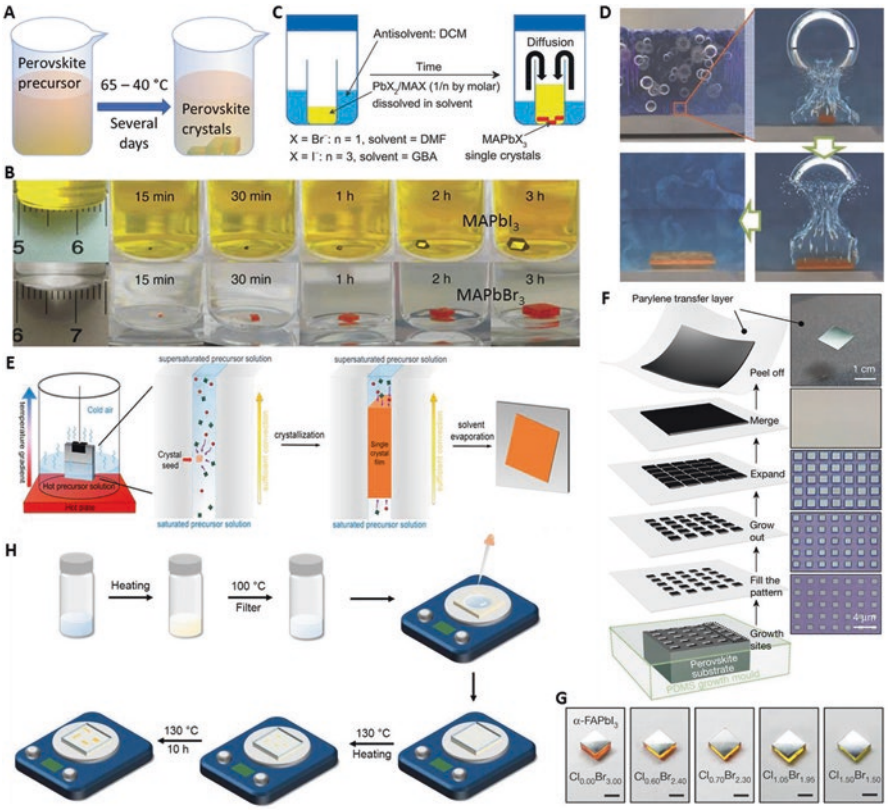

Fig. 3 Solution-based synthesis approaches for both bulk and thin 3D perovskite single crystals. (**a**) Schematic of solution temperature lowering method. Reproduced with permission from Ref. 60, RSC. (**b**) Photos recording the growth process of both $MAPbI_3$ and $MAPbBr_3$ crystals using inverse temperature crystallization method at different time intervals. Reproduced with permission from Ref. 61, Springer Nature. (**c**) Schematic of anti-solvent vapor-assisted crystallization method. Reproduced with permission from Ref. 6, AAAS. (**d**) Schematic of cavitation-triggered asymmetrical method. Reproduced with permission from Ref. 62, Wiley. (**e**) Schematic of space-confined inverse temperature crystallization method for growing perovskite thin crystals. Reproduced with permission from Ref. 63, ACS. (**f**) Solution-based lithography-assisted epitaxial growth method and the obtained samples. Reproduced with permission from Ref. 13, Springer Nature. (**g**) Optical images of the as-grown epitaxial α-$FAPbI_3$ thin crystals. Reproduced with permission from Ref. 14, Springer Nature. (**h**) Schematic of space-confined solution epitaxial growth strategy. Reproduced with permission from Ref. 64, ACS

tal growth and seed-inkjet-printing approach, have thus been developed, beneficial for large-scaled perovskite crystal electronics [16, 23].

Currently, solution-based epitaxy strategies were developed, which has the benefit of establishing stable interfacial chemical bonds between perovskite thin crystals and substrates [68]. In comparison with the conventional vapor-phase epitaxy approaches, solution-processed epitaxy can possess the highly improved active

sample coverage with the adjustable thickness because of the uniform epitaxial contact between perovskite layers and substrates [44]. Solution-based lithography-assisted epitaxial growth approach was reported by Xu's team to synthesize perovskite single-crystal films, with the widely researched bulk perovskite crystals using as substrates (Fig. 3f) [13, 69]. They detailly showed that the crystallization dynamics, like lateral scale, thickness, composition, crystal orientation, dimensionality, and morphology, of perovskite crystals could be controlled and tuned via combining epitaxial growth and micro-fabrication. The similar synthesis process was applied by the same group in the case that the compositions between perovskite thin crystals and perovskite crystal substrates were different (Fig. 3g), where the high lattice strain reaching 2.4% can be effectively formed into the obtained perovskite epitaxial thin crystals [14]. The generated compressive strain, caused by carefully designing the lattice mismatch level, could not only decrease the m^* values and then enhance the carrier mobility, driving the development of electronic devices, but also make the perovskite crystal samples and devices more stable. All-inorganic perovskite $CsPbBr_3$ epitaxial thin crystals were also obtained through the space-confined solution epitaxial growth strategy, with the typical oxide $SrTiO_3$ using as substrates (Fig. 3h) [70]. It was demonstrated that the obtained perovskite epitaxial thin crystals can show the excellent transport properties and defect behaviors, facilitating the electronic devices with significantly optimized stability and high performance; these advanced characteristics could stem from the high-quality epitaxy between perovskite thin crystals and substrates as evidenced by the structural characterizations [70].

Nanostructured Crystals Nanostructured halide perovskite crystals in "structure level", like micro-/nanoplates or micro-/nano-sheets, micro-/nanowires, and quantum dots, have been deemed desirable candidates for various optoelectronic devices [71, 72]. As for the growth of perovskite micro-/nanoplates or micro-/nano-sheets, except for the normally used vapor-phase method [73], solution-phase approaches have also been widely adopted, where the extra introduced solvents (e.g., acetone) and low reaction temperature play the key factors in the shape control [74, 75]. Similarly, perovskite micro-/nanowires can be prepared by both vapor-phase and solution-phase processes; the former ones with precise controls (like the extra solvent(s), reaction time, and reaction pressure) were more widely used for growing all-inorganic perovskite micro-/nanowires in different shapes [76], while the solution-growth ones were more often reported to prepare hybrid perovskite micro-/nanowires [77]. There have been numerous publications on the synthesis of various perovskite quantum dots, of which most are based on solution-processed hot injection approach [78, 79]. For this method, the injection time and the operating temperature play the important roles in controlling the perovskite quantum dots' sizes. Notably, nanostructured perovskite crystals were mainly used in light-emitting applications, due to their unique quantum confinement effect (leading to efficient color emissions), [71, 72] while, in comparison, research on nanostructured perovskite FETs, particularly quantum dots, is still lacking, possibly due to the relatively poor charge transport properties. However, it is expected that, given the con-

figuration advantages, the nanostructured perovskite FETs offer excellent platform to assist in elucidating more underlying physics in these nanostructured perovskites and developing high-performance devices.

3.4.2 Low-Dimensional Perovskite Crystals

Owing to the unique characteristics (in particular, the intrinsic quantum confinement effect and improved stabilities), low-dimensional perovskites in "molecular level", such as 2D layered or 1D linear structures, have recently aroused wide interest [80–83]. As for the layered perovskites, organic cations with long chains can serve as the "barriers", resulting in the adjustable optoelectronic properties, due to the formed quantum confinement effect. Additionally, in the layered perovskites, neighboring layers can be bonded through van der Waals forces with weak interactions, causing the strongly suppressed ion migration and the highly anisotropic charge transport behaviors, favorable for the design of lateral-structure FET devices [18, 21].

As to the synthesis routines, besides the above-discussed approaches for the 3D perovskite crystals that have also been employed to synthesize the layered perovskite crystals [84–86], there have recently some other particular strategies for gaining layered perovskite crystals with high quality. Cooling-temperature approach was used for the growth of $(BA)_2(MA)_{n-1}Pb_nI_{3n+1}$ (BA = $C_4H_9NH_3$, n = 1–4) perovskite crystals, in which the different-ratio precursor chemicals BA, MAI, and PbI_2 were dissolved in HI solvent (57 wt% in H_2O). Following by heating the solution to 130 °C and then cooling down to room temperature with a precise control, layered perovskite crystals with high quality could be gained after washing with diethyl ether and drying for 24 h (Fig. 4a) [81]. Centimeter-sized $(PEA)_2PbBr_4$ thin crystals were obtained by combining cooling-temperature process with seed growth (Fig. 4b) [87]. Additionally, solvent evaporation approach was also widely used in the growth of layered perovskite crystals; via such a method, various layered perovskite crystals, like $(BA)_2(MA)_{n-1}Pb_nI_{3n+1}$ (n = 1, 2, and 3) (Fig. 4c), $(PEA)_2PbBr_4$, and even lead-free $(MA)_2MnCl_4$, could be obtained [82, 84].

In addition, Bakr et al. presented that surface tension could assist in synthesizing large-sized layered perovskite crystals on the solution surface (Fig. 4d) [88]; by this method, $(PEA)_2PbI_4$ and $BA_nMA_{n-1}Pb_nI_{3n+1}$ (n = 1, 2, 3, 4, and ∞) layered crystals could be gotten [64, 90]. Recently, liquid-diffused separation-induced crystallization (LDSC) was reported to synthesize high-quality layered perovskite crystals, such as BA_2PbBr_4, PA_2PbBr_4, and PMA_2PbBr_4, at room temperature [89]. In detail, the oversaturated solution could be obtained by separating the solvent from the related precursor solution, and then the crystallization would occur spontaneously (Fig. 4e). As compared to the heating- and/or cooling-based approaches, such a LDSC method has the advantage of much easier operations at room temperature. It is worth mentioning that, aiming to realize advanced devices based on perovskite crystals, exploring more promising strategies for the synthesis of layered perovskite crystals with controllable sizes will be highly in demand.

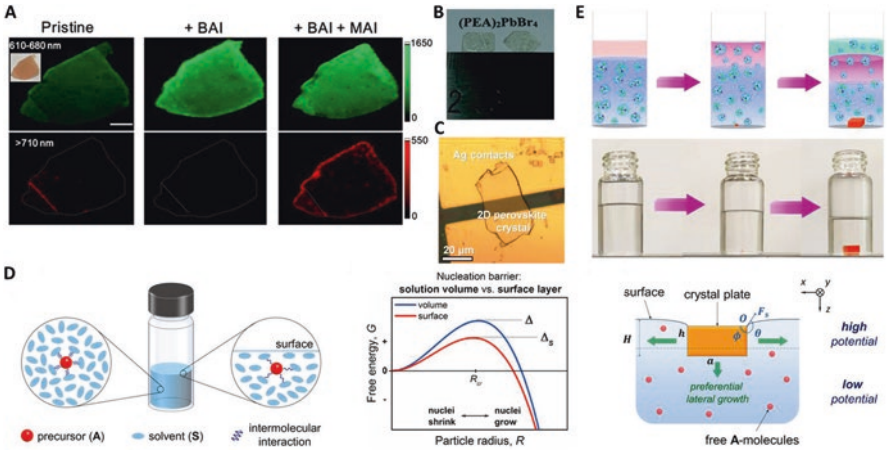

Fig. 4 Solution-based growth approaches for 2D perovskite single crystals. (**a**) Photos of the layered perovskite crystals grown by cooling temperature method. Reproduced with permission from Ref. 81, ACS. (**b**) Large-sized layered perovskite crystals via combining cooling and seed growth methods. Reproduced with permission from Ref. 87, RSC. (**c**) Large-sized layered perovskite crystals grown by solvent evaporation method. Reproduced with permission from Ref. 84, Wiley. (**d**) Schematic of surface tension-assisted growth approach. Reproduced with permission from Ref. 88, ACS. (**e**) Schematic of liquid-diffused separation-induced crystallization method for layered perovskite crystals and related photos recording the growth process. Reproduced with permission from Ref. 89, Springer Nature

3.5 Superior Transport Features

Except for the excellent optical features, perovskite crystals have also demonstrated the superior transport properties, which are essential for the design of high-performance electronics [16–19, 23–25, 44, 46]. Generally, carrier transport behaviors are highly related to the materials' electronic band structures; in detail, the effective mass (m^*) of charge carriers and the mean free time (τ) during the consecutive scattering can determine the carrier mobility (μ), which can be expressed by $\mu = e\tau/m^*$. For the typically used $MAPbI_3$, the m^* values or the electron and hole are $0.2m_0$ and $0.27m_0$ (m_0 is the free-electron rest mass), respectively, because both the conduction and valence bands have the pronounced curvatures (Fig. 5a) [96–98]. Principally, low m^* values of the carriers mean that they should exhibit the high mobilities (surpassing 10^3 cm^2 V^{-1} s^{-1}) [19, 24, 97, 99, 100], extremely desirable for the perovskite transistors and other electronics. Moreover, calculations on the density of states (DOS) demonstrate the elemental contributions to the conduction band (CB) and valence band (VB) (Fig. 5b); that is, the charge carriers in $MAPbI_3$ mainly transport through the $[BX_6]^{4-}$ octahedron, i.e., electrons travel mainly through the Pb-6p states and holes transport via the hybridization of Pb-6 s and I-5p states [96].

Beyond, multiple experimental techniques have been developed to check the perovskite crystals' carrier mobilities, such as Hecht-equation electrical method (Fig. 5c) [91], space-charge-limit-current test (>150 cm^2 V^{-1} s^{-1}, Fig. 5d) [6, 54],

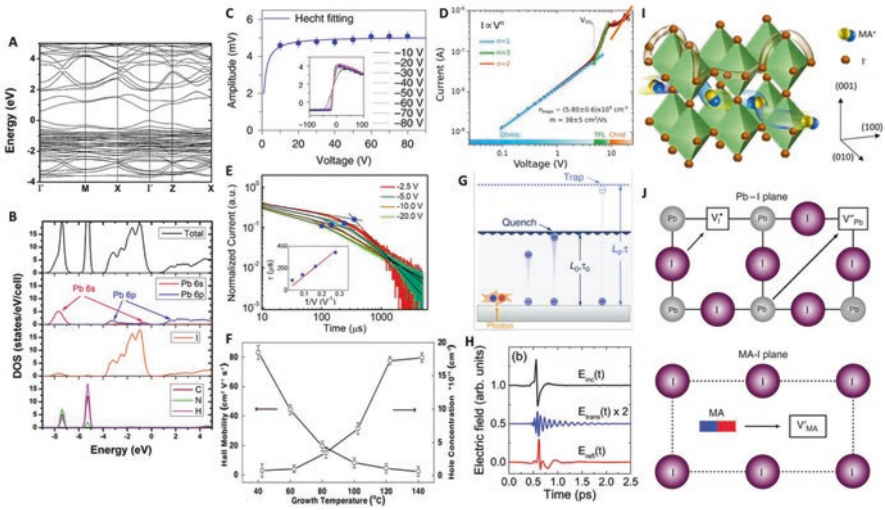

Fig. 5 Electric structures, transport features, and ion migration of perovskites. (**a**) Band structures of $MAPbI_3$ perovskite simulated by using the Perdew-Burke-Ernzerhof (PBE) functionals. (**b**) Total density of states of $MAPbI_3$ perovskite, which is projected onto Pb (6 s and 6p), I, C, N, and H atoms. Reproduced with permission from Ref. 82, RSC. (**c**) Mobility-lifetime product evaluation for holes based on Hecht equation (inset: the relationship between pulse amplitude and applied voltage). Reproduced with permission from Ref. 91, Springer Nature. (**d**) Space-charge-limit-current measurement for $MAPbBr_3$ crystal. Reproduced with permission from Ref. 6, AAAS. (**e**) The transient current curves of perovskite crystal devices. Reproduced with permission from Ref. 92, AAAS. (**f**) Hall-effect measurement of epitaxial $MAPbBr_3$ crystals. Reproduced with permission from Ref. 69, Wiley. (**g**) 1D diffusion-quenching structure: carrier funneling process occurs at the interface between active material and carrier extraction layer. Reproduced with permission from Ref. 93, Springer Nature. (**h**) In the absence of a photoexcitation, the incident (black), transmitted (blue), and reflected (red) multi-THz pulses after interaction with perovskite crystal. Reproduced with permission from Ref. 94, RSC. (**i**) Schematic showing the migration of two major mobile ionic species—I^- and MA^+. (**j**) Schematic of the three ionic transport mechanisms involving conventional vacancy hopping between neighboring positions. Reproduced with permission from Ref. 95, Springer Nature

time-of-flight method (115 $cm^2\ V^{-1}\ s^{-1}$, Fig. 5e) [92, 101, 102], Hall-effect technique (nearly 180 $cm^2\ V^{-1}\ s^{-1}$, Fig. 6f) [69], and FET-based measurement (refer to Sect. 4 for details). Notably, all these simple setup-based methods (e.g., *I–V* curves) primarily measure the carrier mobilities around the respective Fermi levels; therefore, it would be quite different for each measurement due to the nonequilibrium or high-injection-level Fermi level, leading to discrepancies of the obtained results [17, 44]. To address such an issue, some contactless optical characterizations have thus been developed, such as the 3D optical diffusion-quenching method (Fig. 5g) and the terahertz frequency conductivity measurement (Fig. 5h) [16, 93, 94, 105]; these methods could effectively avoid the impacts of contact resistance and/or high electric field. It should be noted that the highly varied mobilities were obtained from different testing methods [17]; thus, to accurately evaluate the carrier mobilities of perovskite crystals, more appropriate approaches should be further introduced.

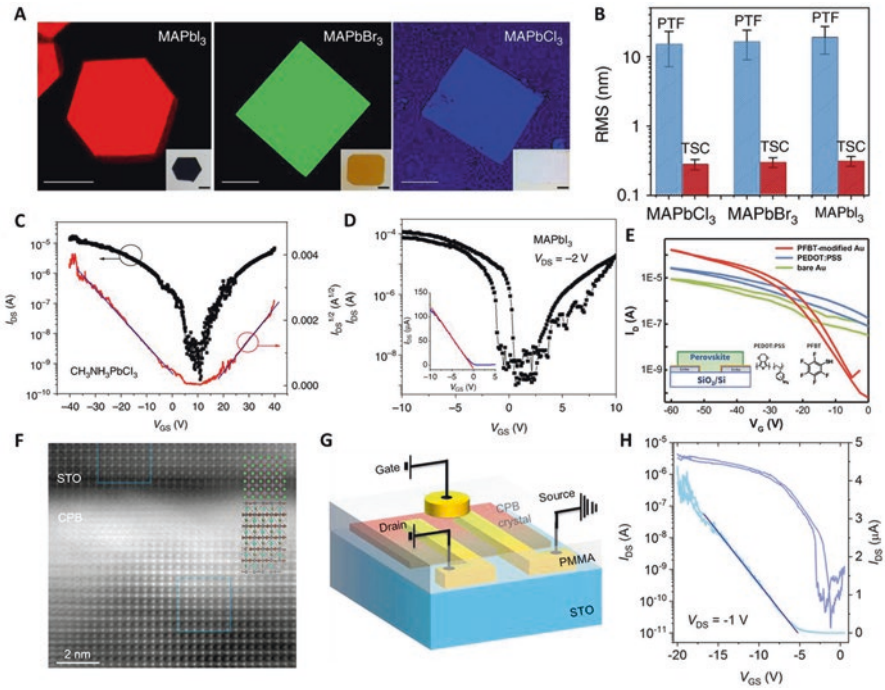

Fig. 6 Transistors based on perovskite thin crystals. (**a**) Fluorescence microscope images of perovskite $MAPbX_3$ thin crystals (X = Cl, Br, and I) excited by 450-, 473-, and 405-nm lasers, respectively. (**b**) Comparisons of the root-mean-square roughness values between perovskite thin crystals and polycrystalline films. (**c**) Transfer characteristics and fitted lines for $MAPbCl_3$ thin-crystal transistor. (**d**) Transfer curves for $MAPbI_3$ thin-crystal device. (**a**–**d**) are reproduced with permission from Ref. 103, Springer Nature. (**e**) Transfer curves for the perovskite crystal transistors using Au and polymer-modified Au electrodes, respectively. Reproduced with permission from Ref. 104. Wiley. (**f**) Cross-section STEM HAADF image of the perovskite crystal/STO interface showing the excellent epitaxial property. (**g**) Schematic of the TCTG-structured transistor based on epitaxially grown perovskite thin crystal. (**h**) Dual-sweep transfer curves of the transistor upon a drain voltage of −1 V. (**f**–**h**) are reproduced with permission from Ref. 70, ACS

Also, these experimentally obtained mobilities of perovskite crystals are not as high as the theoretically predicted values, but they are still much higher than those of the polycrystalline counterparts; moreover, their mobilities can be comparable with those of the traditional inorganic semiconducting materials [6, 16, 17, 30, 56]. These make perovskite crystals the extremely ideal candidates for high-performance FET devices.

Furthermore, to experimentally obtain the carrier mobilities that can be much closer to the predicted values, suitable material processing and novel device design for controlling the possible detrimental factors along with in-depth fundamental research are required. Principally, the intrinsic factors, such as the polar scattering, crystals vibration, and Fröhlich interactions, could affect the charge transport properties of semiconductor materials [17, 46]; these can also apply to the perovskite

crystals. Meanwhile, considering that perovskite crystals are free of grain boundaries, the extrinsic factors affecting their mobilities mainly depend on their defects (like structural or point ones). In general, structural defects in semiconductors can lead to the formation of electronic traps within their bandgap, which could serve as the centers for trapping free charge carriers; hereafter, the trapped charge carriers tend to be annihilated in the deep trap states with high activation energies (the so-called non-radiative recombination), which would be detrimental to the performance of optoelectronic devices [44]. It was reported that the trap densities in perovskite crystals, characterized by capacitance–frequency (*C–f*) or current-voltage (*I–V*) curves, are around five to seven orders of magnitude lower than those of the polycrystalline films, which could also be proven by their highly improved carrier lifetimes [6, 44, 92, 101, 106–108]. In this regard, the highly reduced trap densities could facilitate the suppression of the charge carriers' non-radiative recombination and thus improve the performance electronic devices based on perovskite crystals. Point defects (such as vacancies and interstitials) can also affect charge transport properties through scattering in semiconductor materials caused by Coulomb interaction. Due to the decreased point defect densities and the reduced carrier-phonon coupling, perovskite crystals could exhibit the highly enhanced carrier mobilities [107, 109–111]. Notably, it is highly desirable to carry out more investigations to study defect behaviors and carrier dynamics within perovskite crystals, considering their intrinsic complexity.

3.6 Ion Migration Behaviors

Perovskite halide materials have widely displayed the mixed electronic-ionic conductivity behaviors (Fig. 5i), which could originate from the relatively low activation energy of these ions (Fig. 5j) [95, 112–114]; these would be more intense under the particular operating conditions. Ion migration behaviors have been widely observed in the perovskite optoelectronics which can be related to the appearance of *I–V* hysteresis; in the meanwhile, various techniques, such as Kelvin probe tests or photoluminescence/X-ray photoemission mappings [112, 115–118], have been applied to study the mechanisms of ion migration. In polycrystalline perovskite films, the grain boundaries have been experimentally demonstrated to act as the motion channel for the ionic defects, leading to more severe ion migration with applying electric field [119]. The ion accumulations at the perovskite/electrode interfaces could cause the electric-field screening effect, resulting in obvious *I–V* hysteresis in the related devices, in particular the FETs [19, 20, 120, 121]. Moreover, theoretical calculations showed that ion migration in perovskite materials can occur through the point defects (e.g., vacancies or interstitials), due to their relatively low activation energies [5, 122, 123]. Ion migration behaviors and the related hysteresis issues make the device characterizations complicated by triggering variations under the electric fields, leading to the difficulties for accurately evaluating the device performance; namely, the obtained nonideal *I–V* curves could make the key device

parameters in particular the FET mobilities, under-/overestimation [20]. In addition, ion migration has been considered as the main factor for the faster compositional segregation and decomposition of perovskite materials, thus affecting long-term stabilities of the related devices [124]. Thus, it would be highly crucial to effectively suppress the ion migration in halide perovskites.

As to single-crystal perovskites with the highly enhanced crystallinity, their merits, including free of grain boundaries and highly decreased densities of point defects and impurities, make them the promising candidates for high-performance FETs [19, 20]. Additionally, the suppressed ion migration in single-crystal perovskites could highly weaken the gate electric-field screening effect and hysteresis behaviors, further making for high-repeatability FETs for industrial applications [19, 20].

"Every nutshell has a concave and convex side." Because halide perovskites possess the unique feature of being mixed ionic-electronic conductors, the mobile ions can make some contributions to the transport behaviors under the particular conditions. Recent reports also demonstrated that the independent ion motions in perovskites could account for the mechanism of their ambipolar transport behaviors, especially under light radiation [125], beneficial for designing the electronic devices with multiple functionalities, like inverters and light-emitting transistors. Besides, the mixed ionic-electronic feature of perovskites would also provide new chances for designing other electronic devices, like FET-based memristors [46, 126, 127]. In this regard, while ion migration would affect the device performance and stabilities, such a behavior could simultaneously stimulate more explorations in novel devices like memristors. Till date, the underlying mechanism of ion migration in halide perovskites remains elusive; thereby, in-depth understandings of the ion migration behaviors and their effects play the key role in the developments and designs of innovative electronic devices made by halide perovskites.

4 Single-Crystal Perovskite FETs

As stated above, perovskite crystals with no or fewer grain boundaries and low trap densities process the excellent transport features and improved stabilities, rendering them perfect candidates for FETs. In the following sections, research achievements and ongoing progress in FETs based on perovskite crystals with different forms and dimensions are summarized in detail.

4.1 Transistors Based on 3D Perovskite Thin Crystals

To date, there have been a few reports regarding the FET devices by employing 3D perovskite thin crystals as the active channels. To enable the effective FET functionality, a series of widely used perovskite ($MAPbX_3$, X = Cl, Br, and I) thin crystals

with micrometer-scale thicknesses (Fig. 6a), grown through a spatially confined ITC process, were adopted as channel meterials [103]. Notably, as compared to the polycrystalline films, the obtained perovskite thin crystals feature the highly smooth surfaces with the average root-mean-square (RMS) roughness less than 0.3 nm (Fig. 6b) [103], which could lead to the well-defined interfaces between perovskite channels and electrodes, thus making for high device performance. Both the fabricated BGTC and BGBC FETs made by perovskite thin crystals obviously demonstrated ambipolar transport behaviors (Fig. 6c and d) [103]. In detail, the optimal saturation hole mobility reaching 1.9 $cm^2\ V^{-1}\ s^{-1}$ could be obtained at room temperature in the BGTC FET based on Br-based thin crystal (Fig. 6c), and the BGBC device containing I-based thin crystal could exhibit a maximum hole mobility up to 2.9 $cm^2\ V^{-1}\ s^{-1}$ (Fig. 6d), while a maximum on/off ratio up to 10^5 could be also achieved. Various structural characterization results showed that the obtained thin-crystal facets possess the significantly suppressed roughness and defects, leading to the improved channel-dielectric interface quality, which could be key reason for the high performance of these perovskite crystal FETs.

Except for the perovskite thin-crystal surface quality, the interface between perovskite crystal layers and metal electrodes also has a critical impact on the performance of the related devices. The effect of chemical interaction between perovskite crystal layers and metal electrodes on the FET device performance was systemically studied [104]; it was found that the performance of FETs based on $MAPbBr_3$ thin crystals with Au top electrodes could degrade quickly, regardless of whether the electrodes were prepared through an evaporation method or a gentle, soft lamination process. Such the device performance degradations could be attributed to the electrochemical reactions at the perovskite/Au electrode interfaces, which could form a defective, intermixed layer around the interface, inducing more defects in the perovskite crystal channels. To overcome this problem, some effective strategies were proposed, like treating electrodes via a self-assembled monolayer (SAM)-doped conducting polymer or adopting the BGBC device structure, resulting in the improved device performance. The obvious performance enhancements of the optimized FET devices could be ascribed to the significantly suppressed electrochemical reactions at the perovskite/Au electrode interfaces (Fig. 6e) [104]. In this regard, suppressing the electrochemical reaction at the active perovskite crystal/metal electrode interfaces would be an effective mean for optimizing the performance and yield of the related FET devices.

In addition to hybrid perovskite thin crystals, all-inorganic ones have also attracted immense attention because of their comparable electronic features and improved moisture stabilities. Yang et al. demonstrated that $CsPbBr_3$ epitaxial thin crystals would be obtained by the facile solution-processed epitaxy method with the typical $SrTiO_3$ using as substrate [70]. Structural characterizations indicated that the obtained thin crystals possessed excellent crystalline quality and perfect epitaxial relationship with the substrates (Fig. 6f), leading to the remarkable charge transport features [70]. TCTG-structured FETs containing such the epitaxial thin crystals were fabricated with the PPMA film serving as dielectric (Fig. 6g); impressively, the resultant device exhibited a maximum hole mobility approaching 4.0 $cm^2\ V^{-1}\ s^{-1}$

and a high on/off ratio more than 10^5 at room temperature (Fig. 6h) [70]. Such the obtained excellent device performance with the highly improved stability could originate from the high-quality epitaxial perovskite thin crystals featuring the perfect atomic match with the substrates, thus highly decreasing the ionic defects and the ion migration. Applying the suitable interfacial engineering, such as using epitaxy techniques, could effectively minimize the defect/impurity densities in the active perovskite crystal channels and the related interfaces and thus improve the device performance and stabilities, holding great potentials for high-yield FET applications.

4.2 3D Perovskite Micro-/Nanoplate Transistors

Except for thin crystals, micro-/nanoplate 3D perovskites featuring free of grain boundaries were also used as active channels in FETs. BCBG-structured FETs (with pre-patterned Au electrodes) based on hybrid perovskite microplates (that were synthesized by selective growth method) were successfully fabricated, which displayed the notable-hysteresis transfer characteristics with a maximum saturation electron mobility up to 2.5 $cm^2\ V^{-1}\ s^{-1}$ at low temperature (77 K) (from backward sweep) (Fig. 7a and b) [128]. It was also found the perovskite microplate FET mobilities were greatly dependent on the microplates' thicknesses; the device made by a 300-nm $MAPbI_3$ microplate could have an optimal saturation mobility of around 0.5 $cm^2\ V^{-1}\ s^{-1}$ (Fig. 7c) [129]. Thereafter, graphene stripes were used as the electrodes for the fabrication of the $MAPbI_3$ microplate FETs; tuning the barrier heights between $MAPbI_3$ microplate channels and graphene electrodes could effectively affect the FET performance, and an optimized saturation electron mobility up to 4 $cm^2\ V^{-1}\ s^{-1}$ could be obtained at low temperature (from backward sweep) (Fig. 7d) [130]. In addition, it was found that using thermal annealing treatments could cause the transition of carrier transport types (i.e., from unipolar n-type to ambipolar and then to unipolar p-type) in the perovskite microplate FETs, which could originate from both the slight disintegration of active perovskite microplates and the p-type doping of Pb clusters in the perovskite microplates [130].

All-inorganic perovskite microplates have also gained wide-ranging attention in field of FET devices. Vapor-phase deposited all-inorganic $CsPbBr_3$ microplates and van der Waals epitaxial $CsPbBr_3$ ultrathin platelets through dry-transferring process have been attempted for the FET fabrications, clearly indicating that these micro−/nanoplatelets could serve as promising candidates for FETs with different device structures [132–134]. Except for these dry-processed microplates, solution-grown $CsPbBr_3$ microplates were also successfully applied to produce BGTC-structured FETs, clearly showing ambipolar transport behaviors and high phototransistor performance [131]. Specifically, the optimal saturation electron and hole mobilities could reach approximately 0.19 and 0.02 $cm^2\ V^{-1}\ s^{-1}$, respectively, in the dark condition, while, upon a 50-mW cm^{-2} light radiation, they could increase to 0.40 and 0.34 $cm^2\ V^{-1}\ s^{-1}$, respectively (Fig. 7e and f) [131].

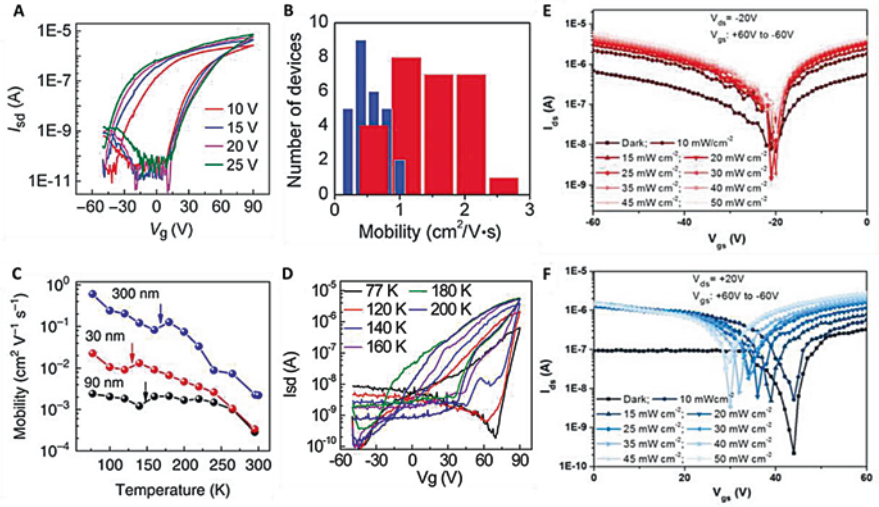

Fig. 7 Transistors based on perovskite micro-/nanoplates. (**a**) Transfer curves for hybrid perovskite microplate transistors. (**b**) Distribution of electron mobilities from 27 perovskite microplate devices tested at 77 K (red, backward sweep mobility; blue, forward sweep mobility). (**a** and **b**) are reproduced with permission from Ref. 128, AAAS. (**c**) Temperature-dependent electron mobilities for microplate devices with different thicknesses. Reproduced with permission from Ref. 129, Springer Nature. (**d**) Transfer curves of graphene-contacted transistors based on perovskite microplates at different temperatures. Reproduced with permission from Ref. 130, Wiley. (**e** and **f**) Transfer characteristics for all-inorganic perovskite microplate transistors applying different power-density illumination and drain voltages, respectively. Reproduced with permission from Ref. 131, Wiley

4.3 Transistors by 2D Layered Perovskite Crystals

FET devices based on layered 2D hybrid perovskite $(C_6H_5C_2H_4NH_3)_2SnI_4$ (PEA_2SnI_4) thin films served as the active channels were first reported by Mitzi et al. [135]; through choosing the suitable metal electrodes, a champion hole mobility reaching 0.62 $cm^2\ V^{-1}\ s^{-1}$ and a high on/off ratio up to 10^4 were obtained at room temperature [135]. Recently, there existed various great efforts, including the active channel morphology/structure optimizations, interface improvements, and molecular engineering of the contained organic group cations, for considerably improving the layered perovskite FET device performance. Among these strategies, using layered perovskite crystals as the active channels can effectively promote the high-performance FET applications. The exfoliated $(PEA)_2SnI_4$ thin crystals were used as the active layers for the fabrications of the BGBC-structured FETs, where a MoO_x hole injection layer was introduced to improve the charge carrier injection (Fig. 8a) [136]. The average saturation hole mobility up to 40 $cm^2\ V^{-1}\ s^{-1}$ could be obtained at room temperature; such the high performance was ascribed to the small structural disorder and low grain boundary density in these exfoliated 2D perovskite crystals (Fig. 8b and c). Notably, not all the exfoliated 2D perovskite crystals

possessed the flat and smooth surfaces for establishing promising contact with the meatal electrodes, thus resulting in the low yield (less than 1%) of the operable FET devices [136].

More recently, the exfoliated $(BA)_2(MA)_{n-1}Pb_nI_{3n+1}$ (n = 2, 3, 4, and 5) thin crystals were employed as the active channel materials to produce the highly reproducible and reliable BGTC-constructed FET devices (Fig. 8d) [137]. It was found that the FETs could exhibit the improving device performance with the decreasing temperature; a maximum mobility reaching 0.087 $cm^2\ V^{-1}\ s^{-1}$ and a high on/off ratio up to 10^6 with the clearly decreased hysteresis could be obtained at 150 K (Fig. 8e), which could originate from the effectively suppressed ion migration at low temperatures. Additionally, it was shown that replacing Au by Ca as electrodes could effectively decrease the carrier injection resistance at the interface between 2D perovskite crystals and metal electrodes. Thereby, the optimized $(BA)_2(MA)Pb_2I_7$ thin-crystal device with Ca using as electrodes could exhibit a maximum linear electron mobility of around 0.129 $cm^2\ V^{-1}\ s^{-1}$ and a high on/off ratio of 10^6 at 150 K (Fig. 8f) [137].

Recent resurgence of interest in 2D layered perovskite FET devices has led to significant progress in the field. It should be noted that layered perovskite FET devices, in particular the single-crystal ones, demonstrated the much higher and more reliable device performance as compared to the ones containing 3D perovskite counterparts, although the theoretically simulated carrier mobilities of 3D perovskites were actually lower than those of 2D layered perovskites [84, 138], which could originate from the significantly suppressed ion migration within 2D perovskites [43]. Also, layered perovskite crystals showed significantly improved stability, in particular the better moisture resistance, which could further make them

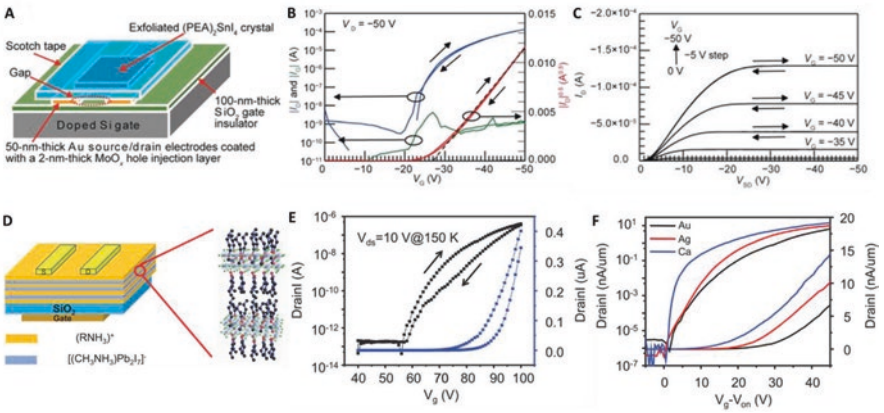

Fig. 8 2D layered perovskite crystal transistors. (**a**) Schematic of BGBC transistor based on exfoliated $(PEA)_2SnI_4$ thin crystal. (**b**) Transfer and (**c**) output curves of the related transistor. (**a**–**c**) are reproduced with permission from Ref. 136, AIP. (**d**) Schematic of BGTC transistor based on exfoliated 2D $(BA)_2(MA)Pb_2I_7$ thin crystals, together with the molecular structure of 2D perovskite. (**e**) Transfer characteristics of a $(BA)_2(MA)Pb_2I_7$ thin-crystal transistor measured at 150 K in the dark. (**f**) Transfer characteristics of the devices with Au, Ag, and Ca working as electrodes. Reproduced with permission from Ref. 137, Wiley

more promising candidates for FET devices. Benefiting from these advantages, it is expected that the continuous improvements of the device performance can be achieved, through further microstructure retouching, molecular tailoring, and device structure designs.

5 Challenges and Outlooks

In this chapter, we comprehensively reviewed the unique features of perovskite crystals, including structural and dimensional versatilities, tunable band structures, charge carrier, and ion transport behaviors, which could facilitate FET devices, the solution-phase growth processes for various formed perovskite crystals, the advances of perovskite crystal FET devices, as well as the facing challenges and possible strategies and opportunities. Notably, single-crystal perovskites have attracted extensive research attention for the broadly ranged energy and optoelectronic applications due to their promising features. Moreover, owing to their excellent charge transport properties and unique ion migration behaviors, as well as the superior thermal and structural stabilities that can be attributed to free of grain boundaries along with the reduced defects and traps, perovskite crystals in different forms and dimensions are also becoming more desirable for FET applications. Moreover, perovskite crystals can be grown through the facile, low-cost solution-based methods in comparison to complicated processes for conventional inorganic semiconductors, demonstrating the significant potentials for enabling high-efficient commercial electronics.

Notably, in comparison to the great achievements in energy and optoelectronic applications, the research on perovskite crystal FETs is still in their infancy, and more efforts are still demanded for addressing the challenges faced by the community toward real-world commercialization. Notably, the general issues, like environmental and health threats, for the polycrystalline halide perovskite devices would still be the concerns for the perovskite crystal FETs. In this sense, the proposed strategies for addressing these general issues from other reviews could be reasonably applied in single-crystal perovskite FETs without any doubt [44, 139, 140]. Moreover, there are also several particular challenges and potential opportunities regarding perovskite crystal FETs, which are detailly discussed as follows:

(1) Optimizing perovskite crystal FET mobilities. The simulations theoretically predicted that the ideal perovskite materials can exhibit the ultrahigh charge carrier mobilities (e.g., larger than 3000 $cm^2\ V^{-1}\ s^{-1}$ in the normally researched $MAPbI_3$), because of their low effective mass (m^*) values [99, 100]. However, the experimentally obtained mobilities in the perovskite FETs (even the single-crystal ones) [26] are still much less than the theoretical predictions. In this sense, the in-depth interpretations on the underlying mechanisms of charge transport behaviors in the single-crystal perovskites, together with the suitable processing of active perovskite crystal channels and electrodes and the novel

device designs (e.g., vertical device construction), are greatly required for gaining the optimal device performance.

(2) Revealing underlying principle of ion migration. Ion migration has been widely recognized as the intrinsic behavior in halide perovskites, causing their transport properties more elusive. Notably, ion migration behaviors have also been found in the single-crystal perovskites and devices (even though they are not that severe as in polycrystalline ones) [2, 16, 19, 20, 27, 44, 46, 125]. Ion migration could affect perovskite crystal FETs, resulting in inaccurate evaluations of device performance (e.g., under-/overestimations of mobilities and on/off ratios) [19, 20, 23–25]. In this sense, getting in-depth understandings regarding ion migration in perovskite crystals is critical for effectively boosting FET device performance and facilitating broad electronics. The efficient strategy to probe ion migration would be to perform tests, combining with computational simulations on the electrical behaviors as a function of temperatures and their temporal responses.

(3) Stabilizing FETs based on perovskite crystals. It is widely acknowledged that single-crystal perovskites can display much higher stabilities than polycrystalline perovskite alternatives, but their stabilities are still not comparable to conventional inorganic semiconductor materials, thus restricting their practical electronic applications. Some attempts have been made to improve the perovskite crystal FET device stabilities, including use of layered perovskite crystals, elemental doping, and novel device structure engineering with protection electrodes and/or layers [19, 20, 23–25, 46]. More effective strategies, possibly component engineering or epitaxial synthesis methods, should be developed for enhancing the stability of perovskite crystal FET devices further.

(4) Integrating arrayed perovskite crystal FETs. To date, there is still a large gap between the initial demonstration of perovskite crystal FETs and the requirements for realizing commercial chips, posing the challenges to clearly elucidate the logical computing functionalitis [23–25, 44]. In this sense, it is greatly beneficial to explore the promising production strategies for the integration of arrayed perovskite crystal FETs, advancing the practical electronic applications. The proposed solution-processed epitaxial growth approach assisted with lithography using the industrially mature lithographic template could be an effective routine to address the issues [13, 64], demonstrating significant potential to realize the industrialization of perovskite crystal electronics.

Despite being faced by these challenges, it is quite reasonable to foresee a promising future of perovskite crystal FETs, considering their remarkable features, mainly including the excellent transport properties and highly improved stabilities related to the ordered lattice arrangement and greatly reduced defect densities, together with their cost-efficiency, simple processability, and superior compatibility. All in all, FET devices made by solution-synthesized perovskite crystals could provide an ideal platform for fundamental studies and in the meanwhile, with impressive device performance, facilitate multiple electronic functionalities; potentially, breakthroughs in the area will drive the niche industrial deployments of novel perovskite electronics that promote next-generation technologies.

References

1. Kim, J. Y., Lee, J.-W., Jung, H. S., Shin, H., & Park, N.-G. (2020). High-efficiency perovskite solar cells. *Chemical Reviews, 120*, 7867–7918.
2. Green, M. A., Ho-Baillie, A., & Snaith, H. J. (2014). The emergence of perovskites solar cells. *Nature Photonics, 8*, 506–514.
3. Yang, T., Li, F., & Zheng, R. (2021). Recent advances in radiation detection technologies enabled by metal-halide perovskites. *Materials Advances, 2*, 6744.
4. Leng, K., Fu, W., Liu, Y., Chhowalla, M., & Loh, K. P. (2020). From bulk to molecularly thin hybrid perovskites. *Nature Reviews Materials, 5*, 482–500.
5. Ball, J. M., & Petrozza, A. (2016). Defects in perovskite-halides and their effects in solar cells. *Nature Energy, 1*, 16149.
6. Shi, D., Adinolfi, V., Comin, R., Yuan, M., Alarousu, E., Buin, A., Chen, Y., Shi, D., Hoogland, S., Rothenberger, A., et al. (2015). Low trap-state density and long carrier diffusion in organolead trihalide perovskite single crystals. *Science, 347*, 519–522.
7. Chen, L., Tan, Y.-Y., Chen, Z.-X., Wang, T., Hu, S., Nan, Z.-A., Xie, L.-Q., Hui, Y., Huang, J.-X., Zhan, C., et al. (2019). Toward long-term stability: Single-crystal alloys of cesium-containing mixed cation and mixed halide perovskite. *Journal of the American Chemical Society, 141*, 1665–1671.
8. Kong, W., Wang, S., Li, F., Zhao, C., Xing, J., Zou, Y., Yu, Z., Lin, C.-H., Shan, Y., Lai, Y. H., et al. (2020). Ultrathin perovskite monocrystals boost the solar cell performance. *Advanced Energy Materials, 10*, 2000453.
9. Fu, M., Tamarat, P., Trebbia, J.-B., Bodnarchuk, M. I., Kovalenko, M. V., Even, J., & Lounis, B. (2018). Unraveling exciton-phonon coupling in individual $FAPbI_3$ nanocrystals emitting near-infrared single photons. *Nature Communications, 9*, 3318.
10. Ni, Z., Bao, C., Liu, Y., Jiang, Q., Wu, W.-Q., Chen, S., Dia, X., Chen, B., Hartweg, B., Yu, Z., et al. (2020). Resolving spatial and energetic distributions of trap states in metal halide perovskite solar cells. *Science, 367*, 1352–1358.
11. Kelso, M. V., Mahenderkar, N. K., Chen, Q., Tubbesing, J. Z., & Switzer, J. A. (2019). Spin coating epitaxial films. *Science, 364*, 166.
12. Shi, E., Yuan, B., Shiring, S. B., Gao, Y., Akriti, Guo, Y., Su, C., et al. (2020). Two-dimensional halide perovskite lateral epitaxial heterostructures. *Nature, 580*, 614–620.
13. Lei, Y., Chen, Y., Zhang, R., Li, Y., Yan, Q., Lee, S., Yu, Y., Tsai, H., Choi, W., Wang, K., et al. (2020). A fabrication process for flexible single-crystal perovskite devices. *Nature, 583*, 790–795.
14. Chen, Y., Lei, Y., Li, Y., Yu, Y., Cai, J., Chui, M.-H., Rao, R., Gu, Y., Wang, C., Choi, W., et al. (2020). Strain engineering and epitaxial stabilization of halide perovskites. *Nature, 577*, 209–215.
15. Zhang, X., Zhang, R., Yang, T., Cheng, Y., Li, F., Li, W., Huang, J., Liu, H., & Zheng, R. (2021). Facile fabrication of hybrid perovskite single-crystalline photocathode for photoelectrochemical water splitting. *Energy Technology, 9*, 2000965.
16. Zhang, X., Li, F., & Zheng, R. (2020). Growth and optimization of hybrid perovskite single crystals for optoelectronics/electronics and sensing. *Journal of Materials Chemistry C, 8*, 13918–13952.
17. Herz, L. M. (2017). Charge-carrier mobilities in metal halide perovskites: Fundamental mechanisms and limits. *ACS Energy Letters, 2*, 1539–1548.
18. Li, J., Han, Z., Gu, Y., Yu, D., Liu, J., Hu, D., Xu, X., & Zeng, H. (2021). Perovskite single crystals: Synthesis, optoelectronic properties, and application. *Advanced Functional Materials, 31*, 2008684.
19. Li, F., & Zheng, R. (2020). *Halide perovskites with ambipolar transport properties for transistor applications*. The Royal Society of Chemistry.

20. Paulus, F., Tyznik, C., Jurchescu, O. D., & Vaynzof, Y. (2021). Switched-on: Progress, challenges, and opportunities in metal halide perovskite transistors. *Advanced Functional Materials, 31*, 2101029.
21. Liang, Y., Li, F., & Zheng, R. (2020). Low-dimensional hybrid perovskites for field-effect transistors with improved stability: Progress and challenges. *Advanced Electronic Materials, 6*, 2000137.
22. Zaumseil, J., & Sirringhaus, H. (2007). Electron and ambipolar transport in organic field-effect transistors. *Chemical Reviews, 107*, 1296–1323.
23. Li, F., Yang, T., & Zheng, R. (2022). Solution-processed perovskite crystals for electronics: Moving forward. *Matter, 5*, 1700–1733.
24. Lin, Y.-H., Pattanasattayavong, P., & Anthopoulos, T. D. (2017). Metal-halide perovskite transistors for printed electronics: Challenges and opportunities. *Advanced Materials, 29*, 1702838.
25. Li, F., Yu, W., Guan, X., & Wu, T. (2022). Emerging transistor applications enabled by halide perovskites. *Accounts of Chemical Research, 3*, 8–20.
26. Liu, A., Zhu, H., Bai, S., Reo, Y., Zou, T., Kim, M.-G., & Noh, Y.-Y. (2022). High-performance inorganic metal halide perovskite transistors. *Nature Electronics, 5*, 78–83.
27. Jeong, B., Veith, L., Smolders, T. J. A. M., Wolf, M. J., & Asadi, K. (2021). Room-temperature halide perovskite field-effect transistors by ion transport mitigation. *Advanced Materials, 33*, 2100486.
28. Winterer, F., Walter, L. S., Lenz, J., Seebauer, S., Tong, Y., Polavarapu, L., & Weitz, R. T. (2021). Charge traps in all-inorganic $CsPbBr_3$ perovskite nanowire field-effect phototransistors. *Advanced Electronic Materials, 7*, 2100105.
29. Shao, S., Talsma, W., Pitaro, M., Dong, J., Kahmann, S., Rommens, A. J., Portale, G., & Loi, M. A. (2021). Field-effect transistors based on formamidinium tin triiodide perovskite. *Advanced Functional Materials, 31*, 2008478.
30. Zhang, F., Lu, H., Tong, J., Berry, J. J., Beard, M. C., & Zhu, K. (2020). Advances in two-dimensional organic-inorganic hybrid perovskites. *Energy & Environmental Science, 13*, 1154–1186.
31. Rose, G. (1839). Description of some new minerals from the Urals. *Annals of Physics, 124*, 551–573.
32. Zhu, Z., Sun, Q., Zhang, Z., Dai, J., Xing, G., Li, S., Huang, X., & Huang, W. (2018). Metal halide perovskites: Stability and sensing-ability. *Journal of Materials Chemistry, C 6*, 10121–10137.
33. Jang, D. M., Park, K., Kim, D. H., Park, J., Shojaei, F., Kang, H. S., Ahn, J.-P., Lee, J. W., & Song, J. K. (2015). Reversible halide exchange reaction of organometal trihalide perovskite colloidal nanocrystals for full-range band gap tuning. *Nano Letters, 15*, 5191–5199.
34. Tao, S., Schmidt, I., Brocks, G., Jiang, J., Tranca, I., Meerholz, K., & Olthof, S. (2019). Absolute energy level positions in tin- and lead-based halide perovskites. *Nature Communications, 10*, 2560.
35. Xiao, K., Lin, R., Han, Q., Hou, Y., Qin, Z., Nguyen, H. T., Wen, J., Wei, M., Yeddu, V., Saidaminov, M. I., et al. (2020). All-perovskite tandem solar cells with 24.2% certified efficiency and area over 1 cm^2 using surface-anchoring zwitterionic antioxidant. *Nature Energy, 5*, 870–880.
36. Lu, H., Liu, Y., Ahlawat, P., Mishra, A., Tress, W. R., Eickemeyer, F. T., Yang, Y., Fu, F., Wang, Z., Avalos, C. E., et al. (2020). Vapor-assisted deposition of highly efficient, stable black-phase $FAPbI_3$ perovskite solar cells. *Science, 370*, eabb8985.
37. Yang, T., Li, F., & Zheng, R. (2019). Recent progress on cesium lead halide perovskites for photodetection applications. *ACS Applied Electronic Materials, 1*, 1348–1366.
38. Kim, G., Min, H., Lee, K. S., Lee, D. Y., Yoon, S. M., & Seok, S. I. (2020). Impact of strain relaxation on performance of a-formamidinium lead iodide perovskite solar cells. *Science, 370*, 108–112.

39. Lee, S. J., Shin, S. S., Im, J., Ahn, T. K., Noh, J. H., Jeon, N. J., Seok, S. I., & Seo, J. (2017). Reducing carrier density in formamidinium tin perovskites and its beneficial effects on stability and efficiency of perovskite solar cells. *ACS Energy Letters, 3*, 46–53.
40. Stranks, S. D., & Snaith, H. J. (2015). Metal-halide perovskites for photovoltaic and light-emitting devices. *Nature Nanotechnology, 10*, 391–402.
41. Dunlap-Shohl, W. A., Zhou, Y., Padture, N. P., & Mitzi, D. B. (2019). Synthetic approaches for halide perovskite thin films. *Chemical Reviews, 119*, 3193–3295.
42. Li, Z., Yang, M., Park, J.-S., Wei, S.-H., Berry, J. J., & Zhu, K. (2015). Stabilizing perovskite structures by tuning tolerance factor: Formation of formamidinium and cesium lead iodide solid-state alloys. *Chemistry of Materials, 28*, 284–292.
43. Zheng, K., Abdellah, M., Zhu, Q., Kong, Q., Jennings, G., Kurtz, C. A., Messing, M. E., Niu, Y., Gosztola, D. J., Al-Marri, M. J., Zhang, X., Pullerits, T., & Canton, S. E. (2016). Direct experimental evidence for photoinduced strong coupling polarons in organolead halide perovskite nanoparticles. *Journal of Physical Chemistry Letters, 7*, 4535–4539.
44. Lei, Y., Chen, Y., & Xu, S. (2021). Single-crystal halide perovskites: Opportunities and challenges. *Matter, 4*, 2266–2308.
45. Mehmood, U., Al-Ahmed, A., Afzaal, M., Al-Sulaiman, F. A., & Daud, M. (2017). Recent progress and remaining challenges in organometallic halides-based perovskite solar cells. *Renewable and Sustainable Energy Reviews, 78*, 1–14.
46. Younis, A., Lin, C.-H., Guan, X., Shahrokhi, S., Huang, C.-Y., Wang, Y., He, T., Singh, S., Hu, L., Retamal, J. R. D., He, J.-H., & Wu, T. (2021). Halide perovskites: A new era of solution-processed electronics. *Advanced Materials, 33*, 2005000.
47. Zhang, W., Eperon, G. E., & Snaith, H. J. (2016). Metal halide perovskites for energy applications. *Nature Energy, 1*, 16048.
48. Li, J., Han, Z., Gu, Y., Yu, D., Liu, J., Hu, D., Xu, X., & Zeng, H. (2020). Perovskite single crystals: Synthesis, optoelectronic properties, and application. *Advanced Functional Materials, 33*, 2008684.
49. Dey, K., Roose, B., & Stranks, S. D. (2021). Optoelectronic properties of low-bandgap halide perovskites for solar cell applications. *Advanced Materials, 33*, 2102300.
50. Ahmadi, M., Wu, T., & Hu, B. (2017). A review on organic-inorganic halide perovskite photodetectors: Device engineering and fundamental physics. *Advanced Materials, 41*, 201605242.
51. Wehrenfennig, C., Liu, M., Snaith, H. J., Johnston, M. B., & Herz, L. M. (2014). Homogeneous emission line broadening in the organo lead halide perovskite $CH_3NH_3PbI_{3-x}Cl_x$. *Journal of Physical Chemistry Letters, 5*, 1300–1306.
52. De Wolf, S., Holovsky, J., Moon, S.-J., Loper, P., Niesen, B., Ledinsky, M., Haug, F.-J., Yum, J.-H., & Ballif, C. (2014). Organometallic halide perovskites: Sharp optical absorption edge and its relation to photovoltaic performance. *Journal of Physical Chemistry Letters, 5*, 1035–1039.
53. Huang, J., Yuan, Y., Shao, Y., & Yan, Y. (2017). Understanding the physical properties of hybrid perovskites for photovoltaic applications. *Nature Reviews Materials, 2*, 17042.
54. Liu, Y., Yang, Z., Cui, D., Ren, X., Sun, J., Liu, X., Zhang, J., Wei, Q., Fan, H., Yu, F., Zhang, X., Zhao, C., & Liu, S. F. (2015). Two-inch-sized perovskite $CH_3NH_3PbX_3$ (X = Cl, Br, I) crystals: Growth and characterization. *Advanced Materials, 27*, 5176–5183.
55. Krogstrup, P., Jørgensen, H. I., Heiss, M., Demichel, O., Holm, J. V., Aagesen, M., Nygard, J., & Fontcuberta i Morral, A. (2013). Single-nanowire solar cells beyond the Shockley-Queisser limit. *Nature Photonics, 7*, 306–310.
56. Herz, L. M. (2016). Charge-carrier dynamics in organic-inorganic metal halide perovskites. *Annual Review of Physical Chemistry, 67*, 65–89.
57. Wang, K., Wang, S., Xiao, S., & Song, Q. (2018). Recent advances in perovskite micro- and nanolasers. *Advanced Optical Materials, 6*, 1800278.
58. Li, F., Ma, C., Wang, H., Hu, W., Yu, W., Sheikh, A. D., & Wu, T. (2015). Ambipolar solution-processed hybrid perovskite phototransistors. *Nature Communications, 6*, 8238.

59. Feng, A., Jiang, X., Zhang, X., Zheng, X., Zheng, W., Mohammed, O. F., Chen, Z., & Bakr, O. M. (2020). Shape control of metal halide perovskite single crystals: From bulk to nanoscale. *Chemistry of Materials, 32*, 7602–7617.
60. Dang, Y., Liu, Y., Sun, Y., Yuan, D., Liu, X., Lu, W., Liu, G., Xia, H., & Tao, X. (2015). Bulk crystal growth of hybrid perovskite material $CH_3NH_3PbI_3$. *CrystEngComm, 17*, 665–670.
61. Saidaminov, M. I., Abdelhady, A. L., Murali, B., Alarousu, E., Burlakov, V. M., Peng, W., Dursun, I., Wang, L., He, Y., Maculan, G., Goriely, A., Wu, T., Mohammed, O. F., & Bakr, O. M. (2015). High-quality bulk hybrid perovskite single crystals within minutes by inverse temperature crystallization. *Nature Communications, 6*, 7586.
62. Peng, W., Wang, L., Murali, B., Ho, K.-T., Bera, A., Cho, N., Kang, C.-F., Burlakov, V. M., Pan, J., Sinatra, L., Ma, C., Xu, W., Shi, D., Alarousu, E., Goriely, A., He, J.-H., Mohammed, O. F., Wu, T., & Bakr, O. M. (2016). Solution-grown monocrystalline hybrid perovskite films for hole-transporter-free solar cells. *Advanced Materials, 28*, 3383–3390.
63. Chen, Y.-X., Ge, Q.-Q., Shi, Y., Liu, J., Xue, D.-J., Ma, J.-Y., Ding, J., Yan, H.-J., Hu, J.-S., & Wan, L.-J. (2016). General space-confined on-substrate fabrication of thickness-adjustable hybrid perovskite single-crystalline thin films. *Journal of the American Chemical Society, 138*, 16196–16199.
64. Wang, K., Wu, C., Yang, D., Jiang, Y., & Priya, S. (2018). Quasi-two-dimensional halide perovskite single crystal photodetector. *ACS Nano, 12*, 4919.
65. Zhang, Y., Liu, Y., Li, Y., Yang, Z., Liu, S., & (F.). (2016). Perovskite $CH_3NH_3Pb(Br_xI_{1-x})_3$ single crystals with controlled composition for fine-tuned bandgap towards optimized optoelectronic applications. *Journal of Materials Chemistry C, 4*, 9172–9178.
66. Wei, H., Fang, Y., Mulligan, P., Chuirazzi, W., Fang, H.-H., Wang, C., Ecker, B. R., Gao, Y., Loi, M. A., Cao, L., & Huang, J. (2016). Sensitive X-ray detectors made of methylammonium lead tribromide perovskite single crystals. *Nature Photonics, 10*, 333.
67. Rao, H. S., Li, W. G., Chen, B.-X., Kuang, D.-B., & Su, C.-Y. (2017). In-situ growth of 120-cm^2 $CH_3NH_3PbBr_3$ perovskite crystal film on FTO glass for narrowband-photodetectors. *Advanced Materials, 29*, 1602639.
68. Xu, S., Shen, Y., Ding, Y., & Wang, Z. L. (2010). Growth and transfer of monolithic horizontal ZnO nanowire superstructures onto flexible substrates. *Advanced Functional Materials, 20*, 1493–1497.
69. Lei, Y., Chen, Y., Gu, Y., Wang, C., Huang, Z., Qian, H., Nie, J., Hollett, G., Choi, W., Yu, Y., et al. (2018). Controlled homoepitaxial growth of hybrid perovskites. *Advanced Materials, 30*, 1705992.
70. Yang, T., Jin, C., Qu, J., Asadpoor Darvish, A., Sabatini, R., Zhang, X., Chen, H., Ringer, S. P., Lakhwani, G., Li, F., Cairney, J., Liu, X., & Zheng, R. (2021). Solution epitaxy of halide perovskite thin single crystal s for stable transistors. *ACS Applied Materials & Interfaces, 13*, 37840–37848.
71. Tong, Y., Ehrat, F., Vanderlinden, W., Cardenas-Daw, C., Stolarczyk, J. K., Polavarapu, L., & Urban, A. S. (2016). Dilution-induced formation of hybrid perovskite nanoplatelets. *ACS Nano, 10*, 10936–10944.
72. Weidman, M. C., Seitz, M., Stranks, S. D., & Tisdale, W. A. (2016). Highly tunable colloidal perovskite nanoplatelets through variable cation, metal, and halide composition. *ACS Nano, 10*, 7830–7839.
73. Zhang, Q., Ha, S. T., Liu, X., Sum, T. C., & Xiong, Q. (2014). Room-temperature near-infrared high-Q perovskite whispering-gallery planar nanolasers. *Nano Letters, 14*, 5995–6001.
74. Akkerman, Q. A., Motti, S. G., Srimath Kandada, A. R., Mosconi, E., D'Innocenzo, V., Bertoni, G., Marras, S., Kamino, B. A., Miranda, L., De Angelis, F., et al. (2016). Solution synthesis approach to colloidal cesium lead halide perovskite nanoplatelets with monolayer-level thickness control. *Journal of the American Chemical Society, 138*, 1010–1016.
75. Tyagi, P., Arveson, S. M., & Tisdale, W. A. (2015). Colloidal organohalide perovskite nanoplatelets exhibiting quantum confinement. *Journal of Physical Chemistry Letters, 6*, 1911–1916.

76. Chen, J., Fu, Y., Samad, L., Dang, L., Zhao, Y., Shen, S., Guo, L., & Jin, S. (2017). Vapor-phase epitaxial growth of aligned nanowire networks of cesium lead halide perovskites ($CsPbX_3$, X = Cl, Br, I). *Nano Letters, 17*, 460–466.
77. Zhu, H., Fu, Y., Meng, F., Wu, X., Gong, Z., Ding, Q., Gustafsson, M. V., Trinh, M. T., Jin, S., & Zhu, X. Y. (2015). Lead halide perovskite nanowire lasers with low lasing thresholds and high-quality factors. *Nature Materials, 14*, 636–642.
78. Protesescu, L., Yakunin, S., Bodnarchuk, M. I., Krieg, F., Caputo, R., Hendon, C. H., Yang, R. X., Walsh, A., & Kovalenko, M. (2015). Nanocrystals of cesium lead halide perovskites ($CsPbX_3$, X = Cl, Br, and I): Novel optoelectronic materials showing bright emission with wide color gamut. *Nano Letters, 15*, 3692–3696.
79. Song, J., Li, J., Li, X., Xu, L., Dong, Y., & Zeng, H. (2015). Quantum dot light-emitting diodes based on inorganic perovskite cesium lead halides ($CsPbX_3$). *Advanced Materials, 27*, 7162–7167.
80. Shang, Q., Wang, Y., Zhong, Y., Mi, Y., Qin, L., Zhao, Y., Qiu, X., Liu, X., & Zhang, Q. (2017). Unveiling structurally engineered carrier dynamics in hybrid quasi-two-dimensional perovskite thin films toward controllable emission. *Journal of Physical Chemistry Letters, 8*, 4431.
81. Zhao, C., Tian, W., Leng, J., Zhao, Y., & Jin, S. (2019). Controlling the property of edges in layered 2D perovskite single crystals. *Journal of Physical Chemistry Letters, 10*, 3950.
82. Zhang, Y., Liu, Y., Xu, Z., Ye, H., Li, Q., Hu, M., Yang, Z., Liu, S. (2019). Two-dimensional $(PEA)_2PbBr_4$ perovskite single crystals for a high-performance UV-detector. Journal of Materials Chemistry C 7, 1584.
83. Saidaminov, M. I., Mohammed, O. F., & Bakr, O. M. (2017). Low-dimensional-networked metal halide perovskites: The next big thing. *ACS Energy Letters, 2*, 889.
84. Li, M. K., Chen, T. P., Lin, Y. F., Raghavan, C. M., Chen, W. L., Yang, S. H., Sankar, R., Luo, C. W., Chang, Y. M., & Chen, C.-W. (2018). Intrinsic carrier transport of phase-pure homologous 2D organolead halide hybrid perovskite single crystals. *Small, 14*, 1803763.
85. Passarelli, J. V., Fairfield, D. J., Sather, N. A., Hendricks, M. P., Sai, H., Stern, C. L., & Stupp, S. I. (2018). Enhanced out-of-plane conductivity and photovoltaic performance in n = 1 layered perovskite through organic cation design. *Journal of the American Chemical Society, 140*, 7313–7323.
86. Li, X., Hoffman, J. M., & Kanatzidis, M. G. (2021). The 2D halide perovskite rulebook: How the spacer influences everything from the structure to optoelectronic device efficiency. *Chemical Reviews, 121*, 2230–2291.
87. Ge, C., Zhai, W., Tian, C., Zhao, S., Guo, T., Sun, S., Chen, W., & Ran, G. (2019). Centimeter-scale 2D perovskite $(PEA)_2PbBr_4$ single crystal plates grown by a seeded solution method for photodetectors. *RSC Advances, 9*, 16779.
88. Zhumekenov, A. A., Burlakov, V. M., Saidaminov, M. I., Alofi, A., Haque, M. A., Turedi, B., Davaasuren, B., Dursun, I., Cho, N., El-Zohry, A. M., Bastiani, M. D., Giugni, A., Torre, B., Fabrizio, E. D., Mohammed, O. F., Rothenberger, A., Wu, T., Goriely, A., & Bakr, O. M. (2017). The role of surface tension in the crystallization of metal halide perovskites. *ACS Energy Letters, 2*, 1782.
89. Yao, F., Peng, J., Li, R., Li, W., Gui, P., Li, B., Liu, C., Tao, C., Lin, Q., & Fang, G. (2020). Room-temperature liquid diffused separation induced crystallization for high-quality perovskite single crystals. *Nature Communications, 11*, 1194.
90. Liu, Y., Ye, H., Zhang, Y., Zhao, K., Yang, Z., Yuan, Y., Wu, H., Zhao, G., Yang, Z., Tang, J., Xu, Z., & Liu, S. (2019). Surface-tension-controlled crystallization for high-quality 2D perovskite single crystals for ultrahigh photodetection. *Matter, 1*, 465.
91. He, Y., Petryk, M., Liu, Z., Chica, D. G., Hadar, I., Leak, C., Ke, W., Spanopoulos, I., Lin, W., Chung, D. Y., et al. (2020). $CsPbBr_3$ perovskite detectors with 1.4% energy resolution for high-energy g-rays. *Nature Photonics, 15*, 36–42.

92. Dong, Q., Fang, Y., Shao, Y., Mulligan, P., Qiu, J., Cao, L., & Huang, J. (2015). Electron-hole diffusion lengths >175 mm in solution-grown $CH_3NH_3PbI_3$ single crystals. *Science, 347*, 967–970.
93. Gong, X., Huang, Z., Sabatini, R., Tan, C.-S., Bappi, G., Walters, G., Proppe, A., Saidaminov, M. I., Voznyy, O., Kelley, S. O., & Sargent, E. H. (2019). Contactless measurements of photocarrier transport properties in perovskite single crystals. *Nature Communications, 10*, 1591.
94. Valverde-Chavez, D. A., Ponseca, C. S., Jr., Stoumpos, C. C., Yartsey, A., Kanatzidis, M. G., Sundstrom, V., & Cooke, D. G. (2015). Intrinsic femtosecond charge generation dynamics in single crystal $CH_3NH_3PbI_3$. *Energy & Environmental Science, 8*, 3700–3707.
95. Eames, C., Frost, J. M., Barnes, P. R. F., O'Regan, B. C., Walsh, A., & Islam, M. S. (2015). Ionic transport in hybrid lead iodide perovskite solar cells. *Nature Communications, 6*, 7497.
96. Du, M. H. (2014). Efficient carrier transport in halide perovskites: Theoretical perspectives. *Journal of Materials Chemistry A, 2*, 9091.
97. Brenner, T. M., Egger, D. A., Kronik, L., Hodes, G., & Cahen, D. (2016). Hybrid organic-inorganic perovskites: Low-cost semiconductors with intriguing charge-transport properties. *Nature Reviews Materials, 1*, 15007.
98. Yin, W.-J., Yang, J.-H., Kang, J., Yan, Y., & Wei, S.-H. (2015). Halide perovskite materials for solar cells: A theoretical review. *Journal of Materials Chemistry A, 3*, 8926.
99. Wang, Y., Zhang, Y., Zhang, P., & Zhang, W. (2015). High intrinsic carrier mobility and photon absorption in the perovskite $CH_3NH_3PbI_3$. *Physical Chemistry Chemical Physics, 17*, 11516.
100. He, Y., & Galli, G. (2014). Perovskites for solar thermoelectric applications: A first principal study of $CH_3NH_3AI_3$ (A = Pb and Sn). *Chemistry of Materials, 26*, 5394.
101. Li, H., Song, J., Pan, W., Xu, D., Zhu, W.-A., Wei, H., & Yang, B. (2020). Sensitive and stable 2D perovskite single-crystal X-ray detectors enabled by a supramolecular anchor. *Advanced Materials, 32*, 2003790.
102. Zhu, H. L., Liang, Z., Huo, Z., Ng, W. K., Mao, J., Wong, K. S., Yin, W.-J., & Choy, W. C. H. (2018). Low-bandgap methylammonium-rubidium cation Sn-rich perovskites for efficient ultraviolet-visible-near infrared photodetectors. *Advanced Functional Materials, 28*, 1706068.
103. Yu, W., Li, F., Yu, L., Niazi, M. R., Zou, Y., Corzo, D., Basu, A., Ma, C., Dey, S., Tietze, M. L., Buttner, U., Wang, X., Wang, Z., Hedhili, M. N., Guo, C., Wu, T., & Amassian, A. (2018). Single crystal hybrid perovskite field-effect transistors. *Nature Communications, 9*, 5354.
104. Wang, J., Senanayak, S. P., Liu, J., Hu, Y., Shi, Y., Li, Z., Zhang, C., Yang, B., Jiang, L., Di, D., Ievlev, A. V., Ovchinnikova, O. S., Ding, T., Deng, H., Tang, L., Guo, Y., Wang, J., Xiao, K., Venkateshvaran, D., Jiang, L., Zhu, D., & Sirringhaus, H. (2019). Investigation of electrode electrochemical reactions in $CH_3NH_3PbBr_3$ perovskite single-crystal field-effect transistors. *Advanced Materials, 31*, e1902618.
105. Ponseca, C. S., Savenije, T. J., Abdellah, M., Zheng, K., Yartsev, A., Pascher, T., Harlang, T., Chabera, P., Pullerits, T., Stepanov, A., et al. (2014). Organometal halide perovskite solar cell materials rationalized: Ultrafast charge generation, high and microsecond-long balanced mobilities, and slow recombination. *Journal of the American Chemical Society, 136*, 5189–5192.
106. Brenner, T. M., Egger, D. A., Rappe, A. M., Kronik, L., Hodes, G., & Cahen, D. (2015). Are mobilities in hybrid organic-inorganic halide perovskites actually "high"? *Journal of Physical Chemistry Letters, 6*, 4754–4757.
107. Liu, Y., Ye, H., Zhang, Y., Zhao, K., Yang, Z., Yuan, Y., Wu, H., Zhao, G., Yang, Z., Tang, J., et al. (2019). Surface-tension-controlled crystallization for high-quality 2D perovskite single crystals for ultrahigh photodetection. *Matter, 1*, 465–480.
108. Ebadi, F., Taghavinia, N., Mohammadpour, R., Hagfeldt, A., & Tress, W. (2019). Origin of apparent light-enhanced and negative capacitance in perovskite solar cells. *Nature Communications, 10*, 1574.
109. Seeger, K. (2004). *Semiconductor physics*. Springer.

110. Chu, Z., Yang, M., Schulz, P., Wu, D., Ma, X., Seifert, E., Liuyang, S., Li, X., Zhu, K., & Lai, K. (2017). Impact of grain boundaries on efficiency and stability of organic-inorganic trihalide perovskites. *Nature Communications, 8*, 2230.
111. Wenger, B., Nayak, P. K., Wen, X., Kesava, S. V., Noel, N. K., & Snaith, H. J. (2017). Consolidation of the optoelectronic properties of $CH_3NH_3PbBr_3$ perovskite single crystals. *Nature Communications, 8*, 590.
112. Li, C., Tscheuschner, S., Paulus, F., Hopkinson, P. E., Kießling, J., Köhler, A., Vaynzof, Y., & Huettner, S. (2016). Iodine migration and its effect on hysteresis in perovskite solar cells. *Advanced Materials, 28*, 2446.
113. Snaith, H. J., Abate, A., Ball, J. M., Eperon, G. E., Leijtens, T., Noel, N. K., Stranks, S. D., Wang, J. T.-W., Wojciechowski, K., & Zhang, W. (2014). Anomalous hysteresis in perovskite solar cells. *Journal of Physical Chemistry Letters, 5*, 1511.
114. Shao, Y., Fang, Y., Li, T., Wang, Q., Dong, Q., Deng, Y., Yuan, Y., Wei, H., Wang, M., Gruverman, A., et al. (2016). Grain boundary dominated ion migration in polycrystalline organic-inorganic halide perovskite films. *Energy & Environmental Science, 9*, 1752–1759.
115. Li, C., Guerrero, A., Huettner, S., & Bisquert, J. (2018). Unravelling the role of vacancies in lead halide perovskite through electrical switching of photoluminescence. *Nature Communications, 9*, 5113.
116. Li, C., Guerrero, A., Zhong, Y., Gräser, A., Luna, C. A. M., Köhler, J., Bisquert, J., Hildner, R., & Huettner, S. (2017). Real-time observation of iodide ion migration in methylammonium lead halide perovskites. *Small, 13*, 1701711.
117. Fassl, P., Ternes, S., Lami, V., Zakharko, Y., Heimfarth, D., Hopkinson, P. E., Paulus, F., Taylor, A. D., Zaumseil, J., & Vaynzof, Y. (2018). Effect of crystal grain orientation on the rate of ionic transport in perovskite polycrystalline thin films. *ACS Applied Materials & Interfaces, 11*, 2490.
118. Birkhold, S. T., Precht, J. T., Giridharagopal, R., Eperon, G. E., Schmidt-Mende, L., & Ginger, D. S. (2018). Direct observation and quantitative analysis of mobile frenkel defects in metal halide perovskites using scanning Kelvin probe microscopy. *Journal of Physical Chemistry C, 122*, 12633.
119. Murali, B., Kolli, H. K., Yin, J., Ketavath, R., Bakr, O. M., & Mohammed, O. F. (2020). Single crystals: The next big wave of perovskite optoelectronics. *ACS Materials Letter, 2*, 184–214.
120. Hong, K., Le, Q. V., Kim, S. Y., & Jang, H. W. (2018). Low-dimensional halide perovskites: Review and issues. *Journal of Materials Chemistry C, 6*, 2189–2209.
121. Zhang, Y., Liu, Y., Xu, Z., Yang, Z., & Liu, S. (2020). 2D perovskite single crystals with suppressed ion migration for high-performance planar-type photodetectors. *Small, 16*, 2003145.
122. Luo, D., Su, R., Zhang, W., Gong, Q., & Zhu, R. (2019). Minimizing non-radiative recombination losses in perovskite solar cells. *Nature Reviews Materials, 5*, 44–60.
123. Motti, S. G., Meggiolaro, D., Martani, S., Sorrentino, R., Barker, A. J., De Angelis, F., & Petrozza, A. (2019). Defect activity in lead halide perovskites. *Advanced Materials, 31*, 1901183.
124. Liu, Y., Ievlev, A. V., Borodinov, N., Lorenz, M., Xiao, K., Ahmadi, M., Hu, B., Kalinin, S. V., & Ovchinnikova, O. S. (2020). Direct observation of photoinduced ion migration in lead halide perovskites. *Advanced Functional Materials, 31*, 2008777.
125. Kerner, R. A., & Rand, B. P. (2018). Ionic-electronic ambipolar transport in metal halide perovskites: Can electronic conductivity limit ionic diffusion? *Journal of Physical Chemistry Letters, 9*, 132–137.
126. Zhu, X., Lee, J., & Lu, W. D. (2017). Iodine vacancy redistribution in organic-inorganic halide perovskite films and resistive switching effects. *Advanced Materials, 29*, 1700527.
127. Ma, F., Zhu, Y., Xu, Z., Liu, Y., Zheng, X., Ju, S., Li, Q., Ni, Z., Hu, H., Chai, Y., Wu, C., Kim, T. W., & Li, F. (2020). Optoelectronic perovskite synapses for neuromorphic computing. *Advanced Functional Materials, 30*, 1908901.
128. Wang, G., Li, D., Cheng, H.-C., Li, Y., Chen, C.-Y., Yin, A., Zhao, Z., Lin, Z., Wu, H., He, Q., Ding, M., Liu, Y., Huang, Y., & Duan, X. (2015). Wafer-scale growth of large arrays

of perovskite microplate crystals for functional electronics and optoelectronics. *Science Advances, 1*, e1500613.
129. Li, D., Wang, G., Cheng, H.-C., Chen, C.-Y., Wu, H., Liu, Y., Huang, Y., & Duan, X. (2016). Size-dependent phase transition in methylammonium lead iodide perovskite microplate crystals. *Nature Communications, 7*, 11330.
130. Li, D., Cheng, H. C., Wang, Y., Zhao, Z., Wang, G., Wu, H., He, Q., Huang, Y., & Duan, X. (2017). The effect of thermal annealing on charge transport in organolead halide perovskite microplate field-effect transistors. *Advanced Materials, 29*, 1601959.
131. Zou, Y., Li, F., Zhao, C., Xing, J., Yu, Z., Yu, W., & Guo, C. (2019). Anomalous ambipolar phototransistors based on all-inorganic CsPbBr3 perovskite at room temperature. *Advanced Optical Materials, 7*, 1900676.
132. Hu, X., Zhou, H., Jiang, Z., Wang, X., Yuan, S., Lan, J., Fu, Y., Zhang, X., Zheng, W., Wang, X., Zhu, X., Liao, L., Xu, G., Jin, S., & Pan, A. (2017). Direct vapor growth of perovskite $CsPbBr_3$ nanoplate electroluminescence devices. *ACS Nano, 11*, 9869–9876.
133. Huo, C., Liu, X., Song, X., Wang, Z., & Zeng, H. (2017). Field-effect transistors based on van-der-Waals-grown and dry-transferred all-inorganic perovskite ultrathin platelets. *Journal of Physical Chemistry Letters, 8*, 4785–4792.
134. Zhou, J., Xie, L., Song, X., Wang, Z., Huo, C., Xiong, Y., Cheng, Z., Wang, Y., Zhang, S., Chen, X., & Zeng, H. (2020). High-performance vertical field-effect transistors based on all-inorganic perovskite microplatelets. *Journal of Materials Chemistry C, 8*, 12632–12637.
135. Kagan, C. R., Mitzi, D. B., & Dimitrakopoulos, C. D. (1999). Organic-inorganic hybrid materials as semiconducting channels in thin-film field-effect transistors. *Science, 286*, 945.
136. Matsushima, T., Leyden, M. R., Fujihara, T., Qin, C., Sandanayaka, A. S. D., & Adachi, C. (2019). Large metal halide perovskite crystals for field-effect transistor applications. *Applied Physics Letters, 115*, 120601.
137. Liu, F., Wang, L., Wang, J., Wang, F., Chen, Y., Zhang, S., Sun, H., Liu, J., Wang, G., Hu, Y., & Jiang, C. (2021). 2D ruddlesden–popper perovskite single crystal field-effect transistors. *Advanced Functional Materials, 31*, 2005662.
138. Milot, R. L., Sutton, R. J., Eperon, G. E., Haghighirad, A. A., Hardigree, J. M., Miranda, L., Snaith, H. J., Johnston, M. B., & Herz, L. M. (2016). Charge-carrier dynamics in 2D hybrid metal–halide perovskites. *Nano Letters, 16*, 7001–7007.
139. Nakamura, T., Yakumaru, S., Truong, M. A., Kim, K., Liu, J., Hu, S., Otsuka, K., Hashimoto, R., Murdey, R., Sasamori, T., et al. (2020). Sn(IV)-free tin perovskite films realized by in situ Sn(0) nanoparticle treatment of the precursor solution. *Nature Communications, 11*, 3008.
140. Lin, R., Xiao, K., Qin, Z., Han, Q., Zhang, C., Wei, M., Saidaminov, M. I., Gao, Y., Xu, J., Xiao, M., et al. (2019). Monolithic all-perovskite tandem solar cells with 24.8% efficiency exploiting comproportionation to suppress Sn (II) oxidation in precursor ink. *Nature Energy, 4*, 864–873.

"Metal Halide Perovskite Solar Modules: The Challenge of Upscaling and Commercializing This Technology"

Angelique M. Montgomery, Nutifafa Y. Doumon, Christa Torrence, Laura T. Schelhas, and Joshua S. Stein

1 Introduction

Metal halide perovskites (MHPs) are favored electronic and optoelectronic semiconductor devices due to their high conversion efficiency and low cost. In 2009, MHPs were used in the development of perovskite solar cells (PSCs) with a power conversion efficiency (PCE) of 3.8% [1]. PCE has risen rapidly to 25.7% [2] in 2022 for single-junction solar cell architectures with area < 0.1 cm^2. With the current focus on low-cost, clean, and renewable energy sources, there is great interest in upscaling this technology to large-area photovoltaic (PV) modules. The Department of Energy (DOE) has defined aggressive goals to reduce the levelized cost of electricity for utility-scale PV to \$0.02/kWh by 2030 [3–5]. Two scenarios are defined to reach this goal: (1) high performance and (2) low cost. The low-cost scenario assumes module efficiency of 20% and a cost of \$0.17/W [4]. To achieve this goal, a module technology must be manufactured at a fraction of the cost of conventional crystalline silicon-based (c-Si) modules. Locally produced, solution, or

A. M. Montgomery (✉) · C. Torrence · J. S. Stein
Sandia National Laboratories, Albuquerque, NM, USA
e-mail: ammontg@sandia.gov; ctorrence@lanl.gov; jsstein@sandia.gov

N. Y. Doumon
National Renewable Energy Laboratory, Golden, CO, USA

Department of Materials Science and Engineering, The Pennsylvania State University, University Park, State College, PA, USA

Alliance for Education, Science, Engineering, and Design with Africa, The Pennsylvania State University, University Park, State College, PA, USA
e-mail: nzd5349@psu.edu

L. T. Schelhas
National Renewable Energy Laboratory, Golden, CO, USA
e-mail: laura.schelhas@nrel.gov

W. Nie, K. (Kris) Iniewski (eds.), *Metal-Halide Perovskite Semiconductors*,
https://doi.org/10.1007/978-3-031-26892-2_14

vapor-processed perovskite PV modules offer a promising pathway to meet this goal. However, challenges exist in upscaling from the cell level (<10 cm^2) to the minimodule (>100–1000 cm^2) or full module level (>1000 cm^2); yet, current PV technologies have overcome similar challenges. While upscaling represents a significant engineering and research effort, it is a common stage in the path to commercializing new PV technologies. In this chapter we outline four critical research areas to be addressed in this path to commercialization: manufacturing, performance characterization, reliability testing, and environmental health and safety. Here, we provide a short introduction to each topic to set the stage for the development landscape.

Manufacturing There are many challenges to upscaling to full-sized MHP modules and developing a commercial manufacturing process. Applying uniform thin films to large areas requires fundamentally different methods than those used for small single cells. Spin coating, which is used for most small area PSC research and development, is not scalable for large areas and mass production. Instead, slot-die coating, blade coating, spray coating, or vapor-based application methods are preferred [6–17]. However, changing the film application method requires changes to the precursor ink rheology and careful attention to the processing steps and the manufacturing environment to ensure a high-quality, uniform film deposition. In addition, module fabrication involves additional processing steps compared to cells. Scribing is used between film deposition steps to divide the film into separate interconnected cells (Fig. 1a). Along with careful deposition, scribe quality and scribing precision are important aspects to module fabrication to minimize electrical losses. Another approach to using perovskites for PV modules is in a tandem structure where the PSC is placed above or below a second solar cell. The additional cell could be a variety of materials, for example, c-Si, CdTe, CIGS, organic, or even other PSCs. Monolithically integrated two-terminal (2 T) and mechanically stacked four-terminal (4 T) tandem solar cells provide a solution to the critical thermalization loss and high transmission phenomenon seen in single-junction architectures. Still, each approach faces different engineering challenges.

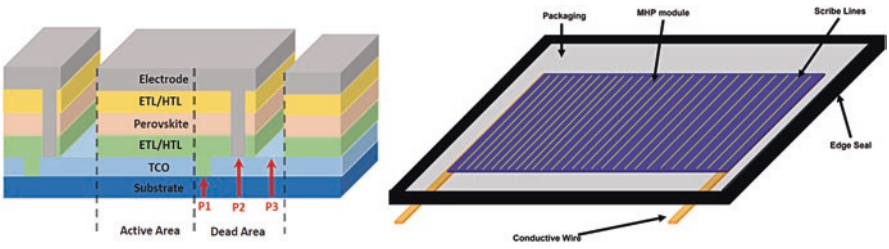

Fig. 1 (**a**) Schematic for MHP thin film including all deposited layers. ETL/HTL is alternated to either an inverted n-*i*-p or planar p-*i*-n structure. This schematic includes the separation of interconnected sub-cells using scribing of P1, P2, and P3. (**b**) Schematic of packaged MHP module with a glass-glass configuration

Performance Characterization Another challenge for commercializing perovskite modules is the difficulty in characterizing module performance due to their relatively slow response and metastability. Conventional c-Si and other thin-film PV modules (e.g., CdTe and CIGS) can be characterized on the production line using a flash test, where the module is exposed to a rapid flash of light (~100 ms or less) during which an *I-V* curve is measured. Like other current PV technologies such as CdTe and CIGS, many PSCs are metastable when initially exposed to light. Meaning their electrical output changes rapidly until it eventually stabilizes, a process that can take several seconds to hours. Preconditioning (or stabilization) is a general technique used to bring a module into a stable state so that a characterization is repeatable. Preconditioning usually involves illuminating the module until performance is stable. However, preconditioning takes time which is non-conducive for a high-speed production line that cannot wait for each module to stabilize during production. Therefore, to satisfy the unmet challenge for rapid production rates and comparable devices in MHP modules, fast measurement techniques need to be developed and validated to support high-speed manufacturing.

Reliability Commercial PV modules are expected to operate outdoors in varied, harsh environments for decades. A commercial thin-film module must be protected from environmental stresses such as mechanical loading, moisture, UV radiation, etc. Typically, thin-film modules are laminated between two sheets of glass to protect the active layers from the environment as shown in Fig. 1b. Perovskites are especially sensitive to moisture exposure; adding an additional packaging requirement to reduce water ingress as much as possible is preferred. Figure 1b shows a conceptual packaging design for prototype minimodules that includes double glass with an edge seal. It is important that the encapsulant material does not degrade and release reaction products that may harm the inner layers. For example, EVA, a common encapsulant material, has a degradation pathway that results in the release of acetic acid, which may degrade the MHP and corrode metal contacts [18–20]. Accelerated testing inside climate chambers can be used to provide confidence that a module can survive harsh conditions in the field. However, the applicability of current accelerated testing standards for MHP modules remains an active area of research.

Environmental Health and Safety Another challenge to commercialization is the fact that MHPs are made using lead (Pb) in the absorber. Most c-Si PV modules also contain lead, which is present in the solder used to connect cells together. However, there is concern that the lead in MHP is much more soluble and could be released into the environment more readily if the module were to break and be exposed to water. Early research investigated these risks using leaching tests where the module is sampled and crushed and placed in solutions of leachate. Alternative perovskite formulations with tin (Sn)-, cesium (Cs)-, and chromium (Cr)-based halide perovskites appear to be less harmful; however, the performance and stability of these alternatives are still under investigation. Alternatively, other materials can be

added to the device stack or included in the encapsulation that bind to lead and decrease transfer to the solute.

This chapter will explore these challenges among others that should be addressed before the commercialization of large-scale MHP modules can be realized.

2 Manufacturing of Perovskite PV Modules

There are two primary methods used to deposit the active perovskite layer and charge transporting layers (CTLs) for large-area modules: (i) solution- or chemical-based deposition (one-step or two-step) [6, 7, 21–33] and (ii) vapor-based deposition [23, 34–37]. Scalable solution methods include blade, slot-die, gravure, and spray coating. Vapor-based methods have been widely adopted in the PV industry for manufacturing CdTe PV modules [38, 39] but can require more challenging setups (e.g., vacuum processing) compared to solution processing methods.

To achieve high-performance modules, high-quality homogeneous films are required. High-quality films are often characterized by uniform coverage and pinhole-free films [33, 40]. However, achieving high-quality films for a seamless production requires a controlled manufacturing environment and atmosphere that includes posttreatments such as substrate heating [41], air-knife assistance [42], co-solvent incorporation [43, 44], antisolvent engineering [45], Lewis acid-base adduct method [46], additive engineering [47–49], and efficient precursor solution chemistries that enable low-defect solvent removal [50]. There are a number of detailed review papers on these topics and therefore will not be covered extensively here [9, 42, 46, 49, 51–72]. Precursor rheology must also be optimized for each application method and deposition technique. Multi-solvent blends are typically developed for large-area depositions to optimize film formation. Common solvents include dimethyl sulfoxide (DMSO), dimethylformamide (DMF), N-methyl-2-pyrrolidone (NMP), γ-butyrolactone GBL (used as cosolvent), THF, 2ME, and others. However, DMF introduces significant health risks, and GBL is subject to legal restrictions in many countries which limits their commercial viability [73]. The need for an environmentally safe nonvolatile solvent to synthesize the active and transport layers is an essential step toward commercial viability [73–77].

Green solvents exist such as ethyl acetate (EA) which is typically used as an antisolvent for perovskite precursor to optimize the perovskite/transporting material interface [78]. However, EA evaporation is slow and could impact the active layer crystallization process [78, 79]. Therefore, developing new green solvent chemistries with more volatile systems are needed for low-energy, low-cost scalable fabrication methods with limited waste and efficient precursor chemistries for large-area manufacturing [61, 74, 75, 77–82].

To make modules, it is necessary to add scribing steps between the deposition of the various layers of the perovskite device (Fig. 1a). The division of the film into separate smaller series-connected sub-cells increases the voltage; however, the

current in the module is limited by the lowest current produced by any of the sub-cells. Therefore, reducing resistive losses and increasing efficiency are dependent on developing homogeneous deposition processes for all functional layers.

Scribing techniques used within the literature rely on three scribing steps P1, P2, and P3. The scribing is repeated depending on the number of sub-cells on a single large-area substrate. P1 patterning defines the width of a sub-cell and isolates the substrate from the front transparent conductive oxide (TCO) layer. After the deposition of the electron/hole transporting layers as well as the absorber layer, P2 scribing is performed. An interconnection of the neighboring sub-cells is produced by selectively removing the top layers of the oxide to expose the TCO layer with mechanical or laser scribing. The precision of the P2 scribe is very important because it is used to establish a series contact between the back and front conductive layers of neighboring cells in the module to ensure optimum charge conductivity [83–85]. If P2 is not precise, the current transport that is formed from the electrical interconnection of sub-cells is limited [32, 84, 86]. The final P3 scribe is performed after the application of the bottom electrode which completes the monolithic series interconnection by producing electrical isolation for the top electrode and the adjacent sub-cells. The bottom electrode is laser scribed to electrically disconnect the back contact from sub-cells to form P3. The region between P1 and P3 is considered the "dead area" because it does not contribute to PV conversion under operational conditions [86, 87]. Scribing methods must be precise, and the purpose of scribing is to achieve good electrical series interconnection with low active area loss. Efficient scribe passivation and a good electrical series interconnection with very low area loss is key for high-performing modules. As more research pivots to the module scale, scribing and passivation will likely become a critical focus of the research community.

Inactive area losses are defined by the geometrical fill factor (GFF): the ratio between active area and total area [88]. By enlarging the module area, the GFF can be enhanced because the ratio of dead area associated with edges for encapsulation and frames is reduced [88, 89]. However, as active area width is lost, the photogenerated carriers are reduced and the efficiency suffers. Therefore, there exists a trade-off between wider cells (lower inactive area with higher resistive losses) and narrower cells (higher inactive area and lower resistive losses) [90, 91]. It is for these reasons that there is still a significant gap between cell and module efficiencies. Panasonic Corporation achieved a PCE of 16.09% for a perovskite module with an aperture area of 802 cm^2 which is 30 cm long, 30 cm wide, and 2 mm thick [92].

The need for a reliable low-cost manufacturing process depends on a reproducible method with high-throughput homogeneous deposition. Roll-to-roll and sheet-to-sheet processing are attractive options for MHP manufacturing. Roll-to-roll is a low-cost operation that allows for flexible substrates, continuous production, and high speeds [93–95]. Sheet-to-sheet processing is less susceptible to damage than roll-to-roll; however, switching to multiple substrates is easier in this method because there is only one roll holder [94, 96]. In either system, reproducibility is

critical with large-area substrates to ensure the manufacturing process yields similar performance properties every time.

Careful characterization and rapid production rates for large-area MHP modules are contingent upon the quality and efficiency in module performance characterization and in-process characterization methods that reflect the unique behavior of MHP. Multiple steps within perovskite module production will rely on fast and efficient in-line characterization methods to validate module performance and identify key parameters that impact production quality for a highly controlled manufacturing process.

3 Performance Characterization

To produce high-quality MHP modules, process control and in-line detection methods that quickly monitor the film quality and performance of modules are needed. Performance loss under illumination is identified depending on its effects in the current–voltage (*I–V*) characteristics of the device [97–99]. Electronic shunts, ohmic loss (voltage drop), recombination loss, and reduced current generation all impact device performance [97]; however, most are manufacturing defects that can be improved with careful large-scale fabrication. MHP undergoes voltage changes when exposed to light and voltage bias with rates affected by temperature. Therefore, fast measurements to monitor the film quality and its electrical characteristics during multiple stages of production are critical to ensure long-term performance for project owners and investors.

Small electronic shunts originate from high resistance between the cell's two contacts that cause local heating (hot spots) and faults that influence hysteresis behavior and reduce the maximum power [100]. Uneven coverage of the absorber and contacts, inhomogeneities between the deposited layers, and rough surfaces can cause shunts that impede the current generation and performance parameters like V_{oc} and FF. As a result, power is reduced, and an undesirable *I–V* hysteresis may result which is mainly related to ion migration in the bulk and at the interface of the device [101–103]. *I–V* curves and electroluminescence (EL) imaging are typically used to monitor shunt behavior at various stages of production.

The PV community reports device performance at a fixed condition, known as standard testing conditions (STC). This is defined as a module temperature of 25 °C, solar irradiance of 1000 W/m^2, and a reference spectrum defined at air mass of AM1.5 [104]. STC creates uniformity in testing conditions for accurate comparisons of module performance from different manufacturers. In an *I–V* measurement, a voltage is swept across a device, and the current is recorded at each stabilized voltage step which typically takes seconds [104]. Ideally, the measured current will be dependent on the measuring conditions (voltage, temperature, irradiance, environmental conditions) and not the prior history of the device [104]. However, perovskites response times (seconds to minutes) require longer sweep times and scan rates to allow for sufficient current stabilization at each voltage step [93]. The

IEC 60904-1 measurement standard describes procedures for *I–V* characteristics of PV devices to ensure basic requirements for *I–V* measurements, define procedures for different measuring techniques, and include practices to minimize measurement uncertainty [105]. However, the IEC 60904-1 standard does not describe the special treatments needed to stabilize the current before performance characterization. Characterization methods typically use simple equipment; however, due to MHP metastability and slow responding device behavior, precise measurements require specialized equipment and expertise.

The primary measurement used to rate modules during production is the maximum output power (P_{max}) ratings at STC. This is an essential parameter for accurate output power rating nameplates and specification data sheets that distinguish between cost-dependent high-performing and low-performing perovskite modules. The higher the power rating, the more watts the module produces and the more expensive the module. Power ratings are critical because they aim to match real-life conditions for a fair understanding about how modules perform outdoors. However, accurate P_{max} is a challenge because it is difficult for a simulator to exhibit real environmental conditions by only varying the temperature and irradiance without the consideration of environmental stressors. Maximum power point (MPP) tracking is a continuous steady-state measurement to find the maximum power by using a perturb-and-observe algorithm to keep the device at its maximum power for some time, and then an average power is reported to represent P_{max}.

Flash tests are a quick method that can be automated on a production line and performed approximately at a rate of once per second by exposing the module to a fast (20–100+ ms) flash of light during which an *I–V* curve is produced and P_{max} is measured. Flash tests are a conventional method used to yield power ratings for current commercial PV technologies. Spectral uniformity match, spatial uniformity, and temporal stability are used to assess the reliability and quality of the measurement. It is performed several times during production, especially after lamination to test the functionality and performance of the completed module. Though flash testing has shown its effectiveness for current commercial PV technologies, it remains a challenge for MHP modules. Song et al. showed that fast *I–V* curves may overestimate I_{sc} and underestimate FF for PSCs compared to a slow asymptotic continuous scan [94, 106–108]. Increasing the scan speed is possible for a flash test; however, it could overestimate performance parameters like V_{oc}. Decreasing the scan speed could easily give time for carrier generation and extraction to come to completion; however, slow scans require different light source and increase the overall testing time. It is difficult to assume that all identical modules will respond identically to a flash test, though this test could give a close enough approximation to a consistent performance measurement to distinguish between best- and worst-performing modules. This is an area of current research.

Dynamic *I–V* or asymptotic *I–V* measurements are like conventional *I–V* in which a stepwise *I–V* is produced; however, at each voltage step, a stabilization period allows the device under test (DUT) sufficient time to complete current collection. Essentially it is a series of stabilized current at fixed voltage (SCFV) measurements over a specific voltage range.

Some MHP cells and modules exhibit different *I–V* behavior depending on the direction of the *I–V* curve (I_{sc} to V_{oc} vs. V_{oc} to I_{sc}) [52]. This *I–V* hysteresis behavior is dependent on parameters such as scan rate, scan direction, bias applied, preconditioning, and device architecture [101, 109–111]. Different electrical characteristics of an *I–V* curve limit reproducibility and lower carrier mobility and collection rates while presenting challenges for a fast-responding stable measurement. The origin of an *I–V* hysteresis is mainly ion migration; however, ferroelectric polarization, ion trapping, and capacitive effects are also potential causes [102, 106, 107, 112–116]. Ion migration in MHP gained much attention when Snaith et al. suggested that it was one of three possible origins for the *I–V* hysteresis phenomenon and showed how device architecture and process control influence the severity of the *I–V* hysteresis behavior [117–119]. They showed that a stabilized power output is possible under operational conditions; however, the *I–V* hysteresis is likely to affect MPP tracking effectiveness. More work in this area should focus on ion migration kinetics and how light illumination and dark storage impact the movement of ionic and electronic species and device stability.

The effect of operating temperature on module performance is an important parameter for yield assessment. Not many studies have been performed to measure these effects on PSCs or MHP modules. Moot et al. studied PSC performance with temperature and found the relationship to be nonlinear [120]. They showed that efficiency vs. temperature for MHPs was influenced by a change in V_{oc} and I_{sc} which is distinct from c-Si which is predominantly affected by V_{oc} [120, 121]. Accurate temperature coefficient calculations are necessary for the commercialization of this technology. More work is needed in this area.

4 Reliability

This section discusses degradation, stability, lifetime, durability, and reliability of MHP modules. Though these terms may seem similar, they have only one thing in common: they are all affected by the degradation mechanisms at the individual cell level and/or the failure modes at the module level. Degradation is the observed deterioration of PV performance parameters due to different stressors resulting from chemical or mechanical effects. Stability is the investigation of the degradation and the mechanisms behind this phenomenon to determine how fast or slow the process occurs over time [122]. The lifetime of a cell or module is how long (in minutes, hours, or years) the cell or module produces power at a reasonable level in a safe manner [123]. The lifetime is usually defined as the time it takes the cell or module to lose 20% or retain 80% of its initial power, often referred to as T_{80} [122, 124–127]. While durability focuses on maintaining output power level of cell or module, reliability focuses on the module's failure [123]. Using our definitions, a MHP technology would be said to be reliable if it performs a specific function for the expected lifetime. On the other hand, it would be durable if it can withstand pressure, wear, or damage while performing its function.

Degradation sources in PV can be generally classified into intrinsic or extrinsic, interfacial, or a bulk device effect. Module failure modes include other external factors, in addition to the individual cell's degradation sources, such as environmental stressors (e.g., wind, UV) and damage to the PV module themselves. The intrinsic degradation of the bulk active layer of the MHP cell can be caused by several stressors resulting in photooxidative degradation [125, 126, 128, 129], thermal degradation [126, 130], general degradation due to morphological changes or heterogeneity of the active film [130–132], and/or interface degradation [126, 132, 133]. The most influential factors in the intrinsic MHP degradation pathways could be (i) diffusion of oxygen (O_2) and/or moisture causing oxidative degradation of the active layer, delamination, interlayer reactions, and/or oxidation of electrodes [128, 129, 134–136]; (ii) temperature effects or heating leading to thermal degradation, pronounced degradation due to thin-film heterogeneity, and/or metal ion diffusion [128, 130, 134, 135, 137, 138]; and (iii) UV-light responsible for light-assisted doping by O_2 and/or photo-induced degradation [129, 132, 134–136]. All three degradation pathways can occur simultaneously in cells and modules. However, in modules there could be additional failure modes due to interconnections and packaging. The performance stability and lifetime measurements of laboratory-scale next-generation PVs including MHP PVs (with specific challenges known to MHP module fabrication) have so far only been limited to a couple of hundreds to thousands of hours [100, 125–127, 139]. However, for the levelized cost of energy metrics to approach SETO's 2030 goal of $0.02/kWh, MHP modules are expected to last at least 20 years in the field [3]. It is worth nothing that groups are exploring avenues for shorter lifetime modules, leveraging recycling, repair, and repowering approaches.

Any number of stressors, defects, or environmental conditions can lead to module failure modes and therefore lead to low module reliability and durability. This is equally true for traditional PV technologies like c-Si or CdTe. Here, we classify these degradation modes generally into two groups based on whether they are visually observable or not. Table 1 shows the detailed classification and some of the tests (discussed later) needed to certify or qualify the modules for field operation. Getting a deeper understanding of the various degradation, defects, and failure modes at the fundamental level, both quantitatively and qualitatively, is essential for advancing the technology. It will be crucial for developing qualification and safety test protocols unique to MHP modules. This is a task currently undertaken by one of SETO's funded joint projects under the Perovskite PV Accelerator for Commercializing Technology (PACT). PACT's protocols are under development and updated regularly [140].

4.1 Qualification and Safety Testing

Since much of the current MHP research has been at the lab and cell level, many researchers use the protocols set under the international summit on organic photovoltaic stability (ISOS) [4, 66]. The ISOS protocols are not meant as a replacement

Table 1 Identified degradation mechanisms and failure modes in MHP PV cells and modules

Visual defects	PV cells within the module	PV module	Environmental factors
Yes	·Cracks/fracture ·Edge seal defects ·Corrosion of cell metallization	·Damages to frame and junction box ·Corrosion and breakage of glass ·Discoloration and delamination (or degradation of back sheet) ·Sealant issues/defects ·Discoloration and delamination of encapsulant (degradation of encapsulant) ·Cracks/fracture ·Electrical arcing	·Shading ·Soiling ·Structural failures due to natural events (rain, sun, wind, snow, hail, fire, dust, etc.)
No	·Light-induced degradation ·Light and elevated temperature-induced degradation ·Potential-induced degradation ·Edge deletion ·Thermal degradation ·Cracking and mechanical delamination of MHP layers (Fig. 1a) ·Shunts due to laser scribing and impurities in the MHP thin film	·Contact failure due to electrochemical corrosion between MHP films and metal electrodes ·Internal circuitry discoloration ·Breaks in electrical circuitry ·Substring in open circuit ·Nonfunctioning bypass diodes ·Thermal degradation ·Cracking and mechanical delamination of MHP cell layers (Fig. 1a) ·Failure of electrical solder bond ·Reversed bias hot spots	·Reverse-biased degradation due to shading on cells connected in series ·Degradation due to natural events (rain, sun, wind, snow, hail, fire, dust, etc.) such as moisture permeation or thermal fatigue

for qualification testing; rather they are to be used as research tools. Researchers and manufacturers follow certain standard protocols to assess how well a module would perform under stressors. We refer to these as accelerated stress tests (ASTs).

At the industry level, a set of ASTs are used to similarly assess any type of PV module. They are qualification testing or type approval testing (in other parts of the world) and safety testing. Passing both qualification and safety testing is a major step in commercializing a PV module. Qualification testing, a set of defined ASTs, is usually derived from a reliability testing program. They are set by the International Electrochemical Commission (IEC) to determine the module quality. In other words, it consists of various module quality tests (MQT) that include application of one or more stressors for a prescribed length of time. Tests are pass/fail with different criteria defined for each MQT. They help detect early known degradation or failure modes of PV modules in particular environments with limitation in duration of test, acceptable costs, and level of quality of individual modules that pass the test.

The qualification testing is a blank pass or fail process, and therefore these tests do not determine a module's entire lifespan.

In today's PV module technologies, there are three such qualification tests depending on the type of PV modules to be tested, either c-Si PV, thin-film PV modules such as a-Si or CdTe, or concentrator PV modules. They are known, respectively, as the IEC 61215, IEC 61646, and IEC 62108 protocols [141]. These standards are revised and improved over time, with the intent of ensuring a rigorous AST standard consistent with reproducible environmental stressors such as temperature, light, and humidity. For instance, the first qualification testing for terrestrial PV modules, the IEC 61215 protocol, was established in 1993. Its third edition, revealed in 2016, has merged IEC 61215 and IEC 61646 protocols, bringing significant changes to the technical content with the inclusion of light exposure, specific to each technology.

Today's qualification tests are a result of the 1975 US government's efforts to improve PV module performance, leading to the jet propulsion laboratory (JPL) block buy program. Modules were designed and produced under contracts by different manufacturers, tested in phases—the block buys—and labeled as Block I to V [142]. The blocks were run through a series of ASTs intended to reproduce field-observed failures. These tests were adapted over time as modules designed were optimized until the modules were discontinued or successfully passed the qualification testing. Details of the blocks by modules and qualification testing can be found in Ref. [142]. Consequently, the PV community does not have to fully reinvent the wheel for MHP module qualification testing. We can take clues and acquired knowledge from the JPL program, learning from it and constantly applying modified versions based on our evolving understanding and insights into MHP module degradation and failure modes.

The other standard test type is safety testing, offered under the IEC 61730 or Underwriters Laboratories (UL 61730). Both tests focus on safety and nonhazardous operation of the PV modules [143]. Currently, there are two protocol versions for the safety testing for the IEC 61730 standard, namely, IEC 61730-1 and the redline version, IEC 61730-2. The safety test demands that fundamental PV module construction requirements are met to provide safe fire, mechanical, and electrical functioning of the modules over their lifetime. It consists of various module safety tests (MST_i), in total around 56 ($0 < i < 57$, with i a natural number) under the IEC 61730-2 protocol requirements. They are important, as they seek to help prevent, during the operation of the modules, personal injuries due to environmental and mechanical hazards, fire hazards, and electrical shocks. The safety concerns and testing for MHP PV modules may have to go beyond the current parameters and consider other environmental and health hazards (i.e., possible leaking of Pb into the surrounding environment of the modules) as discussed in Sect. 15.5.

The current IEC standards for testing are tailored for commercially available PV technologies, with c-Si and a-Si being the baseline. Thus, these tests are unlikely to fully capture and consider all the prevalent failure/degradation modes of the next-generation thin-film PV modules such as MHPs. As indicated, MHP degradation/failure modes are governed by multiple factors that affect the device's long-term

stability, still not fully understood (still under discovery due to differences in materials), and thus may not be well appreciated by the IEC standards. For example, improvements to MHP materials and devices have increased thermal stability, but exposure to light at elevated temperature remains a critical stressor to determine durability. Currently, there is not a light and elevated temperature test as part of the IEC-61215 tests. In addition, existing IEC tests may need to be fine-tuned for the next-generation thin-film modules, especially MHP modules, as the current tests may also cause other failure modes otherwise not observed in the field [144].

Advancing the long-term performance stability of these new technologies is crucial to their commercialization and deployment. However, even at the lab scale, there are a lot of inconsistencies in reported procedures and parameters [126, 145, 146]. For these reasons, some members of the MHP PV community came together to lay down some ground rules based on the ISOS protocols [124, 126] in what came to be known, especially for MHP, as the "consensus statement for stability assessment and reporting for perovskite photovoltaics based on ISOS procedures" [126]. These ground rules guide laboratory-scale research testing, as they are more focused on the MHP devices at the cell level. In addition, SETO went a step further, publishing minimum requirements for durability/reliability performance targets, using modified IEC 61215 protocols combined with the ISOS-L-2 light soaking test [126] of the ISOS protocols, as a baseline for meaningful assessment of MHP module scale qualification testing until an international AST standard is reached. While the details of the ISOS-L-2 and other protocols for lab-scale next-generation PV cells can be found in Ref. [126], SETO's recommended MQT from IEC 61215 comprises of (i) MQT_{10}, UV preconditioning; (ii) MQT_{11}, thermal cycling; (iii) MQT_{13}, damp heat; and (iv) MQT_{21} PID [3]. This set of tests does not consider the humidity freeze test (MQT_{12}) and others, as SETO's focus is on the material and device stability rather than the packaging. It is our opinion that any AST standard considering packaged MHP modules for commercial viability should eventually include all other relevant MQT tests, but this is a good starting point for the technology. Another simple but crucial quality test not mentioned in the SETO recommendation is the electroluminescence (EL) test, capable of unearthing otherwise invisible microscopic defects such as cracks, moisture effects, and welding issues.

One risk with ASTs is the possibility that they will produce degradation not consistent with outdoor field performance. Ideally, ASTs do not reveal degradation that is not observed in real-world operation. Thus, one must always reconcile these differences by quantitatively and qualitatively comparing the outcome of the two tests. These comparisons may help fine-tune the ASTs over time and can be used to improve the IEC protocols. This approach can be used to develop tests that would be acceptable for MHP modules and packaging qualification and safety testing. A critical component to this test development will be field testing of MHP modules in the field in different climate zones (to cover the specificities of the different climate zones in the final international standard protocols). For example, such an effort combining AST and outdoor field performance of Si PV modules is already underway, led by the national renewable laboratory under the Durable Module Materials (DuraMAT) consortium [147]. They focus on accelerating the development and

deployment of durable and high-performance materials for PV module packaging to increase field lifetime and lower the cost of solar-generated electricity. This same approach could be applied to MHP modules to assess the viability of current test protocols and/or inform modifications to the test procedures.

In brief, for reliability and durability testing of PV modules, international standard tests are readily available for module qualification and safety testing. However, these tests may have to be amended, updated, or adjusted to properly validate the next-generation thin-film PV modules, such as MHP modules. It requires that novel approaches to AST protocols attuned to these technologies be explored to, if needed, adequately update the current standards and successfully qualify the next generation of PV modules. Some works are underway, namely, the ISOS consensus at lab scale and SETO's DuraMAT and PACT projects for developing materials and protocols for the module's reliability and durability.

5 Environmental and Health Risks

Most well-performing, highly efficient MHP modules/cells contain a soluble form of lead in the absorber layer which poses environmental and health risks. Tin (Sn), cesium (Cs), and chromium (Cr) show potential for a lead-free alternative; however, these semiconductor material combinations do not perform as well as lead-based semiconductors [148]. In addition, solvents used for precursor fabrication have toxicity risks, but these solvents are essential for the crystallization, nucleation, and growth dynamics of the MHP film. Worker safety regulations help to minimize exposure to workers through indigestion, inhalation, or skin contact. It is important to understand the health risks of MHP PV from its production to its final disposal and examine materials, processes, and unplanned events that can affect its safety.

When exposed to moisture, lead halide perovskites will degrade and ultimately form lead iodide (PbI_2). PbI_2 is highly soluble with a solubility constant (K_{sp}) in the range of $8.3 * 10^{-9}$ to $1.84 * 10^{-8}$ [149–151]. In high temperatures, such as fire, the PbI_2 oxidizes into PbO and PbO_2, both of which are insoluble in water [152, 153]. PbO powder can be absorbed by the skin and stored in soft tissues. After continual exposure, lead is absorbed into the bone and teeth where it has an elimination half-life of 20–30 years.

The US CDC sets upper limits on acceptable Pb blood level, which in the 1960s was set to 60 μg/dL and has been reduced over the years to the present value of 5 μg/dL in adults and 3.5 μg/dL for children [154, 155]. In adults, even a level of 5 μg/dL can lead to anemia and increased blood pressure, and exposure to pregnant women could endanger the fetus [156]. Symptoms of lead poisoning generally become noticeable when blood levels reach 40 μg/dL [157]. Lead is especially dangerous to children because they absorb lead about 4–5x more than adults due to their hand-to-mouth tendencies [158]. Blood levels of 5–10 μg/dL in children cause an interference with brain development, lowered IQ, decreased hearing, and stunted growth—with the impacts amplified as blood levels rise [156, 158, 159]. The Institute for Health Metrics

and Evaluation (IHME) estimates that as of 2019, 62.5% of the world's intellectual disability without an otherwise obvious source is caused by lead [160].

The US Department of Labor's Occupational Safety and Health Administration (OSHA) enforces safety regulations to provide safe and healthful working conditions for workers [161]. OSHA regulates a wide range of workplace hazards including chemical hazards and safe use of equipment [161]. An estimated 1.6 million workers in the USA are potentially exposed to lead, primarily at construction sites and manufacturing facilities. Employers must take compliance actions if airborne lead levels exceed the "action limit" of 30 $\mu m/m^3$, including medical monitoring, more stringent worksite controls, and the use of respirators, gloves, goggles, and other proper personal protection equipment (PPE) [162]. Additionally, if lead dust or lead-containing materials are present in a workspace, employers must provide proper PPE and require good hygiene practices, such as regular handwashing and showering before leaving the workspace. The National Ambient Air Quality Standards (NAAQS) regulates the ambient air concentration of lead, ozone, carbon monoxide, particulate matter, sulfur dioxide, and nitrogen dioxide. The maximum safe lead level in ambient air is defined as 0.15 $\mu g/m^3$ over a 3-month average [163]. Per the US Environmental Protection Agency (EPA), PV modules are categorized as a solid waste and are required to undergo waste characterization prior to disposal. The Comprehensive Environmental Response, Compensation, and Liability Act (CERCLA) of 1980 focuses on the response to a release, or the threatened release, of hazardous substances that may endanger public health or the environment [150, 164]. A site containing high levels of lead in the soil or groundwater meets criteria to be deemed a "superfund site" and qualifies for funding to clean up and rehabilitate the site. CERCLA assesses potential superfund sites for a variety of contaminants, and lead is the most common pollutant. There are currently over 600 recorded superfund sites, 43% of which have lead contamination [164].

Tin (Sn)- and cesium (Cs)-based halide perovskites appear to be less harmful; however, they should not be considered a safe and nontoxic alternative. Tin toxicity is highly dependent on its ionic form. Inorganic tin compounds are expelled from the body quickly but have been found to be harmful in large amounts. Organic tin compounds (organotins), which are commonly used in tin halide perovskites, can cause neurological problems, gastrointestinal symptoms, and respiratory irritation [165, 166]. Tin halide perovskites can degrade to form SnO_2 and SnI_4 [167, 168]. SnI_4 is highly reactive with water forming SnO_2 [167], which can cause respiratory irritation and harm to the aquatic life [169]. Cs-based halide perovskites are attractive due to their high luminescence quantum yield and excellent thermal stability [170]. However, Cs can cause burns and severe irritation to the skin upon contact due to its corrosivity [171]. Inhalation of Cs can result in irritation to the nose, throat, and lungs which may potentially lead to a buildup of fluid in the lungs [172]. In addition, Cs hydroxide also poses a risk to workers in transport and manufacturing due to its intense reactivity with water which could result in burns, inhalation, and ignition of other nearby flammable materials [171].

Events that can result in exposure include accidents, disposal, and module breakage from severe weather or transportation, among others. Accidents during manufacturing include accidental spills, inadequate ventilation, lack of safety protocols,

improper hygiene, and decontamination procedures. Noncompliance with protocols can lead to skin contact, inhalation, or even ingestion of harmful toxins. Storage and transportation of modules present risks. Warehouse storing modules pose fire risk due to the high density of material. Transporting modules present risks of accident, causing module breakage and potential release of hazardous materials that could possess skin contact risk for workers. First Solar, the CdTe thin-film manufacturer, shows that as of 2011 approximately one-third of warranty returns are due to module breakage occurring during the shipping and installation process, corresponding to the return of 0.4% of modules [173].

There are three main exposure pathways of concern: inhalation, ingestion, and skin contact. Inhalation risks stem primarily from fire smoke, but toxic substances in dust or other small particles can be aerosolized from burned or broken modules and cause resultant harm. For some toxic substances, inhalation is the highest-risk exposure pathway due to increased absorption by the body. Common safety practices include maintaining proper ventilation, wearing well-fitting masks with suitable filters, and restricting nonessential workers from accessing specific areas [174]. Ingestion can occur through several routes including contamination of drinking water, children's play areas, or soil used to grow food. Skin contact is an important exposure pathway for liquid solvents, which can cause skin irritation and burns. Some chemicals can also be absorbed into the body through the skin, putting one at risk for both dermal and internal harm. Proper PPE, particularly gloves, is crucial to prevent exposure through skin contact.

In the case of fires, high temperatures can damage modules and release Pb into the air or into the water used to extinguish the fire. Conings et al. (2019) fire exposure experiments quantified the percentage of lead released from a MHP module during a fire [175]. Analysis of nearby surfaces was assessed to determine the amount of lead carried by the smoke and deposited on surfaces in the vicinity of the fire. Glass encapsulation mostly absorbed the Pb from the MHP layer, and Pb found on nearby surfaces was released from the exposed sections of PV modules where the encapsulation was damaged or destroyed [175].

Leaching can occur when material from the module is exposed to a liquid such as rainwater, water from extinguishing fires, or soil pore water in the case that the modules are disposed of in a landfill. The contaminants dissolve into the water forming ions that leach out of the module through cracks or module edges into groundwater, soil, or be absorbed by nearby plants. The EPA specifies a Toxicity Characteristic Leaching Procedure (TCLP) test (Method 1311) under RCRA for waste characterization [176]. The procedure simulates leaching in a landfill to determine whether hazardous elements will leach from the waste. There are currently TCLP limits on eight heavy metals, some of which may be present in MHP modules. Any material with TCLP analytical results above the regulatory limit is deemed hazardous waste and must be disposed of in facilities permitted to accept such waste.

The pursuit of lead-free or "low-lead" semiconductors as a safer alternative would help mitigate the risk of lead release as they may offer a more environmentally safe route to commercialization. However, current challenges in this area include raising the efficiency and increasing stability of these alternative designs. In the near term, researchers have proposed and demonstrated the use of polymeric

materials in the module packaging that bind to free lead in solution preventing excess leaching and transport [177–180].

5.1 Future Work and Challenges

The commercialization of MHP solar modules is a promising technology for achieving the US government's decarbonization goals of 100% carbon-free electricity generation by 2035 [3]. MHP modules are on the cusp of commercialization with several research and manufacturing gaps as final barriers. Reproducible deposition of efficient thin-film MHP solar modules need to be demonstrated at large areas and rapid processing rates. Characterization methods are needed to monitor the quality and performance of products coming off of these high-speed production lines. Validated accelerated test protocols are needed to ensure that modules will survive in the field in a range of climates and conditions. Outdoor performance validation studies in a range of climates are needed to demonstrate that testing protocols are adequate to identify relevant failure and degradation modes. Finally, the safety protocols for workers need to be established, and the environmental risks associated with end of life and/or reuse/recycling need to be considered.

Acknowledgments This material is based upon work supported by the US Department of Energy's Office of Energy Efficiency and Renewable Energy (EERE) under the Solar Energy Technologies Office Award Number 38050.

Sandia National Laboratories is a multimission laboratory managed and operated by National Technology & Engineering Solutions of Sandia, LLC, a wholly owned subsidiary of Honeywell International Inc., for the US Department of Energy's National Nuclear Security Administration under contract DE-NA0003525.

This work was authored in part by the National Renewable Energy Laboratory, operated by Alliance for Sustainable Energy, LLC, for the US Department of Energy (DOE) under Contract No. DE-AC36-08GO28308.

The views expressed in the article do not necessarily represent the views of the DOE or the US government. The US government retains, and the publisher, by accepting the article for publication, acknowledges that the US government retains a nonexclusive, paid-up, irrevocable, worldwide license to publish or reproduce the published form of this work, or allow others to do so, for US government purposes.

References

1. Kojima, A., Teshima, K., Shirai, Y., & Miyasaka, T. (2009). *Organometal halide perovskites as visible-light sensitizers for photovoltaic cells* (Vol. 131, pp. 6050–6051). American Chemical Society.
2. Bellini, E. (2021). *UNIST, EPFL claim 25.6% efficiency world record for perovskite solar cell*.
3. Siegler, T. D. et al. (2022). The path to perovskite commercialization: A perspective from the United States solar energy technologies office. *ACS Energy Letters*, 1728–1734. https://doi.org/10.1021/acsenergylett.2c00698.

4. Smith, B. L., Woodhouse, M., Horowitz, K. A. W., Silverman, T. J., Zuboy, J., & Margolis, R. M. (2021). *Photovoltaic (PV) Module Technologies_ 2020 Benchmark costs and technology evolution framework results*. NREL.
5. Wilson, G. M., et al. (2020). The 2020 photovoltaic technologies roadmap. *Journal of Physics D: Applied Physics, 53*. https://doi.org/10.1088/1361-6463/ab9c6a
6. Pérez-Gutiérrez, E., et al. (2017). Organic solar cells all made by blade and slot–die coating techniques. *Solar Energy, 146*, 79–84. https://doi.org/10.1016/j.solener.2017.02.004
7. Yang, Z., Zhang, W., Wu, S., Zhu, H., Liu, Z., Lui, Z., Jiang, Z., Chen, R., & Zhou, J. (2021). Slot-die coating large-area formamidinium-cesium perovskite film for efficient and stable parallel solar module.
8. Rong, Y., et al. (2018). Toward industrial-scale production of perovskite solar cells: Screen printing, slot-die coating, and emerging techniques. *Journal of Physical Chemistry Letters, 9*, 2707–2713. https://doi.org/10.1021/acs.jpclett.8b00912
9. Liu, C., Cheng, Y. B., & Ge, Z. (2020). Understanding of perovskite crystal growth and film formation in scalable deposition processes. *Chemical Society Reviews, 49*, 1653–1687. https://doi.org/10.1039/c9cs00711c
10. Bishop, J. E., Smith, J. A., & Lidzey, D. G. (2020). Development of spray-coated perovskite solar cells. *ACS Applied Materials & Interfaces, 12*, 48237–48245. https://doi.org/10.1021/acsami.0c14540
11. Lee, D. S., et al. (2022). Fully scalable and stable $CsPbI_2Br$ solar cells realized by an all-spray-coating process. *ACS Applied Materials & Interfaces, 14*, 7926–7935. https://doi.org/10.1021/acsami.1c21644
12. Parida, B. et al. (2022). Recent developments in upscalable printing techniques for perovskite solar cells. *Advanced Science (Weinh)*, e2200308. https://doi.org/10.1002/advs.202200308.
13. Howard, I. A., et al. (2019). Coated and printed perovskites for photovoltaic applications. *Advanced Materials, 31*, e1806702. https://doi.org/10.1002/adma.201806702
14. Castro-Hermosa, S., et al. (2020). Efficient fully blade-coated perovskite solar cells in air with nanometer-thick bathocuproine buffer layer. *Nano Research, 14*, 1034–1042. https://doi.org/10.1007/s12274-020-3147-4
15. Liang, Q., et al. (2022). Manipulating crystallization kinetics in high-performance blade-coated perovskite solar cells via cosolvent-assisted phase transition. *Advanced Materials*, e2200276. https://doi.org/10.1002/adma.202200276.
16. Razza, S., et al. (2015). Perovskite solar cells and large area modules (100 cm^2) based on an air flow-assisted PbI2 blade coating deposition process. *Journal of Power Sources, 277*, 286–291. https://doi.org/10.1016/j.jpowsour.2014.12.008
17. Ouyang, Z., Yang, M., Whitaker, J. B., Li, D., & van Hest, M. F. A. M. (2020). Toward scalable perovskite solar modules using blade coating and rapid thermal processing. *ACS Applied Energy Materials, 3*, 3714–3720. https://doi.org/10.1021/acsaem.0c00180
18. de Oliveira, M. C. C., Diniz Cardoso, A. S. A., Viana, M. M., & Lins, V. D. F. C. (2018). The causes and effects of degradation of encapsulant ethylene vinyl acetate copolymer (EVA) in crystalline silicon photovoltaic modules: A review. *Renewable and Sustainable Energy Reviews, 81*, 2299–2317. https://doi.org/10.1016/j.rser.2017.06.039
19. Li, J., et al. (2021). Encapsulation of perovskite solar cells for enhanced stability: Structures, materials and characterization. *Journal of Power Sources, 485*. https://doi.org/10.1016/j.jpowsour.2020.229313
20. Wang, Y., et al. (2022). Encapsulation and stability testing of perovskite solar cells for real life applications. *ACS Materials Au, 2*, 215–236. https://doi.org/10.1021/acsmaterialsau.1c00045
21. Liu, Z., et al. (2020). A holistic approach to interface stabilization for efficient perovskite solar modules with over 2,000-hour operational stability. *Nature Energy, 5*, 596–604. https://doi.org/10.1038/s41560-020-0653-2
22. Tong, G., et al. (2021). Scalable fabrication of >90 cm^2 perovskite solar modules with >1000 h operational stability based on the intermediate phase strategy. *Advanced Energy Materials, 11*. https://doi.org/10.1002/aenm.202003712

23. Sha, Y., et al. (2020). A scalable integrated dopant-free heterostructure to stabilize perovskite solar cell modules. *Advanced Energy Materials, 11*. https://doi.org/10.1002/aenm.202003301
24. Jiang, Y., et al. (2018). Combination of hybrid CVD and cation exchange for upscaling Cs-substituted mixed cation perovskite solar cells with high efficiency and stability. *Advanced Functional Materials, 28*. https://doi.org/10.1002/adfm.201703835
25. Jiang, Y., et al. (2019). Negligible-Pb-waste and upscalable perovskite deposition technology for high-operational-stability perovskite solar modules. *Advanced Energy Materials, 9*. https://doi.org/10.1002/aenm.201803047
26. Bu, T., et al. (2019). Dynamic antisolvent engineering for spin coating of $10 \times 10\ cm^2$ perovskite solar module approaching 18%. *Solar RRL, 4*. https://doi.org/10.1002/solr.201900263
27. Dai, X., et al. (2019). Scalable fabrication of efficient perovskite solar modules on flexible glass substrates. *Advanced Energy Materials, 10*. https://doi.org/10.1002/aenm.201903108
28. Chiang, C.-H., Nazeeruddin, M. K., Grätzel, M., & Wu, C.-G. (2017). The synergistic effect of H_2O and DMF towards stable and 20% efficiency inverted perovskite solar cells. *Energy & Environmental Science, 10*, 808–817. https://doi.org/10.1039/c6ee03586h
29. Hu, C., et al. (2021). Discovery of a new intermediate enables one-step deposition of high-quality perovskite films via solvent engineering. *Solar RRL, 5*. https://doi.org/10.1002/solr.202000712
30. Im, J.-H., Kim, H.-S., & Park, N.-G. (2014). Morphology-photovoltaic property correlation in perovskite solar cells: One-step versus two-step deposition of $CH_3NH_3PbI_3$. *APL Materials, 2*. https://doi.org/10.1063/1.4891275
31. Liu, Z., et al. (2021). Scalable one-step heating up synthesis of Cu_2ZnSnS_4 nanocrystals hole conducting materials for carbon electrode based perovskite solar cells. *Solar Energy, 224*, 51–57. https://doi.org/10.1016/j.solener.2021.05.089
32. Christians, J. A., et al. (2018). Stability at scale: Challenges of module interconnects for perovskite photovoltaics. *ACS Energy Letters, 3*, 2502–2503. https://doi.org/10.1021/acsenergylett.8b01498
33. Yang, M., et al. (2017). Perovskite ink with wide processing window for scalable high-efficiency solar cells. *Nature Energy, 2*. https://doi.org/10.1038/nenergy.2017.38
34. Nair, S., Patel, S. B., & Gohel, J. V. (2020). Recent trends in efficiency-stability improvement in perovskite solar cells. *Materials Today Energy, 17*. https://doi.org/10.1016/j.mtener.2020.100449
35. Qiu, L., et al. (2019). Hybrid chemical vapor deposition enables scalable and stable Cs-FA mixed cation perovskite solar modules with a designated area of 91.8 cm^2 approaching 10% efficiency. *Journal of Materials Chemistry A, 7*, 6920–6929. https://doi.org/10.1039/c9ta00239a
36. Leyden, M. R., Jiang, Y., & Qi, Y. (2016). Chemical vapor deposition grown formamidinium perovskite solar modules with high steady state power and thermal stability. *Journal of Materials Chemistry A, 4*, 13125–13132. https://doi.org/10.1039/c6ta04267h
37. Li, J., et al. (2020). Highly efficient thermally co-evaporated perovskite solar cells and mini-modules. *Joule, 4*, 1035–1053. https://doi.org/10.1016/j.joule.2020.03.005
38. Compaan, A. D., Gupta, A., Lee, S., Wang, S., & Drayton, J. (2004). High efficiency, magnetron sputtered CdS/CdTe solar cells. *Solar Energy, 77*, 815–822. https://doi.org/10.1016/j.solener.2004.06.013
39. Ramanujam, J., et al. (2020). Flexible CIGS, CdTe and a-Si:H based thin film solar cells: A review. *Progress in Materials Science, 110*. https://doi.org/10.1016/j.pmatsci.2019.100619
40. Han, G. S., et al. (2019). Spin-coating process for 10 cm × 10 cm perovskite solar modules enabled by self-assembly of SnO_2 nanocolloids. *ACS Energy Letters, 4*, 1845–1851. https://doi.org/10.1021/acsenergylett.9b00953
41. Park, N.-G., & Zhu, K. (2020). Scalable fabrication and coating methods for perovskite solar cells and solar modules. *Nature Reviews Materials, 5*, 333–350. https://doi.org/10.1038/s41578-019-0176-2

42. Cheng, R., et al. (2019). An air knife-assisted recrystallization method for ambient-process planar perovskite solar cells and its dim-light harvesting. *Small, 15*, e1804465. https://doi.org/10.1002/smll.201804465
43. Zhang, X., Yang, W., Qi, J., & Hu, Y. (2020). Preparing ambient-processed perovskite solar cells with better electronic properties via preheating assisted one-step deposition method. *Nanoscale Research Letters, 15*, 178. https://doi.org/10.1186/s11671-020-03407-9
44. Li, P., Omer Mohamed, M. I., Xu, C., Wang, X., & Tang, X. (2020). Electrical property modified hole transport layer (PEDOT:PSS) enhance the efficiency of perovskite solar cells: Hybrid co-solvent post-treatment. *Organic Electronics, 78*. https://doi.org/10.1016/j.orgel.2019.105582
45. Li, C.-Y., et al. (2021). Anti-solvent mixture-mediated reduction of photocurrent hysteresis in high-impurity perovskite precursor based MAPbI3 solar cells. *Solar Energy, 214*, 86–92. https://doi.org/10.1016/j.solener.2020.11.062
46. Lee, D.-K., Lim, K.-S., Lee, J.-W., & Park, N.-G. (2021). Scalable perovskite coating via anti-solvent-free Lewis acid–base adduct engineering for efficient perovskite solar modules. *Journal of Materials Chemistry A, 9*, 3018–3028. https://doi.org/10.1039/d0ta10366g
47. Zhang, F., & Zhu, K. (2019). Additive engineering for efficient and stable perovskite solar cells. *Advanced Energy Materials, 10*. https://doi.org/10.1002/aenm.201902579
48. Liu, Y., et al. (2021). Ionic additive engineering for stable planar perovskite solar cells with efficiency >22%. *Chemical Engineering Journal, 426*. https://doi.org/10.1016/j.cej.2021.130841
49. Li, Y., Dailey, M., Lohr, P. J., & Printz, A. D. (2021). Performance and stability improvements in metal halide perovskite with intralayer incorporation of organic additives. *Journal of Materials Chemistry A, 9*, 16281–16338. https://doi.org/10.1039/d1ta05252g
50. Conings, B., et al. (2015). The impact of precursor water content on solution-processed organometal halide perovskite films and solar cells. *Journal of Materials Chemistry A, 3*, 19123–19128. https://doi.org/10.1039/c5ta06199g
51. Sakai, N., et al. (2017). Controlling nucleation and growth of metal halide perovskite thin films for high-efficiency perovskite solar cells. *Small, 13*. https://doi.org/10.1002/smll.201602808
52. Cheng, Y., Peng, Y., Jen, A. K. Y., & Yip, H.-L. (2021). Development and challenges of metal halide perovskite solar modules. *Solar RRL*, https://doi.org/10.1002/solr.202100545.
53. Zhong, J. X., Wu, W. Q., Ding, L., & Kuang, D. B. (2020). Blade-coating perovskite films with diverse compositions for efficient photovoltaics. *Energy & Environmental Materials, 4*, 277–283. https://doi.org/10.1002/eem2.12118
54. Gao, L.-L., Li, C.-X., Li, C.-J., & Yang, G.-J. (2017). Large-area high-efficiency perovskite solar cells based on perovskite films dried by the multi-flow air knife method in air. *Journal of Materials Chemistry A, 5*, 1548–1557. https://doi.org/10.1039/c6ta09565h
55. Abdelsamie, M., et al. (2020). Impact of Processing on Structural and Compositional Evolution in Mixed Metal Halide Perovskites during Film Formation. *Advanced Functional Materials, 30*. https://doi.org/10.1002/adfm.202001752
56. Zhang, H., et al. (2022). A universal co-solvent dilution strategy enables facile and cost-effective fabrication of perovskite photovoltaics. *Nature Communications, 13*, 89. https://doi.org/10.1038/s41467-021-27740-4
57. Liu, R., et al. (2020). The synergistic effect of co-solvent engineering and thermal engineering towards phase control two-dimensional perovskite solar cells. *Solar Energy, 209*, 446–453. https://doi.org/10.1016/j.solener.2020.09.006
58. Ha, S. T., Su, R., Xing, J., Zhang, Q., & Xiong, Q. (2017). Metal halide perovskite nanomaterials: Synthesis and applications. *Chemical Science, 8*, 2522–2536. https://doi.org/10.1039/c6sc04474c
59. Sun, J., Li, F., Yuan, J., & Ma, W. (2021). Advances in metal halide perovskite film preparation: The role of anti-solvent treatment. *Small Methods, 5*, e2100046. https://doi.org/10.1002/smtd.202100046

60. Li, M., et al. (2017). Enhanced efficiency and stability of perovskite solar cells via anti-solvent treatment in two-step deposition method. *ACS Applied Materials & Interfaces, 9*, 7224–7231. https://doi.org/10.1021/acsami.7b01136
61. Lee, D. S., et al. (2019). Grain quality engineering for organic metal halide perovskites using mixed antisolvent spraying treatment. *Solar RRL, 4*. https://doi.org/10.1002/solr.201900397
62. Moot, T., et al. (2020). CsI-antisolvent adduct formation in all-inorganic metal halide perovskites. *Advanced Energy Materials, 10*. https://doi.org/10.1002/aenm.201903365
63. Lee, J. W., Kim, H. S., & Park, N. G. (2016). Lewis acid-base adduct approach for high efficiency perovskite solar cells. *Accounts of Chemical Research, 49*, 311–319. https://doi.org/10.1021/acs.accounts.5b00440
64. Wang, S., et al. (2020). Lewis acid/base approach for efficacious defect passivation in perovskite solar cells. *Journal of Materials Chemistry A, 8*, 12201–12225. https://doi.org/10.1039/d0ta03957h
65. Jia, Q., et al. (2020). Large-grained all-inorganic bismuth-based perovskites with narrow band gap via lewis acid-base adduct approach. *ACS Applied Materials & Interfaces, 12*, 43876–43884. https://doi.org/10.1021/acsami.0c14512
66. Abbas, M., et al. (2020). A critical review on crystal growth techniques for scalable deposition of photovoltaic perovskite thin films. *Materials (Basel), 13*. https://doi.org/10.3390/ma13214851
67. Reddy, S. S., et al. (2019). Lewis acid-base adduct-type organic hole transport material for high performance and air-stable perovskite solar cells. *Nano Energy, 58*, 284–292. https://doi.org/10.1016/j.nanoen.2019.01.041
68. Heo, Y. J., et al. (2021). Enhancing performance and stability of tin halide perovskite light emitting diodes via coordination engineering of lewis acid–base adducts. *Advanced Functional Materials, 31*. https://doi.org/10.1002/adfm.202106974
69. Sun, H., et al. (2021). Strategies and methods for fabricating high quality metal halide perovskite thin films for solar cells. *Journal of Energy Chemistry, 60*, 300–333. https://doi.org/10.1016/j.jechem.2021.01.001
70. Liu, C., et al. (2020). Tailoring C60 for efficient inorganic $CsPbI_2$ Br perovskite solar cells and modules. *Advanced Materials, 32*, e1907361. https://doi.org/10.1002/adma.201907361
71. Abdelsamie, M., et al. (2021). Mechanism of additive-assisted room-temperature processing of metal halide perovskite thin films. *ACS Applied Materials & Interfaces, 13*, 13212–13225. https://doi.org/10.1021/acsami.0c22630
72. Liu, Z., Ono, L. K., & Qi, Y. (2020). Additives in metal halide perovskite films and their applications in solar cells. *Journal of Energy Chemistry, 46*, 215–228. https://doi.org/10.1016/j.jechem.2019.11.008
73. Ling, J., et al. (2021). A perspective on the commercial viability of perovskite solar cells. *Solar RRL, 5*. https://doi.org/10.1002/solr.202100401
74. Vesce, L., et al. (2021). Ambient air blade-coating fabrication of stable triple-cation perovskite solar modules by green solvent quenching. *Solar RRL, 5*. https://doi.org/10.1002/solr.202100073
75. Tian, S., et al. (2019). A facile green solvent engineering for up-scaling perovskite solar cell modules. *Solar Energy, 183*, 386–391. https://doi.org/10.1016/j.solener.2019.03.038
76. Zhang, M., Xin, D., Zheng, X., Chen, Q., & Zhang, W.-H. (2020). Toward Greener solution processing of perovskite solar cells. *ACS Sustainable Chemistry & Engineering, 8*, 13126–13138. https://doi.org/10.1021/acssuschemeng.0c04289
77. Hoang, M. T., et al. (2021). Towards the environmentally friendly solution processing of metal halide perovskite technology. *Green Chemistry, 23*, 5302–5336. https://doi.org/10.1039/d1gc01756j
78. Cui, Y., Wang, S., Ding, L., & Hao, F. (2020). Green–solvent–processable perovskite solar cells. *Advanced Energy and Sustainability Research, 2*. https://doi.org/10.1002/aesr.202000047

79. Ahmed, D. S., Mohammed, B. K., & Mohammed, M. K. A. (2021). Long-term stable and hysteresis-free planar perovskite solar cells using green antisolvent strategy. *Journal of Materials Science, 56*, 15205–15214. https://doi.org/10.1007/s10853-021-06200-w
80. Bu, T., et al. (2017). Synergic interface optimization with green solvent engineering in mixed perovskite solar cells. *Advanced Energy Materials, 7*. https://doi.org/10.1002/aenm.201700576
81. Worsley, C., et al. (2021). γ-Valerolactone: A nontoxic green solvent for highly stable printed mesoporous perovskite solar cells. *Energy Technology, 9*. https://doi.org/10.1002/ente.202100312
82. Worsley, C., et al. (2022). Green solvent engineering for enhanced performance and reproducibility in printed carbon-based mesoscopic perovskite solar cells and modules. *Materials Advances, 3*, 1125–1138. https://doi.org/10.1039/d1ma00975c
83. Rakocevic, L., et al. (2017). Interconnection optimization for highly efficient perovskite modules. *IEEE Journal of Photovoltaics, 7*, 404–408. https://doi.org/10.1109/jphotov.2016.2626144
84. Yang, M., et al. (2018). Highly efficient perovskite solar modules by scalable fabrication and interconnection optimization. *ACS Energy Letters, 3*, 322–328. https://doi.org/10.1021/acsenergylett.7b01221
85. Bailie, C., Eberspacher, C., Gehan, E., Bramante, R., & Hest, M. (2019). In *IEEE 46th photovoltaic specialists conference*, 1–5.
86. Kim, D. H., Whitaker, J. B., Li, Z., van Hest, M. F. A. M., & Zhu, K. (2018). Outlook and challenges of perovskite solar cells toward terawatt-scale photovoltaic module technology. *Joule, 2*, 1437–1451. https://doi.org/10.1016/j.joule.2018.05.011
87. Razza, S., Pescetelli, S., Agresti, A., & Di Carlo, A. (2021). Laser processing optimization for large-area perovskite solar modules. *Energies, 14*. https://doi.org/10.3390/en14041069
88. Rong, Y., et al. (2018). Challenges for commercializing perovskite solar cells. *Science, 361*. https://doi.org/10.1126/science.aat8235
89. Di Giacomo, F., et al. (2020). Upscaling Inverted perovskite solar cells: Optimization of laser scribing for highly efficient mini-modules. *Micromachines (Basel), 11*. https://doi.org/10.3390/mi11121127
90. Klaus Ellmer, A. K. B. R. (2007). *Transparent conductive zinc oxide* (Vol. 104). Springer.
91. Walter, A., et al. (2018). Closing the cell-to-module efficiency gap: A fully laser scribed perovskite minimodule with 16% steady-state aperture area efficiency. *IEEE Journal of Photovoltaics, 8*, 151–155. https://doi.org/10.1109/jphotov.2017.2765082
92. Tamai, H., & Sato, T. (2020). *Japan's NEDO and panasonic achieve the world's highest conversion efficiency of 16.09% for largest-area perovskite solar cell module*. https://www.businesswire.com/news/home/20200206006046/en/Japan%E2%80%99s-NEDO-and-Panasonic-Achieve-the-World%E2%80%99s-Highest-Conversion-Efficiency-of-16.09-for-Largest-area-Perovskite-Solar-Cell-Module
93. Li, H., et al. (2020). Recent progress towards roll-to-roll manufacturing of perovskite solar cells using slot-die processing. *Flexible and Printed Electronics, 5*. https://doi.org/10.1088/2058-8585/ab639e
94. Angmo, D., et al. (2021). A lab-to-fab study toward roll-to-roll fabrication of reproducible perovskite solar cells under ambient room conditions. *Cell Reports Physical Science, 2*. https://doi.org/10.1016/j.xcrp.2020.100293
95. Martin, B., Amos, D., Brehob, E., van Hest, M. F. A. M., & Druffel, T. (2021). Techno-economic analysis of roll-to-roll production of perovskite modules using radiation thermal processes. *Applied Energy*. https://doi.org/10.1016/j.apenergy.2021.118200
96. Zhong, Z. W., Shan, X. C., & Wong, S. J. (2011). Roll-to-roll large-format slot die coating of photosensitive resin for UV embossing. *Microsystem Technologies, 17*, 1703–1711. https://doi.org/10.1007/s00542-011-1344-5
97. Moon, S.-J., et al. (2015). Laser-scribing patterning for the production of organometallic halide perovskite solar modules. *IEEE Journal of Photovoltaics, 5*, 1087–1092. https://doi.org/10.1109/jphotov.2015.2416913

98. Meroni, S. M. P., et al. (2020). Scribing method for carbon perovskite solar modules. *Energies, 13*. https://doi.org/10.3390/en13071589
99. Markauskas, E., Gečys, P., Repins, I., Beall, C., & Račiukaitis, G. (2017). Laser lift-off scribing of the CZTSe thin-film solar cells at different pulse durations. *Solar Energy, 150*, 246–254. https://doi.org/10.1016/j.solener.2017.01.074
100. Castriotta, L. A., et al. (2022). Reducing losses in perovskite large area solar technology: Laser design optimization for highly efficient modules and minipanels. *Advanced Energy Materials*, https://doi.org/10.1002/aenm.202103420.
101. Taheri, B., et al. (2021). Laser-scribing optimization for sprayed SnO_2-based perovskite solar modules on flexible plastic substrates. *ACS Applied Energy Materials, 4*, 4507–4518. https://doi.org/10.1021/acsaem.1c00140
102. Lee, D.-K., & Park, N.-G. (2021). Materials and methods for high-efficiency perovskite solar modules. *Solar RRL*, https://doi.org/10.1002/solr.202100455.
103. Jung, E. H., et al. (2019). Efficient, stable and scalable perovskite solar cells using poly(3-hexylthiophene). *Nature, 567*, 511–515. https://doi.org/10.1038/s41586-019-1036-3
104. Deng, Y., et al. (2018). Surfactant-controlled ink drying enables high-speed deposition of perovskite films for efficient photovoltaic modules. *Nature Energy, 3*, 560–566. https://doi.org/10.1038/s41560-018-0153-9
105. International Standard IEC 60904-1{ed2.0). (2006–09).
106. Silverman, T., Jahn, U., Apolloni, M., Louwen, A., Schweiger, M., Bellurado, G., Wagner, J., Tetzlaff, A., Ingenhoven, P., & Moser, D. (2014). Characterisation of performance of thin film PV technologies. (International Energy Agency Project: IEA PVPS Task 13).
107. Silverman, T. J., Jahn, U., Friesen, G., Pravettoni, M., Apolloni, M., Louwen, A., van Sark, W. G. J. H. M., Schweiger, M., Belluardo, G., Wagner, J., Tetzlaff, A., Ingenhoven, P., & Moser, D. (2020). In *IEA International Energy Agency* (SFOE NREL, 2020).
108. Silverman, T., Jahn, U., Friesen, G., Pravettoni, M., Apolloni, M., Louwen, A., Schweiger, M., Bellurado, G., Wagner, J., Tetzlaff, A., & Moser, I. D. (2014). IEA-PVPS_T13-02_2014_Characterization_ThinFilm_Modules.
109. Bardizza, G., Müllejans, H., Pavanello, D., & Dunlop, E. D. (2021). Metastability in performance measurements of perovskite PV devices: A systematic approach. *Journal of Physics: Energy, 3*. https://doi.org/10.1088/2515-7655/abd678
110. Fu, Y. (2022). Stabilization of metastable halide perovskite lattices in the 2D limit. *Advanced Materials, 34*, e2108556. https://doi.org/10.1002/adma.202108556
111. Fell, C. J. (2019). Standardising current–voltage measurements for metastable solar cells. *Journal of Physics: Energy, 2*. https://doi.org/10.1088/2515-7655/ab55cc
112. Silverman, T. J., M. G. D., Marion, B., Krutz, S. R. (2014). In *2014 IEEE 40th Photovoltaic Specialist Conference (PVSC)*.
113. Yan, X., et al. (2022). Ion migration in hybrid perovskites: Classification, identification, and manipulation. *Nano Today, 44*. https://doi.org/10.1016/j.nantod.2022.101503
114. Deceglie, M. G., et al. (2015). Validated method for repeatable power measurement of cigs modules exhibiting light-induced metastabilities. *IEEE Journal of Photovoltaics, 5*, 607–612. https://doi.org/10.1109/jphotov.2014.2376056
115. Zhang, S., et al. (2022). Improved performance and stability of perovskite solar modules by interface modulating with graphene oxide crosslinked CsPbBr3 quantum dots. *Energy & Environmental Science, 15*, 244–253. https://doi.org/10.1039/d1ee01778k
116. Kim, H. S., et al. (2015). Control of I–V hysteresis in $CH_3NH_3PbI_3$ perovskite solar cell. *Journal of Physical Chemistry Letters, 6*, 4633–4639. https://doi.org/10.1021/acs.jpclett.5b02273
117. Yan, X., W. F., Cheng, F., Sun, H., Xu, C., Wang, L., Kang, Z., Zhang, Y. (2022). Ion migration in perovskite solar cells. *Science Direct*.
118. Xiaoxue Ren, L. Z., Yongbo Yuan, Liming Ding. (2021). Ion migration in perovskite solar cells. *Journal of Semiconductors*. https://doi.org/10.1088/1674-4926/42/1/010201.

119. Zhu, W., et al. (2022). Ion migration in organic-inorganic hybrid perovskite solar cells: current understanding and perspectives. *Small, 18*, e2105783. https://doi.org/10.1002/smll.202105783
120. Elumalai, N. K., & Uddin, A. (2016). Hysteresis in organic-inorganic hybrid perovskite solar cells. *Solar Energy Materials and Solar Cells, 157*, 476–509. https://doi.org/10.1016/j.solmat.2016.06.025
121. Martiradonna, L. (2018). Riddles in perovskite research. *Nature Materials, 17*, 377. https://doi.org/10.1038/s41563-018-0072-y
122. Doumon, N. Y. (2019). The degradation of organic solar cells: From chemistry to device physics through materials. https://doi.org/10.33612/diss.98539626.
123. Wohlgemuth, J. (2020). *Photovoltaic Module Reliability*.
124. Reese, M. O., et al. (2011). Consensus stability testing protocols for organic photovoltaic materials and devices. *Solar Energy Materials and Solar Cells, 95*, 1253–1267. https://doi.org/10.1016/j.solmat.2011.01.036
125. Asuo, I. M., et al. (2020). Ambient condition-processing strategy for improved air-stability and efficiency in mixed-cation perovskite solar cells. *Materials Advances, 1*, 1866–1876. https://doi.org/10.1039/d0ma00528b
126. Khenkin, M. V., et al. (2020). Consensus statement for stability assessment and reporting for perovskite photovoltaics based on ISOS procedures. *Nature Energy, 5*, 35–49. https://doi.org/10.1038/s41560-019-0529-5
127. Doumon, N. Y., Yang, L., & Rosei, F. (2022). Ternary organic solar cells: A review of the role of the third element. *Nano Energy, 94*. https://doi.org/10.1016/j.nanoen.2021.106915
128. Schelhas, L. T., et al. (2019). Insights into operational stability and processing of halide perovskite active layers. *Energy & Environmental Science, 12*, 1341–1348. https://doi.org/10.1039/c8ee03051k
129. Bryant, D., et al. (2016). Light and oxygen induced degradation limits the operational stability of methylammonium lead triiodide perovskite solar cells. *Energy & Environmental Science, 9*, 1655–1660. https://doi.org/10.1039/c6ee00409a
130. Mundt, L. E., et al. (2021). Mixing matters: Nanoscale heterogeneity and stability in metal halide perovskite solar cells. *ACS Energy Letters, 7*, 471–480. https://doi.org/10.1021/acsenergylett.1c02338
131. Song, Z., et al. (2015). Impact of processing temperature and composition on the formation of methylammonium lead iodide perovskites. *Chemistry of Materials, 27*, 4612–4619. https://doi.org/10.1021/acs.chemmater.5b01017
132. Luchkin, S. Y., et al. (2017). Reversible and irreversible electric field induced morphological and interfacial transformations of hybrid lead iodide perovskites. *ACS Applied Materials & Interfaces, 9*, 33478–33483. https://doi.org/10.1021/acsami.7b01960
133. Wang, J., et al. (2021). Tuning an electrode work function using organometallic complexes in inverted perovskite solar cells. *Journal of the American Chemical Society, 143*, 7759–7768. https://doi.org/10.1021/jacs.1c02118
134. Schulz, P., Cahen, D., & Kahn, A. (2019). *Halide perovskites: Is it all about the interfaces?* (Vol. 119, pp. 3349–3417). American Chemical Society.
135. Dunfield, S. P., et al. (2020). From defects to degradation: A mechanistic understanding of degradation in perovskite solar cell devices and modules. *Advanced Energy Materials, 10*. https://doi.org/10.1002/aenm.201904054
136. Motti, S. G., et al. (2019). Controlling competing photochemical reactions stabilizes perovskite solar cells. *Nature Photonics, 13*, 532–539. https://doi.org/10.1038/s41566-019-0435-1
137. Akriti *et al.* Layer-by-layer anionic diffusion in two-dimensional halide perovskite vertical heterostructures. Nature Nanotechnology 16, 584–591, doi:https://doi.org/10.1038/s41565-021-00848-w (2021).
138. Cho, J., Mathew, P. S., DuBose, J. T., & Kamat, P. V. (2021). Photoinduced halide segregation in ruddlesden-popper 2D mixed halide perovskite films. *Advanced Materials, 33*, e2105585. https://doi.org/10.1002/adma.202105585

139. Ding, Y., et al. (2022). Single-crystalline TiO_2 nanoparticles for stable and efficient perovskite modules. *Nature Nanotechnology, 17*, 598–605. https://doi.org/10.1038/s41565-022-01108-1
140. Rehman, A. U., et al. (2021). Electrode metallization for scaled perovskite/silicon tandem solar cells: Challenges and opportunities. *Progress in Photovoltaics: Research and Applications*. https://doi.org/10.1002/pip.3499
141. S. Kurtz, J. Wohlgemuth, M. Kempe, N. Bosco, P. Hacke, D. Jordan, D. C. Miller, T. J. Silverman. (2013). *Photovoltaic module qualification plus testing*.
142. Smokler, M. I., Otth, D. H., & Ross, R. G. Jr. (1985). In *Proceedings of the 18th IEEE photovoltaic specialists conference* (Las Vegas, Nevada).
143. Doyle, T., Desharnais, R., & Lorico, T. E. (2020). *2020 PVEL PV module reliability scorecard*.
144. Owen-Bellini, M., et al. (2020). Advancing reliability assessments of photovoltaic modules and materials using combined-accelerated stress testing. *Progress in Photovoltaics: Research and Applications, 29*, 64–82. https://doi.org/10.1002/pip.3342
145. Jeong, S.-H., et al. (2020). Characterizing the efficiency of perovskite solar cells and light-emitting diodes. *Joule, 4*, 1206–1235. https://doi.org/10.1016/j.joule.2020.04.007
146. Dunbar, R. B., et al. (2017). How reliable are efficiency measurements of perovskite solar cells? The first inter-comparison, between two accredited and eight non-accredited laboratories. *Journal of Materials Chemistry A, 5*, 22542–22558. https://doi.org/10.1039/c7ta05609e
147. *DuraMat Durable Module Materials Consortium*.
148. Torrence, C. E., Libby, C. S., Nie, W., Stein, J. S. (2023) Environmental and health risks of perovskite solar modules: Case for better test standards and risk mitigation solutions. iScience, 26(1), 105807. https://doi.org/10.1016/j.isci.2022.105807
149. Angelidis, T. N., & Kydros, K. A. (1995). Selective gold dissolution from a roasted auriferous pyrite-arsenopyrite concentrate. *Hydrometallurgy, 37*, 75–88.
150. Clever, H. L., & Johnston, F. J. (1980). The solubility of some sparingly soluble lead salts: An evaluation of the solubility in water and aqueous electrolyte solution. *Journal of Physical and Chemical Reference Data, 9*, 751–784. https://doi.org/10.1063/1.555628
151. Lichty, D. M. (1903). The solubility of the chloride, the bromide, and the iodide of lead, in water, at temperatures from 0° upward. *ACS, 25*, 469–474. https://doi.org/10.1021/ja02007a002
152. New Jersey Department of Health. Hazardous Substance Fact Sheet Cesium Hydroxide. (2007).
153. Garcia, G., et al. (2018). Influence of chromium hyperdoping on the electronic structure of $CH_3NH_3PbI_3$ perovskite: A first-principles insight. *Scientific Reports, 8*, 2511. https://doi.org/10.1038/s41598-018-20851-x
154. Galvao, J., et al. (2014). Unexpected low-dose toxicity of the universal solvent DMSO. *The FASEB Journal, 28*, 1317–1330. https://doi.org/10.1096/fj.13-235440
155. Agency for Toxic Substances and Disease Registry (ATSDR) What are the physiologic effects of chromium exposure? (Center for Disease Control, Agency for Toxic Substances and Disease Registry (ATSDR) Environmental Health and Medicine Education, 2013).
156. Lee, K. P., Chromey, N. C., Culik, R., Barnes, J. R., & Schneider, P. W. (1987). Toxicity of N-methyl-2-pyrrolidone (NMP)_Teratogenic, subchronic, and two-year inhalation studies. *PubMed, 9*. https://doi.org/10.1016/0272-0590(87)90045-5
157. Scailteur, V., & Lauwerys, R. R. (1987). Dimethylformamide (DMF) hepatotoxicity. *Toxicology, 43*, 231–238. https://doi.org/10.1016/0300-483x(87)90082-5
158. Foxall, K. (Ed.). (2007). *Chemical and Environmental hazards UK HPA Centre for Radiation*.
159. Sinha, P., Balas, R., Krueger, L., & Wade, A. (2012). Fate and transport evaluation of potential leaching risks from cadmium telluride photovoltaics. *Environmental Toxicology and Chemistry, 31*, 1670–1675. https://doi.org/10.1002/etc.1865
160. Labor, U. S. D. o. *Occupational safety and health administration* <https://www.osha.gov/solvents>.

161. Li, J., et al. (2020). Biological impact of lead from halide perovskites reveals the risk of introducing a safe threshold. *Nature Communications, 11*, 310. https://doi.org/10.1038/s41467-019-13910-y
162. Natasha, et al. (2020). Risk assessment and biophysiochemical responses of spinach to foliar application of lead oxide nanoparticles: A multivariate analysis. *Chemosphere, 245*, 125605. https://doi.org/10.1016/j.chemosphere.2019.125605
163. Conings, B., Babayigit, A., & Boyen, H.-G. (2019). Fire safety of lead halide perovskite photovoltaics. *ACS Energy Letters, 4*, 873–878. https://doi.org/10.1021/acsenergylett.9b00546
164. (ed US Environmental Protection Agency) (1994).
165. Townsend, T., Y. C. J., Tolaymat, T. (ed University of Florida) (2003).
166. Alsalloum, A. Y., et al. (2020). Low-temperature crystallization enables 21.9% efficient single-crystal MAPbI3 inverted perovskite solar cells. *ACS Energy Letters, 5*, 657–662. https://doi.org/10.1021/acsenergylett.9b02787
167. Boopathi, K. M., et al. (2017). Solution-processable antimony-based light-absorbing materials beyond lead halide perovskites. *Journal of Materials Chemistry A, 5*, 20843–20850. https://doi.org/10.1039/c7ta06679a
168. Chen, M., et al. (2019). Highly stable and efficient all-inorganic lead-free perovskite solar cells with native-oxide passivation. *Nature Communications, 10*, 16. https://doi.org/10.1038/s41467-018-07951-y
169. Hu, W., et al. (2020). Bulk heterojunction gifts bismuth-based lead-free perovskite solar cells with record efficiency. *Nano Energy, 68*. https://doi.org/10.1016/j.nanoen.2019.104362
170. Ito, N., et al. (2018). Mixed Sn-Ge perovskite for enhanced perovskite solar cell performance in air. *Journal of Physical Chemistry Letters, 9*, 1682–1688. https://doi.org/10.1021/acs.jpclett.8b00275
171. Jain, S. M., et al. (2018). An effective approach of vapour assisted morphological tailoring for reducing metal defect sites in lead-free, (CH3NH3)3Bi2I9 bismuth-based perovskite solar cells for improved performance and long-term stability. *Nano Energy, 49*, 614–624. https://doi.org/10.1016/j.nanoen.2018.05.003
172. Jeon, N. J., et al. (2018). A fluorene-terminated hole-transporting material for highly efficient and stable perovskite solar cells. *Nature Energy, 3*, 682–689. https://doi.org/10.1038/s41560-018-0200-6
173. Llanos, M., Yekani, R., Demopoulos, G. P., & Basu, N. (2020). Alternatives assessment of perovskite solar cell materials and their methods of fabrication. *Renewable and Sustainable Energy Reviews, 133*. https://doi.org/10.1016/j.rser.2020.110207
174. Lyu, M., et al. (2016). Highly compact and uniform CH3NH3Sn0.5Pb0.5I3 films for efficient panchromatic planar perovskite solar cells. *Science Bulletin, 61*, 1558–1562. https://doi.org/10.1007/s11434-016-1147-2
175. Qiu, J., Xia, Y., Chen, Y., & Huang, W. (2019). Management of crystallization kinetics for efficient and stable low-dimensional ruddlesden-popper (lDRP) lead-free perovskite solar cells. *Advanced Science (Weinh), 6*, 1800793. https://doi.org/10.1002/advs.201800793
176. Singh, A., et al. (2018). Photovoltaic performance of vapor-assisted solution-processed layer polymorph of Cs3Sb2I9. *ACS Applied Materials & Interfaces, 10*, 2566–2573. https://doi.org/10.1021/acsami.7b16349
177. Li, Z., et al. (2021). Sulfonated graphene aerogels enable safe-to-use flexible perovskite solar modules. *Advanced Energy Materials, 12*. https://doi.org/10.1002/aenm.202103236
178. Li, X., et al. (2021). On-device lead-absorbing tapes for sustainable perovskite solar cells. *Nature Sustainability, 4*, 1038–1041. https://doi.org/10.1038/s41893-021-00789-1
179. Jiang, Y., et al. (2019). Reduction of lead leakage from damaged lead halide perovskite solar modules using self-healing polymer-based encapsulation. *Nature Energy, 4*, 585–593. https://doi.org/10.1038/s41560-019-0406-2
180. Li, X., et al. (2020). On-device lead sequestration for perovskite solar cells. *Nature, 578*, 555–558. https://doi.org/10.1038/s41586-020-2001-x

Perovskite Polycrystalline Film for X-Ray Imaging

Hao Hu, Jun Liu, and Guangda Niu

1 Introduction

X-ray medical imaging is of ultra-importance in modern society. It plays an irreplaceable role on in situ living inspection of pathological changes of tissues for early tumor diagnosis, which is vital for human health [1, 2]. This technique dates back to the first human hand X-ray image pictured by Rontgen in 1895. After over one century's development, modern X-ray medical imaging systems (such as computerized tomography (CT)) have been digitalized with photoelectric detectors transforming photon signals into electrical signals, and these detectors are the core of X-ray medical imaging systems [3, 4].

From the higher perspective, X-ray detectors bear basic physical resemblance to other photoelectric detectors such as visible-light and infrared detectors. However, the detection system is quite different. The visible-light imagers such as everyday CMOS or CCD imager in cameras or smart phones are based on modern chip technology. Integrated with optical focusing system, tiny imaging chip can deliver wide-angle large-area views [5]. However, due to the close-to-1 refractive index of X-ray in most materials, one cannot focus X-ray easily like visible and infrared light [6]. Therefore, large imager is needed for X-ray imaging. And in this case, large-area imaging matrixes are preferred to construct the electric circuits for imaging panels in a similar way to the display panel [7, 8].

H. Hu · J. Liu
Hubei Jiufengshan Laboratory, Wuhan, P. R. China
e-mail: huhao@jfslab.comc.m; liujun@jfslab.com.cn

G. Niu (✉)
Sargent Joint Research Center, Wuhan National Laboratory for Optoelectronics & School of Optical and Electronic Information & National Engineering Research for Laser Processing, Huazhong University of Science and Technology, Wuhan, P. R. China
e-mail: guangda_niu@hust.edu.cn

W. Nie, K. (Kris) Iniewski (eds.), *Metal-Halide Perovskite Semiconductors*,
https://doi.org/10.1007/978-3-031-26892-2_15

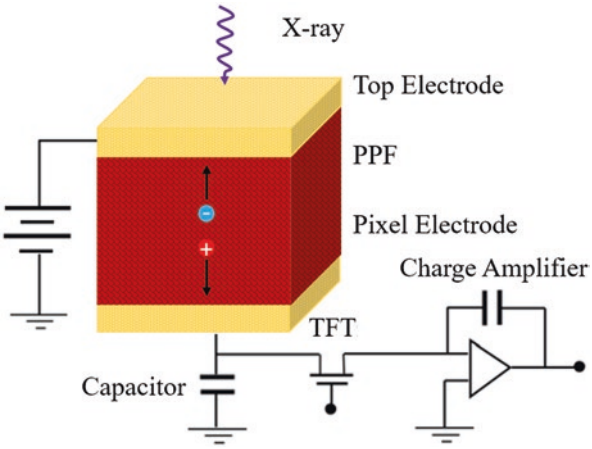

Fig. 1 The schematic diagram of PPF TFT detector

This systematic difference seems inessential, but it actually shapes the whole technology roadmap for X-ray imagers. The detection scheme needs to be compatible with the current large imaging matrix techniques such as thin-film transistor (TFT), spliced silicon photomultipliers (SiPM), and so on for successful commercialization. For instance, CsI and α-Se X-ray imagers, the current workhorses of flat panel detector (FPD), pave their way toward commercialization, due to the feasible integration of CsI and α-Se on TFT backplanes through thermal evaporation [9, 10].

Recently, there have been increasing reports on the X-ray imaging applications with perovskite polycrystalline films (PPFs) on TFT array backplane (as shown in Fig. 1). There are several advantages of PPF rendering it suitable for this technique including:

1. A high stopping power for the X-ray. The large penetration depth of high-energy photons makes plenty of semiconductors such as silicon inadequate for efficient X-ray attenuation and detection. Thanks to the high average atomic number, PPF could more effectively absorb X-ray for sensitive detection [11].
2. High intrinsic carrier mobility-lifetime ($\mu\tau$) product. Though the mobility of PPF is moderate, the defect tolerance nature of perovskite material renders its polycrystalline state relatively long carrier lifetime. This unique advantage of PPF distinguishes it from other semiconductor materials whose polycrystalline films could suffer from severe trap-mediated recombination [12].
3. Feasible integration technique. A convenient deposition method of PPF for the integration with TFT panels is the prerequisite of commercial production. Techniques such as paste blading and compression molding are under development to satisfy the requirement of low-temperature integration with TFT backplanes, which have led to successful development of prototype imaging panels in recent reports [13, 14].

In this chapter, we focus on the specific topic of the integration of PPF with TFT for X-ray imaging. Firstly, we give an introduction of the current progresses in this specific area. Afterward, we would discuss the figures of merit for this flat panel detector. Moreover, we will address some specific issues including the optimal film thickness, the blocking interface, and the measurement protocol. Lastly, an outlook of the current challenges pending to be tackled for commercialized applications is provided.

2 Recent Progresses

Integrating PPFs on TFT active pixel array backplane is one major step toward practical imaging applications. Such projects require not only the PPFs but also the matched TFT and readout circuit for successful demonstration of X-ray imaging, which have been pushed ahead with industrial resources. Park et al. firstly demonstrated the integration of $MAPbI_3$ PPF on TFT by paste doctor blading technique [14]. A polyimide (PI)-perovskite composites layer was inserted between the PPF and electrodes to enhance the adhesion of PPF to TFT backplane and reduce the dark current (Fig. 2a). An impressive sensitivity of 11,000 μC Gy_{air}^{-1} cm^{-2} was achieved with a spatial resolution of 3.1 lp mm^{-1} (as shown in Fig. 2b).

The paste-based process can achieve the direct deposition of perovskite PPFs on TFT without extra bonding processes, which is apparently advantageous. On the other hand, Deumel et al. developed an alternative strategy which can readily bond the pre-pressed free-standing perovskite PPF wafer with the TFT backplane [13]. The bonding process involved the liquification of perovskite power under methylamine atmosphere and recrystallization after the removal of excessive methylamine. This solidification process provided the adhesion force between the TFT substrate and perovskite wafer. It is worth mentioning an additional photoresist grid was prefabricated on the backplane before the bonding process to enhance the mechanical adhesion (Fig. 2c). Eventually, an ultralow detection limit of 0.22 nGy_{air} per frame under an electrical field of 0.03 V μm^{-1} was achieved (Fig. 2d). The detection limit in the unit of nGy_{air} per frame can be transformed to more universal nGy_{air} s^{-1} under the given frame rate. And the detector showed an overall sensitivity of 1060 μC Gy_{air}^{-1} cm^{-2} and a spatial resolution of 6.0 lp mm^{-1} (Fig. 2e, f).

In addition to the normal TFT panel whose active layer is amorphous silicon (α-Si), indium-gallium-zinc oxide (IGZO)-based TFT has also been used to integrate with PPFs. Park et al. deposited guanidinium-doped $MAPbI_3$ PPFs on the IGZO TFT backplane by the doctor blading technique [15]. Besides the IGZO channel material with higher mobility than α-Si, the utilized TFT had a top-gate structure with a pressure-sensitive air-dielectric layer (Fig. 2g). And the resulting detector had two sensory modalities including the X-ray and tactile pressure. The imaging demonstration by placing a live rat's foot on the detector highlighted the potential to

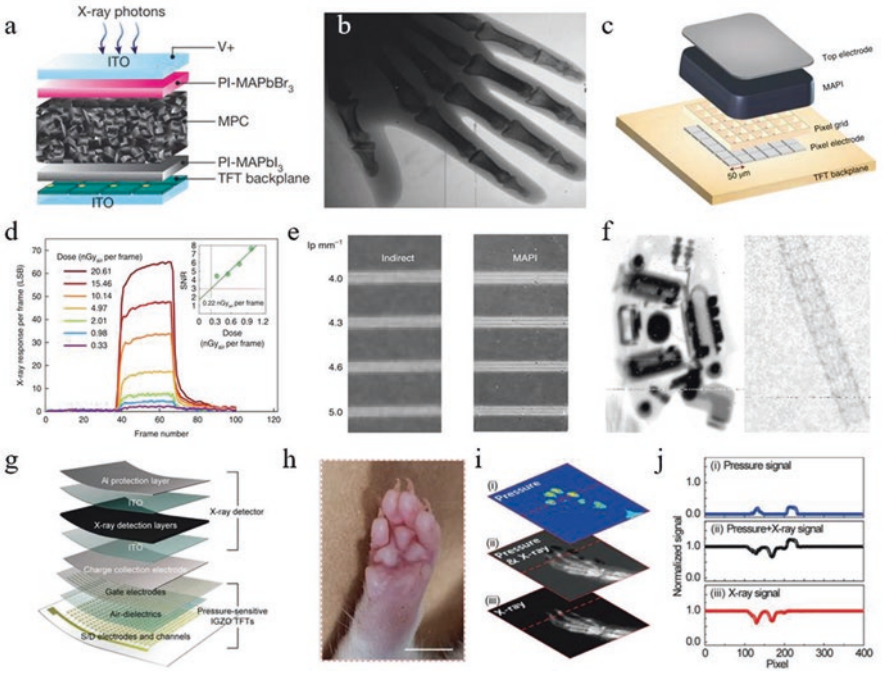

Fig. 2 Perovskite TPF devices integrated with TFT. (**a**) Illustration of an all-solution-processed digital X-ray detector. (**b**) A hand phantom X-ray image obtained. Reproduced with permission [14]. (**c**) Exploded view of the different elements of the X-ray imager. (**d**) X-ray response as a function of dose. (**e**) X-ray image with the resolution of phantom structures taken by the indirect conversion (left) and $MAPbI_3$ detector (right). (**f**) X-ray image of the hearing aid (left) and coronary stent (right) taken by the pixelated $MAPbI_3$ detector at a dose of 4.17 μGy_{air} per frame. Reproduced with permission [13]. (**g**) Schematic layouts of the multiplexed detector that consisted of pressure-sensitive IGZO TFTs and X-ray detectors. In vivo imaging of the (**i**) X-ray and (**j**) the pressure on (**h**) rat's foot. Reproduced with permission [15]. Copyright 2021, Wiley

inspect and diagnose nonplanar objects (Fig. 2h, i, j). Moreover, the imaging sensor could distinguish two adjacent objects that were only 100 μm apart.

Despite the abovementioned progresses, there are more related studies listed in Table 1 most of which are not integrated with pixelated TFT backplanes. Note that the summary is limited to thick three-dimensional hybrid PPF X-ray detection due to its leading position toward TFT integration and application.

From Table 1, one can see that a variety of detector parameters has been reported. For example, the thickness ranges from 200 to 1000 μm [16, 18] and the biasing field from 65.8 to 6000 V cm^{-1} [19, 24]. There have been different detector architectures/X-ray tube voltages, and the resulting detectors perform vastly different. Actually, in its infancy, there remains blurred lines regarding the detection scheme in this field. In the following sections, we shall try to untangle some topics which require close examinations.

Table 1 The summary of X-ray detectors based on thick three-dimensional hybrid PPFs

Material	μτ product ($cm^2\ V^{-1}$)	Deposition method and film thickness	Device/measurement parameters	Sensitivity (μC $Gy_{air}^{-1}\ cm^{-2}$)	Detection limit ($nGy_{air}\ s^{-1}$)	Spatial resolution (lp mm^{-1})	Reference
$MAPbI_3$	1.0×10^{-4}	Doctor blading 860 μm	Vertical ITO/PI-MAPbBr3/PPF/PI-MAPbI3/TFT 100 kVp, 2400 V cm^{-1}	1.1×10^4	–	3.1	[14]
$MAPbI_3$	1.3×10^{-4}	Doctor blading 200 μm	Vertical Electrode/polymer/PPF/electrode 90 kVp, 5000 V cm^{-1}	1.35×10^4	–	–	[16]
$MAPbI_3$	–	Hot press 570 μm	Vertical Au/PCBM/PPF/Spiro-OMeTAD/Au 40 kVp, ~260 V cm^{-1}	3.13×10^4	–	–	[17]
$MAPbI_3$	$\sim 2 \times 10^{-4}$	Hydraulic press 1000 μm	Vertical ITO/PEDOT:PSS/PPF/PCBM/ZnO/Ag 70 kVp, 2000 V cm^{-1}	~2527	–	–	[18]
$MAPbI_3$	5.46×10^{-3}	Hot press 760 μm	Vertical Au/PPF/Au 40 kVp, 65.8 V cm^{-1}	4.2×10^5	350 (measured at 13.2 V cm^{-1})	–	[19]
$MAPbI_3$	3.84×10^{-4}	Hot press 800 μm	Vertical Au/PCBM/PPF/Au 40 kVp, 125 V cm^{-1}	1.22×10^5	–	–	[20]

(continued)

Table 1 (continued)

Material	μτ product (cm^2 V^{-1})	Deposition method and film thickness	Device/measurement parameters	Sensitivity (μC Gy_{air}^{-1} cm^{-2})	Detection limit (nGy_{air} s^{-1})	Spatial resolution (lp mm^{-1})	Reference
$MAPbI_3$	4×10^{-4}	Hydraulic press 230 μm	Vertical Au/PPF/ITO RQA5 spectrum, 1700 V cm^{-1}	9300	6.3 (measured at 300 V cm^{-1})	6 (measured at 300 V cm^{-1})	[13]
$MAPbI_3$ TMTA mix	6.8×10^{-4}	Doctor blading ~400 μm	Vertical Au/PPF/ITO 50 kVp, 5000 V cm^{-1}	1.74×10^4	76 (measured at 50 V cm^{-1})	–	[21]
$GA_{0.1}MA_{0.9}PbI_3$	–	Doctor blading ~300 μm	Vertical ITO/PEDOT:PSS/ PPF/TiO_2/ITO 50 kVp, 1000 V cm^{-1}	6740	–	–	[15]
$MAPb(I_{0.9}Cl_{0.1})_3$	1.5×10^{-3}	Solution fill 240 μm	Vertical Cr/BCP/C_{60}/PPF/Cr 60 kVp, 500 V cm^{-1}	8696 ± 228	–	4.0	[22]
$Cs_{0.15}FA_{0.85}Pb_{I3}/Cs_{0.15}FA_{0.85}Pb($ $I_{0.15}Br_{0.85)3}$ PPF heterojunction	8.47×10^{-3}	Solution fill ~520 μm	Vertical Cr/BCP/C_{60}/PPF/ Carbon 60 kVp, ~480 V cm^{-1}	1629 ± 27	26.1 ± 0.54	–	[23]
$PEA_2MA_8Pb_9I_{28}$	2.6×10^{-5}	Doctor blading 300 μm	Vertical ITO/PPF/Au 50 kVp, 6000 V cm^{-1}	10,980	69 (measured at ~167 V cm^{-1})	–	[24]

3 The Figures of Merit

To start, there are various figures of merit available for X-ray imagers which are fundamental and essential to evaluate their performances. In the following we divide them into groups and give a brief introduction.

3.1 Sensitivity and Detection Limit

Sensitivity with the unit of μC Gy_{air}^{-1} cm^{-2} is one of the most widely used parameters to evaluate the performance of X-ray detectors. It is defined by dividing the photocurrent density by the dose rate. This quantity is similar to responsivity (*A* W^{-1}) employed in visible and infrared detection, representing the response magnitude property of corresponding detectors [25].

Not only the response magnitude but also the background noise level would determine if a signal is detectable or not. According to the definition of International Union of Pure and Applied Chemistry [26], the detection limit *D* is the equivalent dose rate to produce a signal greater than three times the noise level which can be formulated as:

$$D = \frac{3 \times i_{n-\text{dark}}}{A \times s} \propto \frac{3}{A \times \text{SNR}}$$

where i_{n-dark} is the noise current under dark condition, *A* is the area of the active region, and s is the sensitivity. This parameter indicates the lowest detectable dose rate. For medical X-ray detection, a lower dose is favored to avoid potential ionizing radiation damage to the DNA molecules. Therefore, the detection limit, which reflects both the noise and response magnitude levels, is a vital and more comprehensive detector parameter. For infrared and visible sensor, specific detectivity (*D**) has been widely used and defined as:

$$D^* = \frac{\sqrt{A \times \Delta f}}{\text{NEP}} \propto \sqrt{(A \times \Delta f)} \times \text{SNR}$$

where *A* is the area of the active region of the detector, Δf the bandwidth, and NEP the noise equivalent power [27]. One can see that *D* and *D** have similar underlying physical meanings. It is worth mentioning that as the noise level is dependent on the sampling frequency, the Δf should be noted when measuring the detection limit [13, 28].

3.2 Dark Current

The dark current or called leakage current is an important parameter of FPD. It is worth mentioning that the shot noise has been suggested as the main noise source in perovskite detectors, and the amplitude of the shot noise is proportional to the square root of the dark current [29]. However, as the detection limit already takes the noise level into consideration, one doesn't necessarily need to use dark current to measure the significance of noise.

The importance of dark current lies mainly on the systematic level. In actual application, during the shutter open time, the dark current and photoresponse will store charges in corresponding capacitors. As the volume of capacitors is limited due to size constraints in TFT backplanes, the magnitude of the dark current directly poses an upper limit to the dynamic range [30]. In extreme cases, the dark current could fully fill the capacitors under given shutter open time, and all the pixels would be "overexposed" masking the sensor's photoresponse completely.

Therefore, the dark current itself is an irreplaceable criterion, not to measure the device's property but to evaluate the integration availability of the corresponding detectors with TFT panels.

3.3 Spatial Resolution and Detective Quantum Efficiency

Not like the figures of merit discussed above, the spatial resolution and detective quantum efficiency (DQE) are not the property of discrete device, but the whole imaging system.

The spatial resolution equals the spatial frequency when the modulation transfer function (MTF) of the corresponding imager drops to 0.2 [31]. Generally speaking, based on the imaging of a line-pair test phantom with a series of spatial frequencies, the MTF values at the corresponding spatial frequency can be calculated as:

$$\mathrm{MTF} = \frac{I_{\max} - I_{\min}}{I_{\max} + I_{\min}}$$

where $I_{\max}$ and $I_{\min}$ are the brightest and darkest intensity for certain line pair. The MTF can also be extracted by Fourier transform of a knife-edge image which is more convenient in some circumstances [32].

The spatial resolution is an intuitive parameter which is the final evaluation index of an imaging system. But it depends on many more influence factors other than the detectors' quality itself. For example, the X-ray source intensity and pixel size would significantly determine the imager's spatial resolution [33].

DQE defines the ability of the imaging system to transfer the signal with different spatial frequencies from input to output as [34]:

$$\mathrm{DQE}(\mathrm{f}) = \frac{\mathrm{SNR}_{\mathrm{out}}^2(\mathrm{f})}{\mathrm{SNR}_{\mathrm{in}}^2(\mathrm{f})}$$

Ideally, an imaging system should have a DQE equals unity, but in practice all imager would increase the noise and the DQE would deviate from unity. As the MTF can be defined as the redistribution of image quanta, $\mathrm{SNR}_{\mathrm{out}}(\mathrm{f})$ is proportional to MTF(f). Overall, DQE is a more comprehensive parameter for the imager reflecting the properties of both the single detector and whole system [35].

3.4 *Image Lag and Ghosting*

The image lag and ghosting reflect the dynamic features of image sensors. As shown in Fig. 3, the image lag means the carryover of signals from previous X-ray exposure to the subsequent image frame. In other words, the charge carriers generated by one exposure will induce signals in several following frames. Ghosting, on the other hand, means that the sensitivity of X-ray detectors changes along with its exposure to X-rays, and usually it would decline [36].

Generally speaking, these properties are of no concern for a single-shot image, but of vital significance for dynamic medical imaging applications such as CT and

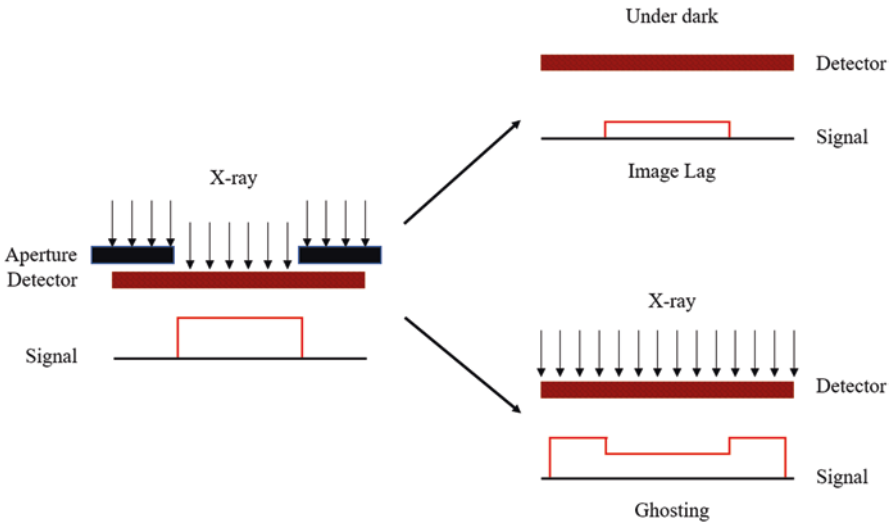

Fig. 3 Illustration of image lag (up) and ghosting (down) after exposing a detector through an aperture

dynamic digital radiography [37, 38]. These parameters, though defined on systematic level, are largely determined by single detector's properties. The image lag is determined by the carrier trapping profile in corresponding detectors while ghosting by detector's stability against X-ray illumination.

4 Specific Topics

In this section, we will address several specific topics regarding PPF FPD focusing on optimizing these figures of merit discussed above. Firstly, we would discuss about the proper PPF thickness for optimal detector performance. Secondly, we provide our perspective on detector structures and blocking interfaces. Lastly, we will check the measurement protocols for proper determination of detector parameters.

4.1 Film Thickness

The optimal thickness of PPF for X-ray detection is a nontrivial question at present. The film thickness is one major parameter dominating the signal output amplitude, influencing the sensitivity and detection limit of corresponding detectors. The current PPF X-ray detectors have been reported with a thickness from hundreds of nm to hundreds of μm [39, 40]. However, different thickness PPF would require completely different deposition techniques. For films with a thickness below 10 μm, spin coating is a widely used mature technique [41]. Extensive experience from the perovskite solar cell community can conveniently help prepare the corresponding high-quality PPFs. On the other hand, if films over 100 μm are needed, vastly different techniques such as paste blading or compression molding need to be developed. Enormous technical problems will need to be addressed such as the slurry handling, voids removal, and substrate integration. Therefore, it is of prime importance to ascertain the optimal thickness for PPF X-ray detection.

Usually regarding this question, the absorption of X-ray by PPFs is considered. According to Beer-Lambert's Law, the intensity of X-ray would decline exponentially with the distance from surface, and the absorption can be calculated accordingly:

$$I(z) = I_0 e^{-\alpha z}$$

$$A(z) = 1 - e^{-\alpha z},$$

where z is the depth, α is the attenuation coefficient, I_0 is the incident X-ray intensity, and $I(z)$ and $A(z)$ is the X-ray intensity and absorption ratio with a depth of z.

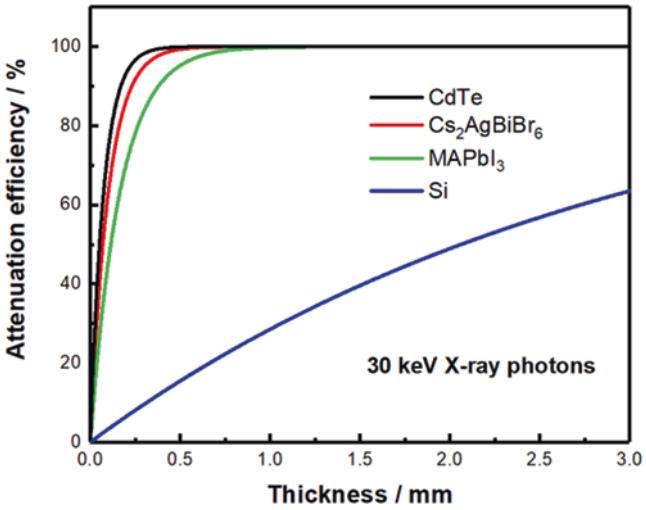

Fig. 4 The attenuation efficiency of 30 keV X-ray photons of typical semiconductor materials with varying thicknesses

The absorption curve with different film thicknesses can be calculated with certain material composition and X-ray photon energy (as shown in Fig. 4). Sandro et al. suggested a thickness with 90% absorption as a guideline for optimal X-ray detectors [42]. They claimed that as one prime advantage of direct detection is that the spatial resolution doesn't degrade with increasing thickness, a thick PPF could best take this advantage yielding the potentially highest signal.

This argument is ideally valid; however, in practice there may be more factors to consider. Firstly, one needs to realize that this statement assumes an upper limit of signal, which is true in scintillator detectors, solar cells, et al. However, in some other device architectures such as photoconductive detectors, the origin of response signal is mainly the gain effect which is directly dictated by the charge carrier density profile under radiation [43]. In this case, the carrier density (cm^{-3}) rather than the integral carrier generation profile (cm^{-2}) is more influential. But as the PPF X-ray FPD, in our understanding, should best be photovoltaic, a thicker PPF would be advantageous.

Secondly, even for the photovoltaic devices, the current performance is still far from taking full advantage of a thick PPF. In Fig. 5, Qianqian Lin et al. reported the current density-voltage behavior of a photovoltaic PPF device with a thickness ranging from 1 to 10 μm [44]. Under 100 mW cm^{-2} white-light illumination (as shown in Fig. 5a), the thinnest 1 μm film shows the highest current output due to the better carrier extraction ability with a stronger electric field. Under 80.3 $\mu Gy_{air}\ s^{-1}$ X-ray irradiation, on the other hand, 6 μm PPF yields the highest current output at −1 V (seen in Fig. 5b). This result suggests that though thicker PPF could better absorb the X-ray, it may not deliver a higher signal due to the incomplete charge collection. Due to the low intensity of X-ray radiation in practice, the trap-assisted

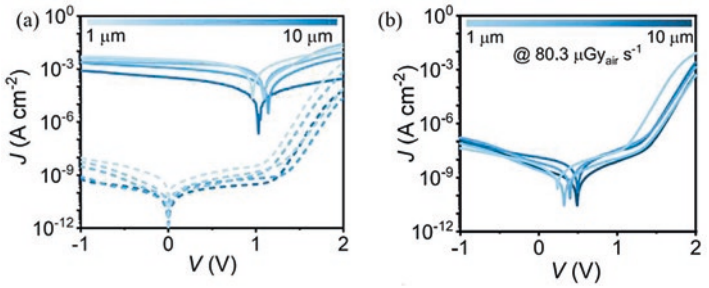

Fig. 5 (**a**) Comparison of J–V curves measured in the dark (dashed lines) and under 100 mW cm^{-2} white-light illumination (solid lines) of $(BA_2PbBr_4)_{0.5}FAPbI_3$ devices with various film thicknesses. (**b**) J–V curves of $(BA_2PbBr_4)_{0.5}FAPbI_3$ thick junctions with various thicknesses under 80.3 μGy_{air} s^{-1} X-ray irradiation. Reproduced with permission [44]. Copyright 2022, Elsevier

recombination is more prominent, and larger electric fields are needed to collect the carriers. Therefore, at this stage, it is not clear whether a thick PPF is beneficial absorbing more X-ray photons or detrimental diminishing the internal field. Applying high biases could give thick PPFs an advantage over thin PPFs, but there are always limitations to the practicable operating voltage such as the bias stability and acceptable dark current limit of the corresponding detectors.

Another potential advantage of using thick PPF is to avoid the potential damage of X-ray radiation to the flat panel circuit for radiography applications. This concern is plausible but only partly true. The current commercial sensor matrixes include different species such as charge-coupled device (CCD), complementary metal-oxide-semiconductor transistor (CMOS), amorphous silicon (α-Si), low-temperature polycrystalline silicon (LTPS), and amorphous indium-gallium-zinc oxide (α-IGZO). These different transistor panels have different resistivity against X-ray radiation. Amorphous TFTs such as α-Si are highly resistive to X-ray radiation, while CMOS technology has a limited radiation hardness [45–47]. In our understanding, as the α-Si TFT is the main radiography imager for X-ray detection (such as scintillators and α-Se), the radiation damage is not a big concern for thin PPFs. On the other hand, if a CMOS image chip is employed for certain applications (e.g., the small pixel CMOS chips for micro-CT product), a thick PPF to completely attenuate the incident X-ray and protect the image circuit is necessary.

In short summary, in this section the underlying factors for the optimal PPF thickness in X-ray detectors are discussed. Due to the potentially higher dark current of photoconductive detectors, photovoltaic detectors are preferred at present to integrate with TFT backplanes which would require a thick PPF. However, at the present stage, the advantages of over 100 μm PPF for X-ray imaging are not fully explored. With unoptimized charge extraction ability, the benefits of higher X-ray attenuation may be completely cancelled out by lower charge collection. The benefit of thick PPFs to screen the imaging panel underneath from X-ray radiation is not compulsory for TFT backplanes.

4.2 Blocking Interface

The blocking interface is one core concept for PPF X-ray detector and distinguishes photovoltaic detectors from photoconductive detectors. Fundamentally, the photoconductive detectors possess the gain effect due to an enhanced charge carrier injection from adjacent electrodes in the absence of a well-performed blocking interface under illumination. The blocking interface would suppress the charge injection under dark (reduce the dark current) and under illumination (lead to the photovoltaic behavior if the charge collection profile is ideal), which is preferred to facilitate the integration with TFT panels.

One might still wonder if the blocking interface would be essential for PPF X-ray FPD to reduce the dark current. A semi-insulating PPF seems to also suffice with a low equilibrium charge carrier density (given the mobility of PPF is more or less fixed). However, this strategy may not be valid considering the space-charge-limited current (SCLC) effect. The space charge is the net charge injected by the contacts, breaking the condition of charge neutrality implying there will be more carriers under bias voltage than the background charge carriers [48]. The SCLC follows the well-known Mott and Gurney equation:

$$J = \frac{9}{8}\varepsilon\mu\frac{V^2}{L^3},$$

where μ is the mobility of the conducting carrier, V is the applied bias, and L is the device thickness. One can tell that the magnitude of SCLC is not limited to the material equilibrium carrier concentration, but to the mobility. Therefore, a semi-insulating PPF would not reduce the amplitude of SCLC. The theoretical SCLC density is estimated for conventional perovskites using reported ε_r and μ values of 25 and 1 $cm^2\ V^{-1}\ s^{-1}$, respectively. For a 500 μm PPF, the result is 20 V^2 nA cm^{-2}. This result means a very low working bias (< 0.3 V) is needed to maintain the dark current below 1 nA cm^{-2}, which would greatly diminish the device's detection ability. To go further, for photoconductive detectors with the SCLC contributing to the dark current, the light-to-dark current ratio depends largely on the nonequilibrium carrier concentration under illumination, which further relies on the light intensity and carrier lifetime. Therefore, for weak light application such as X-ray imaging and non-photoresistor type of materials, the photoconductive detector is not a preferable option.

A plausible and confusing argument is that semi-insulating active layer could guarantee a low dark current and be used in photoconductive detectors. The above discussion indicates it is not the case. Indeed, for the widely studied α-Se FPD with an α-Se layer of higher resistivity, the detector is still made photovoltaic, either through Schottky barriers or injection blocking layers [9, 49].

There are several strategies to produce blocking interfaces with adequate barrier heights. The simplest one is to select the right electrodes which can form high-quality Schottky barrier with PPFs. In Fig. 6, we show three typical examples of the

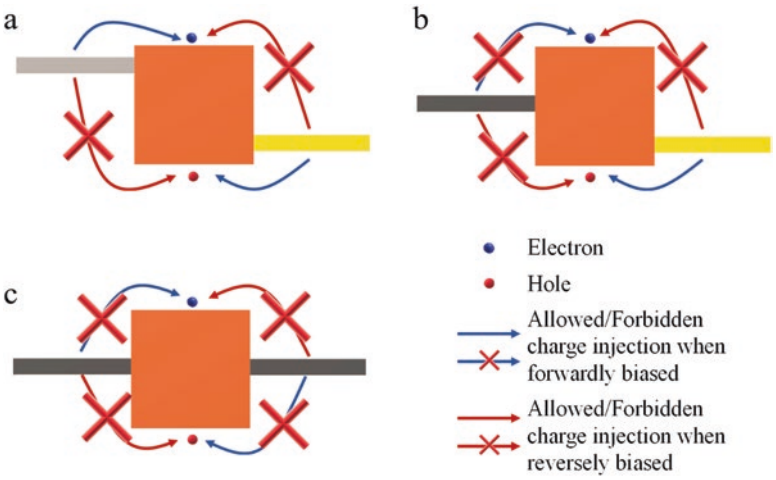

Fig. 6 The potential energy band diagrams of Schottky-type detectors. (**a**) Asymmetric electrode structure with large Schottky barrier. (**b**) Asymmetric structure with medium Schottky barrier. (**c**) Symmetric electrode structure with small Schottky barrier

energetic structures of Schottky junctions. The blocking effect theoretically depends on the barrier height which is energy-level differences between the low work function electrode with the valence band edge and the high work function electrode with the conduction band edge. To evaluate the Schottky diode behavior, one should take both interfaces and bias directions into consideration. If one interface cannot provide rectifying effect, it would already jeopardize the whole device. For example, in Fig. 6b and c, the work function of certain electrode sits in the middle of the perovskite band gap leading to moderate barrier height for both electrons and holes. This may ideally block the injection of electrons and holes effectively or not form competent rectifying interface at all. Which direction to go largely relies on the band gap width of the semiconductors. And for the X-ray FPD application, a ~1.5 eV band gap width of iodine-based perovskites is, in our idea, too narrow to support adequate rectifying effect. Therefore, the energetic structure in Fig. 6a is more advantageous necessitating a careful selection of both interface electrodes. Considering the possible pinning and metal alloying effect, the surface states of PPFs and chemical reactions with metals will both exert an influence and complicate the final rectifying effect [50, 51].

Inserting blocking interlayers is an alternative to suppress the dark current of PPF detectors. There are extensive experiences of certified electron and hole blocking materials for iodine-based perovskites from the perovskite solar cell community. But practical difficulties emerge when implementing this strategy. For the PPF, the surface roughness is much larger [14]. For perovskite solar cells, a very flat thin perovskite layer can be easily covered by tens of nm blocking layers, while for PPF, thicker blocking layer in the μm range would be necessary which leads to a large series resistance. Huang et al. have developed to use perovskites of different band

structures to form the barrier for suppressed dark currents [23]. One benefit of this scheme is to directly produce the barrier during the fabrication of PPF saving the trouble of depositing thick blocking layer afterward. However, there may be risks of halide ion interdiffusion which would change the barrier profile and rectifying effect in the long-term run [52].

To sum up, in this section we address the necessity of blocking interfaces for PPF detectors to reduce dark currents. We note that a Schottky diode type of detector working at reversed bias would be ideal if the proper metal electrodes can be picked out. Otherwise, blocking interlayers are needed. Right now, one tricky problem is the surface roughness of PPF which requires further planarization treatments for high-quality contact fabrication.

4.3 Measurement Protocols

How to conduct precise and meaningful measurements is no simple question in various scientific fields. Back during the early development of perovskite solar cells, due to the notorious hysteresis behavior, preconditioning and long-time maximal power point tracking were gradually promoted for a precise evaluation of the cell performance [53]. For perovskite X-ray detectors, the measurement protocol is also not mature and requires close examination.

The detector's sensitivity is one important parameter as discussed above. Right now, a highest value of 4.2×10^5 μC Gy_{air}^{-1} cm^{-2} has been reported for a 760 μm hot-pressed $MAPbI_3$ film [19]. Such a high value implies the contributions of gain effect in the photoconductive detector. Besides the fact that photoconductive detector probably cannot satisfy the requirements to integrate with TFT panels, one troublesome problem is that the sensitivity of a photoconductive detector is, to a great extent, limited by the external voltage applied. As the bias increases, the photoresponse also increases producing a higher sensitivity. Therefore, the value may be in the end absurdly determined by the measurement range of the source meter. Another tricky fact is the dependance of the sensitivity on the beam quality including the dose rate and energetic spectrum of X-ray. Figure 7a presents the X-ray sensitivity measured under different tube voltages and dose rates with a Schottky photovoltaic $CsPbBr_3$ device [54]. With different X-ray filters, the X-ray has different photon energy distributions. And with harder X-ray, a larger sensitivity is obtained with the same detector. The value varies from 15 to 5111 μC Gy_{air}^{-1} cm^{-2} which indicates the huge impact of beam quality.

Therefore, we suggest that the sensitivity should be more carefully referred. It should be marked clearly if it is the sensitivity of a photovoltaic or photoconductive detector. And for photoconductive detectors, we suggest a unified biasing condition for intercomparison between different researches. Given the current reported conditions, an electric field of 100 V cm^{-1} is an acceptable condition which doesn't damage the detectors in most studies. Note this value is far lower than the optimal field (>1000 V cm^{-1}) for charge collection in $CsPbBr_3$ γ-ray detectors [51, 55]. On the

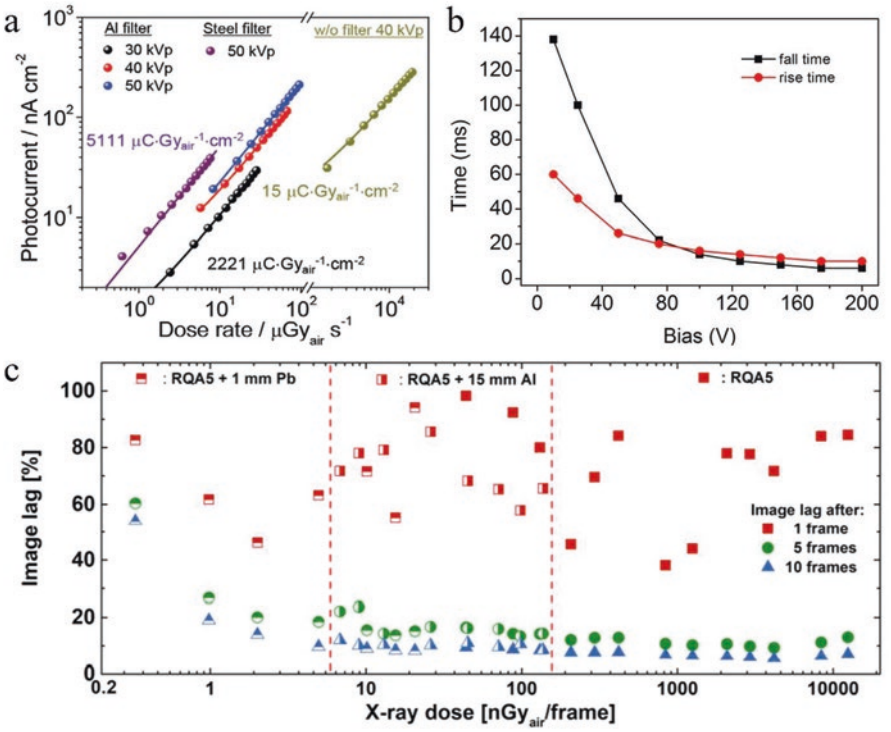

Fig. 7 (**a**) X-ray sensitivity corresponding to specific tube voltage and dose rate by the Schottky $CsPbBr_3$ device. Reproduced with permission [54]. Copyright 2022, Wiley. (**b**) Rise and fall time response dependent on the applied bias. Reproduced with permission [14]. (**c**) Image lag of the X-ray response after one frame (35 ms, red square), five frames (green dots), and ten frames (blue triangles) for the exposition with the RQA5 spectrum, RQA5 + 15 mm Al filtration, and RQA5 + 1 mm Pb. Within the scope of measurement accuracy, the image lag is independent of the dose and the exposed X-ray spectrum. Reproduced with permission [13]

other hand, the IEC 62220–1-1:2015 International Standard provides comprehensive guidelines how to capture and analyze X-ray images to characterize digital X-ray detectors where the beam quality is also defined such as RQA5 and RQA7 [34]. And we suggest the beam qualities should be modulated to fit with the RQA5 or RQA7 criterion.

Cao et al. provide a practical procedure to determine the detection limit of perovskite X-ray detectors [28]. As the detection limit is also subject to the sampling frequency (which can influence the noise current level), given that typical X-ray dynamic imagers operate with a frame rate of 30 fps, we suggest a sampling frequency of 30 Hz to be employed when measuring the fluctuation of the dark current [56]. Also, we suggest to use the same biasing condition as in the sensitivity measurement to extract the detection limit for consistency.

Besides the above discussed sensitivity and detection limit, dark current is another important figure of merit. Generally, measuring the dark current is simple,

but the determination of the dark current density is thought-provoking. It is worth questioning that when shrunk to tens of μm range, would the detectors still maintain the same dark current profile as they are in the mm range? Actually, the unspoken assumption that the dark current density is universal, no matter for large or small pixel size, is not eternally right. Serious uniformity issues might arise as large-area pixel averages the output current [57]. Therefore, one should provide the dark current results of various pixel sizes for a meaningful evaluation of this parameter.

The detector's bandwidth is an often-neglected property for PPF X-ray detector which may be due to unspecified application requirements. Recently, the emergence of single-photon counting CT technique inspires an evaluation of X-ray detector's bandwidth to extract the maximal counting rates [58, 59]. For PPF detectors, given a hole carrier mobility of 1 $cm^2\ V\ s^{-1}$, the mean carrier drift time across a 0.5 mm thick detector is about 0.5 ms at 100 $V\ cm^{-1}$. This means, ideally, the detector would run out of the X-ray generated charge carriers in 0.5 ms after the X-ray is switched off, corresponding to a theoretical bandwidth of 2000 Hz. This value is much lower than the sampling frequency of CT due to the low mobility and bias endurance of polycrystalline perovskites, but seems to satisfy the requirements of dynamic digital radiography [60]. Due to the charge trapping effect, the detector's bandwidth ends up lower in practice leading to the image lag phenomenon. Due to the lack of modulation means, it is difficult to measure the bandwidth of PPF X-ray detectors. As the switching speed of X-ray tube is slow, one possible means is to use a chopper system to generate the X-ray pulses with target repetition rates [61, 62]. One may also gather some relevant information from the temporal profile of signal rising/falling processes. Lee et al. presented the rise and fall time responses of corresponding PPF detectors under a series of applied biases. Around 10 ms rise/fall time was obtained under high biasing condition (as shown in Fig. 7b) [14]. It is worth noting that the fall time only depends on the fast decay process of the signal, while the slow decay process can also bring about the image lag. In Fig. 7c, Deumel reported that the lag after 35 ms was 71 ± 18% of the original value, but after 350 ms the lag decreased down to 7 ± 1% [13].

To summarize, in this section we provide our perspectives on the characterizations of detector parameters. We think the sensitivity should be compared under controlled measurement conditions. The detection limit is a more comparable parameter given the noise level is measured under the consistent sampling frequency. To rule out the influence of pixel size, the dark current density should be extracted from a series of different sizes of detectors. As the temporal response of PPF X-ray detectors is one key property for high-speed dynamic imaging applications, the characterization of detector bandwidth requires further clarifications.

5 Conclusion

Perovskites have been the wonder material of the last decade and expected with widespread applications. To integrate with TFT backplanes for X-ray imaging is one of the most promising scenarios for perovskites. PPF possesses a high X-ray

attenuation ability, decent carrier transport ability, and feasible large-area deposition technique, which make it one of few semiconductors suitable for this application. Compared to commercial α-Se detector, PPF X-ray FPD supports X-ray imaging of higher energy ranges under lower operating voltages, which can become a game changer.

Therefore, this project has been continuously attracting industrial attention with a series of reports on the protype FPD. This chapter is focused on this specific topic of PPF X-ray FPD. An overview of the recent developments is provided, followed by the key figures of merit of the detection scheme. Moreover, we share our understandings on some poorly defined topics in this area. Currently, there have been interesting relevant studies based on rather thin solar-cell-type perovskite film or reporting very high sensitivity with a large gain factor. Though these projects could contribute to flexible or photoconductive detection techniques, we suggest for TFT-based X-ray FPD, a rather thick PPF with blocking interfaces is preferred.

Despite the bright prospect and rapid progress, there remain thorny challenges. One most prominent one is the overlarge dark current. Blocking interfaces constituted of either metal electrodes or selective transporting layers need to be further developed. This problem is closely related to the PPF quality. The surface states of PPF directly impact the barrier height of the blocking interface, and the surface roughness also influences the resulting junction quality. Therefore, to construct a reliable blocking interface is a systematic project. On the other hand, further increasing the working bias or mobility of PPF detectors would open up new application fields toward fast-speed imaging, which sets up a long-term goal [63]. Overall, with continuously devoted research efforts, rapid technique breakthroughs are anticipated, and the commercial PPF X-ray FPD is just around the corner.

Acknowledgments The authors would like to acknowledge financial support from the National Key Research and Development Project (2021YFB3201000), National Natural Science Foundation of China (62101200, 62074066).

References

1. Ayala-Domínguez, L., & Brandan, M. E. (2018). Quantification of tumor angiogenesis with contrast-enhanced X-ray imaging in preclinical studies: A review. *Biomedical Physics & Engineering Express, 4*(6), 062001.
2. Takeda, T., et al. (1998). Phase-contrast X-ray CT image of breast tumor. *Journal of Synchrotron Radiation, 5*(3), 1133–1135.
3. Neitzel, U. (2005). Status and prospects of digital detector technology for CR and DR. *Radiation Protection Dosimetry, 114*(1–3), 32–38.
4. Goldman, L. W. (2007). Principles of CT and CT technology. *Journal of Nuclear Medicine Technology, 35*(3), 115–128.
5. Bigas, M., et al. (2006). Review of CMOS image sensors. *Microelectronics Journal, 37*(5), 433–451.
6. Mayo, S. C., Stevenson, A. W., & Wilkins, S. W. (2012). In-line phase-contrast X-ray imaging and tomography for materials science. *Materials, 5*(5), 937–965.

7. Liu, X., et al. (2016). Highly photosensitive dual-gate a-Si:H TFT and array for low-dose flat-panel X-ray imaging. *IEEE Photonics Technology Letters, 28*(18), 1952–1955.
8. Antonuk, L., et al. (1994). High-resolution, high-frame-rate, flat-panel TFT array for digital X-ray imaging. *Medical Imaging* 1994. Vol. 2163. SPIE.
9. Huang, H., & Abbaszadeh, S. (2020). Recent developments of amorphous selenium-based X-ray detectors: A review. *IEEE Sensors Journal, 20*(4), 1694–1704.
10. Howansky, A., et al. (2019). Comparison of CsI:Tl and Gd2O2S:Tb indirect flat panel detector x-ray imaging performance in front- and back-irradiation geometries. *Medical Physics, 46*(11), 4857–4868.
11. Cuzin, M. (1987). Some new developments in the field of high atomic number materials. *Nuclear Instruments and Methods in Physics Research Section A: Accelerators, Spectrometers, Detectors and Associated Equipment, 253*(3), 407–417.
12. Kleppinger, J. W., et al. (2022). Influence of carrier trapping on radiation detection properties in CVD grown 4H-SiC epitaxial layers with varying thickness up to 250 µm. *Journal of Crystal Growth, 583*, 126532.
13. Deumel, S., et al. (2021). High-sensitivity high-resolution X-ray imaging with soft-sintered metal halide perovskites. *Nature Electronics, 4*(9), 681–688.
14. Kim, Y. C., et al. (2017). Printable organometallic perovskite enables large-area, low-dose X-ray imaging. *Nature, 550*(7674), 87–91.
15. Jang, J., et al. (2021). Multimodal digital X-ray scanners with synchronous mapping of tactile pressure distributions using perovskites. *Advanced Materials, 33*(30), 2008539.
16. Datta, A., Zhong, Z., & Motakef, S. (2020). A new generation of direct X-ray detectors for medical and synchrotron imaging applications. *Scientific Reports, 10*(1), 20097.
17. Jia, S., et al. (2022). Ion-accumulation-induced charge tunneling for high gain factor in P–I–N-structured perovskite $CH_3NH_3PbI_3$ X-ray detector. *Advanced Materials Technologies*, 2100908.
18. Shrestha, S., et al. (2017). High-performance direct conversion X-ray detectors based on sintered hybrid lead triiodide perovskite wafers. *Nature Photonics, 11*(7), 436–440.
19. Xiao, Y., et al. (2021). Grain and stoichiometry engineering for ultra-sensitive perovskite X-ray detectors. *Journal of Materials Chemistry A, 9*(45), 25603–25610.
20. Hu, M., et al. (2020). Large and dense organic–inorganic hybrid perovskite $CH_3NH_3PbI_3$ wafer fabricated by one-step reactive direct wafer production with high X-ray sensitivity. *ACS Applied Materials & Interfaces, 12*(14), 16592–16600.
21. Xia, M., et al. (2022). Compact and large-area perovskite films achieved via soft-pressing and multi-functional polymerizable binder for flat-panel X-ray imager. *Advanced Functional Materials, 32*(16), 2110729.
22. Zhao, J., et al. (2020). Perovskite-filled membranes for flexible and large-area direct-conversion X-ray detector arrays. *Nature Photonics, 14*(10), 612–617.
23. Zhou, Y., et al. (2021). Heterojunction structures for reduced noise in large-area and sensitive perovskite X-ray detectors. *Science Advances, 7*(36), eabg6716.
24. He, X., et al. (2022). Quasi-2D perovskite thick film for X-ray detection with low detection limit. *Advanced Functional Materials, 32*(7), 2109458.
25. Zhang, D., et al. (2013). High-responsivity GeSn short-wave infrared p-i-n photodetectors. *Applied Physics Letters, 102*(14), 141111.
26. (1978). Nomenclature, symbols, units and their usage in spectrochemical analysis—II. Data interpretation Analytical chemistry division. *Spectrochimica Acta Part B: Atomic Spectroscopy*, *33*(6), 241–245.
27. Jones, R. C. (1960). Proposal of the detectivity D** for detectors limited by radiation noise†. *Journal of the Optical Society of America, 50*(11), 1058–1059.
28. Pan, L., et al. (2021). Determination of X-ray detection limit and applications in perovskite X-ray detectors. *Nature Communications, 12*(1), 5258.
29. Wu, H., et al. (2021). Metal halide perovskites for X-ray detection and imaging. *Matter, 4*(1), 144–163.

30. Simone, G., et al. (2020). Organic photodetectors and their application in large area and flexible image sensors: The role of dark current. *Advanced Functional Materials, 30*(20), 1904205.
31. Sones, R. A., & Barnes, G. T. (1984). A method to measure the MTF of digital X-ray systems. *Medical Physics, 11*(2), 166–171.
32. Viallefont-Robinet, F., et al. (2018). Comparison of MTF measurements using edge method: towards reference data set. *Optics Express, 26*(26), 33625–33648.
33. Wang, J., & Fleischmann, D. (2018). Improving spatial resolution at CT: Development, benefits, and pitfalls. *Radiology, 289*(1), 261–262.
34. Michail, C., et al. (2016). Determination of the detective quantum efficiency (DQE) of CMOS/CsI imaging detectors following the novel IEC 62220-1-1: 2015 International Standard. *Radiation Measurements, 94*, 8–17.
35. Moy, J.-P. (2000). Signal-to-noise ratio and spatial resolution in X-ray electronic imagers: Is the MTF a relevant parameter? *Medical Physics, 27*(1), 86–93.
36. Zhao, W., DeCrescenzo, G., & Rowlands, J. (2002). Investigation of lag and ghosting in amorphous selenium flat-panel X-ray detectors. *Medical Imaging*. Vol. 4682. 2002: SPIE.
37. Mail, N., et al. (2008). An empirical method for lag correction in cone-beam CT. *Medical Physics, 35*(11), 5187–5196.
38. Adachi, S., et al. (2000). Experimental evaluation of a-Se and CdTe flat-panel X-ray detectors for digital radiography and fluoroscopy. *Medical Imaging*. Vol. 3977. 2000: SPIE.
39. Gao, Y., et al. (2021). Ultrathin and ultrasensitive direct X-ray detector based on heterojunction phototransistors. *Advanced Materials, 33*(32), 2101717.
40. Demchyshyn, S., et al. (2020). Designing ultraflexible perovskite X-ray detectors through interface engineering. *Advanced Science, 7*(24), 2002586.
41. Park, N.-G., & Zhu, K. (2020). Scalable fabrication and coating methods for perovskite solar cells and solar modules. *Nature Reviews Materials, 5*(5), 333–350.
42. Deumel, S., et al. (2022). Organometal halide perovskite imager: A comparison 1.5 years after fabrication. *SPIE Medical Imaging*. Vol. 12031. SPIE.
43. Keyes, R. J. (2013). *Optical and infrared detectors*. Vol. 19. Springer Science & Business Media.
44. Peng, J., et al. (2022). Ion-exchange-induced slow crystallization of 2D-3D perovskite thick junctions for X-ray detection and imaging. *Matter, 5*(7), 2251–2264.
45. Boudry, J. M., & Antonuk, L. E. (1996). Radiation damage of amorphous silicon, thin-film, field-effect transistors. *Medical Physics, 23*(5), 743–754.
46. Park, S., et al. (2021). Effect of X-ray irradiation on a-IGZO and LTPS thin-film transistors for radiography applications. *Applied Surface Science, 550*, 149237.
47. Zentai, G. (2011). Comparison of CMOS and a-Si flat panel imagers for X-ray imaging. In *2011 IEEE international conference on imaging systems and techniques*.
48. Marsh, O. J., & Viswanathan, C. R. (1967). Space-charge-limited current of holes in silicon and techniques for distinguishing double and single injection. *Journal of Applied Physics, 38*(8), 3135–3144.
49. Johanson, R. E., et al. (1998). Metallic electrical contacts to stabilized amorphous selenium for use in X-ray image detectors. *Journal of Non-Crystalline Solids, 227–230*, 1359–1362.
50. Pan, L., et al. (2020). Comparison of Zr, Bi, Ti, and Ga as metal contacts in inorganic perovskite $CsPbBr_3$ gamma-ray detector. *IEEE Transactions on Nuclear Science, 67*(10), 2255–2262.
51. He, Y., et al. (2018). High spectral resolution of gamma-rays at room temperature by perovskite $CsPbBr_3$ single crystals. *Nature Communications, 9*(1), 1609.
52. Funk, H., et al. (2020). In situ TEM monitoring of phase-segregation in inorganic mixed halide perovskite. *The Journal of Physical Chemistry Letters, 11*(13), 4945–4950.
53. Zimmermann, E., et al. (2016). Characterization of perovskite solar cells: Towards a reliable measurement protocol. *APL Materials, 4*(9), 091901.
54. He, Y., et al. (2022). Sensitivity and detection limit of spectroscopic-grade perovskite CsPbBr3 crystal for hard X-ray detection. *Advanced Functional Materials, 32*(24), 2112925.
55. He, Y., et al. (2021). $CsPbBr_3$ perovskite detectors with 1.4% energy resolution for high-energy γ-rays. *Nature Photonics, 15*(1), 36–42.

56. Moy, J.-P. (2000). Recent developments in X-ray imaging detectors. *Nuclear Instruments and Methods in Physics Research Section A: Accelerators, Spectrometers, Detectors and Associated Equipment, 442*(1), 26–37.
57. Roch, A. L., et al. (2020). Comparison of X-ray and electron radiation effects on dark current non-uniformity and fluctuations in CMOS image sensors. *IEEE Transactions on Nuclear Science, 67*(1), 268–277.
58. Badea, C., et al. (2022). Co-clinical photon counting CT research for multi-contrast imaging. In *Seventh international conference on image formation in X-ray computed tomography (ICIFXCT 2022)*. Vol. 12304. SPIE.
59. Schroeder, C., et al. (2004). Lag measurement in an active matrix flat-panel imager. *Medical Physics, 31*(5), 1203–1209.
60. Oppelt, A. (2006). *Imaging systems for medical diagnostics: Fundamentals, technical solutions and applications for systems applying ionizing radiation, nuclear magnetic resonance and ultrasound*. Wiley.
61. Cammarata, M., et al. (2009). Chopper system for time resolved experiments with synchrotron radiation. *Review of Scientific Instruments, 80*(1), 015101.
62. Förster, D. F., et al. (2015). Phase-locked MHz pulse selector for X-ray sources. *Optics Letters, 40*(10), 2265–2268.
63. Zefreh, K. Z., Welford, F. M., & Sijbers, J. (2016). Investigation on the effect of exposure time on scintillator afterglow for ultra-fast tomography acquisition. *Journal of Instrumentation, 11*(12), C12014.

Index

W. Nie, K. (Kris) Iniewski (eds.), *Metal-Halide Perovskite Semiconductors*,
https://doi.org/10.1007/978-3-031-26892-2